NASA SP-252

THE ENTRY PLASMA SHEATH AND ITS EFFECTS ON SPACE VEHICLE ELECTROMAGNETIC SYSTEMS

VOLUME I

A symposium held at
LANGLEY RESEARCH CENTER
Hampton, Virginia
October 13–15, 1970

NATIONAL AERONAUTICS AND SPACE ADMINISTRATION

NASA SP-252

THE ENTRY PLASMA SHEATH AND ITS EFFECTS ON SPACE VEHICLE ELECTROMAGNETIC SYSTEMS VOLUME I

Fourth Plasma Sheath Symposium
held at
Langley Research Center
Hampton, Virginia
October 13–15, 1970

Prepared by Langley Research Center

Scientific and Technical Information Office 1971
NATIONAL AERONAUTICS AND SPACE ADMINISTRATION
Washington, D.C.

For sale by the National Technical Information Service, Springfield, Virginia 22151 — Price $3.00

PREFACE

This symposium is the fourth in a series on the plasma sheath. The first three were held in Boston, Massachusetts, and were sponsored by the Air Force Cambridge Research Laboratories.

The papers included in the symposium cover theoretical and experimental results of research and flight tests of many different specific aspects of the general problem of plasma sheath degradation of reentry vehicle electromagnetic systems. Only the newer advances and more recent developments in the field are included in the Fourth Plasma Sheath Symposium, with no particular attempt being made to review the general background and history of the problem or to cover those aspects discussed in the previous symposia. Flight data from both NASA and DOD programs are included.

The symposium proceedings are published in three NASA special publications, which include the unclassified (present volume), confidential (NASA SP-253), and secret (NASA SP-254) material. Information concerning access to the classified volumes is given in CSTAR (Classified Scientific and Technical Aerospace Reports - an NASA semimonthly abstract journal).

The responsibility for the technical content of each paper lies with the author. The Langley staff was responsible for the organization and assembly of the proceedings.

Finally, we would like to express appreciation to the following individuals who participated in the planning of the symposium program. These include: W. C. Taylor and T. Morita of Stanford Research Institute (SRI), M. G. Dunn of Cornell Aeronautical Laboratory, Inc., R. L. Fante of AVCO Systems Division, W. Rotman of Air Force Cambridge Research Laboratories, and J. S. Evans and C. J. Schexnayder of Langley Research Center.

Paul W. Huber, Chairman
Norman D. Akey, Vice-Chairman
W. F. Croswell, Technical Program Chairman
C. T. Swift, Publications Chairman

CONTENTS

ALLEVIANTS

M. G. Dunn, Chairman

A BRIEF HISTORY OF THE LANGLEY REENTRY COMMUNICATIONS PROGRAM

By C. H. Nelson
NASA Langley Research Center

The keynote of this Fourth Plasma Sheath Symposium is that the technology concerning reentry communications has finally reached a reasonable state of maturity. Results of experiments conducted both in flight and in the laboratory are beginning to agree quite well with theoretical predictions. Consequently, excellent techniques and tools are now available for spacecraft with velocities equivalent to earth orbital entry. These achievements represent about a decade of accomplishment.

It was, in fact, about 10 years ago that the Langley Research Center became heavily engaged in the development of multiple-stage vehicles which achieved the velocities required to support the growing need for aerodynamic data at Mach numbers corresponding to orbital entry. Flight tests were needed to verify research work concerning aerodynamic configurations, stability and control, heat protection systems, etc., being carried out in various ground test facilities. As the test velocities increased, the payload data systems became degraded because of the radio-frequency interference caused by the plasma sheath. Also, during this same early period the Langley Research Center was developing the Scout solid-propellant boost vehicle and frequently data loss due to severe rocket-exhaust attenuation was experienced at high altitudes.

It became vitally important to the planning and conduct of future flight programs in the ionizing region that methods be found to eliminate this signal interference. Other typical programs of national concern at that time included the planned Dyna-Soar test flights, manned spacecraft return from earth orbit, planetary atmosphere probes, and Department of Defense ballistic-missile and anti-ballistic-missile development. Similar communications problems were being encountered in these programs.

A Langley data transmission panel was formed to investigate the problem and provide means for its practical solution. After surveying the situation, the data panel recommended a broad research program which was called project RAM (Radio Attenuation Measurements). The goals of RAM covered (1) flight verification of attenuation theory and ground test data, (2) study of the ionization effects on various antenna designs, (3) development of methods for measuring the profiles of the flow-field parameters, such as ion density, and (4) development of techniques for eliminating data loss involving the use of higher signal frequencies, aerodynamic shaping of payloads, optimization of material addition, and other approaches such as magnetic fields near the antenna.

Subsequently, the project mounted eight flight experiments and numerous ground tests in a wide range of facilities. The first four flights were made at entry velocities of 18 000 feet per second for the purpose of investigating

flow-field ionization resulting from payloads with nose radii from 1 inch to 4 inches and carrying out initial experiments concerning magnetic windows, water injection, and plasma diagnostics.

In March 1965, a water injection experiment was carried out on Gemini 3, which reentered at 25 000 feet per second, to prove the validity of the technique on large blunt bodies.

The three flight experiments in the RAM C series were conducted about a year apart with 6-inch-nose-radius payloads at entry velocities of about 25 000 feet per second. The third and final RAM C payload was launched September 30, 1970, and carried several important experiments including Langmuir probes for flow-field measurements, multifrequency transmitters from VHF to X-band, diagnostic S-band antenna, two different material injection experiments, and many other onboard measuring devices as well as an extensive array of ground data-receiving apparatus. All spacecraft experiments returned important data, the details of which are covered in this publication.

OVERVIEW OF THE AF AVIONICS LABORATORY REENTRY ELECTROMAGNETICS PROGRAM

By Robert Rawhouser
AF Avionics Laboratory

SUMMARY

The Air Force Avionics Laboratory has been engaged in studies of wave propagation through plasma since 1959. Interest was initially generated by the Dynasoar program, which was to be a manned space vehicle. AFAL ran some model tests in the Hotshot tunnels of the Arnold Engineering Development Center. More significant than the results was the realization of the magnitude of the problem. A program was inaugurated to study the problem from numerous approaches. Many theoretical problems have been solved and reports issued. Shock-tube and tunnel experiments on various configurations have yielded results. Reflectometers to yield antenna impedance measurements in the presence of plasma have been installed on some early Atlas missiles, ASSET vehicles, and Trailblazer II vehicles. Four Trailblazers have been instrumented and flown to obtain data on wave propagation through plasma and plasma noise. Considerable effort has been placed on methods of alleviating the effects of plasma. Methods chosen for the AFAL program have been the aerodynamic gas spike, a strong steady magnetic field, and the modulated electron beam. The latter two have been difficult to instrument and are still under development. In addition, the laboratory has sponsored two Athena missile flights to investigate plasma influence on electromagnetic countermeasures.

INTRODUCTION

Communication with hypersonic vehicles during reentry into the earth's atmosphere is severely hampered by the plasma sheath surrounding the vehicles. The sheath is formed by collision of the vehicle with the ambient air especially at surfaces perpendicular to the direction of motion. At these stagnation points the air is stopped with respect to the vehicle, and kinetic energy of the vehicle is transferred to the gas molecules. The resulting gas temperature is high enough to cause dissociation of the molecules, excitation of atoms, and ionization of molecules and atoms. The resulting plasma (ionized gas but macroscopically neutral) flows around the vehicle from the stagnation points forming many different regions with different plasma states depending on the vehicle shape and orientation. From the standpoint of radio wave propagation, the most important constituent of the plasma is the free electrons. The electrons react to the electromagnetic field of a passing wave while the heavy ions are relatively immobile. The periodic vibrations of the electrons may be interrupted by collisions with the numerous neutral particles thereby extracting energy from the wave and converting it into the heat of the gas. The important parameters of the plasma are electron density, electron collision frequency (related to gas density and pressure), and electron and gas temperatures. In addition to the

plasma parameters, the frequency and polarization of the electromagnetic wave is important. For a given electron density, there is associated a plasma oscillation frequency, also called critical or cutoff frequency. If an external magnetic field is also present, the plasma has a gyrofrequency. The relation of the wave frequency to these frequencies and to the direction of propagation gives many possibilities of behavior. Figure 1 shows regions of plasma for a simple body of rotation.

EARLY DYNASOAR SUPPORT

Interest in the subject was initially generated in the Air Force in getting test data from intercontinental ballistic missiles and then accelerated by the Dynasoar project. The latter was to be a manned space vehicle which would have an appreciable blackout time. Very little data existed at the time, and the flow-field and plasma calculations were rather crude. In order to obtain data on the effects of plasma on electromagnetic waves, some experiments were run in the Hotshot tunnels at the Arnold Engineering Development Center. Both of the tunnels were of the blow-down type, wherein a chamber of pressurized gas is suddenly heated by an arc discharge, the gas bursts a diaphragm and flows over a model. Experiments were made at both S- and X-band frequencies. The equipment employed was essentially an interferometer. One path went through the plasma from an antenna in the model. The other path is direct from transmitter to receiver with an attenuator and phase shifter in the line. Sum and difference signals provide the necessary data for both attenuation and phase shift caused by the plasma. A number of runs were made in both the Hotshot I and Hotshot II tunnels. Perhaps the most significant result obtained was the documentation of the difficulties of simulation of the airborne case by laboratory facilities. The Hotshot II tunnel could accommodate relatively large models but produced an unexpected difficulty. It had magnetic storage for the gas chamber heating and discharge. The resulting circulating currents produced considerable interference in sensitive experimental instruments. Hotshot I with capacitive storage was easier to work with, but one had to be very careful of tunnel contamination from the arc discharge chamber. The reduced data agreed fairly well with simple theory of attenuation through plasma produced by gas flow over a simple model.

REFLECTOMETER FLIGHT MEASUREMENTS

The work in the Hotshot tunnels showed that one of the easiest ways of getting useful information on plasma about a hypersonic body would be by means of four-probe reflectometers on antenna feed lines in the vehicle. The four probes spaced three-eighths of a wavelength apart give all the voltages needed to calculate the complex impedance of the antenna and its changes as plasma builds up and decays. The four signals are easily combined into two voltages which must be transmitted to ground on telemetry channels, either on a carrier above the blackout frequency or delayed and replayed after blackout ends. The reflectometers, besides providing considerable data, have the advantage that they can be made quite small and add little weight to the payload.

The first use of the reflectometers was in 1960 and 1961 when they were installed on three Atlas missile flights on a noninterference basis. There was rather bad luck on these attempts and little reliable data. On the best effort the common missile experiment power supply changed drastically because of an equipment failure on another experiment. This necessitated a postflight calibration check on a similar reflectometer at the reduced voltages for which it was not designed. This allowed analysis of data but with little confidence.

Reflectometers were installed on four ASSET vehicles from 1963 to 1965, also on a noninterference basis. One of these was on an X-band coaxial feed line, and three were on the telemetry lines at 240 megahertz. Only one reflectometer was carried on any particular vehicle. Three of these flights were very successful, and reflectometer data were obtained, as well as the relative attenuation of the signal as received on the ground. The latter data could be referred to the vehicle position, attitude, velocity, and known antenna pattern. The two sets of data gave considerable information which compared in general but with some difference. This result is not unexpected in view of the difficulty of precision measurement in this type of work.

The antennas on the ASSET vehicle were located on the fins near the rear end. This position was deliberately chosen as having the least plasma and still being in a position to radiate to selected ground sites. This, of course, was contrary to our particular desires. As was expected, there was very little effect on the X-band transmissions. The VHF data were very interesting and complicated. The ASSET vehicle was the first glide reentry vehicle flown, all previous ones being bodies of revolution. The added complication of variations in three dimensions made the analysis difficult. The ASSET reentered the atmosphere at a velocity of 25 000 ft/sec and an angle of attack in the neighborhood of 40°, in contrast to very small angles of attack for nose cones. The result was very different flow fields from those previously encountered. Not only was there flow from forward to the rear but also around the edges and upward over the side. This part of the flow field was separated from the body. It was deduced from the reflectometer and attenuation data that a trough had been formed by the body and the plasma sheath and resulted effectively in a leaky waveguide (fig. 2). Some of the radiated power could have been conducted along this trough and radiated to the rear. There was not enough instrumentation around all the needed places to definitely detect everything that occurred. Nevertheless, the hypothesis of a leaky trough waveguide is quite reasonable and compatible with the data.

Very good reflectometer data were obtained in the Trailblazer flights, which were sponsored by the AF Avionics Laboratory. Four flights were flown in February 1966, October 1966, October 1967, and November 1968; the payload in each case was built and integrated with the boosters by the Ohio State Unviersity Research Foundation. The flights were conducted at NASA Wallops Station. In these flights the payload was totally ours so the design of the experiments was not affected by others and was limited only by the small size of the vehicle and, of course, safety factors. A "standard" nose cone was adopted consisting of a 12-inch-diameter hemisphere with an antenna ring around the "equator" of the nose section. This hemisphere is followed by a cone flared at 9° to the axis and extending to a 19-inch base. The total length of the hemisphere-cone

body is 28 inches. The weight vs reentry velocity tradeoff limits the total weight of this reentry body including the fourth-stage motor to 65 pounds in order to get 18 000 ft/sec reentry velocity.

The first three Trailblazers flown were instrumented with reflectometers along with other equipment to be discussed later. The third flight had a failure of the third-stage ignition; therefore the reentry velocity was too low for the experiment, and this flight will be ignored. In flight number one, reflectometer data were obtained at S-band and C-band. Samples of the data plotted on a Smith impedance chart are shown in figures 3 and 4. The points marked are in seconds after launch of the vehicle and can be related to altitude and velocity by radar data. The antennas were not well matched to free space to start, but the Smith chart shows wide excursions in impedance with the changing plasma conditions. Changes start around 270 000 feet altitude and continue until at 422 seconds the payload is down to 60 000 feet and the velocity is 4000 ft/sec. The plasma has disappeared and the antenna has returned to the initial conditions. The three lines in each graph show the antenna impedance for different attitudes of the payload. It was spinning at 13.75 rps and had an initial angle of attack of 10.5°. The resultant precession varied the impedance on both sides of the mean value for each revolution of the payload as the stagnation point described a circle around the center of the nosecap and hence moved nearer and farther from each antenna (fig. 5). The curves labeled A are at times when the stagnation point was closest to the antenna, curves C when they were farthest apart, and B the mean position. The impedance wandered back and forth between A and C every 0.04 sec. The complete zigzag path of the impedance with time would be too confusing to plot on one chart. At no time in the flight did the reflection become so large as to produce a serious loss of signal. In fact, with the antennas untuned as they were, the plasma sheath generally gave a better antenna match. Any signal loss in this case was only from absorption within the plasma.

PLASMA DIAGNOSIS FROM REFLECTOMETER DATA

With the trajectory, attitude, velocity, and shape of the vehicle known, much progress has been made by many workers in calculating the plasma sheath and then the attenuation and reflection of radio waves of known frequency from a known antenna. The results are then compared with the data obtained in flight. The inverse problem can be considered. Given the impedance data, what can be inferred of the plasma about the body? If a plasma model is chosen with n parameters, then n quantities must be measured which are not redundant. This amounts to a solution of n equations (not linear) in n unknowns. As part of the program the plasma model shown was postulated (fig. 6). In this model the electron density is represented by two Gaussian curves specified by the parameters α_1, α_2, α_3, and α_4. These parameters correspond physically to the fall-off of electron density toward the metal wall, the decay on the space side, the distance from the metal wall to the maximum of the sheath, and the maximum density. Since a measurement of impedance at a single frequency gives two parameters, the resistive and reactive components of the impedance, or alternately, the standing wave ratio and phase angle, at least two different measurements are required. This model assumes a given constant collision frequency.

More inputs are needed for a fuller model. Equations were formulated and a computer program written for solving the parameters. With these results the reflections can be computed and the process repeated until an error minimization criterion is achieved. This method has produced a reasonable fit of the plasma profile obtained from impedance data with the profile calculated from flight data. The main difference is in the tail-off of the curve out toward space, but since the calculated density there is small, the effect on radio frequency propagation is negligible.

TRAILBLAZER REFLECTION DATA

Considerably more data have been obtained from Trailblazer flights. Numerous radars have tracked each shot and signal-level recordings are available. The first two vehicles launched contained two small corner reflectors opposite each other on the flank of the cone. Only at C-band did these reflectors give an appreciable radar echo modulation at twice the spin frequency (fig. 7). A lengthy analysis was required to separate the effect of the plasma sheath because of the continually changing aspect angle of the payload due to spin, precession, and descent. By digitizing and computerizing the radar data and the trajectory data and comparing with echo data of the payload taken on the ground, it was possible to obtain a measure of the plasma attenuation. The results were found to be compatible with other measurements made during the flights.

The corner reflectors were omitted on later shots. It was found that the spin effect showed up in other records, for example the reflectometers, and the corner reflectors were unnecessary. The second flight was instrumented primarily to monitor the rf noise produced by the plasma. This noise is of no importance during transmission from the vehicle since the signal level is high compared to the noise generated in the frequency band. However, during reception the desired signal is at a low level and the noise is effectively a nearby jammer over the receiver bandwidth. A radiometer was installed in the Trailblazer to measure the rf noise. It operated at 2250 MHz with 80-MHz bandwidth. Antennas were placed at the payload nose, in the shoulder antenna ring, and 5 inches back on the flank. The hemispherical nose was made of beryllium so that there were no ablation products affecting the two forward antennas. The antenna on the flank is in the midst of ablative material. The radiometer was time-shared between the three antennas, a matched load to the radiometer, and a noise source for automatic calibration. Data were sent to the ground on an X-band telemetry system.

PLASMA SHEATH NOISE

Noise is usually measured as an effective temperature which may or may not be the same as the temperature of the plasma. At the nose the noise temperature was found to be comparable to the stagnation temperature (fig. 8). The curve with time also followed the curve of the power reflection coefficient. On the side antennas the data showed the same variation with the spin rate as

the reflectometer had when the antenna faced the windward and leeward sides. The flank antenna which is farthest from the nose measured a decreased noise temperature, and the data do not correspond with reflectometer data. Ablation products could affect the plasma in this region.

Laboratory measurements connected with this project showed that plasma noise had essentially a "white" spectrum over the band from 400 MHz to 35 GHz. Water injection could reduce the noise by 6 to 8 decibels. A high-power transmitter can cause additional ionization and raise the noise level as monitored by a separate frequency.

AERODYNAMIC GAS SPIKE EXPERIMENT

Considerable effort on the project has been pointed toward a study of plasma alleviation techniques. Since other organizations studied material additions to plasma, that alleviation possibility we have not studied. We have concentrated on admittedly less promising techniques, namely the aerodynamic gas spike, the magnetic window, and electron-beam plasma modulation.

It is known that a sharp-nosed cone has a thin plasma sheath around it on reentry into the atmosphere. Furthermore, the electron density of the sheath is less than that of a blunt body. The problem for a spike is to keep it from eroding away and becoming blunt. One idea is to inject a gas into the region before an antenna to be protected and have a nozzle to make the gas form a spike. This method was studied to determine the possibilities and the parameters needed, such as the kind of gas, pressure, flow velocity, mass of gas, and angle of attack all related to the ambient conditions.

Equipment to test the gas-spike concept was built and eventually tested on Trailblazer flight number 4. The gas used was helium stored at a pressure of 6500 psi (fig. 9). This gas was ejected at the nose of the reentry vehicle through a nozzle, which also doubled as a stub antenna at a frequency of 235 MHz (fig. 10). The primary action is the simulated pointed nose produced by the gas and the altered shock shape. Cooling of the plasma by the helium is also a consideration. The valve system of the gas supply was designed to adjust the helium flow according to pressure changes. In the actual experiment the gas was turned on at an altitude much too low to be effective. A spike was not formed, and hence, this was not a true test of the gas spike. The flight was productive, however, in obtaining data on propagation in the VHF region. Besides the transmission, the antenna was time-shared with a reflectometer and a radiometer. Measurable plasma was observed for about 10 seconds during reentry, from an altitude of about 250 000 ft down to 60 000 ft. The maximum attenuation observed was about 18 decibels and at no time was there complete loss of signal until payload disintegration. Postflight calculations have shown that almost all the attenuation was due to the thermal boundary layer. The plasma in the boundary layer was considerably overdense at the frequency used. The fact that it did not produce a higher attenuation is due to the boundary layer being only a small fraction of a wavelength. This means that

despite the high attenuation rate, the total attenuation is not as great as it would be at a higher frequency. This performance has been mentioned many times as a means of communicating through the plasma sheath, but it has not been used in practice. The voltage reflection coefficient never rose above 0.53 except at the end of flight. This corresponds to a loss of transmitted power due to reflection of 1.5 dB. Thus, the principal loss mechanism was by absorption.

The radiometer had a 20-MHz bandwidth centered at 260 MHz. The frequency used was different from that of the transmitter to avoid mutual interference. However, there was considerable interference from other transmitters in the area because of the wide bandwidth and heavy use of the VHF band. Separating out what is considered external interference gave a noise temperature in the neighborhood of 3400° K. This temperature is somewhat lower than that of the thermal boundary layer where most of the noise originates. A noise measurement of this kind provides an integrated result favoring the portion of plasma closest to the wall, and there is a thermal gradient near the surface. Even so, the measured noise would be sufficient to cause an additional degradation of 15 to 20 dB in the signal-to-noise ratio in receiving.

Study indicates a gas-spike system will be effective over only a limited range of operating conditions. The angle of attack must be below 5°, and the asymmetrical flow observed during flight makes this figure probably too high. The spike length must be comparable to the nose radius for a significant effect on the shock shape.

MAGNETIC WINDOW

The magnetic-window technique is well known from theory and some laboratory experiments. An external constant magnetic field converts a plasma to an anisotropic medium with different propagation constants in different directions. There is a gyromagnetic frequency defined which enters the equations as well as the plasma and signal frequencies. By using right-handed circular polarization in the direction of the external field, a frequency well below the plasma frequency can be propagated. A rather strong magnetic field, in the range of 13 000 gauss, is required for a signal frequency in S-band and a plasma frequency near X-band. Obtaining such a magnetic field requires either a large and heavy power supply or a superconducting coil. We tried to get a flyable package by means of the superconducting techniques. The appearance of superconducting alloys such as niobium-tin makes the possibility feasible, but of course, it still requires very cold temperatures, in the neighborhood of liquid helium, i.e., near 4° K. The idea is to get the coil superconducting and the magnet energized on the ground. The power supply can be removed, and the current in the coil will circulate as long as it is kept in the superconducting state. This requires a flyable dewar to prevent heating during the time of launch and flight.

The first flyable cryogenic dewar did not meet the required specifications. Recently a second attempt has been made in light of more recent cryogenic techniques, and the contractor has designed it for holding the coil in the

superconducting phase for 12 hours (fig. 11). This dewar is ready to be tested along with all the environmental specifications needed for missile hardware. Despite much effort and plans, we have never been able to flight-test the magnetic-window device.

PLASMA MODULATION TECHNIQUE

The other alleviation technique we have pursued actively is modulation of the plasma sheath by an electron beam. This idea has some elements of the idea of a traveling wave tube. The electron beam is passed through a microwave cavity which modulates it into bunches. This bunched beam passes through the plasma and causes oscillations in it. At a discontinuity, such as a shock edge, the modulated plasma causes radiation into space. This transition radiation has been studied by several people. A T-shaped plasma facility was used to study the parameters with an electron beam crossing the plasma column. The phenomenon of attenuation of waves by a plasma has been displaced by problems of beam focus and transition radiation. There appears to be a region of ambient conditions where the beam modulation scheme would be useful. The practical equipment being built for a flight test ran into the trouble of arc-over at the cathode as gas from the external environment flows back into the electron gun. This can be controlled by a cryogenic pump but has added to the problem of beam focus. A small aperture is needed to prevent gas leakage back to the gun, whereas the electron beam tends to spread over the additional distance needed with the cryogenic pump. A parametric study is being made and a compromise design is well on the way. This design will have to be extensively tested in the laboratory before any flight test is contemplated.

A review of proposed alleviation techniques shows that each of them is accompanied by grave problems. Any one adds weight to the payload package either in equipment or expendable material. This must be carefully considered in view of the mission and achievement of only partial effectiveness. The selection of an alleviation system can be made only with a specific system in mind. Even with a positive answer as to the effectiveness of the technique, considerable development is still necessary to implement the system.

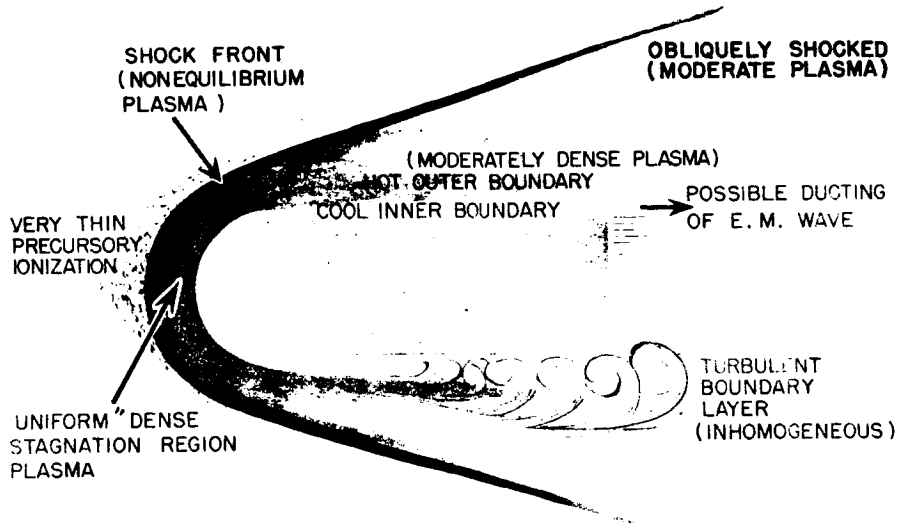

Figure 1.- Sketch of the principal plasma regions existing around a hypersonic vehicle.

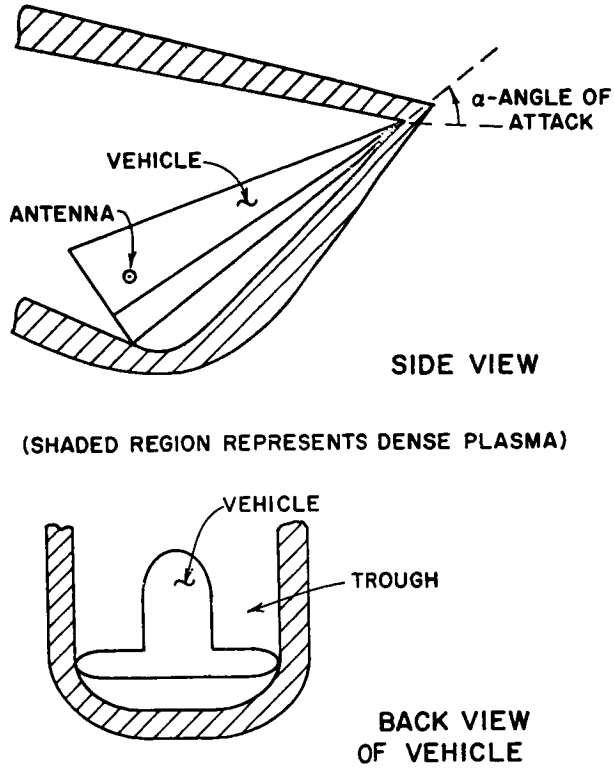

Figure 2.- Geometry of reentry problem.

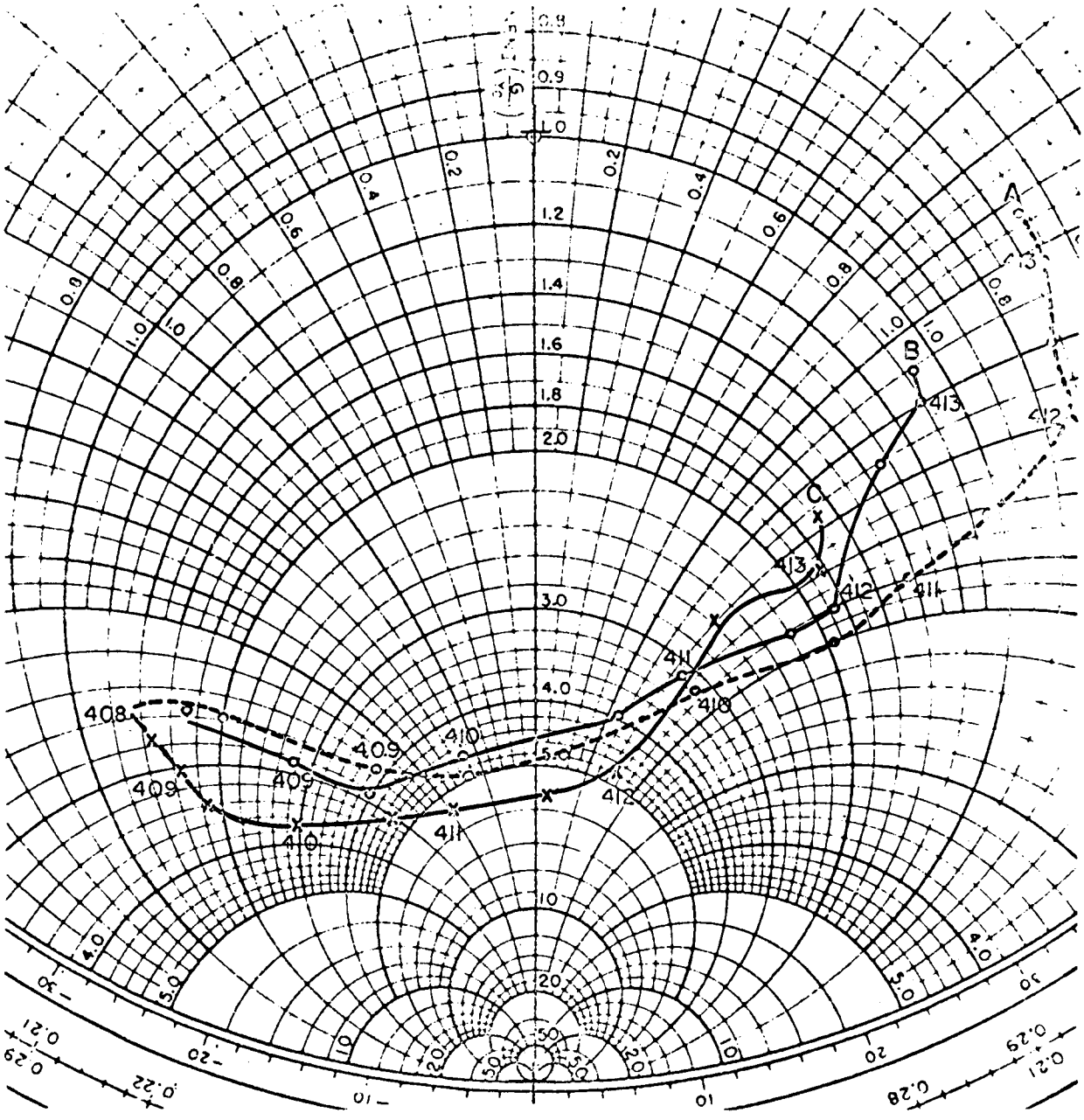

Figure 3.- S-band antenna impedance during plasma buildup.

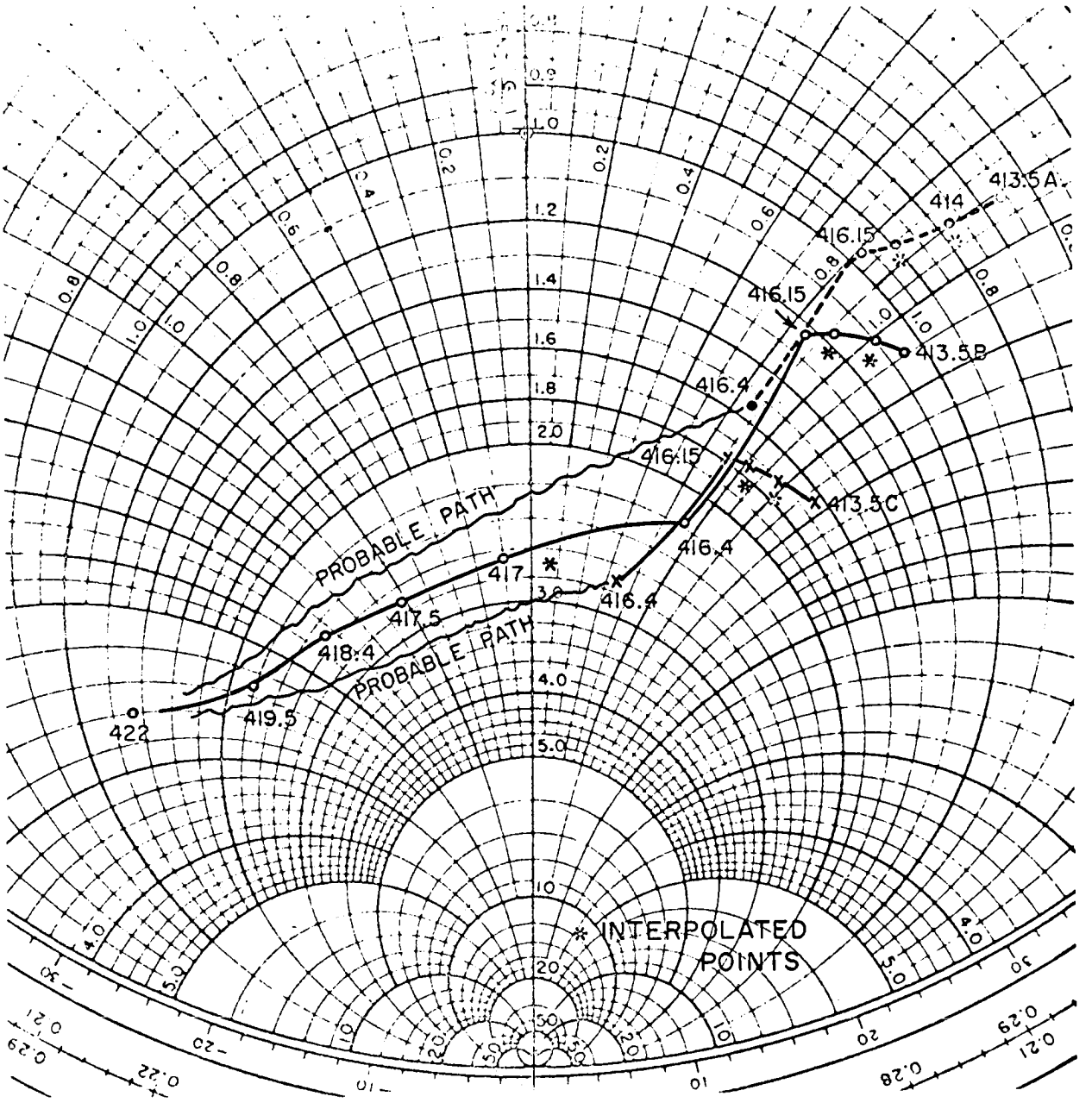

Figure 4.- S-band antenna impedance during plasma decay.

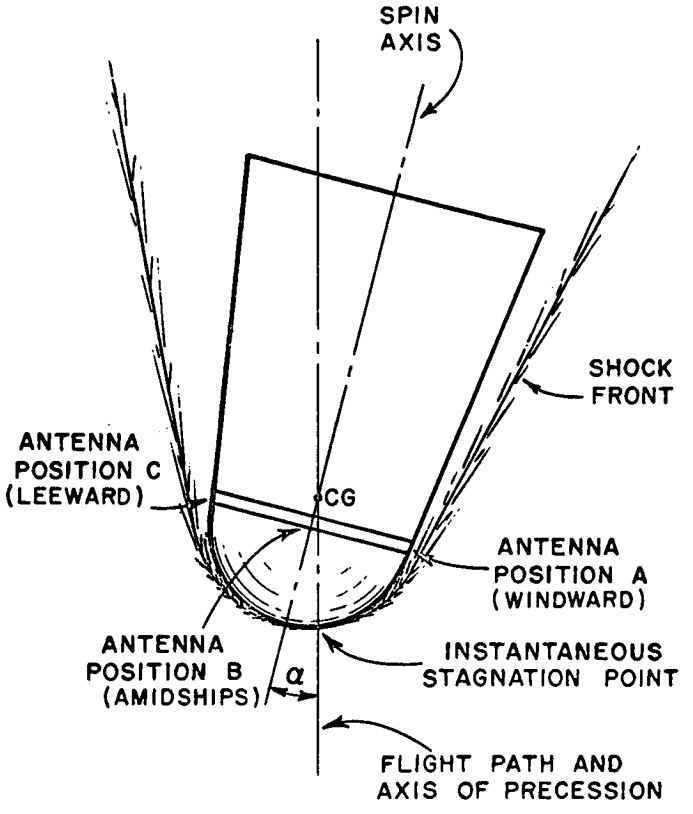

Figure 5.- Relative antenna positions during reentry.

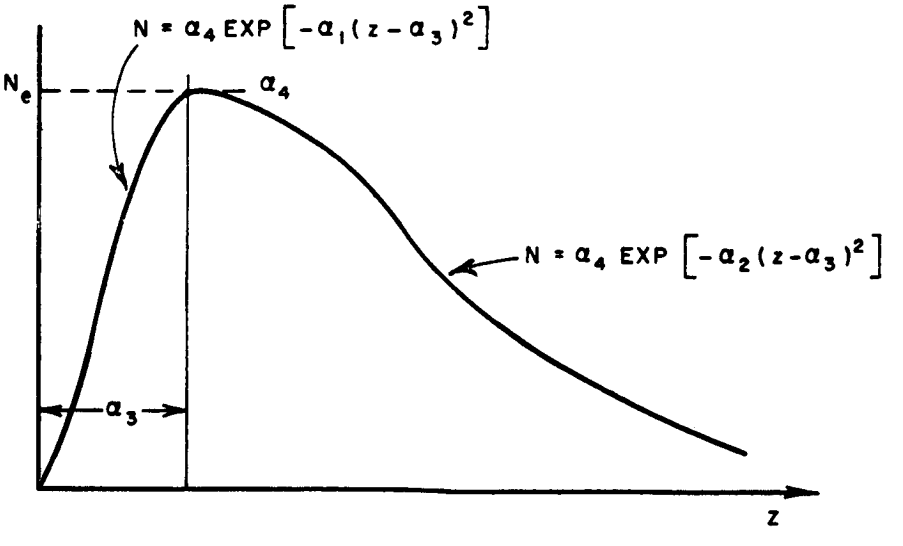

Figure 6.- A parameterized model of the electron density.

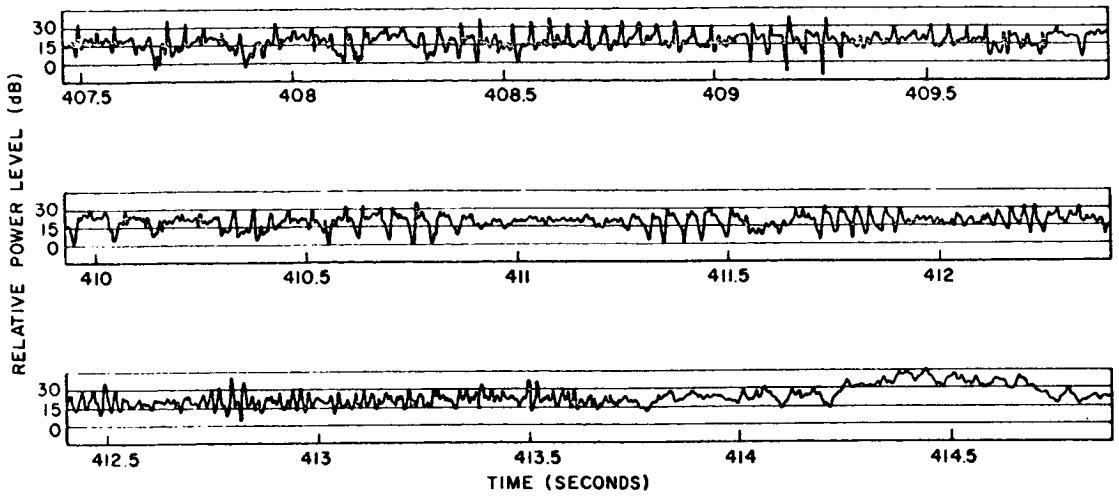

Figure 7.- C-band radar fast AGC record.

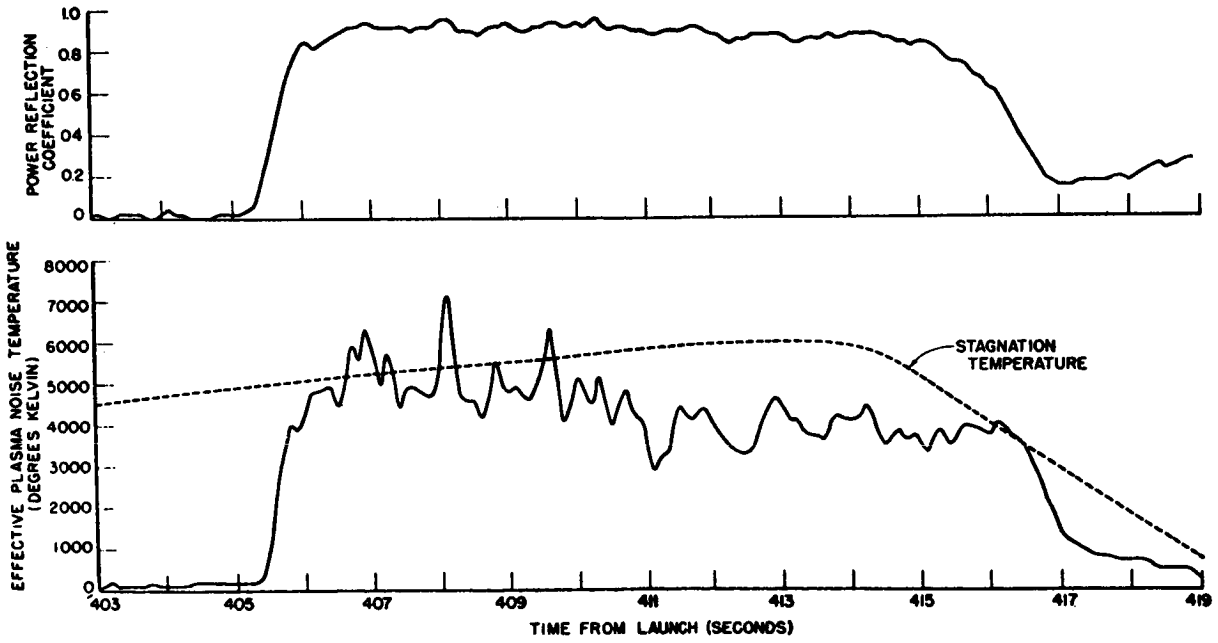

Figure 8.- Nose antenna parameters during reentry.

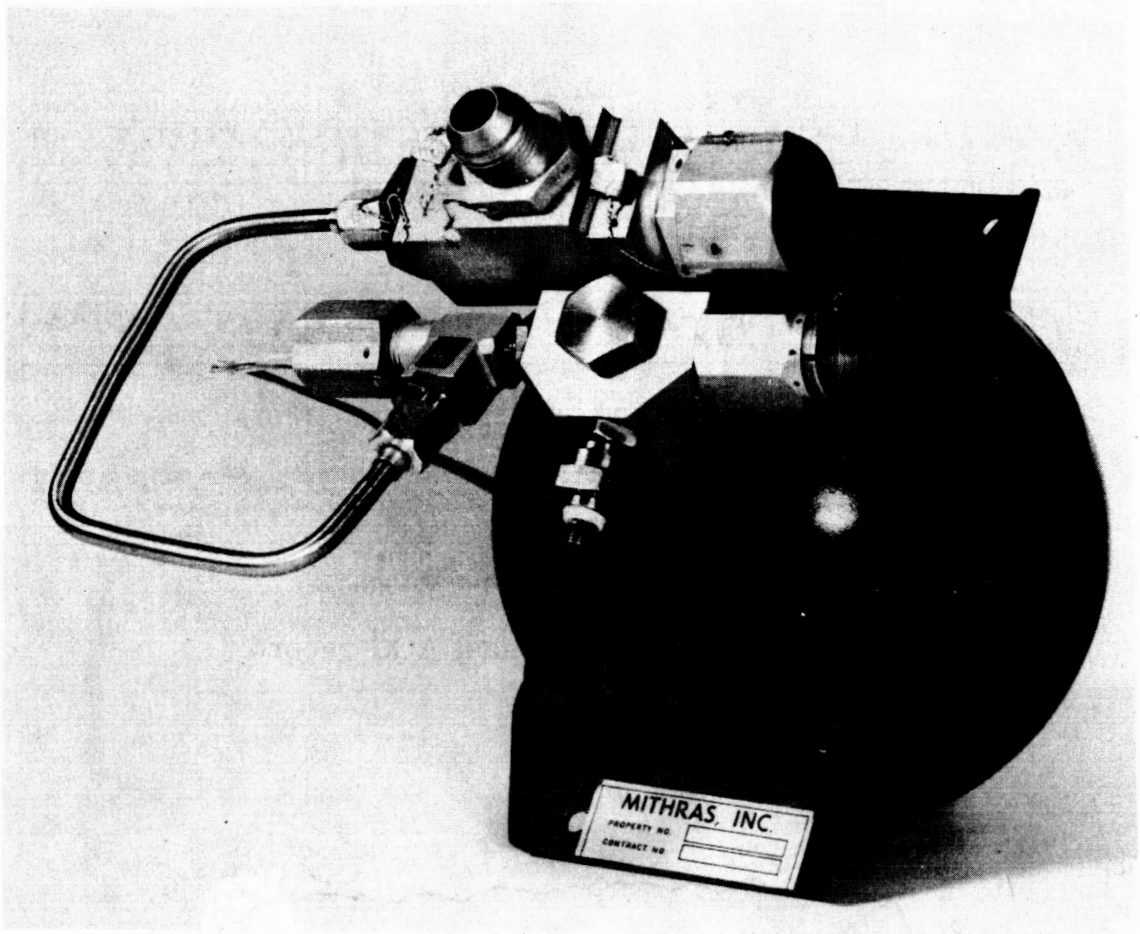

Figure 9.- Aerospike gas storage and supply system.

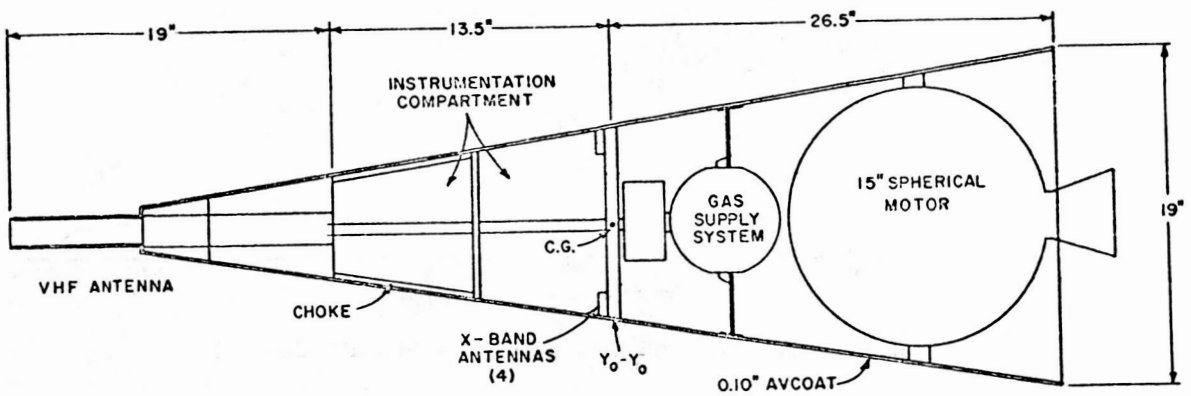

Figure 10.- Outline drawing of the Trailblazer payload.

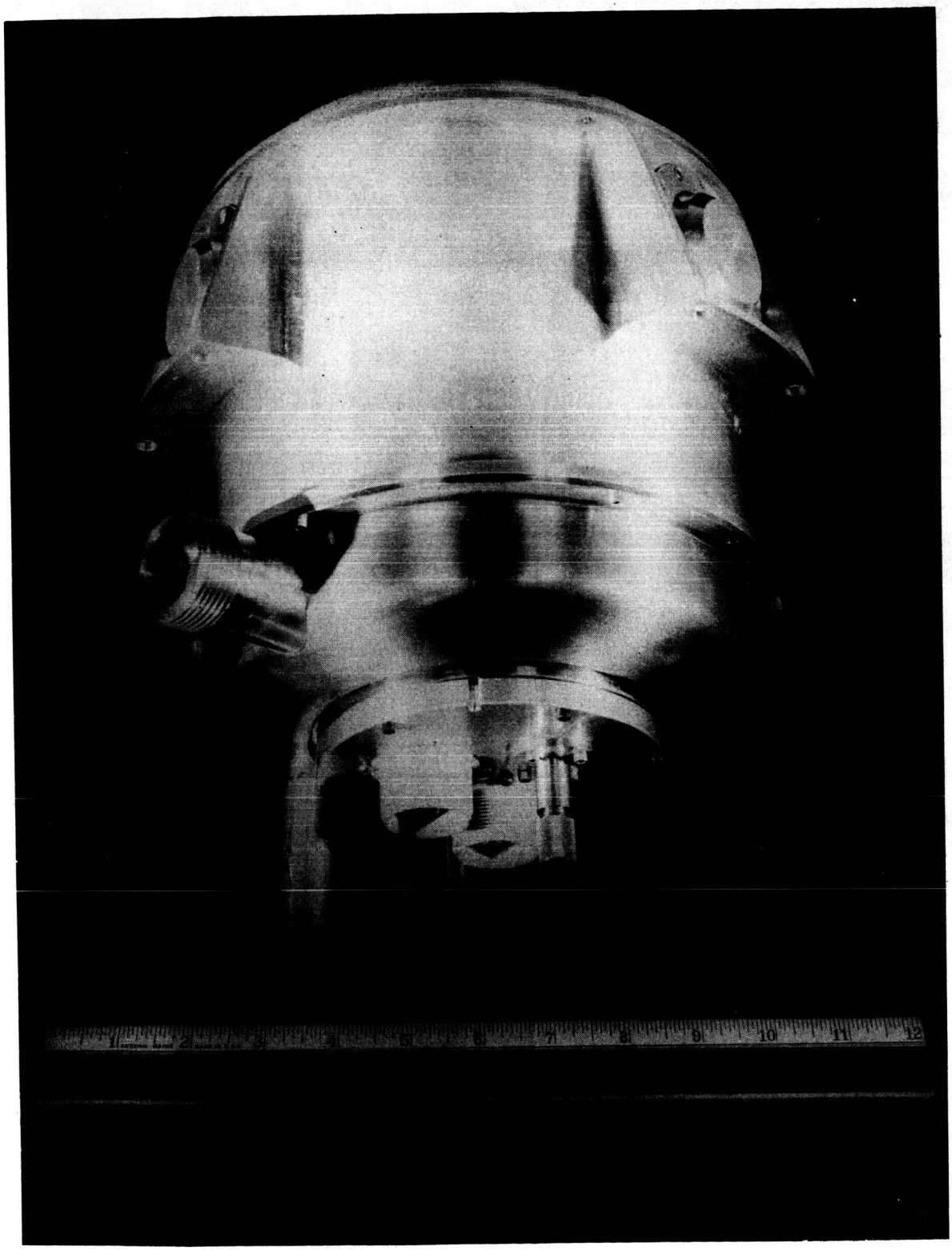

Figure 11.- Flyable dewar.

OVERVIEW OF RAM REENTRY MEASUREMENTS PROGRAM

By Norman D. Akey
NASA Langley Research Center

INTRODUCTION

The NASA Langley Research Center Project RAM (Radio Attenuation Measurements) began studies in the area of reentry communications problems about 1960. Since that time, project RAM has theoretically studied velocity regimes up to 25 000 ft/sec and has provided carefully controlled ground and flight measurements for development and improvement of these theoretical concepts. Several methods for maintaining communications during the blackout period have been demonstrated. Related phenomena such as rocket exhaust attenuation have also been studied.

RAM FLIGHT TESTS

Table I gives a summary of the seven successful RAM flights. The first four flights (RAM A and B series) were conducted at 18 000 ft/sec and the last three (RAM C series) at 25 000 ft/sec. These flights have (1) measured attenuation for frequencies ranging from 30 MHz to 10 GHz, (2) shown effects of antenna location and design, (3) studied the effect of vehicle scaling for 2-inch (RAM A series), 8-inch (RAM B series), and 12-inch (RAM C series) nose diameters, (4) made plasma diagnostic measurements of the flow field at discrete spacecraft locations, and (5) shown the relative merits of material addition, magnetic fields, aerodynamic shaping, and higher-than-normal signal frequencies as methods of overcoming the blackout problem. Results of the RAM A and B series flights have been reported in references 1 to 18 and the RAM C results are presented in references 19 to 23.

SUPPORTING RESEARCH AND TECHNOLOGY

In addition, a strong RAM supporting research and technology program (SRT) has been maintained in conjunction with the RAM flight experiments. This program has involved both theoretical studies and extensive testing in ground research facilities. Figure 1 comprises a summary chart of the entire RAM program, tying in the SRT work with the flights in a historical progression. It is, for the most part, self-explanatory. There are, however, some areas of fairly recent unreported work which are of current interest to other reentry communication programs and merit further discussion now. Test results are not given, as they are too detailed to report in this paper, but the investigators and the types of tests are given for reference. The details of SRT work done to date are given in references 8, and 24 to 78.

The injection slot size requirements tests noted in figure 1 were conducted by T. G. Campbell of the Langley Research Center. A dielectric shroud was placed over the RAM C-III payload and attenuated antenna patterns measurements were taken with various slot sizes and configurations cut out of the shroud. It was determined from these measurements what slot width and length, or what size "window," it was necessary to produce using material injection over a given antenna in order to achieve signal recovery. These test results are being correlated with the RAM C-III flight results.

Extensive tests to determine penetration and spreading of water and electrophilic liquids injected into the flow field of a hypersonic body were conducted by W. L. Weaver of Langley. The tests were performed at both the Langley and the Ames Research Centers using flat-plate models and a 3/8-scale model of the RAM C-III payload. The studies included effects of injection orifice sizes, angles of injection, arrangements of multiple orifices, shielding of one jet by another, injection pressure, free-stream dynamic pressure, mixing of side-by-side jets, and the slot width cut by a given configuration.

An analysis of the RAM C series X-band signal strength records to determine plasma effects on antenna patterns has been conducted by C. L. Britt, of Research Triangle Institute, under contract NAS1-8837.

It was observed in ground tests that electrophilic liquids injected from a model into a hot-flow facility appeared to have greater spreading characteristics than did water. This apparent diffusion effect is being studied for correlation with the RAM C-III flight data. L. C. Schroeder of Langley is pursuing this effort both in-house and by contract as part of the RAM C-III data analysis.

A continuing effort is underway to verify calibrations of the RAM C series diagnostic devices for specific flight regimes. This work is both in-house and contractual and involves C. T. Swift, W. L. Jones, Jr., W. L. Grantham, and W. F. Croswell, all of Langley; M. G. Dunn of Cornell Aeronautical Laboratories; and W. C. Taylor of Stanford Research Institute.

CONCLUDING REMARKS

Project RAM will, upon completion of the RAM C data analysis, have accomplished its goals set forth in 1960. Learning to understand the flow field in order to achieve better blackout predictions for specific NASA applications has taken us through a natural sequence of starting with the rather simple equilibrium and frozen flow calculations and sequentially adding in the effects of simplified nonequilibrium, finite-rate chemistry kinetics, boundary-layer displacement, ablation products, and high altitude ambipolar diffusion.

Project RAM has developed an understanding of the flow-field interference with RF propagation and has used this knowledge in the areas of optimizing antenna design and developing plasma diagnostic techniques.

Finally, extensive work in developing and testing blackout alleviation techniques has been done. These include aerodynamic shaping, the magnetic window, high frequency transmission, and material addition to the flow field.

There are no future flights planned in the RAM program. The knowledge which has been gained will be applied in providing definition of reentry communication problems during the mission design phase of future NASA programs. Such definition would probably include recommendations for antenna design and placement. Blackout alleviation techniques and systems will be considered and utilized as appropriate.

REFERENCES

1. Beckwith, Ivan E.; and Bushnell, Dennis M.: Effect of Intermittent Water Injection on Aerodynamic Heating of a Sphere-Cone at Flight Velocities to 18 000 Feet Per Second. NASA TM X-1128, 1965.

2. Cuddihy, W. F.; and Hughes, J. Kenrick: Simulated Reentry Tests of a Method for Reducing Radio Blackout by Material Addition to Ionized Flow Field. NASA TM X-988, 1964.

3. Cuddihy, William F.; Beckwith, Ivan E.; and Schroeder, Lyle C.: RAM B2 Flight Test of a Method for Reducing Radio Attenuation During Hypersonic Reentry. NASA TM X-902, 1963.

4. Cuddihy, William F.; Beckwith, Ivan E.; and Schroeder, Lyle C. (With appendix A by Ivan E. Beckwith, Dennis M. Bushnell, and James L. Hunt; appendix B by Ivan E. Beckwith and Sadie P. Livingston; and appendix C by Ivan E. Beckwith): Flight Test and Analysis of a Method for Reducing Radio Attenuation During Hypersonic Flight. NASA TM X-1331, 1967.

5. Grantham, William L.: Analysis of Plasma-Sheath Electron Density Measurements at Entry Velocities. NASA paper presented at Third Symposium on the Plasma Sheath (Boston, Mass.), Sept. 1965.

6. Grantham, William L.: Preliminary Analysis of Plasma-Sheath Electron Density Measurements at Entry Velocities. NASA TM X-1035, 1964.

7. McIver, Duncan E., Jr.: Study of the Effects of a Rocket Exhaust on Radio Frequency Signal Attenuation by the Use of a Recoverable Camera on the NASA Scout Vehicle. NASA TM X-888, 1963.

8. Anon.: Proceedings of the NASA Conference on Communicating Through Plasmas of Atmospheric Entry and Rocket Exhaust. NASA SP-52, 1964.

9. Raper, James L.; Keynton, Robert J.; and Woodbury, Gerard E.: Detailed Description and Flight Performance of the Ram B Vehicle. NASA TN D-2437, 1964.

10. Schroeder, Lyle C.: Gemini Reentry Communications Experiment. NASA paper presented at Third Symposium on the Plasma Sheath (Boston, Mass.), Sept. 1965.

11. Schroeder, Lyle C.; Sims, Theo E.; and Cuddihy, William F.: Experiment T-1, Reentry Communication on Gemini III. Manned Space Flight Experiments Symposium - Gemini Missions III and IV, NASA, Oct. 1965, pp. 81-103.

12. Schroeder, Lyle C.: Flight Results of Gemini Reentry Communications Experiment. Conference on Langley Research Related to Apollo Mission, NASA SP-101, 1965, pp. 205-216.

13. Sims, Theo E.; and Jones, Robert F.: Rocket Exhaust Effects on Radio Frequency Propagation From a Scout Vehicle and Signal Recovery During the Injection of Decomposed Hydrogen Peroxide. NASA TM X-529, 1961.

14. Sims, Theo E.; and Jones, Robert F.: Flight Measurements of VHF Signal Attenuation and Antenna Impedance for the RAM A1 Slender Probe at Velocities up to 17,800 Feet Per Second. NASA TM X-760, 1963.

15. Sims, Theo E.: Measurement of VHF Signal Attenuation and Antenna Impedance During the Ascending Flight of a Slender Probe at Velocities up to 17,800 Feet Per Second. NASA paper presented at Second Symposium on the Plasma Sheath (Boston, Mass.), Apr. 1962.

16. Schroeder, Lyle C.; and Russo, Francis P. (With appendix by Francis P. Russo and Aubrey E. Cross): Flight Investigation and Analysis of Alleviation of Communications Blackout by Water Injection During Gemini 3 Reentry. NASA TM X-1521, 1968.

17. Akey, Norman D.; Cross, Aubrey E. (With appendix A by Thomas G. Campbell; appendix B by Fred B. Beck; and appendix C by W. Linwood Jones, Jr.): Radio Blackout Alleviation and Plasma Diagnostic Results From a 25 000 Foot Per Second Blunt-Body Reentry. NASA TN D-5615, 1970.

18. Grantham, William L.: Flight Results of a 25 000-Foot-Per-Second Reentry Experiment Using Microwave Reflectometers to Measure Plasma Electron Density and Standoff Distance. NASA TN D-6062, 1970.

19. Schroeder, Lyle C.: Flight Measurements at 25 000 Feet Per Second of Blackout Alleviation by Water and Electrophilic Injection. The Entry Plasma Sheath and Its Effects on Space Vehicle Electromagnetic Systems - Vol. II, NASA SP-253, 1971, pp. 77-100.

20. Croswell, William F.; and Jones, W. Linwood, Jr.: Effects of Reentry Plasma on RAM C-I VHF Telemetry Antennas. The Entry Plasma Sheath and Its Effects on Space Vehicle Electromagnetic Systems - Vol. I, NASA SP-252, 1971, pp. 183-201.

21. Grantham, William L.: Reentry Plasma Measurements Using a Four-Frequency Reflectometer. The Entry Plasma Sheath and Its Effects on Space Vehicle Electromagnetic Systems - Vol. I, NASA SP-252, 1971, pp. 65-107.

22. Jones, W. Linwood, Jr.; and Cross, Aubrey E.: Electrostatic Probe Measurements of Plasma Surrounding Three 25 000 Foot Per Second Reentry Flight Experiments. The Entry Plasma Sheath and Its Effects on Space Vehicle Electromagnetic Systems - Vol. I, NASA SP-252, 1971, pp. 109-136.

23. Swift, C. T.; Beck, F. B.; Thomson, J.; and Castellow, S. L., Jr.: RAM C-III S-Band Diagnostic Experiment. The Entry Plasma Sheath and Its Effects on Space Vehicle Electromagnetic Systems - Vol. I, NASA SP-252, 1971, pp. 137-155.

24. Beckwith, Ivan E.; and Huffman, Jarrett K.: Injection and Distribution of Liquids in the Flow Fields of Blunt Shapes at Hypersonic Speeds. NASA TM X-989, 1964.

25. Beckwith, Ivan E.; and Bushnell, Dennis M.: Depletion of Free Electrons by Water Injection Into the Flow Fields of Hypersonic Vehicles. NASA paper presented at Third Symposium on the Plasma Sheath (Boston, Mass.), Sept. 1965.

26. Beckwith, Ivan E.; Bushnell, Dennis M.; and Huffman, Jarrett K.: Investigation of Water Injection on Models of Gemini Vehicle and Resulting Predictions for GT-3 Reentry Communications Experiment. NASA TM X-1200, 1966.

27. Beckwith, Ivan E.; Bushnell, Dennis M.; and Huffman, Jarrett K.: Fluid Mechanics Aspects of the Gemini Reentry Communications Experiment. Conference on Langley Research Related to Apollo Mission, NASA SP-101, 1965, pp. 217-237.

28. Brummer, E. A.: X-Band Telemetry Systems for Reentry Research. Pap. No. CP 63-663, Inst. Elec. Electron. Eng., Apr. 1963.

29. Bushnell, Dennis M.; and Gooderum, Paul B.: Atomization of Superheated Water Jets at Low Ambient Pressures. J. Spacecraft Rockets, vol. 5, no. 2, Feb. 1968, pp. 231-232.

30. Bushnell, Dennis M.; and Huffman, Jarrett K.: Forward Penetration of Liquid Water and Liquid Nitrogen Injected From an Orifice at the Stagnation Point of a Hemispherically Blunted Body in Hypersonic Flow. NASA TM X-1493, 1968.

31. Cockrell, C. R.: Higher-Order-Mode Effects on the Aperture Admittance of a Rectangular Waveguide Covered With Dielectric and Plasma Slabs. NASA TN D-4774, 1968.

32. Croswell, William F.: Antennas Under Ablation Material. Conference on Langley Research Related to Apollo Mission, NASA SP-101, 1965, pp. 239-265.

33. Croswell, William F.; Taylor, William C.; Swift, C. T.; and Cockrell, Capers R.: The Input Admittance of a Rectangular Waveguide-Fed Aperture Under an Inhomogeneous Plasma: Theory and Experiment. IEEE Trans. Antennas Propagation, vol. AP-16, no. 4, July 1968, pp. 475-487.

34. Cuddihy, W. F.; Beckwith, I. E.; and Schroeder, L. C.: A Solution to the Probelm of Communications Blackout of Hypersonic Reentry Vehicles. AMRAC Proceedings, Vol. IX, Pt. II, Inst. Sci. Technol., Univ. of Michigan, 1963, pp. 187-231. (Available from DDC as AD 344 601 (4613-59-X, pt. II).)

35. Dow, Marvin B.; Pittman, Claud M.; and Croswell, William F.: Thermal Performance and Radio-Frequency Transmissivity of Several Ablation Materials. NASA TN D-1896, 1964.

36. Evans, John S.: Reduction of Free Electron Concentration in a Reentry Plasma by Injection of Liquid. Vol. III of Proceedings of the Third Symposium on the Plasma Sheath - Plasma Electromagnetics of Hypersonic Flight, W. Rotman, H. Moore, R. Papa, and J. Lennon, eds., AFCRL-67-0280 (Vol. III), U.S. Air Force, May 1967, pp. 343-361.

37. Evans, John S.; and Schexnayder, Charles J., Jr.: Analysis of Theoretical and Experimental Electron Concentrations for RAM B3 Flight. NASA TM X-1412, 1967.

38. Evans, John S.; and Huber, Paul W.: Calculated Radio Attenuation Due to Plasma Sheath on Hypersonic Blunt-Nosed Cone. NASA TN D-2043, 1963.

39. Evans, John S.: Charge Recombination on Water Droplets in a Plasma. NASA TM X-1186, 1965.

40. Falanga, Ralph A.; Hinson, William F.; and Crawford, Davis H.: Exploratory Tests of the Effects of Jet Plumes on the Flow Over Cone-Cylinder-Flare Bodies. NASA TN D-1000, 1962.

41. Gilreath, Melvin C.; Croswell, William F.; and Castellow, Stark L., Jr.: Radiofrequency Transmission Characteristics of Several Ablation Materials. NASA TN D-4879, 1968.

42. Gooderum, Paul; Bushnell, Dennis; and Huffman, Jarrett: Mean Droplet Size for Cross-Stream Water Injection Into a Mach 8 Air Flow. J. Spacecraft Rockets, vol. 4, no. 4, Apr. 1967, pp. 534-536.

43. Harrington, R. F.; Brummer, E. A.; and Southall, W. A.: A 3-Pound, 1,000-Watt X-Band Reentry Telemetry System. New Links to New Worlds, PTGSET Record, IEEE, Oct. 1963, paper 1.1.

44. Hinson, William F.; and Falanga, Ralph A.: Effect of Jet Pluming on the Static Stability of Cone-Cylinder-Flare Configurations at a Mach Number of 9.65. NASA TN D-1352, 1962.

45. Huber, Paul W.; and Sims, Theo E.: The Entry-Communications Problem. Astronaut. Aeronaut., vol. 2, no. 10, Oct. 1964, pp. 30-40.

46. Huber, Paul W.: Hypersonic Shock-Heated Flow Parameters for Velocities to 46,000 Feet Per Second and Altitudes to 323,000 Feet. NASA TR R-163, 1963.

47. Huber, Paul W.: Considerations of the Communications Loss During Planetary Atmospheric Entry. Guidance, Control, and Communications, NASA TM X-50120, 1963, pp. 35-49.

48. Huber, Paul W.; and Sims, Theo E.: Research Approaches to the Problem of Reentry Communications Blackout. Vol. II of Proceedings of the Third Symposium on the Plasma Sheath - Plasma Electromagnetics of Hypersonic Flight, W. Rotman, H. Moore, R. Papa, and J. Lennon, eds., AFCRL-67-0280 (Vol. II), U.S. Air Force, May 1967, pp. 1-33.

49. Huber, Paul W.: Research Approach to Reentry Communications Blackout. Conference on Langley Research Related to Apollo Mission, NASA SP-101, 1965, pp. 189-203.

50. Huber, Paul W.; and Nelson, Clifford H.: Plasma Frequency and Radio Attenuation. Proceedings of the NASA-University Conference on the Science and Technology of Space Exploration, Vol. 2, NASA SP-11, 1962, pp. 347-360. (Also available as NASA SP-25.)

51. Huber, Paul W.; and Evans, John S.: Theoretical Shock-Layer Plasma Flow Properties for the Slender Probe and Comparison With the Flight Results. NASA paper presented at Second Symposium on the Plasma Sheath (Boston, Mass.), April 1962.

52. Huber, Paul W.: Deduction of Reentry Plasma Properties About Manned Orbital Spacecraft From Radio Signal Attenuation Data. NASA TN D-4118, 1967.

53. Huber, Paul W.: Relation Between Reentry Plasma Knowledge and Flight Data. NASA paper presented at Conference on Applications of Plasma Studies to Reentry Vehicle Communications (Wright-Patterson AFB), Oct. 1967. (Available as NASA TM X-60771.)

54. Leonard, William F.: Determination of Plasma Temperature and Electron Density Distributions Using Millimeter Waves. NASA TN D-2892, 1965.

55. Levine, Jack: Performance and Some Design Aspects of the Four-Stage Solid-Propellant Rocket Vehicle Used in the RAM A1 Flight Test. NASA TN D-1611, 1963.

56. McIver, Duncan E., Jr.; Jones, W. Linwood; and Cuddihy, William F.: Effects of External Material Injection on Radio-Signal Transmission Through a Rocket Exhaust. NASA TM X-1049, 1965.

57. McIver, Duncan E., Jr.: Radio-Frequency Signal Attenuation by Plasmas of Rocket Exhaust Gases. A Compilation of Recent Research Related to the Apollo Mission. NASA TM X-890, 1963, pp. 135-144.

58. Russo, Anthony J.: Estimates of Attenuation and Reflection of Telemetering Signals by Ionized Flow Fields Surrounding Typical Reentry Bodies. NASA TN D-1778, 1963.

59. Russo, F. P.; and Hughes, J. K.: Measurements of the Effects of Static Magnetic Fields on VHF Transmission in Ionized Flow Fields. NASA TM X-907, 1964.

60. Sims, Theo E.: Reentry Communications Research at Langley Research Center. IEEE Int. Conv. Record, vol. 13, pt. 4, 1965, pp. 99-104.

61. Sims, Theo E.: Communication Through Reentry Plasma. Conference Record - 1966 Winter Convention on Aerospace & Electronic Systems, Vol. I, IEEE, c.1966, pp. IB-21 - IB-28.

62. Sims, T. E.; and Grantham, W. L.: Reentry Plasma Studies. Proceedings of the Conference on the Applications of Plasma Studies to Reentry Vehicle Communications, Vol. II, Avionics Lab., U.S. Air Force, 1967.

63. Swift, Calvin T.: Radiation Patterns of a Slotted-Cylinder Antenna in the Presence of an Inhomogeneous Lossy Plasma. IEEE Trans. Antennas Propagation, vol. AP-12, no. 6, Nov. 1964, pp. 728-738.

64. Swift, C. T.; and Knop, C. M.: Equatorial Patterns of an Axially-Slotted Cylinder Coated With a Critically Dense Plasma. IEEE Trans. Antennas Propagation, vol. AP-12, no. 4, July 1964, pp. 498-502.

65. Swift, C. T.: A Reciprocity Theorem for the Interaction of Electromagnetic Plane Waves With a One-Dimensional Inhomogeneous Slab. Proc. IEEE (Correspondence), vol. 51, no. 9, Sept. 1963, pp. 1268-1269.

66. Knop, C. M.; Swift, C. T.; and Hodara, H.: Radiation Patterns and Admittance of an Axial Slot on a Plasma Covered Cylinder. Vol. I of Proceedings of the Third Symposium on the Plasma Sheath - Plasma Electromagnetics of Hypersonic Flight, W. Rotman, H. Moore, R. Papa, and J. Lennon, eds., AFCRL-67-0280 (Vol. I), U.S. Air Force, May 1967, pp. 41-116.

67. Swift, C. T.; and Hodara, H.: Effects of the Plasma Sheath on Antenna Performance. Presented at the AGARD/IRC Meeting on "Radio Wave Propagation Factors in Space Communications" (Rome, Italy), Sept. 1965.

68. Swift, Calvin T.: Radiation From Slotted-Cylinder Antennas in a Reentry Plasma Environment. NASA TN D-2187, 1964.

69. Swift, Calvin T.; and Evans, John S.: Generalized Treatment of Plane Electromagnetic Waves Passing Through an Isotropic Inhomogeneous Plasma Slab at Arbitrary Angles of Incidence. NASA TR-172, 1963.

70. Swift, Calvin T.: Input Admittance of a Coaxial Transmission Line Opening Onto a Flat, Dielectric-Covered Ground Plane. NASA TN D-4158, 1967.

71. Swift, Calvin T.: Input Admittance of a Rectangular Waveguide-Fed Aperture Antenna Radiating Into an Inhomogeneous Lossy Dielectric Slab. NASA TN D-4197, 1967.

72. Swift, Calvin T.; and Hatcher, Douglas M.: The Input Admittance of a Rectangular Aperture Antenna Loaded With a Dielectric Plug. NASA TN D-4430, 1968.

73. Swift, C. T.; Croswell, W. F.; and Evans, J. S.: Diagnosis of Planetary Atmospheres From Effects of Entry Plasma on Antenna Impedance. AIAA Pap. No. 68-137, Jan. 1968.

74. Weaver, William L.; and Hinson, William F.: Water Injection From a 9° Hemisphere-Cone Into a Hypersonic Airstream. NASA TN D-5739, 1970.

75. Taylor, W. C.: Shock-Tube Measurement of Admittance of RAM C and RAM C-C Diagnostic Antennas. The Entry Plasma Sheath and Its Effects on Space Vehicle Electromagnetic Systems - Vol. I, NASA SP-252, 1971, pp. 157-182.

76. Kurzius, Shelby C.; Raab, Fredrik H.; and Revolinski, Richard L.: Ionization Suppression in High Temperature Low-Pressure Plasmas by Electrophilic Vapors and Sprays. NASA CR-1701, 1970.

77. Dunn, Michael G.: Comparison Between Predicted and Measured Blackout Boundaries for Earth Entry of Apollo. The Entry Plasma Sheath and Its Effects on Space Vehicle Electromagnetic Systems - Vol. 1, NASA SP-252, 1971, pp. 33-45.

78. Schexnayder, Charles J., Jr.; Evans, John S.; and Huber, Paul W.: Comparison of Theoretical and Experimental Electron Density for RAM C Flights. The Entry Plasma Sheath and Its Effects on Space Vehicle Electromagnetic Systems - Vol. I, NASA SP-252, 1971, pp. 277-303.

TABLE I.- HISTORY OF RAM FLIGHTS

Flight	Prime experiment	Peak velocity, ft/sec	Launch date
RAM A-1	Aerodynamic shaping	18 000	August 30, 1961
RAM A-2	Aerodynamic shaping and magnetic window	18 000	February 21, 1962
RAM B-1	Multifrequency	18 000	September 21, 1962 (rocket failure)
RAM B-2	Water addition	18 000	May 28, 1963
RAM B-3	Plasma diagnostic (reflectometers)	18 000	April 10, 1964
RAM C-I	Water addition and plasma diagnostics (electrostatic probes)	25 000	October 19, 1967
RAM C-II	Plasma diagnostics (reflectometers and electrostatic probes)	25 000	August 22, 1968
RAM C-III	Water and electrophilic injection, plasma diagnostics	25 000	September 30, 1970

Notes: Additional experiments on these flights have included the evaluation of antenna design and performance in a plasma environment, and the correlation of theoretical predictions of electromagnetic radiation with flight results at various frequencies.

A water injection experiment was successfully conducted on Gemini GT-3, March 23, 1965.

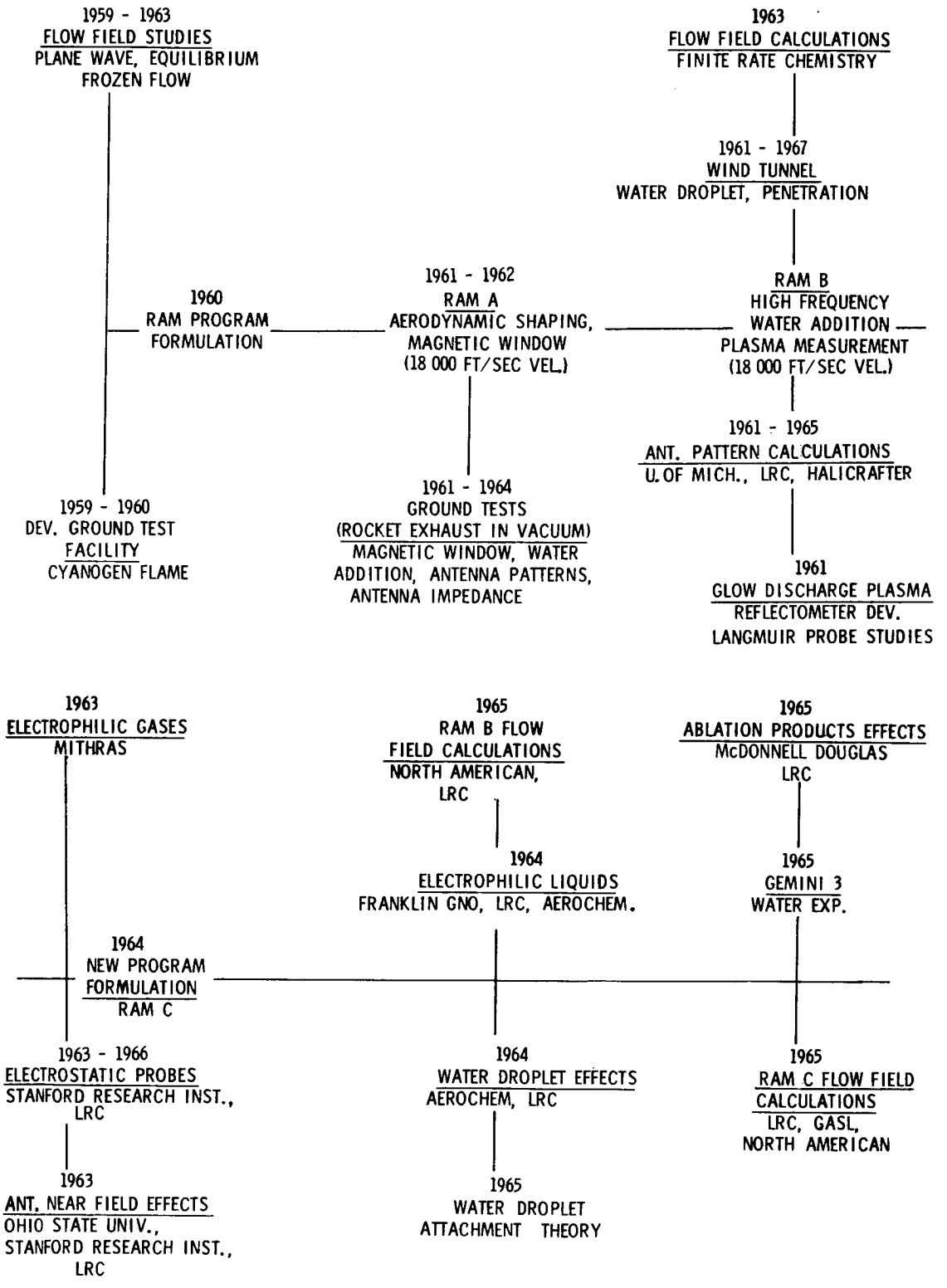

Figure 1.- Summary of project RAM flights and SRT.

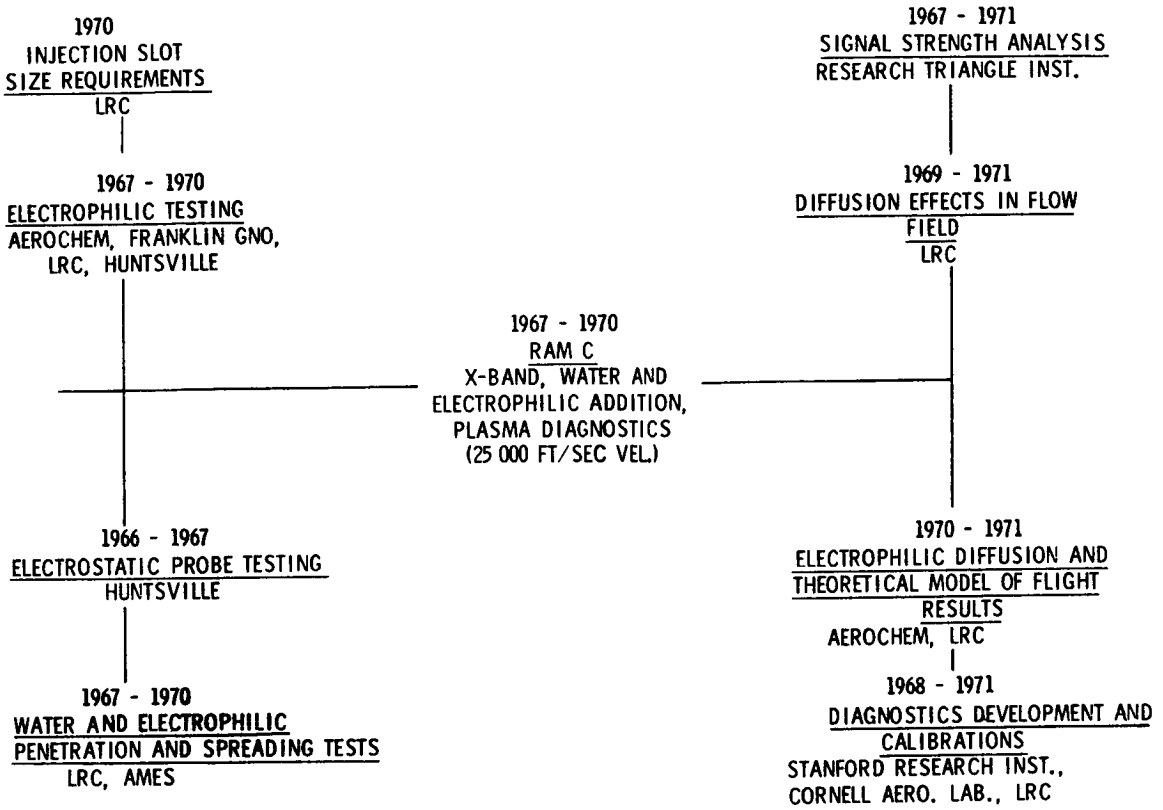

Figure 1.- Concluded.

COMPARISON BETWEEN PREDICTED AND MEASURED BLACKOUT BOUNDARIES FOR EARTH ENTRY OF APOLLO[+]

By Michael G. Dunn

Cornell Aeronautical Laboratory, Inc.
Buffalo, New York 14221

ABSTRACT

A semiempirical technique has been developed to calculate the non-equilibrium flow electron-density and collision-frequency distributions in the plasma surrounding an Apollo vehicle during earth-atmosphere entry. Utilizing the results of these calculations, the communication-blackout boundaries were constructed for a carried frequency of 2.287 GHz for an entry velocity range of 14,000 to 35,000 ft/sec. For any arbitrary entry velocity in this range, the altitude uncertainty band is ± 5000 ft. The predicted boundaries are compared to in-flight data gathered by the NASA[*] for Apollo 4, 6, 7, 8, and 10. The agreement between the predicted and measured blackout boundaries is reasonably good.

INTRODUCTION

Prior to the initiation of the Apollo program, experience with the Mercury and Gemini earth-orbiting space vehicles had indicated that communications with the craft at customary radio frequencies was impossible during a significant portion of the entry trajectory as a result of free electrons in the surrounding plasma. The increased entry velocity associated with Apollo upon return from lunar missions implied considerably higher electron densities than previously experienced and thus an extended period of time over which signal transmissions would be significantly degraded (blackout). For the purposes of the flight data communications blackout will be defined as that point in the trajectory at which the received signal becomes equal to the

---

[+]This paper is based on research sponsored by the NASA, Goddard Space Flight Center, under Contract NAS5-9978. Many people at Cornell Aeronautical Laboratory have contributed to this work. A complete list of credits is given in CAL Report No. AI-2187-A-17.

[*]These data were recently supplied to the author by Dr. Richard Lehnert, National Aeronautics and Space Administration, Goddard Space Flight Center, Greenbelt, Maryland.

receiver threshold. The most desirable solution to this difficulty would be to reduce the electron density to an acceptable level. It soon became apparent that alleviation might not be practical and therefore an accurate prediction of the trajectory position of onset and termination of signal degradation was the next best solution. It was this latter interest that motivated the research reported in this paper.

The Apollo vehicle is very blunt and enters the earth atmosphere at a large (approximately 20°) angle of attack. Early in the program it was determined that if accurate estimates of the communication blackout boundaries were to be made, then significantly more information about chemical kinetics, flow-field predictions, separated flow, and ablation products would be required. Each of these areas was investigated in some detail and the results are summarized in Reference 1. The material presented in this paper is a much condensed version of that outlined in Reference 1.

As an initial step in this program streamline locations and pressure distributions in the asymmetric inviscid flow field were obtained from the time-dependent solution of Bohachevsky and Mates.[2] This information was then used[3] to perform nonequilibrium chemical kinetics calculations by means of a streamtube technique. The results of this effort were helpful in determining the important chemical reactions and for which of the reactions rate coefficient data were needed. With this information, an experimental program was initiated to measure the important reaction-rate coefficients under laboratory conditions.

The inviscid flow-field calculation noted above was a good starting point, but it was clear that at altitudes greater than approximately 250,000 ft the thin boundary-layer approximation begins to break down for flow around the Apollo body and thus could not be used. The influence of the transport properties is spread across the shock layer, and even the shock wave itself may not be thin compared to the stand-off distance. Solutions for the gasdynamic variables and chemical compositions were therefore obtained[4-6] for these low-density flows using an approximate analysis based on an integral method.

The experimentally determined reaction-rate coefficient data for the electron-depletion reactions and the theoretical analyses developed were integrated, and calculations were performed at selected trajectory points in order to arrive at a prediction of the communication-blackout boundaries for the Apollo entry upon return from lunar missions. The entry trajectory is such that two different flow-field regimes were necessarily considered in order to calculate the gasdynamic parameters and chemical compositions. During the early portion (high altitude) the flow field is viscous. At lower altitudes, below about 250,000 ft, the thin boundary-layer assumption becomes valid and inviscid-flow calculations are appropriate for calculation of the plasma properties.

In the remainder of this paper the calculations performed to obtain the predicted boundaries will be briefly described. Comparison will be made between the predictions and flight data from Apollo 4, 6, 7, 8, and 10 flights.

CONSTRUCTION OF INVISCID FLOW FIELD

The calculation technique of Reference 2 was not used in the later stages of this research because of the wealth of experimental data that became available. It was more realistic and less expensive to use these data to construct the shock envelope and flow field in the pitch plane for an Apollo vehicle at a 20 degree angle of attack. The flow field was divided into the subsonic-transonic forebody region and the supersonic afterbody region. Ablation effects were not included in these calculations because they were previously considered by Huber[7]. His results are compared to the pure-air chemistry blackout boundaries later in the paper.

The shock envelope in the forebody region was determined using the empirical correlation functions of Kaattari[8] for a twenty degree angle of attack and a normal-shock density ratio of sixteen. The shock-wave shape in the vicinity of the round (toroid) windward corner was also determined by the procedure suggested in Reference 8.

In order to simplify the supersonic flow-field calculations, a single family of characteristics was used to predict the flow expansion around the rounded windward and leeward corners of the body. The pressure and flow inclination angle are constant along each characteristic. Since the corner-region expansion fan is assumed to be isentropic, the procedure does not take into account the entropy gradients due to the curved shock wave. Also, since only one family of characteristics is considered the reflections from the shock wave and streamlines are neglected; this should not have a large influence on the results since these reflections tend to cancel each other.

The experimentally determined surface-pressure distribution for a 0.05-scale model of the Apollo vehicle was used to determine the leading and trailing characteristics of the expansion fan around the rounded leeward and windward corners in the pitch plane. The expansion fan was constructed graphically utilizing the local flow inclination angle of the Apollo vehicle surface and tabulated Prandtl-Meyer functions[9] for $\gamma = 1.4$. The pressure ratio P_2 / P_s is constant along each characteristic since the expansion is assumed to be isentropic. The local pressure along the characteristic is P_2 and the stagnation pressure behind the shock is P_s .

The flow inclination angle computed from the conservation equations for a given pressure ratio P_2 / P_∞ was not the same as the flow inclination angle at the body surface along a given characteristic because of entropy gradients produced by the curved shock which will alter the location of the characteristics. To account for the entropy gradients in a simple manner, it was assumed that the flow deflection angle varied linearly from the flow angle at the surface to the flow angle imposed by the conservation equations at the shock wave along each characteristic. Selected streamlines can then be constructed graphically since the local flow inclination angles are now known. The locations of the streamlines in the subsonic forebody region were determined by enforcing the conservation of mass for axisymmetric flow. The product $\rho \vec{q}$ of the density and velocity vector was assumed to be constant along normals to the forebody surface.

Figure 1 illustrates the location of nine streamlines that were constructed in the plane of symmetry. The oblique-shock calculations indicated that the shock-wave envelope is independent (within 6%) of the flight conditions considered here. In addition to the above streamlines, two streamlines were assumed to originate at the stagnation point and to expand around the body with a pressure distribution that matches the experimentally observed surface-pressure distribution. The leeward side streamline then was assumed to depart from the body surface in the corner region with a flow-inclination angle consistent with the trailing characteristic as determined by the afterbody pressure. This streamline was called the separation streamline since it did not follow the afterbody surface. The windward streamline almost follows the afterbody surface and indicates that a thin, viscous boundary layer exists along the windward side of the vehicle with no apparent separation region.

Having determined the shock shape and the location of several streamlines within the shock layer, the initial conditions on the streamlines just behind the shock wave were calculated for frozen composition and vibrational equilibrium. The nonequilibrium electron-density and collision-frequency histories were then calculated[10] utilizing the initial conditions and the pressure distribution along the streamlines. The oblique shock-wave solutions provided the initial conditions for each streamline with the exception of the windward- and leeward-surface streamlines which used stagnation conditions determined from normal-shock solutions.

CHEMICAL KINETICS CALCULATIONS

The inviscid flow field briefly outlined above was used to obtain estimates of the electron-density and collision-frequency distributions in the plasma surrounding the Apollo vehicle. Trajectory points for which calculations were performed are given in Table 1 below. Note that for two of the last three trajectory points given in this table, it is necessary to account for viscous-flow influences. This correction has been made and is discussed later.

TABLE 1

TRAJECTORY POINTS FOR WHICH INVISCID FLOW-FIELD CALCULATIONS WERE PERFORMED

VELOCITY, ft/sec	ALTITUDE, ft
10,000	150,000
14,000	120,000
16,000	180,000
16,000	210,000
21,000	240,000
21,000	250,000
26,000	280,000
32,000	320,000
34,000	220,000

Species-distribution plots similar to those shown in Figures 2 and 3 (34,000 ft/sec at 220,000 ft) were obtained for each trajectory point of Table 1 and were used in constructing the blackout bounds presented in Figure 4 for 2.287 GHz communication. The system of chemical reactions used here was the same as that used in Reference 3 with the major exception that the rate coefficients for the electron depletion reactions $NO^+ + e^- \longrightarrow N + O$, $N_2^+ + e^- \longrightarrow N + N$ and $O_2^+ + e^- \longrightarrow O + O$ were those measured[11-13] as part of this research. In obtaining the blackout boundaries, the decision was made to define blackout on the basis of the critical electron density. Rays were then drawn from the antenna location through the plasma and across the shock envelope. If the local electron density along the particular ray exceeded the critical electron density (6.5×10^{10} e^-/cm^3 for 2.287 GHz communications), then the signal strength was assumed sufficiently degraded so as to be not useful. It was further assumed that the acute included angle between the shock envelope and the ray must be greater than 5^o before communications would be possible, even if the local electron density along the ray did not exceed critical.

Figure 4 illustrates typical rays drawn from the S-band antenna location through the leeward-side plasma. For this particular flight condition, the electron density along ray A exceeded critical n_e for a significant portion of the path making communications impossible. Along ray B the number density was again significantly greater than critical for much of the propagation path. However, along ray C the number density is near but almost always less than critical, making communications marginal. Ray C crosses the shock envelope at approximately 12.5^o, suggesting that within the constraints of our assumptions this trajectory point would be classified as marginal communications.

No rays were drawn through the windward-side plasma for the trajectory condition of Figure 4 because the electron-density profile for this condition was such as to suggest that the exit path for the E-M wave could not be a direct one. The conclusion should not be drawn, however, that communications through the leeward-side plasma was most likely for all trajectory points. For flight velocities greater than 21,000 ft/sec, the results suggested that the best chances for communications were in fact through the leeward-side plasma. However, for lower velocities and lower altitudes the communications through the windward-side plasma was more likely. This effect is a result of the nonequilibrium chemistry of the reactions involving charged particles and the manner in which they proceed in the respective expansion environment (leeward vs. windward).

Figure 5 presents the prediction (for pure-air flow) of the communication-blackout boundaries for 2.287 GHz with an estimated uncertainty of approximately + 5000 ft altitude. Each of the calculated trajectory points is noted on this plot as communications should not be degraded (⊡), marginal communications (⊙), and communications should be blacked out (△). It is emphasized that these are calculated points and not in-flight data points.

Also included on Figure 5 are the blackout bounds estimated by Huber[7] considering only ablation-product impurity ionization. At the higher velocities, it can be generally concluded that blackout boundary for Apollo

earth-atmosphere entry conditions is controlled by the pure-air chemistry. For flight velocities between 24,000 and 27,000 ft/sec and between 15,000 and 17,000 ft/sec, the ablation-controlled boundary falls within the lower altitude limit of the uncertainty band of the pure-air chemistry. It is thus suggested that in these flight regimes the pure-air and ablation chemistry are of equal importance. The early prediction of Lehnert and Rosenbaum[14] is also included on Figure 5 for comparison purposes. Their estimate differs from the current estimate for velocities greater than 21,000 ft/sec and for velocities lower than 16,000 ft/sec.

VISCOUS FLOW-FIELD CALCULATIONS

For altitudes greater than 250,000 ft, the thin boundary-layer approximation is no longer applicable for analyzing the flow around the Apollo body. The influence of the transport properties is spread across the shock layer, and even the shock wave itself may not be thin compared to the shock stand-off distance. Thus a new formulation is needed in analyzing the viscous flow around the body at low Reynolds numbers. The flow regimes of interest are the viscous layer, the incipient-merged layer, and part of the fully merged layer, viz., $O(\epsilon) \leq \epsilon K^2 \leq O(10^4)$. The term K^2 is the parameter defined by Cheng.[15] In particular, $K^2 = \left(\frac{\rho_\infty U_\infty a}{\mu_*}\right)\epsilon(T_*/T_0)$, $\epsilon = (\gamma-1)/2\gamma$, γ signifying the specific heat ratio, $\rho_\infty U_\infty$ the free-stream mass flux, a the nose radius of the body, T_0 the stagnation temperature, T_* and μ_* the reference temperature and viscosity, respectively. As $K^2 \longrightarrow \infty$, the flow approximates continuum, thin boundary-layer flow, while $K^2 \rightarrow 0$ signifies free-molecule flow conditions. It has been found from the analysis[16] of the stagnation region that the term K^2 may still be used as a meaningful parameter delineating various flow regimes even for the case of mass injection. Thus the present viscous-flow analysis for an Apollo-type body is applicable at altitudes between approximately 250,000 ft and 400,000 ft.

The viscous flow-field analysis performed for the purposes of this contract began by considering the axisymmetric flow over the forebody region of an Apollo body with large mass injection at the wall due to ablation. The flow was in the incipient-merged-layer and the viscous-layer regimes. In these regimes, the Navier-Stokes equations may be used. The equations were simplified by assuming a very thin shock layer compared with the body radius.

The equations thus simplified are similar in form to the conventional boundary-layer equations with the important exceptions that the entire flow field is now viscous, instead of a very thin layer near the wall and that the normal pressure gradient may not be assumed negligible. The latter condition results because of the non-negligible momentum change in the direction normal to the body surface. An approximate analysis based on an integral method was formulated which takes into account large mass injection at the body surface as well as transport phenomena across the shock wave.

Results were initially obtained[4] for hypersonic, low Reynolds-number flow in the stagnation region of a blunt body at high altitudes by application of

the integral method. Significant influences of mass injection on the heat transfer, the "skin-friction," changes in flow conditions across the shock wave in the incipient-merged layer and the viscous-layer flow regimes were observed. Attention was subsequently concentrated on analyzing the viscous-flow phenomena downstream from the stagnation point in these flow regimes, and the results obtained from the stagnation-region analysis provided the initial conditions.

Solutions were then obtained[5] for the viscous, hypersonic shock layer in the forebody region of the Apollo body at high altitudes for the case of a non-reacting gas. This analysis yielded the streamline distributions within the viscous shock layer for various mass-injection rates. These results are particularly significant since they afford a means of assessing the importance of the viscous flow field on the plasma chemical kinetics. Solutions were obtained both with and without mass injection at the body surface. For the zero mass-injection case, the mass flowing in the viscous shock layer consists entirely of the free-stream mass entering through the shock wave; thus the stagnation streamline becomes the dividing streamline along the body and coincides with the body surface. When mass is now injected uniformly along the body at the surface, the layer in the immediate vicinity of the body surface consists of the injected mass and the dividing streamline is now pushed outward from the body. The thickening of the shock layer and the noticeably changed streamline patterns as a result of very large blowing was observed. Since the present analysis is based on a thin shock-layer assumption, it should be kept in mind that the justification of this assumption comes into question when the viscous shock layer becomes very thick (due to blowing) compared with the characteristic length of the body, which in this case is the body nose radius.

The viscous shock-layer work was continued in that an analysis of the chemical nonequilibrium flow in the forebody region of the Apollo body at high altitudes was formulated.[5] At the time, there were no previous analyses dealing with nonequilibrium flow around a blunt body that were directly applicable to the present problem. One analysis that should be mentioned is that performed by Lee and Zierten,[17] who considered the merged-layer ionization in the stagnation region of a blunt body without mass injection (ablation) at the body surface. These authors found that the inviscid theory overestimates the peak electron density by as much as two orders of magnitude.

Results were subsequently obtained for the binary-species nonequilibrium flow in the viscous shock layer for a fully catalytic surface. In analyzing the problem, the momentum and the energy equations and their solutions[5] were used as known inputs, under the assumption that the Lewis number is unity and effectively decoupling[14] the chemical considerations from the momentum and the energy considerations. An integral-method approach was used for the solution of the atom-concentration distributions along the body surface at various altitudes. In these calculations the only charged species were assumed to be e^- and NO^+.

The electron-density level was found[6] to be approximately two orders of magnitude below that predicted by an inviscid analysis. These results demonstrate a sizable influence of flow viscosity on the electron-density level at

high altitudes and that an inviscid analysis yields an upper-bound prediction of these levels. It is thus evident that analysis of the viscous shock layer was necessary in order to assess correctly the magnitudes of the electron-density levels existing in the forebody region of a blunt body at high altitudes. The results obtained for the viscous shock layer were incorporated in the communication-blackout boundaries presented in Figure 5.

COMPARISON BETWEEN PREDICTION AND FLIGHT DATA FOR 2.287 GHz COMMUNICATIONS

The in-flight communications blackout points reported here for Apollo 4 were taken directly from References 18, those for Apollo 6, 7, and 8 from Reference 19 and those for Apollo 10 from Reference 20. The measured signal strengths were obtained using the NASA instrumented aircraft 427 and 432, the Apollo range instrumented aircraft (ARIA), ground based Unified S-Band stations, and the reentry ships "Watertown," "Redstone" and "Huntsville." Typical signal strength data records and a detailed discussion of the instrumentation are presented in Reference 19. Figure 6 presents a comparison between the predicted communication-blackout boundaries and the in-flight data. Data points for Apollo 4, 8, and 10 were obtained for a velocity of approximately 35,000 ft/sec and are all in agreement as shown. The ARIA aircraft obtained data points for Apollo 4 for a freestream velocity of approximately 21,000 ft/sec at an altitude of approximately 240,000 ft which are in reasonable agreement with the prediction. The Apollo 6 blackout was obtained by both the NASA airplane and the "Watertown" and is also shown to be in agreement with the prediction. The ARIA 8 aircraft and the "Huntsville" both acquired signals from Apollo 10 for a velocity of approximately 16,000 ft/sec at an altitude of approximately 195,000 ft. These data points are approximately 20,000 ft above the predicted boundary.

The Apollo 7 results are somewhat more uncertain than the other measurements. In Reference 19 it is suggested that the high altitude loss of signal by NASA 427 aircraft, Merritt Island, and Grand Bahamas Island was anomalous because the ARIA 5 aircraft, which had a much different look angle, observed a signal strength decrease at the reported signal blackout, but continued to record signals beyond this time. It was concluded that the ARIA 5 aircraft lost signal at the trajectory point shown on Figure 6 but no positive evidence of plasma induced blackout was observed. The data for this flight exhibit significant disagreement with the predicted blackout boundaries. However, with the exception of this latter flight, the data appear to be in reasonable agreement with the predicted boundaries.

CONCLUSIONS

A map of the communication-blackout boundary for a carrier frequency of 2.287 GHz has been calculated for the earth-atmosphere entry of an Apollo

vehicle for the entry-velocity range 14,000 ft/sec to 35,000 ft/sec. The estimated altitude uncertainty for a given velocity in this range is $\pm$ 5000 ft. The comparison between predicted and measured blackout boundaries for Apollo 4, 6, 7, 8, and 10 is reasonably good.

REFERENCES

1. Dunn, M. G., "Predicted Communication Boundaries for Earth-Atmosphere Entry of the Apollo Vehicle," Final Report Contract No. NAS5-9978, Cornell Aeronautical Laboratory Report No. AI-2187-A-17, June 1969.

2. Bohachevsky, I. O. and Mates, R. E., "A Direct Method for Calculation of the Flow About an Axisymmetric Blunt Body at Angle of Attack," AIAA Journal, Vol. 4, No. 5, pp. 776-782 (1966).

3. Dunn, M. G., Daiber, J. W., Lordi, J. A. and Mates, R. E., "Estimates of Nonequilibrium Ionization Phenomena in the Inviscid Apollo Plasma Sheath," Cornell Aeronautical Laboratory Report No. AI-1972-A-1, September 1965.

4. Kang, S. W. and Dunn, M. G., "Integral Method for the Stagnation Region of a Hypersonic Viscous Shock Layer with Blowing," AIAA Journal, Vol. 6, No. 10, pp. 2031-2033, October 1968.

5. Kang, S. W., "Hypersonic, Low Reynolds-Number Flow over a Blunt Body with Mass Injection," AIAA Journal, Vol. 7, No. 8, pp. 1546-1552, August 1969.

6. Kang, S. W., "Nonequilibrium, Ionized, Hypersonic Flow over a Blunt Body at Low Reynolds Number," AIAA Journal, Vol. 8, No. 7, pp. 1263-1270, July 1970.

7. Huber, P. W., Addendum #2 to Minutes of the Eleventh Meeting of the Apollo Reentry Communications Blackout Working Group, July 18, 1967.

8. Kaattari, G. E., "Shock Envelopes of Blunt Bodies at Large Angles of Attack," NASA TN D-1980, December 1963.

9. Ames Research Staff, "Equations, Tables, and Charts for Compressible Flow," NACA Report 1135, 1953.

10. Lordi, J. A., Mates, R. E., and Mosselle, J. R., "Computer Program for the Numerical Solution of Nonequilibrium Expansions of Reacting Gas Mixtures," Cornell Aeronautical Laboratory Report AD-1689-A-6 (June 1965).

11. Dunn, M. G., and Lordi, J. A., "Measurement of Electron Temperature and Number Density in Shock-Tunnel Flows: Part II, $NO^+ + e^-$ Dissociative Recombination Rate in Air," to be published in AIAA Journal.

12. Dunn, M. G. and Lordi, J. A., "Measurement of $N_2^+ + e^-$ Dissociative Recombination in Expanding Nitrogen Flows," AIAA Journal, Vol. 8, No. 2, pp. 339-345, February 1970.

13. Dunn, M. G. and Lordi, J. A., "Measurement of $O_2^+ + e^-$ Dissociative Recombination in Expanding Oxygen Flows," AIAA Journal, Vol. 8, No. 4, pp. 614-618, April 1970.

14. Lehnert, R. and Rosenbaum, B., "Plasma Effects on Apollo Re-Entry Communications," NASA TN D-2732 (March 1965).

15. Cheng, H. K., "Hypersonic Shock-Layer Theory of the Stagnation Region at Low Reynolds Number," Proc. 1961 Heat Transfer and Fluid Mechanics Institute, Univ. of So. California, Stanford U. Press, pp. 161-175 (1961).

16. Chen, S. Y., Aroesty, J. and Mobley, R., "The Hypersonic Viscous Shock Layer with Mass Injection," Rand Corp. Memo RM 4631-PR (May 1966).

17. Lee, R. H. C. and Zierten, T. A., "Merged Layer Ionization in the Stagnation Region of a Blunt Body," 1967 Heat Transfer and Fluid Mechanics Inst., La Jolla, California, pp. 452-468 (June 1967).

18. Marini, J., "Apollo 4 Blackout Test Results, Mares Island Entry," NASA, Goddard Space Flight Center, X-551-68-419, November 1968.

19. Marini, J. W. and Hager, F. W., "Apollo 6, 7 and 8 Blackout Test Results," NASA, Goddard Space Flight Center, X-550-69-277, July 1969.

20. Private Communication with Dr. Richard Lehnert, National Aeronautics and Space Administration, Goddard Space Flight Center, July 2, 1970.

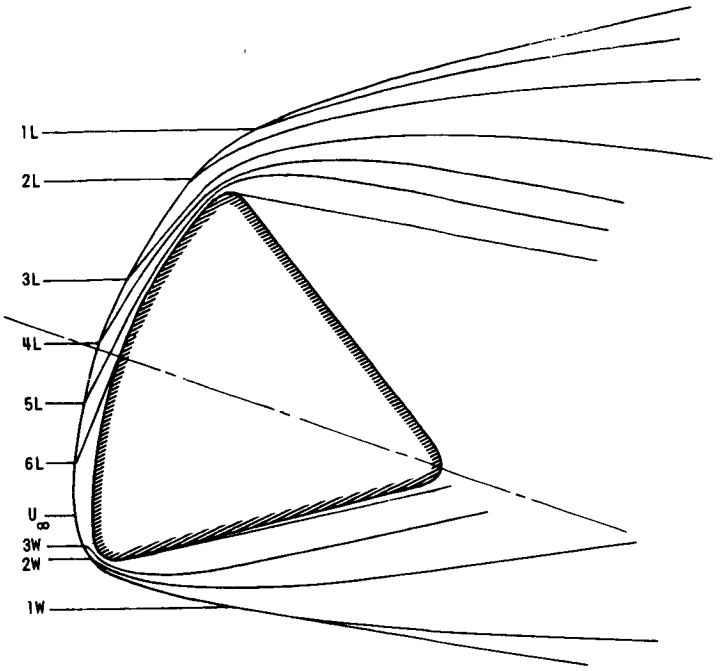

Figure 1.- Streamline pattern in the plane of symmetry.

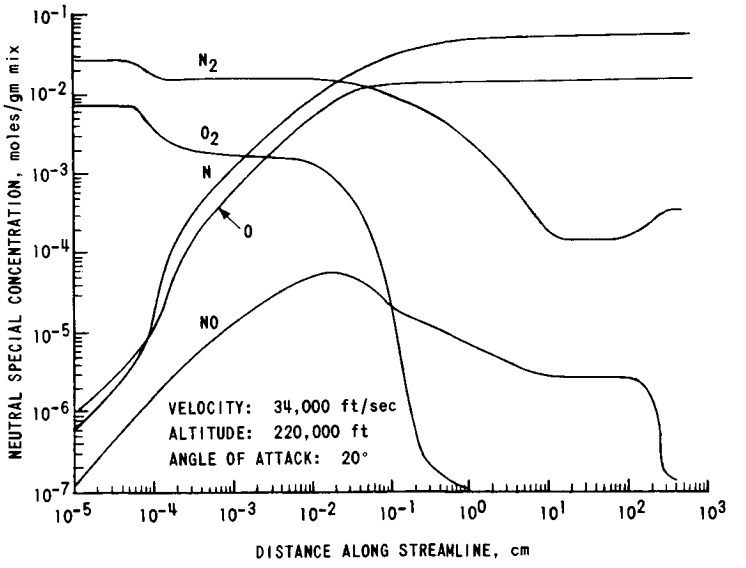

Figure 2.- Nonequilibrium species distribution along streamline 4L in plane of symmetry.

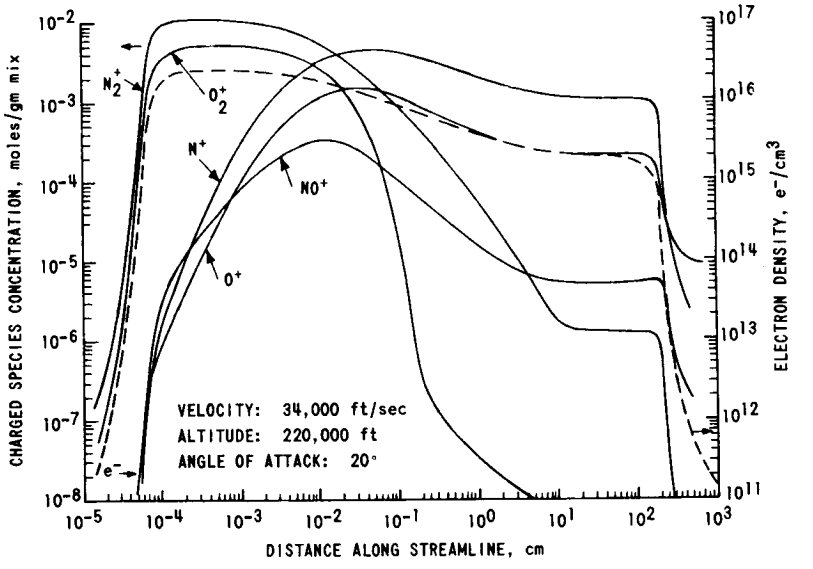

Figure 3.- Nonequilibrium species distribution along streamline 4L in plane of symmetry.

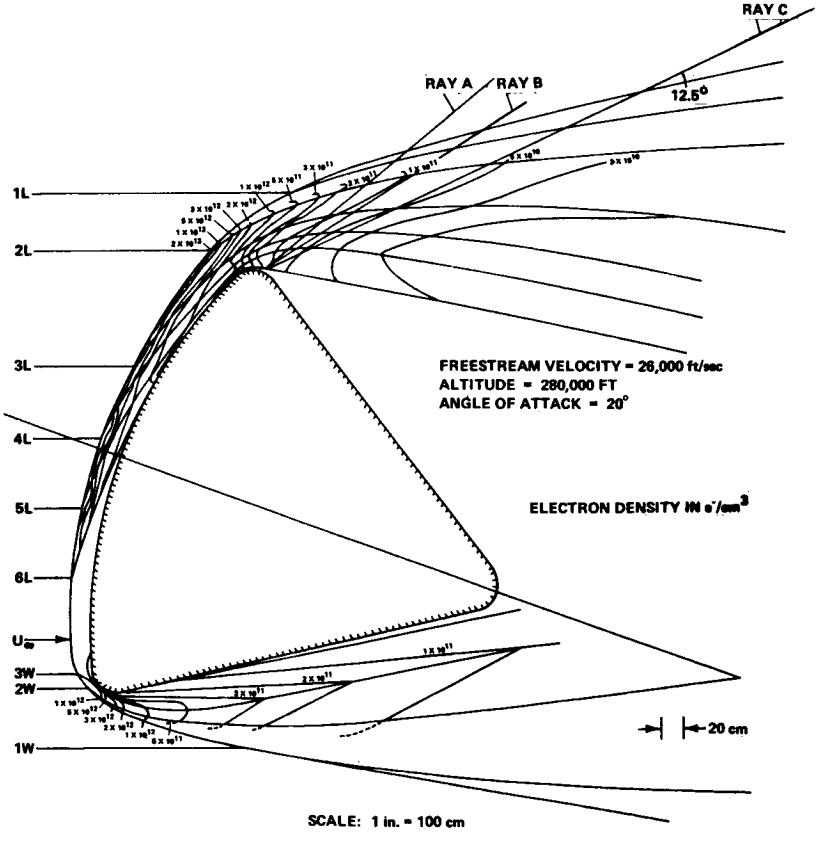

Figure 4.- Electron density distribution in plane of symmetry for Apollo command module.

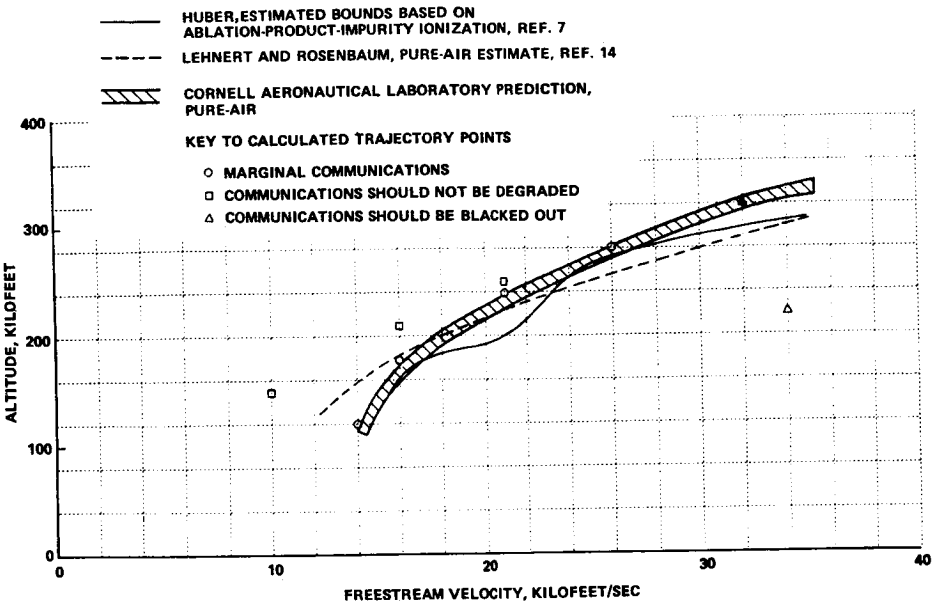

Figure 5.- Predicted blackout bounds for 2.287 GHz communication during Apollo earth-atmosphere entry.

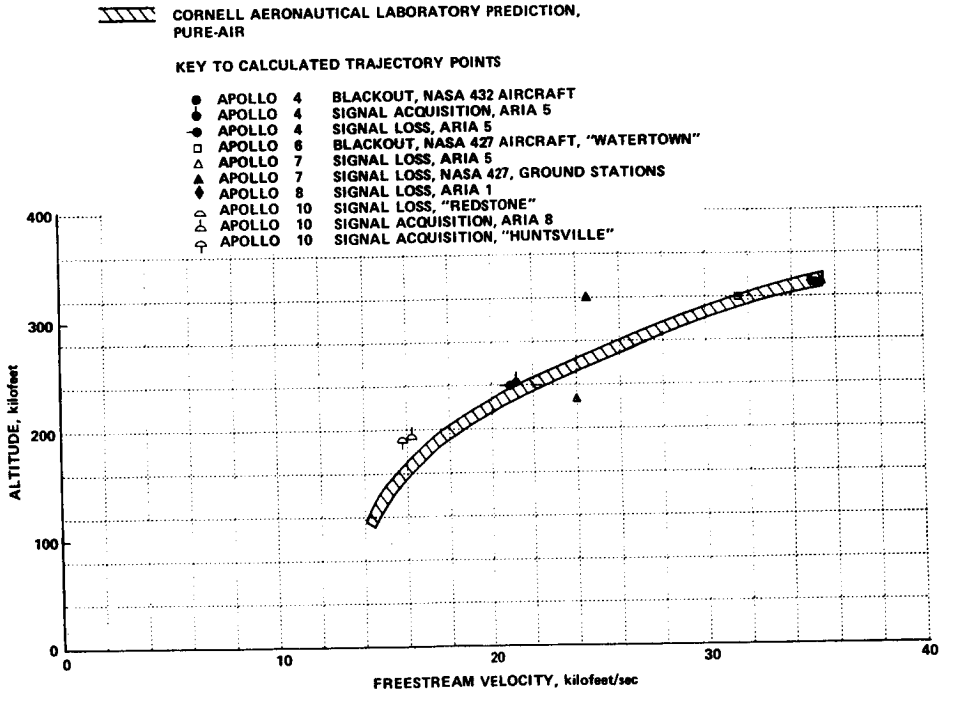

Figure 6.- Comparison between predicted and flight data blackout boundaries.

INVESTIGATIONS ON A CYLINDRICAL ANTENNA AS A DIAGNOSTIC PROBE FOR ISOTROPIC AND MAGNETIZED PLASMAS

L. D. Scott and Bharathi Bhat
Gordon McKay Laboratory, Harvard University

and

B. Rama Rao
M.I.T. Lincoln Laboratory

SUMMARY

This paper reports some investigations on the impedance behavior of a short, cylindrical antenna in the vicinity of the resonance and cut-off frequencies of a weakly ionized, collision-dominated plasma. The impedance results are utilized to explore the possibility of using such an antenna as a diagnostic probe for measuring plasma parameters. Since the antenna is electrically short, the values of the electron density and collision frequency are averaged over the 'near field' region of the antenna, the dimensions of which are quite small, so that it becomes possible to get information on the local characteristics of the plasma. An r.f. probe of this type is likely to be useful for diagnostic measurements in high-pressure, rare-gas laboratory discharge plasmas, shock-tube plasmas, some types of re-entry plasmas, and also in the D-region of the ionosphere. A knowledge of the impedance behavior of dipole antennas radiating inside plasmas is useful for accurately interpreting the data obtained from cosmic-noise intensity measurements [1] and top-side sounding experiments [2]. Both isotropic and magnetized plasmas are considered in this study and the results are summarized.

5

CYLINDRICAL ANTENNA IN AN ISOTROPIC PLASMA

The first part of this paper reports on investigations that were made to determine the effect of interparticle collisions on the antiresonant impedance characteristics of a short cylindrical dipole in the vicinity of the plasma frequency of an isotropic, collision-dominated, non-Maxwellian plasma. The experimental results were analyzed using the theory proposed by King, Harrison, and Denton [3] for an antenna in a cold lossy isotropic plasma. In order to estimate the contribution from the electroacoustic mode to the antenna impedance, the results were also compared with the theory proposed by Balmain [4]

for a warm plasma based on a linearized hydrodynamic model. The theory proposed by King et al. also assumes a Lorentzian conductivity model for the plasma, which is accurate only for a Maxwellian gas. The dependence of the electron-neutral collision frequency on the electron energy has been taken into account by postulating a complex effective collision frequency suggested by Molmud [5], which relates the Lorentzian model for plasma conductivity with the more precise value obtained from kinetic theory considerations.

The experimental apparatus is similar to that shown in figure 1. The plasma chamber consisted of a hot-cathode, Helium d.c. discharge tube, 14 cm in diameter and 38 cm in length. The antenna was a copper rod, 4 mm in diameter and 3.5 cm in length. The length of the antenna is very short at the r.f. signal frequency used in the experiment, which typically varies from 200 to 600 MHz. The electron density and electron temperature were determined by a planar Langmuir probe. The collision frequency was determined from the experimental data by using the following procedure: (a) precision impedance measurements were made on the antenna at 11 frequencies over a 2 to 1 range, typically from 300 to 600 MHz, which includes the plasma frequency; (b) using a fourth degree interpolation polynomial, the frequencies at which the maximum values of the resistance R^{meas} and the magnitude of the impedance $|Z^{meas}|$ occur are determined as well as the values themselves; (c) using the frequency of $|Z^{meas}_{max}|$ as the plasma frequency ω_p, R^{meas}_{max} is matched to R^{theo}_{max} from a family of resistance curves derived from King's theory, with the same plasma frequency, but with collision frequency as a parameter; (d) the value of the collision frequency is then obtained from the complex collision frequency formula of Molmud [5]; (e) to obtain an estimate of the accuracy of the results, the electron-neutral collision frequency obtained in this way is compared with the theoretical values of collision frequency calculated using the collision cross-section data of Golden and Bandel [6]. The comparison between theoretical and experimental results for measurements made at neutral gas pressures of 140, 300 and 750 microns of Hg are shown in figure 2. It can be seen from this figure that there is good agreement between theory and experiment for values of ω_p/ω between 0.8 and 1.6. This demonstrates that the shape of the theoretical curve is correct and that King's theory [3] gives a good description of the impedance behavior of the antenna in the vicinity of the plasma frequency of a collision-dominated plasma. In figure 3 the experimental values for the collision frequency are compared with the theoretical values obtained from the collision cross-section data of Golden and Bandel [6]. Once again it is seen that there is fairly good agreement although the experimental values are somewhat greater than that predicted by theory.

ANTENNA IN A MAGNETOPLASMA

The second part of this paper discusses investigations on the impedance characteristics of a cylindrical antenna immersed in a magnetized plasma with the static magnetic field applied parallel to the axis of the antenna. It is convenient to describe the plasma in terms of the symbols $X = \omega_p^2/\omega^2$, $Y = \omega_c/\omega$ and $Z = \nu_c/\omega$ where ω_p is the angular plasma frequency, ω_c is the angular cyclotron frequency, ν_c is the collision frequency, and ω is the angular signal frequency of the antenna. Measurements of the input impedance of the antenna have been made in the vicinity of the transition regions described by the following plasma parameters: (1) upper hybrid resonance f_u where $X = 1 - Y^2$; (2) plasma cut-off condition f_p given by $X = 1$; (3) cyclotron resonance f_c given by $Y = 1$. The experimental data for the antenna impedance has been compared with the theory proposed by Balmain [7]. The experimental equipment is shown in figure 1. The axial magnetic field in the solenoid was measured by a Hall effect probe and the antenna was placed in the uniform field region at the center of the solenoid. A transistorized power supply with a current regulation of 1 part in 10^5 and with a precision control for fine magnetic field adjustments was used in the experiments. The electron density and electron temperature were measured by using a spherical Langmuir probe. Figure 4 shows the variation in the measured input resistance of the antenna as a function of the signal frequency for several fixed values of the applied magnetic field. The input resistance shows a pronounced maximum near $X = 1$ when $\omega_c = 0$; as the magnetic field is increased, the resistance peak decreases in magnitude and for sufficiently high magnetic fields two distinct resistance peaks appear: one near the upper hybrid resonance frequency ($X = 1 - Y^2$) and the other near the plasma cut-off ($X = 1$). These results are in qualitative agreement with the theoretical predictions of Seshadri [8]. Figure 5 shows the measured input conductance and susceptance of the antenna as a function of signal frequency for two fixed values of cyclotron frequencies 238 MHz and 280 MHz. It can be seen that the antenna conductance shows a maximum at the cyclotron resonance $Y = 1$ as predicted by Balmain [7] and Seshadri [8]. In figure 6 the experimental results of antenna impedance at the cyclotron frequency 224 MHz are compared with Balmain's theory. The theoretical curve is computed by using the frequency corresponding to $|Z_{max}^{meas}|$ as the upper hybrid resonance frequency f_u and by matching R_{max}^{meas} with R_{max}^{theo} with collision frequency as the varying parameter. The experimental results are in good agreement with theory in general. However, it is interesting to note that Balmain's theory does not

predict the resistance maximum near the plasma frequency (X = 1) for the collisional magnetized plasma. The resistance peaks near the upper hybrid frequency ($X = 1 - Y^2$) and the plasma frequency (X = 1) present the possibility of measuring the electron density of a magnetoplasma by using a short r.f. antenna. The impedance results reported in this paper are in qualitative agreement with the in-flight measurements made by Stone, Alexander, and Weber [9] using a short dipole mounted on a rocket.

REFERENCES

1. Harvey, C. C.: Results from the UK-2 Satellite. Annales D'Astrophysique, No. 1, 1965, pp. 248-254.

2. Calvert, W. and Goe, G. B.: Plasma Resonances in the Upper Ionosphere. Journal of Geophysical Research, Vol. 68, No. 22, Nov. 15, 1963, pp. 6113-6120.

3. King, R. W. P., Harrison, C. W., Jr., and Denton, D. H., Jr.: The Electrically Short Antenna as a Probe for Measuring Free Electron Densities and Collision Frequencies in an Ionized Region. J. Res. NBS, Vol. 65D, No. 4, July/August 1961, pp. 371-384.

4. Balmain, K. G.: Impedance of a Short Dipole in a Compressible Plasma. Radio Science, Vol. 69D, No. 4, April 1965, pp. 559-566.

5. Molmud, P.: Langevin Equation and the A.C. Conductivity of non-Maxwellian Plasmas. Phys. Rev., Vol. 114, April 1959, pp. 29-32.

6. Golden, D. E. and Bandel, H. W.: Absolute Total Electron Helium Atom Scattering Cross-Sections for Low Electron Densities. Phys. Rev., Vol. 138, April 1965, pp. A14-A21.

7. Balmain, K. G.: The Impedance of a Short Dipole Antenna in a Magnetoplasma. IEEE Transactions, Vol. AP-12, September 1964, pp. 605-617.

8. Seshadri, S. R.: Input Admittance of a Cylindrical Antenna in a Magnetoionic Medium. Journal of Applied Physics, Vol. 39, No. 5, April 1968, pp. 2407-2412.

9. Stone, R. G., Weber, R. R. and Alexander, J. K.: Measurement of Antenna Impedance in the Ionosphere, I. Planet. Space Sci., Vol. 14, 1966, pp. 631-639; Measurement of Antenna Impedance in the Ionosphere, II. Planet. Space Sci., Vol. 14, 1966, pp. 1007-1016.

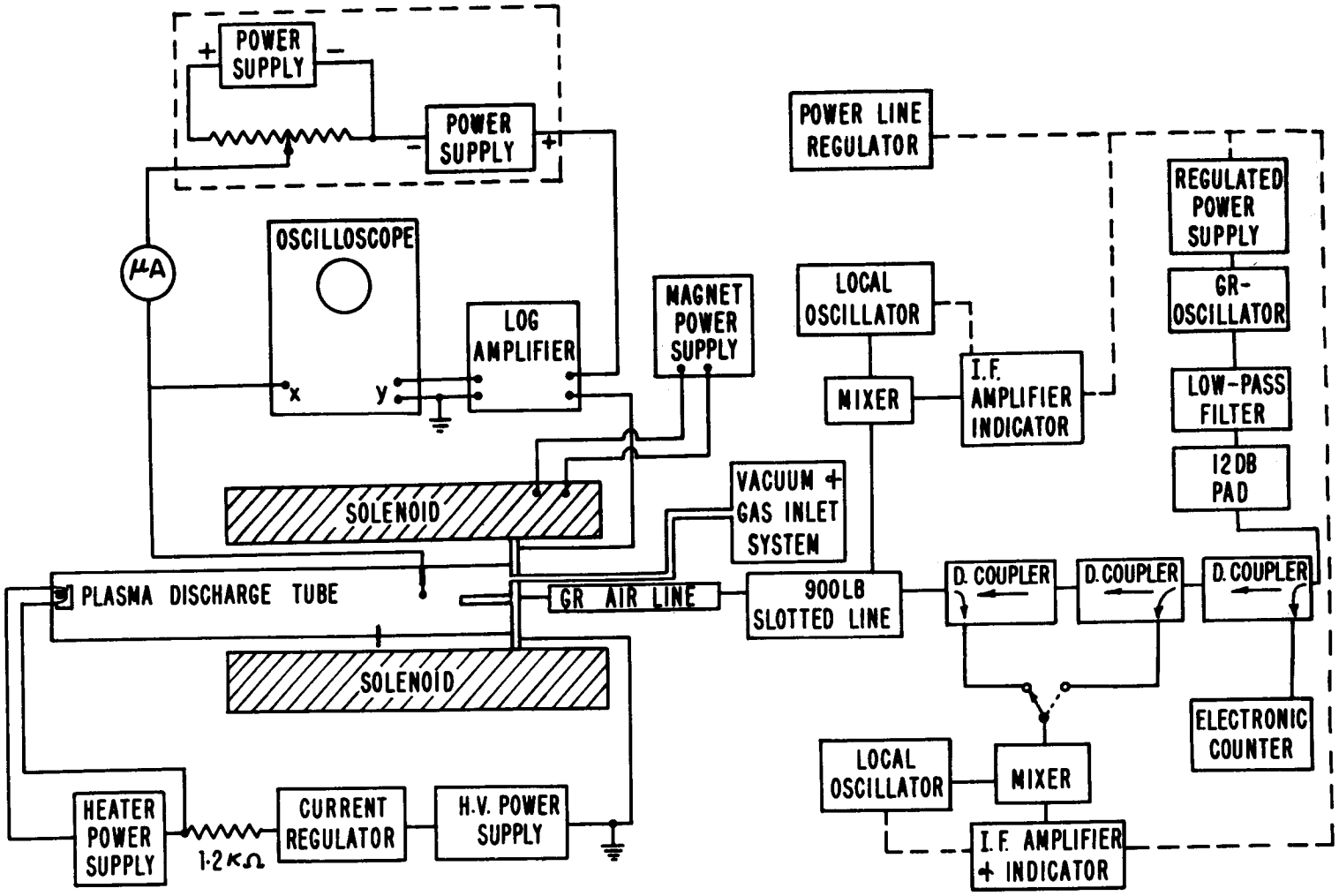

Figure 1.- Block diagram of the experimental apparatus.

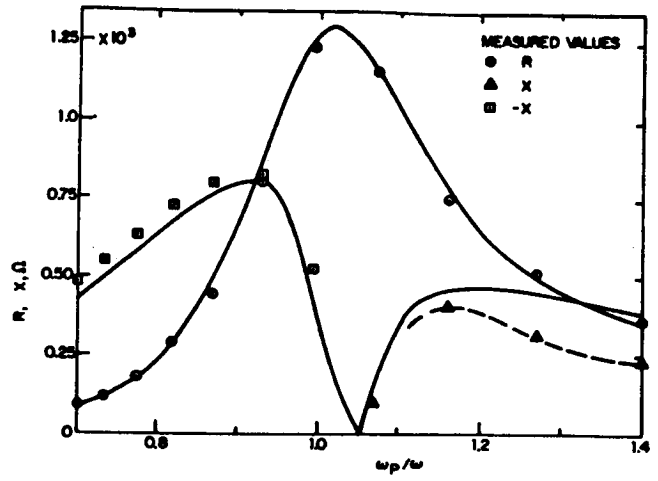

(a) Pressure, 140μ Hg; measured plasma frequency, 418 MHz; measured collision frequency, 7.288×10^8 sec^{-1}.

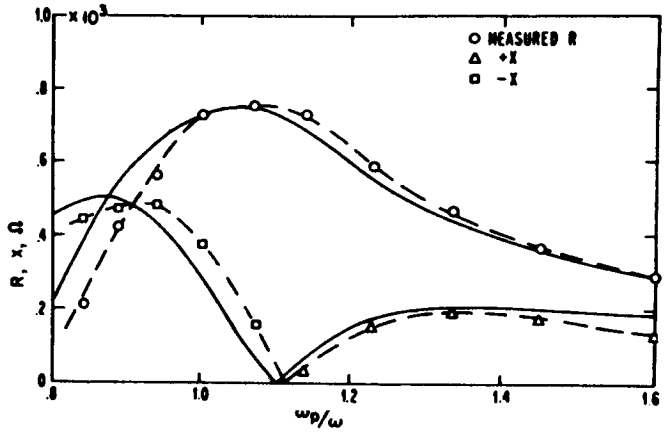

(b) Pressure, 300μ Hg; measured plasma frequency, 477 MHz; measured collision frequency, 12.79×10^8 sec^{-1}.

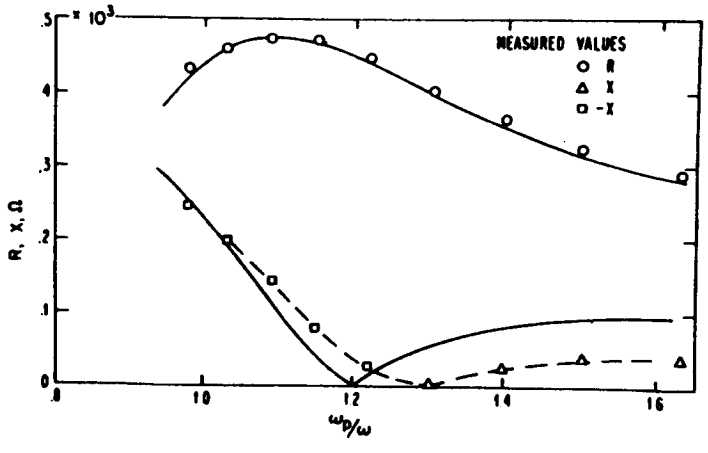

(c) Pressure, 730μ Hg; measured plasma frequency, 587 MHz; measured collision frequency, 21.19×10^8 sec^{-1}.

Figure 2.- Comparison of theoretical and experimental results for the impedance of a short dipole antenna in a plasma. Gas, helium; h = 3.49 cm; r = 2.13 mm.

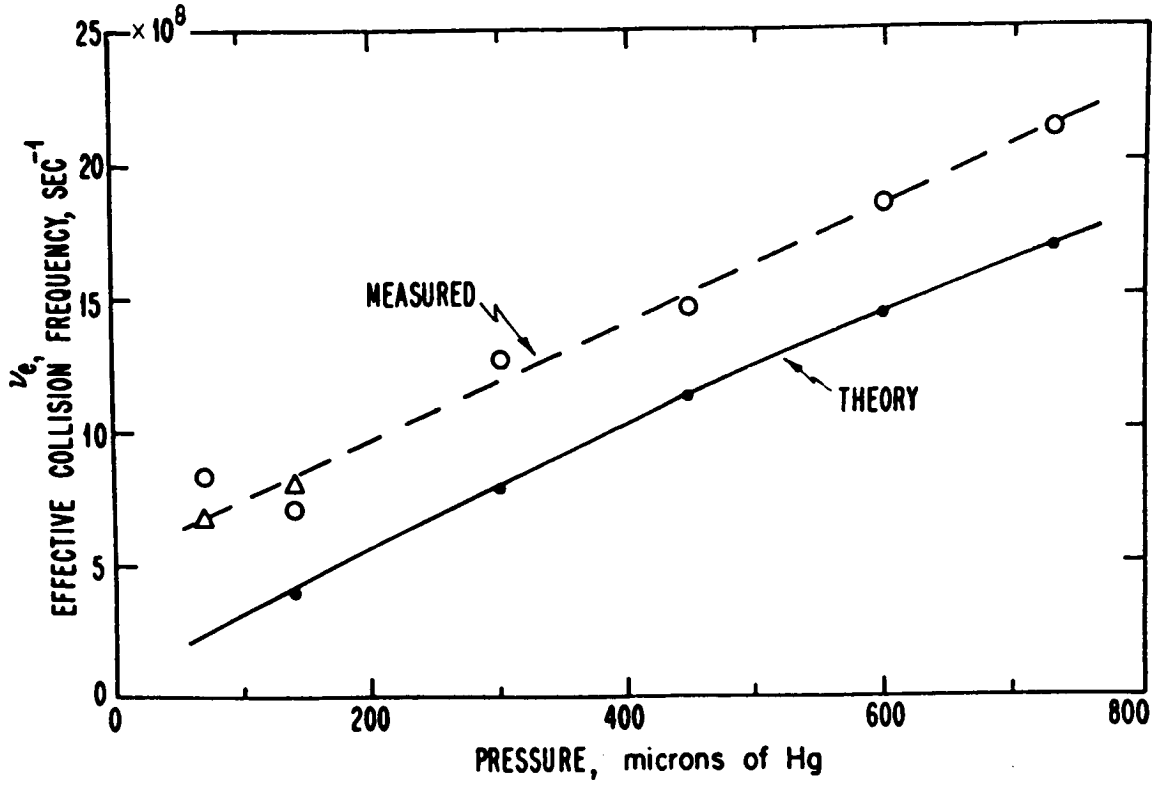

Figure 3.- Comparison between measured and theoretical values for effective electron-neutral collision frequency for momentum transfer.

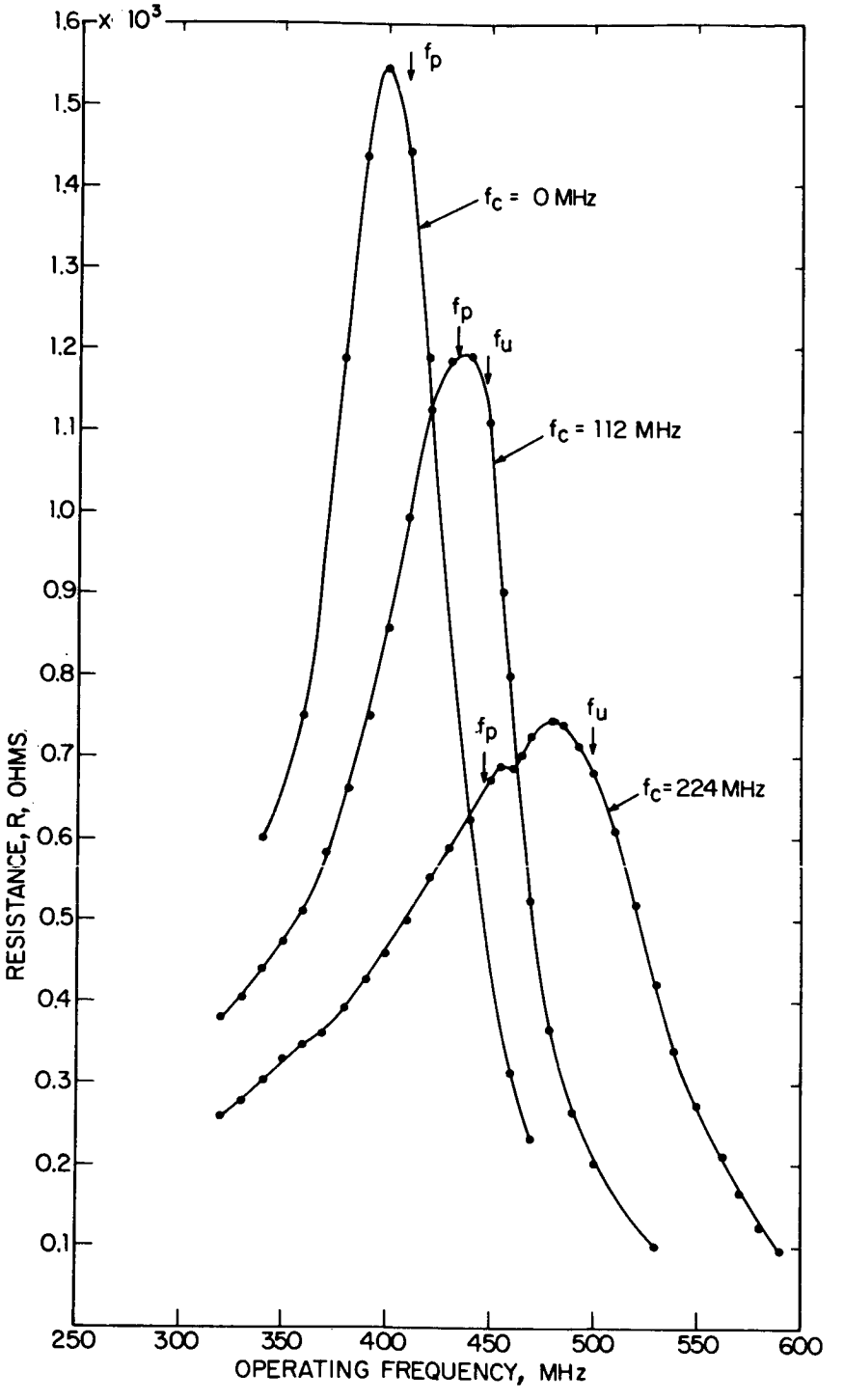

Figure 4.- Resistance of dipole antenna in a magnetoplasma. Experimental results; gas, helium; neutral gas pressure, 110μ Hg.

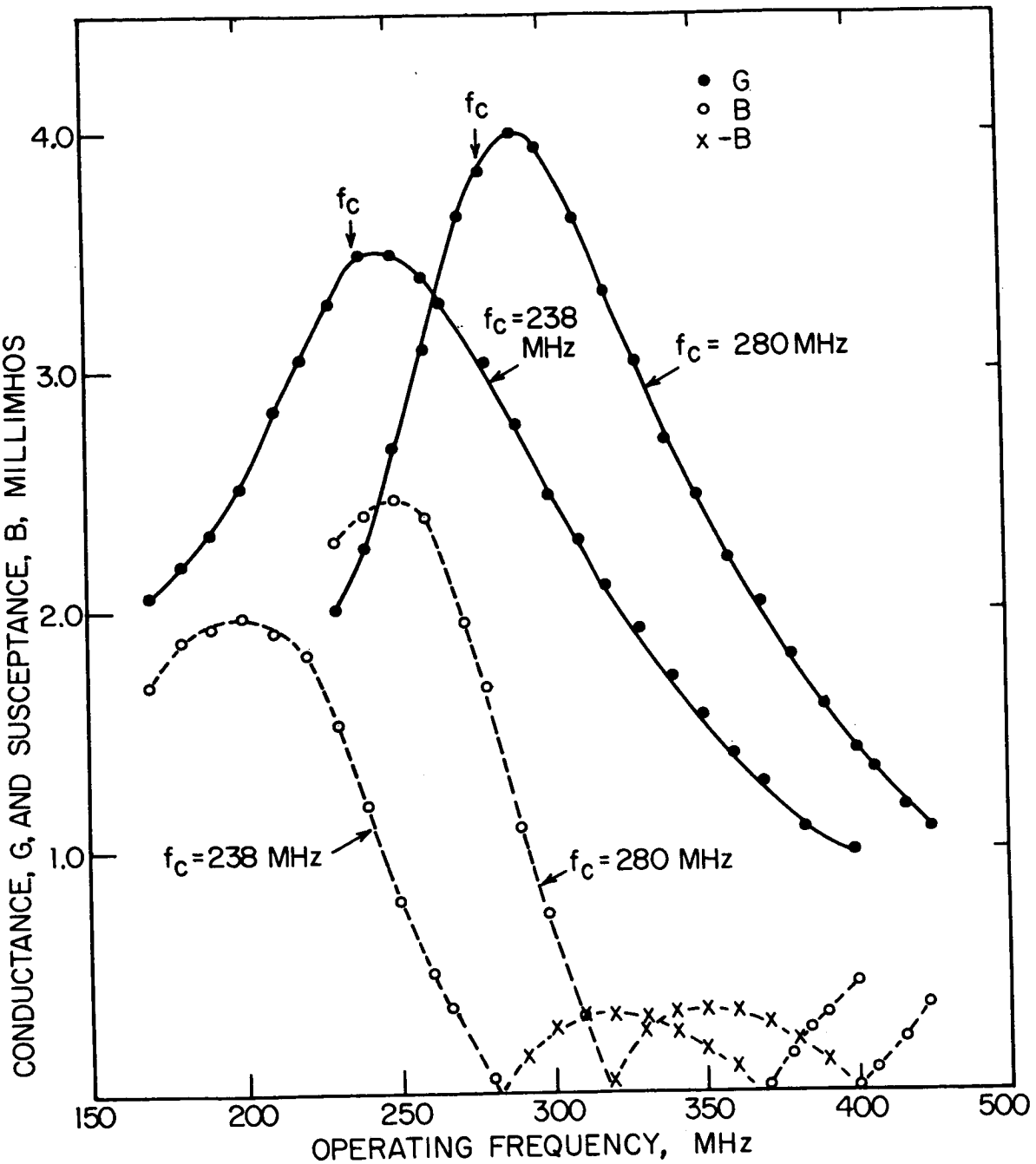

Figure 5.- Admittance of dipole antenna in a magnetoplasma in the vicinity of cyclotron resonance. Experimental results; gas, helium; neutral gas pressure, 110μ Hg.

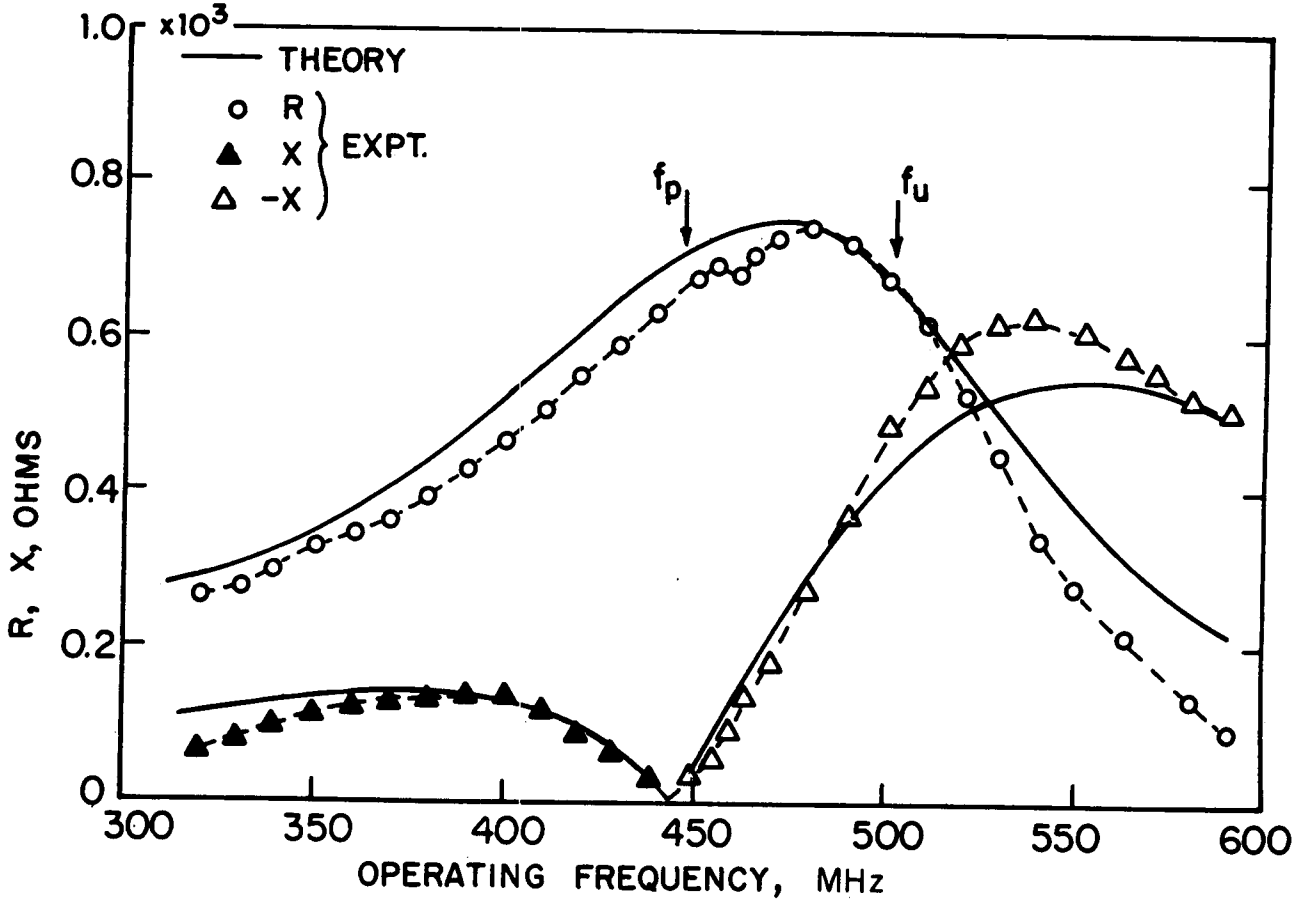

Figure 6.- Comparison of theoretical (Balmain) and experimental results for the impedance of dipole antenna in a magnetoplasma. Gas, helium; gas pressure, 110μ Hg; cyclotron frequency, 224 MHz; measured collision frequency, 9.2×10^8 sec^{-1}.

THE USE OF ELECTROACOUSTIC RESONANCES TO DETERMINE ELECTRON DENSITY PROFILES[†]

By A. W. Baird III and C. D. Lustig

Sperry Rand Research Center, Sudbury, Massachusetts

SUMMARY

A technique is described for deducing an unknown electron density profile from observed electroacoustic resonance frequencies, which uses a simple resonance condition derived from the WKB approximation. The density profile is approximated by a step model, piecewise-linear model, modified piecewise-linear model and polynomial model in both active and afterglow plasmas. Good agreement is obtained between the profile determined by this technique and one obtained theoretically by Parker, Nickel and Gould. (See ref. 1.) The method is applicable to the determination of reentry electron density profiles where at least the first- and second-order resonances can be observed.

INTRODUCTION

Electroacoustic resonance has been observed (refs. 2 and 3) during the reentry of Trailblazer II vehicles flown in 1967 and 1969. From these measurements it was possible to deduce a value for the electron density gradient close to the vehicle surface. However, since only one resonance was detected, only a linear approximation to the density profile was obtained. In this paper we examine the methods by which the electron density profile, assumed not to be linear, can be calculated when conditions are suitable for the observation of higher order electroacoustic resonances.

DISCUSSION

Electroacoustic waves are excited in a reentry plasma sheath by a coaxial antenna mounted flush with the vehicle surface. The waves propagate in the underdense region of the plasma and are reflected when the local plasma frequency ω_p equals the wave frequency ω. Resonance occurs when standing electroacoustic waves are set up between the reflecting layer and the surface of the vehicle.

[†] Work supported by the Air Force Cambridge Research Laboratories under Contract No. F19628-70-C-0092.

Good agreement has been obtained between observed and calculated electroacoustic resonance frequencies for plasmas in which the electron density gradient can be calculated (ref. 1). This involved the use of the first two moments of the Vlasov equation together with the quasistatic approximation of Poisson's equation. These equations were combined into a fourth-order ordinary differential equation, and solutions were obtained numerically on a computer. For the problem of deducing an unknown electron density from observed resonance frequencies, we have used the simpler resonance condition, derived from the WKB approximation, as follows.

$$\left(m-\frac{1}{4}\right)\pi = \int_0^{x_{T_m}} \left[\frac{\omega_m^2 - \omega_p^2(x)}{3v_T^2}\right]^{\frac{1}{2}} dx \qquad (1)$$

$$m = 1, 2, 3, \ldots$$

v_T is the thermal velocity, $(kT_e/m)^{1/2}$. Integration starts at the edge of the plasma $(x=0)$, and x_T is the point at which $\omega_p(x) = \omega$.

If the density profile is assumed to be linear, so that $\omega_p^2(x) = Ax$, then from equation (1) the coefficient A can be determined by

$$A = \frac{2\omega_m}{3\sqrt{3}\pi\left(m-\frac{1}{4}\right)v_T} \qquad (2)$$

For a linear profile, $\omega_m/(m-1/4)$ should be constant. However, this condition is not satisfied in laboratory plasmas, indicating a considerable departure from linearity.

We have determined electron density profiles, including departures from linearity, from measurements of high-order (up to $m=5$) electroacoustic resonances in laboratory plasmas. It is not possible to solve analytically for $\omega_p^2(x)$, so it is necessary to approximate it by a general function which will describe the profile when the appropriate coefficients are used in the function.

The simplest way to describe the profile is to let $\omega_{p_n}^2(x) = \omega_{n-1}^2$ for $L_{n-1} < x < L_n$, where the different L's are to be determined from equation (1). The result of this approach is a step-like profile, with a step for each measured resonance frequency.

An improvement to the step-like model is the piecewise-linear approximation:

$$\omega_{p_n}^2(x) = \left(\frac{\omega_n^2 - \omega_{n-1}^2}{L_n - L_{n-1}}\right) x + \frac{\omega_{n-1}^2 L_n - \omega_n^2 L_{n-1}}{L_n - L_{n-1}} \qquad (3)$$

$$\text{for } L_{n-1} \le x \le L_n \ , \ \omega_0 = 0 \ , \ L_0 = 0 \ .$$

L_n is the distance into the plasma for which $\omega_{p_n}^2(L_n) = \omega_n^2$, and represents the penetration into the plasma of the resonance of order n at a frequency ω_n . It can be shown that if the density profile is given by equation (3), then equation (1) can be written as

$$\left(m - \frac{1}{4}\right)\pi = \frac{2}{3\sqrt{3}\, v_T} \sum_{n=1}^{m} \left(\frac{L_n - L_{n-1}}{\omega_n^2 - \omega_{n-1}^2}\right) \left\{ \left(\omega_m^2 - \omega_{n-1}^2\right)^{\frac{3}{2}} - \left(\omega_m^2 - \omega_n^2\right)^{\frac{3}{2}} \right\} \qquad (4)$$

and solved for L_m .

A further refinement is to represent $\omega_p^2(x)$ as an nth order polynomial where the first n resonance frequencies are known. In theory it should be possible to determine the coefficients of the polynomial by solving for them in equation (1) since there would be a system of n equations and n unknowns. Unfortunately, there is no known analytic solution for equation (1) when n is greater than two, so the problem must be solved by numerical methods. The system of equations for the nth order polynomial has been coded and run on a digital computer, using a root-finder program to determine the values of the coefficients.

Both the piecewise-linear approximation and the polynomial solution have been used to describe the profile of a neon afterglow plasma in which the first five electroacoustic resonance frequencies were obtained. The results of the calculations are shown in figure 1. It can be seen that the piecewise-linear model is a good approximation to the computed polynomial profile. All of these solutions are very near to the wall, extending into the plasma only 0.035 cm, whereas the plasma column had a 0.525 cm radius. A microwave cavity was used to measure the average density of the plasma at the same time in the afterglow that the resonance data were obtained. The value of $\langle \omega_{p_0}^2 \rangle$ was found to be 2.35×10^{20} . If the usual

$J_0\left(\frac{2.4x}{a}\right)$ profile is assumed, then it can be compared with the calculated profile. This is plotted in figure 1, and it can be seen that in this region, where $J_0\left(\frac{2.4x}{a}\right)$ is nearly linear, the plasma profile is significantly different from the normally assumed J_0 profile.

The electroacoustic resonance method has also been used to measure the electron density profile in an active discharge in which the electron density, electron collision frequency and electron temperature closely approximate those in a high-altitude reentry plasma. The plasma was generated in an annular inverse brush cathode discharge in neon. The average electron density is of the order of 10^{11} electrons/cm^3, with an electron temperature of about 0.5 eV and an electron collision frequency of roughly 5×10^7/second.

When the piecewise-linear model was used to describe this electron density profile, no solution was found. This is because the density is low out to 0.02 cm and then increases very rapidly. Consequently, the piecewise-linear model is a poor approximation in this case and was modified to include a step for the first resonance and a continuation of the piecewise-linear model for the remainder of the profile.

It was also found that an nth order polynomial would not adequately describe the profile for the active plasma beyond the third resonance, so that it was necessary to break the profile into two regions and use a different polynomial to describe each region.

Figure 2 shows the profile as determined by the first two resonance frequencies for an active discharge for the step-like model, modified piecewise-linear model, and polynomial. For this particular plasma, x^5 is a good approximation to the profile, which explains why the piecewise-linear model would not work near the wall since it varies only as x. It should be noted that this profile extends almost three times as far into the plasma at the second resonance as did the afterglow plasma profile in figure 1; this is because the temperature is about ten times higher in the active plasma.

To check the validity of this method of determining a density profile, we have used the data of Parker, Nickel, and Gould (ref. 1). In their paper, the density profile was obtained theoretically by solving numerically the problem formulated by Tonks and Langmuir for a plasma composed of a Maxwellian electron gas contained by its radial electric field, and ions which are generated with zero velocity at a rate proportional to the local electron density and fall freely to the walls under the influence of the radial electric field. This profile was incorporated in a theory to predict the frequency at which an electroacoustic resonance would occur for a given electron temperature, density and tube radius. There was excellent agreement between theory and experiment.

By using the resonance data of Parker, Nickel, and Gould (ref. 1), the electron density profile determined by our technique should be similar to the calculated one. This comparison has been made using the piecewise-linear approximation and measured resonance frequencies taken from figure 4 of Parker, Nickel, and Gould. Figure 3 shows the profile determined in this way, together with the theoretical profile for a 3 eV mercury discharge in a 0.5 cm radius tube for $r_w^2/\lambda_d^2 = 4.5 \times 10^3$. Figure 3 shows good agreement between the two profiles.

CONCLUDING REMARKS

Measurement of high order electroacoustic resonances in a reentry sheath would yield detailed information on the electron density profile close to the vehicle surface. In this paper we have outlined the mathematical methods by which profiles can be calculated from observed resonance frequencies. Figure 3 shows that good approximation to the profile is obtained even if only two resonance frequencies are known.

REFERENCES

1. Parker, J. V., Nickel, J. C., and Gould, R. W.: Resonance Oscillations in a Hot Nonuniform Plasma. Phys. Fluids 7, 1489, 1964.

2. Poirier, J. L., Rotman, W., Hayes, D. T. and Lennon, J. F.: Effect of the Reentry Plasma Sheath on Microwave Antenna Performance; Trailblazer II Rocket Results of 18 June 1967. AFCRL Report 69-0354, August 1969.

3. Maloney, L. R.: Trailblazer II Reentry Communications Program. 19th Annual Symposium on USAF Antenna Research and Development, University of Illinois, October 14-16, 1969.

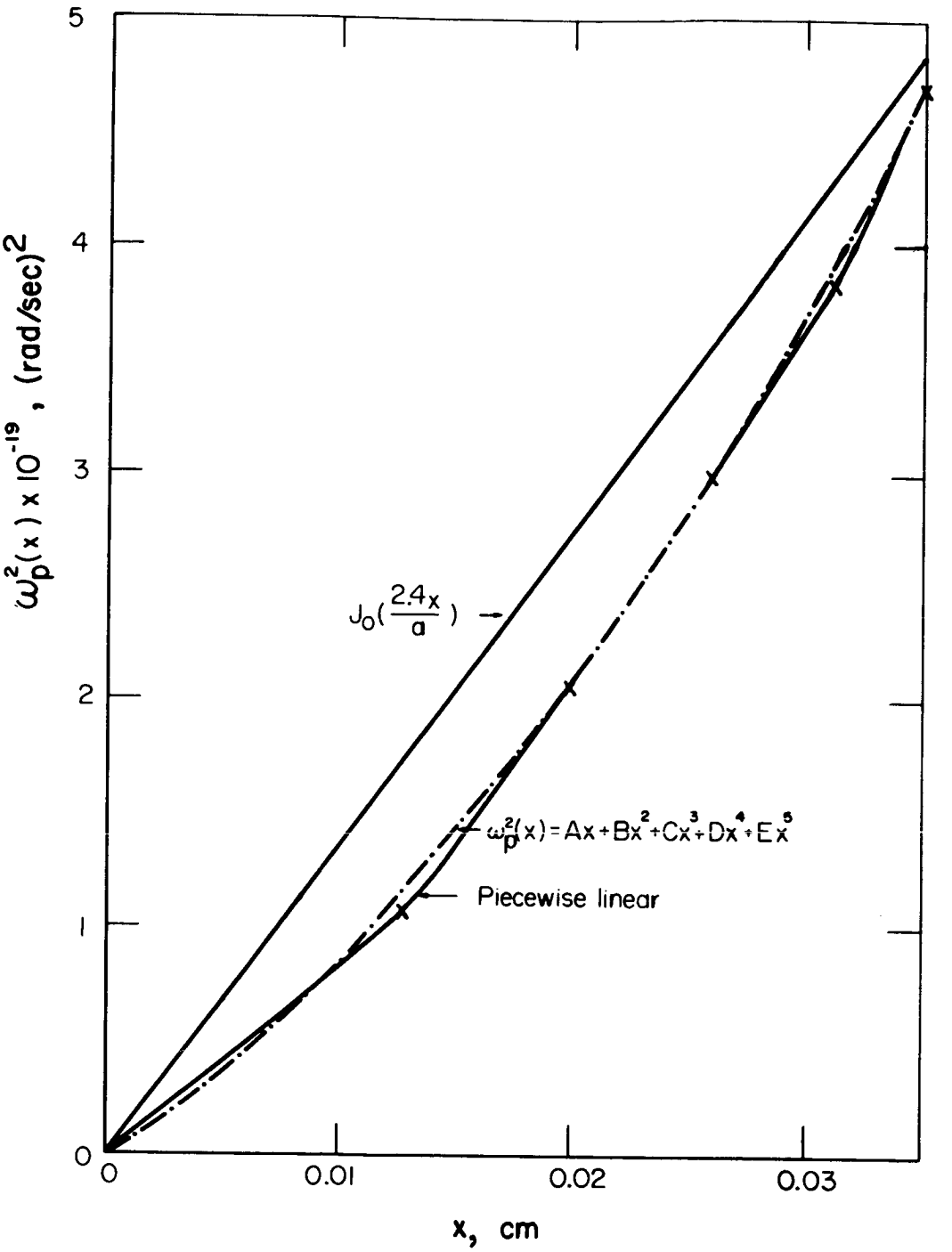

Figure 1.- Density profile as a function of distance from wall for piecewise-linear, fifth-order polynomial, and J_0 profile models in afterglow plasma from measurement of five electroacoustic resonances.

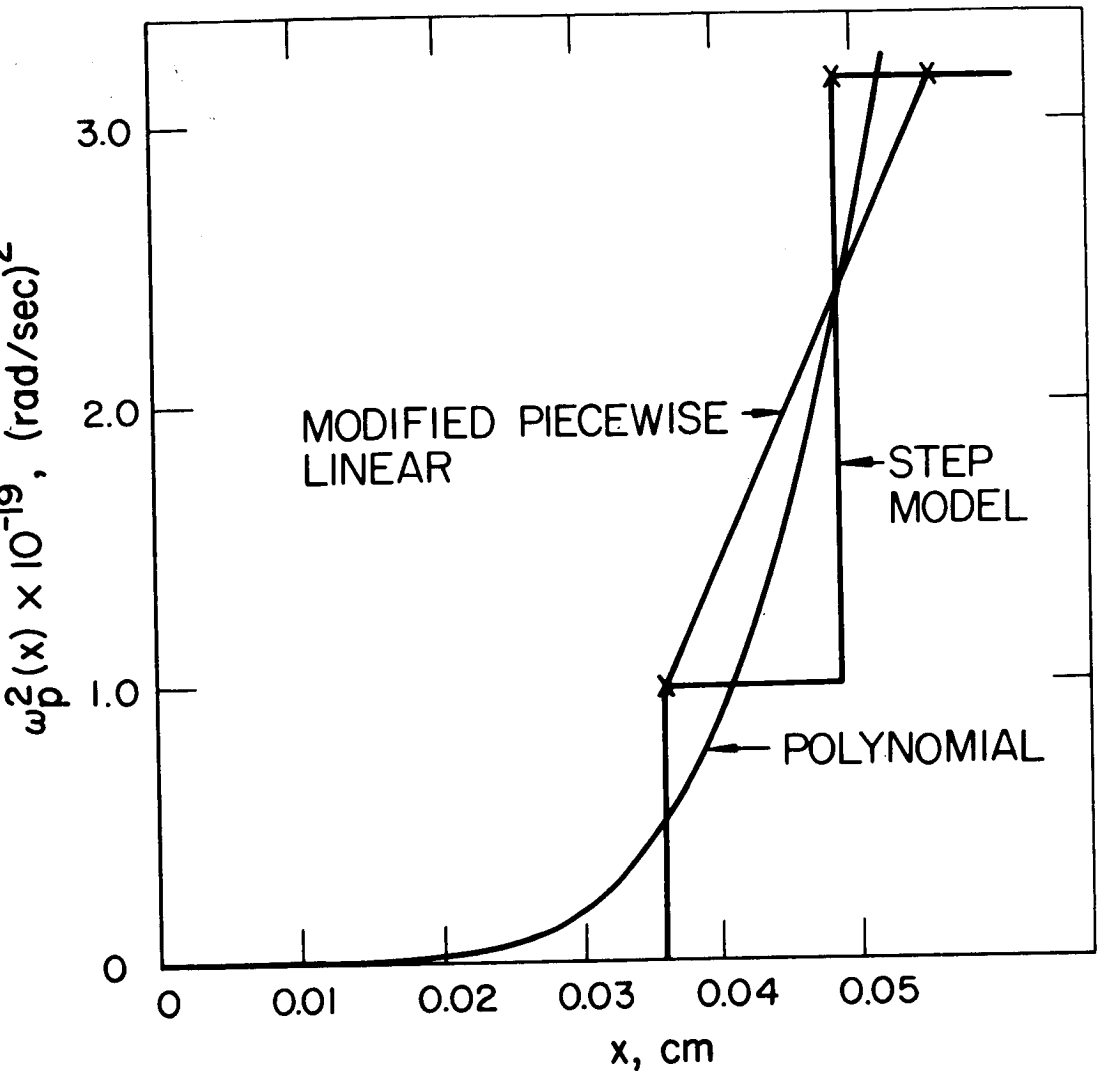

Figure 2.- Density profile as a function of distance from wall for step, modified piecewise-linear, and polynomial model in active plasma for measurement of two electroacoustic resonances.

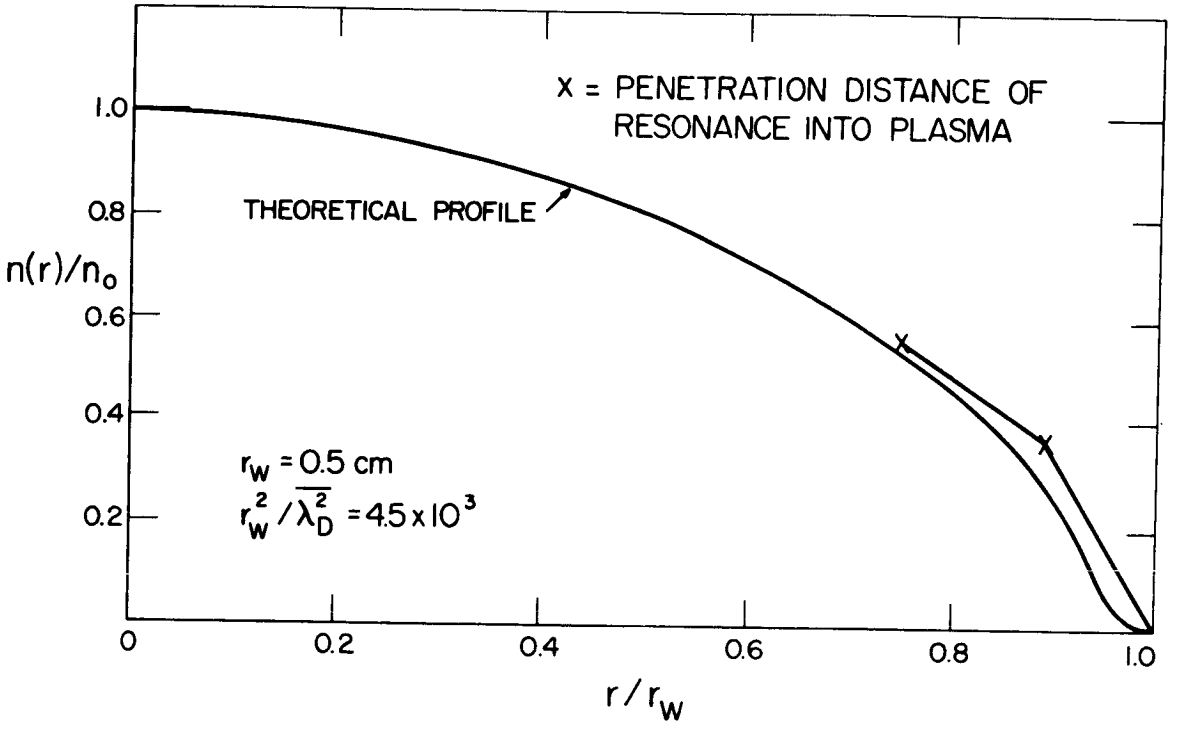

Figure 3.- Comparison of profile determined with piecewise-linear approximation for two resonance frequencies with theoretical profile for 3-eV mercury discharge (from data in ref. 1).

REENTRY PLASMA MEASUREMENTS USING A FOUR-FREQUENCY REFLECTOMETER

By William L. Grantham
NASA Langley Research Center

SUMMARY

The results of a reentry plasma diagnostic experiment made at 25 000 ft/sec are presented for comparison with theoretical flow-field values. Flow-field plasma properties were inferred by use of a four-frequency microwave reflectometer having an electron density measurement range from approximately 10^{10} to 10^{13} electrons/cm^3. The reflectometer technique uses the sharp rise of reflection coefficient to indicate when the plasma approaches critical density. Good correlation exists between the reflectometer-determined plasma values and those derived from electrostatic probes in the aft flow field.

A simple spacecraft shape (hemisphere-cone) was used to minimize the difficulty of flow-field calculations. Also, to render the flow field free of influencing ablation products, a heat-sink beryllium nose cap was employed. The cap was pyrotechnically ejected at 185 000 feet, as its temperature approached the melting point of beryllium; thus, the primary data period (clean flow-field period) ended. During the remainder of the flight a teflon nose cap was used. Measured and computed plasma electron densities presented by Schexnayder, Evans, and Huber in NASA SP-252 generally agree in the primary data period; however, some deviation is noted above 230 000 feet. In the aft region a substantial electron density level difference is indicated at high altitudes and is attributed to ambipolar diffusion mechanisms not included in the theoretical flow-field model. Plasma standoff distance measurements indicate strong electron density gradients near the vehicle surface as expected from sheath calculations.

At altitudes below about 100 000 feet, the interpretation of reflectometer data becomes more difficult because of the high electron-neutral collision frequency and the changes in antenna length caused by heat-shield ablation. The interpretation problems in the low-altitude region make the comparison of measured and computed electron density less meaningful. It is believed, however, that measurement errors in the aft flow field greater than a factor of 3 or 4 are unreasonable. Even with this factor of 3 or 4 error in the measured value, there still remains a factor of 10 difference between measured and computed densities.

INTRODUCTION

A spacecraft reentering the earth's atmosphere is enveloped by a plasma sheath which can cause radio blackout. Accurate definition of the plasma-sheath

properties is, therefore, important for determining radio blackout boundaries and for designing blackout alleviation systems.

Several in-flight plasma-sheath measurements have been made in order to upgrade the theoretical plasma model where necessary and to improve confidence in the model. References 1 and 2 describe electron density measurements made at 18 000 ft/sec velocity, which were compared with calculations. A favorable comparison was obtained except at the higher altitudes (above 200 000 ft) where theoretical values were a factor of 2 greater than measured electron densities.

References 3 and 4 describe ion density measurements made with electrostatic probes at 25 000 ft/sec which indicated that at high altitudes the aft plasma layer was much thicker and had a lower ion density than was expected.

Calculation of aft plasma profiles requires a knowledge not only of the local chemical kinetics but of the entire gas history from the shock entry point of each streamline to the aft point of interest. This experiment was designed to improve knowledge of the flow field in both the nose and the aft regions. Data are presented for a reentry experiment on a spacecraft which had plasma sensors (microwave antennas) at four locations and was traveling at a velocity of 25 000 ft/sec.

The microwave reflectometer technique employed to diagnose the plasma uses the reflectivity of the plasma as an indication of the electron density level. The phase of the reflected wave was measured to infer the critical-density location in the nonhomogeneous plasma from which the general nature of the profile shape can be determined.

The use of a simple blunt-body spacecraft shape (hemisphere-cone) and a nonablation nose cap minimized the difficulty of theoretical calculations and provided a favorable environment for comparing measured and "clean air" computed values. Ejection of the nonablation nose cap at 185 000 feet ended the primary data period (clean flow-field period) and, for the remainder of the flight, an ablating teflon nose cap was used.

The data taken below 185 000 feet are of interest even though clean-air assumptions are no longer valid. Also at some point below this altitude, laminar-to-turbulent boundary-layer transition occurred and probably influenced the plasma. Interpretation of the reflectometer data becomes less accurate at the low altitudes because of high collision frequencies and recession of the microwave antennas. A comparison of reflectometer data with flow-field calculations presented by Schexnayder, Evans, and Huber in reference 5 shows general agreement in the primary data period; however, some deviation is noted above 230 000 feet. In the aft region a substantial electron density level difference is indicated at high altitudes and is attributed to ambipolar diffusion mechanisms not included in the theoretical flow-field model. Plasma standoff distance measurements indicate strong electron density gradients near the vehicle surface as expected from sheath calculations.

This flight experiment is the second in the "C" series of project RAM and is designated RAM C-II. The primary experiment for the C-I flight was a blackout alleviation test using water injection. (See ref. 3.)

SYMBOLS

D	nose diameter of payload
d	distance between antenna aperture and reflecting boundary, cm
ΔdB	diode level relative to value when $\Gamma_p = 0$, dB
f	electromagnetic frequency, Hz
N_e	electron density, electrons/cm^3
x	distance along spacecraft axis
Γ	reflection coefficient at aperture
θ	phase shift of reflected wave, deg
λ	wavelength, cm
ν	electron-neutral collision frequency, collisions/sec
ρ	voltage reflection coefficient at probe unit
ϕ	angular coordinate for payload, deg
ω	electromagnetic frequency, rad/sec

Subscripts:

cr	critical
d	distance
m	measured
o	free space
p	power
pk	peak
r	reflecting boundary
sc	short circuit

DESCRIPTION OF VEHICLE AND PAYLOAD

Vehicle

A four-stage solid-propellant Scout vehicle was used to place the payload on the desired reentry trajectory. The launch was made from Wallops Island, Virginia, and reentry occurred near Bermuda, where tracking and telemetry stations were located. (See fig. 1.)

During the ascending phase of the flight, a heat shield protected the payload from aerodynamic heating. This heat shield was jettisoned at 724 000 feet. The first two stages of the Scout were used to achieve an apogee of about 747 000 feet. Just before apogee the vehicle was oriented to -15° entry angle and the third stage was ignited. As a result, the payload was driven back into the earth's atmosphere with a velocity of 24 900 ft/sec at fourth-stage burnout. Further acceleration of the payload due to gravity raised the velocity to a maximum of 25 190 ft/sec.

Payload spinup was initiated just prior to fourth-stage ignition to maintain small angles of attack during fourth-stage thrusting and the reentry period. This spin also allowed the electron density sensors to alternately monitor windward and leeward plasma conditions about every 166 msec. Retromotors separated the fourth stage from the payload at about 350 000 feet altitude.

Payload

The payload had a 6-inch-radius hemispherical nose with a 9° half-angle conical afterbody. (See fig. 2.) A heat-sink beryllium nose cap was used during the early part of the reentry period to maintain the flow field free of ablation products. Since the nose-cap temperature was expected to approach the melting point of beryllium at the low altitudes, the cap was ejected pyrotechnically at 185 000 feet. A teflon hemispherical nose $\left(1\frac{1}{2}\right.$ inches thick and 6.325 inches in radius$\left.\right)$ was used for the remainder of the flight. A photograph of the flight backup payload in this configuration is shown in figure 3. The payload conical section had a 0.3-inch-thick teflon heat shield.

Special attention was given to minimizing the alkali metal content in the teflon ablator material. Raw-material selection and heat-shield fabrication were controlled to keep the easily ionizable material out of the teflon and, thus, out of the flow field during reentry. A neutron activation technique was used to measure the quantities of sodium, potassium, rubidium and cesium in the teflon and showed the heat shield to have less than 5 ppm total alkali metal content.

Four frequencies were used in the reflectometer system at L-, S-, X-, and K_a-bands. The exact frequencies used are listed in table I. Components of each of the reflectometer systems used in the flight experiment consisted of a

microwave signal source, an isolator, a four-way power divider (three-way for L-band) to split the signal so that several antennas could be used for the same frequency, bidirectional couplers on each of the four lines to measure transmitted and reflected power levels, a unit with four electric field probes spaced at about $\frac{1}{8}$-wavelength intervals on each line to measure the phase and magnitude of the wave reflected by the plasma, and antennas to launch the electromagnetic wave into the plasma. The K_a-band had only two probes each at stations 2, 3, and 4. A dc-to-dc converter was used to drive the microwave tubes from a 28-volt battery supply.

A block diagram of a typical reflectometer (S-band) is shown in figure 4, and figure 5 is a photograph of the individual components for the four frequencies used. Only one antenna (station 3 type) and probe unit is shown for each frequency in the photograph.

All rf components were interconnected with 0.141-inch semirigid coaxial cable at L-, S-, and X-bands. A flexible waveguide was used at the K_a-band. Strip transmission line components were used for the three lower frequencies, and a rigid waveguide was used for the K_a-band.

Reflectometer antennas were located at four stations along the spacecraft (table II) so that a detailed study of the fore and aft plasma regions could be made. At station 1 (x/D = 0.15) on the hemisphere nose, circular waveguides (TE_{11} mode) were brought through the teflon nose by using thin (1 to 10 microns thick) metallic sleeves as waveguide walls to feed the quartz-filled circular antennas in the beryllium cap. All four stations had an antenna for each of the four frequencies except station 1, which did not have an L-band antenna because of lack of space. This gave a total of 15 reflectometer antennas on the payload. Stub tuners were used to tune out VSWR's introduced by the dielectric plugs and aperture mismatch. Details concerning the antenna design are given in reference 6.

REFLECTOMETER MEASUREMENT TECHNIQUE

Reflection Magnitude and Phase Coefficient

Reflection coefficients were obtained by use of the bidirectional coupler diode outputs, and phase coefficients were derived by use of diode outputs from the electric-field-probe units. (See fig. 4.) Diodes in these components were calibrated, and voltage divide networks were used in the flight payload to adjust the diode outputs to about 40 mV for telemetry purposes. Temperatures were monitored on each component having diodes so that calibration adjustments could be made if necessary. No adjustments were needed, however, since the temperature changes during flight were less than 3° F.

Preflight reference levels were obtained by shorting the antennas with a reflecting foil. The level of coupler output compared with the preflight

levels expressed in decibels (ΔdB) was used to compute the power reflection coefficient Γ_p from the equation $\Gamma_p = 10^{-\Delta dB/10}$. Corrections were made for any changes in forward power between the preflight level and the level at the time of interest. These corrections were generally less than 0.1 decibel. Phase coefficients were determined from the four probes by use of a least squares curve fitting program to fit the data to a standing-wave curve. When probe data were restricted to less than three probe levels, the phase was computed from the standing-wave equation by use of the probe levels and the reflection coefficient measured by the coupler. Details concerning the technique and accuracy of reflection and phase coefficient measurements are given in reference 6.

Electron Density

The microwave reflection coefficient has been used for some time to indicate plasma electron density. (See refs. 7 and 8.) The technique described in this paper uses the sharp rise of reflection coefficient (hereafter called the slope technique) to indicate when the peak plasma electron density approaches the critical value $\left(N_{e,cr} = \left(1.237 \times 10^{-8}\right) f^2\right)$ in the dynamically changing reentry plasma. A three-decade measurement range from approximately 10^{10} to 10^{13} was obtained by use of four different microwave frequencies. Figure 6 shows this measurement principle applied to the station 2 reflectometer data. A reflection coefficient of 20 percent is used to indicate the peak-to-critical electron density ratio $\left(N_{e,pk}/N_{e,cr}\right)$ of 0.63 to give a minimum electron density error. (See ref. 6.) By fairing between the data points, an estimate can be made of the ionization history throughout the reentry period for each station on the payload. Data indicated by the open symbols (fig. 6) at the low altitudes are subject to inaccuracy due to high collision frequencies and antenna length changes caused by ablation. By using the slope technique, electron density measurement accuracy is less dependent on the absolute magnitude of the reflection coefficient. A normalized collision frequency (ν/ω) value of less than 0.4 is required to have a sharp increase of reflection near critical density. This requirement is satisfied during the primary data period (down to 185 000 ft). At lower altitudes, collision frequency effects tend to decrease the sharpness and, thus, the accuracy of the measurement.

The reflectometer technique is clearly dependent on the sharp rise of reflection near the critical density, which is predicted by plane-wave theory and by recent theoretical formulations that more correctly determine impedance values for plasma-clad antennas (refs. 9 and 10). Experimentally, this sharp rise has been observed under a variety of aperture-plasma conditions (refs. 10 and 11) including two of the three flight antenna designs used in this experiment (ref. 12), specifically, an open-ended circular guide and a conical horn. The L-band rectangular aperture design was not tested.

Although the flight antennas are different in some respects from those having theoretical solution, the shock-tube experimental results presented in

references 12 and 13 show that the differences do not alter the sharp rise of reflection level near critical density (figs. 7(a) and 7(c)). A comparison is shown in figure 7 between the shock-tube data and theoretical values for the plasma-covered circular apertures. (Changes have been made in the circular aperture model (ref. 9) by Dr. John Q. Howell of the Langley Research Center to include matching of the antennas to free space as they were in the shock-tube and flight experiments.) Comparable plane-wave values (ref. 14) are also shown for the same nonhomogeneous profile for reference purposes. Electron densities derived from the mean reflection coefficient curve fall within about 50 percent of those derived from the circular-aperture theoretical curves for reflection levels below 0.5. Possible reasons for the deviations above 0.5 are discussed in reference 13. Also, the slopes of the individual curves coincide with the theoretical slope except for a systematic lateral displacement along the electron density axis. The lateral displacement between individual runs is attributed to errors in shock-tube electron density values derived from the Langmuir probes.

The close agreement between the theoretical and experimental reflection coefficient values shows the applicability of the circular-aperture theoretical model to that particular antenna design. The effect of high collision frequencies for the X-band aperture is shown in figure 8. The two lower collision frequencies 2.51×10^9 and 2.5×10^{10} are typical for altitudes of 150 000 and 100 000 feet, respectively, for stations 2, 3, and 4. The third collision frequency 2.51×10^{11} is typical for station 1 at 100 000 feet. Interpretation of the low-altitude reflectometer data should be made considering the effect of finite collision frequency. In this report the low collision case is assumed.

Plasma Standoff Distance

In addition to determining electron density from reflectometer data, the phase measurements can be used to infer the nature of the plasma profile shape. Specifically, normal distance from the vehicle surface to the critical density boundary can be determined if the plasma is overdense $\left(\frac{N_{e,pk}}{N_{e,cr}} \geq 10\right)$ and if the reflection coefficient is large enough to permit an accurate phase measurement. Plane-wave concepts are used to develop a simple approximate model for interpreting the phase in terms of this plasma standoff distance. This simple model will be shown to be a reasonable approximation to the more sophisticated circular-aperture theoretical model.

From a plane-wave point of view, the phase coefficient can be considered to be the sum of two phases $(\theta = \theta_d + \theta_r)$: θ_d, the phase shift experienced by a wave of wavelength λ_o in propagating a distance 2d from the antenna to the reflecting boundary and back, $\theta_d = \frac{360(2d)}{\lambda_o}$ degrees; and θ_r, the phase shift at the reflecting boundary. In solving for reflector distance

$d = \left(\theta - \theta_r\right)\frac{\lambda_o}{720}$, it can be seen that d and θ are linearly related. Phase measurements made on the X-band flight-type conical horn and S-band open-ended guide antenna verify this linear dependence for a metal sheet reflector which simulates an overdense plasma. Measurements with teflon slab reflectors $\left(\Gamma_p < 1.0\right)$ also show that the linear dependence is not controlled by the reflection coefficient level. (See fig. 9.) Another important feature shown by figure 9 is that the measured phase deviates from the normal pattern when the external reflection level is near or below the system residual reflection level (Region A).

In the plasma case, θ_r is primarily a function of N_e and asymptotically approaches 180° for $N_{e,pk}/N_{e,cr} > 10$. For that overdense condition, θ_r can be set at 180°. The overdense condition exists for a given frequency during the flight if the next higher frequency is being reflected, since any two adjacent critical densities are different by about a factor of 10.

Interpretation of the flight phase measurements are made in terms of normal critical-density standoff distances by use of the equation $d = \theta_m \frac{\lambda_o}{720}$ where the measured phases θ_m are made relative to the preflight phase values determined for the short-circuited antenna $\left(\theta_{r,sc} = 180^\circ\right)$. Collision frequency effects have a minimum influence on phase values. (See fig. 8(b).)

FLIGHT DATA AND DISCUSSION

All payload systems operated satisfactorily during the reentry experiment. Telemetry signals were reacquired as the payload emerged from radio blackout and the reentry heat pulse. X-band telemetry reacquisition was delayed because of tracking difficulties caused by its narrow-beam receiving antenna at Bermuda. The flight trajectory determined from Bermuda radar and payload instrumentation is shown in figures 10 and 11 and table III. Continuous tracking of the payload was achieved from radar horizon through apogee down to 185 000 feet. Apparently, the radar tracked the ejected beryllium cap below that altitude. Computation of the trajectory below this altitude was determined from payload instrumentation data. Payload accelerometer data indicated that the angle of attack was less than 6° during the reentry period. (See fig. 12.) Because of low accelerometer levels at the high altitudes, absolute values of angle of attack are less accurate. Relative changes, however, should be correct.

Reflection Coefficient Data

Microwave reflection and phase coefficient data taken from the commutated telemetry channels are shown in figures 13 and 14 for the reentry data period.

The reflection values presented, phase and magnitude, are relative to preflight levels measured when a short circuit (aluminum foil) was placed over each antenna except as noted in figure 13(a). The foil was assumed to have a reflection coefficient of 1.0 and a phase coefficient of 180°.

The reflection coefficient data for the most forward body location (fig. 13(a), x/D = 0.15) have several features that are important to note. First, ejection of the beryllium cap is clearly indicated by the K_a-band reflection change at 185 000 feet. This was the only antenna badly mismatched when the cap was removed. Because of the mismatch and antenna losses, the reference level was used as noted. Before lift-off, each station 1 antenna was matched to free space with the beryllium cap on. No mismatch effects due to cap removal are noticeable at S- and X-bands, which have already experienced plasma reflection at about 277 000 feet and 264 000 feet, respectively. A sharp change was observed in the phase coefficients (fig. 14(a)) due to the change in electrical length of the antenna when the cap was ejected.

The K_a-band sensor at station 1 did detect critical density at about 236 000 feet, but because the plasma was offset from the vehicle surface, the reflection coefficient was low and the coupler was unable to detect the weak signal. Therefore, the more sensitive probe levels were used to indicate the presence of critical density. Very slight variation of reflecting boundary distance in the windward and leeward plasmas caused the phase to change; thus, the standing-wave envelope was shifted back and forth across the stationary probes. The resulting probe level modulations (approximately 1 dB) were used to indicate when the plasma became reflecting.

At very low altitudes (below about 110 000 ft) plasma density decreased and the reflection coefficients dropped off. Thickness changes in the teflon ablation cover caused the reflection level to oscillate from maximum to minimum for every quarter-wavelength change in teflon thickness. More oscillations are seen on the K_a-band record since it has the shortest wavelength. The heavy ablation period is identified on the abscissa.

Measurements at station 1 just before and after cap ejection gave a unique opportunity to determine the electron density for a reentry body with a hot wall surface and, a fraction of a second later, with a cold wall. Close examination of the reflectometer data reveals no significant difference in reflection phase or magnitude before and after cap ejection except for those caused by the antenna length change.

Electron densities derived from the reflection coefficient data by use of the 20-percent criterion already discussed are given in figure 15 and table IV. The low collision case is assumed.

At station 2 just aft of the tangency point, the reflection data (fig. 13(b)) show characteristics similar to those at station 1. The L-band data are included here. Two points of interest are that after the onset of plasma reflection, the S- and X-band data show rapid oscillations in the 125 000-foot altitude region where the angle of attack was large (fig. 12). This type of modulation has been observed on other spinning reentry payloads

and is due to the impedance change experienced by the antenna when it exposed to the windward and leeward plasmas. Enlargements of figure 13 are given in reference 6 to show fine structure of the data. A detailed analysis of these rapid oscillations and the very slow L- and S-band level changes during their overdense periods requires further study. It is evident, however, that the aft plasma is undergoing major changes in the 125 000-foot altitude region. The VHF signal strengths recorded at USNS Range Recoverer (fig. 16) show increases above noise level during the "blackout" period, particularly at the time of beryllium-cap ejection and around 125 000 feet altitude, where angle of attack increased. All other receiving stations showed similar effects at VHF but to lesser degree. These signal strength modulations generally confirm reflectometer indications that the aft flow field is strongly affected by the relatively small spacecraft body motions. Electron densities derived from the station 2 reflectometer data (fig. 15(a)) indicated a maximum value slightly above 10^{13} at about 110 000 feet altitude.

Station 3 reflection data (fig. 13(c)) again show a very sharp rise for the L- and S-bands as the plasma exceeds their respective critical densities, but not for the X-band. This can be explained by assuming that the electron density increases steadily through L- and S-band critical density and then begins to plateau near X-band critical density. The plateau near 10^{12} electrons/cm^3 is evident in figure 15(b) for this body station. The most aft (station 4) X-band data show the same type of gradual rise in reflection coefficient. (See fig. 13(d).) Note that there is very little difference between the inferred densities at stations 3 and 4. (See fig. 15(b).) Ion densities derived from the electrostatic probe (ref. 4) in the aft flow field agree closely with station 4 reflectometer values. (See fig. 15(b).)

Station 4 reflection-coefficient data (fig. 13(d)) show strong reflection-coefficient oscillations again where angle of attack is large and show no residual reflection after plasma decay except at the K_a-band, since there is very little change in teflon heat-shield thickness (~0.1 inch).

The S-band level shifts in reflection coefficient at stations 3 and 4 (around 115 000 ft) are attributed to a significant change in profile shape possibly caused by laminar-to-turbulent boundary-layer transition, with ablation products in the thick (3 cm) boundary layer playing an important part. Thickening of the innermost subcritical plasma layer at the low altitudes is also shown by the phase data.

Phase Coefficient Data

The phase data (fig. 14) do not change as dramatically near critical density as does the reflection coefficient, but the afterbody phase values do show the same type of oscillations due to angle of attack. Phase measurements are accurate only when the power reflection coefficient (ρ^2) is above 0.1 at the four-probe units. Altitude and time regions where this condition exists are shown. Cases where less than four probes were used are identified on the figures. For any given station, the phase values approach the short-circuit value

as the plasma density becomes overdense for each frequency, as would be expected.

Measured phase coefficients have been used to determine distance between the spacecraft and the critical-density boundary for each of the body stations. (See fig. 17.) For good distance measurements, the phase coefficient must be accurate and the plasma should be at least a factor of 10 overdense so that θ_r approaches 180°. These conditions are satisfied for the data shown. At all stations the critical density is indicated to be near the spacecraft with larger separations occurring in the aft flow field. The measured profile shapes generally agree with those computed in references 15 and 16. The critical-density layer generally moves closer to the vehicle surface as electron density increases to its peak value, as would be expected. At the aft station 3, however, the S-band data at 115 000 feet altitude show a definite increase in critical-density distance. Note also that the reflection coefficient drops off (fig. 13(c)) for the S-band at that same station. It is clear from these data and from the decrease in the X-band reflection coefficient that the profile shape undergoes some major changes around 115 000 feet. The source of these changes is most likely related to laminar-to-turbulent boundary-layer transition and the presence of electrophilic ablation products (teflon).

Windward and leeward variations of standoff distance are evident in the aft plasma. (See figs. 17(c) and (d).) As might be expected, the nose-region (station 1, fig. 17(a)) measurements show no sensitivity to the angle-of-attack variations. Plasma calculations have not been made for angles of attack other than zero; therefore, a comparison of theoretical and measured values cannot be made.

Electrostatic probe measurements on both RAM C-I and C-II flight experiments also indicate strong electron density gradients near the vehicle surface and show the aft plasma thickness to be in excess of 7 cm. The reflectometer does not verify the entire profile shape measured by the probes, since it is sensitive only to the inner part of the profile. Attenuation effects due to absorption of the signal by the plasma and directivity of the antennas tend to mask the outer profile properties from the reflectometer-measured quantities.

CONCLUDING REMARKS

Reflectometer measurements have been made on a 25 000-ft/sec reentry payload from which plasma-sheath electron-density and critical-density standoff distances have been inferred. Measured electron density levels exceed 10^{13} electrons/cm^3 in the nose region and are around 10^{12} in the aft flow-field regions. In the aft region there are no strong electron density gradients along the body. Electrostatic probe measurements generally agree with reflectometer-inferred plasma properties at altitudes where both measurements were made.

REFERENCES

1. Grantham, William L.: Preliminary Analysis of Plasma-Sheath Electron Density Measurements at Energy Velocities. NASA TM X-1035, 1964.

2. Evans, John S.; and Schexnayder, Charles J., Jr.: Analysis of Theoretical and Experimental Electron Concentrations for RAM B3 Flight. NASA TM X-1412, 1967.

3. Akey, Norman D.; and Cross, Aubrey E. (With appendix A by Thomas G. Campbell; appendix B by Fred B. Beck; and appendix C by W. Linwood Jones, Jr.): Radio Blackout Alleviation and Plasma Diagnostic Results From a 25 000 Foot Per Second Blunt-Body Reentry. NASA TN D-5615, 1970.

4. Jones, W. Linwood, Jr.; and Cross, Aubrey E.: Electrostatic Probe Measurements of Plasma Surrounding Three 25 000 Foot Per Second Reentry Flight Experiments. The Entry Plasma Sheath and Its Effects on Space Vehicle Electromagnetic Systems - Vol. I, NASA SP-252, 1971, pp. 109-136.

5. Schexnayder, Charles J., Jr.; Evans, John S.; and Huber, Paul W.: Comparison of Theoretical and Experimental Electron Density for RAM C Flights. The Entry Plasma Sheath and Its Effects on Space Vehicle Electromagnetic Systems - Vol. I, NASA SP-252, 1971, pp. 277-303.

6. Grantham, William L.: Flight Results of a 25 000 Foot-Per-Second Reentry Experiment Using Microwave Reflectometers to Measure Plasma Electron Density and Standoff Distance. NASA TN 6062, 1970.

7. Anisimov, A. I.; Vinogradov, N. I.; Golant, V. E.; and Konstantinov, B. P.: Method of Investigating Electron Spatial Distribution in a Plasma. Sov. Phys. - Tech. Phys., vol. 5, no. 9, Mar. 1961, pp. 939-948.

8. Golant, V. E.: Microwave Plasma Diagnostic Techniques. Sov. Phys. - Tech. Phys. vol. 5, no. 11, May 1961, pp. 1197-1310.

9. Croswell, W. F.; and Bailey, M. C.: A Study of the Effect of Boundary Layer Plasma Profile Shapes Upon the Admittance of Aperture Antennas. 1968 International Antenna and Propagation Symposium, 68C 29AP, Inst. Elec. Electron. Eng., Inc., c.1968, pp. 39-45.

10. Croswell, William F.; Taylor, William C.; Swift, C. T.; and Cockrell, Capers R.: The Input Admittance of a Rectangular Waveguide-Fed Aperture Under an Inhomogeneous Plasma: Theory and Experiment. IEEE Trans. Antennas and Propagation, vol. AP-16, no. 4, July 1968, pp. 475-487.

11. Taylor, W. C.: Study of the Effects of a Plasma in the Near Zone Field of an Antenna. NASA CR-611, 1966.

12. Taylor, W. C.: Shock-Tube Measurement of Admittance of RAM C and RAM C-C Diagnostic Antennas. The Entry Plasma Sheath and Its Effects on Space Vehicle Electromagnetic Systems - Vol. I, NASA SP-252, 1971, pp. 157-182.

13. Taylor, W. C.: An Experimental Investigation of the Interaction of Plasma With Antennas. NASA CR-1727, 1970.

14. Swift, Calvin T.; and Evans, John S.: Generalized Treatment of Plane Electromagnetic Waves Passing Through an Isotropic Inhomogeneous Plasma Slab at Arbitrary Angles of Incidence. NASA TR R-172, 1963.

15. Webb, H., Jr.; Dresser, H.; Korkan, K.; and Raparelli, R.: Theoretical Flow Field Calculations for Project RAM. NASA CR-1308, 1969.

16. Huber, P. W.; Evans, J. S.; and Schexnayder, C. J.: Comparison of Theoretical and Flight-Measured Ionization in a Blunt Body Reentry Flow Field. AIAA Pap. No. 70-756, June-July 1970.

TABLE I.- RAM C-II RADIO-FREQUENCY SYSTEMS

Purpose	Frequency band	Antenna type	Antenna location		Power	Type ground plane
			x/D*	x, in. (cm)		
Real-time telemetry	VHF (259.7 MHz)	Array of circumferential slots	3.20	38.35 (97.41)	6.6 W (average)	Teflon covered
Delayed-time telemetry	VHF (225.7 MHz)	Array of circumferential slots	3.76	45.15 (114.68)	6.9 W (average)	
Real-time telemetry	X (9210 MHz)	Four rectangular horns	2.65	31.74 (80.62)	600 W (peak)	
Radar beacon	C (5800 MHz)	One rectangular horn	3.50	42.04 (106.78)	840 W (peak)	
Reflectometer experiment	†L (1116 MHz)	See table IV	0.15	1.76 (4.47) (Sta. 1)	≈75 mW (average)	See table IV
	S (3348 MHz)		.76	9.12 (23.16) (Sta. 2)		
	X (10 044 MHz)		2.30	27.58 (70.05) (Sta. 3)		
	K_a (35 000 MHz)		3.48	41.75 (106.04) (Sta. 4)		

†No L-band antenna at station 1.

*D = 12 in. (30.48 cm).

TABLE II.- ANTENNA AND ELECTROSTATIC PROBE LOCATIONS ON RAM C-II PAYLOAD

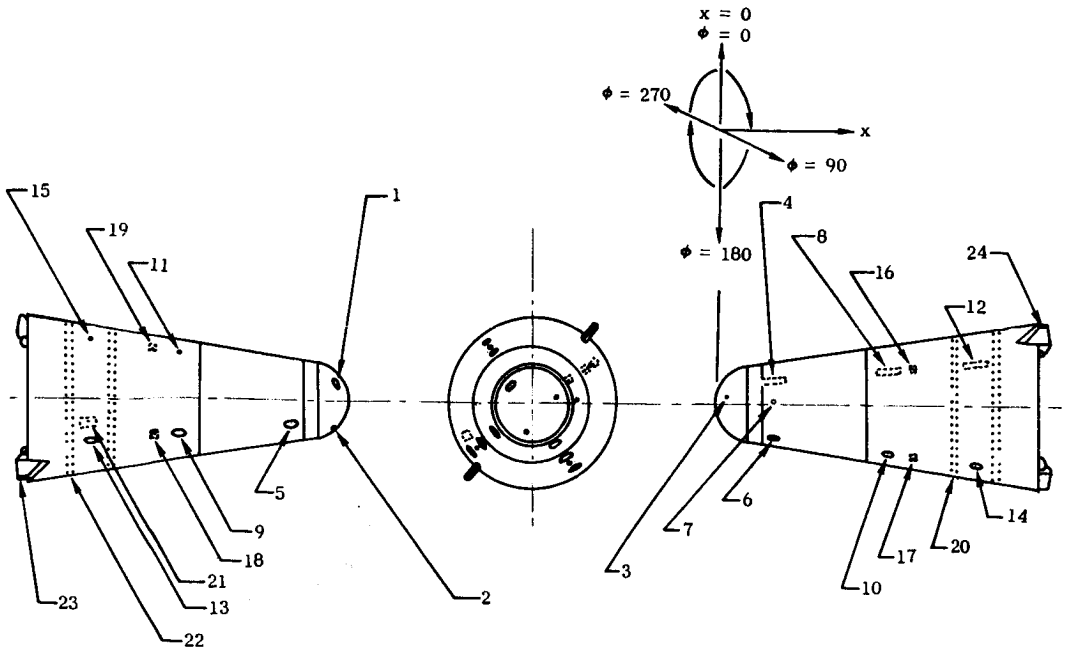

Part		x,† in. (cm)	x/D*	Body station	ϕ,† deg
Number	Function				
	Reflectometer antenna:				
1	**S-band**	1.76 (4.47)	0.15	1	310
2	**X-band**				190
3	**K_a-band**				70
	Reflectometer antenna:				
4	L-band	9.12 (23.16)	0.76	2	55
5	S-band				235
6	X-band				145
7	K_a-band				87
	Reflectometer antenna:				
8	L-band	27.58 (70.05)	2.30	3	55
9	S-band				235
10	X-band				145
11	K_a-band				325
	Reflectometer antenna:				
12	L-band	41.75 (106.04)	3.48	4	55
13	S-band				235
14	X-band				145
15	K_a-band				325
16	X-band telemetry horn (9210 MHz)	31.74 (80.62)	2.65	---	55
17					145
18					235
19					325
20	VHF ring antenna (259.7 MHz)	38.35 (97.41)	3.20	---	---
21	C-band rectangular horn (5800 MHz)	42.04 (106.78)	3.50		252
22	VHF ring antenna (225.7 MHz)	45.15 (114.68)	3.76		---
	Probe:				
23	Electrostatic	48.59 (123.42)	4.05	---	220
24	Thermocouple				40

†Center-line location of parts.
*D = 12 in. (30.48 cm).

TABLE III.- ALTITUDE, VELOCITY, AND TIME OF RAM C-II REENTRY TRAJECTORY

Altitude		Velocity		Time from lift-off, sec
ft	km	ft/sec	km/sec	
450×10^3	137.16	24.9×10^3	7.59	363.9
445	135.64	24.9	7.59	364.6
440	134.11	24.9	7.59	365.4
435	132.59	24.9	7.59	366.2
430	131.06	24.9	7.59	366.9
425	129.54	24.9	7.59	367.7
420	128.02	24.9	7.59	368.4
415	126.49	24.9	7.59	369.3
410	124.97	24.9	7.59	370.0
405	123.44	24.9	7.59	370.8
400	121.92	24.9	7.59	371.6
395	120.40	25.0	7.62	372.3
390	118.87	25.0	7.62	373.1
385	117.35	25.0	7.62	373.8
380	115.82	25.0	7.62	374.7
375	114.30	25.0	7.62	375.4
370	112.78	25.0	7.62	376.2
365	111.25	25.0	7.62	376.9
360	109.73	25.0	7.62	377.7
355	108.20	25.0	7.62	378.5
350	106.68	25.0	7.62	379.3
345	105.16	25.0	7.62	380.1
340	103.63	25.0	7.62	380.5
335	102.11	25.0	7.62	381.6
330	100.58	25.0	7.62	382.3
325	99.06	25.0	7.62	383.1
320	97.54	25.0	7.62	383.8
315	96.01	25.1	7.65	384.7
310	94.49	25.1	7.65	385.4
305	92.96	25.1	7.65	386.2
300	91.44	25.1	7.65	386.9
295	89.92	25.1	7.65	387.7
290	88.39	25.1	7.65	388.5
285	86.87	25.1	7.65	389.3
280	85.34	25.1	7.65	390.0
275	83.82	25.1	7.65	390.8
270	82.30	25.1	7.65	391.6
265	80.77	25.1	7.65	392.3
260	79.25	25.1	7.65	393.1
255	77.72	25.1	7.65	393.8
250	76.20	25.1	7.65	394.7
245	74.68	25.1	7.65	395.4
240	73.15	25.1	7.65	396.2
235	71.63	25.1	7.65	396.9

Altitude		Velocity		Time from lift-off, sec
ft	km	ft/sec	km/sec	
230×10^3	70.10	25.1×10^3	7.65	397.7
225	68.58	25.1	7.65	398.4
220	67.06	25.1	7.65	399.3
215	65.53	25.1	7.65	400.0
210	64.01	25.1	7.65	400.8
205	62.48	25.1	7.65	401.6
200	60.96	25.1	7.65	402.3
195	59.44	25.1	7.65	403.1
190	57.91	25.1	7.65	403.8
185	56.39	25.1	7.65	404.7
180	54.86	25.1	7.65	405.4
175	53.34	25.0	7.62	406.2
170	51.82	25.0	7.62	406.9
165	50.29	25.0	7.62	407.8
160	48.77	24.9	7.59	408.5
155	47.24	24.9	7.59	409.3
150	45.72	24.8	7.56	410.1
145	44.20	24.7	7.53	410.8
140	42.67	24.5	7.47	411.7
135	41.15	24.4	7.44	412.4
130	39.62	24.2	7.38	413.2
125	38.10	24.0	7.32	414.0
120	36.58	23.7	7.22	414.8
115	35.05	23.3	7.10	415.7
110	33.53	22.8	6.95	416.5
105	32.00	22.3	6.80	417.3
100	30.48	21.5	6.55	418.3
95	28.96	20.7	6.31	419.2
90	27.43	19.7	6.00	420.1
85	25.91	18.4	5.61	421.1
80	24.38	16.8	5.12	422.2
75	22.86	15.1	4.60	423.3
70	21.34	12.9	3.93	424.8
65	19.81	10.8	3.29	426.3
60	18.29	8.4	2.56	428.3
55	16.76	6.1	1.86	430.8
50	15.24	4.2	1.28	434.1
45	13.72	2.5	.76	438.9
40	12.19	1.29	.39	446.2

TABLE IV.- REFLECTOMETER-DETERMINED ELECTRON DENSITIES

Body station	x/D	Frequency band	Time from lift-off, sec, at –		Altitude, ft (km), at –	
			Onset of 20% reflection level[a]	Decay of 20% reflection level[a]	Onset[a]	Decay[a]
1	0.15	S	390.3	[b]424.3	277×10^3 (84)	[b]72.6×10^3 (22.1)
		X	392.3	420.0	264 (80)	90.3 (27.5)
		K_a	[c]397.3	[d]419.0	[c]236 (72)	[b c]95.0 (29.0)
2	0.76	L	390.3	423.4	277×10^3 (84)	74.7×10^3 (22.8)
		S	393.8	422.3	254.8 (77.7)	79.6 (24.3)
		X	397.8	419.2	229 (70)	[b]93.7 (28.6)
		K_a	414.0	417.8	125 (38)	102 (31)
3	2.30	L	391.6	421.8	269×10^3 (82)	81.8×10^3 (24.9)
		S	395.8	420.8	242 (74)	86.3 (26.3)
		X	[e]406.8	[e]417.8	[e]170 (52)	[e]102 (31)
		K_a	------	------	----------	----------
4	3.48	L	392.8	421.0	262×10^3 (80)	85×10^3 (26)
		S	397.0	419.6	234.8 (72)	92 (28)
		X	[e]407.8	[e]415.3	[e]164 (50)	[e]117 (36)
		K_a	------	------	----------	----------

[a]At these conditions, $N_{e,pk}/N_{e,cr} = 0.63$ for each respective frequency.

[b]At low altitudes, antenna detuning due to length changes prevents reflection coefficient from crossing through 20 percent point where plasma is dropping below critical density. Sharp cessation of reflected signal modulation (due to windward-leeward plasma variations) is interpreted to be plasma decay.

[c]Not derived from 20-percent-reflection-level criterion (see discussion in text).

[d]Effects of gross antenna detuning caused by antenna length changes and removal of beryllium cap makes determination of this critical density decay time somewhat ambiguous.

[e]Oscillations in measured reflection coefficients due to windward-leeward plasma changes cause some ambiguity in this data point. A mean of reflection-coefficient curve was used to estimate this data point.

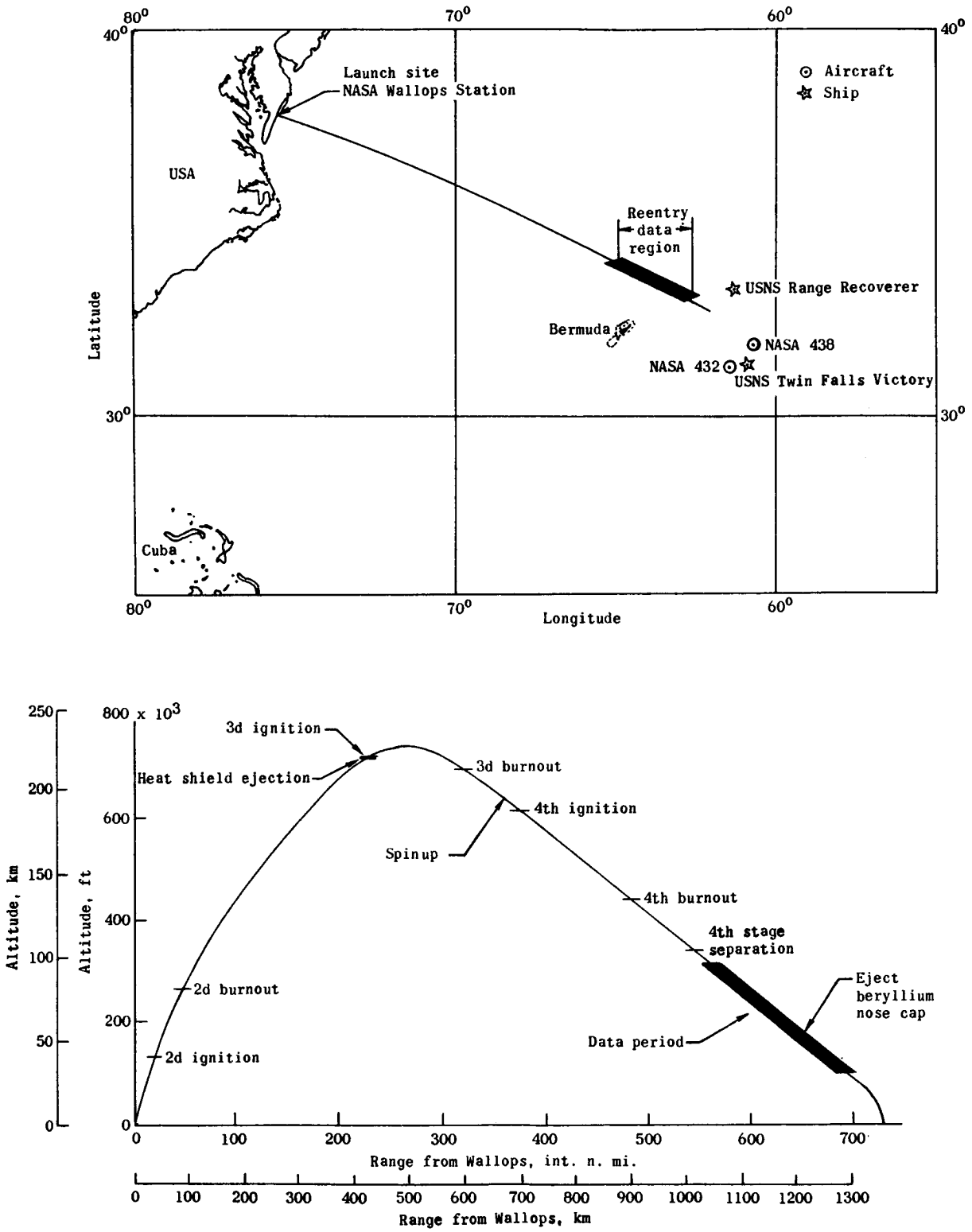

Figure 1.- Trajectory plan view and reentry events.

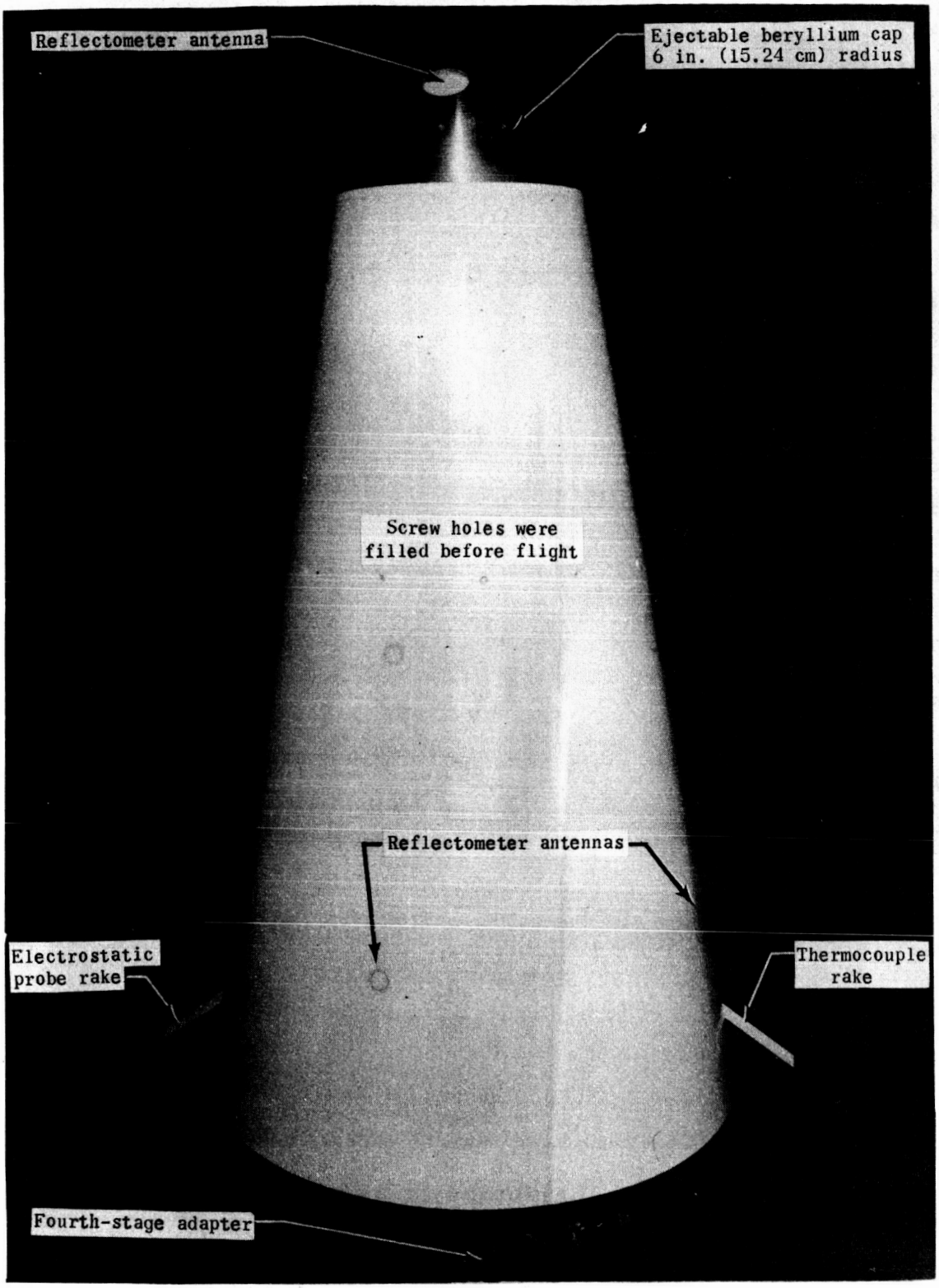

L-68-4975.1

Figure 2.- Flight payload with beryllium nose cap on.

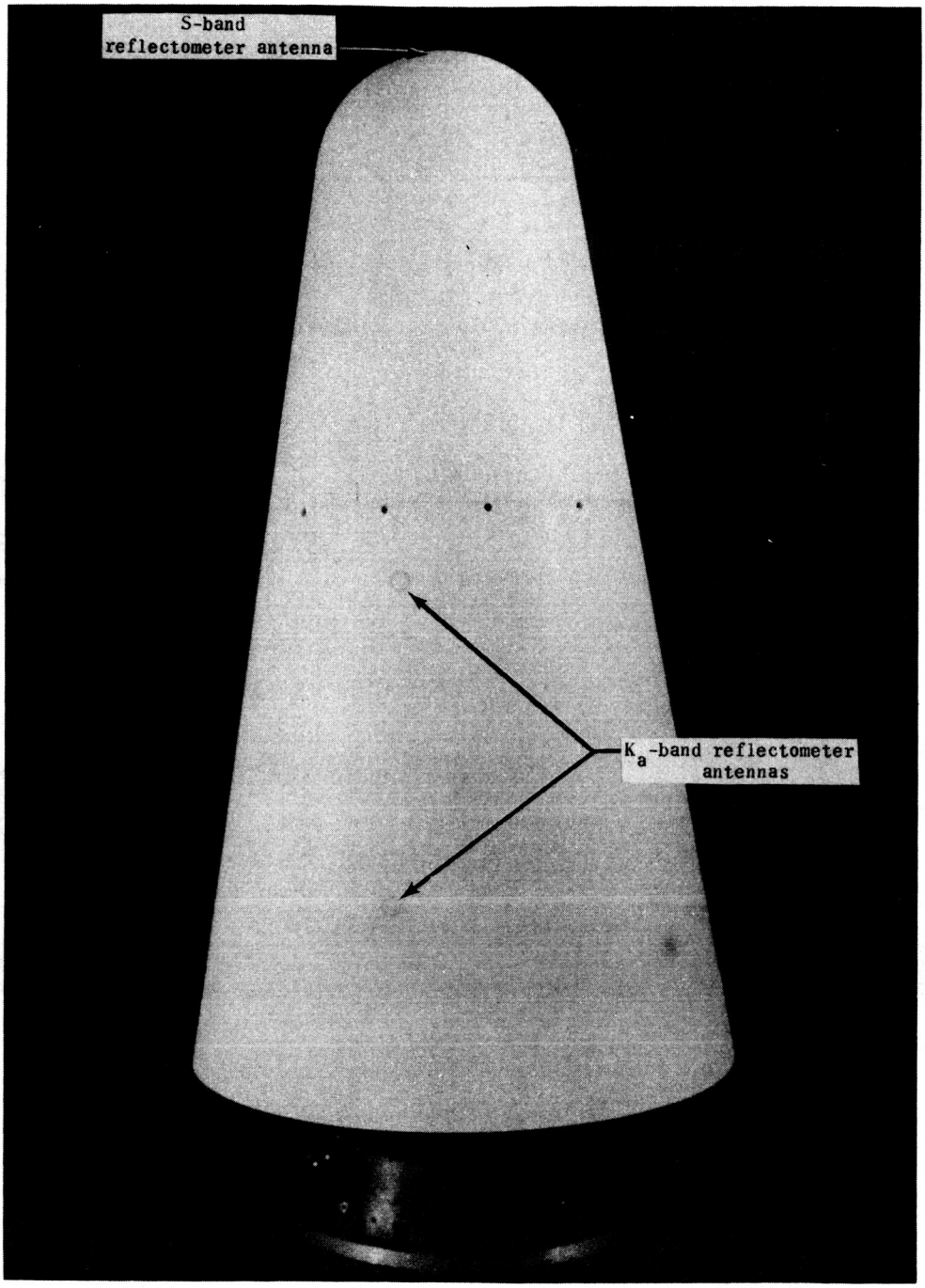

L-70-624.1

Figure 3.- RAM C-II payload with beryllium nose cap off.

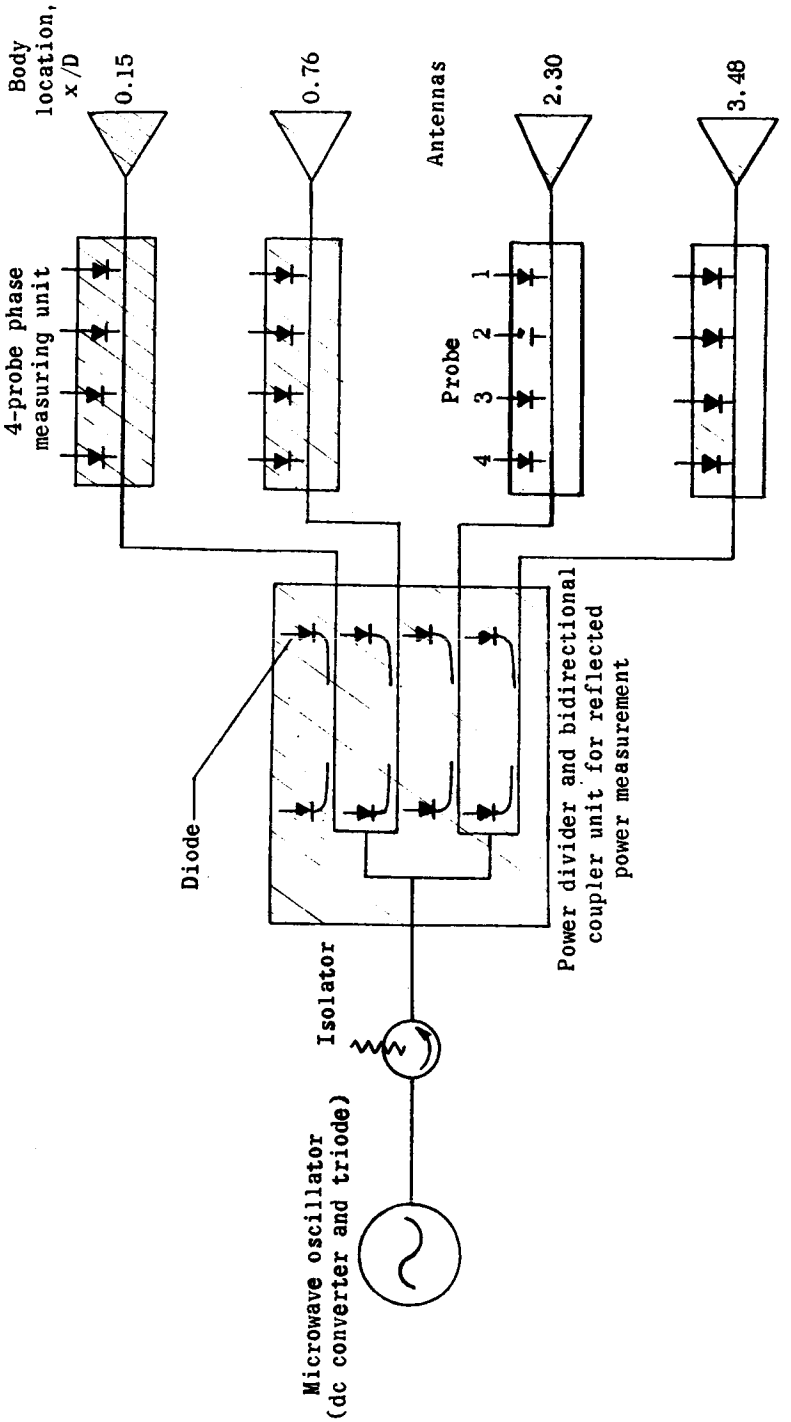

Figure 4.- Block diagram of S-band reflectometer.

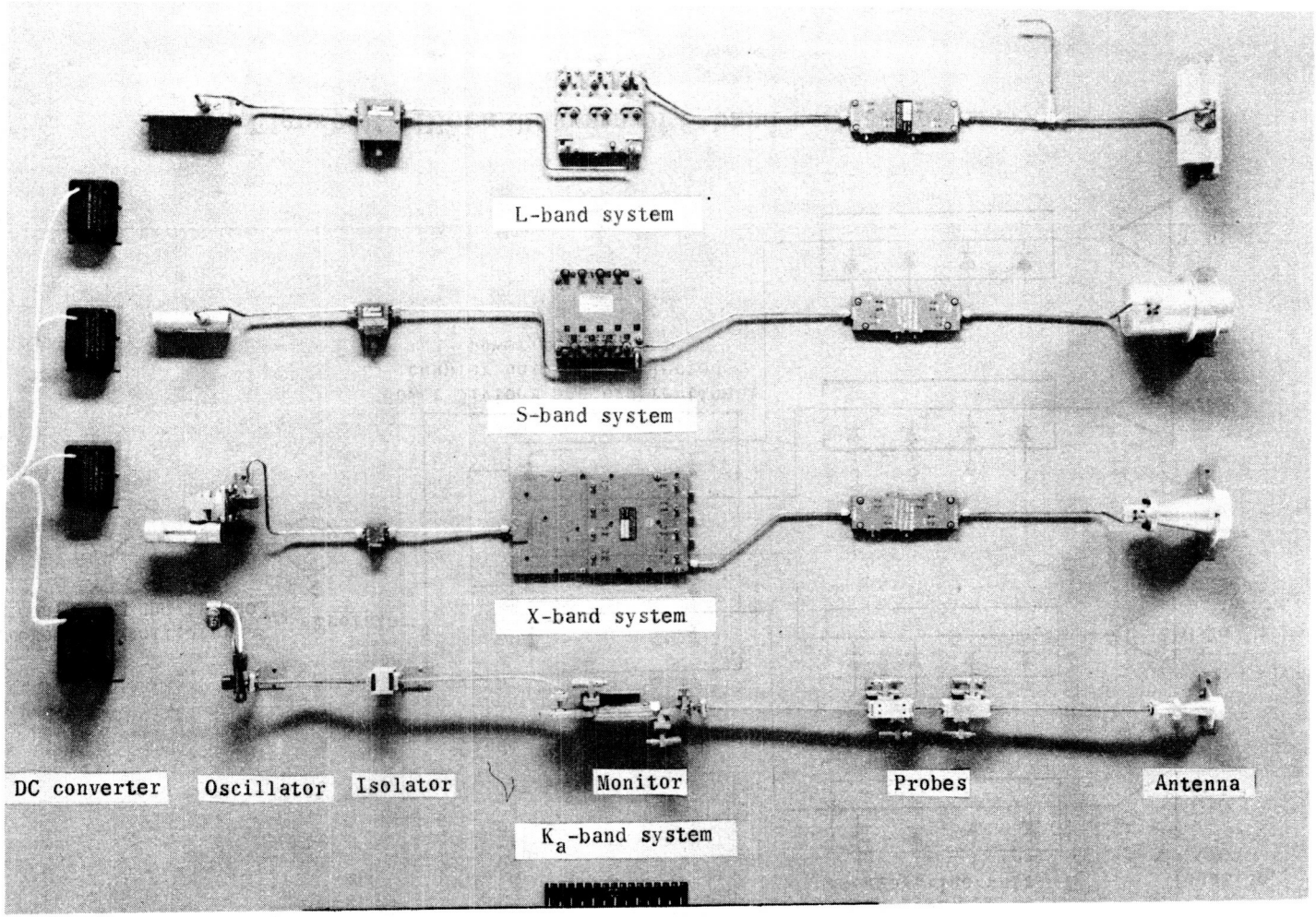

L-70-1389.1

Figure 5.- Reflectometer flight components (only one probe unit and antenna shown for each frequency).

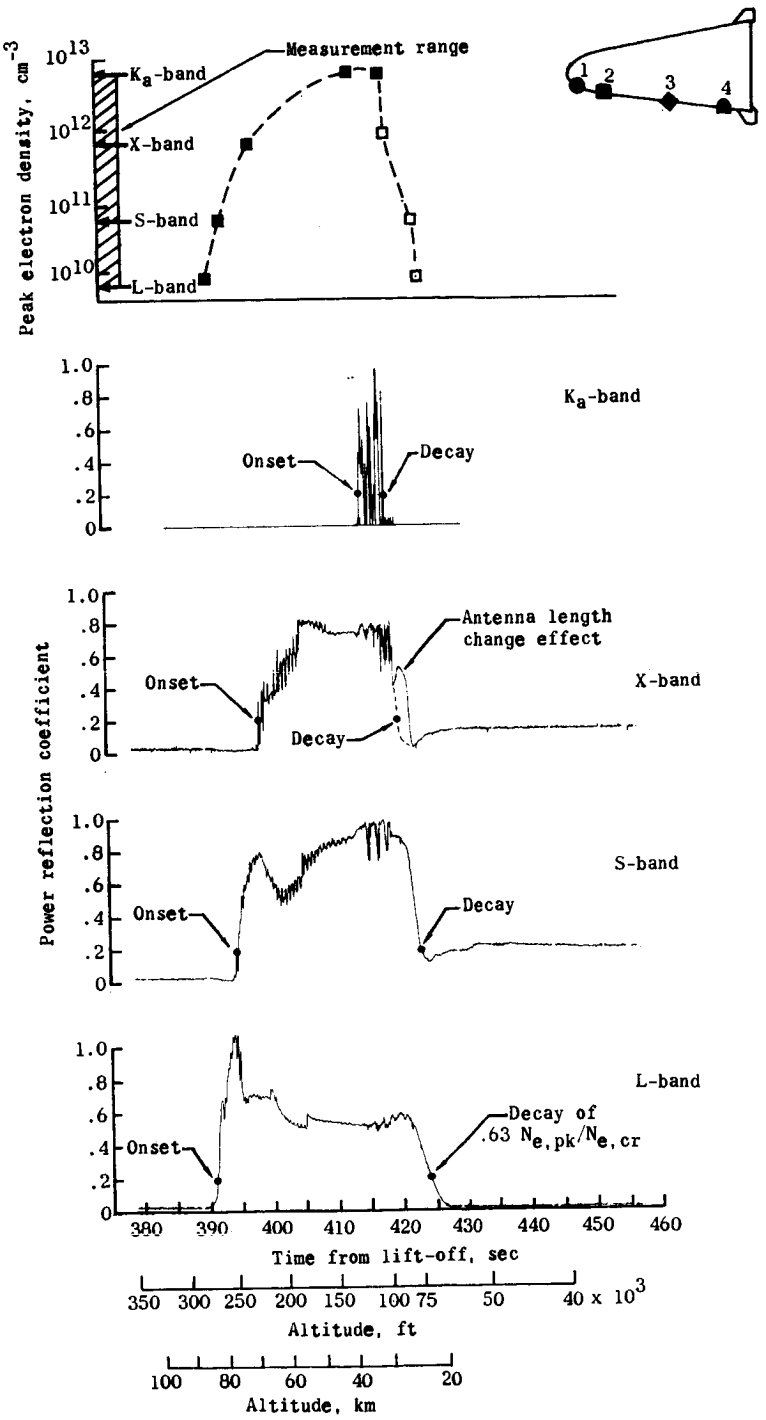

Figure 6.- Electron density determined from reflectometer data at station 2. Data noted by open symbols subject to errors.

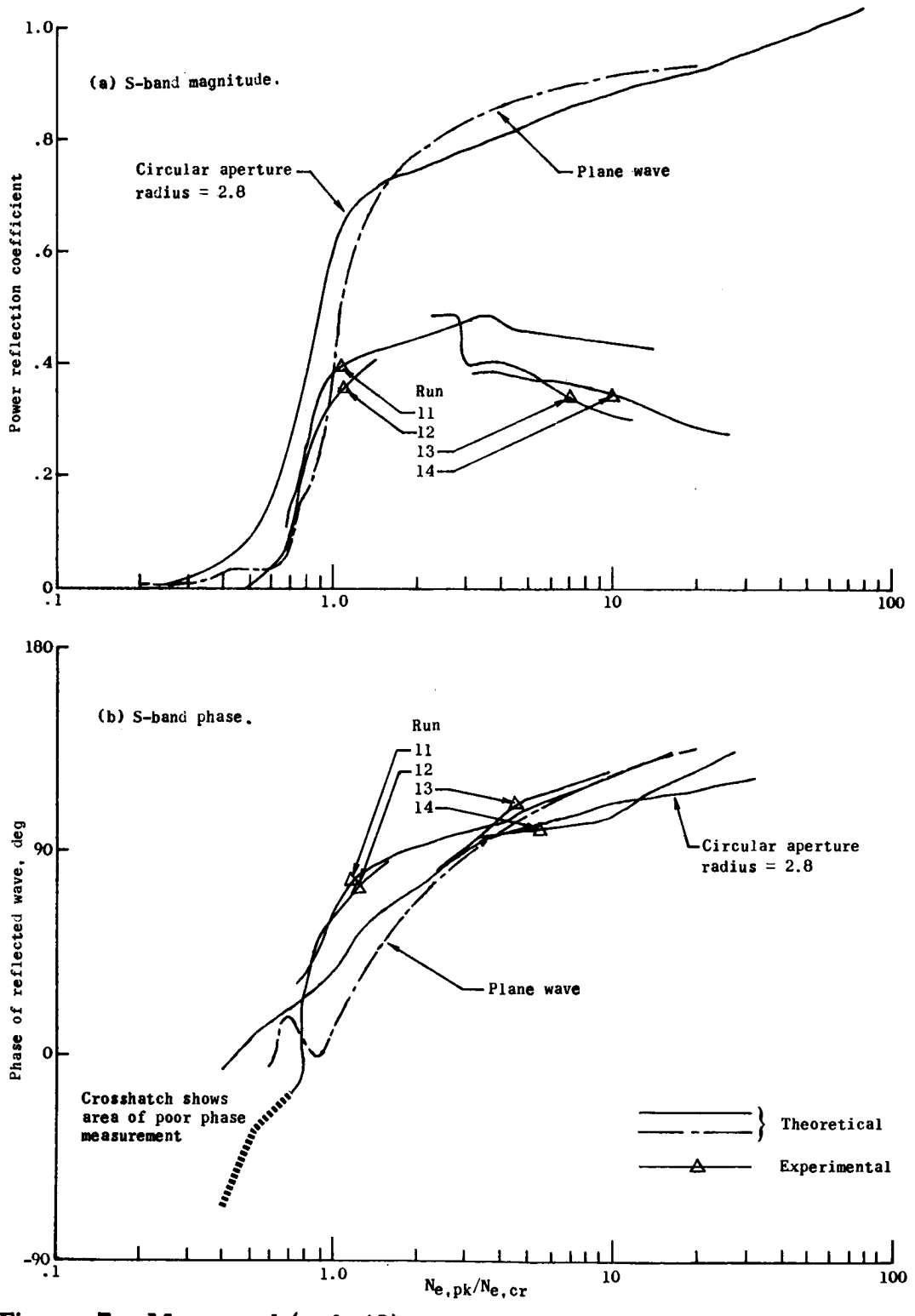

Figure 7.- Measured (ref. 12) and computed reflection coefficients. Parabolic plasma profile (ref. 9); $\nu = 2.51 \times 10^9$; half-density thickness, 0.234 cm; total plasma thickness, 15.24 cm.

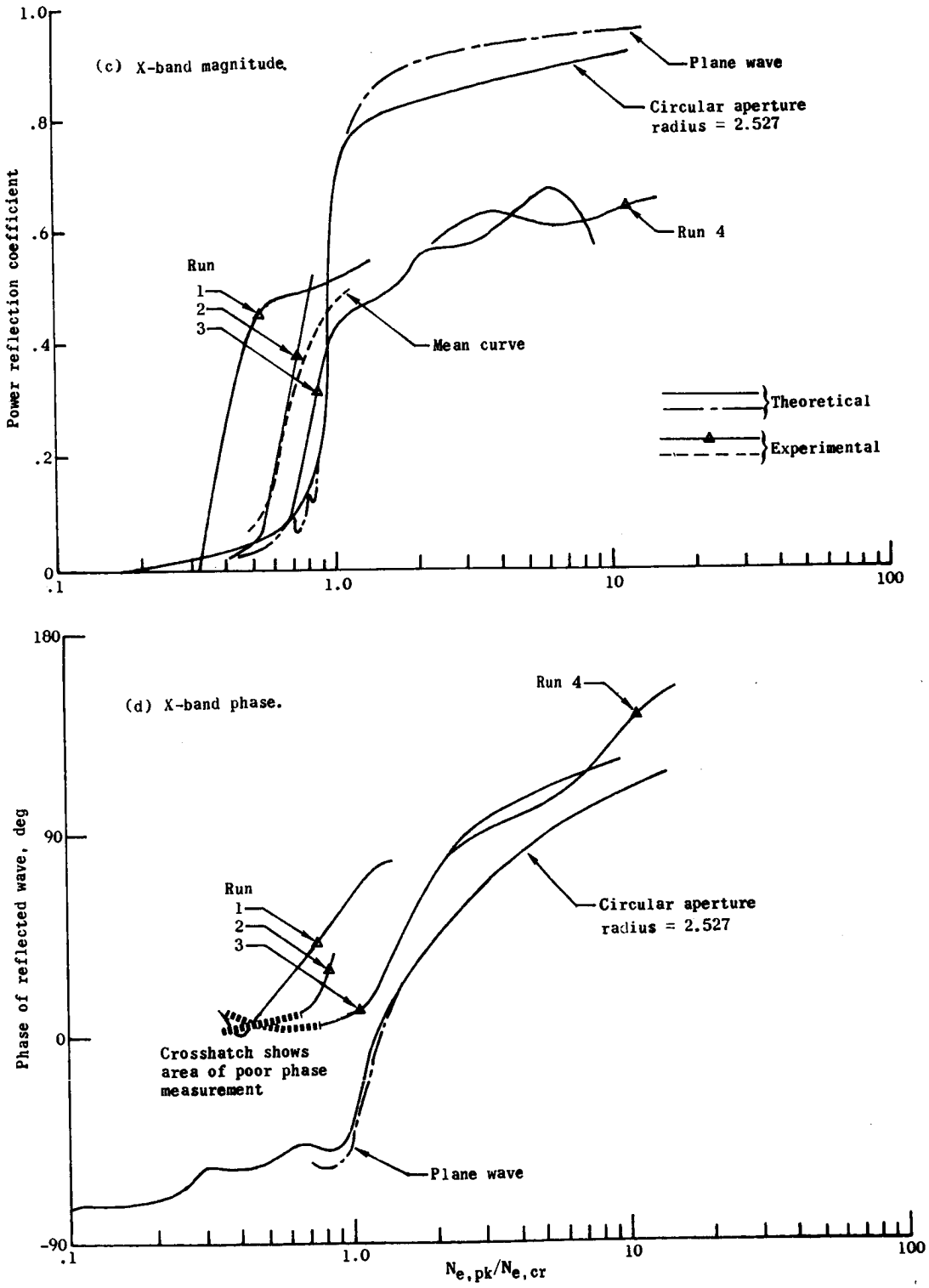

Figure 7.- Concluded.

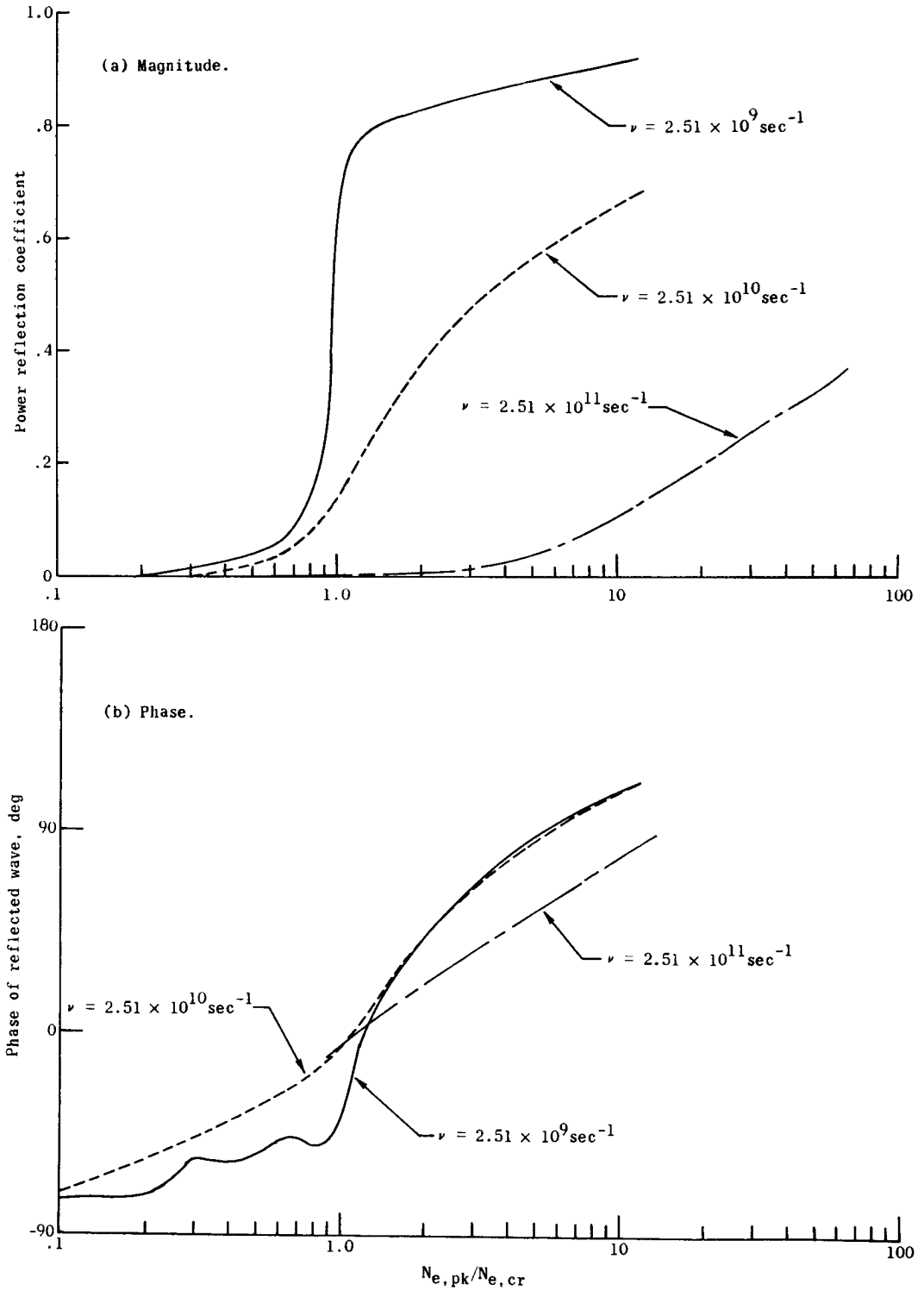

Figure 8.- Computed collision-frequency effect on circular-aperture reflection coefficient. Radius, 2.527 cm (X-band conical horn, stations 2, 3, and 4); frequency, 10.044 MHz; total plasma thickness, 15.24 cm; parabolic plasma profile (ref. 12), half-density thickness, 0.234 cm.

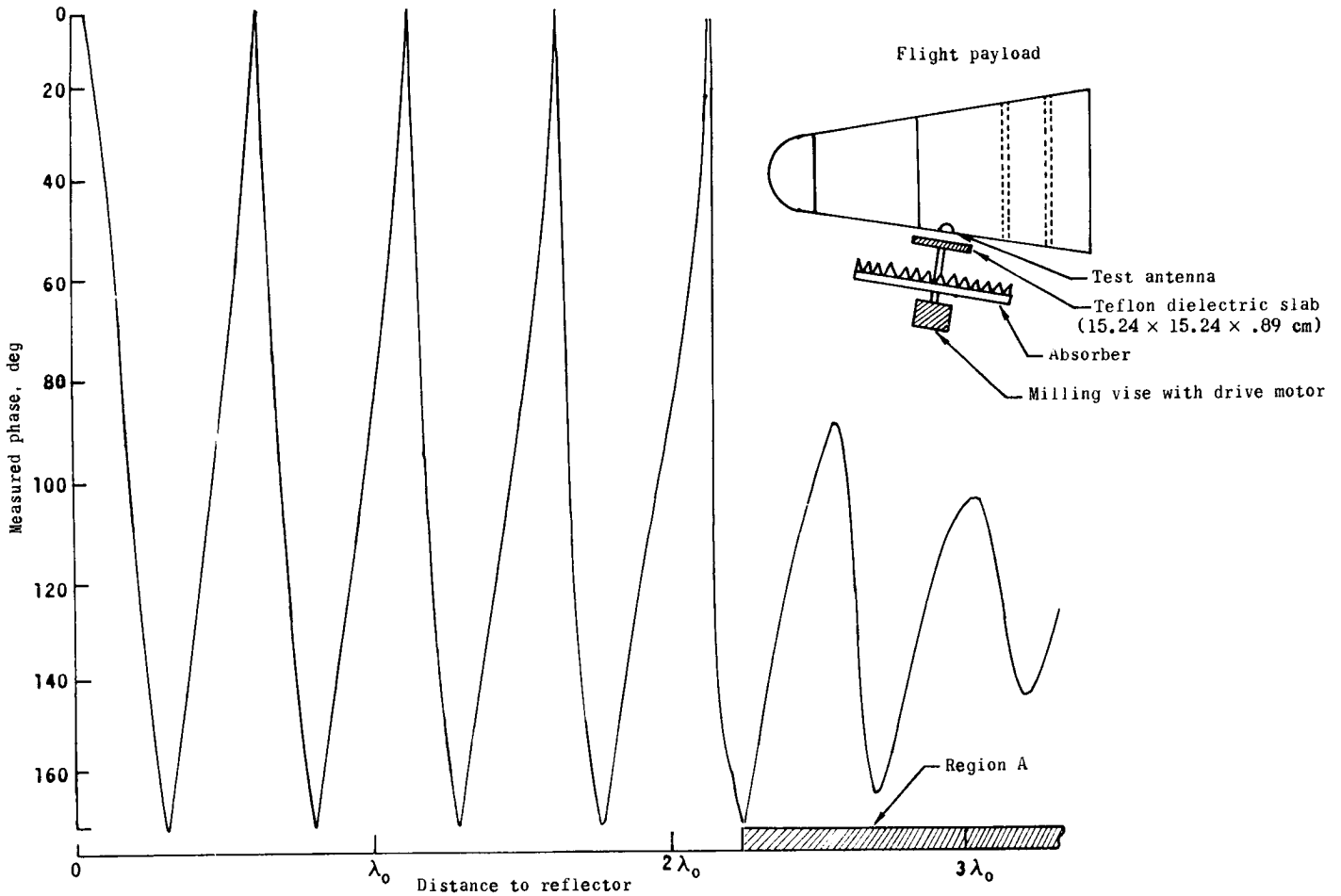

Figure 9.- Variation of phase with reflector distance for X-band station 3 conical horn.

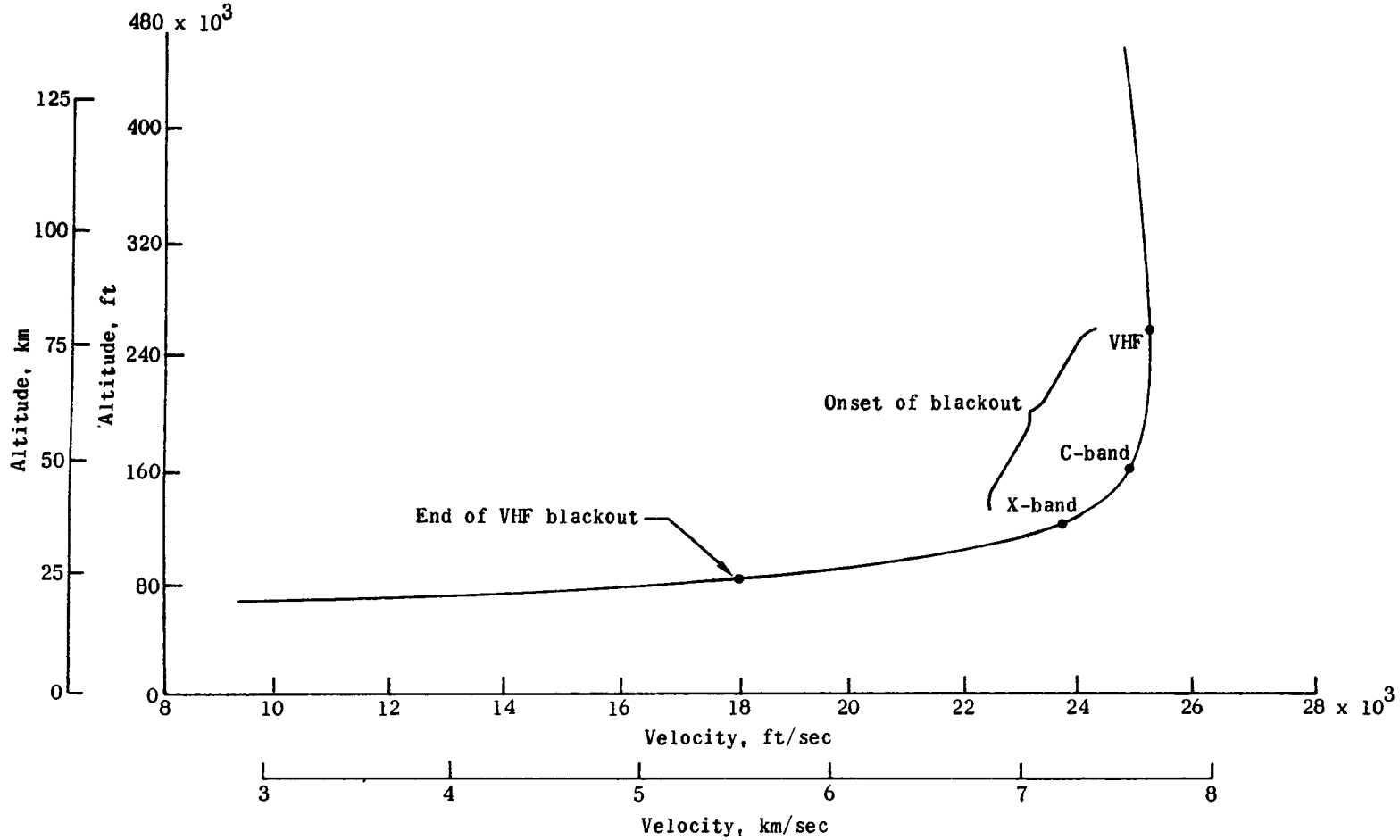

Figure 10.- RAM C-II reentry trajectory showing onset and end of rf signal blackout. X-band and C-band reacquisition was delayed because of tracking difficulties.

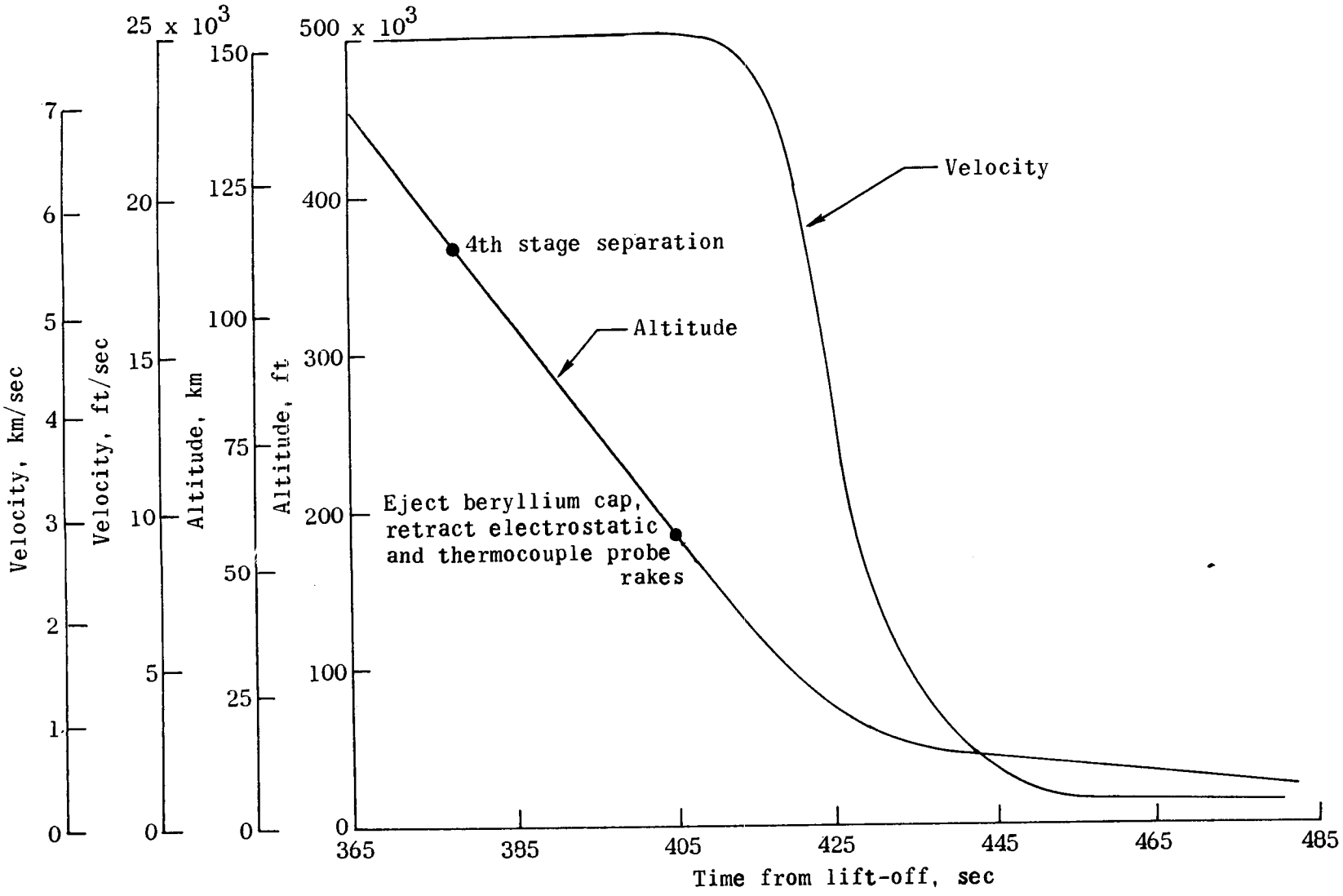

Figure 11.- RAM C-II reentry altitude and velocity time histories.

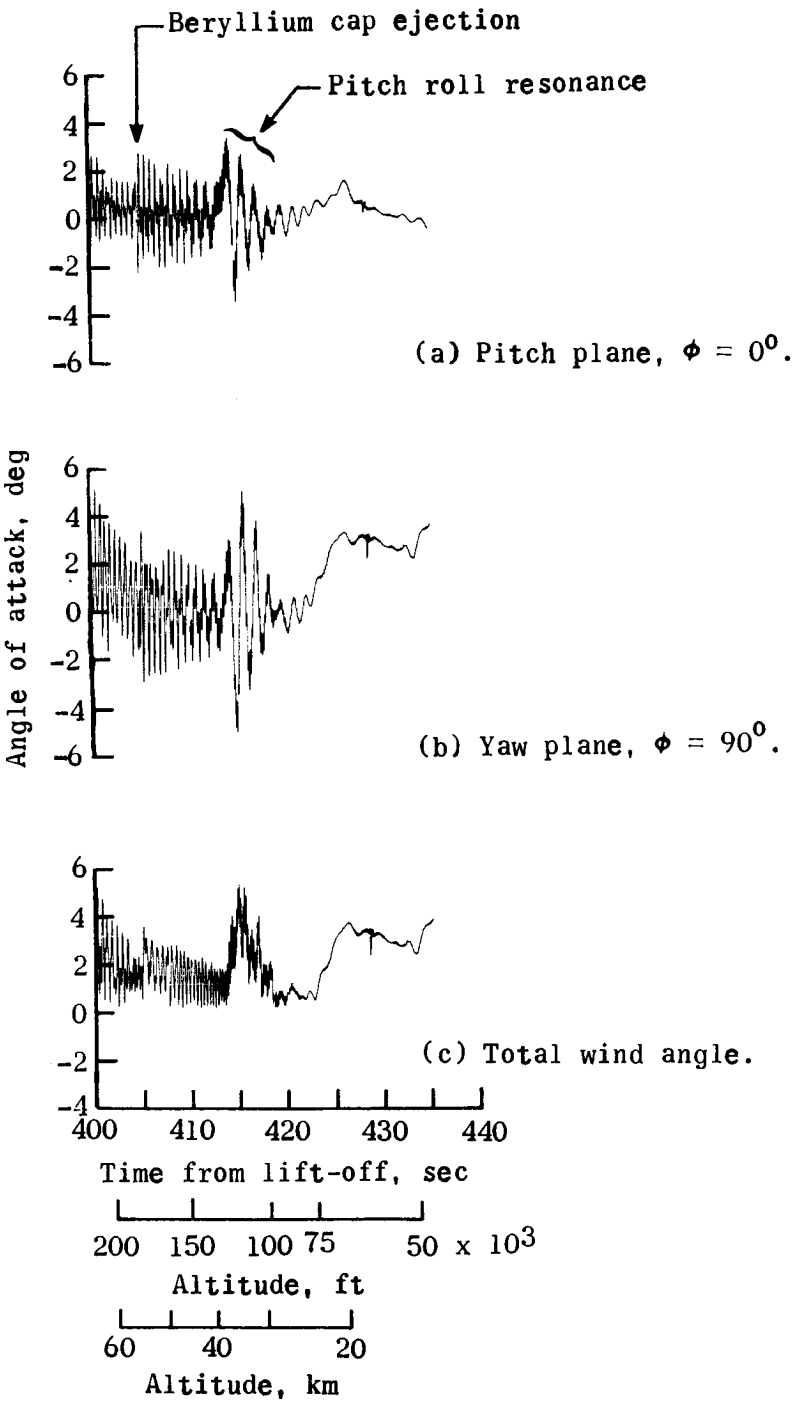

Figure 12.- Payload angle-of-attack time history.

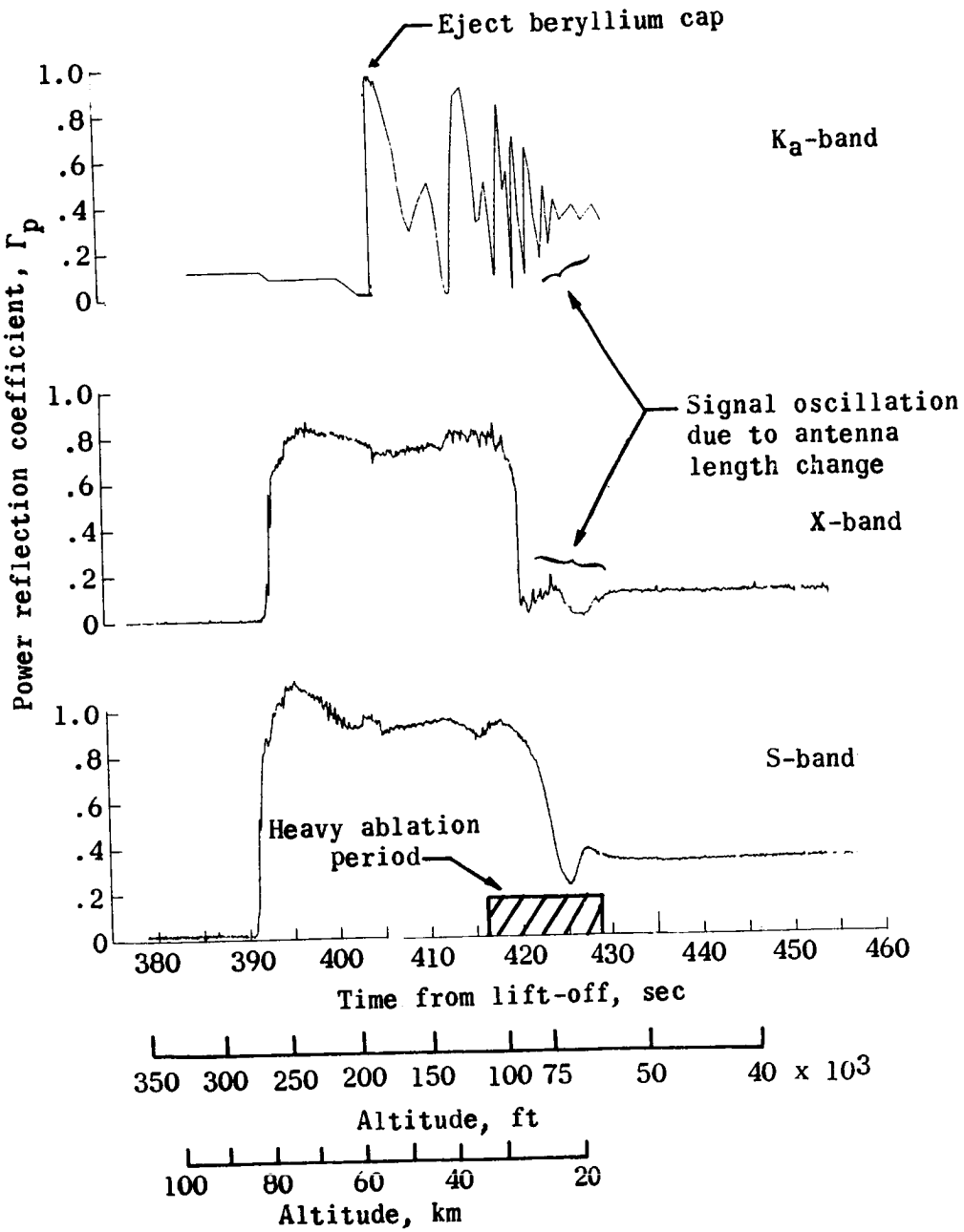

(a) Station 1 (x/D = 0.15). K_a-band is relative to maximum level during flight.

Figure 13.- Measured reflection coefficient magnitudes relative to short circuit at aperture with beryllium cap on.

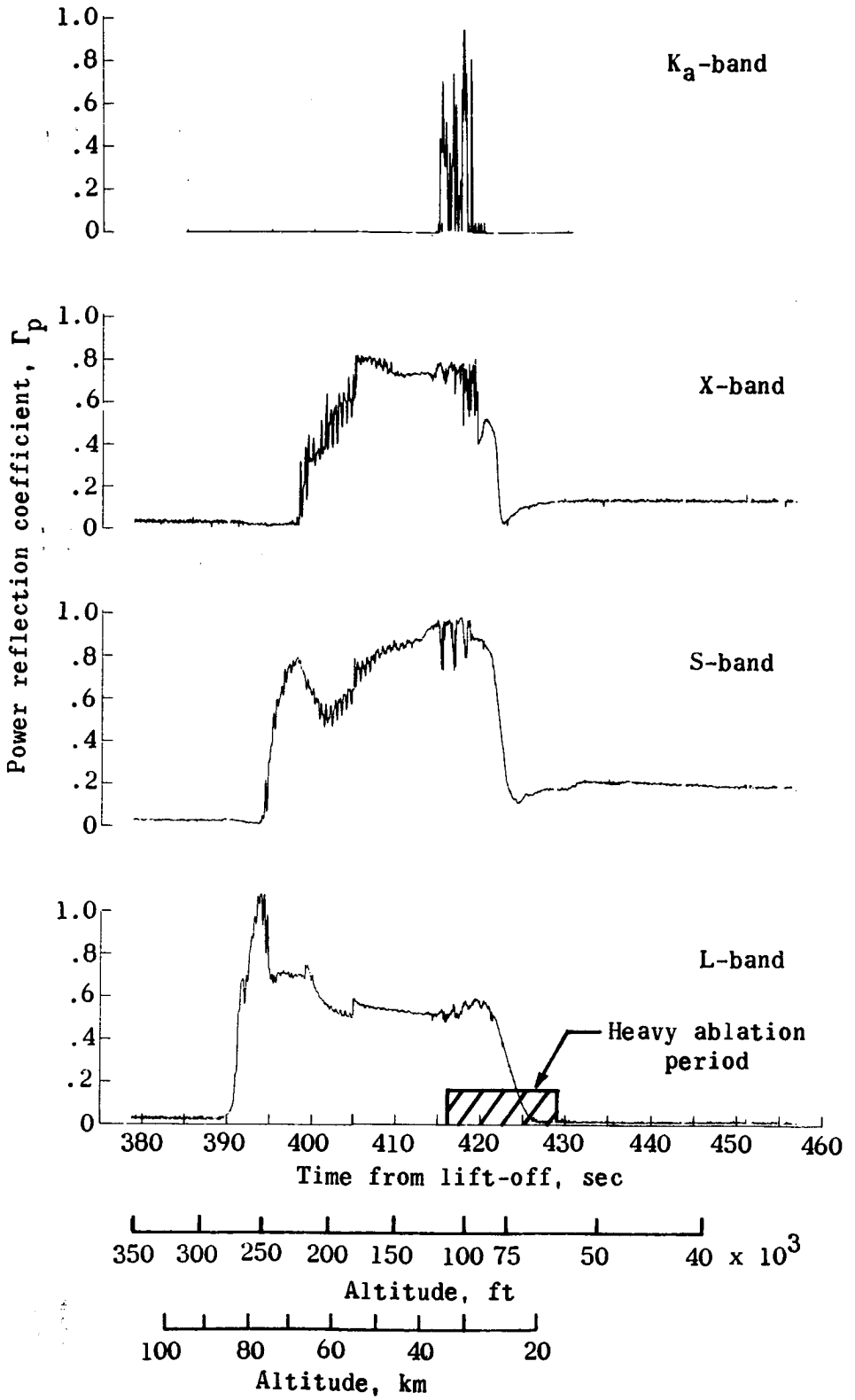

(b) Station 2 (x/D = 0.76).

Figure 13.- Continued.

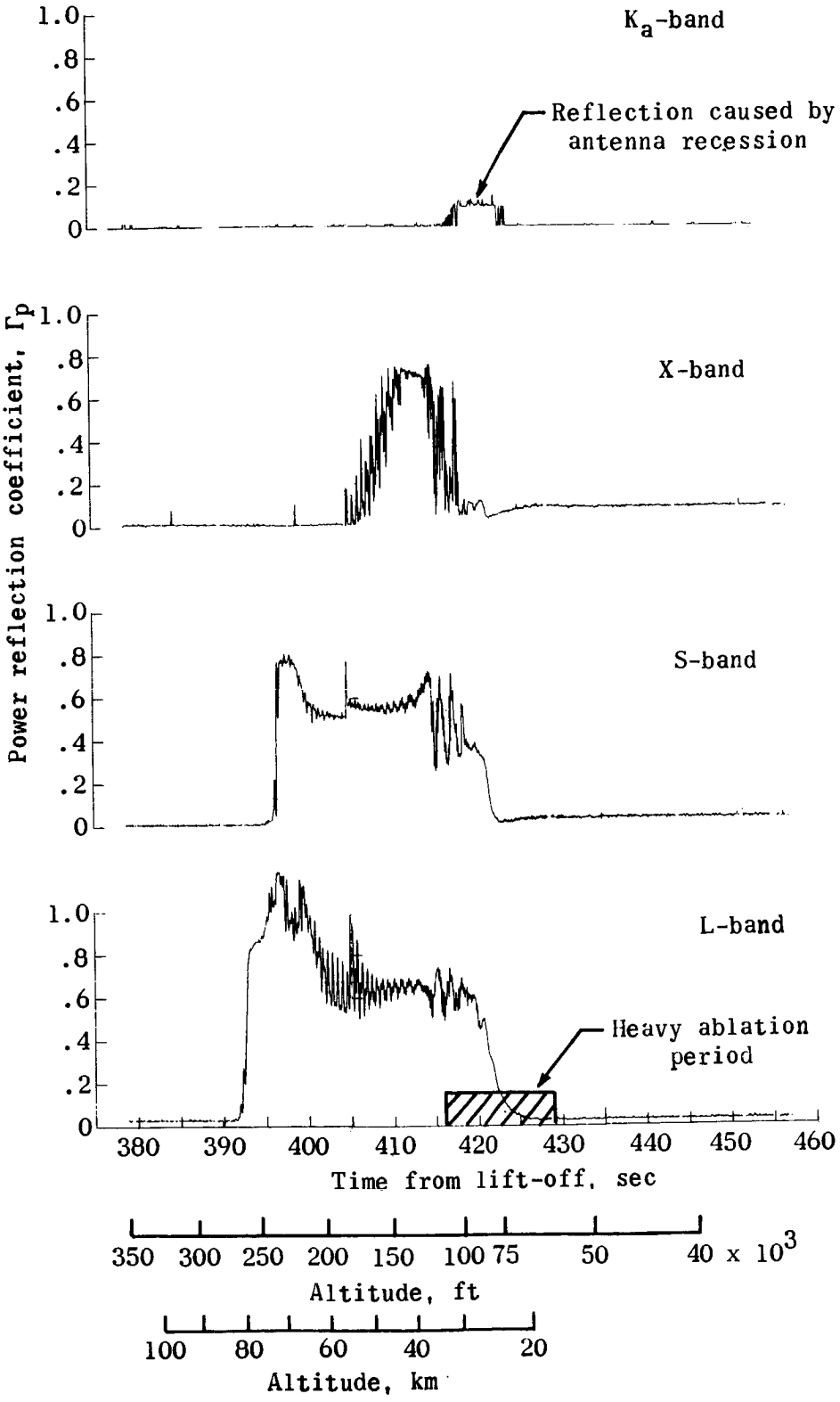

(c) Station 3 (x/D = 2.30).

Figure 13.- Continued.

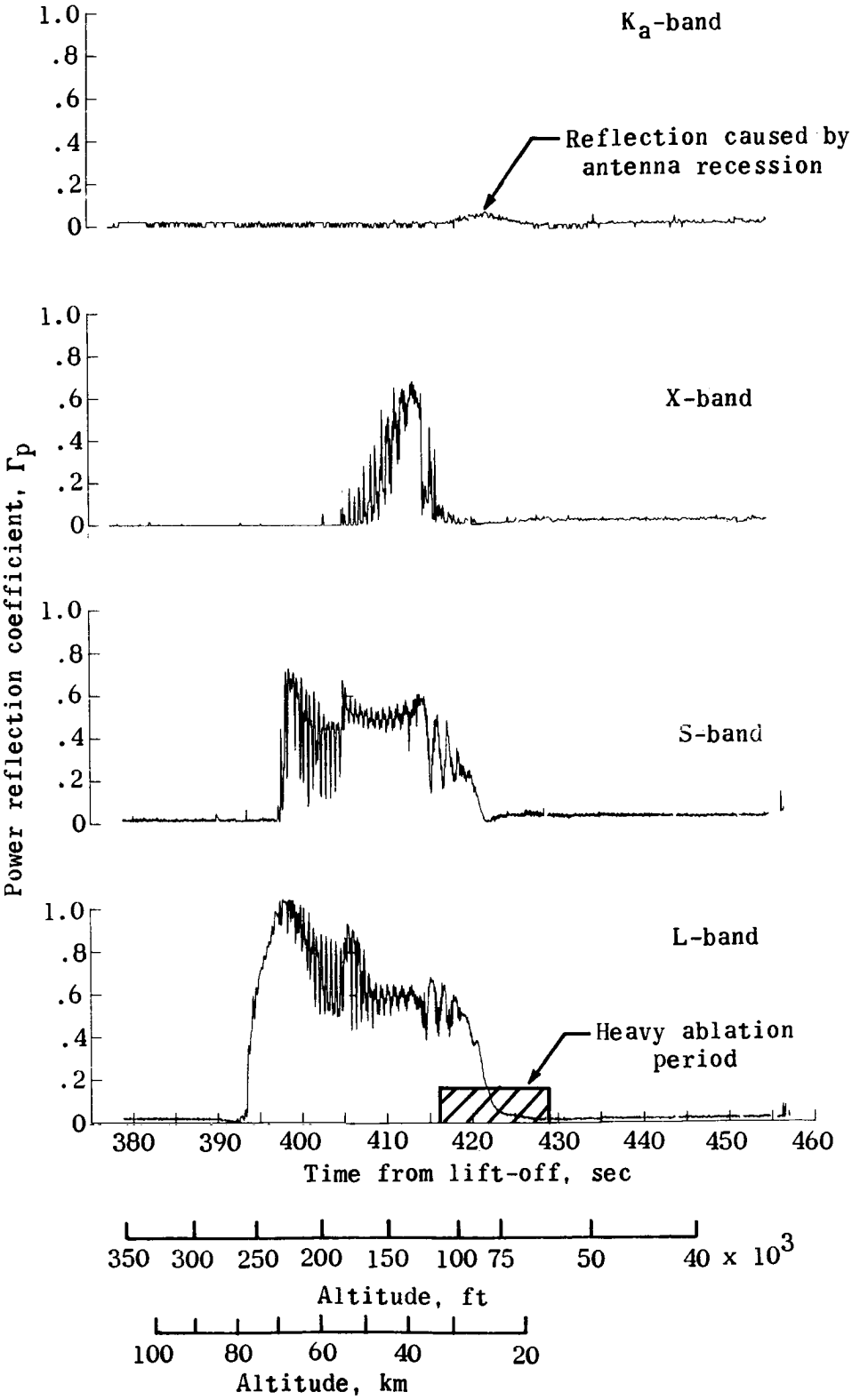

(d) Station 4 (x/D = 3.48).

Figure 13.- Concluded.

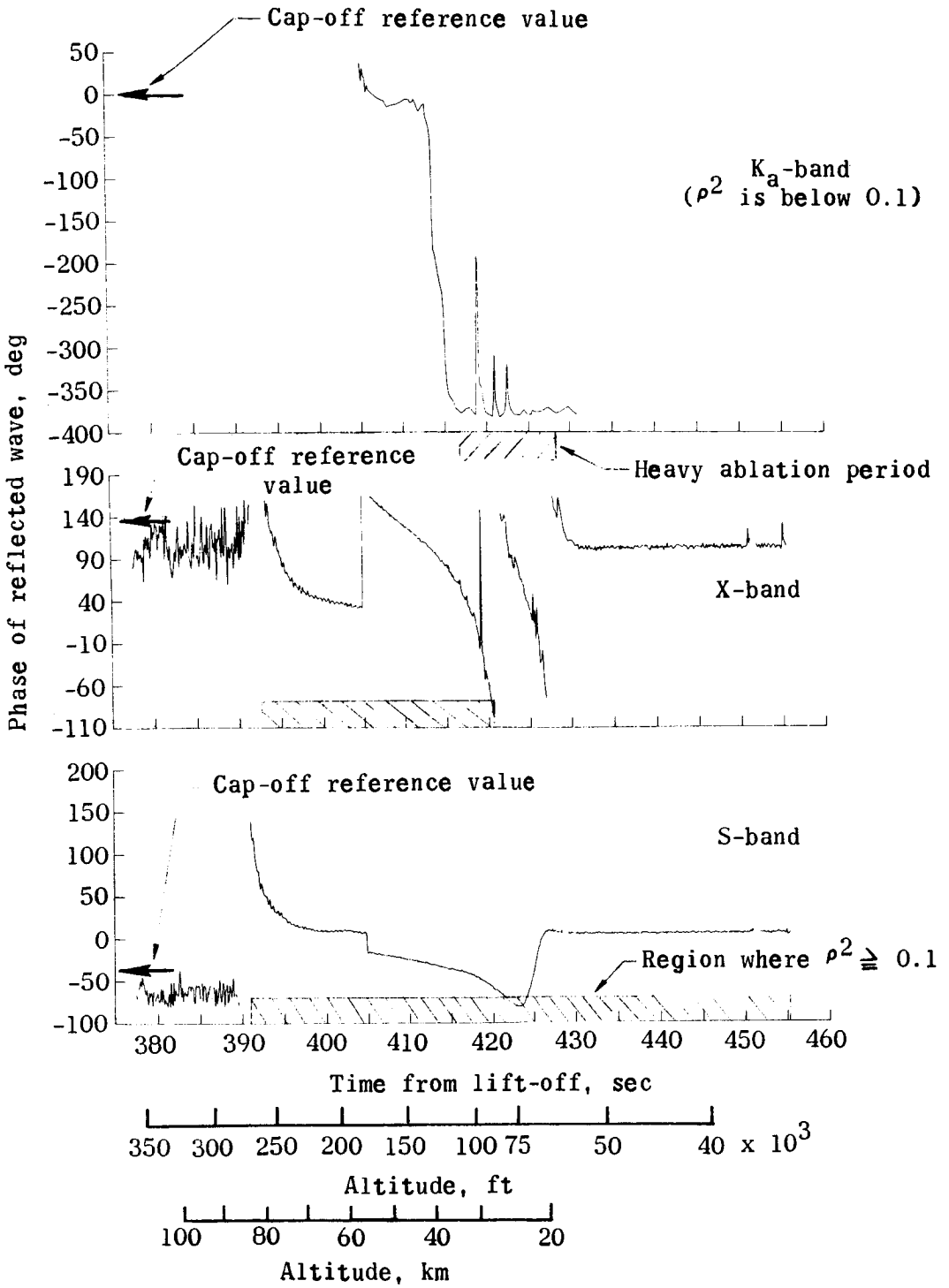

(a) Station 1 (x/D = 0.15).

Figure 14.- Measured phase coefficients relative to the short-circuited aperture with beryllium cap on.

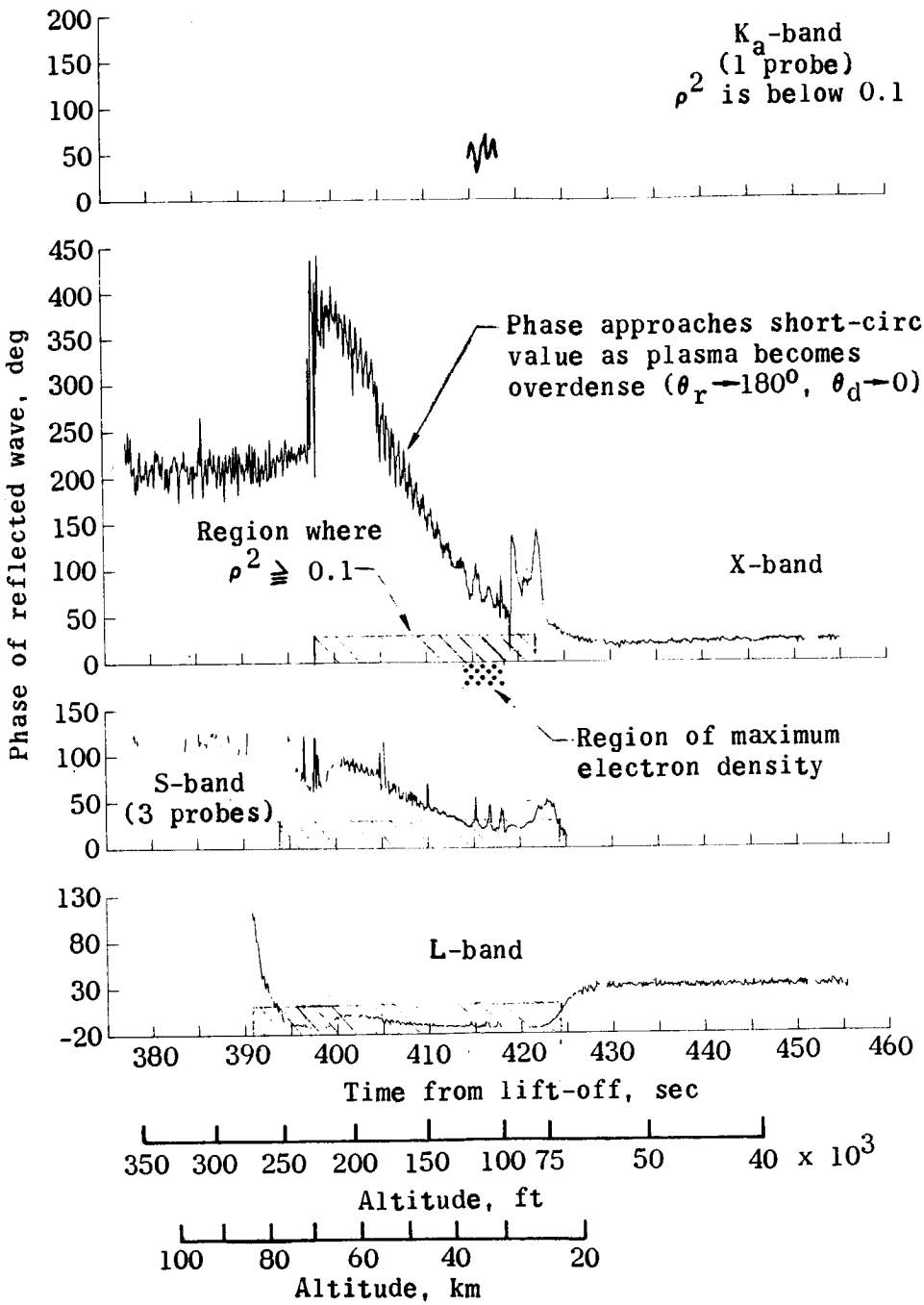

(b) Station 2 (x/D = 0.76).

Figure 14.- Continued.

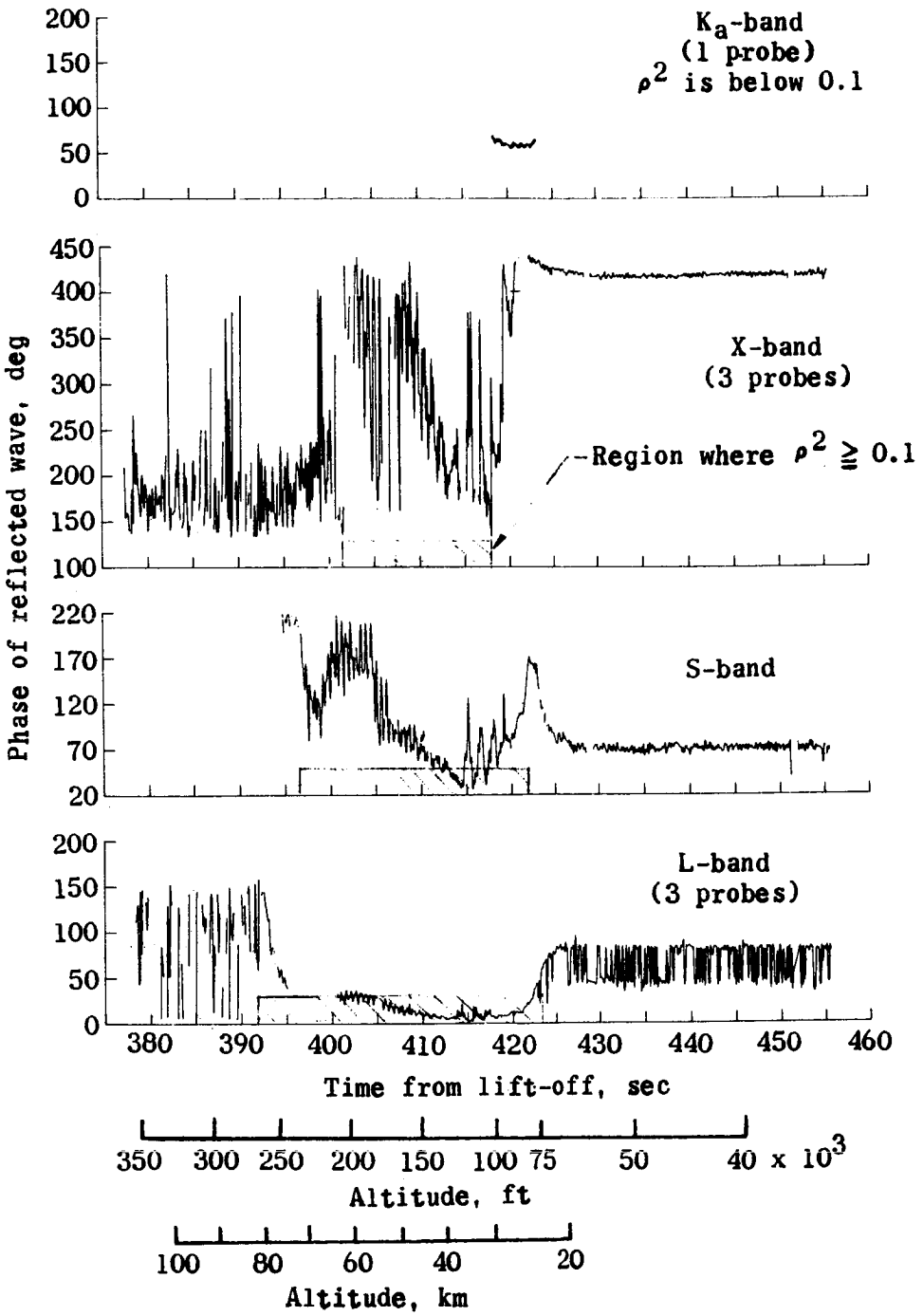

(c) Station 3 (x/D = 2.30).

Figure 14.- Continued.

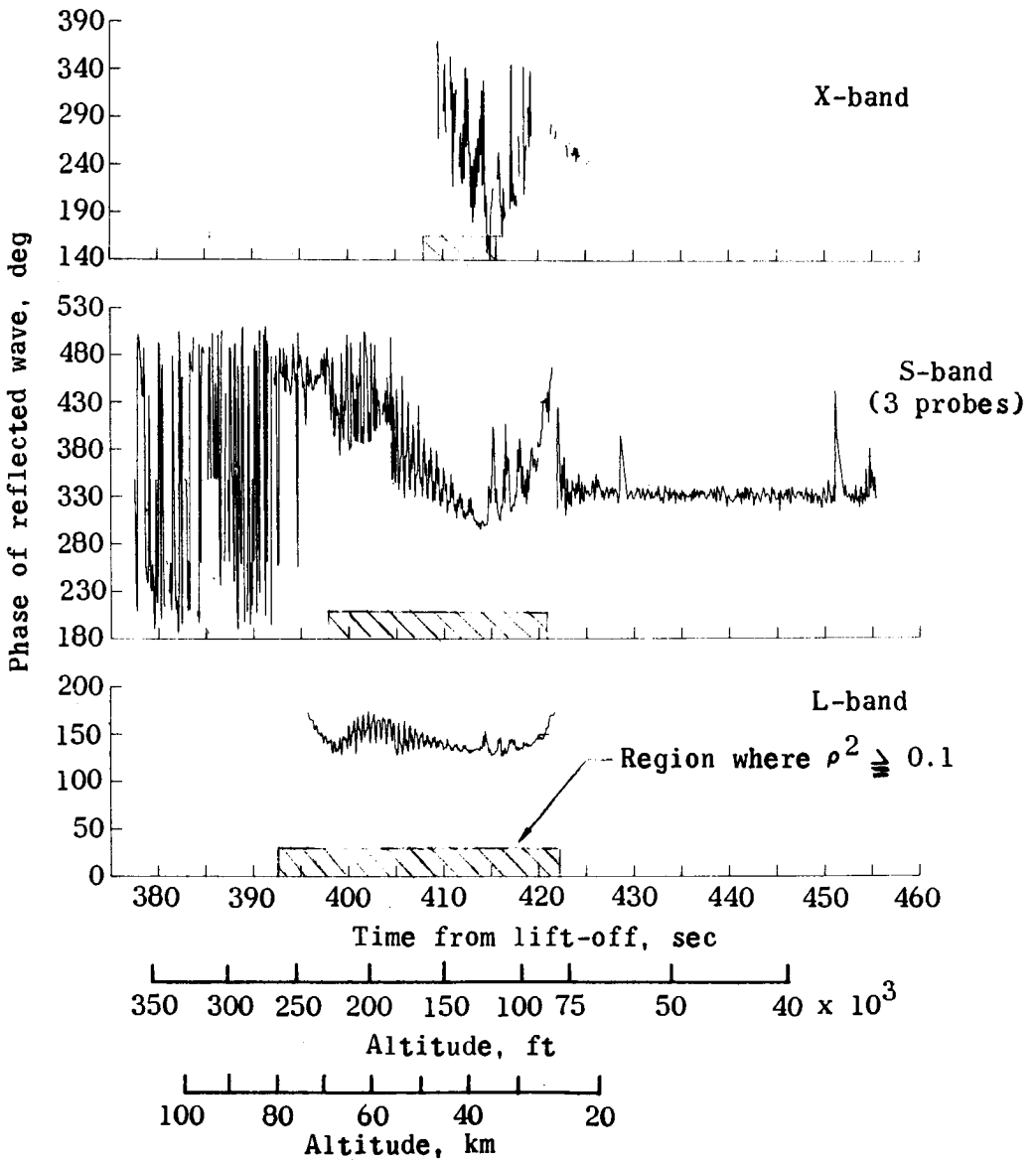

(d) Station 4 (x/D = 3.48).

Figure 14.- Concluded.

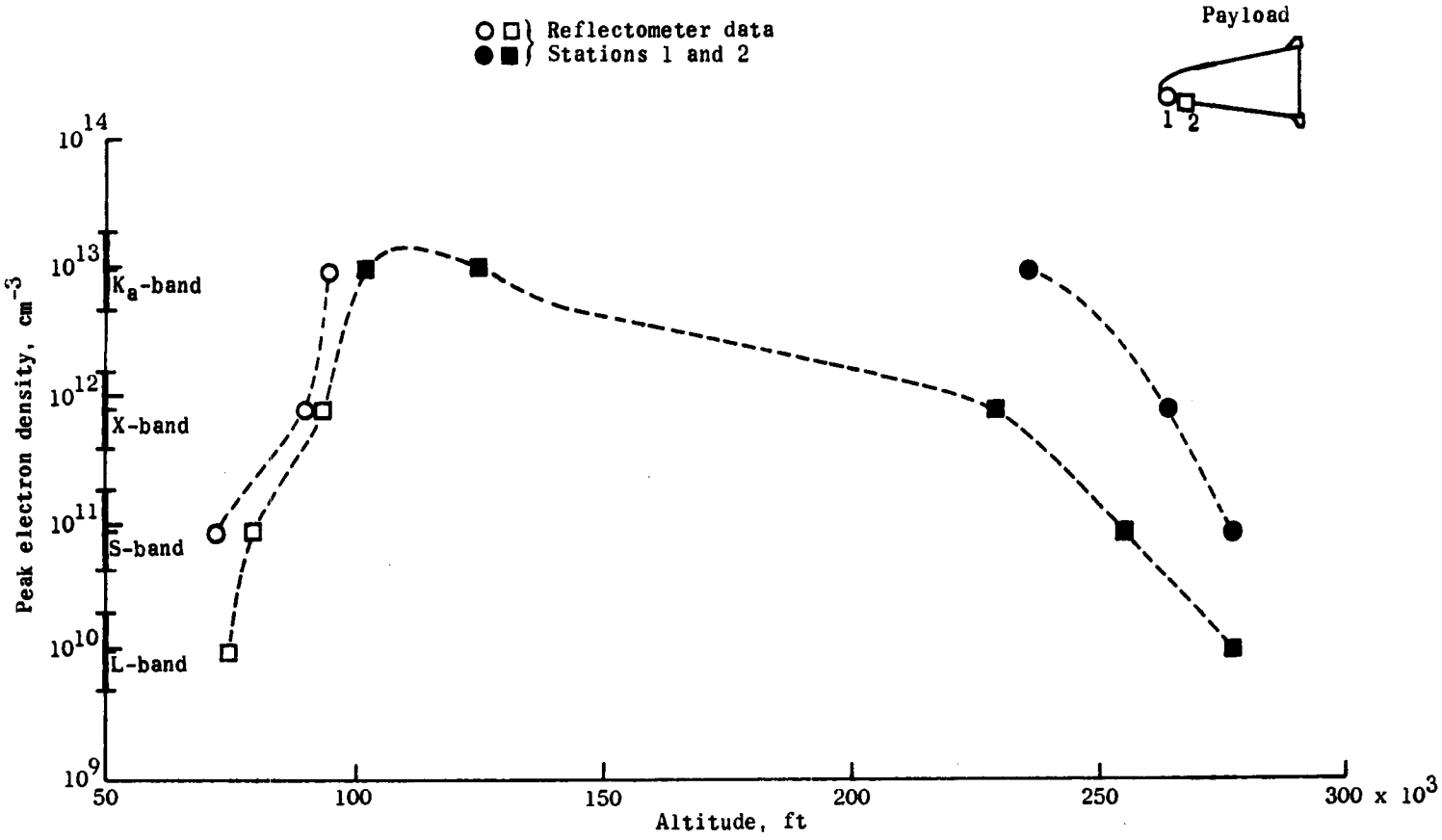

(a) Stations 1 and 2.

Figure 15.- Measured and calculated electron density. Open symbols data subject to errors (see text).

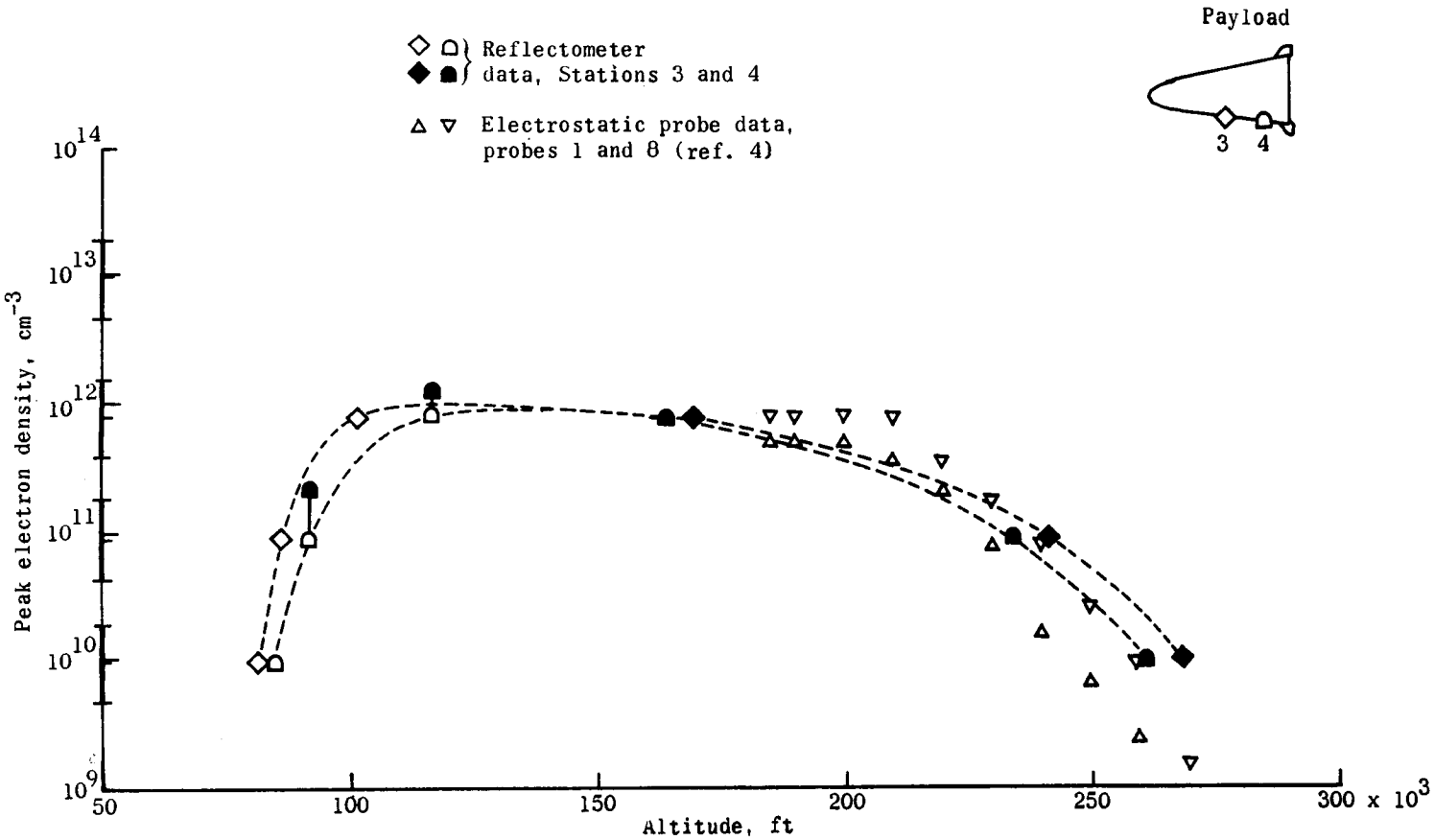

(b) Stations 3 and 4.

Figure 15.- Concluded.

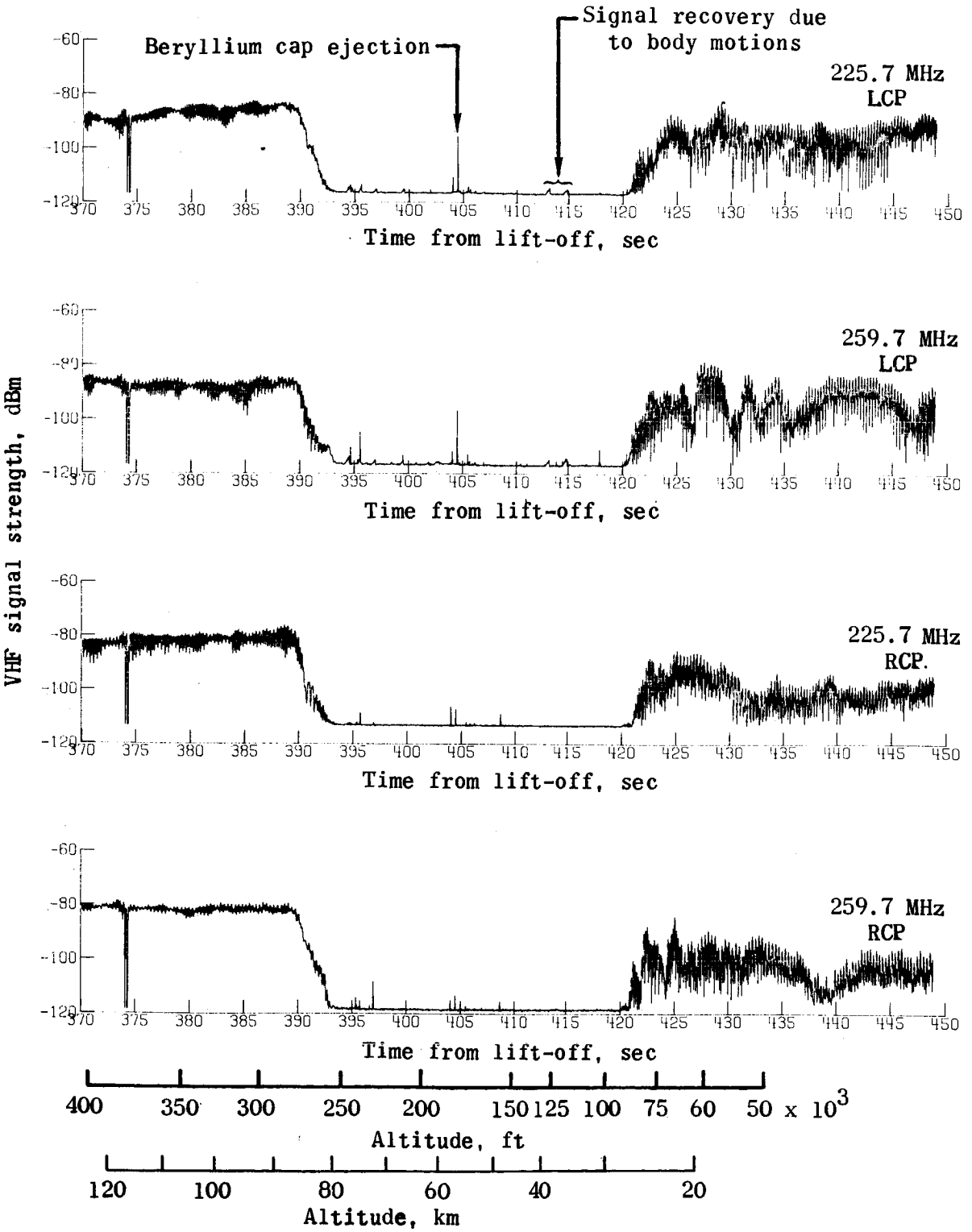

Figure 16.- VHF signal strength at USNS Range Recoverer. Left- and right-hand circular polarization (LCP and RCP).

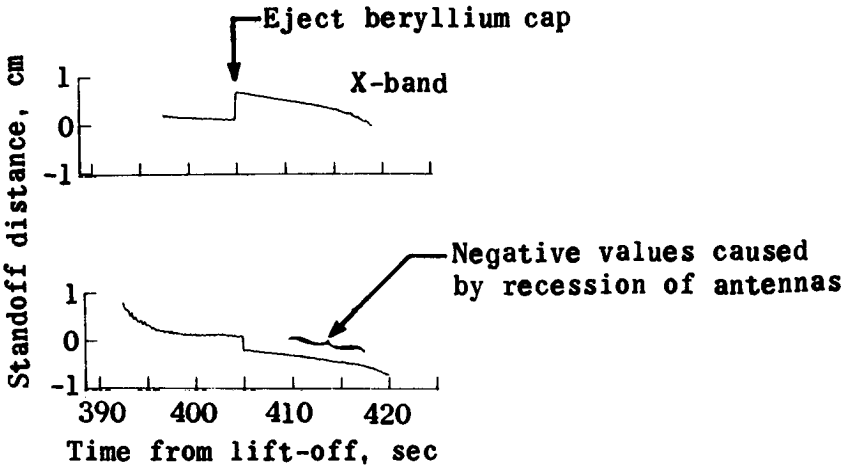

(a) Station 1 (x/D = 0.15).

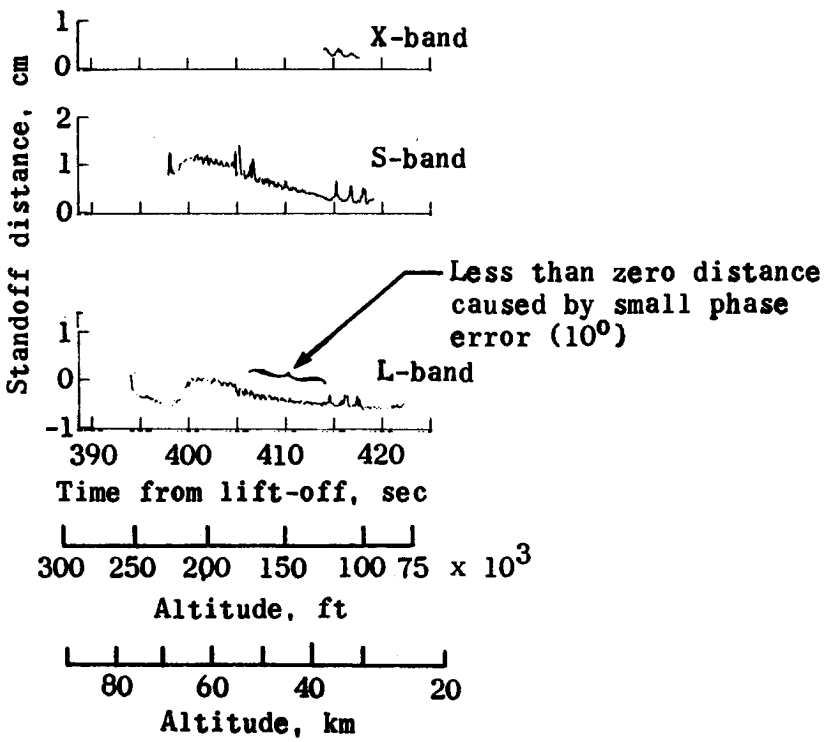

(b) Station 2 (x/D = 0.76).

Figure 17.- Reflectometer-determined critical-density standoff distances.

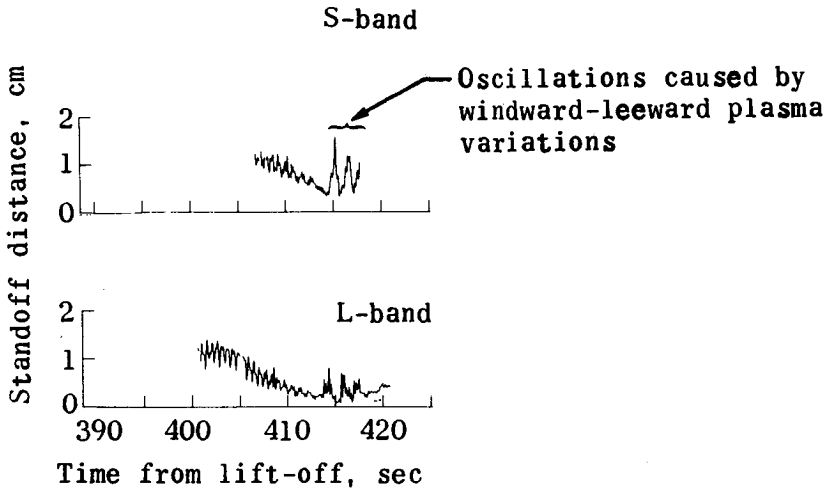

(c) Station 3 ($x/D_i = 2.30$).

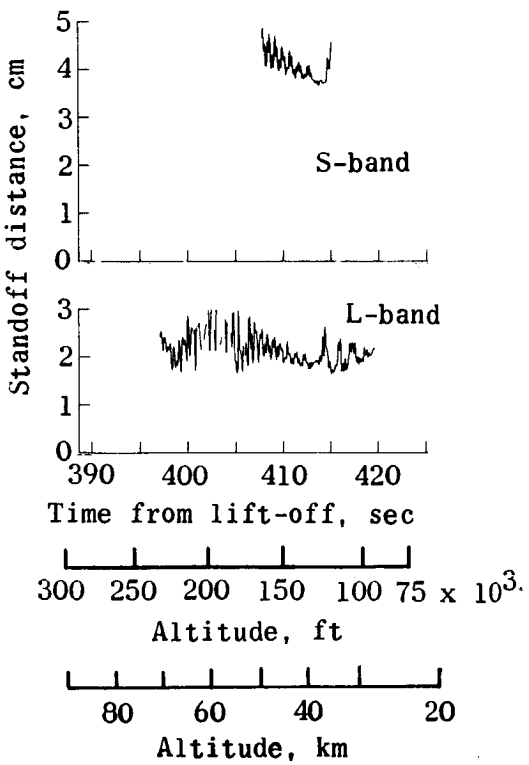

(d) Station 4 ($x/D = 3.48$).

Figure 17.- Concluded.

ELECTROSTATIC PROBE MEASUREMENTS OF PLASMA SURROUNDING THREE 25 000 FOOT PER SECOND REENTRY FLIGHT EXPERIMENTS

By W. Linwood Jones, Jr., and Aubrey E. Cross
NASA Langley Research Center

SUMMARY

A high-altitude electrostatic probe experiment is described and data are presented for three RAM C reentries at velocities of approximately 25 000 feet per second. The electron density profiles inferred from the probe measurements are compared with theoretical calculations, and the probable cause of significant disagreement is briefly discussed. Probe measurements during material-addition sequences for radio-blackout alleviation are presented, and comparisons of probe measurements with other pertinent diagnostic measurements are made.

INTRODUCTION

An electrostatic probe rake is an effective sensor for obtaining electron density profiles in the high-altitude plasma flow field surrounding reentering bodies. Unique measurements were obtained by using this technique during three of the RAM C reentry flight experiments conducted by the Langley Research Center. The results of these measurements have proven invaluable for determining plasma positive-ion and electron distributions in the flow field to assess the validity of present theoretical flow-field models, for evaluating the performance of material injection into the flow field as a blackout alleviant, for sensing vehicle angle-of-attack motions in the rarefied atmosphere where accelerometers are insensitive, and for correlation with other in-flight diagnostic measurements.

EXPERIMENTAL DESCRIPTION

Electrostatic probe measurements for three RAM flights whose individual objectives were somewhat different are described herein. A brief description of the launch vehicles and payloads is given followed by a comprehensive description of the electrostatic probe system. Also briefly covered are the material-injection systems on RAM C-I and C-III, the microwave-reflectometer system on RAM C-II, the S-band diagnostic experiment on RAM C-III, and the VHF telemetry systems on all flights. A complete description of RAM C-I, its instrumentation, and the data obtained is given by Akey and Cross in reference 1, and RAM C-II is described by Grantham in reference 2.

Launch Vehicles

Similar four-stage solid-fuel Scout vehicles were used to launch RAM C-I, C-II, and C-III from the NASA Wallops Station. The launch vehicles transported their respective payloads to apogees greater than 720 000 feet before driving them back into the earth's atmosphere. Prior to reentry each payload was spin-stabilized at approximately 3 rps to prevent large angle-of-attack perturbations. The reentry flight-path angle for all payloads was a nominal -15°, and all payloads reached their maximum velocities at an altitude of about 220 000 feet. The approximate time history of altitude and velocity for all three flights is shown in figure 1, with important events noted. Pertinent vehicle-payload identification and launch information is given in the following table:

Designation		Launch	
Scout vehicle	Payload	Date	Time, GMT
S-159	RAM C-I	10-19-67	17:33:00
S-168	RAM C-II	8-22-68	15:16:00
S-171	RAM C-III	10-1-70	20:06:29.1

Payloads

The three payload configurations are shown in figure 2. Each payload had a hemispherical nose having a radius of about 6 inches, a 9° half-angle conical body, and an overall length of about 51 inches. Both the RAM C-I and C-III configurations had a charring phenolic-graphite ablator as a heat protection material covering the hemispherical nose, whereas RAM C-II had a beryllium-cap heat sink which was ejected at the time of surface melting (185 000-foot altitude), then exposing a teflon-covered nose. The charring ablation material on C-I and C-III was selected to maintain the integrity of material-injection nozzles during the ablation period. The beryllium cap was selected to keep the flow field relatively free of ablation contaminants for comparison of measured plasma characteristics with "clean air" theoretical calculations. Compared with the nonablating beryllium nose cap, chemical analysis of the charring-ablator nose material disclosed easily ionizable alkali-metal contents of 1000 to 4000 ppm, primarily sodium. The ablative phenolic-graphite therefore fed easily ionizable alkali metal into the flow field. In addition, all three flow fields were contaminated with teflon ablation products from the conical body.

Electrostatic Probe Experiment on RAM C-I, C-II, and C-III

Design philosophy.- The ability to compute theoretically realistic electron density profiles is essential for accurate prediction of electromagnetic wave attenuation. The electrostatic probe experiment was designed to determine the positive-ion density profiles in the aft flow field so that calculated profiles could be compared with those measured. The range of densities to be

measured and the location of the ion collectors were selected based on flow-field calculations as shown in figure 3 and presented in unpublished calculations.[1] Data from reference 3 are also shown. Although it was desirable to make measurements over the entire blackout data period (280 000 to 80 000 ft), the high heating rates predicted for the intermediate altitude range necessitated the retraction of the probe rake into the base of the spacecraft at 185 000 feet.

Mechanical configuration of electrostatic probes.- The electrostatic probe rake was located on the aft portion of each payload with a thermocouple probe rake located diametrically opposite (fig. 2). The thermocouple probe rake monitored the rise in temperature of the leading edge due to aerodynamic heating. Detailed drawings and tables of probe dimensions are given in figure 4.

In figure 4(a) the exterior physical configuration of the electrostatic probe rake, a sectional view of the leading edge, and standoff dimensions of the ion collectors are shown. Each of the iridium ion collectors extended 0.010 inch beyond the wedge-shaped beryllium oxide leading edge of the rake. The two larger iridium pieces, one on each side of the rake, served as electron collectors. The beryllium oxide leading edge was a 60° wedge with a leading-edge radius of 0.010 inch and was inclined at an angle of 45° with respect to the payload surface. The main body of the probe was constructed of a phenolic fiber-glass ablation material.

The geometry of the thermocouple probe rake, shown in figure 4(b), was the same as that of the electrostatic probe rake. Instead of electrodes, however, three thermocouples were imbedded 0.025 inch from the leading edge of the wedge, as shown in the sectional view of the leading edge. The thermocouples were platinum/platinum—13-percent-rhodium and were located 2, 4, and 6 cm from the payload surface. The useful measurement range of the thermocouples was from 0° to 3100° F. It is believed that below 2000° F there are no significant thermal effects upon the probe materials.

Probe electronic circuitry.- A fixed bias of -5.0 volts, referenced to the electron collectors, was applied continuously to all ion collectors to attract positive ions. Figure 5 gives a simplied schematic drawing of the probe electronic system on both the RAM C-I and C-II payloads. As the probe continuously collected plasma current, the mechanical commutator sampled the voltage developed across the probe load resistors and calibrate resistors and fed the signals to the quasi-logarithmic amplifier at the rate of 300 samples per second. The quasi-logarithmic amplifier converted the logarithmic input to a linear output which drove a telemetry subcarrier oscillator. The power supply provided bias for the probes and regulated power for the quasi-logarithmic amplifier.

Other than using different serialized components for the two flights, the circuits were identical, with the following exception. The quasi-logarithmic amplifier output on the C-I experiment was connected single-ended to the input

---

[1]Memorandum from John S. Evans and Charles J. Schexnayder, Jr., to RAM Project Files, dated September 1966, concerning revisions to "Report of Calculated Nonequilibrium Flow-Field Properties for RAM C."

of the subcarrier oscillator and thereby placed the low side of the amplifier output at payload ground potential. The output of the logarithmic amplifier on the C-II experiment was connected to a differential-input subcarrier oscillator. The C-II configuration was necessary because of an anomaly that occurred during the C-I flight. This anomaly was the result of a difference in the floating potential of the electron collectors and the spacecraft metallic skin. This extemporaneous voltage developed between the input of the logarithmic amplifier and the low side of the single-ended output, which caused the internal input diodes of the amplifier to switch and thereby made the output of the logarithmic amplifier zero. The anomaly was simulated by bench tests using a -1.85 volt potential between the electron collector and payload ground. The duration of the actual flight anomaly was ascertained by the onboard logarithmic-amplifier calibrate portion of the telemetered data. The differential connection used on the C-II system corrected the situation by effectively connecting a large resistance (10 megohms) in series with this unwanted bias and thereby preventing the diodes from switching.

Probe-experiment characteristics and data format.- A peak plasma density of 10^{12} electrons/cm^3 and a corresponding ion current of 10^{-3} ampere were anticipated in the vicinity of the probes during the prime data period. This upper limit of current through the 400-ohm input load resistor of the logarithmic amplifier represents a useful measurement range of 10^{-7} to 10^{-3} ampere, corresponding to an approximate electron density range from 10^8 to 10^{12} electrons/cm^3.

A typical data format of electrostatic probe information from the logarithmic amplifier output, including currents from the probes and from the calibrates, is presented in figure 6. Shown in the figure is one complete data frame which has a duration of 100 msec. There are five calibrate levels at the beginning and end of each frame, which are repetitive in every frame. The calibrate levels correspond to currents of 0 to 0.1, 1.0, 10.0, 100.0, and 1000.0 μA. Between the calibrate levels are three consecutive samplings or distributions of each of the eight ion collectors. One distribution represents 26.4 msec or about 8 percent of a complete payload roll motion.

Electrostatic probe experiment on RAM C-III.- The RAM C-III payload had two electrostatic probe rakes located diametrically opposite each other at the base of the spacecraft (fig. 2). One was similar to the ion density measuring rakes used on RAM C-I and C-II except that it was slimmer (30° wedge angle) and it extended farther into the flow field. The second rake contained four cylindrical wires alined parallel to the flow from which both electron temperature and density were determined from the swept-voltage characteristic of the probe. This rake also contained six thermocouples to measure heating. The physical configurations of the electrostatic probe rakes, sectional views of the leading edges, and standoff dimensions of the current collectors are given in figures 7(a) and 7(b).

The electronic system for the RAM C-III ion-probe rake was identical to that for the C-II except for the data format (fig. 8). The odd-numbered probes are sampled first, then the even-numbered probes, then the odd are resampled, and finally the calibration is performed.

The electronic system[2] for the electron-probe rake is shown in figure 9. The probes were sequentially swept with a linear voltage ramp from -6.0 to +5.0 volts in a 20-msec period. The probe switching and voltage sweeping were synchronized by a master clock. The frequency response of the system was approximately 600 hertz. The data format is shown in figure 10. A low and a high range of current sensitivity was obtained by selecting either a 6-ohm or a 120-ohm load resistor, respectively. The probe current was monitored by a differential-input voltage controlled oscillator connected across the appropriate load resistor.

Probe theory.- The theory used to interpret the fixed-bias probe measurements is discussed by Dunn in reference 4 and that used for the swept-voltage probes by Laframboise in reference 5. The estimated accuracy of the probe measurements is ±20 percent for densities on the order of 10^{10} to 10^{11} electrons/cm^3 and at least a factor of two over the entire range of 10^8 to 10^{13} electrons/cm^3 (ref. 6).

Material-Injection System on RAM C-I and C-III

During the RAM C-I flight, water was injected into the flow field from the spacecraft nose at varying rates with specific idealized penetrations to provide for electron density reductions in the peak attenuating layer of the flow field (ref. 1). Water and an electrophilic material (Freon E-3) were used as alleviants during the C-III flight, and their relative effectiveness in reducing ionization is discussed by Schroeder in reference 7. For both flights, the injection sequence began at an altitude of approximately 280 000 feet and consisted of a 0.2-second period of injection followed by a 0.3-second period of no injection. A typical injection sequence for each flight is shown in figure 11. Two VHF slot antennas and the electrostatic probe rakes were located in line with the injection sites and were the principle diagnostic instrumentations for assessing the plasma alleviation.

Microwave-Reflectometer System on RAM C-II

The microwave-reflectometer technique, employed to diagnose the RAM C-II flow field, used the reflectivity measurements of the plasma as an indication of electron density. Phase measurements were used to determine the critical density location in the nonhomogeneous plasma and thereby to indicate the general nature of the profile shape. Fifteen microwave antennas were positioned at four locations along the payload (fig. 2). A plasma-density measurement range of three decades was provided by the four-frequency reflectometer system; thus, peak electron densities from 10^{10} to 10^{13} electrons/cm^3 could be ascertained. Greater detail on the microwave-reflectometer system is presented by Grantham in reference 8.

---

[2]Developed by Winn R. Vaughan and Charles D. Nichols of Langley Research Center.

S-Band Diagnostic Experiment on RAM C-III

The S-band diagnostic experiment on RAM C-III consisted of onboard measurements of antenna input admittance and received signal strength measurements by a Bermuda telemetry station. The signal strength measurements gave the time history of the integrated value of the electron density; and the onboard measurements yielded peak electron density and profile shape information. The details of the flight system and flight results are given by Swift, Beck, Thomson, and Castellow in reference 9.

VHF Telemetry System

The VHF telemetry systems on all three payloads used the same frequencies for data transmission, 225.7 MHz and 259.7 MHz; however, the physical location and the types of antennas used were quite different. For the RAM C-I and C-III payloads, two diametrically opposed, axially oriented, 259.7-MHz cavity-backed slot antennas transmitted the real-time telemetry, and an aft-positioned 225.7-MHz circumferential slot array antenna transmitted the delayed-time telemetry. In comparison, on the RAM C-II payload, the real-time and delayed-time telemetry systems utilized a pair of aft-located circumferential slot arrays. The effects of the reentry plasma on the VHF antenna patterns and correlation with electrostatic probe measurements are described by Croswell and Jones in reference 10.

RESULTS AND DISCUSSION[3]

Electrostatic Probe Measurements

Measured electron densities for selected probes are presented as a function of altitude in figure 12. The effects of material injection are clearly seen on the RAM C-I and C-III curves for all probes. During an injection cycle the sequential increase in flow rates is readily seen as corresponding decreases in electron density. Distribution profiles during the side injection portion of cycle 3 of RAM C-I are shown in figure 13. The curve labeled "No flow" represents the average distribution during the no-injection periods of injection cycle 3. The data points for each profile represent instantaneous interpolations of electron density from plots such as those of figure 12. The calculated change in signal attenuation at VHF obtained by using plane-wave—homogeneous-plasma slab theory is in agreement with the observed changes in electron density profile for flow rates 2, 3, and 4 (ref. 1).

Small oscillatory variations can be seen in the electron density curves of all probes for all flights, although they are more clearly seen on C-II probes since these are not disturbed by material injection. These variations are due to an unsymmetrical flow field about the payload while it is at a nonzero angle

[3]All flight data presented for RAM C-III are preliminary and are subject to change.

of attack. Since the probes are fixed on the payload, they sense a varying electron density as they move windward to leeward at the vehicle spin rate of 3 rps.

A comparison of vehicle angle of attack,[4] as determined from accelerometer data, with electrostatic probe measurements from the C-II flight is shown in figure 14. The data from the normal accelerometer strongly correlate with density fluctuations observed by the probe. When the vehicle is undergoing a positive normal acceleration or positive angle of attack, the electrostatic probes are on the windward side of the vehicle and they sense a compression of the flow field. Conversely, for a negative normal acceleration or negative angle of attack, the probes sense the leeward (less dense) side of the flow field. Small angle-of-attack motions (less than $\pm 5^{\circ}$) produce peak-to-peak fluctuations in electron density at collector 1 of ± 50 percent of the average.

Comparative electrostatic probe measurements during the essentially identical flight trajectories of the three flights indicate no appreciable change in ionization levels in the aft flow field.

Based on an equilibrium assumption, it was believed that alkali ablation products from the charring nose of RAM C-I could have caused a significant increase in the ionization levels over those of RAM C-II. At these higher altitudes, the mass ratio of ablatant to air is as great as it is at some lower altitudes where increased ionization due to ablation has been noted. A detailed discussion of alkali-ablation-product contamination of the RAM C flow field is given by Schexnayder, Evans, and Huber in reference 11.

Measured electron density profiles for RAM C-II are shown for four altitudes in figure 15. The probe data are the time-average electron densities with the bars representing the density excursion due to body motions. These data infer profiles that rise steeply from the spacecraft wall to the first probe (0.96 cm) and then rise gradually to the outermost probe (7.08 cm).

Microwave Reflectometer Measurements

The electron density profiles inferred by the electrostatic probe on the RAM C-II payload agree in magnitude and shape with those inferred by the microwave reflectometer over the full altitude range of meaningful probe measurements. The good correlation between these two diagnostic measurements is illustrated in figure 16. The time-average peak electron density, as indicated by the microwave reflectometer and the time-average value for probes 1 and 8 are plotted against distance along the body for four altitudes. The bar on the probe data represents the peak-to-peak density fluctuation due to body motions.

[4] Analysis performed by William L. Weaver of Langley Research Center.

Other Diagnostic Measurements

Good correlation exists between electron densities inferred from electrostatic probes, VHF antenna pattern data, and the S-band diagnostic experiment data. Figure 17 is a plot of electron density against altitude for these systems and the RAM C-II reflectometer. Probe data represent the envelope of maximum to minimum value for all probes for RAM C-II. All densities are corrected for body location and are referred to the probe station by use of figure 16.

Comparison of Theoretical and Experimental Electron Density Profiles

A comparison of the RAM C-II inferred electron density profiles (fig. 15) with theoretical profiles (fig. 3) indicated that the plasma distribution was much thicker than theoretically predicted. Subsequent calculations were performed (ref. 11) and are shown in figure 18 with the RAM C-II and C-III measured data. The data bars represent the envelope of probe data (due to body motions) and the "hatched" region represents C-III data taken during the onset of probe heating. Until a complete analysis is performed, it is not known whether heating effects are present in these hatched data.

When ambipolar diffusion is considered, the theoretical and experimental values of peak electron density compare favorably although the shape of the profile inferred from the probe data is not falling off rapidly as theoretically estimated. At 263 000 ft the C-III profile is still rising at 14 cm. At about 233 000 ft, however, a detailed examination of the C-III records indicated that the peak of the profile does move within the 14-cm distance as the probes move leeward to windward.

CONCLUDING REMARKS

Electron density profiles have been inferred from electrostatic probe measurements obtained during three reentry experiments. Good correlative agreement exists between peak electron densities inferred from probe data and those inferred from other independent diagnostic measurements.

A comparison of results from RAM C-I and C-III (ablation-contaminated flow field) with those from RAM C-II (clean-air flow field) indicates no significant increase in flow-field ionization levels due to ablation products for altitudes above 200 000 feet.

A comparison of theoretical and electrostatic-probe-inferred electron density profiles indicates that ambipolar diffusion effects must be included in theoretical plasma-flow-field models for altitudes above 200 000 feet.

REFERENCES

1. Akey, Norman D.; and Cross, Aubrey E. (With appendix A by Thomas G. Campbell; appendix B by Fred B. Beck; and appendix C by W. Linwood Jones, Jr.): Radio Blackout Alleviation and Plasma Diagnostic Results From a 25 000 Foot Per Second Blunt-Body Reentry. NASA TN D-5615, 1970.

2. Grantham, William L.: Flight Results of a 25 000-Foot-Per-Second Reentry Experiment Using Microwave Reflectometers To Measure Plasma Electron Density and Standoff Distance. NASA TN D-6062, 1970.

3. Webb, H., Jr.; Dresser, H.; Korkan, K.; and Raparelli, R.: Theoretical Flow Field Calculations for Project RAM. NASA CR-1308, 1969.

4. Dunn, Michael G.: Laboratory Measurements of Electron Density and Electron Temperature With RAM Flight Probes. The Entry Plasma Sheath and Its Effects on Space Vehicle Electromagnetic Systems - Vol. I, NASA SP-252, 1971, pp. 261-276.

5. Laframboise, James G.: Theory of Spherical and Cylindrical Langmuir Probes in a Collisionless, Maxwellian Plasma at Rest. Rep. No. 100, Inst. Aerosp. Studies, Univ. Toronto, June 1966. (Available from DDC as AD 634596.)

6. Scharfman, W. E.; and Bredfeldt, H. R.: Use of the Langmuir Probe To Determine the Electron Density and Temperature Surrounding Re-Entry Vehicles. NASA CR-66275, 1966.

7. Schroeder, Lyle C.: Flight Measurements at 25 000 Feet Per Second of Blackout Alleviation by Water and Electrophilic Injection. The Entry Plasma Sheath and Its Effects on Space Vehicle Electromagnetic Systems - Vol. II, NASA SP-253, 1971, pp. 77-100.

8. Grantham, William L.: Reentry Plasma Measurements Using a Four-Frequency Reflectometer. The Entry Plasma Sheath and Its Effects on Space Vehicle Electromagnetic Systems - Vol. I, NASA SP-252, 1971, pp. 65-107.

9. Swift, C. T.; Beck, F. B.; Thomson, J.; and Castellow, S. L., Jr.: RAM C-III S-Band Diagnostic Experiment. The Entry Plasma Sheath and Its Effects on Space Vehicle Electromagnetic Systems - Vol. I, NASA SP-252, 1971, pp. 137-155.

10. Croswell, William F.; and Jones, W. Linwood, Jr.: Effects of Reentry Plasma on RAM C-I VHF Telemetry Antennas. The Entry Plasma Sheath and Its Effects on Space Vehicle Electromagnetic Systems - Vol. I, NASA SP-252, 1971, pp. 183-201.

11. Schexnayder, Charles J., Jr.; Evans, John S.; and Huber, Paul W.: Comparison of Theoretical and Experimental Electron Density for RAM C Flights. The Entry Plasma Sheath and Its Effects on Space Vehicle Electromagnetic Systems - Vol. I, NASA SP-252, 1971, pp. 277-303.

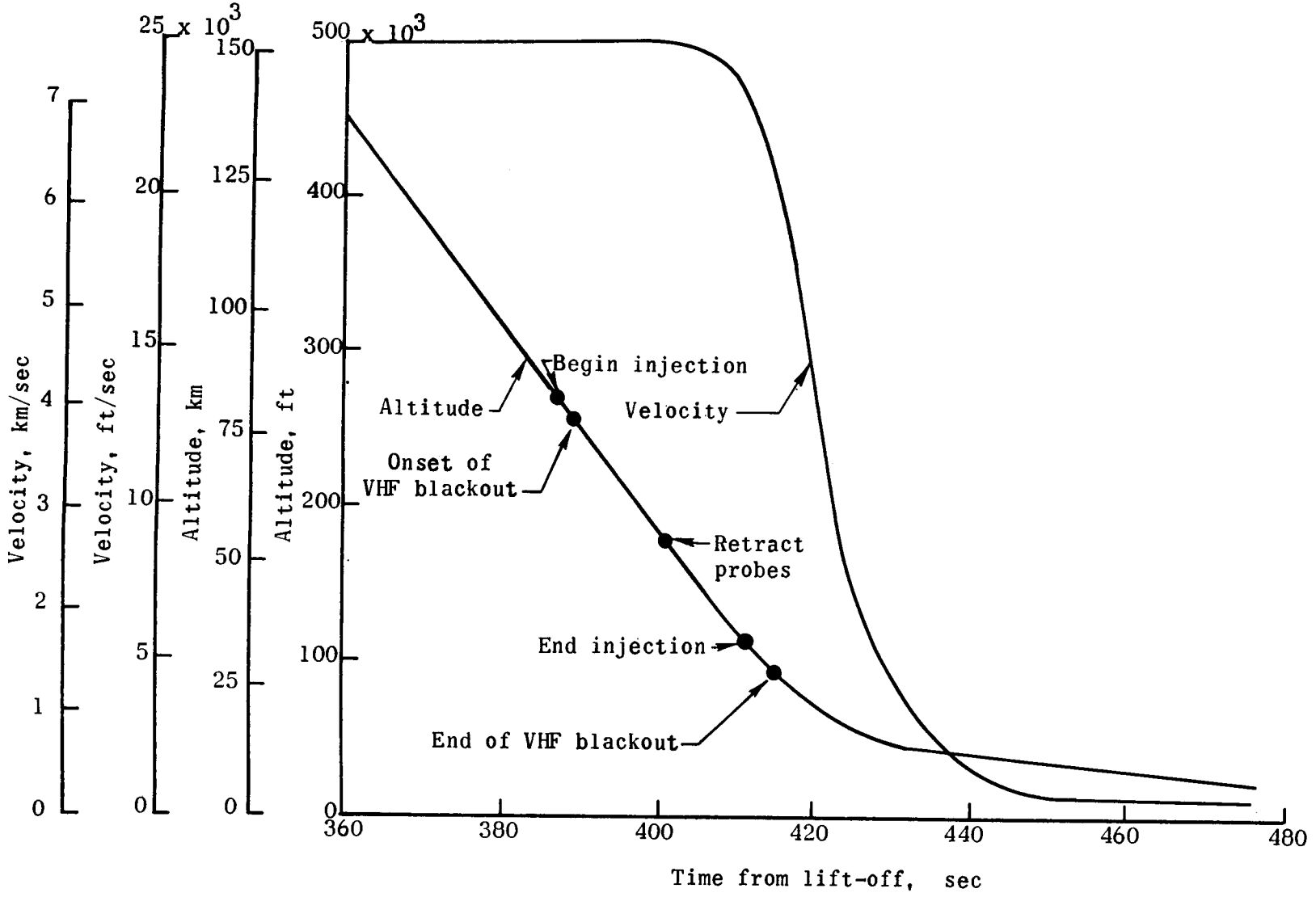

Figure 1.- Typical reentry trajectory for the RAM C flights.

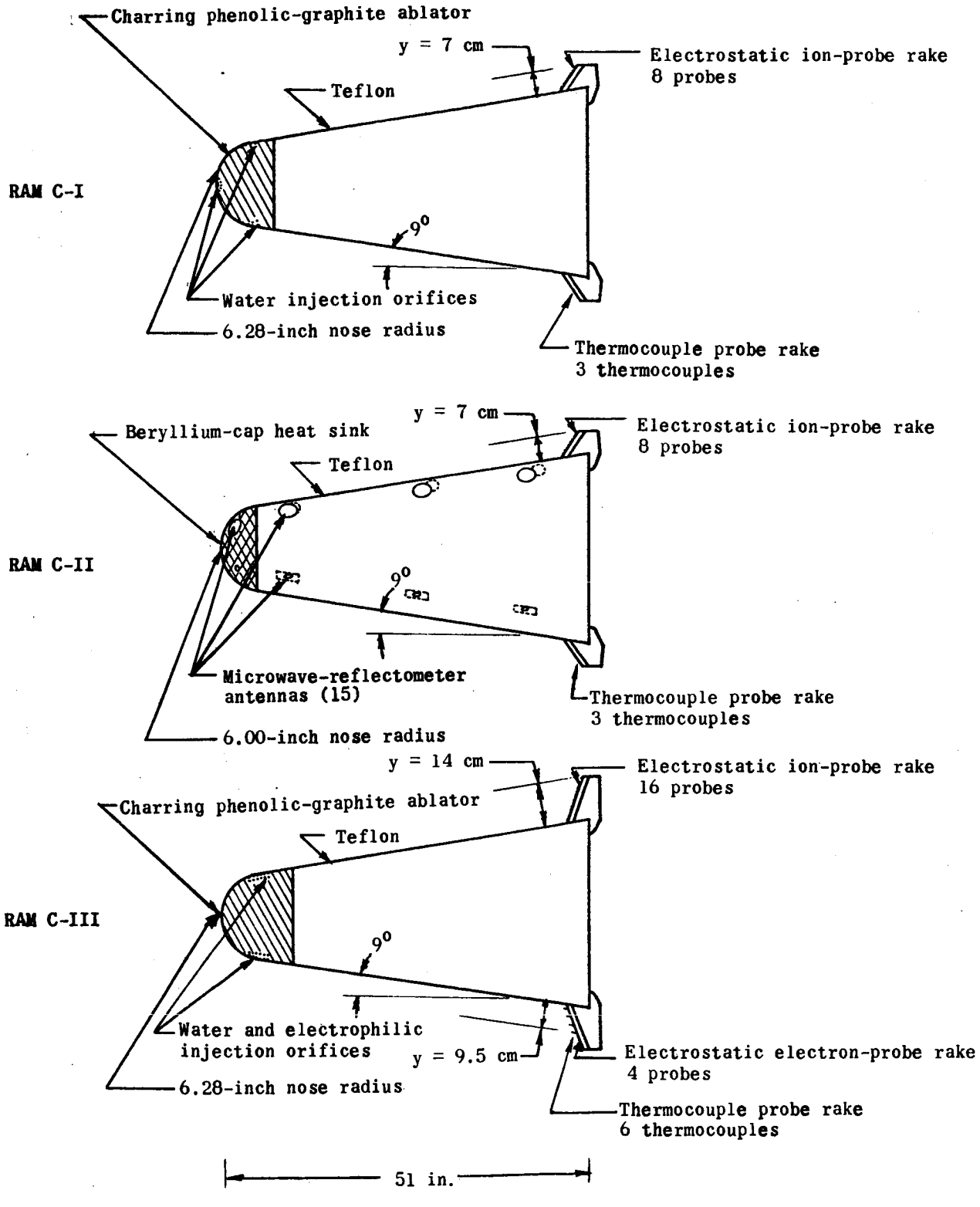

Figure 2.- RAM C-I, C-II, and C-III payload configurations.

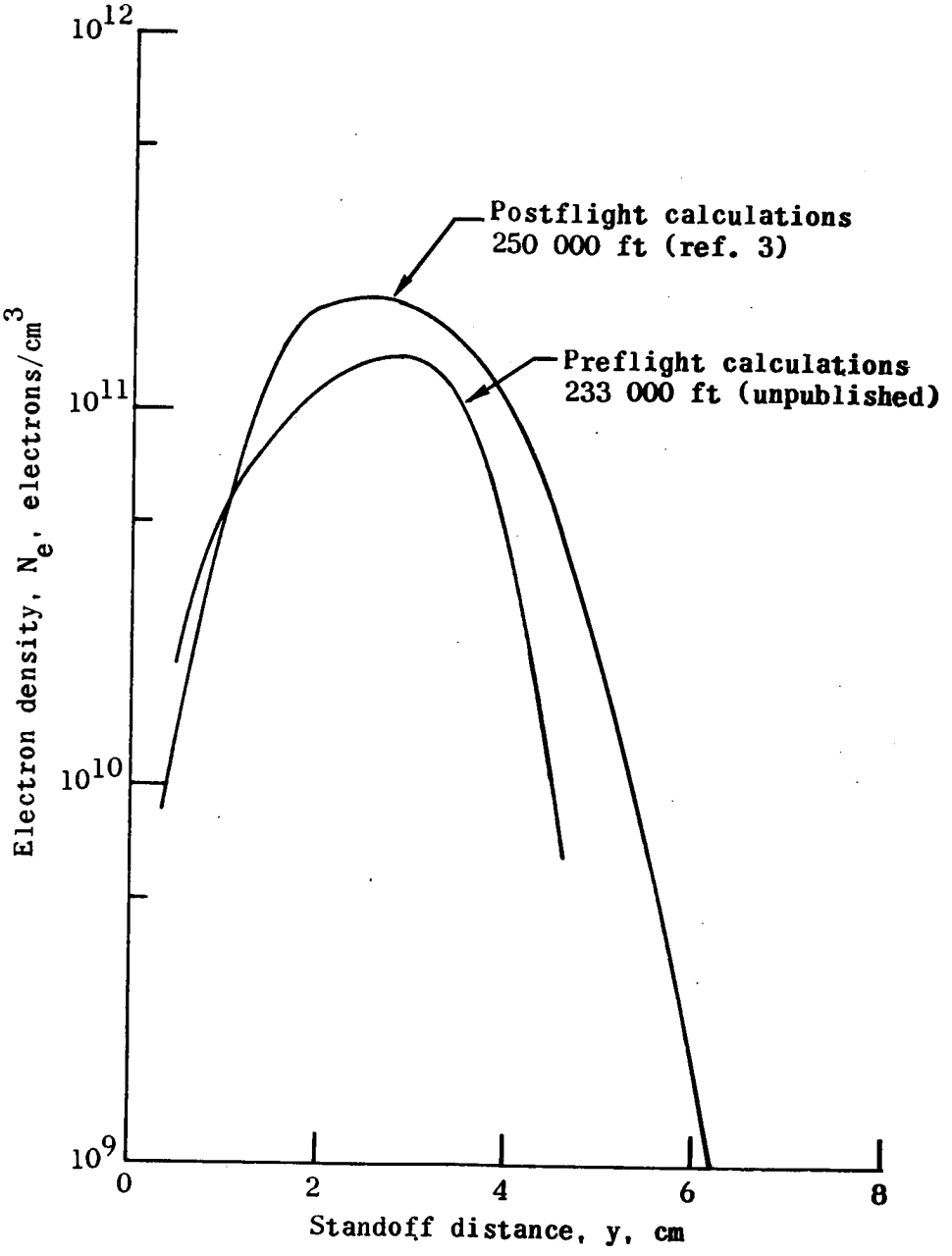

Figure 3.- RAM C-I and C-II boundary-layer-corrected flow-field calculations.

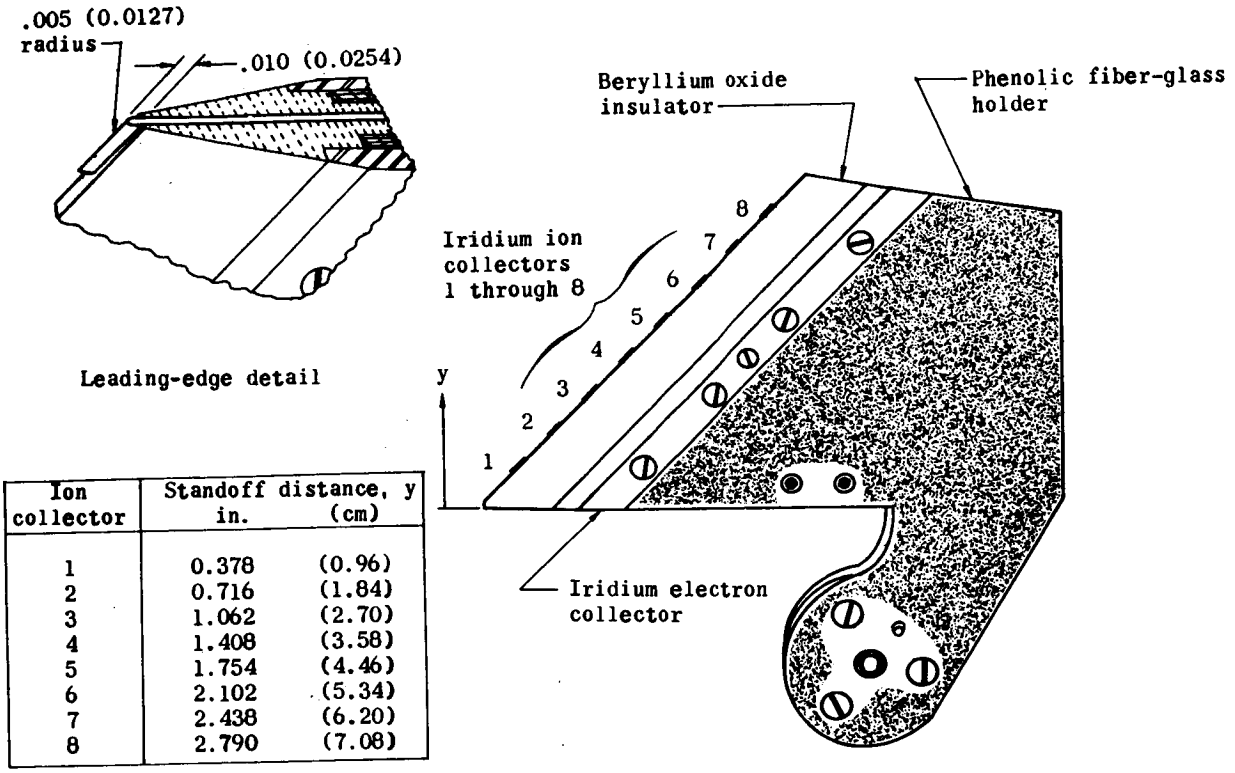

Ion collector	Standoff distance, y in.	(cm)
1	0.378	(0.96)
2	0.716	(1.84)
3	1.062	(2.70)
4	1.408	(3.58)
5	1.754	(4.46)
6	2.102	(5.34)
7	2.438	(6.20)
8	2.790	(7.08)

(a) Electrostatic probe configuration.

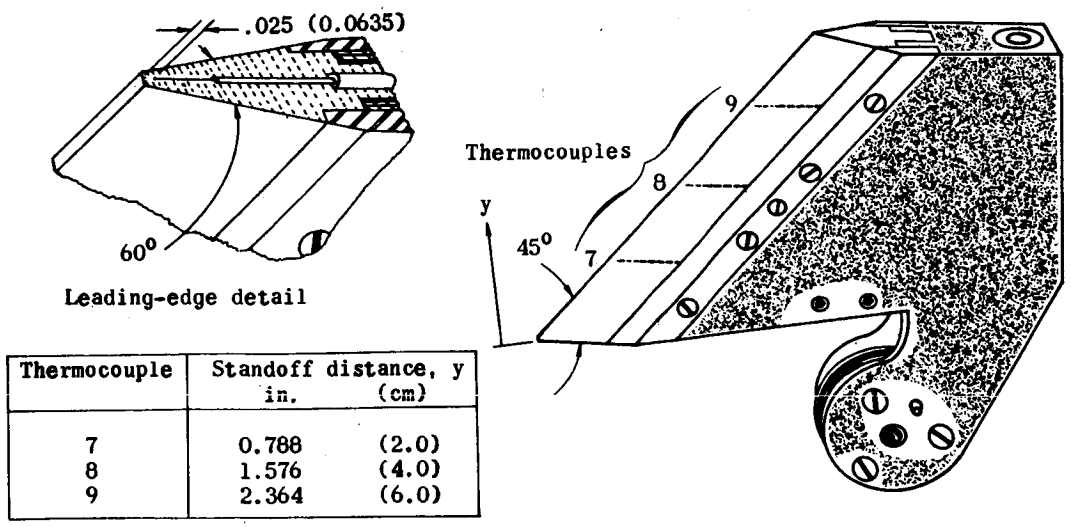

Thermocouple	Standoff distance, y in.	(cm)
7	0.788	(2.0)
8	1.576	(4.0)
9	2.364	(6.0)

(b) Thermocouple probe configuration.

Figure 4.- Body configurations of the RAM C-I and C-II electrostatic and thermocouple probes. All linear dimensions are in inches (centimeters).

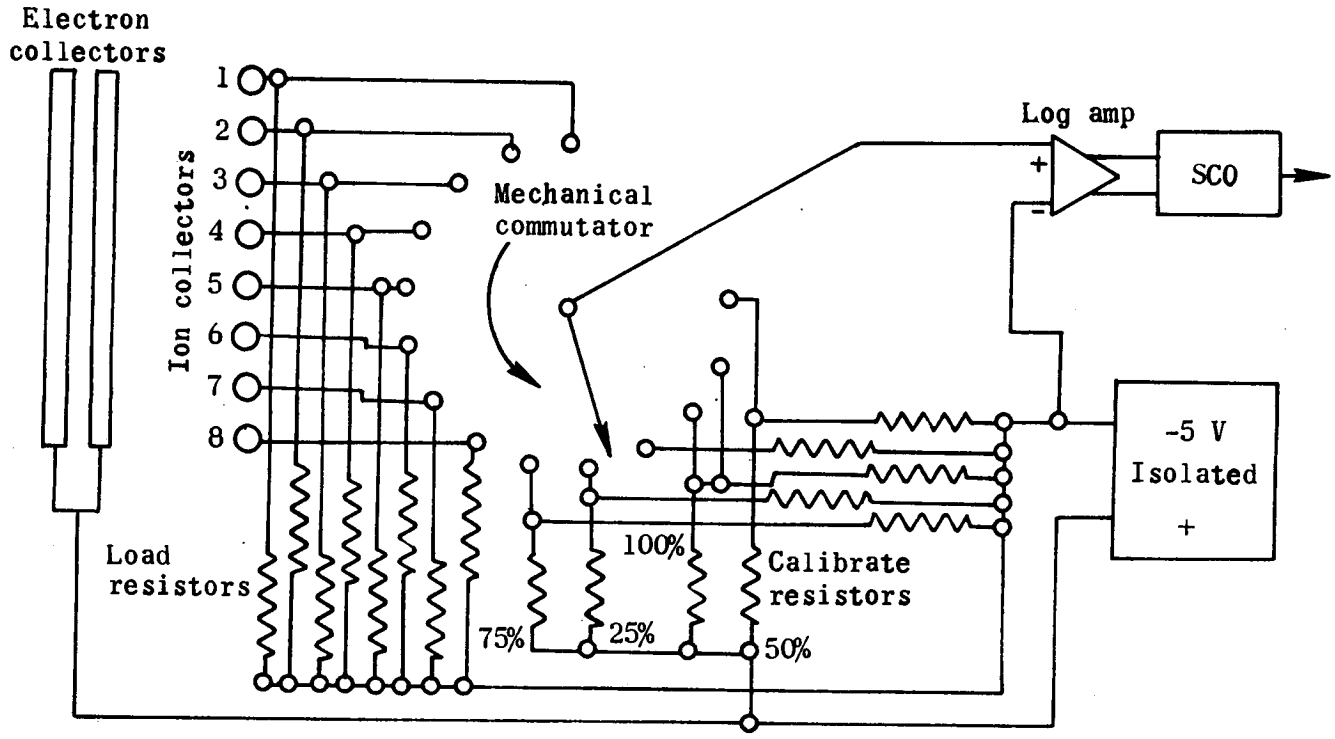

Figure 5.- Simplified schematic of fixed-bias probe electronic systems on RAM C-I and C-II.

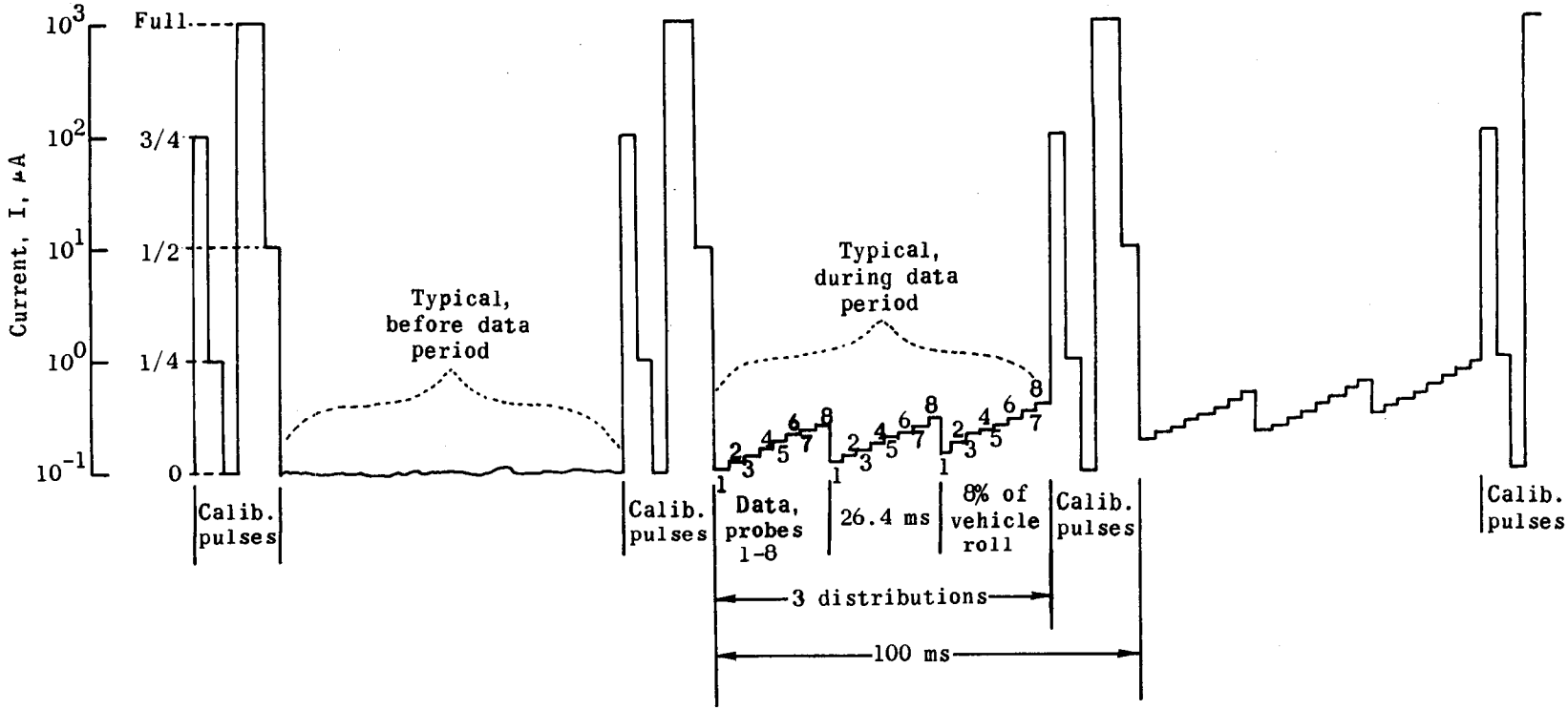

Figure 6.- Typical electrostatic probe data format for RAM C-I and C-II.

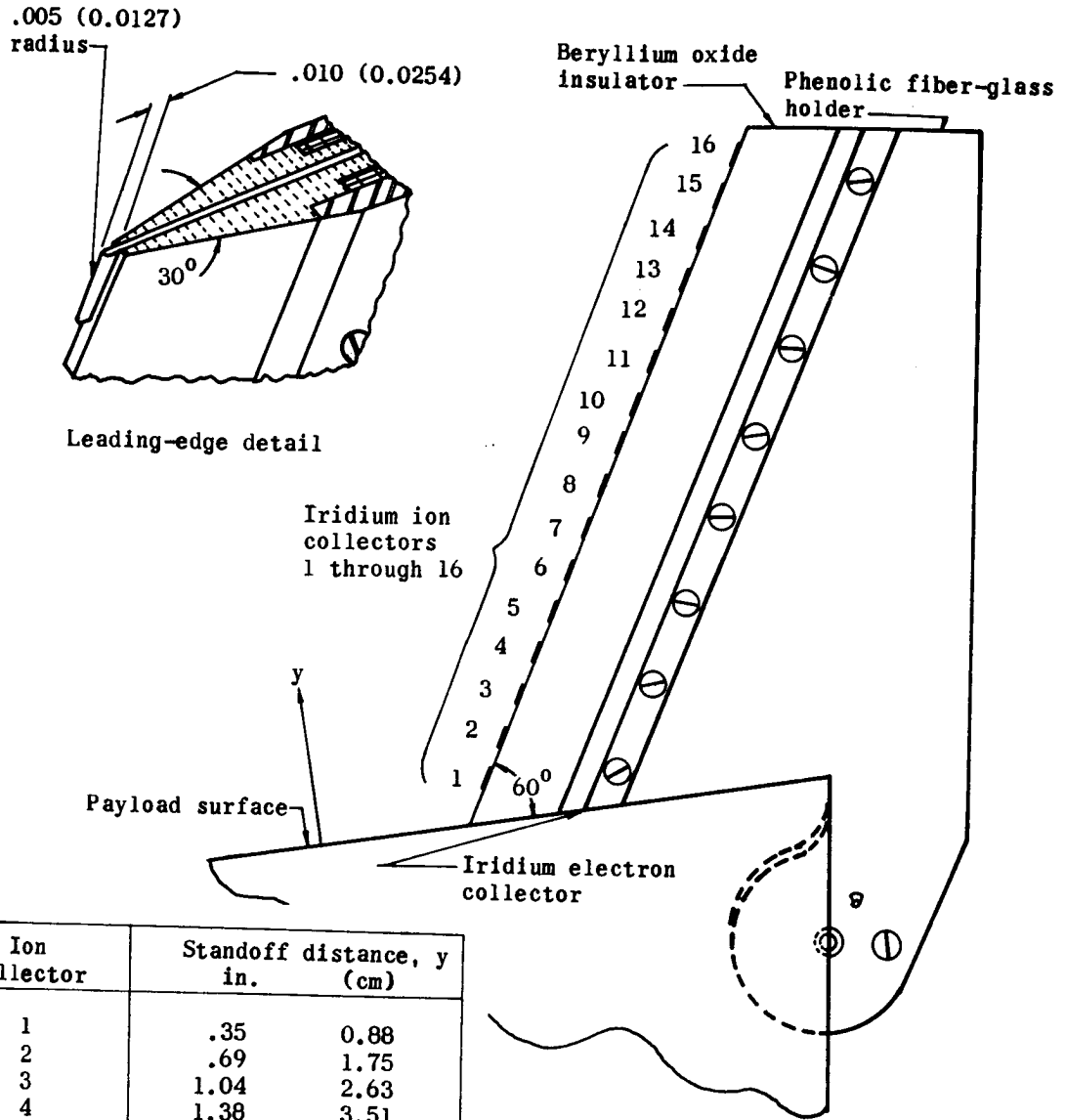

Ion collector	Standoff distance, y in.	(cm)
1	.35	0.88
2	.69	1.75
3	1.04	2.63
4	1.38	3.51
5	1.72	4.38
6	2.07	5.26
7	2.42	6.14
8	2.76	7.01
9	3.10	7.89
10	3.45	8.77
11	3.80	9.64
12	4.14	10.52
13	4.48	11.39
14	4.83	12.27
15	5.18	13.15
16	5.52	14.02

(a) Ion-probe rake.

Figure 7.- Physical configuration of the electrostatic probe rakes on the RAM C-III payload. All linear dimensions are in inches (centimeters).

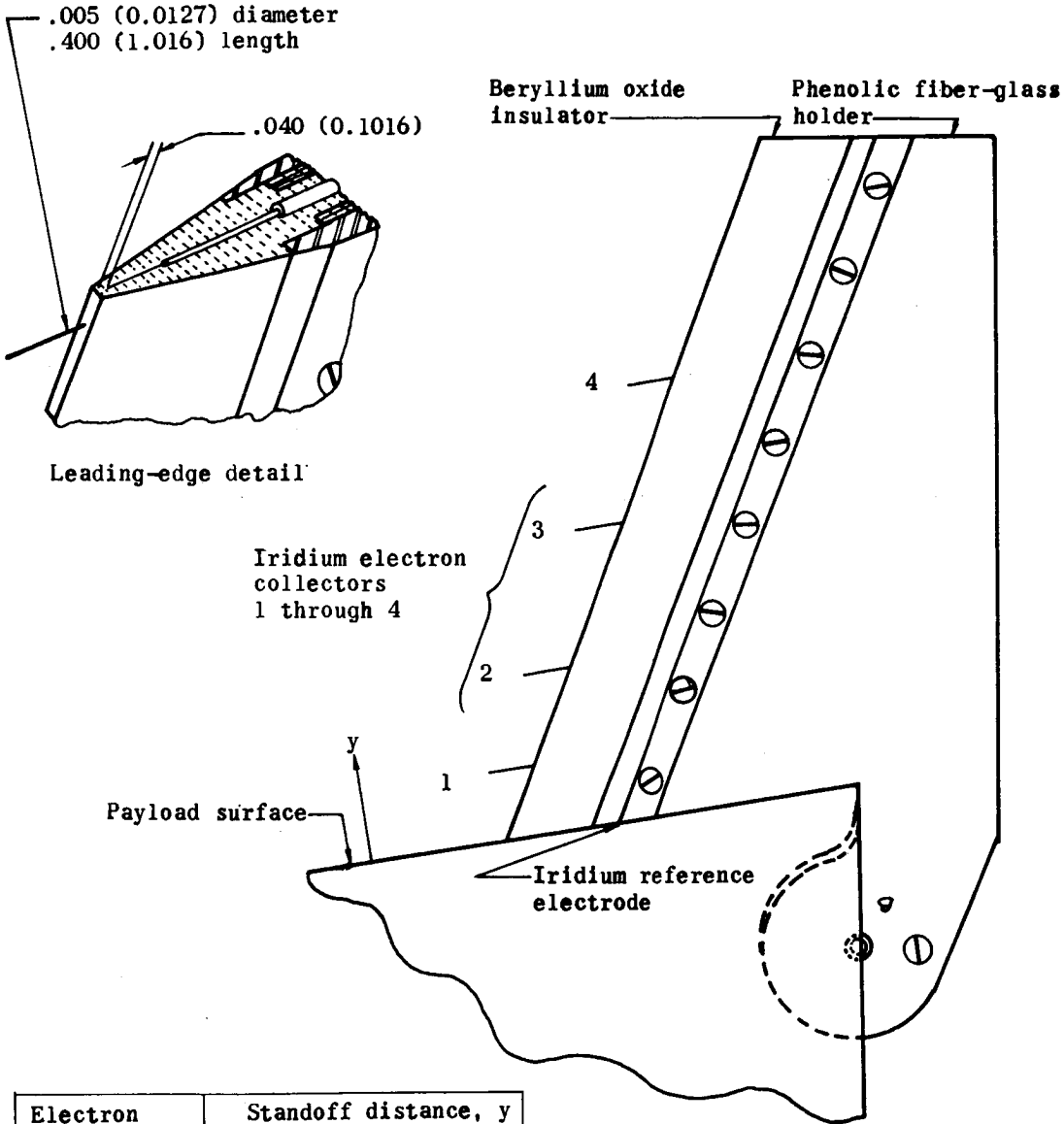

Electron collector	Standoff distance, y	
	in.	(cm)
1	.59	1.5
2	1.38	3.5
3	2.56	6.5
4	3.74	9.5

(b) Electron-probe rake.

Figure 7.- Concluded.

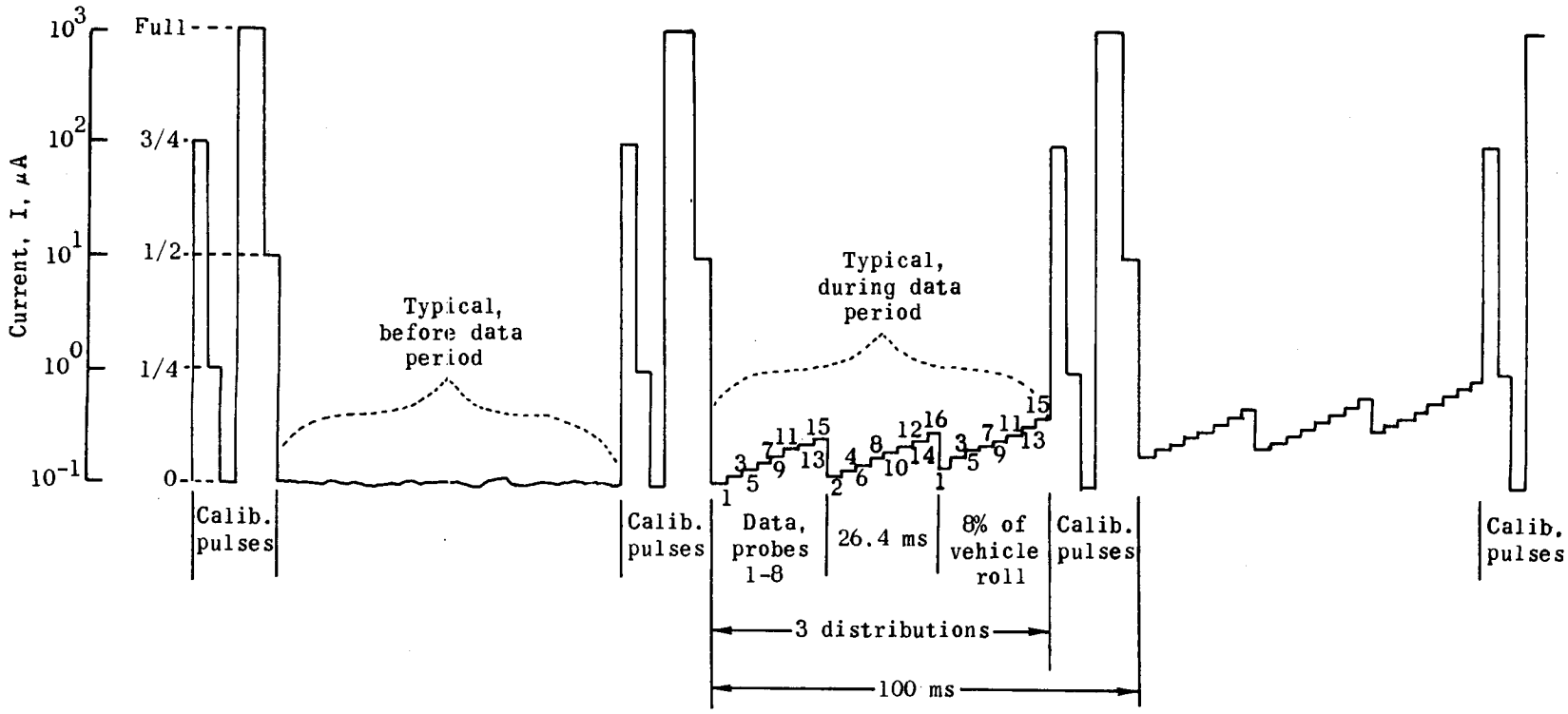

Figure 8.- Typical electrostatic probe data format for RAM C-III.

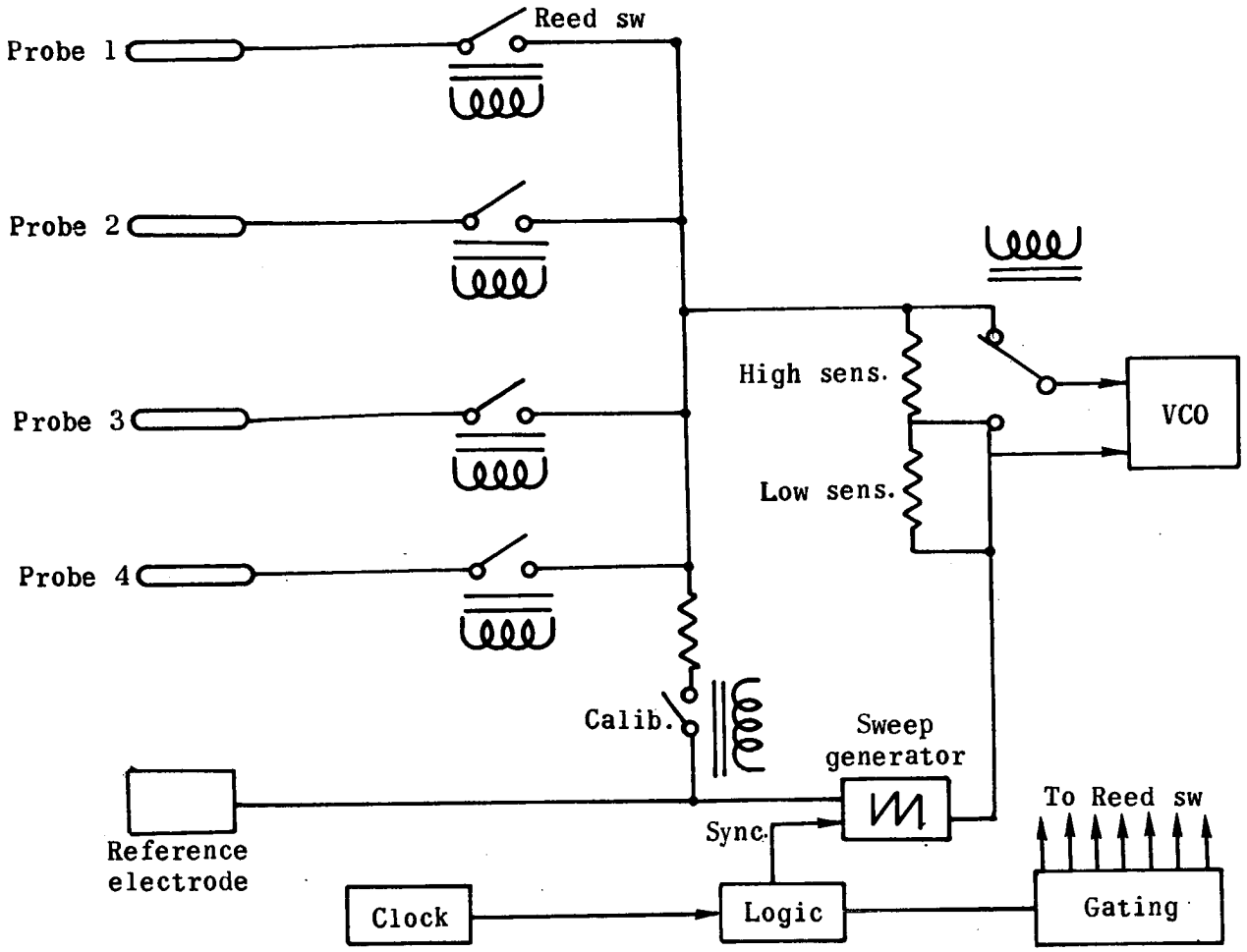

Figure 9.- Simplified schematic of RAM C-III swept-voltage probe electronic system.

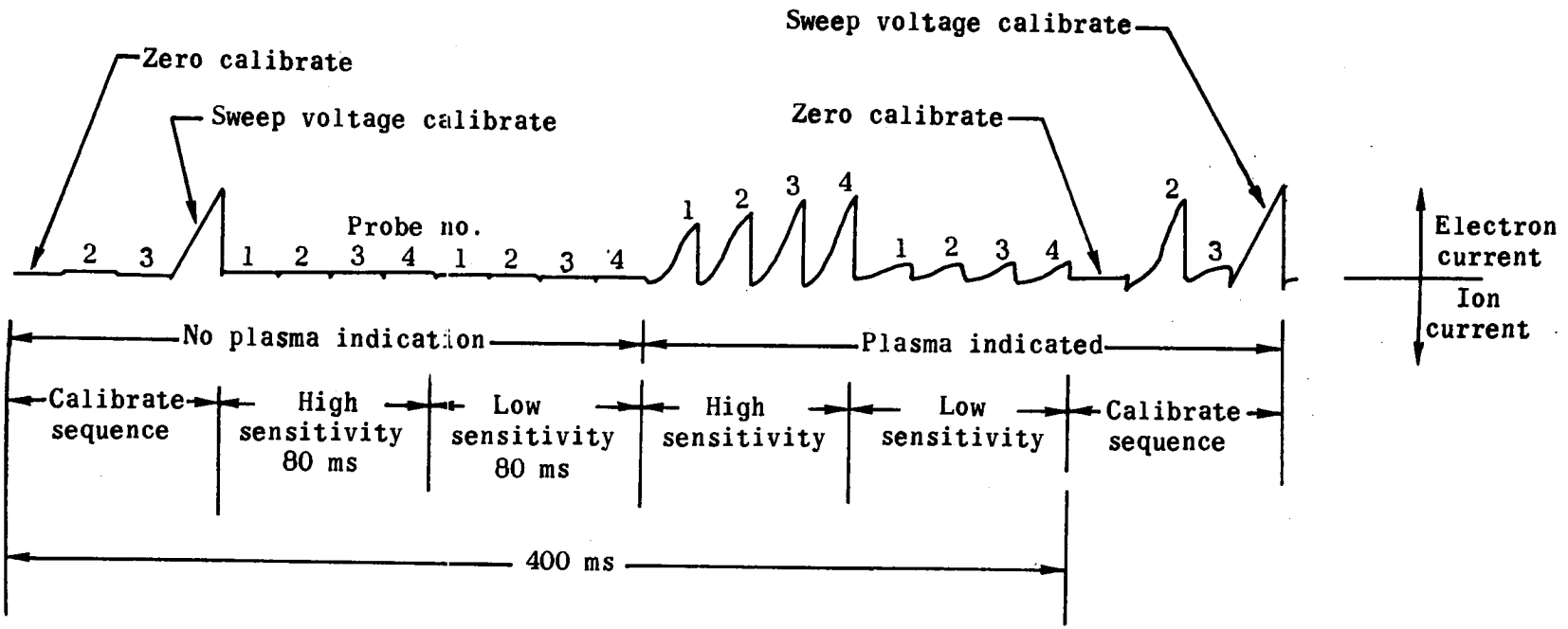

Figure 10.- Data format of RAM C-III swept-voltage probes.

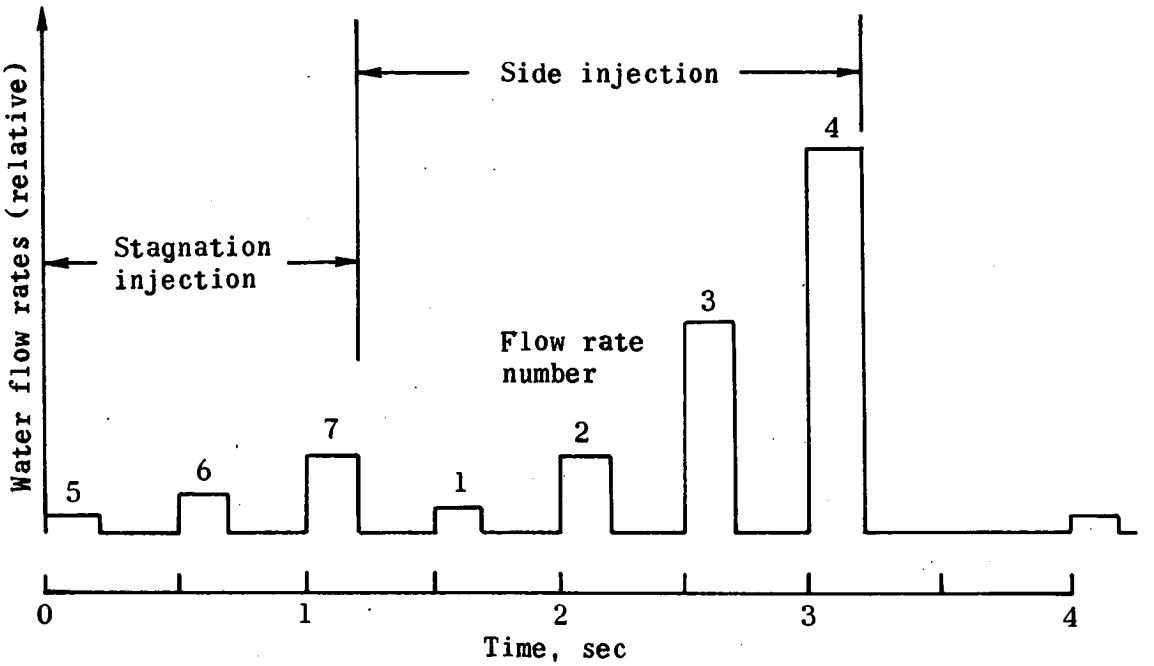

(a) Water-injection sequence for RAM C-I.

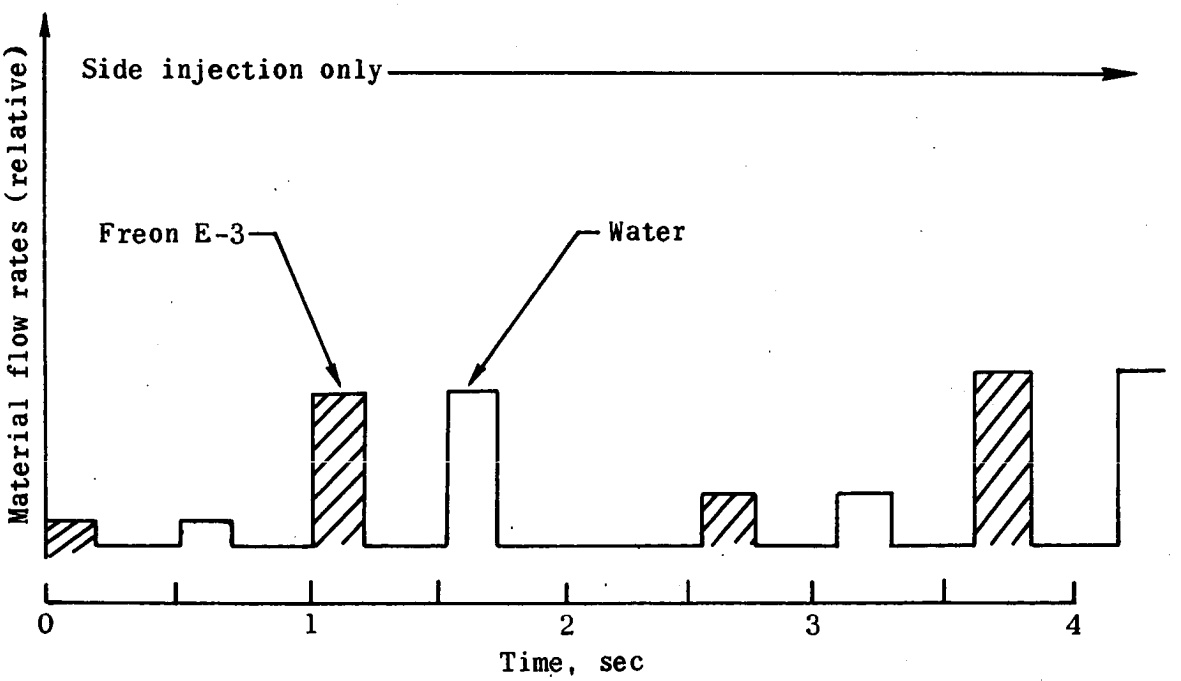

(b) Material-injection sequence for RAM C-III.

Figure 11.- Typical material-injection sequences for RAM C-I and C-III.

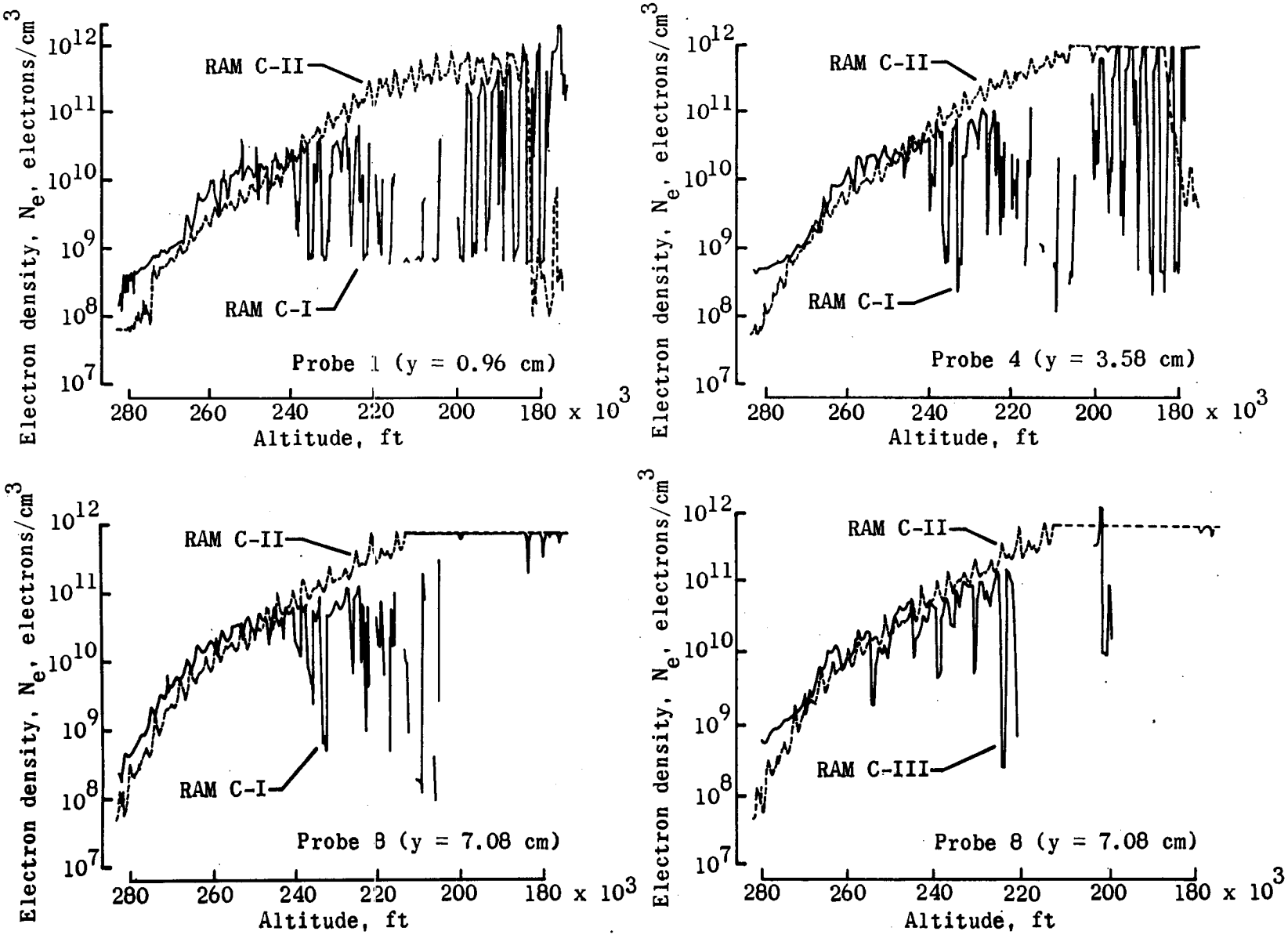

Figure 12.- Measured electron densities for selected probes from RAM C-I, C-II, and C-III.

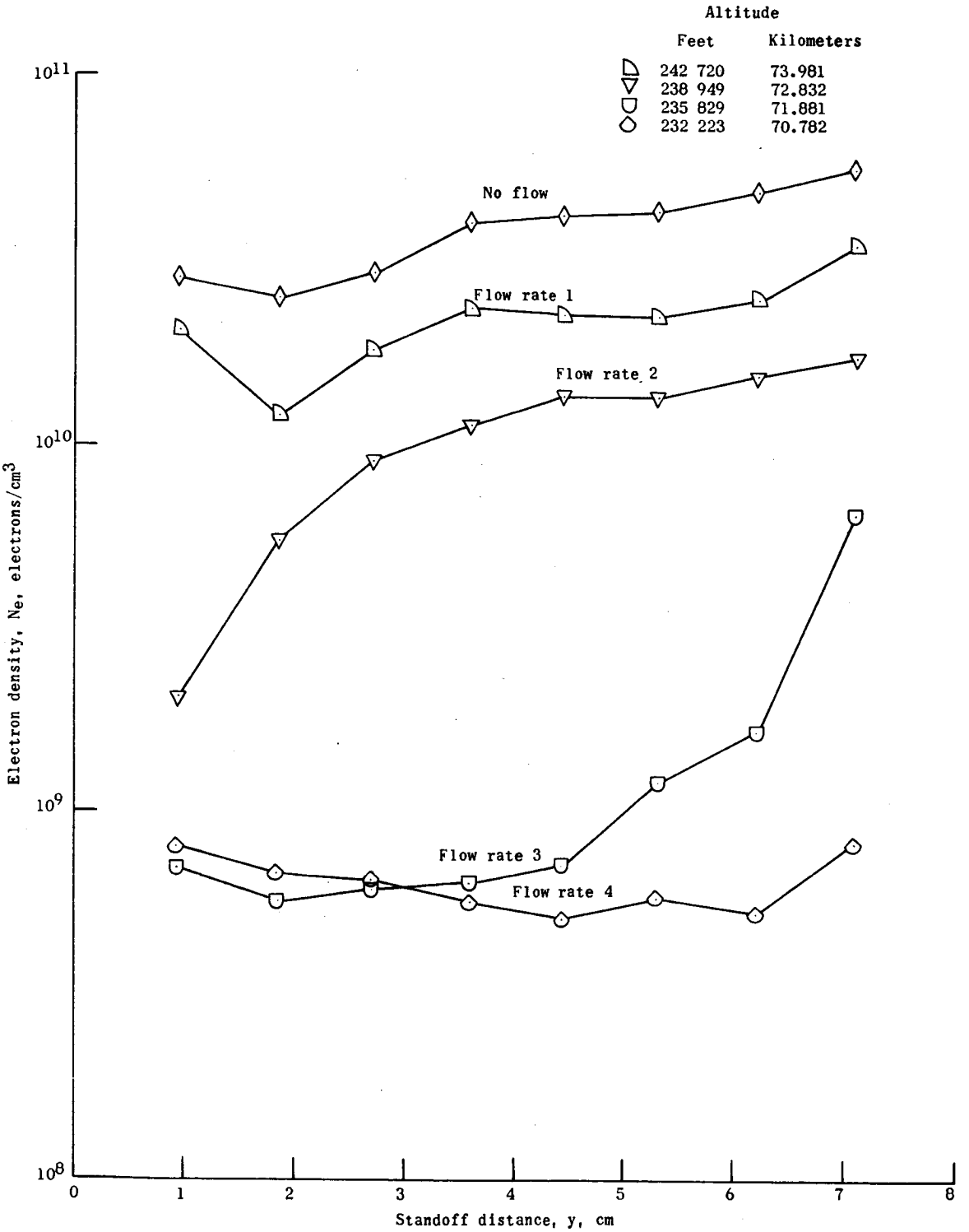

Figure 13.- RAM C-I electron density distribution profiles during side injection portion of cycle 3.

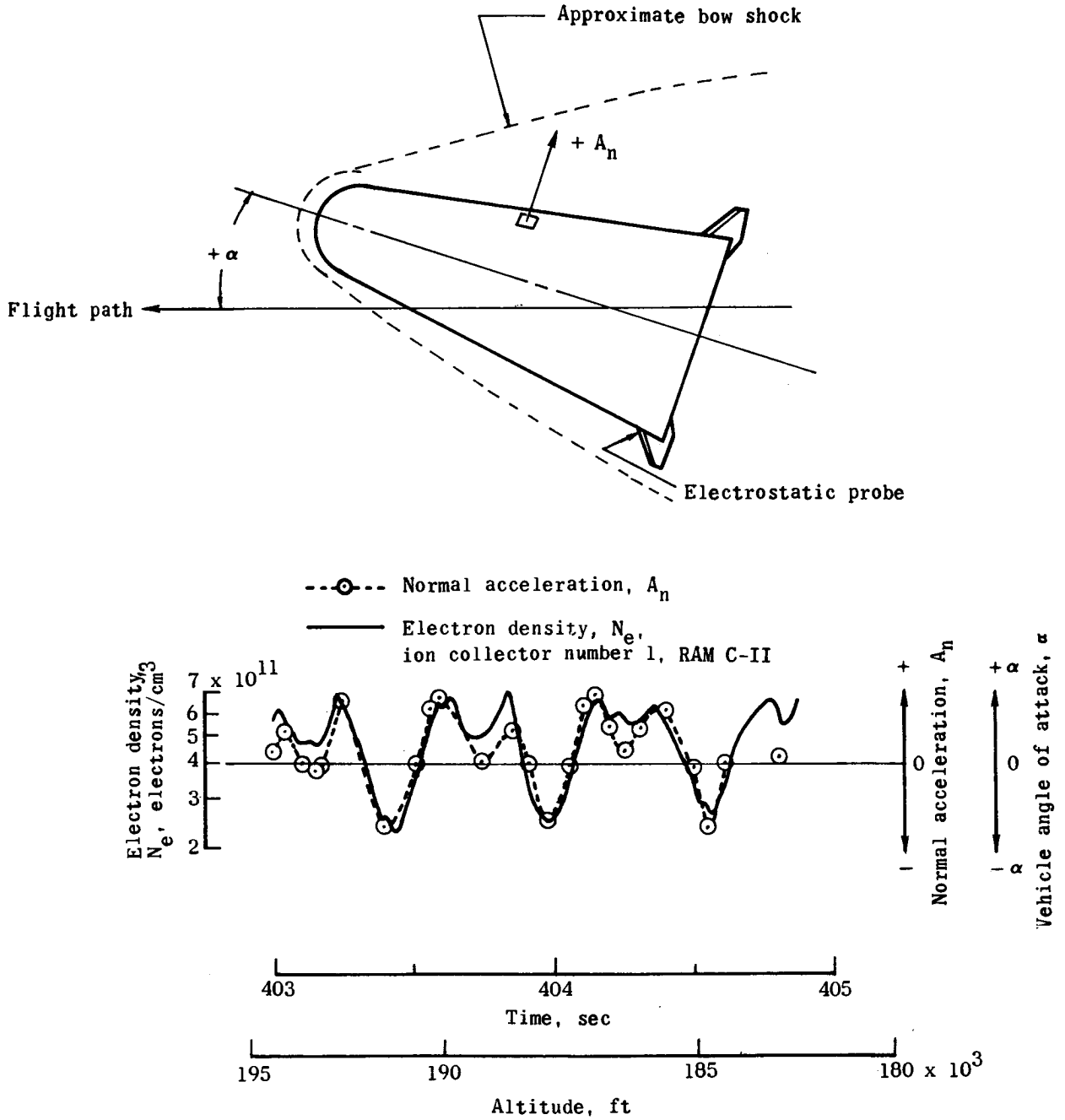

Figure 14.- Correlation of RAM C-II electrostatic probe measurements with vehicle angle-of-attack motions.

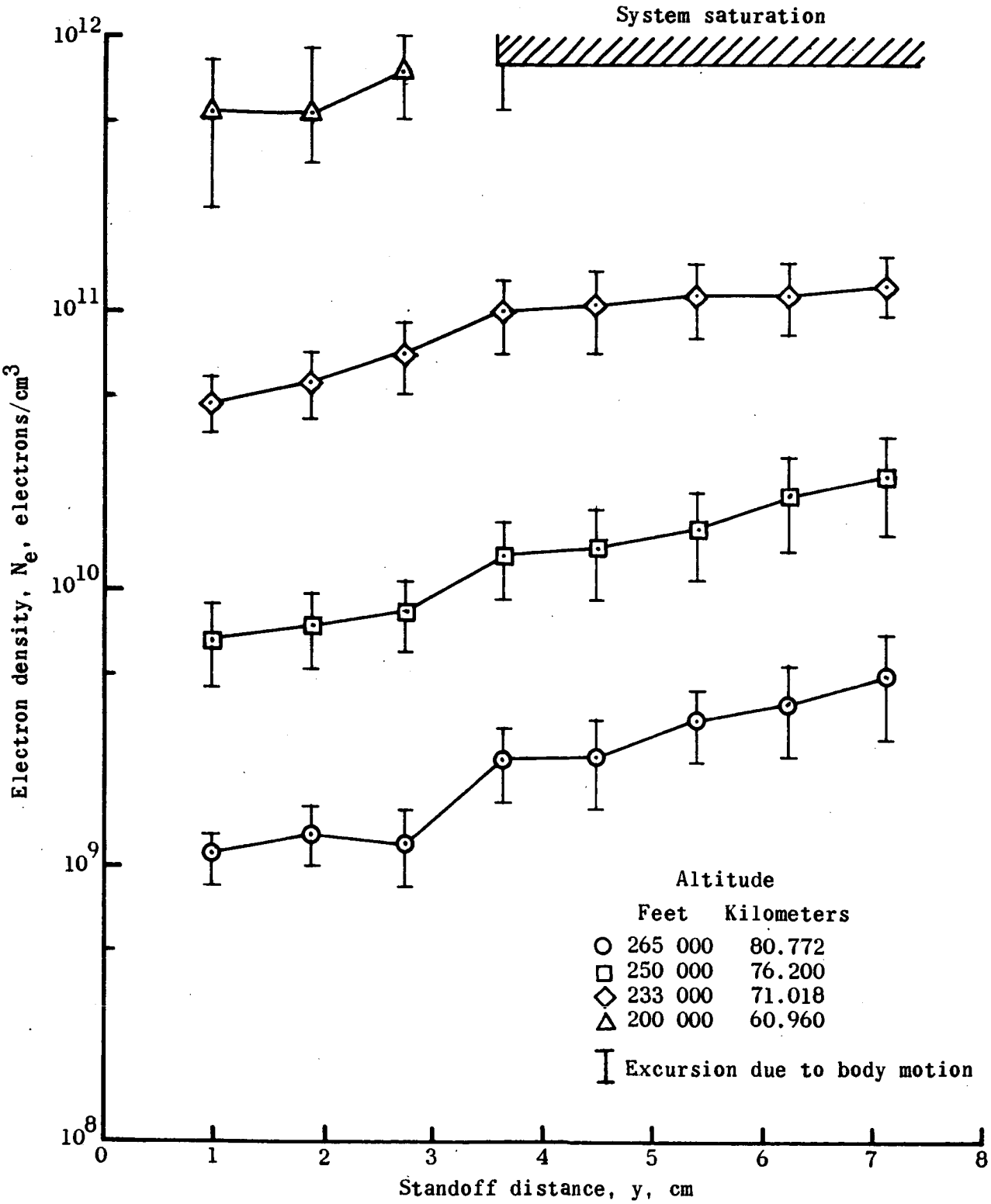

Figure 15.- Measured time-average electron density profiles for RAM C-II at four altitudes.

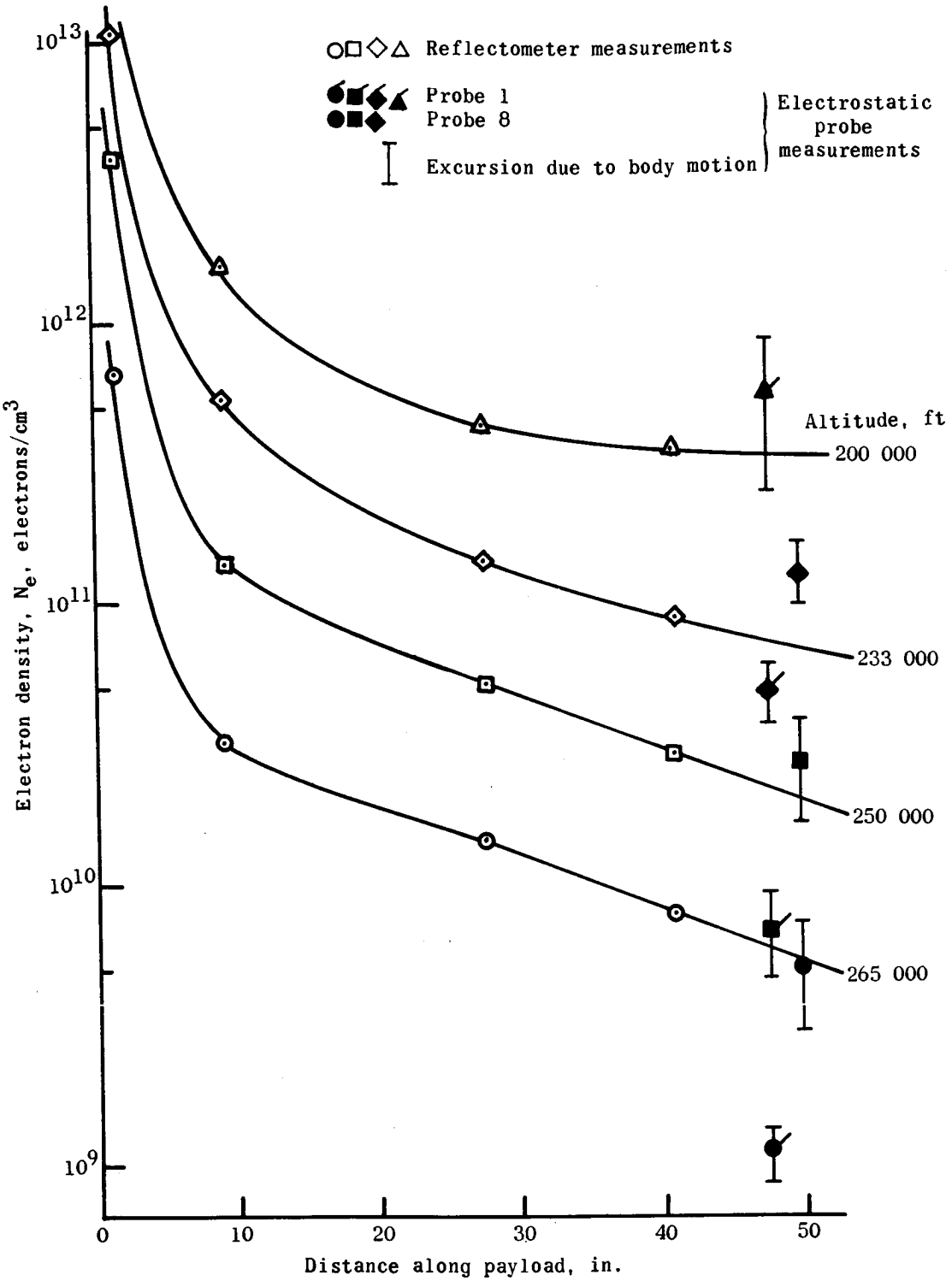

Figure 16.- Correlation of electrostatic probe measurements with reflectometer measurements.

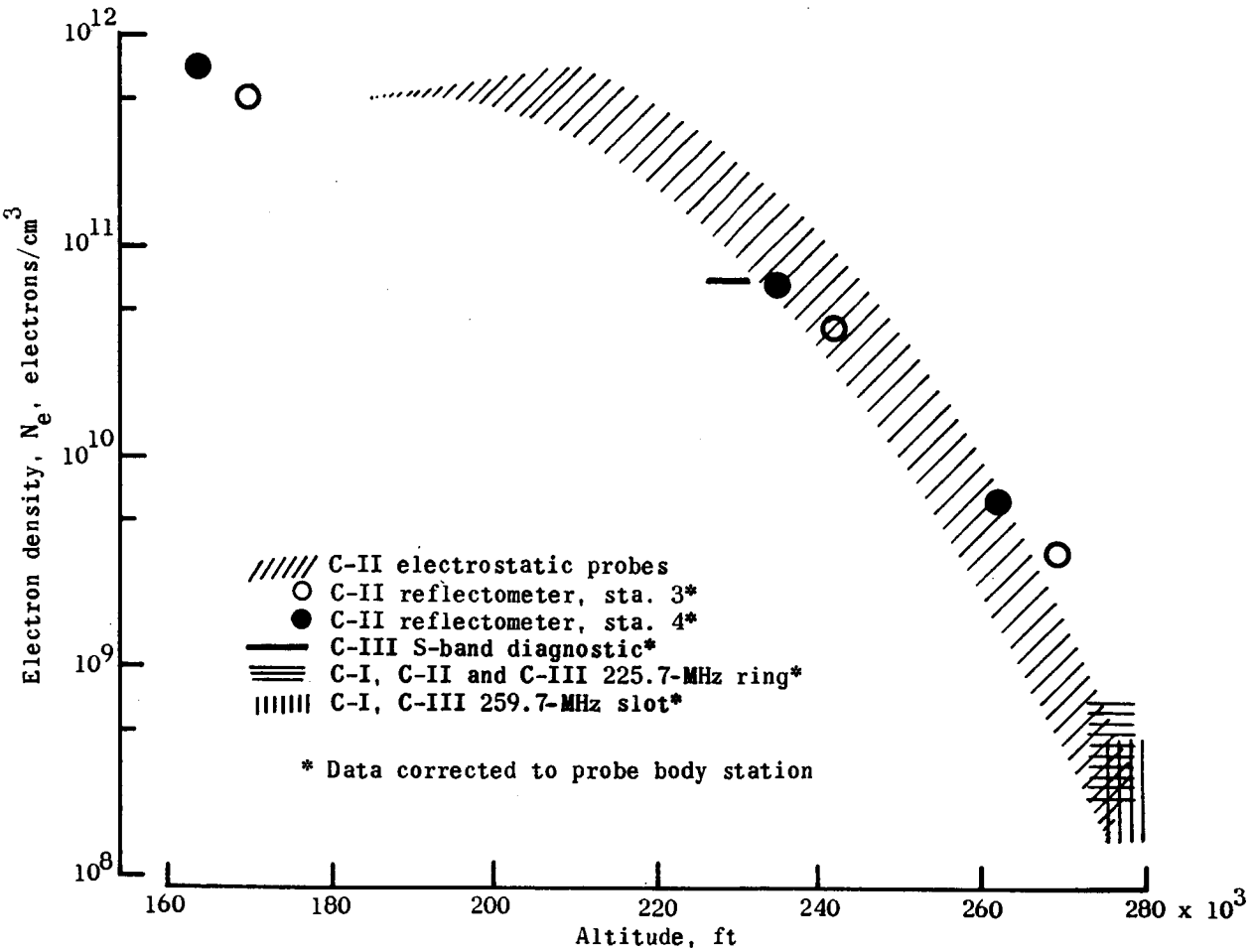

Figure 17.- Comparison of electron densities as inferred from RAM C-I, C-II, C-III diagnostic experiments.

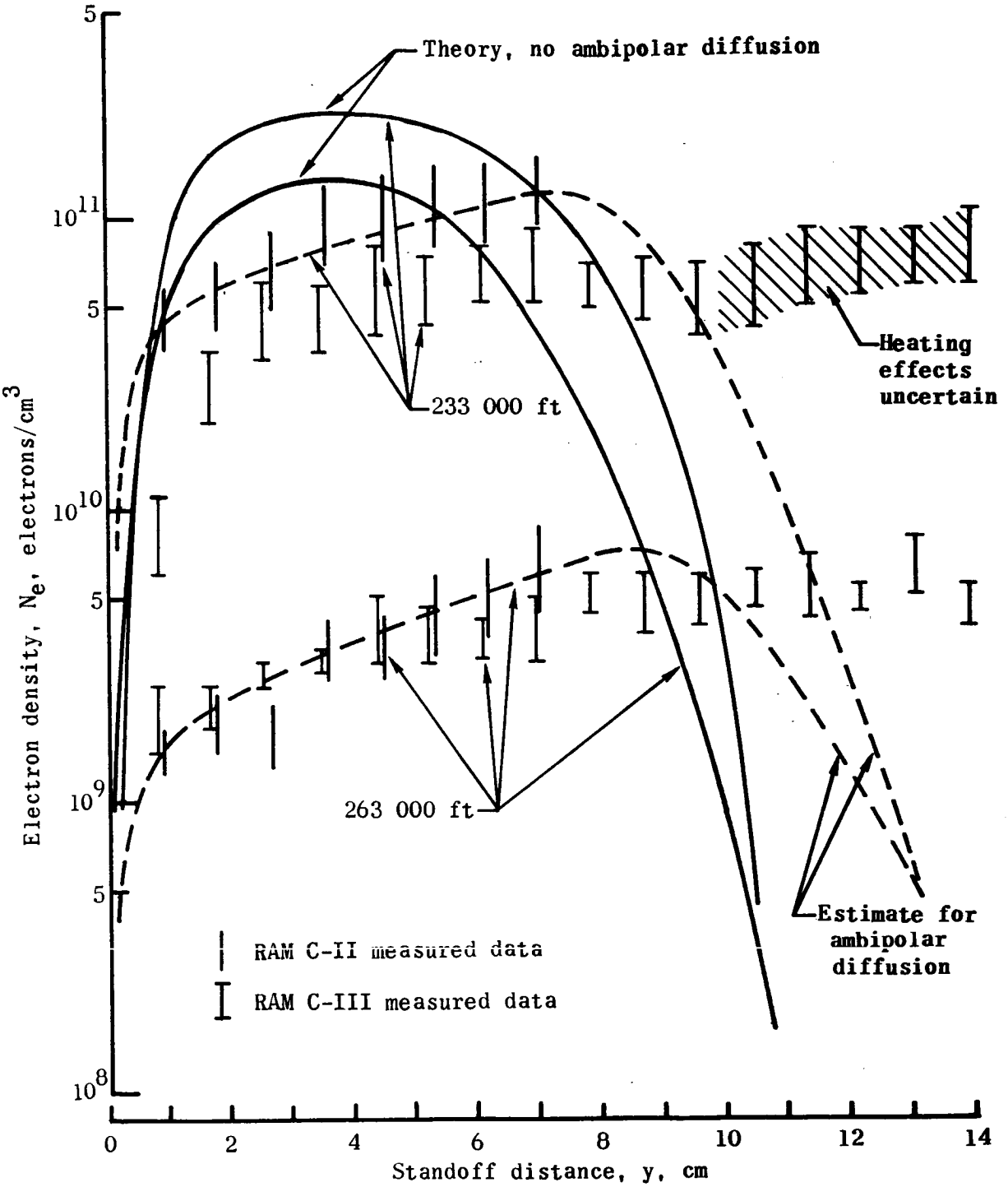

Figure 18.- Comparison of experimental and theoretical electron density profiles for RAM C.

RAM C-III S-BAND DIAGNOSTIC EXPERIMENT

By C. T. Swift, F. B. Beck, J. Thomson,
and S. L. Castellow, Jr.
NASA Langley Research Center

INTRODUCTION

One of the experiments on the September 30, 1970, flight of RAM C-III vehicle consisted of an S-band system which was designed to provide diagnostic information about the electron density in the flow field. The level and distribution of electron density near the surface of the RAM vehicle was to be inferred by measuring the input admittance of the S-band antenna. Signal transmission was also monitored to infer integrated electron density.

The antenna consists of an aperture fed by a circular section of waveguide excited in the TE_{11} mode. The design was based on the work of Bailey and Swift (ref. 1) and was selected for a number of reasons to be discussed, the most pertinent of which was the desire to use an antenna which is amenable to theoretical analysis.

The first part of this paper is concerned with the justification of the input admittance diagnostic method and a description of the flight systems. The latter part of the paper discusses preflight calculations and preliminary flight data.

BACKGROUND

The geometry is shown in figure 1. An aperture antenna opens into an infinite, perfectly conducting flat ground plane, which is coated with an inhomogeneous plasma. The aperture-admittance expression of this antenna is given by

$$Y_{ap} = \frac{1}{\left|V_o\right|^2} \iint_{\text{Aperture}} \left(\vec{E}_{ap} \times \vec{H}^*\right)_{z=0} \cdot d\vec{S} \qquad (1)$$

where V_o is the applied voltage, $\vec{E}_{ap}$ is the assumed electric field at $z = 0$, $\vec{H}$ is the external magnetic field intensity evaluated at $z = 0$, and $d\vec{S}$ is the elementary area of the aperture. The specified form of $\vec{E}_{ap}$ is usually assumed to correspond to the dominant mode of the particular type of waveguide feeding the aperture. Details of the mathematical approach, as applied to specific types of waveguide configurations with experimental verification, are given in references 1 to 5.

Typical numerical results for a rectangular waveguide-fed aperture covered with an inhomogeneous plasma are shown in figure 2. Here the magnitude $|\Gamma|$ and phase ϕ of the reflection coefficient are plotted as a function of the peak value of the ratio ω_p/ω, where ω_p and ω are the plasma frequency and frequency of propagation, respectively. Figure 2 essentially exhibits a plot of admittance as a function of increasing electron density, since ω is normally assumed constant and $\omega_p = 2\pi(8.97 \times 10^3)N_e$, where N_e is the electron density.

The parameter δ/λ of the profile shown in the inset is the distance in free-space wavelengths at which the electron density is one-half its maximum value and is therefore an indication of the inhomogeneity of the plasma. When the plasma is overdense, the slope of $|\Gamma|$ is small so that little change occurs in $|\Gamma|$ as $(\omega_p/\omega)^2$ increases. When $\frac{\delta}{\lambda} = 0$, $|\Gamma|$ asymptotically approaches 1, whereas for other values of δ/λ, the asymptote assumes a somewhat lower value. This leads to the conclusion that $|\Gamma|$ provides a measurement of the inhomogeneity and the phase provides a measurement of electron density. However, specific conclusions relating to other antennas and other types of electron density profiles can be made only after several additional parametric calculations have been completed in cooperation with flow-field specialists.

SYSTEM DESCRIPTION AND ANTENNA DESIGN

For reasons which will be discussed, S-band was selected as the most desirable frequency range for the RAM C-III microwave diagnostic experiment. The specific frequency of 3.348 GHz was chosen because flight-proven components designed to operate at this frequency were readily available from the RAM C-II flight.

A block diagram of the RAM C-III S-band system is shown in figure 3. The converter, isolator, and oscillator had previously been qualified for the RAM C-II flight. The stripline assembly, which contained diodes to measure forward and reflected power and the electric field at four points $\lambda/8$ apart, was new to this flight. In RAM C-II, the coupler and four-probe units were separate items. The environmental flight-acceptance test levels under which the components were subjected are listed in table I.

Because of packaging requirements, a circular waveguide antenna was more desirable than a rectangular one. It was also necessary to cut an aperture in the spacecraft structure, and a round hole was much easier to cut than a rectangular one. A diameter of 2.65 inches was selected so that the guide would be large enough to allow unattenuated propagation of the TE_{11} mode and yet be small enough to damp the higher order waveguide modes. These parameters fix the diameter-to-wavelength ratio of the aperture at $2a/\lambda = 0.75$ and the guide wavelength at $\lambda_g = \lambda\sqrt{1 - \left(\frac{1.84\lambda}{2\pi a}\right)^2} = 5.61$ inches.

In order to build a suitable waveguide-to-coax adaptor, the feed should be placed approximately $\lambda_g/4$ from the back wall of the cavity, and the aperture should be located approximately $\lambda_g/2$ from the feed to assure proper damping of the higher order modes induced by the feed. This arrangement therefore requires a total cavity depth of about $\frac{3}{4}\lambda_g$, or 4.2 inches. The maximum depth allowed by constraint of other experiments was 4.5 inches. Thus, the restriction on the cavity depth requires a frequency of S-band or greater in order to insure proper interpretation of the impedance data.

A drawing of the antenna is shown in figure 4. The aperture section of the antenna was bonded to the skin of the vehicle, and a teflon plug was inserted and bonded flush to the aperture. This was necessary to preserve the structural integrity of the vehicle and to support the ablation material above the aperture. The feed section was built as a separate part because the volume of the antenna was too large to allow removal of the telemetry package. The relative axial location of the antenna in the vehicle is shown in figure 5. The location in azimuth was 30° from the chord connecting the Langmuir probes.

The coaxial feed was designed by mounting the antenna on a flat ground plane and then varying the length and diameter of the feed until the measurements of impedance agreed with the calculations of reference 1. Additional checks were then provided by comparing calculations and measurements of the admittance of an aperture backed by a dielectric-loaded section of waveguide (ref. 6) radiating into a dielectric-covered ground plane. Some of the results are shown in figure 6, which shows the calculated admittance as a function of plug thickness for (1) no external dielectric cover and (2) a 0.32-inch external teflon cover. The experimental data are well within the scatter of the experimental results given in reference 1. Other data taken with 1/2-inch and 1/8-inch quartz sheets over the aperture also gave satisfactory agreement between theory and experiment. Dielectric-covered ground planes having the same radius of curvature as the surface of the RAM vehicle were also used, and no observable change in the admittance as a function of curvature was noted.

MEASUREMENT TECHNIQUES OF THE FLIGHT SYSTEM

The equation for the electric field within the stripline unit is given by

$$E = E_o e^{-j4\pi z/\lambda}\left[1 + |\Gamma| e^{2j\left(\frac{2\pi z}{\lambda}+\phi\right)}\right] \tag{2}$$

and the power is

$$P = \frac{1}{2} EE^* = P_o\left[1 + |\Gamma|^2 + 2|\Gamma|\cos 2\left(\frac{2\pi z}{\lambda} + \phi\right)\right] \tag{3}$$

where $E_o(P_o)$ is the incident electric field (power), and $|\Gamma|$ and ϕ are the magnitude and phase of the reflection coefficient, respectively. In order to determine unique values of P_o, $|\Gamma|$, and ϕ, a minimum of three samples are required. The system described herein contained a fourth probe for redundancy and a directional coupler to measure forward and reflected power.

The operation of the diodes in the sampling unit extended beyond the square law region. Therefore, measurements of the characteristic curves were necessary in order to convert the output voltage of the diode V_{OUT} to a normalized input voltage $\frac{V_{in}}{V_{Po}} = \sqrt{\frac{P}{P_o}}$. A typical calibration curve is shown in figure 7. The upper curve was obtained by placing a short at the output point z_o, where $\cos 2\left(\frac{2\pi z_o}{\lambda} + \phi\right)$ is maximum, and then varying the input power. The other curve was similarly obtained by placing a matched load at the output. The curves should agree except for a constant factor of 4 in input power; hence, the difference represents errors due to internal losses and mismatches.

It is interesting to note that the four-probe technique permits laboratory measurements of admittance to be made which are as accurate as those obtained with a slotted line, even though the mismatch error per probe can be quite large.

TRANSMISSION EXPERIMENT

In order to provide supplementary diagnostic information, a customized S-band receiving station was built to monitor signal attenuation. Although the transmitter was a cw system, modulation was provided by using the directionality of the antenna patterns (figs. 8(a) and 8(b)) and the spin rate of the vehicle to add a 3-Hz AM tone to the signal. One problem was the amount of noise introduced into the system because of the 6-MHz receiver bandwidth necessary to account for oscillator drift. This problem was resolved by using a bank of comb filters with independent detectors to select and narrow-band the received signal and thereby improve the overall signal-to-noise ratio.

A system performance analysis done by Samuel Sokol of NASA Langley Research Center verified the transmission experiment. His calculations are given in table II.

PREFLIGHT CALCULATIONS

The estimated contaminant-free preflight electron density profiles at the S-band antenna location are shown in figure 9. Generally, the peak value of electron density occurs at a considerable distance from the vehicle at the

higher altitudes and moves in as the spacecraft descends. The corresponding calculations of the input admittance of the antenna are shown in figure 10. A counterclockwise rotation of more than 360° is predicted to occur as the peak value of electron density increases to its maximum value. (The limiting value of admittance is the starred point in figure 10, which is that obtained by placing a perfect conductor on top of the ablation layer.) As the vehicle slows down at the lower altitudes, the electron density decreases, and the admittance returns to a value which differs from that obtained prior to entry. This is due to a thickness change in the outer teflon cover which occurs because of ablation. It should be noted in passing that the choice of an 0.8-inch teflon plug yielded the maximum amount of counterclockwise phase rotation in the Smith chart. This particular plug thickness was therefore selected in order to give the maximum dynamic range to the experiment.

Figure 11 shows the admittance obtained when the plasma layer is homogeneous. A comparison with figure 10 vividly indicates that the boundary layer can have a profound effect on the admittance. The initial response of the antenna should therefore provide estimates of the boundary-layer thickness. Information concerning peak electron density should be contained in the data as the plasma becomes overdense.

The preflight calculations were made only to establish criteria for proper antenna design. These data did not include effects of impurities introduced by the Narmco nose-cone and material injectants.

PRELIMINARY FLIGHT RESULTS

The VHF telemetry system transmitted information both in real time and on a 45-second delay link provided by an onboard tape recorder. Figure 12 shows the delayed S-band data. In this figure, the output voltages of eight telemetry channels are displayed as a function of time, which increases from left to right. The distance between grid markers represents 10 seconds. The quality of the figure is only fair because it was reproduced directly from the oscillographic records. The top trace is proportional to the forward power; the next is proportional to the reflected power; the outputs of sampling diodes 1, 2, 3, 4, the thermistor output, and the programer output. The programer trace marks the time at which material was injected into the flow field to quench electrons. The noise to the extreme left of the figure is due to real-time blackout, and to the right represents loss of signal due to payload impact. The telemetry traces of all eight channels are flat prior to the data period. Then, as the electron density builds up to its critical value, the diodes respond in such a way that high frequency noise appears to be superimposed on the output. It will be shown that these oscillations correlate well with the injection of material into the flow field. After the injection sequence ends, the output voltages exhibit a much more gradual change throughout the remaining part of the data period. If a "no-injection" envelope is drawn through each output probe, the preliminary value of the inferred admittance indicates that the plasma is more homogeneous at the higher altitude than anticipated.

The primary objective of the RAM C-III flight was to develop methods of quenching the reentry plasma by injecting liquids into the flow field. The two fluids used in the experiment were water and Freon E-3. The latter is an electrophilic, which chemically depletes electrons. The injection sequence was as follows: (1) low flow rate of freon, (2) low flow rate of water, (3) high flow rate of freon, (4) high flow rate of water. Ten such cycles occurred during reentry. The programer output, which marks the time at which fluid is released, is shown at the bottom of figure 13. The top trace is an expanded plot of the reflected-power monitor output. The presence of material in the flow field has no effect on the reflection coefficient until the fourth injection cycle begins. In the fourth cycle, the electrons are almost completely depleted except during the time increment between pulses 2 and 3. All four injection pulses cause a dip in the reflection coefficient during cycles 5, 6, and 7. In cycle 8, the low flow rate of water shows no effect, and in cycle 9, only the freon is effective. Nothing appears to happen during the last injection sequence.

Figure 14 shows the transmitted signal plotted as a function of time, increasing from right to left (opposite from the admittance data). The time scale is the same as that used in figure 12. The six traces correspond to the six detectors of the receiving system, as previously described. It is believed that the "blips" occurring on the record at approximately 6-second intervals are due to interference from a scanning radar on a ship in the vicinity of the receiving station. The envelope of spikes in the third trace is the received signal. (The spurious radar pulses were artistically removed from this trace.) Each spike is separated from its neighbor by approximately 1/3 second, which corresponds to the spin rate of the vehicle. As the spacecraft descends, blackout occurs and the envelope disappears into the noise. During blackout, a total of five recovery pulses occur which correlate with the injection of material. The one labeled with a question mark may or may not be a recovery pulse. It does appear to correlate with fluid injection.

Several minor problems developed in connection with the transmission experiment. The electronics was designed to receive both vertical and horizontal polarization; however, only the horizontal-polarization receiving channel was operative during the mission. Another problem was that the signal-to-noise ratio of the system fell short of achieving the -126 dBm minimum detectable signal arrived at in table II. The reason for this difference requires further investigation. The last problem that occurred was that the payload lost its high rate of spin during the blackout period; hence, the AM tone was significantly lower in frequency than it was prior to entry. The three irregular pulses at the extreme left of the data trace are the postentry received signals.

The reflected and transmitted signals are plotted on the same time scale in figure 15. As expected, the reflection coefficient rises and falls as the signal goes into blackout and subsequently recovers.

CONCLUDING REMARKS

The RAM C-III S-band diagnostic antenna was successfully flown on September 30, 1970. As the payload descended into the atmosphere, the electron density exceeded the critical value which resulted in a rise in reflection coefficient and an attenuation of the transmitted signal. When water and an electrophilic were injected into the flow, improved signal transmission and a lowering of the reflection coefficient was observed to occur. At the lower altitudes, the electrophilic seems to spread or diffuse around the payload more so than water does and was very effective in removing electrons contiguous with the surface of the vehicle.

The data presented here should be treated as preliminary. A great deal of data reduction will be required before quantitative conclusions can be drawn.

ACKNOWLEDGEMENTS

The authors would like to express their gratitude to the following individuals of the NASA Langley Research Center: W. Robert Young and Ernest C. Hooper of the Flight Instrumentation Division for their assistance in the design and construction of the S-band receiving station; William L. Grantham of the Flight Instrumentation Division for data pertaining to the RAM C-II flight; and Paul W. Huber, Charles J. Schexnayder, Jr., and John S. Evans of the Hypersonic Vehicles Division for the contribution of figure 9.

REFERENCES

1. Bailey, Marion C.; and Swift, Calvin T.: Input Admittance of a Circular Waveguide Aperture Covered by a Dielectric Slab. IEEE Trans. Antennas Propagation, vol. AP-16, no. 4, July 1968, pp. 386-391.

2. Swift, Calvin T.: Input Admittance of a Rectangular Waveguide-Fed Aperture Antenna Radiating Into an Inhomogeneous Lossy Dielectric Slab. NASA TN D-4197, 1967.

3. Croswell, William F.; Taylor, William C.; Swift, C. T.; and Cockrell, Capers R.: The Input Admittance of a Rectangular Waveguide-Fed Aperture Under an Inhomogeneous Plasma: Theory and Experiment. IEEE Trans. Antennas Propagation, vol. AP-16, no. 4, July 1968, pp. 475-487.

4. Swift, Calvin T.: Input Admittance of a Coaxial Transmission Line Opening Onto a Flat, Dielectric-Covered Ground Plane. NASA TN D-4158, 1967.

5. Croswell, William F.; Rudduck, Roger C.; and Hatcher, Douglas M.: The Admittance of a Rectangular Waveguide Radiating Into a Dielectric Slab. IEEE Trans. Antennas Propagation, vol. AP-15, no. 5, Sept. 1967, pp. 627-633.

6. Swift, Calvin T.; and Hatcher, Douglas M.: The Input Admittance of a Rectangular Aperture Antenna Loaded With a Dielectric Plug. NASA TN D-4430, 1968.

TABLE I.- ENVIRONMENTAL TESTS REQUIRED FOR COMPONENTS (FLIGHT LEVELS)

Vibration test:

Duration, minutes	Sweep, octaves/minute	Frequency, Hz	Acceleration,[a] Sine (±g)	Random (grms)
---	4	10 to 24	0.2 inch D.A.	----
---	4	24 to 2000	6 inch D.A.	----
1	---	20 to 2000		10.0

Acceleration test:

An acceleration of 55g is applied to each of the three orthogonal axes for 1 minute each.

Shock test:

One impact per direction in each of three orthogonal axes. Each impact is 15g of duration 10 to 15 milliseconds.

Temperature test:

With the test specimen nonoperating, the chamber temperature and the test specimen are stabilized at 20° F. The test specimen is then operated for 20 minutes. The temperature is raised to 60° F and the specimen is operated for 20 minutes. The temperature is raised at a rate of 2° F/minute until 140° F is reached. The specimen is operated for 20 minutes, lowered to room temperature over a 20-minute time period, and operated for 20 minutes.

Vacuum test:

Not required for components (entire payload taken through vacuum test).

[a] g = acceleration due to gravity; grms = g's- root mean square; D.A. = double amplitude.

TABLE II.- SYSTEM PERFORMANCE ANALYSIS

Receiver noise figure	7.5 dB		
Noise temperature (NF-1)290	1350° K		
Antenna noise temperature (assumed)	100° K		
Cable noise temperature (1 dB loss)	75° K		
Total noise temperature	1525° K =	31.6 dB	
Boltzmann's constant (k)		-198.6 dBm	
Effective receiver bandwidth (if): B = 1 MHz		60 dB	
Effective receiver noise power (kTB)			-107 dBm
Spacecraft antenna gain (assumed)		9 dBi	
Ground antenna gain (10-foot dish, 45% efficiency)		37 dBi	
Transmitted power (rated at 50 milliwatts)		17 dBm	
$(\lambda/4\pi R)^2$ at range R of 200 nautical miles		-155 dB	
Polarization loss		-3 dB	
Tracking at half-power points on both antennas		-6 dB	
Miscellaneous unknown losses		-6 dB	
Expected signal level into the receiver at 200 n. mi.			-107 dBm

Carrier-to-noise ratio at 200 n. mi. . . . 0 dB in 1-MHz if bandwidth Signal-to-noise ratio at 200 n. mi. . . . . 50 dB in 10-Hz video bandwidth	Acquisition at 200 n. mi. from Bermuda
Improvement with decreased range . . . . . 6 dB Signal-to-noise ratio (no plasma effects) . . . . . 56 dB Minimum detectable signal (approximately) . . . . . -126 dBm Dynamic range of detectable signal fluctuations . . . . . 25 dB	Data period starts at 100 n. mi. from Bermuda

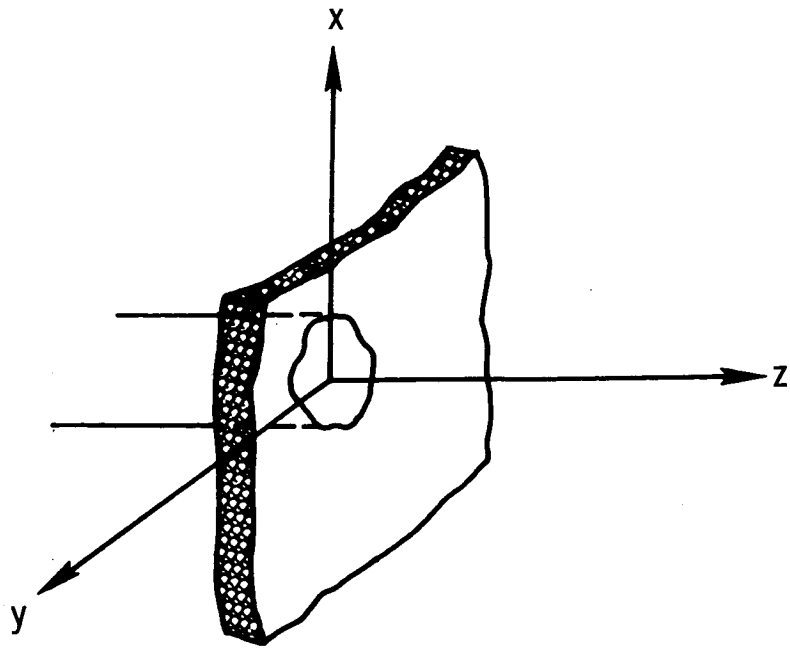

Figure 1.- Geometry of aperture antenna.

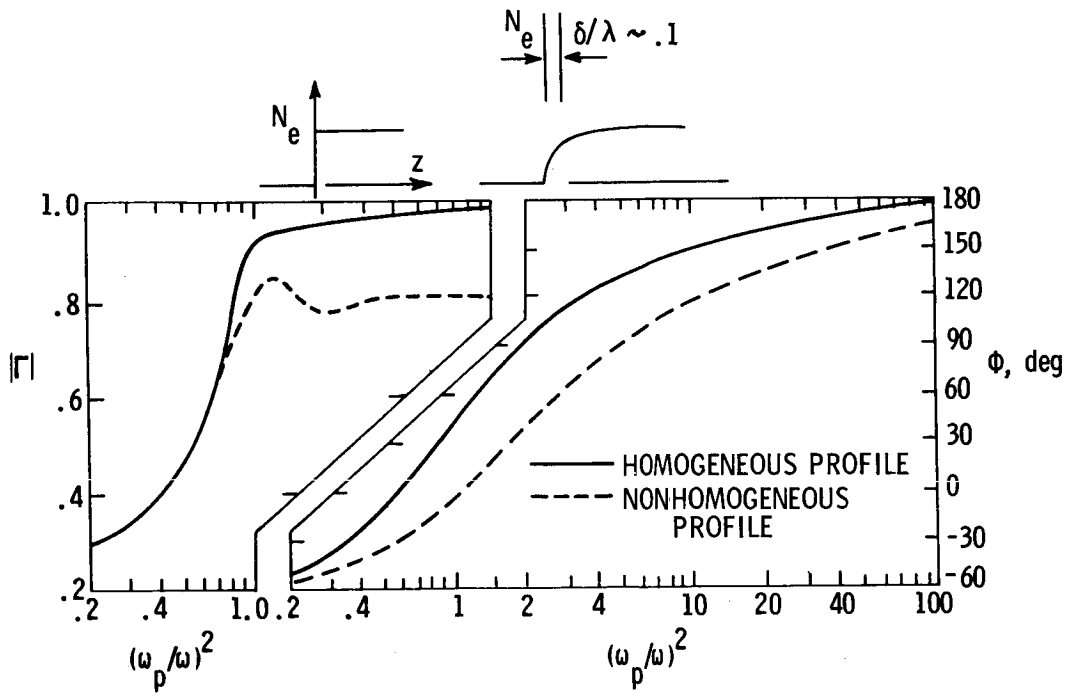

Figure 2.- Magnitude and phase of reflection coefficient for a rectangular waveguide-fed aperture covered with an inhomogeneous plasma.

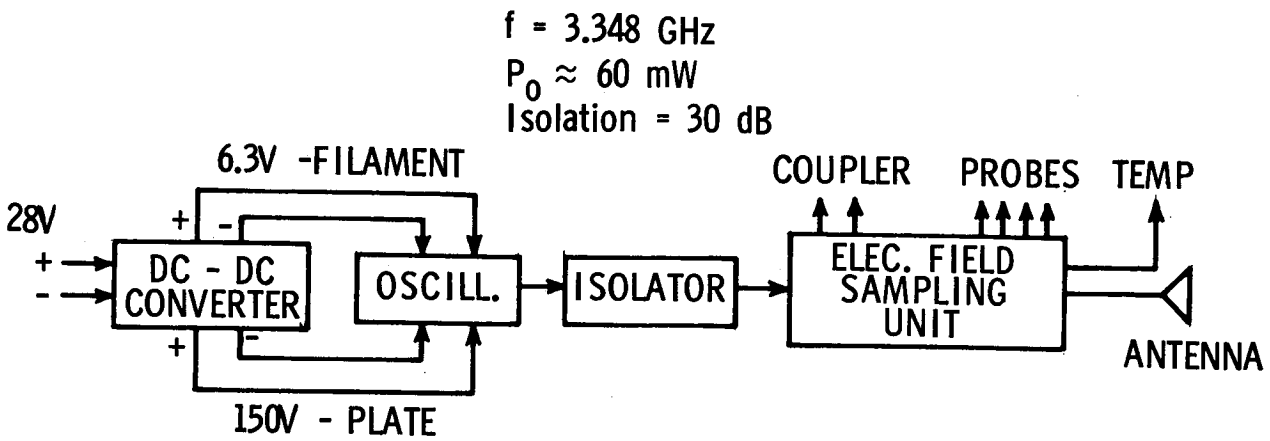

Figure 3.- Block diagram of the RAM C-III S-band system.

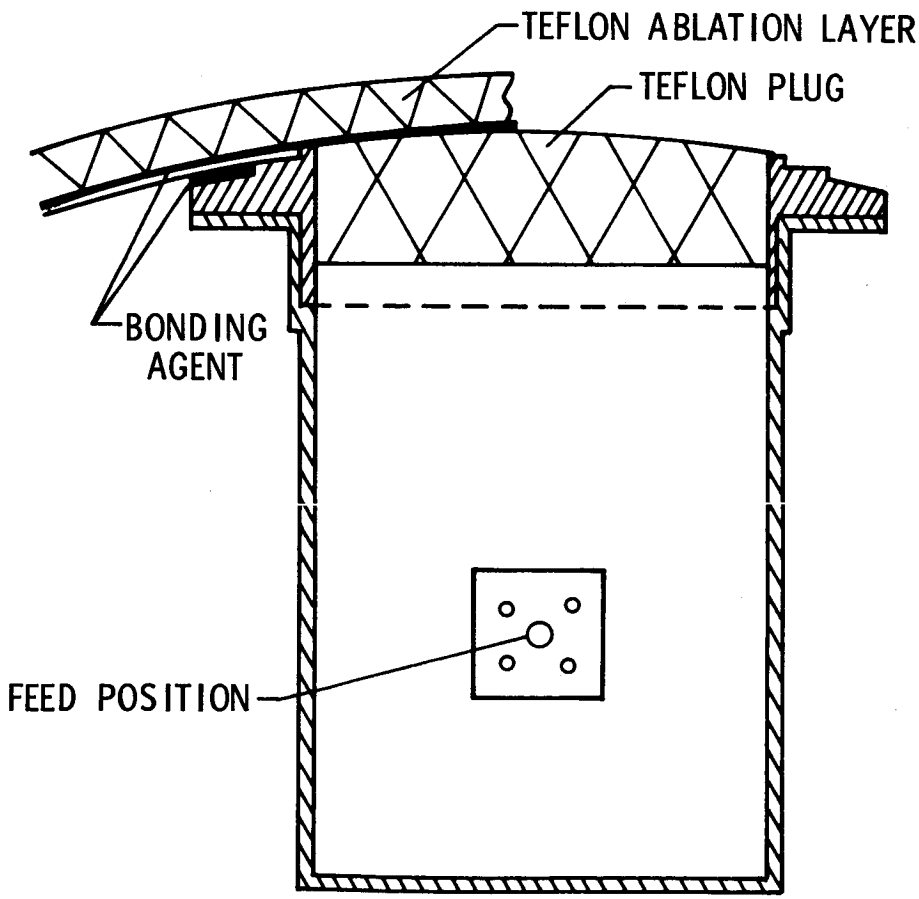

Figure 4.- Drawing of the RAM C-III S-band antenna.

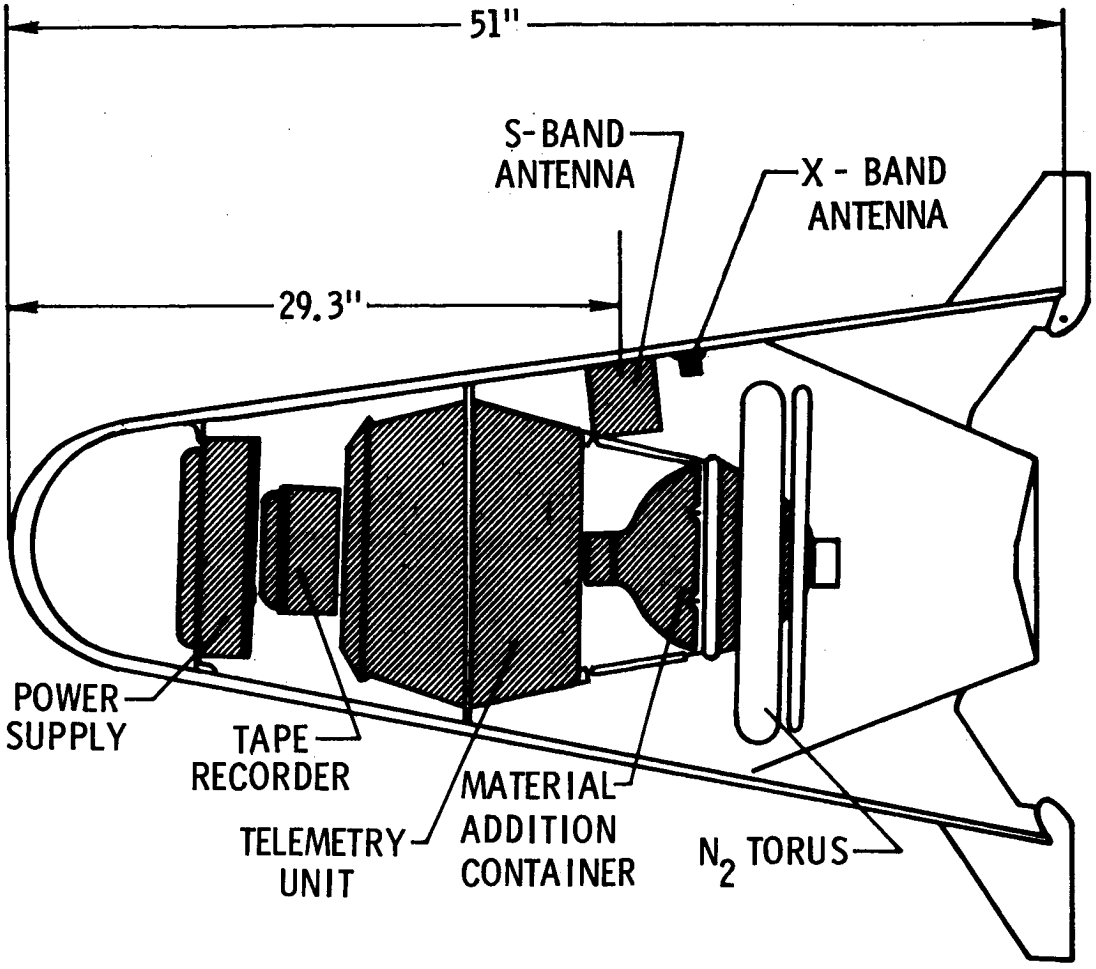

Figure 5.- Cutaway of the RAM spacecraft showing relative location of the S-band antenna.

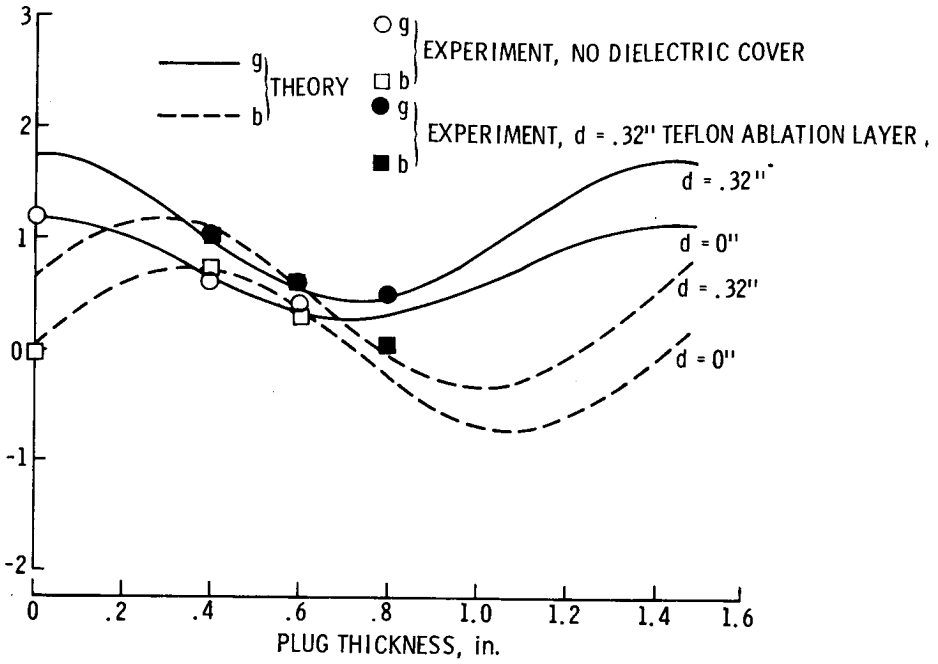

Figure 6.- Calculated and measured admittance of teflon-plug-loaded circular-aperture antennas. (g = Normalized conductance; b = Normalized susceptance.)

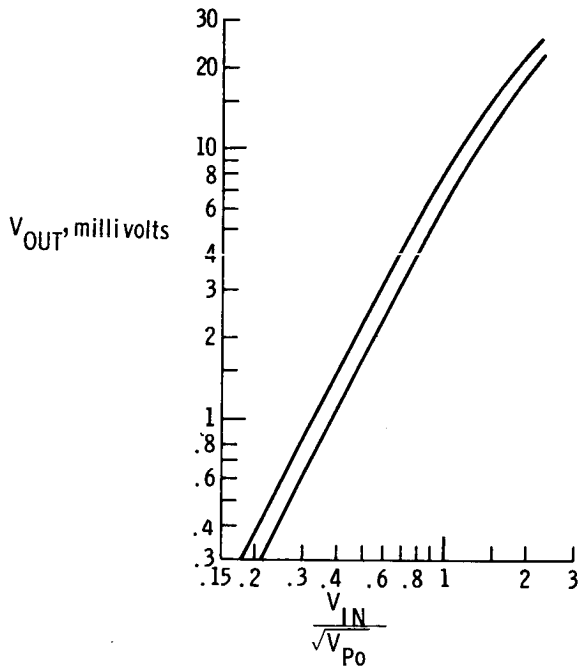

Figure 7.- Diode calibration curve. P_o = 60 mW; diode 2.

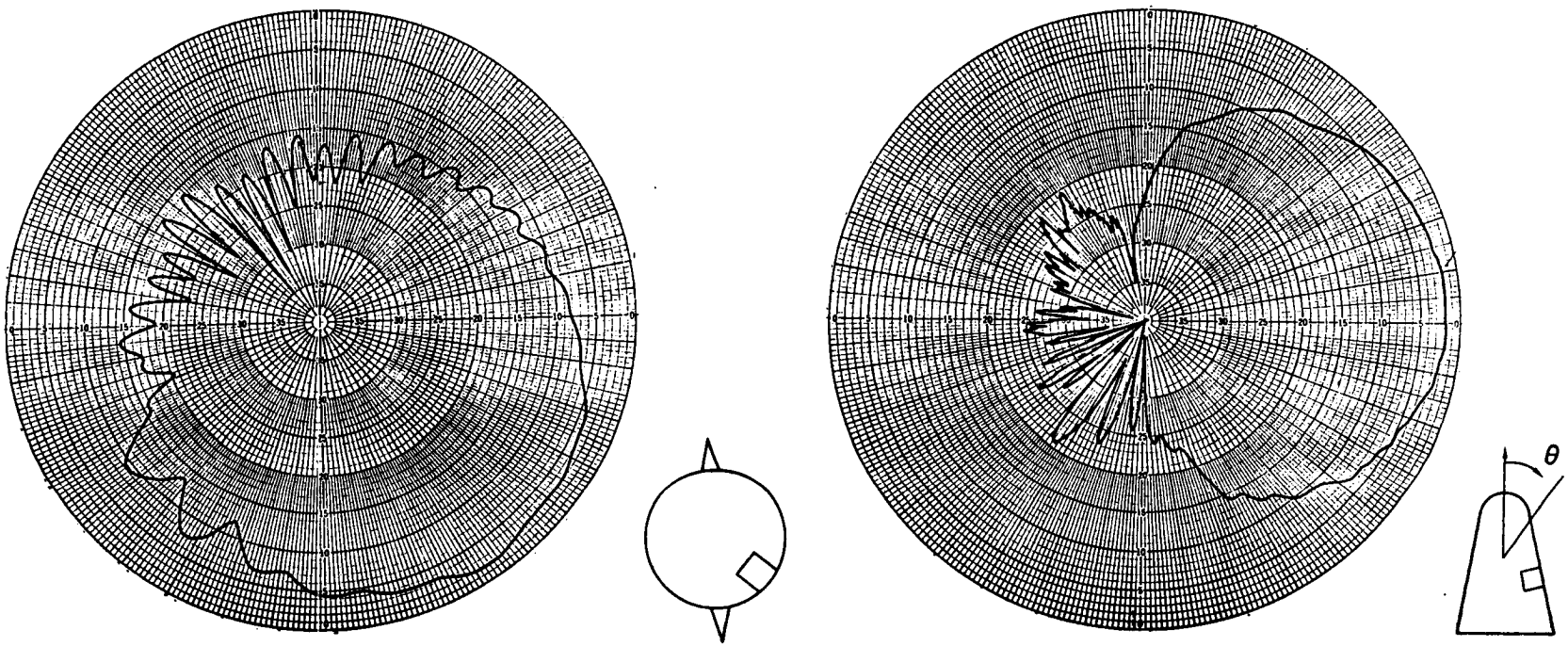

(a) Equatorial pattern.

(b) Elevation pattern.

Figure 8.- Antenna pattern of the S-band antenna.

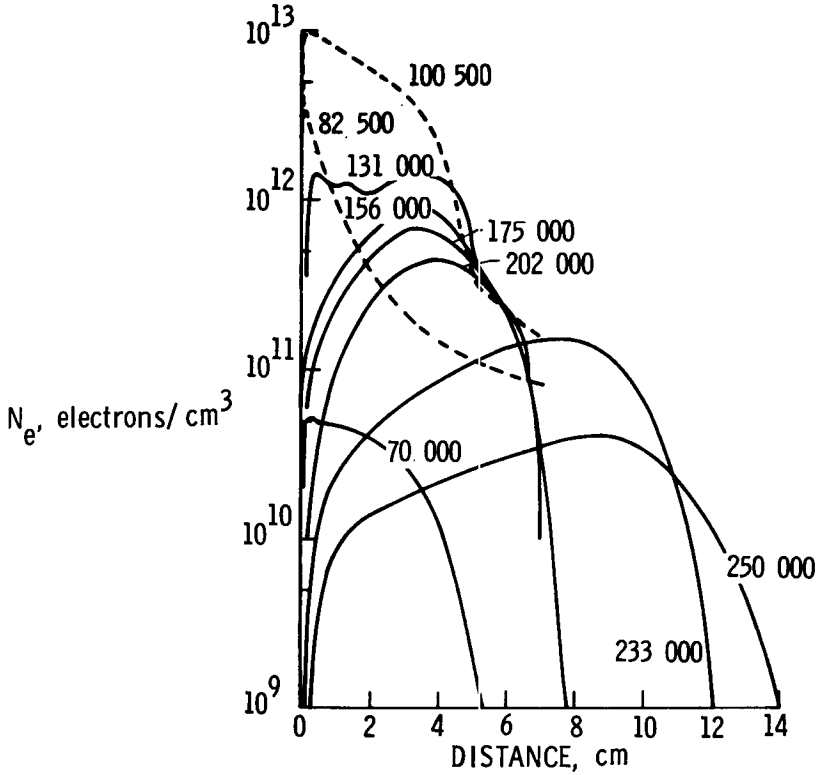

Figure 9.- Calculated preflight contaminant-free electron density profiles.

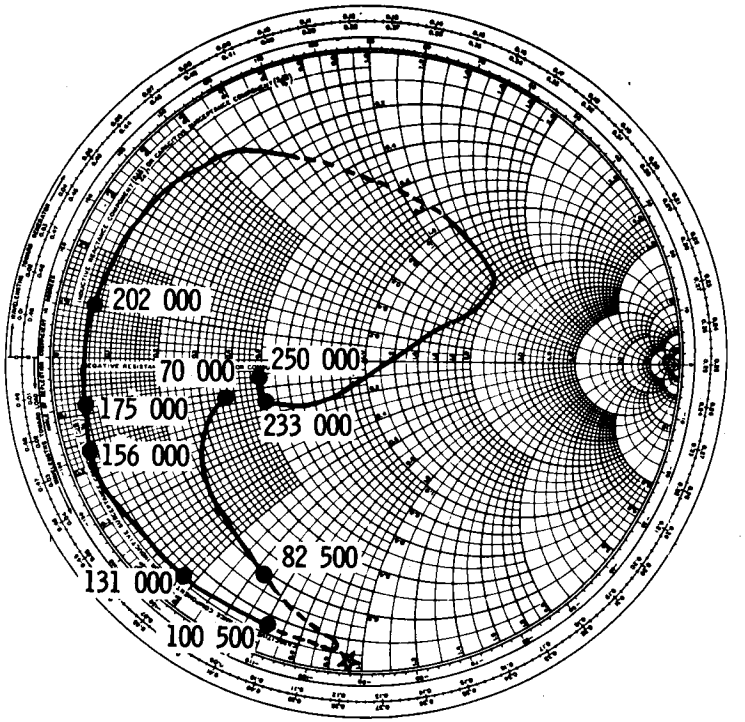

Figure 10.- Admittance of the S-band antenna as a function of the electron density profiles shown in figure 9.

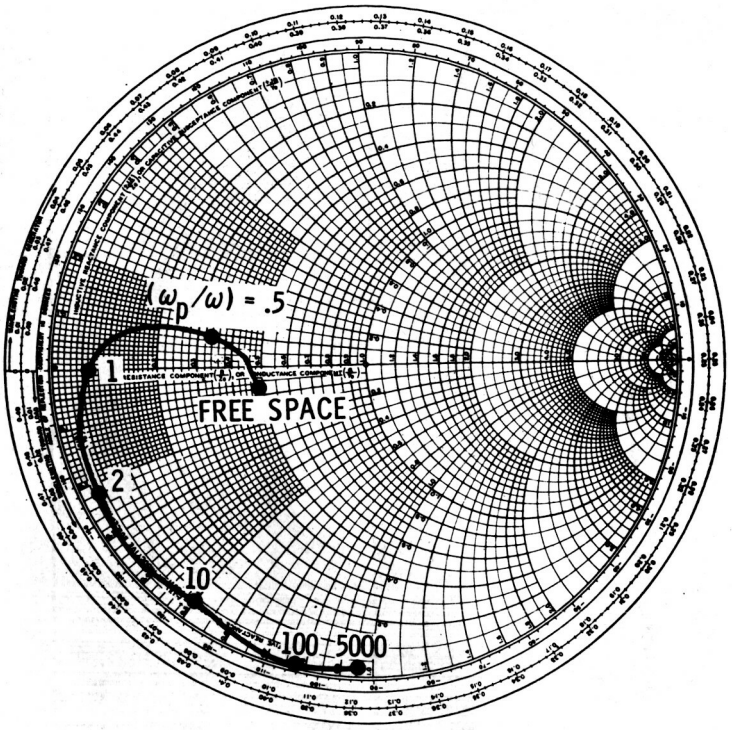

Figure 11.- Admittance of the S-band antenna as a function of increasing electron density (homogeneous profile assumed).

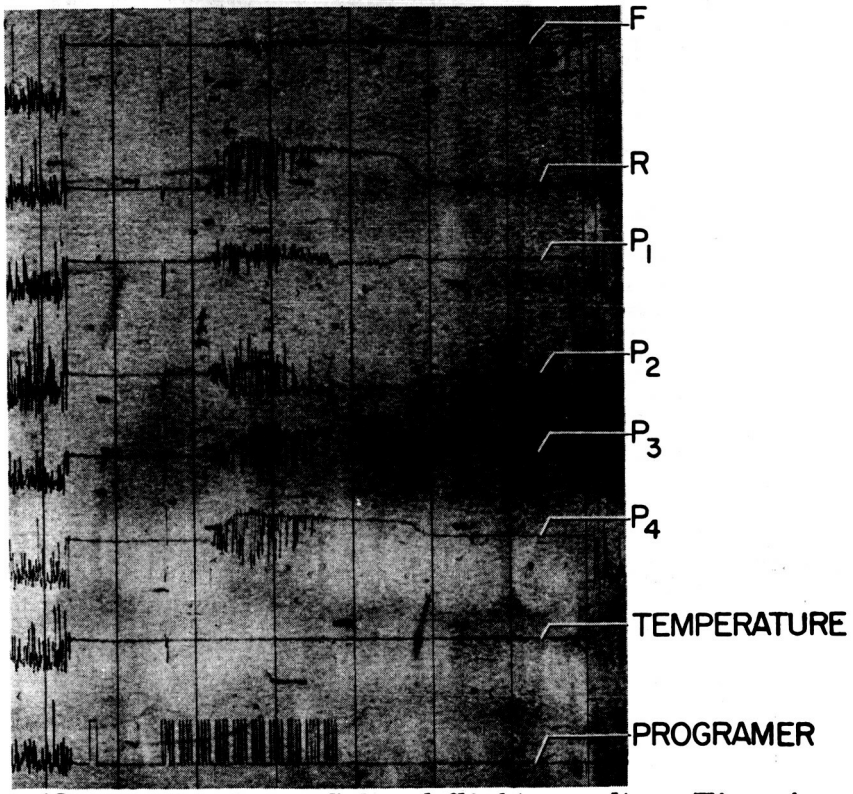

Figure 12.- Preliminary S-band flight results. Time increases from left to right.

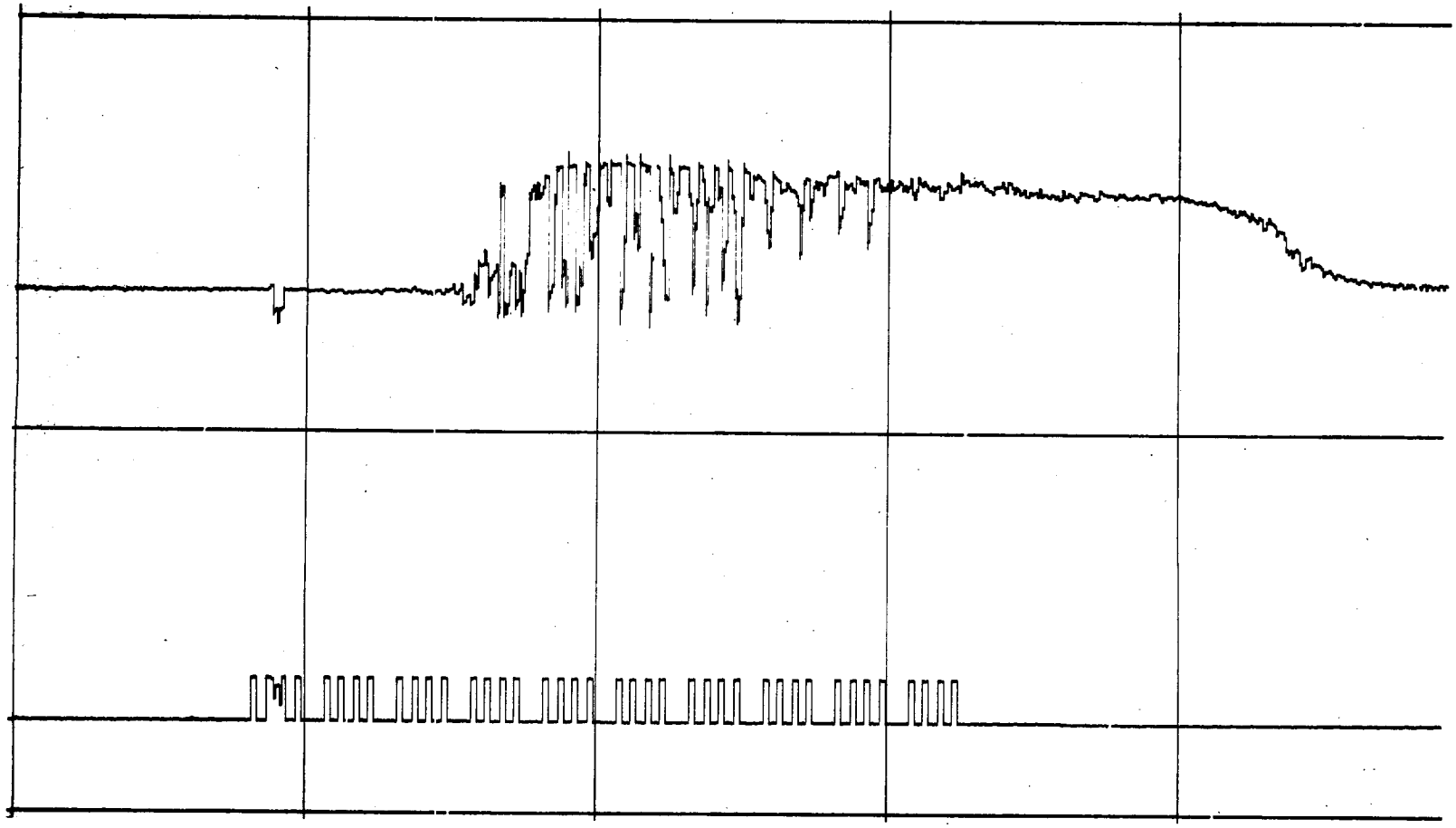

Figure 13.- Expanded plot of reflected power monitor (top trace) and programer output (bottom trace).

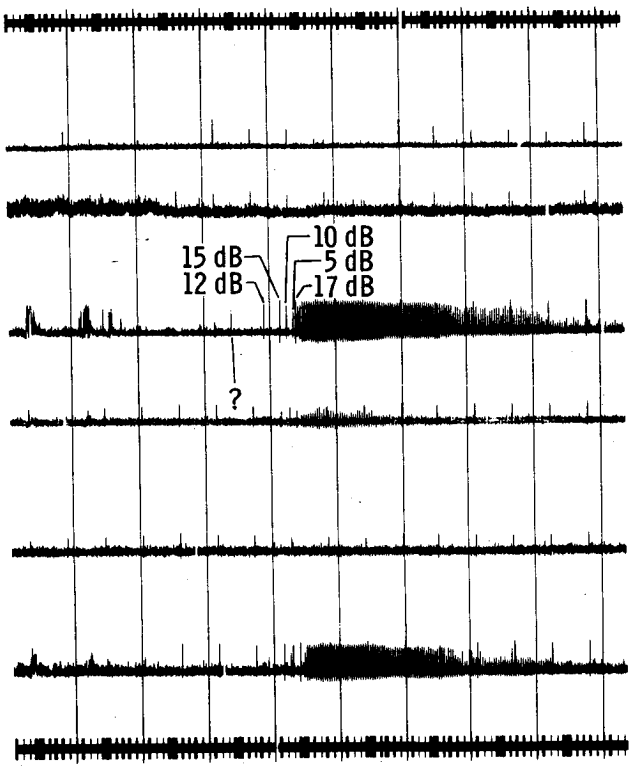

Figure 14.- Transmission data. Time increase from right to left.

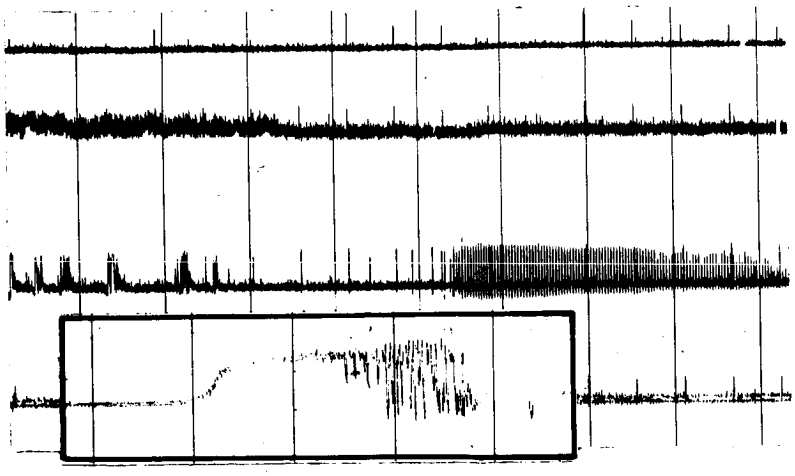

Figure 15.- Transmission data and reflected power monitor. Time increases from right to left.

SHOCK-TUBE MEASUREMENT OF ADMITTANCE OF RAM C AND RAM C-C DIAGNOSTIC ANTENNAS*

By W. C. Taylor

Stanford Research Institute

SUMMARY

A program of measurements was performed in the SRI 12-inch shock tube to determine the accuracy of inferring electron density from measurements of the admittance of three different antennas used in the RAM flight-test program. Measurements were made at air densities corresponding to approximately 125,000 and 175,000 feet altitude. Electron density was varied from 5×10^{10} to 10^{13} cm^{-3}. Within a factor of two in electron density, admittance agreed with theoretical calculations of Croswell** for all three antennas except for conductance at overcritical densities, which was always higher than calculated. However, the results showed that susceptance is a good indicator of peak electron density in the above-critical regime.

INTRODUCTION

A well-known electrical characteristic of antennas immersed in plasmas is the large rise in reflection coefficient near the plasma critical density. However, the admittance of the antenna, especially the susceptance, continues to vary as electron density is increased. These features can be used for plasma diagnostics in both laboratory and flight-test plasmas if the measured antenna parameters can be related to the plasma parameters. By the use of separate diagnostics of the laboratory plasma (using ion probes), a relationship between plasma parameters and antenna admittance can be established and compared with theory.

---

*Editor's note: The flights are incorrectly identified in this paper. The one the author refers to as RAM C is actually RAM C-II, and the one he refers to as RAM C-C is actually RAM C-III.

**W. F. Croswell, personal communication.

Two of the antennas tested in the program of measurements reported here were flown on the RAM C test flight , and one is scheduled to be flown momentarily on the RAM C-C test flight. These measurements were performed under contract to NASA (ref. 1), following two earlier series of measurements with rectangular apertures (refs. 2 and 3).

SYMBOLS

b	Normalized susceptance
f	Microwave frequency
g	Normalized conductance
i_p	Electrostatic-probe current
n	Electron density
n_c	Critical electron density
p_1	Initial shock-tube pressure
t	Time
V_i	Microwave voltage corresponding to incident wave
V_p	Microwave-probe voltage
$\|\Gamma\|$	Magnitude of reflection coefficient
δ	Distance to half-peak-density point
ν	Collision frequency
ω	Microwave radian frequency
ω_p	Plasma radian frequency

DESCRIPTION OF ANTENNAS AND SHOCK-TUBE MOUNTING

The SRI arc-driven 12-inch shock tube is described in ref.3. For the measurements reported here, it was desirable to mount the antennas in the tube such that the reflective metal shock-tube wall was not directly opposite the antennas. For this reason, an auxiliary fiberglass tube 10-inches in diameter (inside) was designed and fabricated to essentially extend the tube test section into the existing 36-inch-diameter dump tank. This auxiliary tube is shown in figure 1, showing two antennas mounted on a curved ground plane and attached at the downstream end of the fiberglass tube. The sharp leading edge of the fiberglass tube was located upstream of the dump tank, such that the tube served as a channel for most of the test slug to flow unexpanded into the dump-tank area where the antennas were located. Figure 2 shows the sharp leading edge of the Teflon coating on the curved ground plane, fashioned to allow the test slug of hot air to pass essentially undisturbed between the Teflon layer and the fiberglass. Figure 3 shows the side of the ground plane over which the test plasma passed. The test plasma over the ground plane was about six inches deep and ten inches wide. Also shown is the window that was cut in the fiberglass to reduce the reflection coefficient without plasma to a minimum level. This window was covered by thin Mylar on the inside surface to preserve the surface continuity. Microwave absorber was placed between the fiberglass and the dump tank to isolate the metal tank walls from the antennas. Before the antennas were mounted on it, the fiberglass tube was inserted in the shock tube for some 0.1-torr test shots. A rake of wire probes across the downstream end of the tube showed that the fiberglass did not measurably affect the electron density in the test slug at this pressure.

Figure 3 also shows the array of six 10-mil-diameter wire probes used to map the test-plasma electron density for the low-pressure shots. For the high-pressure shots, two wedge probes were placed just downstream of the apertures at distances of 1/8-inch and 7/8-inch off the Teflon layer. Both types of probes were described in ref. 3.

On the basis of measurements reported earlier (ref. 4), estimates can be made of the electron-density boundary-layer thickness. In terms of the distance δ from the Teflon surface out to the half-peak-density point, the results are: for the S-band antennas, δ = 2 mm at 0.1 torr and 0.7 mm at 1 torr; further downstream, for the X-band antenna, δ = 2.5 mm at 0.1 torr and 0.9 mm at 1 torr .

Figure 2 shows the two RAM C antennas designed for use as reflectometers on RAM flight tests. The main purpose of these antennas was to indicate by a precipitous change in reflection coefficient, the time at which the plasma density went through a small range of electron density near the critical value. The antenna on the left in figure 2 is the S-band one, radiating at 3348 MHz, and on the right is the X-band one, at a frequency of 10.044 GHz. Both have tuning screws for providing a free-space match. The metal conducting walls of both antennas were extended through the Teflon coating to achieve the greatest possible proximity to the plasma .

Measurements were also conducted of the admittance of the S-band diagnostic RAM C-C antenna. This antenna, also circular, was designed to provide a calculable scattering matrix so that the plasma conditions over the aperture could be related to the measured terminal admittance over a wide range of electron density.

Block diagrams of the microwave circuitry used to measure the rapidly changing admittance of the antennas are shown in figure 4 (S-band) and figure 5 (X-band). The main feature of the S-band system is the slotted line with three microwave probes used to detect the local electric field standing wave. If the incident power is determined by other means, only two probes are needed to determine admittance, but a third probe at a still different electrical location in the line improves the precision of the measurement. (During early measurements, the S-band system consisted of two probes and a reflected directional coupler, but the three-probe method was found to be more accurate when coaxial equipment is used.) The tuners were needed to cancel out the susceptance introduced by the couplings in the somewhat complicated transmission lines between the microwave instrumentation external to the dump tank and the antenna terminals in the approximate center of the tank. The X-band system also included a directional coupler to monitor the incident level, similar to that shown for the S-band system.

It had been found earlier (ref. 3) that in the low-pressure shots the use of a liquid-nitrogen trap in the shock tube to remove the water vapor from the test air served to increase the length of the nominally uniform test plasma between the shock front and the driver gases. This procedure was used in these tests especially since the larger aperture sizes (~3 inches) presented a more stringent requirement for test-plasma length than in the previous work (ref. 3). It was initially planned that only 0.1-torr measurements would be made, but some 1.0-torr shots were fired toward the end of the program.

It was found early in the admittance tests that, although liquid nitrogen was being used for a water-vapor trap to improve the quality and duration of the test period, there was a high incidence of poor-quality test plasmas as evidenced by very short test times on some of the probes. Many test shots were run to isolate the source of the trouble, and it turned out that almost all the shots when the microwave absorber was not in the tube gave very good test slugs. As a result, the absorber was placed in a Mylar vacuum enclosure of its own to isolate it from the test air. The subsequent results were consistently good. It is assumed that outgassed impurities from the absorber in the test air caused the problem, but it is not understood how. The absorber used was Eccosorb AN-75.

RESULTS OF MEASUREMENTS ON RAM C ANTENNAS

Preliminary Tests and Calibrations

The RAM C S-band antenna installed on the segment of cylindrical ground plane was found to have a VSWR of 1.12 when radiating into free space, while the X-band VSWR was 1.06. But when the ground plane was mounted on the fiberglass auxiliary tube, the S-band VSWR was found to be greater than 1.3. Solutions were sought until the window shown in figure 3 was cut out, giving a VSWR no greater than 1.1 for both antennas. This was maintained when the apparatus was installed in the shock tube, provided microwave absorber was used between the fiberglass and the metal dump-tank wall.

In each case, measurements were made of the phase shift between the aperture (covered with a short circuit made with metal foil) and shorted terminals of the antenna so that the measured terminal admittance could be transformed to aperture admittance if it was assumed that only a phase rotation was needed to do so. For the S-band antenna, the nulls with the

aperture shorted were located 0.121 guide wavelengths toward the load from the nulls with the terminals shorted. In the X-band system, the nulls with the aperture shorted were located 0.107 guide wavelengths toward the generator from the nulls with the terminals shorted.

The losses in the transmission lines between the slotted line and the antenna terminals were measured and taken into account in both cases. The use of RG-9/U coaxial cable kept the S-band one-way loss to 1.1 dB. The use of the 10-dB directional coupler in the X-band circuit between the slotted line and the antenna contributed to the total effective X-band line loss of 1.3 dB (one-way).

The X-band detector monitoring reflected signal was calibrated by putting a short at the antenna terminals and setting the attenuator at various appropriate levels. The detector levels were recorded on photographs, using the same Polaroid camera for a given detector that was subsequently used to record the shot data from this detector.

The slotted-line detectors were calibrated using a matched load to achieve a flat line. When the load admittance varies arbitrarily over the complete range from 0 to ∞, it is possible that the voltage detected by a probe in a slotted line, V_p, varies from 0 to $2V_i$, where V_i is the voltage corresponding to the incident wave alone. However, with some line losses and plasma density varying over a finite range, it was known from earlier experience that the voltage excursions could be expected to be almost always in the range of $0.4\ V_i$ to $1.6\ V_i$. After setting the incident power at a known level, the calibration levels were recorded photographically, varying the attenuator levels both higher and lower than the attenuator setting that was used for the shots. This latter setting, usually 4 dB, corresponded in the calibration levels to V_i. Figure 6, showing an example of the calibration levels, illustrates the precision available in these measurements. Since V_i corresponds to the radius of a Smith-chart when the admittance is inferred from the probe levels, a Smith-chart radius is equivalent to approximately a 3-cm scale on the oscilloscope face. This could be improved, for example, by the use of single-trace oscilloscopes rather than the dual ones. However, as many as 12 channels were needed (six ion probes, three S-band, and three X-band) on some of the shots in addition to any auxiliary measurements such as shock-speed monitoring. Indeed, in some cases, M-type multiple-trace heads were used to minimize the number of oscilloscopes needed.

Results of 0.1-Torr Measurements

Figure 7 shows the pertinent data collected on a 0.1-torr shot. For this shot, the three S-band probes were placed at eighth-wavelength intervals with the center one (No. 2) at a point corresponding to the terminal's position. The two X-band probes were placed three-sixteenths and one-eighth wavelength, respectively, from the equivalent terminals' position. Since all traces shown were triggered simultaneously, the shock arrived at the S-band aperture first, then at the X-band aperture, and then at the ion probes. The X-band aperture and probes were centered approximately 85 and 125 mm, respectively, downstream from the S-band centerline. It is seen that the ion probes are generally consistent with each other in this shot for at least the first 80 μs following the front, with the exception of a short burst on ion probe No. 5. (Ion probe No. 1, shown at the top of figure 3, was not monitored on this shot, and ion probe No. 2 current is not shown in figure 7.) Although the admittance generally seemed most strongly related to the electron density inferred from No. 4 (the center probe just over surface), the data was not used unless it could be seen that at least three other probes showed essentially the same density. The inferred electron density on this shot ranged from 3.2×10^{11} (just after the front) to 1.7×10^{12} (where the ion probe traces go off scale).

Since it was found that both antennas respond largely only to the plasma over the central 1.5-inch core of the aperture, corresponding to a flow time of about 10 μs, the gradient in electron density over the aperture for the 80-μs test time was no greater than approximately 20 percent. Thus, this and similar shots with a slow axial variation in electron density yielded essentially a continuum of data over this range. For data reduction and plotting, discrete points were taken at approximately 10-μs intervals. It is seen that the precipitous jumps in the X-band probe voltages and reflection coefficient (at approximately 65 μs following the front) occur while the electron density and the S-band probe voltages are changing relatively gradually. The biggest jump in the S-band data occurs at the arrival of the shock front because the density just behind the front is over critical for this frequency. Note that the S-band probes respond to the front in a "rise time" of about 10 μs. It appears from the microwave data on this shot that the

electron density kept increasing for a total of about 175 μs starting at the front, but the ion probe currents went off-scale such that neither density nor uniformity of the plasma is known after about 80 μs.

The composite S-band aperture admittance data are shown in figure 8. The "ticked" circles are from the data on figure 7. The data from the three microwave probes were converted to radii of arcs plotted on the Smith Chart from the appropriate electrical points around the perimeter. The size of a given admittance data "point" is an indication of how far the three arcs missed intersecting at a single point. The phase rotation with increasing electron density is counterclockwise, as indicated by the approximate-electron-density indicators around the periphery of the chart. The voltage-reflection-coefficient values corresponding to these data, but corrected for line loss, are plotted in figure 9 as a function of electron density. The data from figure 7 are indicated, with a line drawn connecting the points, since a continuum of values is available from the shot. Because such shots are so fruitful, only a few are needed to adequately indicate the admittance as a function of time. The data from other, similar shots are also represented in figure 9 by lines interconnecting the points.

Figure 10 shows the X-band aperture admittance data, with the points from figure 7 identified by tick marks. Figure 11 shows the corresponding voltage-reflection-coefficient values versus electron density, compared with calculations by W. F. Croswell for a somewhat smaller circular aperture. It is seen that the measurements fall within a factor of two of the theory up to $|\Gamma| = 0.7$, and that the slope of the curves from single shots agrees quite well with the theory. Since the maximum slope is largely determined by collision frequency the agreement in slope is an indication that the collision frequency was close to the value calculated from the shock speed and pressure--2.5×10^9.

The admittance data of figure 10 were plotted in figure 12 as a function of n, and compared with theoretical aperture admittance calculated by Croswell. (The electron density corresponding to the two points well above 10^{13} in figure 10 is not known.) It is seen that the conductance values agree well only up to critical, as does the reflection coefficient in figure 11. It is possible that above critical the discrepancy in both conductance and reflection coefficient is due to the fact that the theory applies to an antenna terminating in a conducting ground plane, whereas the RAM C antennas terminate at the surface of the Teflon. It is possible that a larger conductance arises because the energy can be radiated through the Teflon off to the side of the ground plane, rather than being confined to

the narrow layer of undercritical plasma next to the surface. The susceptance data agree quite well with the theory except for translation in electron density for the various shot groupings. Since the ion-probe determination of electron density may be uncertain by as much as a factor of two, it is expected that the theory for susceptance is applicable to this antenna.

Thus it appears that the RAM C antennas not only accomplished the purpose of indicating by a sharp change in reflection coefficient when the electron density passed through the narrow range near critical, but in addition the phase information from the X-band antenna appears valuable in determining electron density in a larger range above the critical density.

Results of Measurements at 1.0 Torr

Figure 13 shows the pertinent data collected on a 1.0 torr shot. Only the reflection coefficient of the X-band antenna was measured for the 1.0-torr shots. The S-band microwave probes were located electrically as for figure 7. These data show one example of various "anomalies" that seemed to happen more on the 1.0-torr shots than on the low-pressure ones: the dip in X-band reflection coefficient at about 150 μs after the front is not accompanied by a corresponding dip in the probe current, which rises monotonically in time during the first 250 μs of the test. Such anomalies seem to be the cause of the large scatter in the 1.0-torr data compared with the lower-pressure shots, as illustrated below. One would expect the typical steep slopes of the X-band and S-band reflection coefficients near the critical value to be separated by an order of magnitude. Figure 13 shows that they are separated by only a factor of 2 or 3. For instance, at a point 180 μs from the arrival of the shock, where the inferred electron density is only 3.5×10^{11}, $|\Gamma|_x = 0.58$ and $|\Gamma|_s = 0.65$.

Figure 14 shows both S- and X-band reflection-coefficient data from the 1-torr shots, compared with theoretical predictions of Croswell. It is noted that up to $|\Gamma| \approx 0.6$, the theoretical curves are a fair fit if they are translated in electron density in opposite directions--i.e., if the S-band curve is moved a factor of 1.7 higher and if the X-band curve is moved a factor of 2 lower than predictions. Most of the measured points fall within a factor of two of the translated curve in each case up to $|\Gamma| \approx 0.6$.

It is suspected that the problem of larger scatter in the 1.0-torr data than in the low-pressure shots was caused to some extent by less homogeneous plasmas (transverse to the flow direction). Since the fiberglass tube was required to be qualified by preliminary tests only for the less stringent low-pressure shots, where the mean free path is greater than the scale of roughness of the surfaces, this tube may have contributed much of the problem by giving rise to secondary wave structure in the plasma. This explanation helps in understanding only the scatter in the data, but has no bearing on why the response of the two antennas in terms of electron density is not as far apart (essentially one order of magnitude) as in the case of both the 0.1-torr measurements and theory.

RAM C-C RESULTS

The RAM C-C (S-band) antenna had a VSWR of 1.60 in bench measurements and 1.68 when installed in the shock tube, compared with the theoretical prediction of 2.0. Since no conducting walls of this antenna extend through the 0.32-inch-thick Teflon ground-plane cover, it was expected that significant radiation may occur off the edge of the ground-plane under any conditions, especially when the plasma is overdense. A metal foil reflector with the same lateral extent as the plasma was used to simulate the limiting case of $n \to \infty$. This gave $|\Gamma| = 0.84$. Since the flight configuration is completely enveloped by plasma, this indicates that the experiments in the shock tube with the limited ground plane would fail to duplicate the flight configuration by this extent in terms of voltage-reflection coefficient. As will be seen below, the maximum value of $|\Gamma|$ measured with plasma was 0.78, corresponding to the maximum value of n, which was 10^{13}.

Figure 15 shows the measured values of aperture admittance for $p_1 = 0.1$ torr, covering the range from just below critical to two orders of magnitude above.* These values are not corrected for line loss. Figure 16 shows the corresponding reflection-coefficient values, except that they are corrected

---

* The phase relationship between the terminal admittance and aperture admittance was 0.19 guide wavelengths for this antenna.

for line loss. Also shown are additional data from two other pressure conditions. It is seen that the 1.0-torr data show considerably more scatter than the 0.1-torr data, just as for the RAM C data. Also shown in figure 16 are predictions for this antenna by Croswell and Swift reduced by 16 percent to form an approximate theory appropriate to the experimental configuration, where the maximum possible $|\Gamma|$ is 0.84. Even with this reduction, the agreement is not very good, although the location of the maximum slopes of the curves is at essentially the same electron density.

In the range $(\omega_p/\omega)^2 \gtrsim 1$, the magnitude of the reflection coefficient is largely determined by the aperture conductance, which is sensitive to the limited lateral extent of the plasma. This antenna was also designed for determining electron density above critical mainly by the dependence of the susceptance on n in this region. Figure 17 shows the measured susceptance plotted against n. Figure 17 appears to confirm that the susceptance is an accurate measure of electron density in the two-order-of-magnitude range above critical. It is seen in figures 16 and 17 that several points, actually representing a continuum of data, were derivable from each of four shots. For each shot, the slope of the lines interconnecting the points is virtually identical with the theoretical curve.

REFERENCES

1. W. C. Taylor, "An experimental Investigation of the Interaction of Plasmas with Antennas," Final Report, Contract NAS1-8889, SRI Project 7729, Stanford Research Institute, Menlo Park, California (June 1970).

2. W. C. Taylor, "Study of the Effects of a Plasma in the Near-Zone Field of an Antenna," NASA CR-611 (1966).

3. W. C. Taylor, "The Effects of a Plasma in the Near-Zone Field of an Antenna--II," NASA CR-1149 (1968).

4. H. R. Bredfeldt, W. E. Scharfman, H. Guthart, and T. Morita, "The Use of Ion Probes in Re-Entry Physics," Tech. Report 26, Contract SD-103 under ARPA Order 281-62, SRI Project 3857, Stanford Research Institute, Menlo Park, California (May 1965).

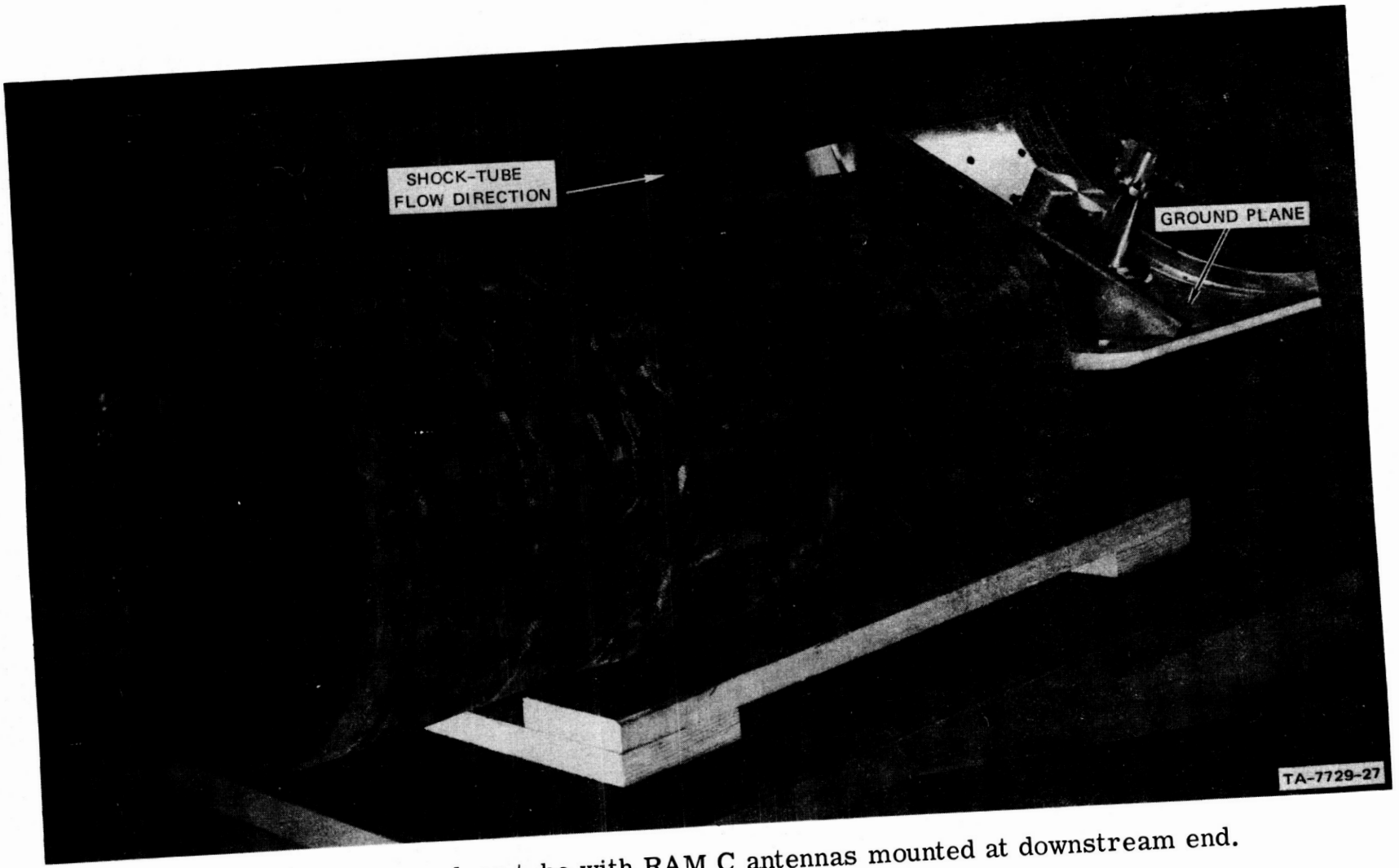

Figure 1.- Fiberglass tube with RAM C antennas mounted at downstream end.

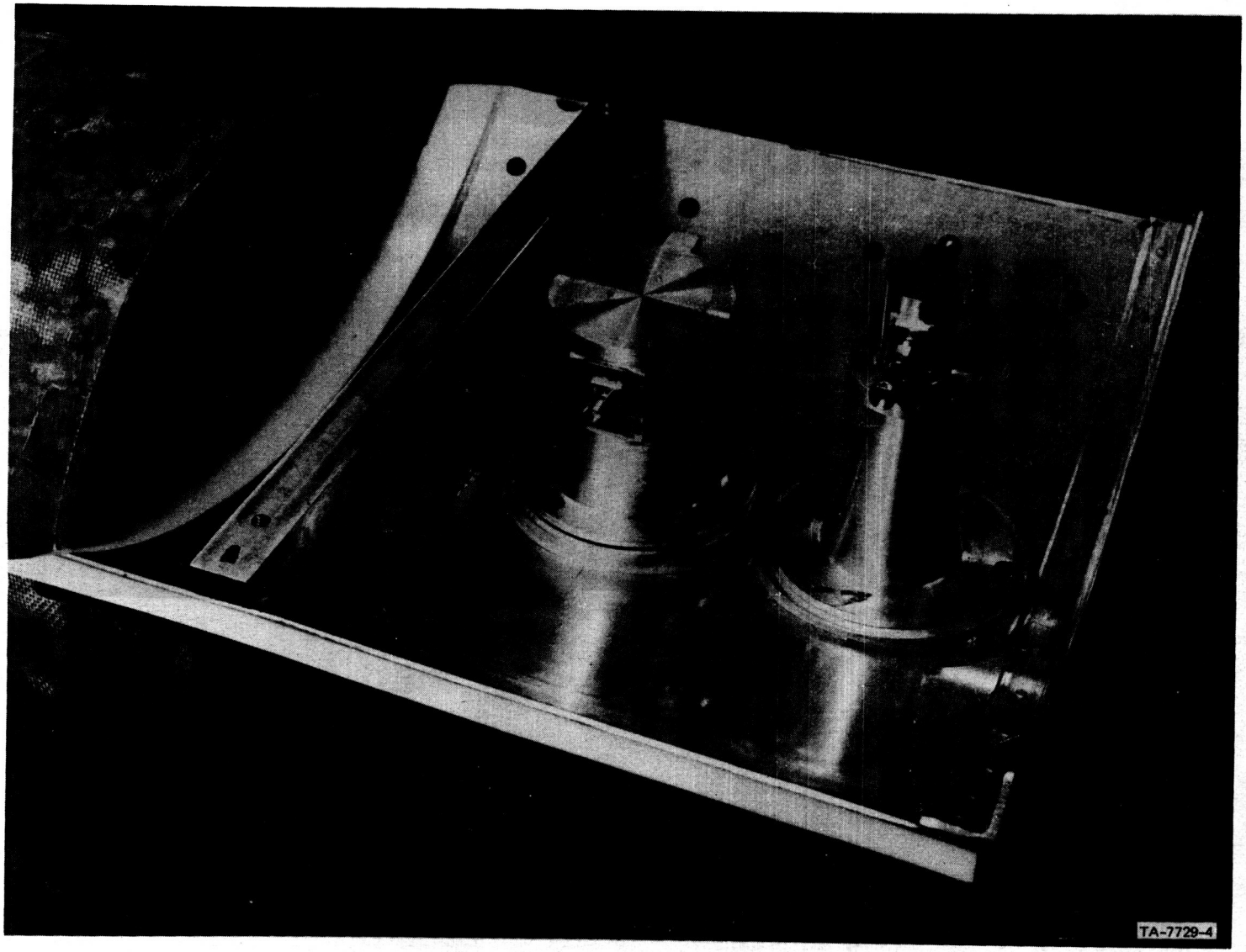

Figure 2.- RAM C antennas mounted on ground plane.

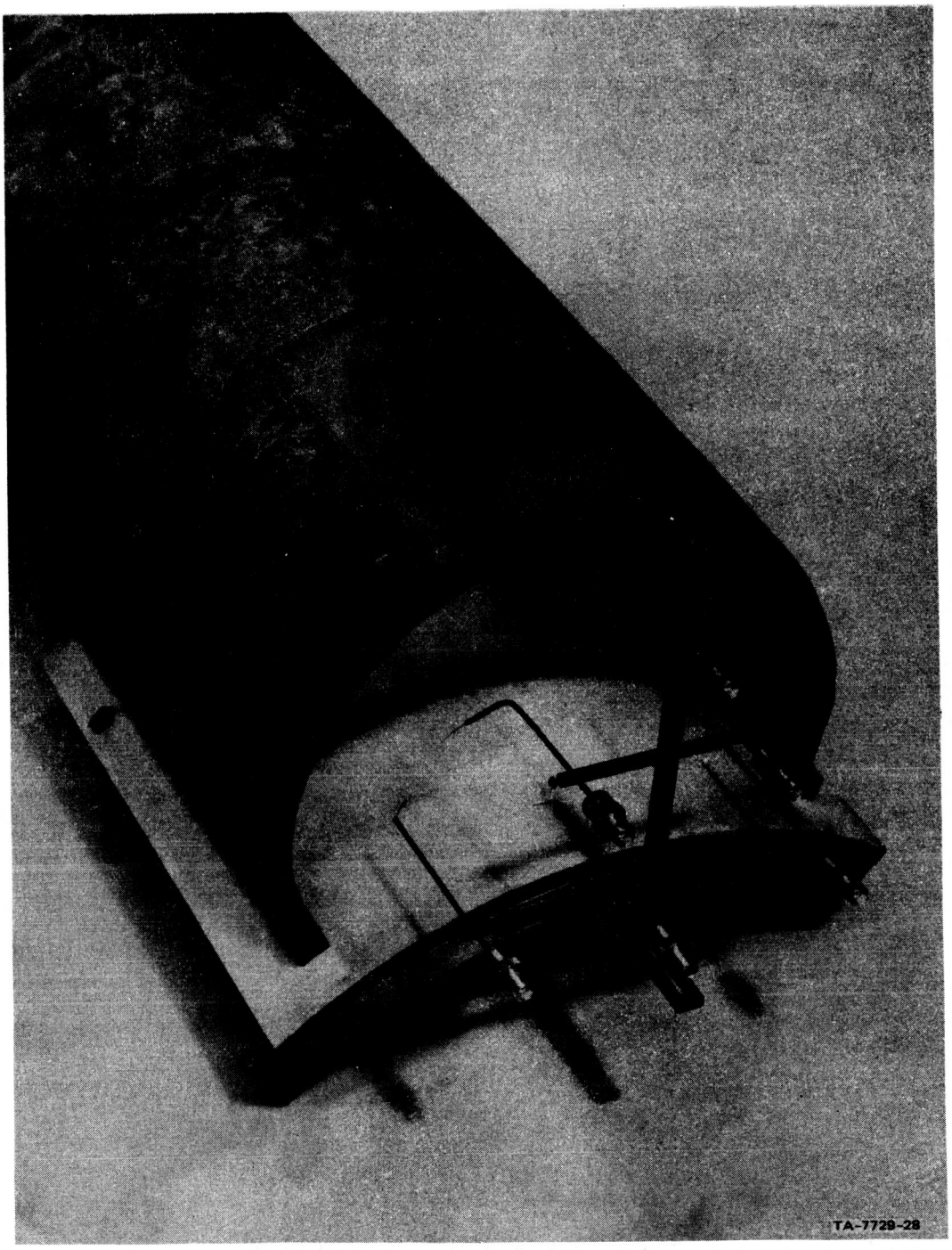

Figure 3.- View of test facility including electrostatic probe array and window in fiberglass (antenna aperture covered by Teflon layer).

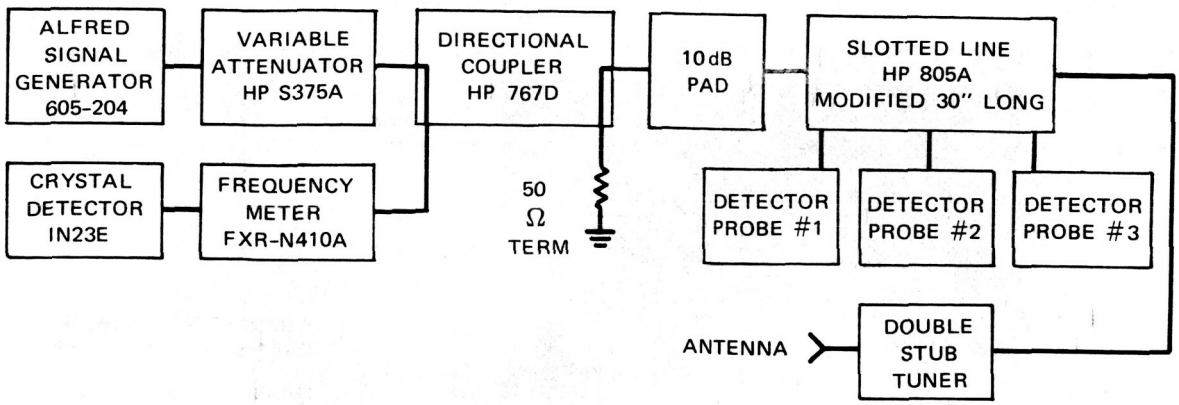

Figure 4.- Block diagram of S-band equipment for admittance measurements.

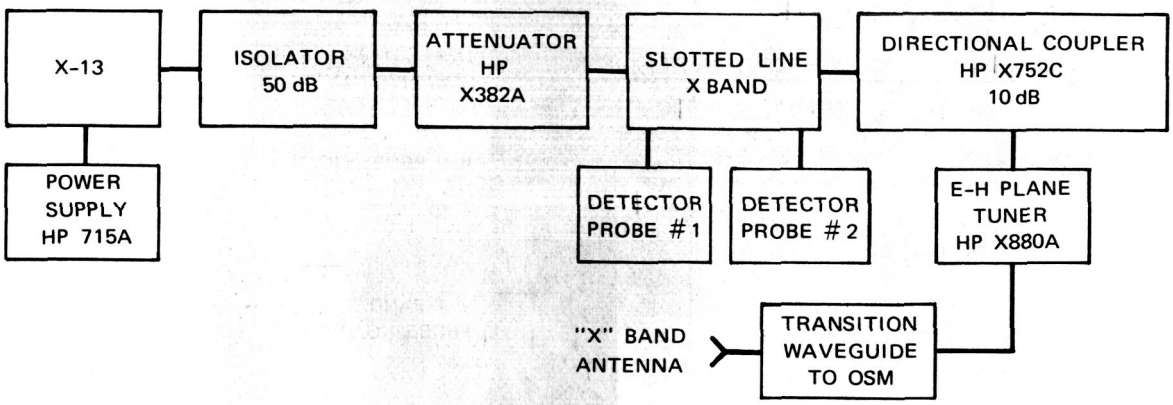

Figure 5.- Block diagram of X-band equipment for admittance measurements.

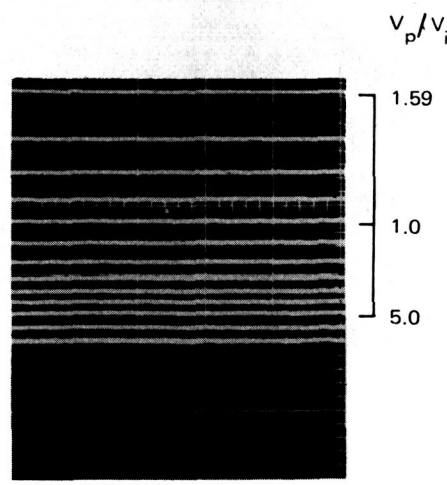

Figure 6.- Example of slotted-line microwave-probe-detector calibration levels.

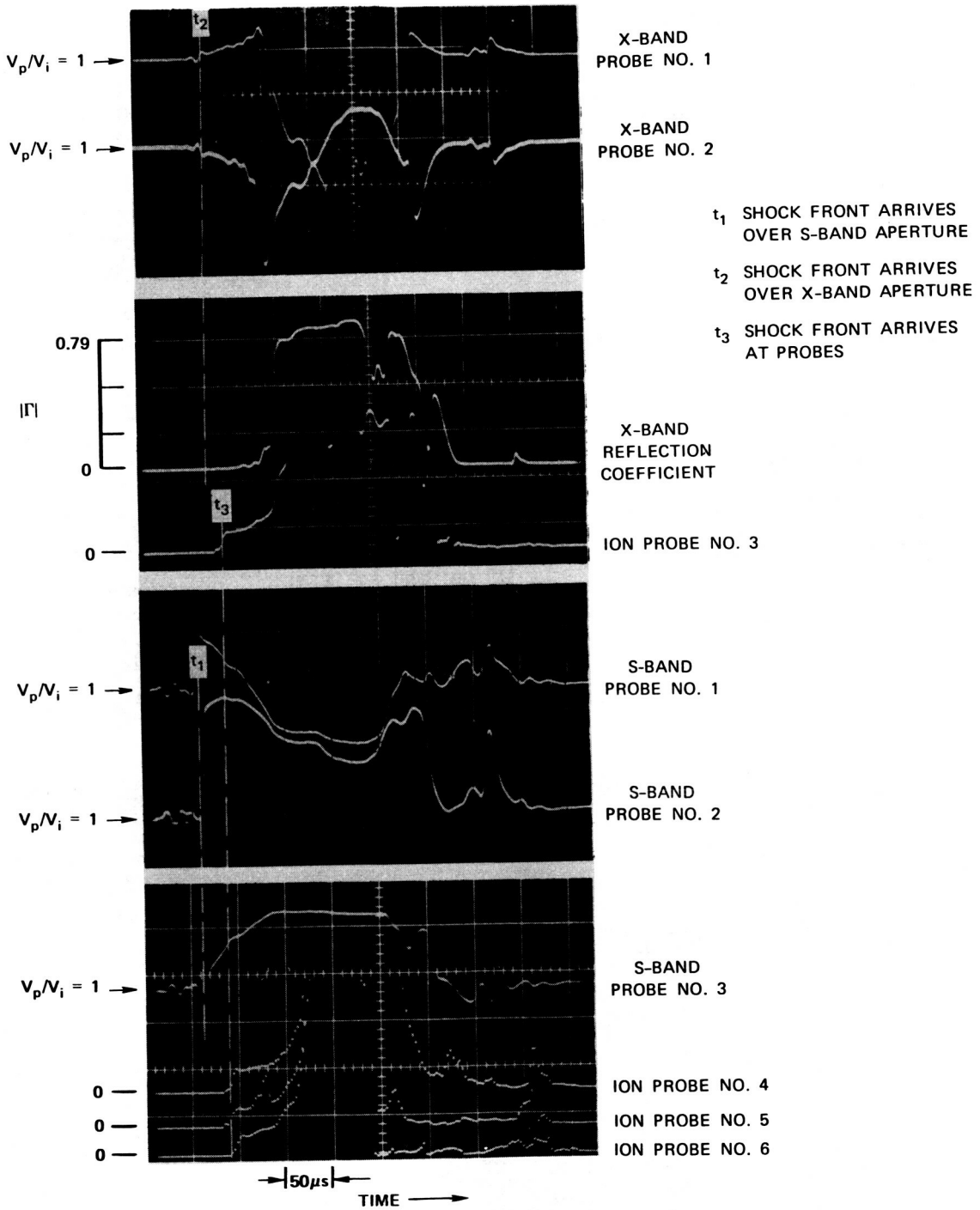

Figure 7.- Example of 0.1-torr shot data on RAM C antennas.

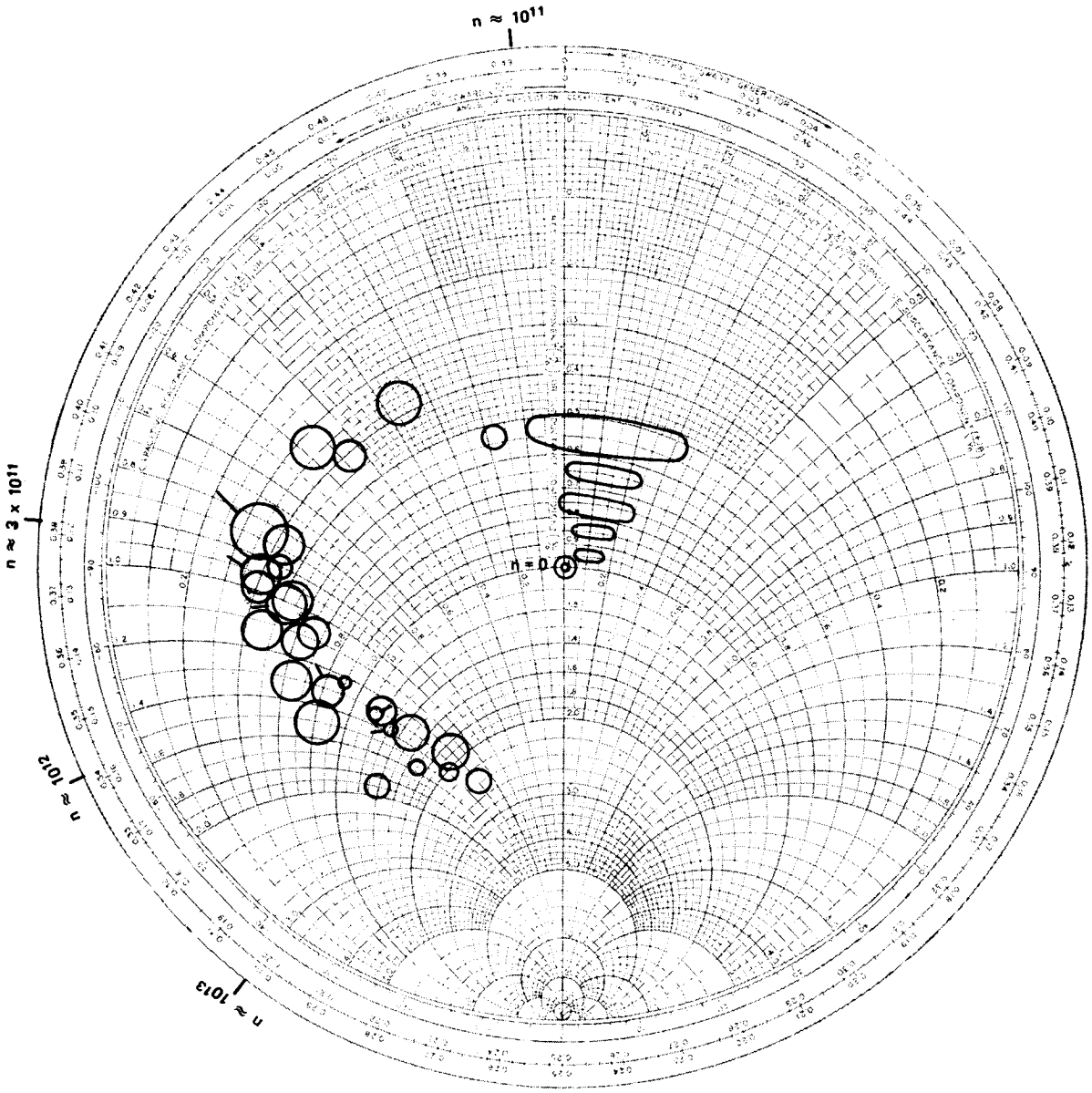

Figure 8.- RAM C S-band admittance data referenced to aperture (not corrected for line loss) – 0.1 torr.

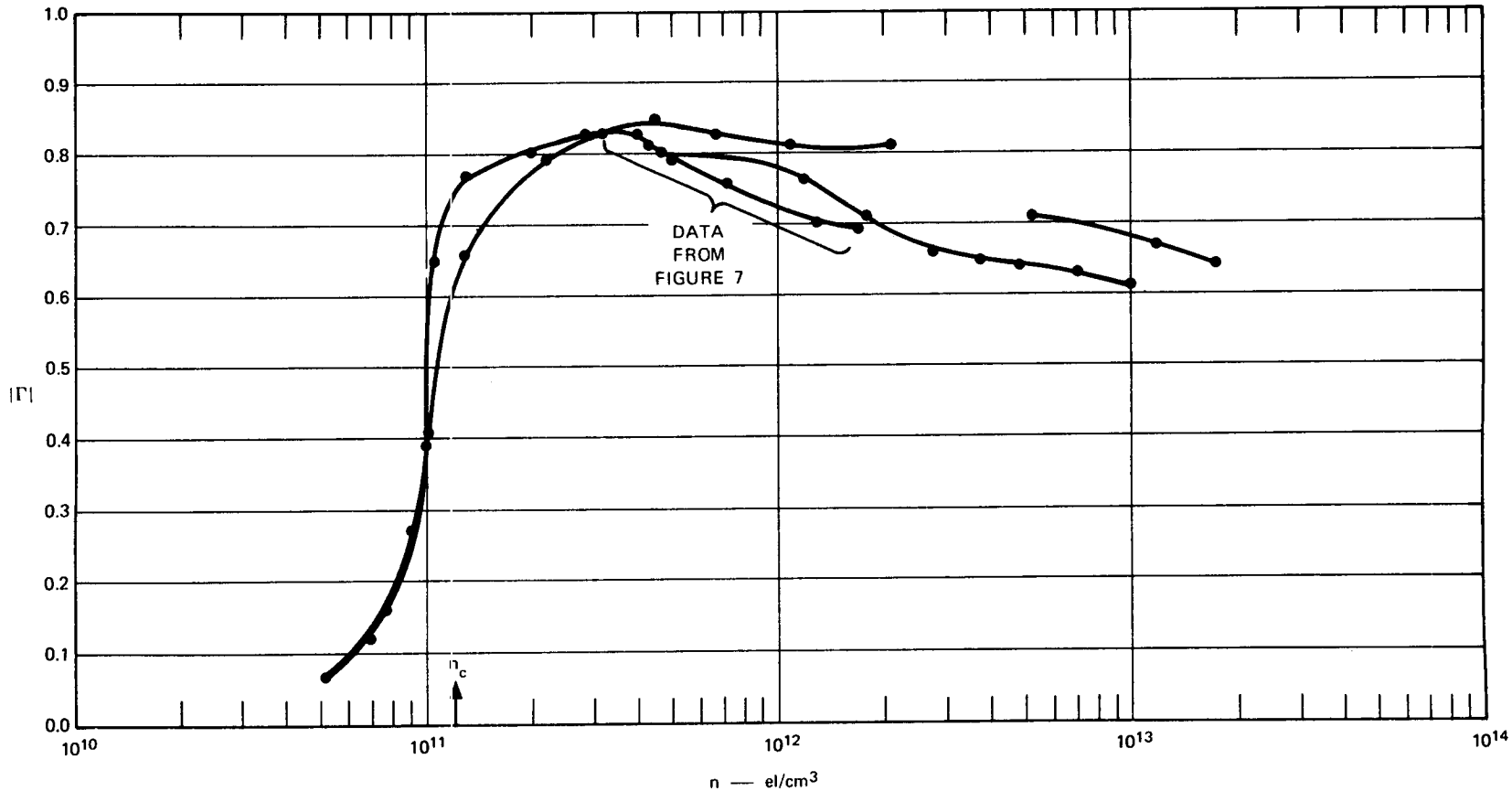

Figure 9.- RAM C S-band reflection coefficient as a function of electron density – 0.1 torr.

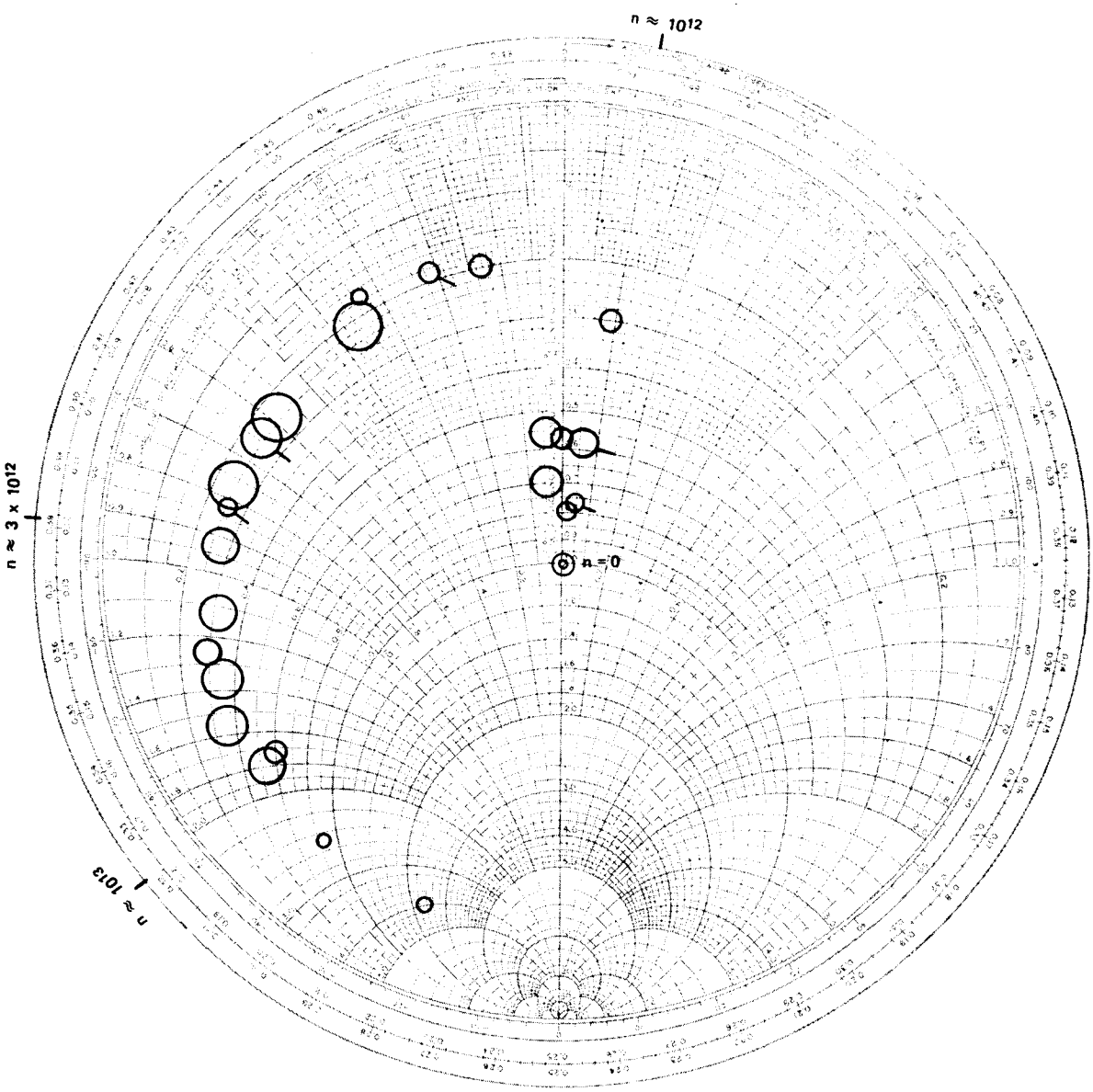

Figure 10.- RAM C X-band aperture admittance (line-loss corrected) – 0.1 torr.

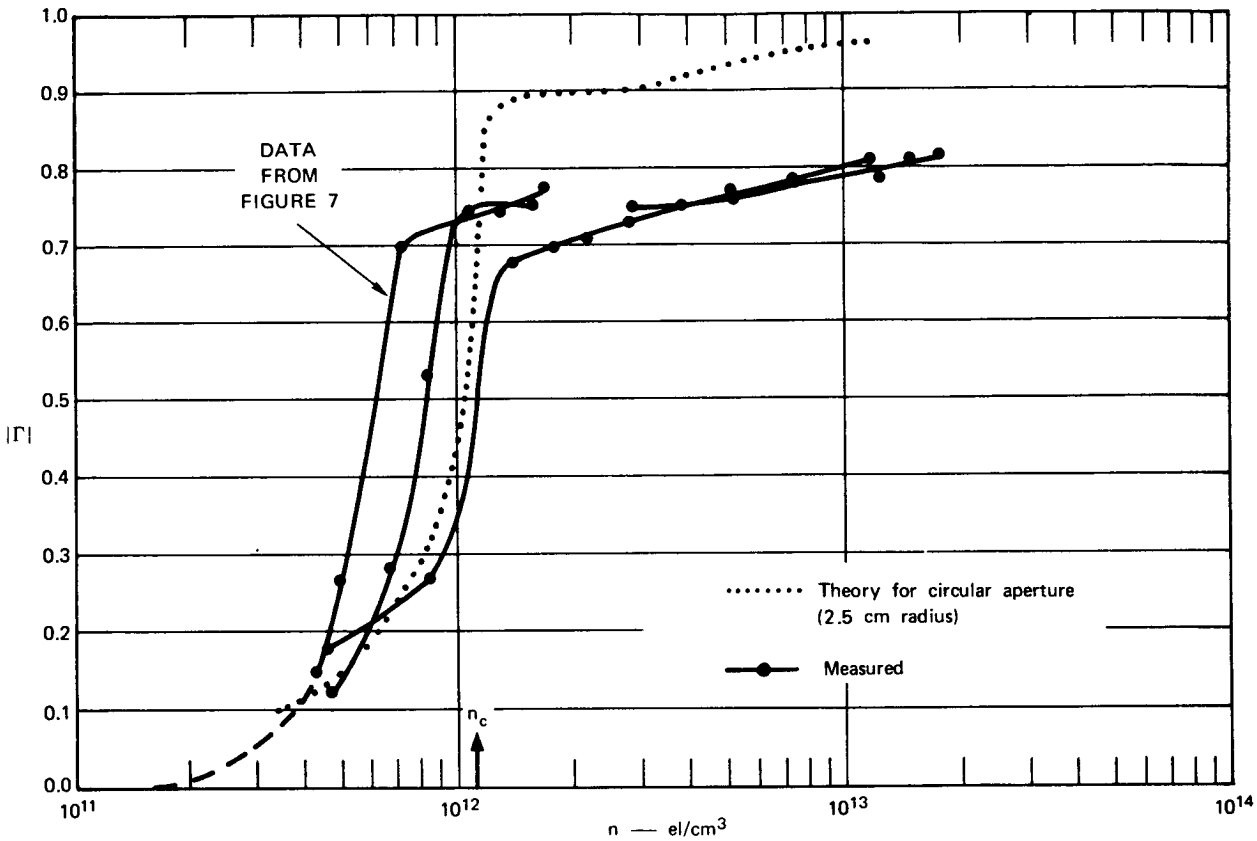

Figure 11.- RAM C X-band reflection coefficient as a function of electron density, measured and theory – 0.1 torr.

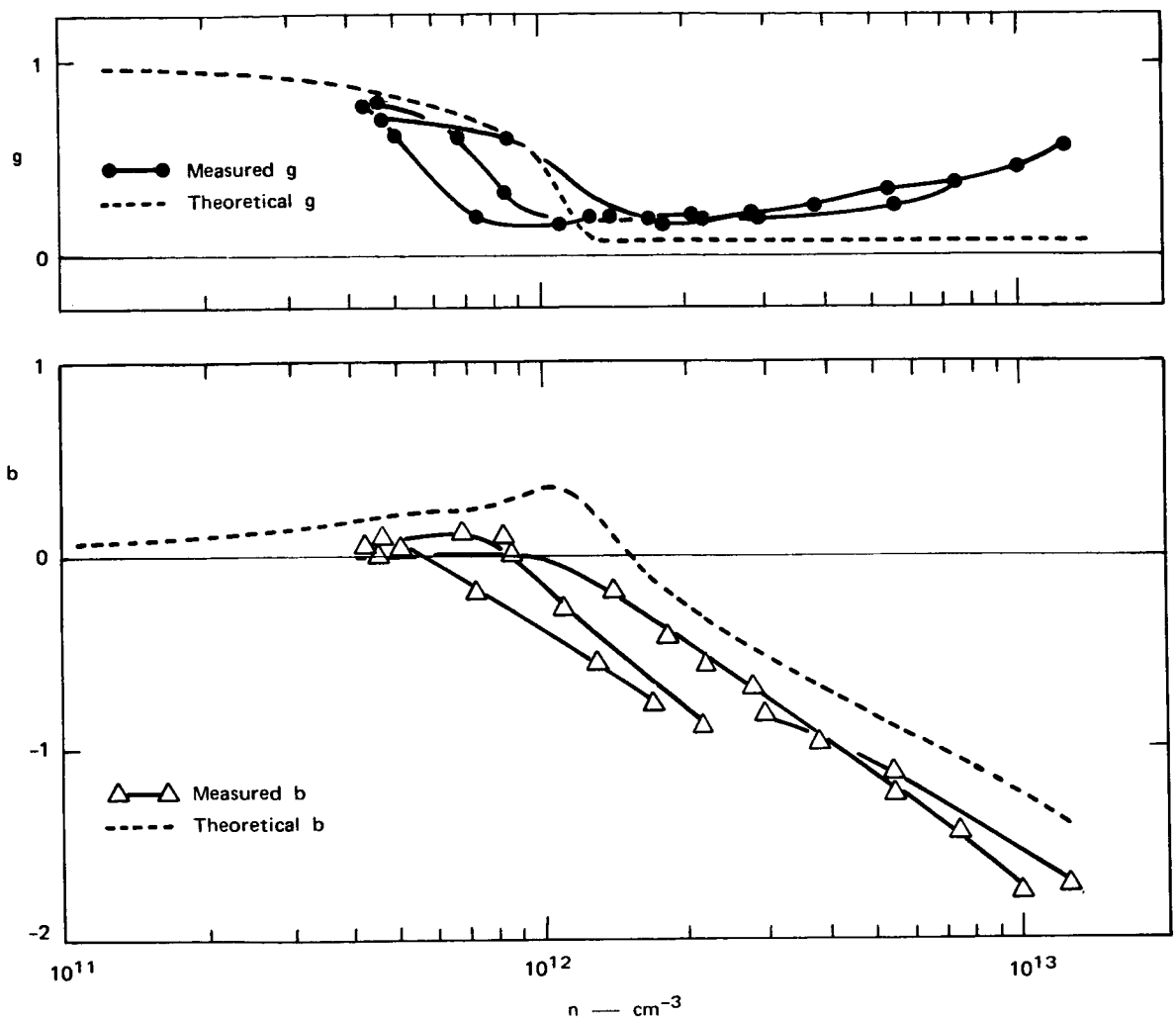

Figure 12.- Comparison of measured RAM C X-band aperture admittance with theory – 0.1 torr.

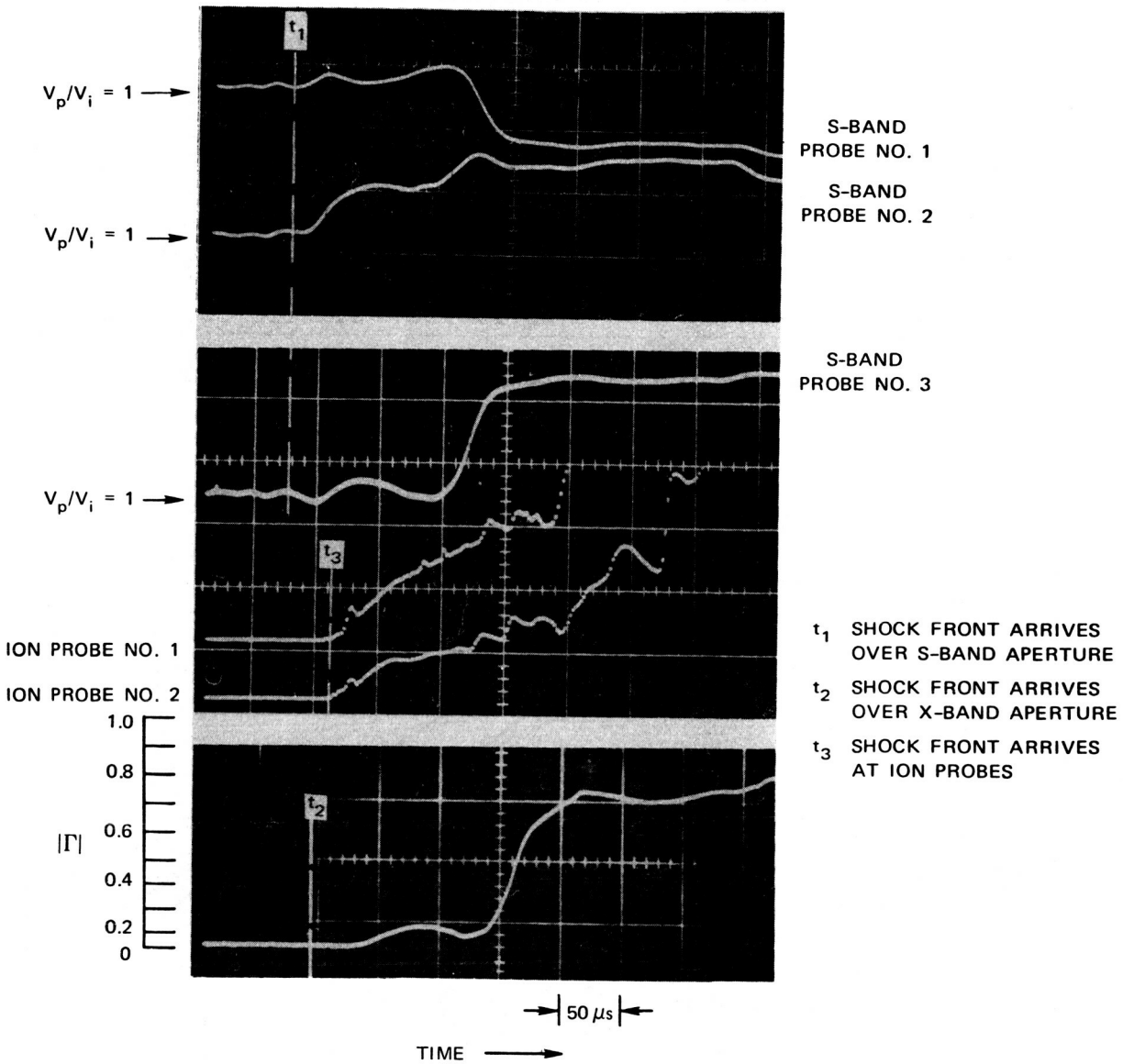

Figure 13.- Example of 1.0-torr shot data on RAM C antennas.

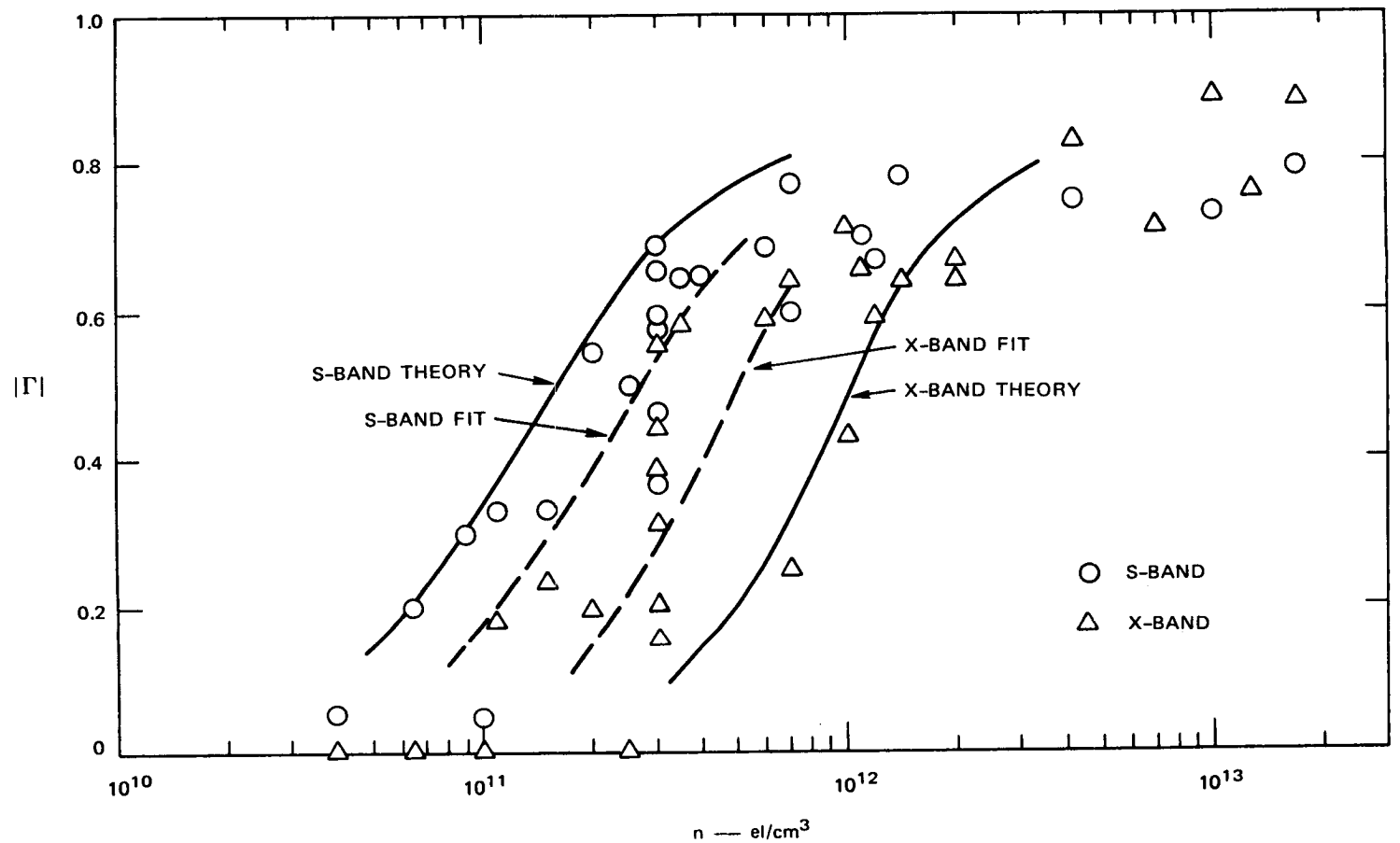

Figure 14.- RAM C reflection coefficient data as a function of electron density, compared with theory – 1.0 torr.

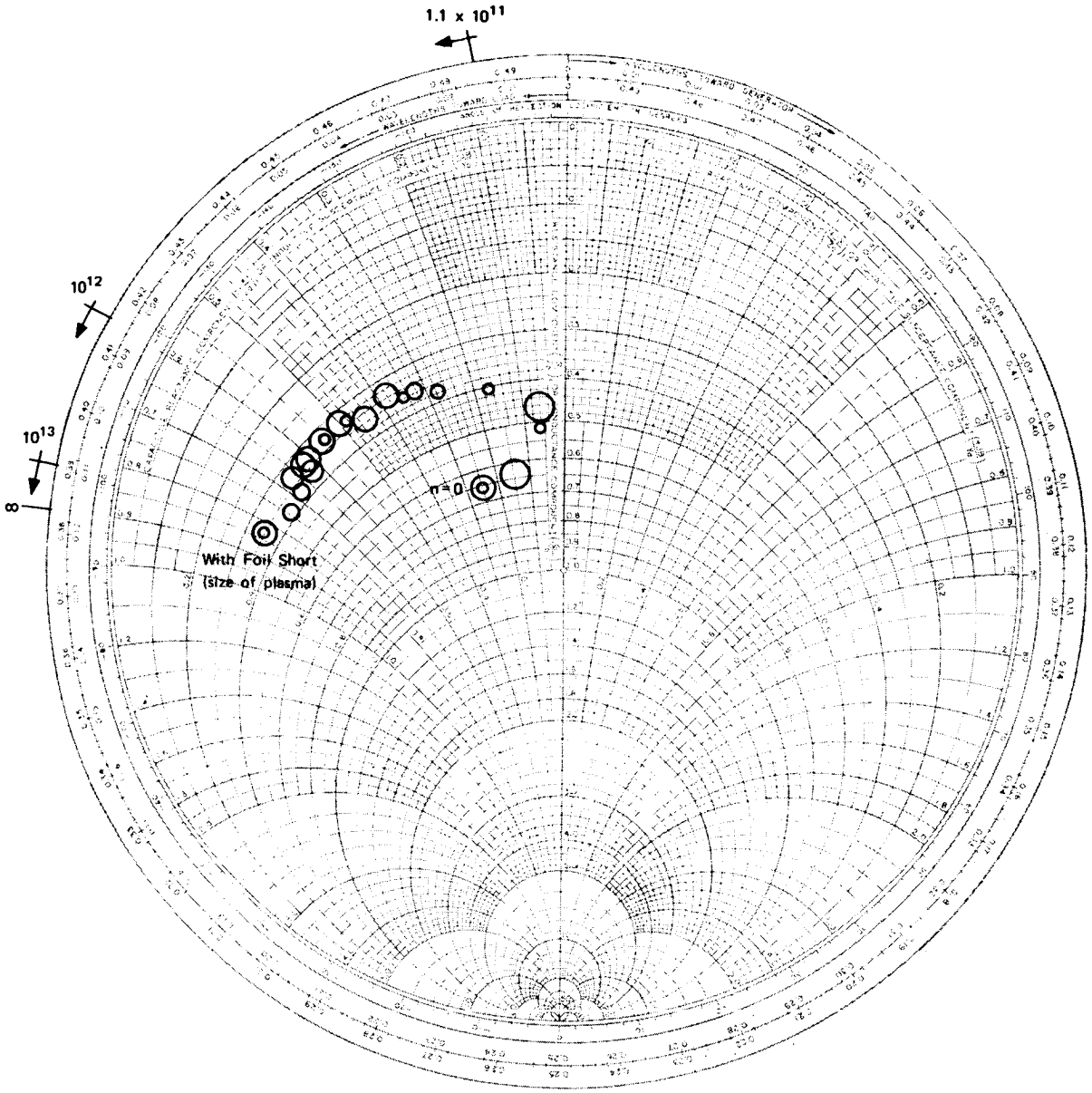

Figure 15.- Measured admittance of RAM C antenna $(p_1 = 0.1$ torr$)$, referenced to aperture.

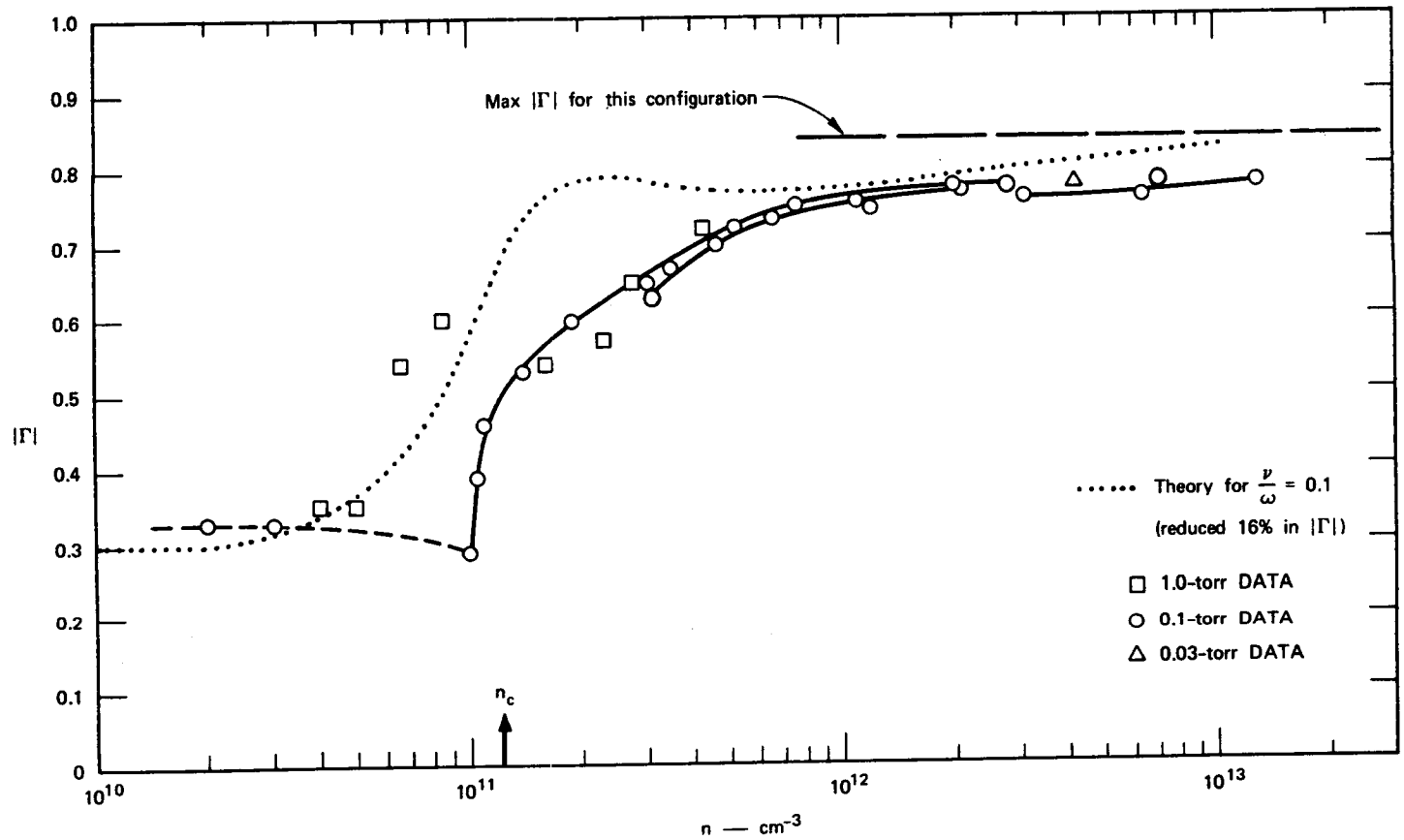

Figure 16.- Reflection coefficient of RAM C-C antenna as a function of electron density, compared with theory.

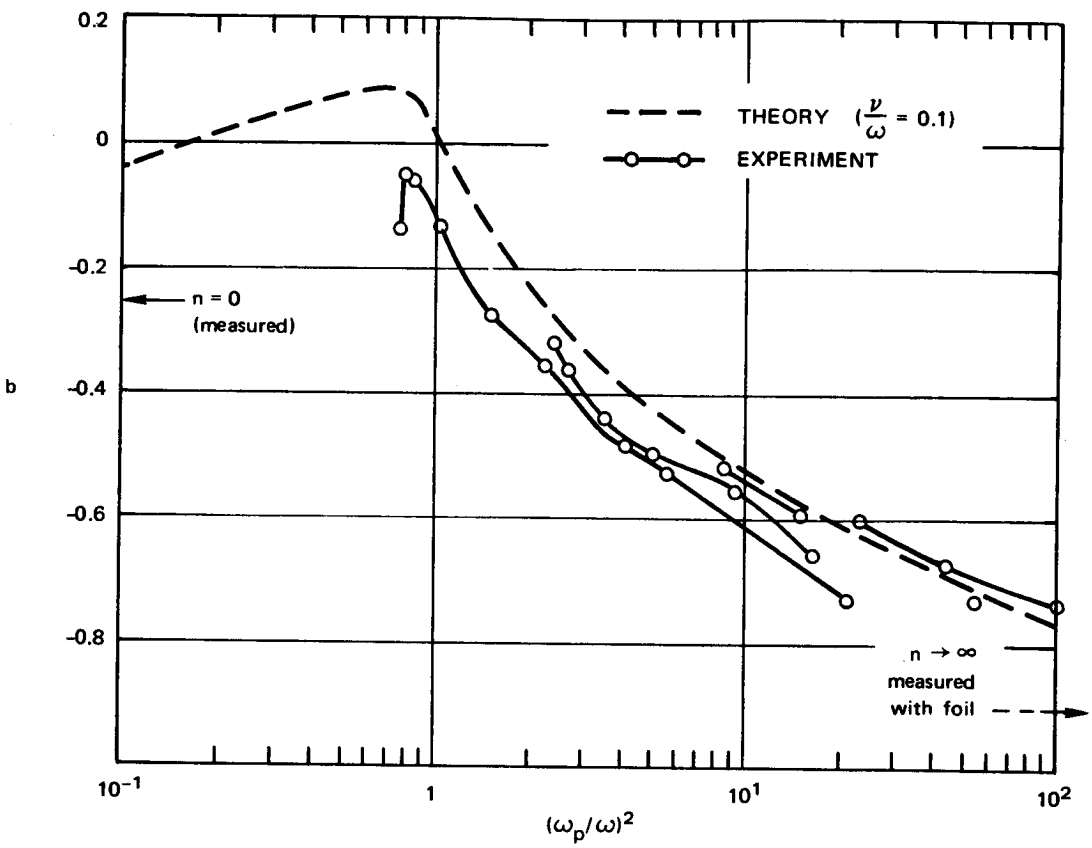

Figure 17.- Aperture susceptance, RAM C-C, theory versus experiment – 0.1 torr.

EFFECTS OF REENTRY PLASMA ON RAM C-I VHF TELEMETRY ANTENNAS

By William F. Croswell and W. Linwood Jones, Jr.
NASA Langley Research Center

SUMMARY

Upon careful inspection of the VHF signal strength recorded at several ground stations during the RAM C-I flight, antenna pattern changes are noted that are uniquely related to observer aspect angles. These aspect angles range from 75° to 88° when the receiving station is located broadside to the RAM configuration, and the aspect angle is 0° when the receiving station is directly down range (nose on). The antenna pattern changes are shown to occur in the altitude-velocity interval where the electron density, inferred from a rake of electrostatic probes, is equal to critical electron density occurring over the antenna physical aperture and where the corresponding measured reflected power from the same antennas rises to very large values. These results should be of interest to those designers desiring antennas that have forward-looking patterns during reentry.

DESCRIPTION OF EXPERIMENT

Payload

A diagram showing the pertinent parts of the RAM C-I payload is given in figure 1. The particular items discussed in this paper are the pair of cavity-backed slot antennas used for the real-time telemetry link (f = 259.7 MHz) and labeled "4" and "5" in figure 1, the four-slot array of cavity-backed slot antennas used for the delayed-time telemetry link (225.7 MHz) and labeled "10" in figure 1, and the rake of electrostatic probes labeled "12" in figure 1. A limited description of the antennas is given in a subsequent section; further details are given in reference 1 (appendix A). The detailed description of the electrostatic probe rake, as well as how the electron density is inferred from ion current measurements, is given in reference 1 (appendix C) and reference 2. For purposes of clarity in this paper, it can be simply stated that the electrostatic probe rake consists of eight iridium ion collectors spaced nearly equally apart 0.96 cm to 7.08 cm away from the vehicle surface.

Trajectory Parameters

The RAM C-I vehicle was launched and traveled along the ground track shown in figure 2. In particular, note that (1) the telemetry tracking ship USNS Twin Falls Victory is located directly down range of the payload nose (observer aspect angle θ of 0°) and that (2) the Bermuda station is located approximately broadside during the data period. The variation of the trajectory parameters as observed from the Bermuda receiving station is given in figure 3. Of

particular interest to this paper, which concerns critical electron density effects at VHF frequencies, is the region from 390 to 392 seconds from lift-off. Note that in this region the aspect angle relative to the vehicle nose ranges from 75° to 88° and the elevation angle as measured from Bermuda ranges from 21° to 20°.

Antennas

Real-time telemetry antenna.- The real-time telemetry antenna, operating at a frequency of 259.7 MHz, was designed primarily to determine the effectiveness of the injection experiment; similar antennas were used in all past RAM injection experiments. The basic antenna consists of a cavity-backed slot, with slot dimensions of 1/2 inch by 10 inches (1.27 cm by 25.40 cm). Two of these antennas were used in case the pressurization provided in one cavity should fail. The two cavity-backed slot antennas were fed with equal amplitude and 90° phase shift. The primary antenna patterns in the equatorial and polar plane are given in figure 4. The final impedance characteristics are given in figure 5. Several observations concerning the antenna patterns are important. First, since the vehicle is spin stabilized, one should observe about a 30- to 35-dB ripple in the received signal at Bermuda; signals observed at this station radiate approximately from the equatorial plane of the payload. Second, one should observe a small ripple in the nose-on radiated signal received at the USNS Twin Falls Victory ship. In addition, since the direct telemetry antenna has a -5-dB gain in the nose region and the delayed-time telemetry antenna has +3.5-dB gain in the nose region, the difference in the received signal of the two frequencies should be at least 17 dB.

Delayed-time telemetry antenna.- The delayed-time telemetry antenna, operating at a frequency of 225.7 MHz, was designed primarily to provide good pattern coverage for tracking airplanes and ships after blackout; the payload has an onboard tape recorder. The antenna consists of four circumferential cavity-backed slots, with slot dimensions of 1 inch by 16 inches (2.54 cm by 40.64 cm). The slots were connected in pairs and each pair was phased relative to the other pair to produce a forward-looking lobe. The primary antenna patterns in the equatorial plane and polar plane are given in figures 6(a), 6(d), and 6(g). The other patterns given in figure 6 are for other possible phase shifts ϕ between pairs for azimuthal angles Φ of 0°, 20°, and 40°. The impedance of this antenna is given in figure 7. Two observations about these antenna patterns are of importance in the interpretation of data later. First, one should observe about a 30-dB ripple in the received signal at the Bermuda station. Second, at the nose-on receiving station, about a 1- to 2-dB ripple should be observed.

Langmuir Probes

The RAM C-I Langmuir probes consisted of eight iridium strips mounted on a retractable sting. The probes were spaced approximately equal distances apart measured perpendicular to the spacecraft surface. Of interest in later data analysis, probe number 1 is located 0.96 cm from the payload surface and probe number 8 is located 7.08 cm from the payload surface.

A typical electron density profile for high altitudes inferred from measured ion current is given by the hatched area in figure 8. The upper and lower bounds on the hatched area represent the range of excursion of the measured ion current due to body motions. Correlation of such excursions in ion current with body motion is given in reference 2. The theoretical calculations are estimates of electron density including diffusion and are given in reference 3. It should be noted that preliminary results from similar probes on RAM C-III which extended 14 cm away from the payload surface indicate that the electron density profile is essentially flat even out to 14 cm.

Regardless of the total extent of the plasma, it appears that the VHF antennas will have a fairly uniform plasma slab that scales through critical density with decreasing altitude.

RESULTS

Signal-Strength Records

The signal strengths recorded at the Bermuda station and the USNS Twin Falls Victory station are given in figure 9 and figure 10, respectively. The arrows marked on these records indicate the altitude or time in the descending trajectory at which, first, probe number 8 and, second, probe number 1 of the Langmuir probe rake pass through critical electron density at the respective operating frequency. The region of interest to this paper is the time period from 385 to 394 seconds. The spikes evident in these records from 394 to 420 seconds are either due to fluid injection in the flow field or to problems related to digital conversion of the data. The increase in signal strength at about 420 seconds indicates the emergence of the RAM C-I payload from blackout. The signal-strength record between 420 and 435 seconds is subject to tracking errors as well as signal-strength variations from low-elevation-angle multipath effects.

Now carefully observe the region of interest between 385 and 394 seconds in figures 9 and 10. In figure 9, for instance, the pattern ripple for the delayed-time antenna is about 30 dB prior to the critical electron density region indicated by the arrows. This ripple value agrees with the measured free-space patterns in the equatorial plane as predicted earlier. Notice that the ripple structure of the signal strength diminishes remarkedly in the region indicated by the arrow markers; the signal strength resumes a ripple structure as attenuation due to overdense plasma occurs. Notice also in figure 9 that the ripple structure agrees approximately with the free-space equatorial pattern for the real-time antenna and that a similar sequential change in the real-time antenna-pattern ripple structure also occurs in a similar time frame.

A related change in the pattern ripple structure was also observed for both antennas in the signal received at the USNS Twin Falls Victory, which was located directly down range of the payload nose (observer aspect angle of 0°). The region of interest is between 386 and 394 seconds in figure 10. Notice that at 394 seconds, where the plasma electron density over the antennas is very small,

the antenna-pattern ripple structure is about ±2 dB. This value of pattern ripple factor agrees quite well with the nose-on free-space pattern ripple structure predicted in figures 4(a) and 6(a). Also notice that the mean level of the signal received at 386 seconds at the two frequencies is different by about 16 to 20 dB in absolute level, which was predicted earlier from pattern levels and absolute gain values.

Now closely observe the received signal in the time period from 390 to 392 seconds in figure 10. Notice that there is a temporary 20-dB sharp dip in the received signal level which corresponds to the occurrence of critical electron density over the delayed-time antenna aperture. A similar but smaller signal-level dip also occurs for the real-time antenna, but is time shifted to correspond to the occurrence of critical electron density over the antenna aperture. The time of occurrence of these amplitude dips in the received nose-on signal closely corresponds to the time period in figure 9 where a significant decrease in pattern ripple observed from the broadside direction is noted.

Forward-Power and Reflected-Power Records

The records of measured forward and reflected power for both the real-time and delayed-time antennas are given in figure 11. Noted in these records by arrows are those altitudes where critical electron density was observed on probe number 8 and probe number 1, in that order, for the descending trajectory. Notice that a sharp rise in the reflected power occurs in the region between the arrows for both antennas. The changes in the forward power and ultimately a limitation on the accuracy of this measurement were the result of a measured low directivity for this miniaturized flight directional coupler. In any event, however, the sharp rise or increase in reflected power with the simultaneous occurrence of critical electron density over the antenna aperture corresponds to that altitude range where the ripple changes were noted in figures 9 and 10.

CONCLUDING REMARKS

The perturbations in the signals received at the two strategically placed prime receiving stations clearly indicate that very large changes occurred in the shape of the VHF antenna patterns when the electron density surrounding the RAM C-I vehicle passed through the critical electron density region. Such changes are quite remarkable indeed since the maximum dimension of the vehicle at the highest VHF frequency is only about 1 wavelength. The nature of this pattern change is to diminish the nose-on level of received signal strength and to cause the equatorial pattern of both the circumferential and axial slot arrays to smooth out considerably. The pattern change (and therefore the subsequent nose-on decrease in signal) is probably due to diffraction rather than absorption since the collision frequency at this altitude is quite low.

The patterns of both antennas tend to return to the general form of the free-space pattern at altitudes after the initial occurrence of critical

electron density. The change in the ripple structure may be due to field changes in the slot antennas caused by the high impedance mismatch.

REFERENCES

1. Akey, Norman D.; and Cross, Aubrey E. (With appendix A by Thomas G. Campbell; appendix B by Fred B. Beck; and appendix C by W. Linwood Jones, Jr.): Radio Blackout Alleviation and Plasma Diagnostic Results From a 25 000 Foot Per Second Blunt-Body Reentry. NASA TN D-5615, 1970.

2. Jones, W. Linwood, Jr.; and Cross, Aubrey E.: Electrostatic Probe Measurements of Plasma Surrounding Three 25 000 Foot Per Second Reentry Flight Experiments. The Entry Plasma Sheath and Its Effects on Space Vehicle Electromagnetic Systems – Vol. I, NASA SP-252, 1971, pp. 109-136.

3. Schexnayder, Charles J., Jr.; Evans, John S.; Huber, Paul W.: Comparison of Theoretical and Experimental Electron Density for RAM C Flights. The Entry Plasma Sheath and Its Effects on Space Vehicle Electromagnetic Systems – Vol. I, NASA SP-252, 1971, pp. 277-303.

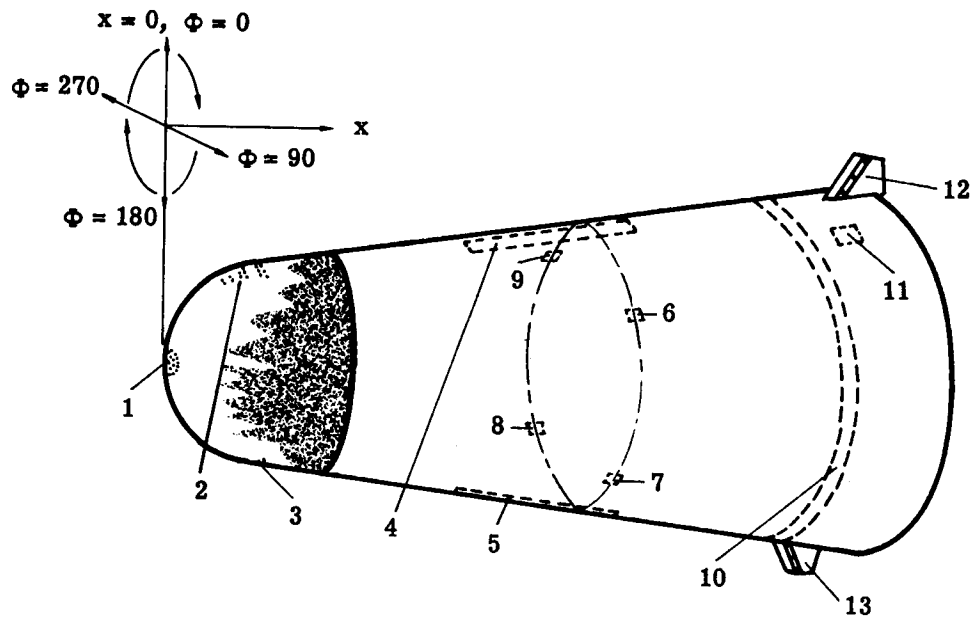

Part		x,		Φ,	x/D
Number	Function	in.	(cm)	deg (a)	(b)
	Water injection nozzle:				
1	Stagnation	0	(0)	---	0
2	Lateral	6.0	(15.2)	0	.48
3	Lateral	6.0	(15.2)	180	.48
	Antenna:				
4	VHF slot (259.7 MHz)	29.6	(75.2)	0	2.36
5	VHF slot (259.7 MHz)	29.6	(75.2)	180	2.36
6	X-band horn (9210 MHz)	32.6	(82.8)	60	2.60
7	X-band horn (9210 MHz)	32.6	(82.8)	150	2.60
8	X-band horn (9210 MHz)	32.6	(82.8)	240	2.60
9	X-band horn (9210 MHz)	32.6	(82.8)	330	2.60
10	VHF ring (225.7 MHz)	43.0	(109.2)	---	3.42
11	C-band horn (5700 MHz)	46.6	(118.4)	30	3.71
	Probe:				
12	Electrostatic	48.6	(123.4)	0	3.87
13	Thermocouple	48.6	(123.4)	180	3.87

[a]Center-line location of parts.

[b]Nose diameter D is 12.56 in. (31.90 cm).

Figure 1.- Diagram showing location of the pertinent parts of the RAM C-I configuration.

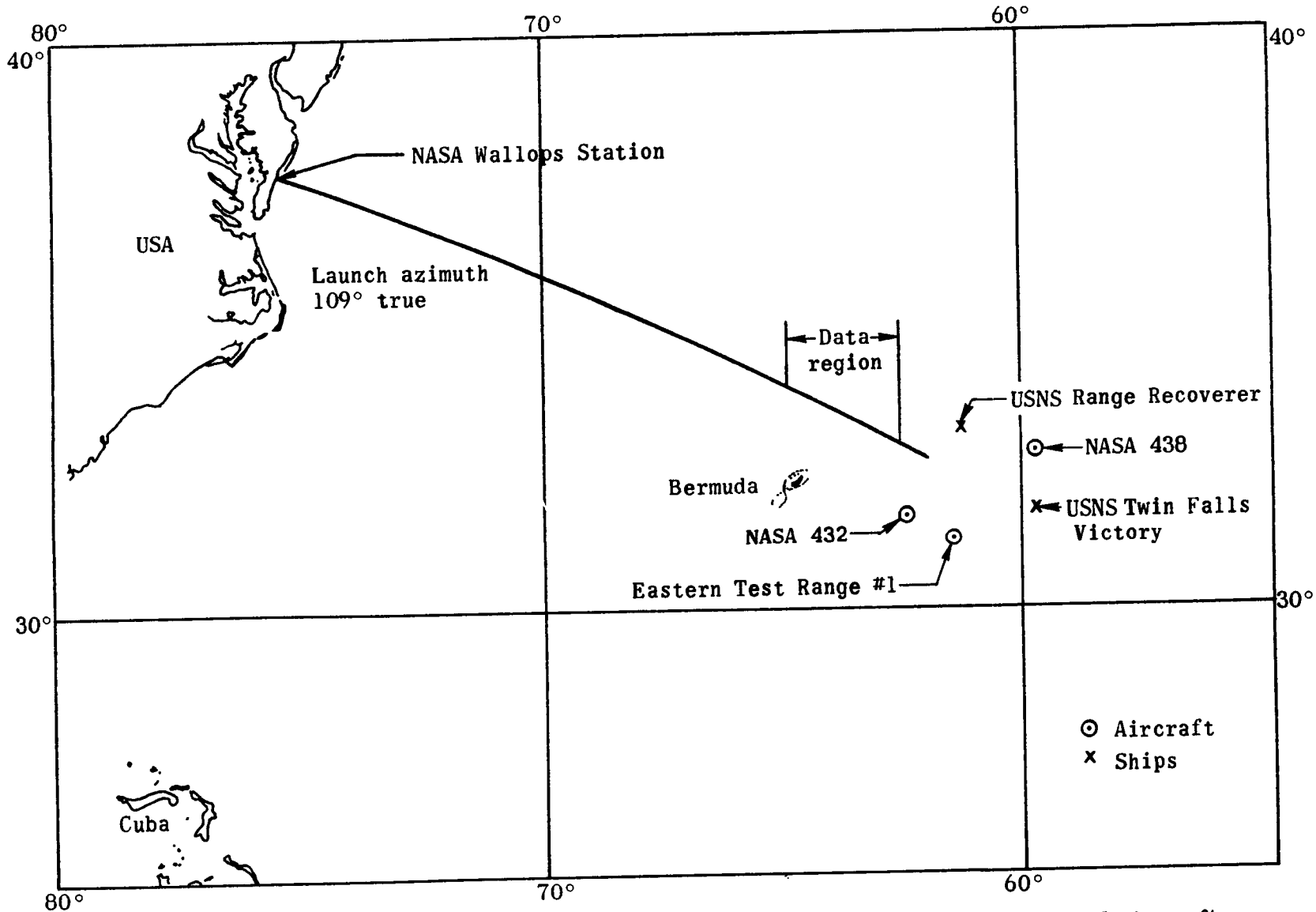

Figure 2.- RAM C-I ground track with relative locations of tracking ships and aircraft.

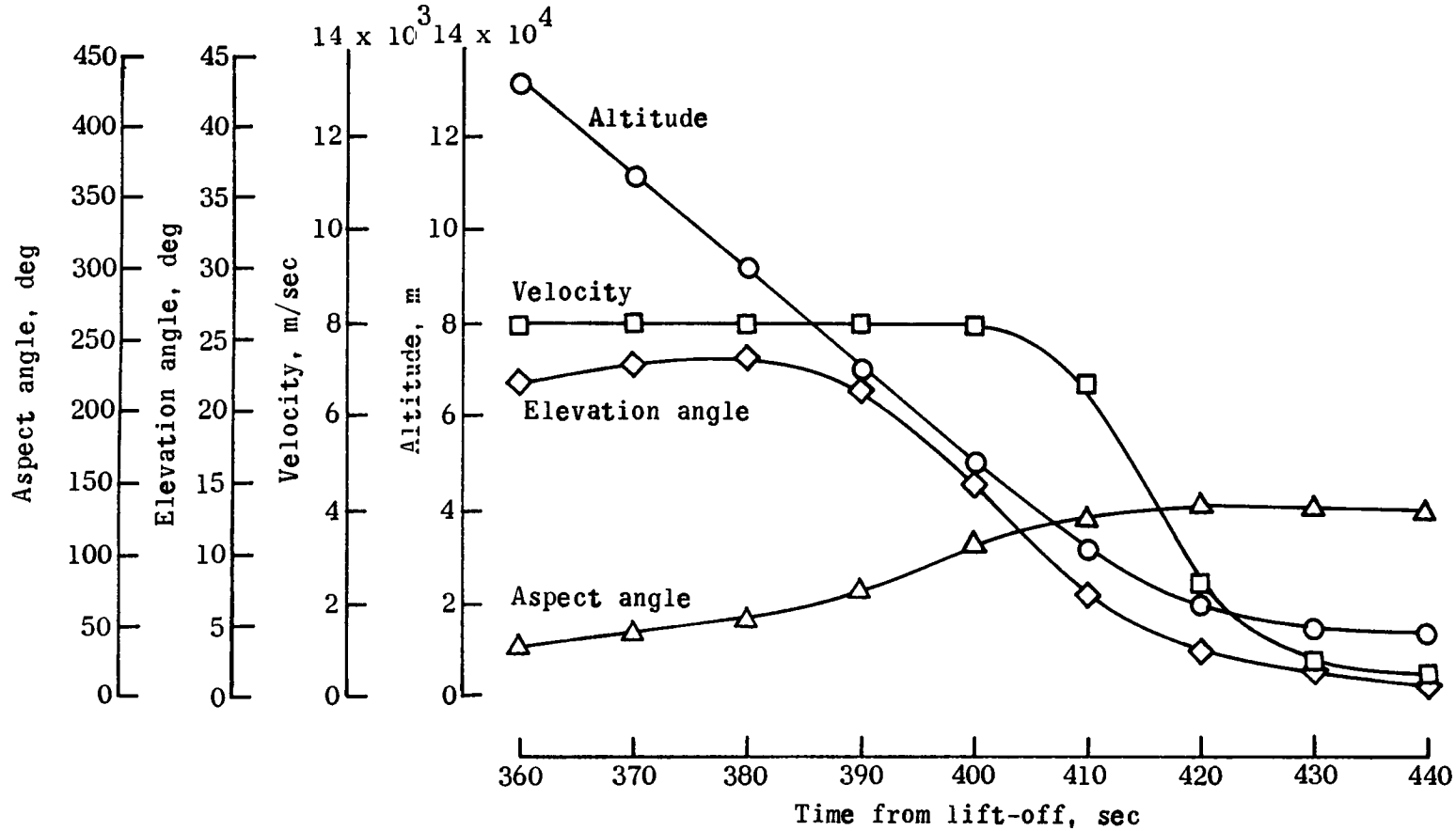

Figure 3.- Variation of RAM C-I altitude, velocity, elevation angle, and aspect angle with time from lift-off (as observed from the Bermuda receiving station).

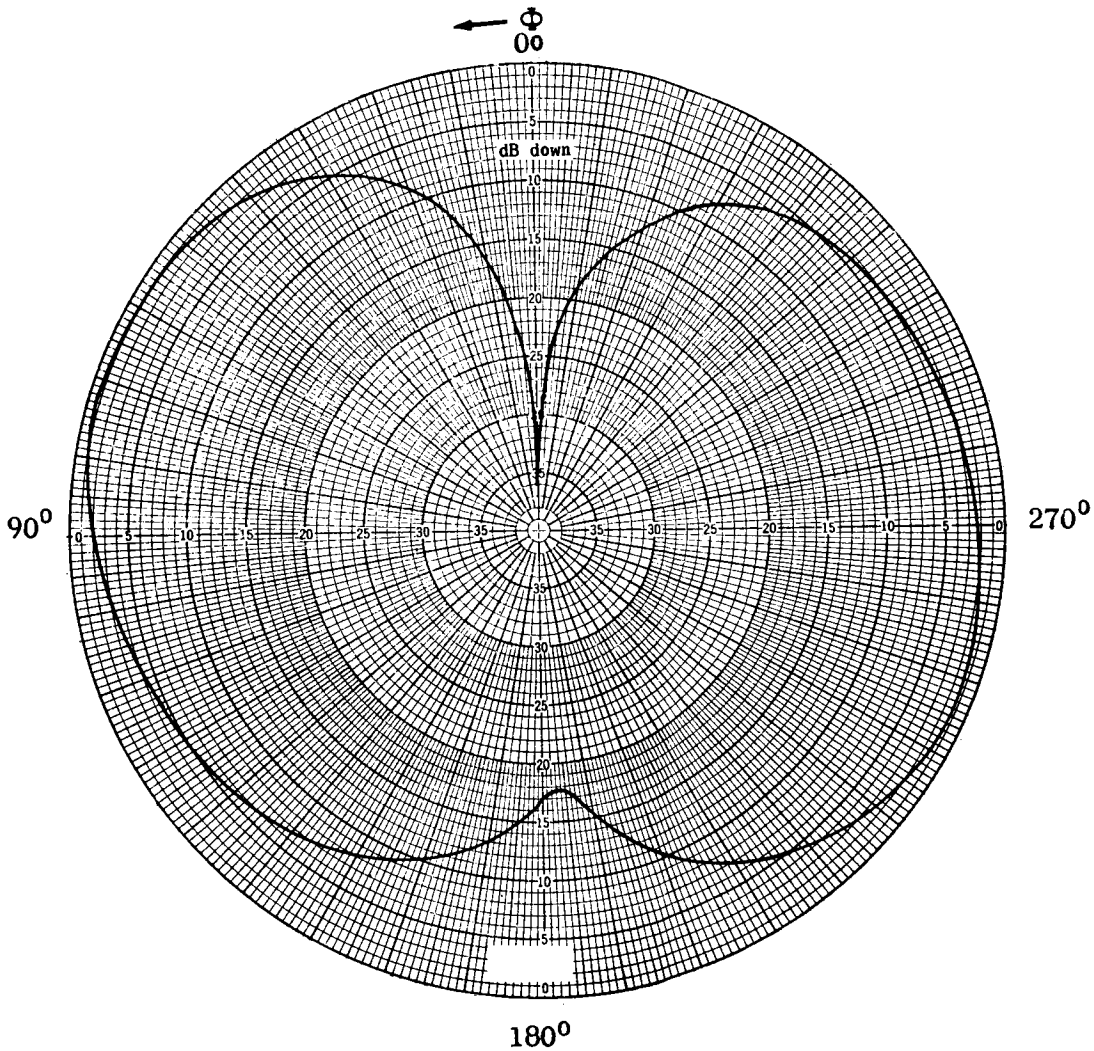

(a) Equatorial plane.

Figure 4.- Orthogonal plane patterns of the direct telemetry antenna (free space).

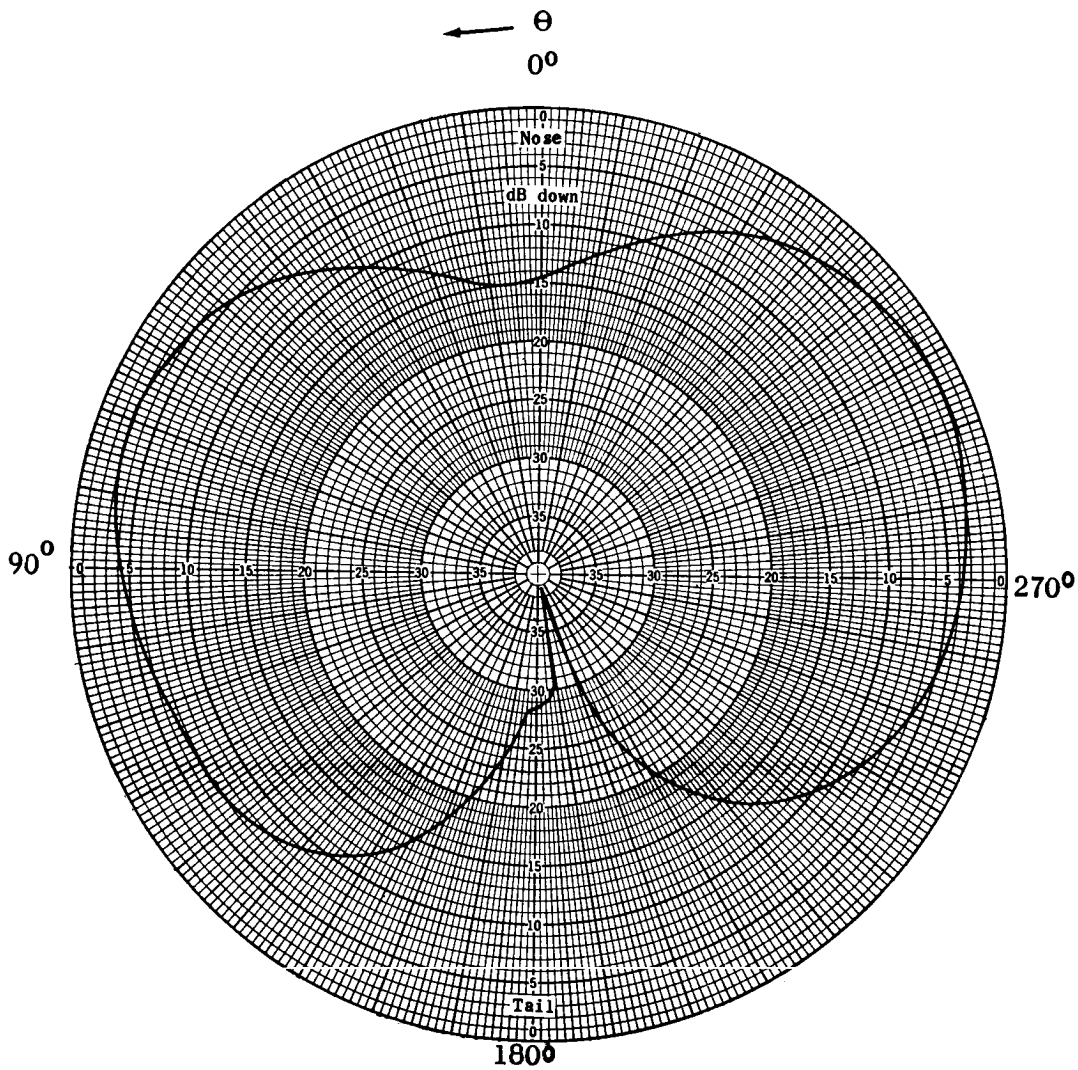

(b) Polar plane.

Figure 4.- Concluded.

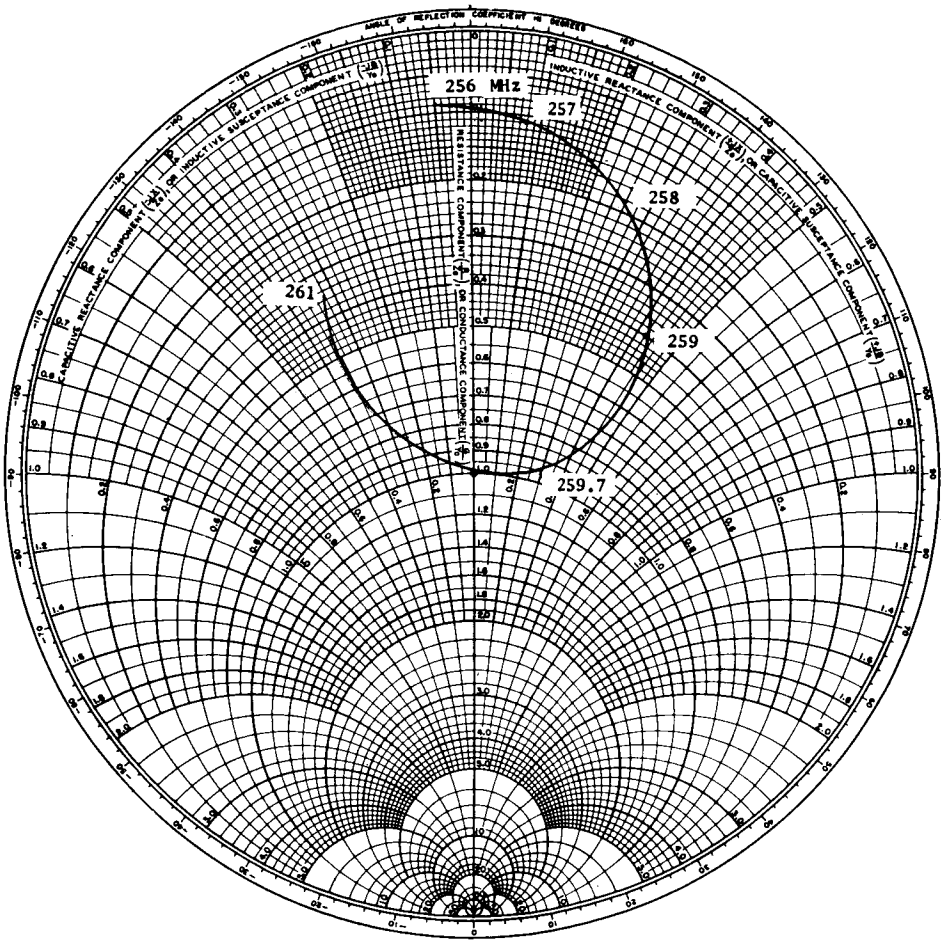

Figure 5.- Final impedance characteristics of direct telemetry antenna (free space).

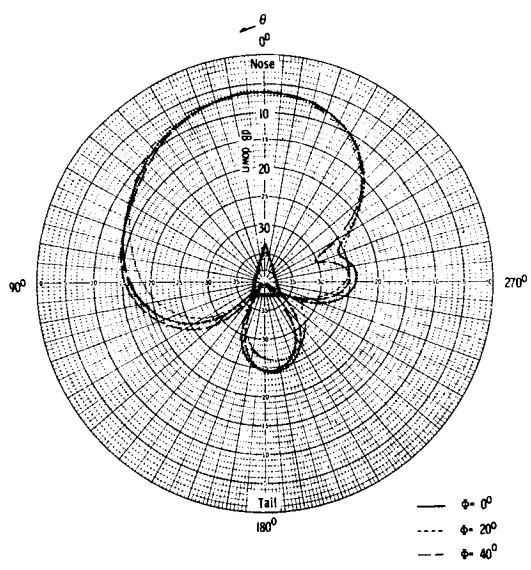

(a) Left-hand circular. $\phi = 0^{o}$.

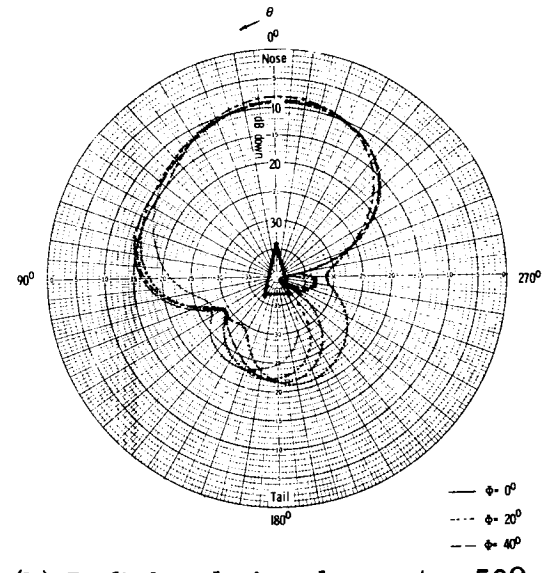

(b) Left-hand circular. $\phi = 50^{o}$.

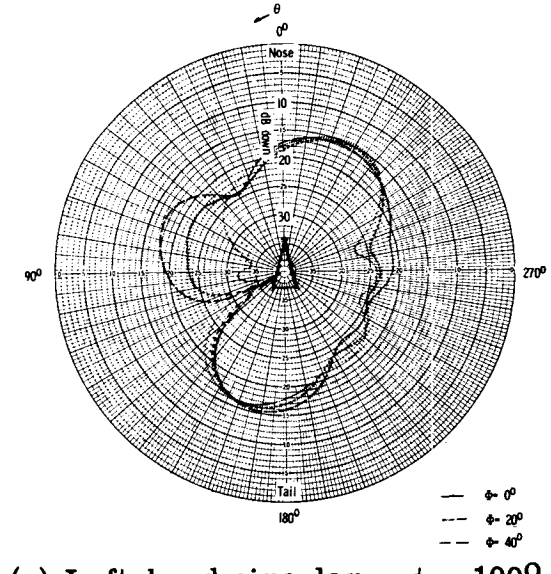

(c) Left-hand circular. $\phi = 100^{o}$.

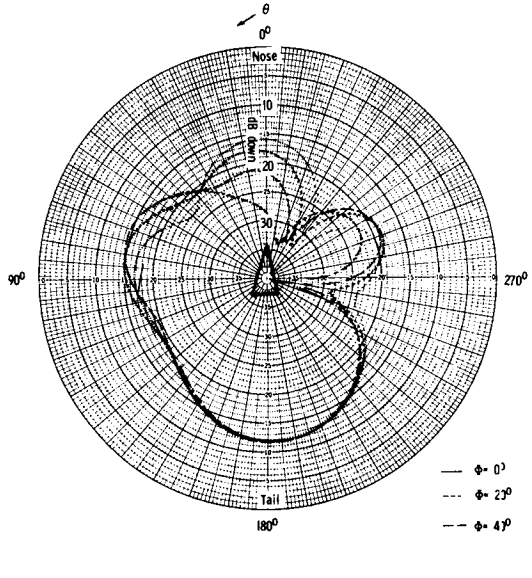

(d) Right-hand circular. $\phi = 0^{o}$.

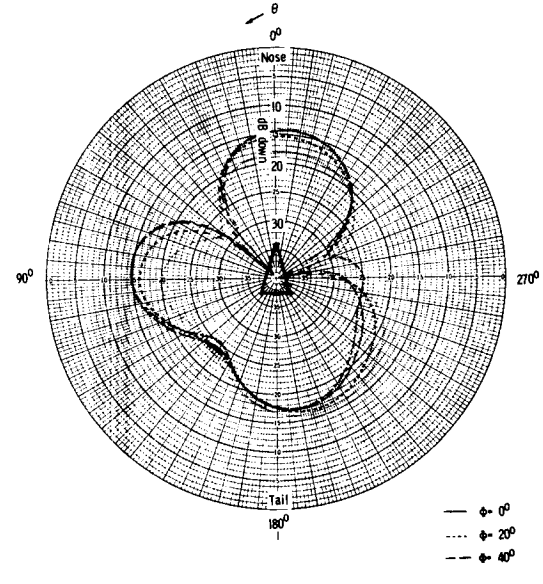

(e) Right-hand circular. $\phi = 50^{o}$.

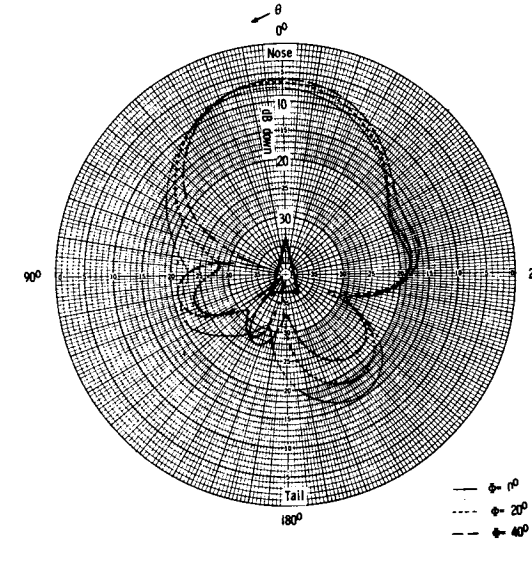

(f) Right-hand circular. $\phi = 100^{o}$.

Figure 6.- Patterns of the delayed-time telemetry antenna at various angles and polarizations.

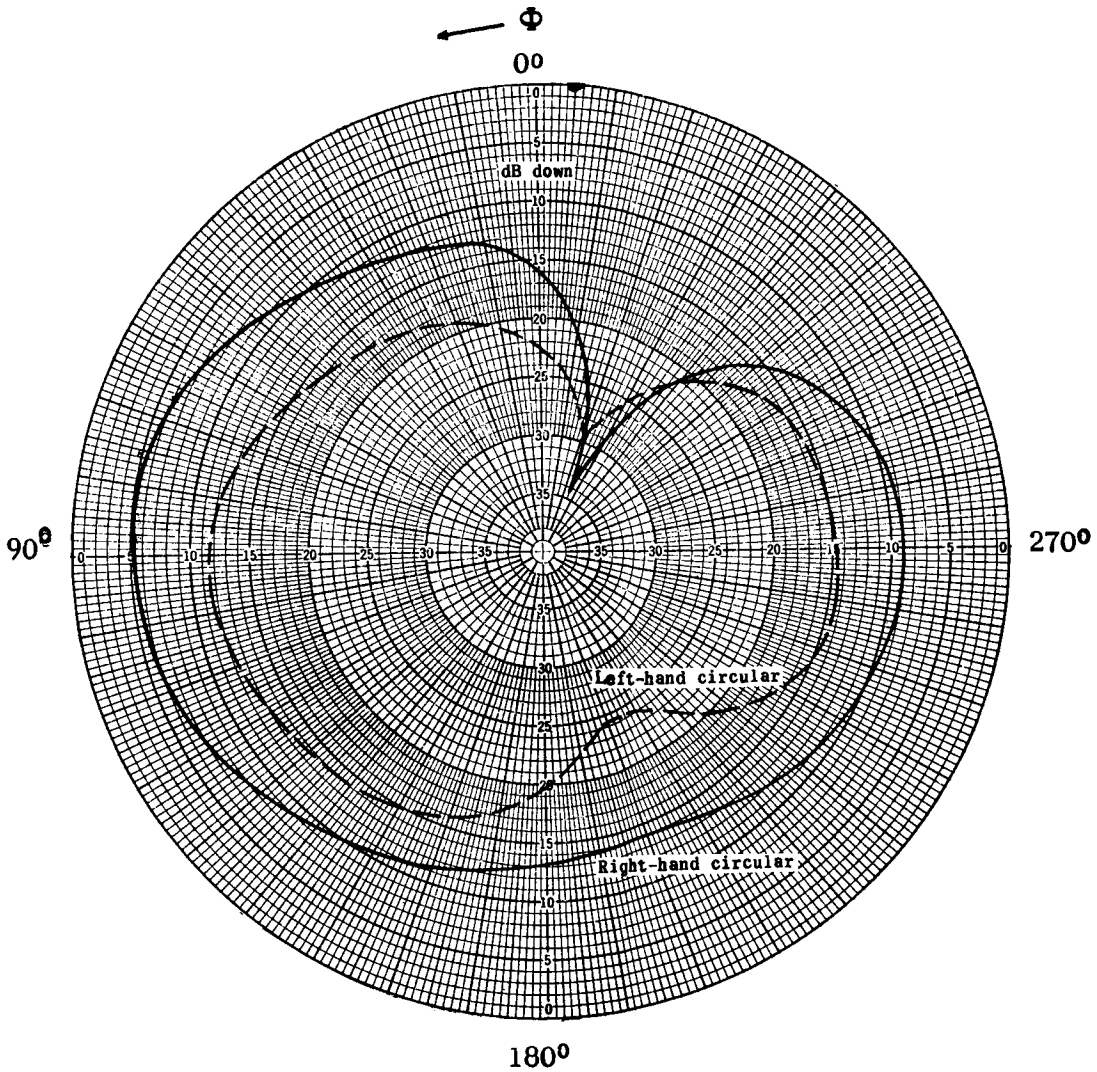

(g) Equatorial-plane patterns.

Figure 6.- Concluded.

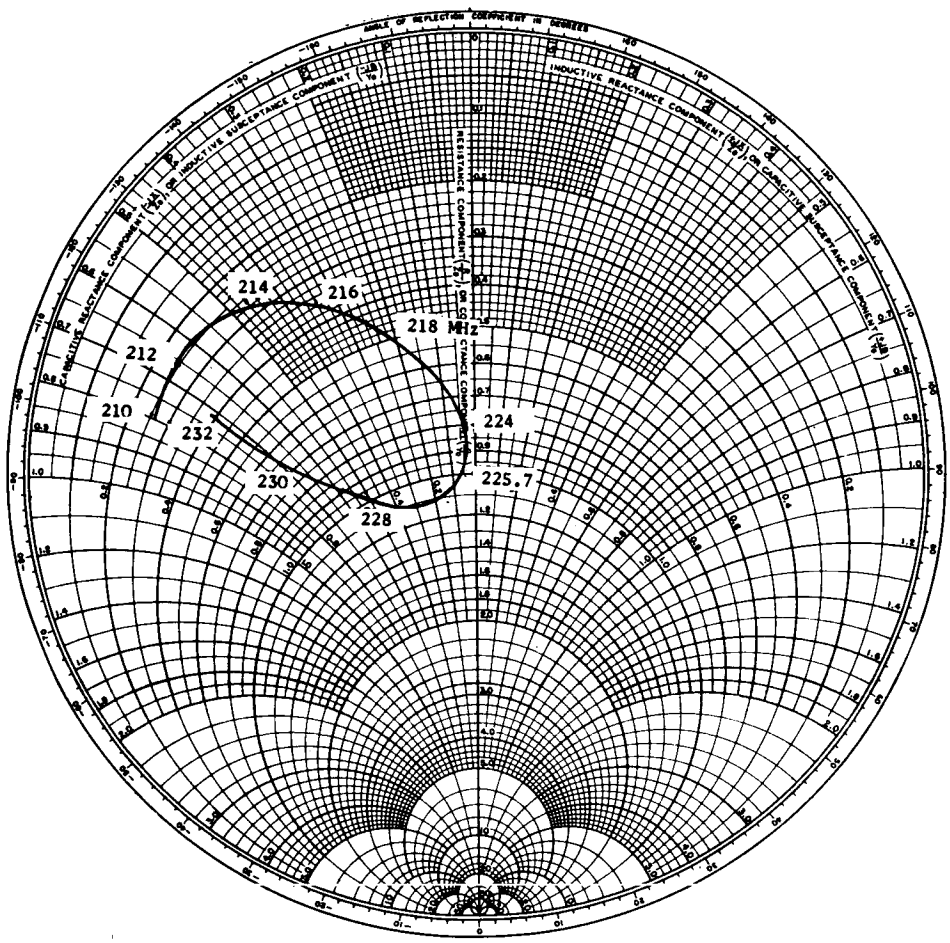

Figure 7.- Final impedance characteristics of delayed-time antenna (free space).

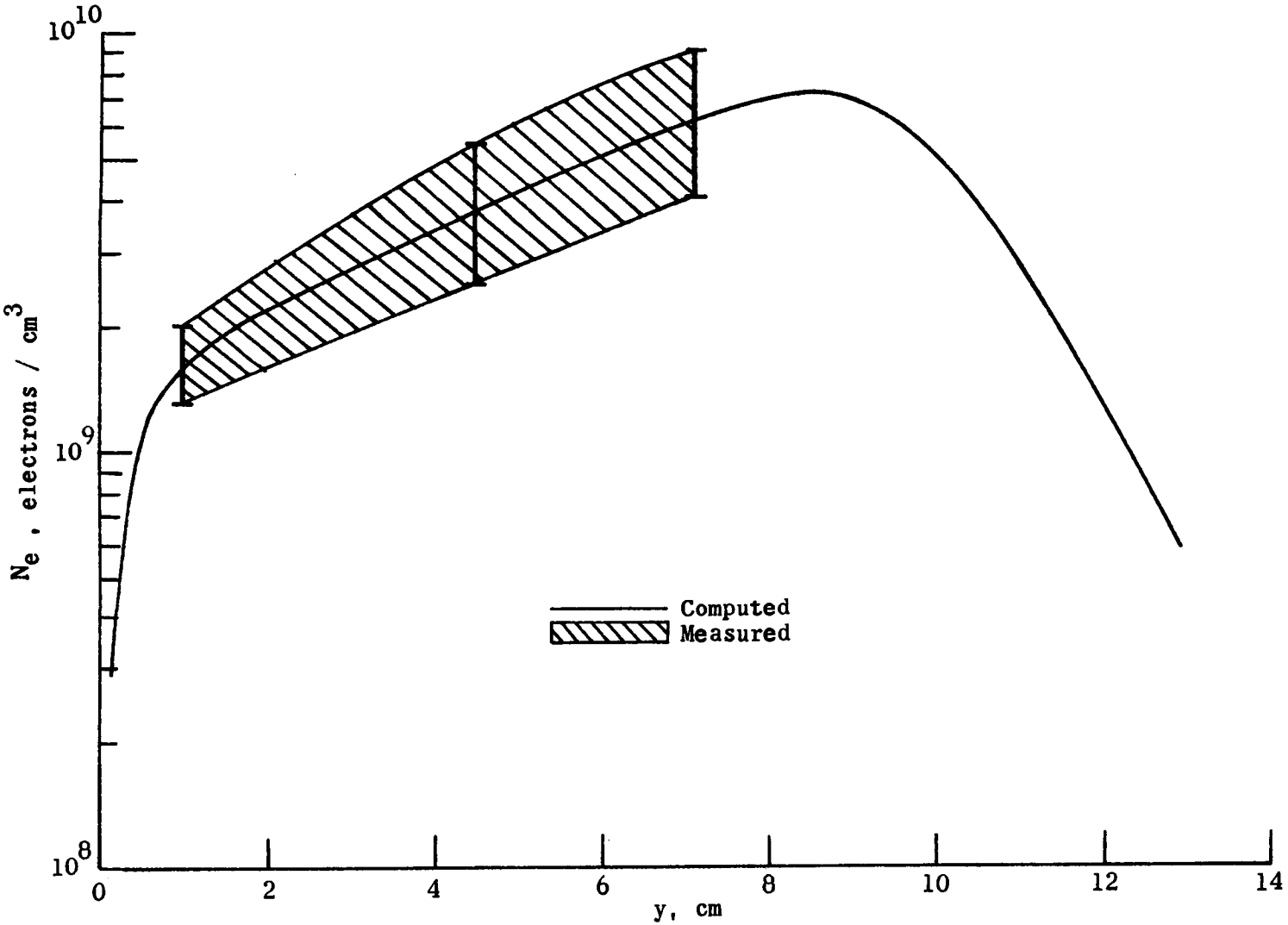

Figure 8.- Electron density N_e inferred from Langmuir probe ion density measurements compared with theoretical calculations (y is perpendicular distance from payload surface).

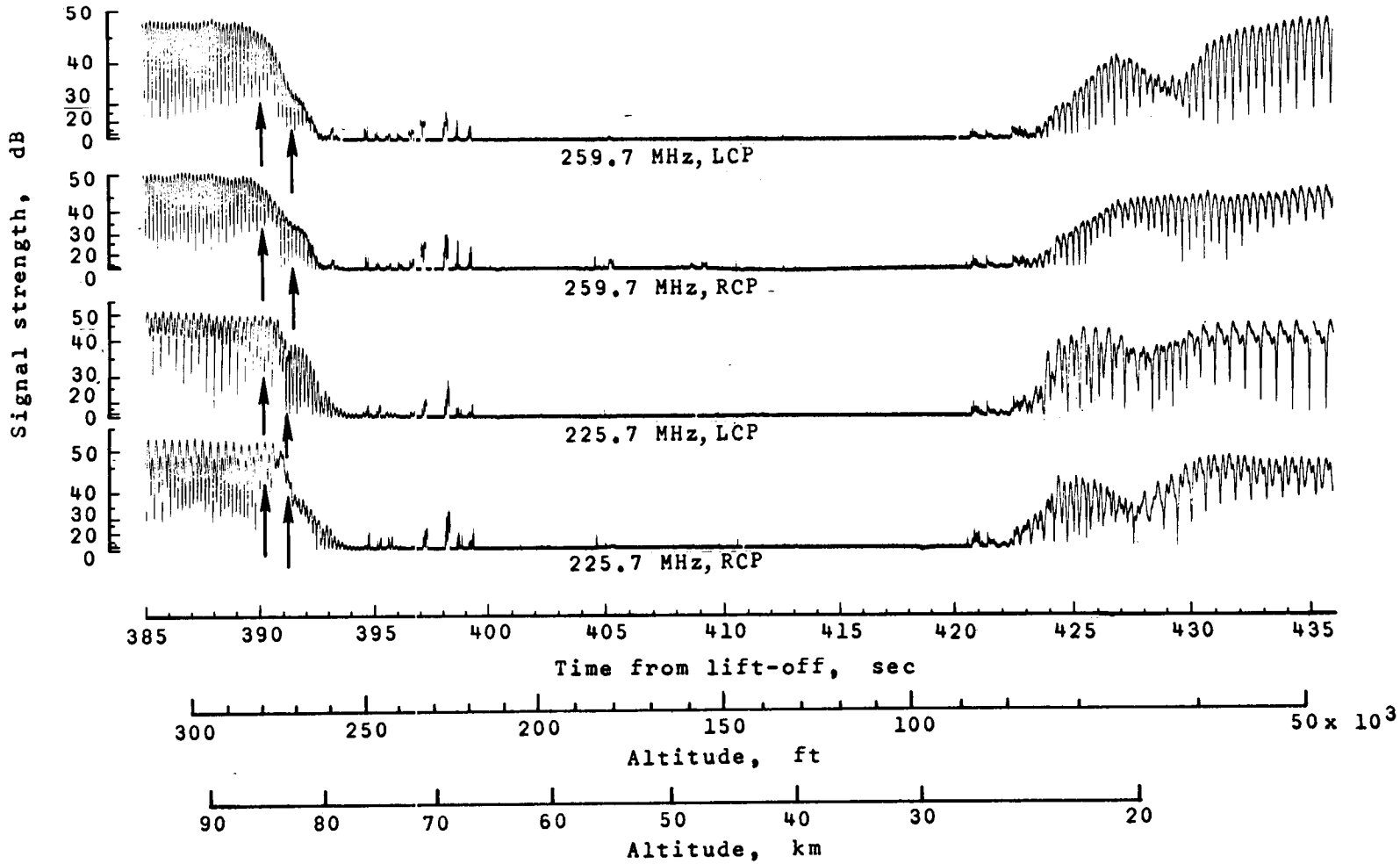

Figure 9.- Received signal at the Bermuda station. (LCP, left circular polarization; RCP, right circular polarization.)

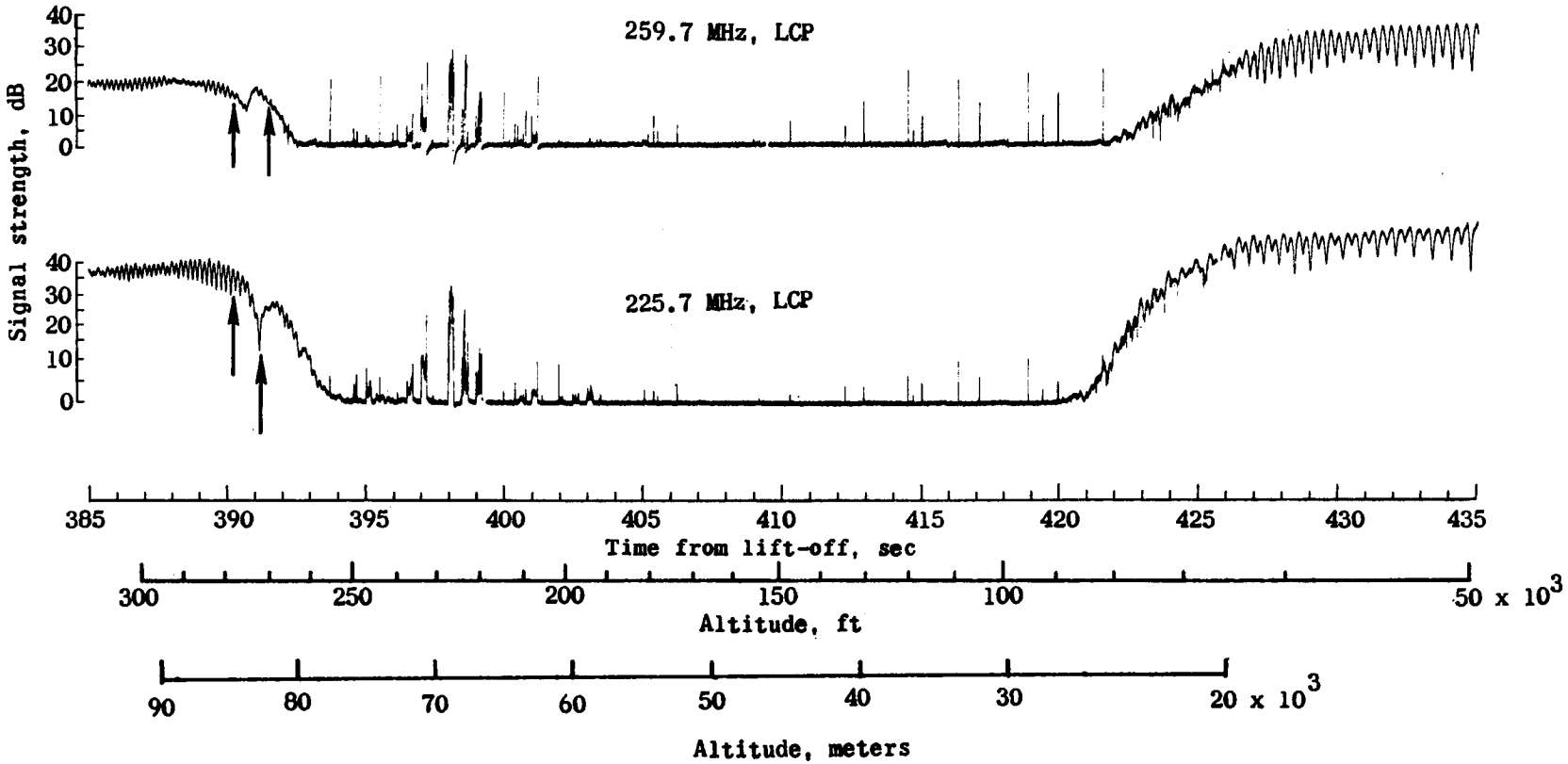

Figure 10.- Received signal at the USNS Twin Falls Victory station.

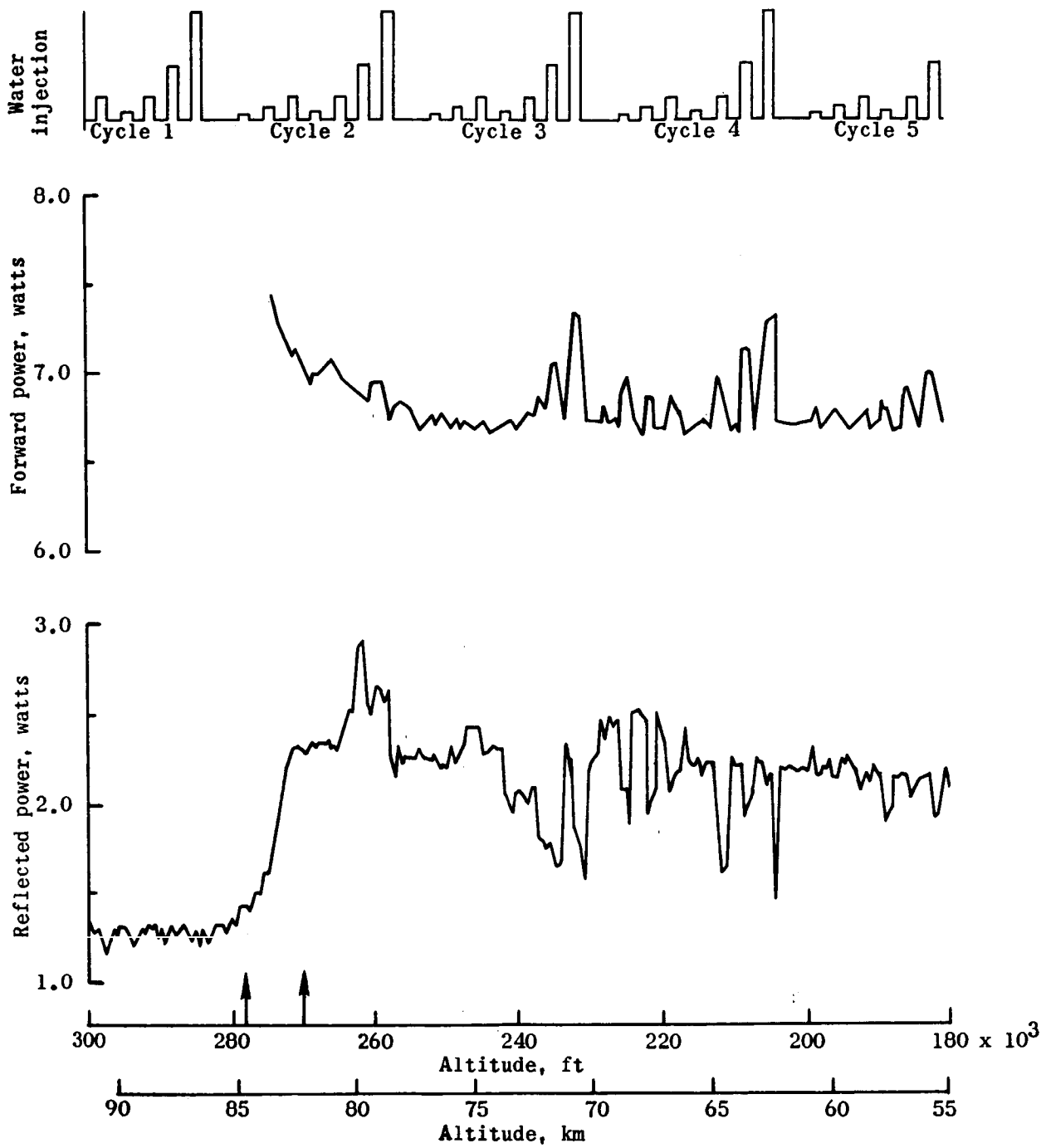

(a) 259.7-MHz system.

Figure 11.- Measured forward and reflected power of VHF telemetry systems as a function altitude.

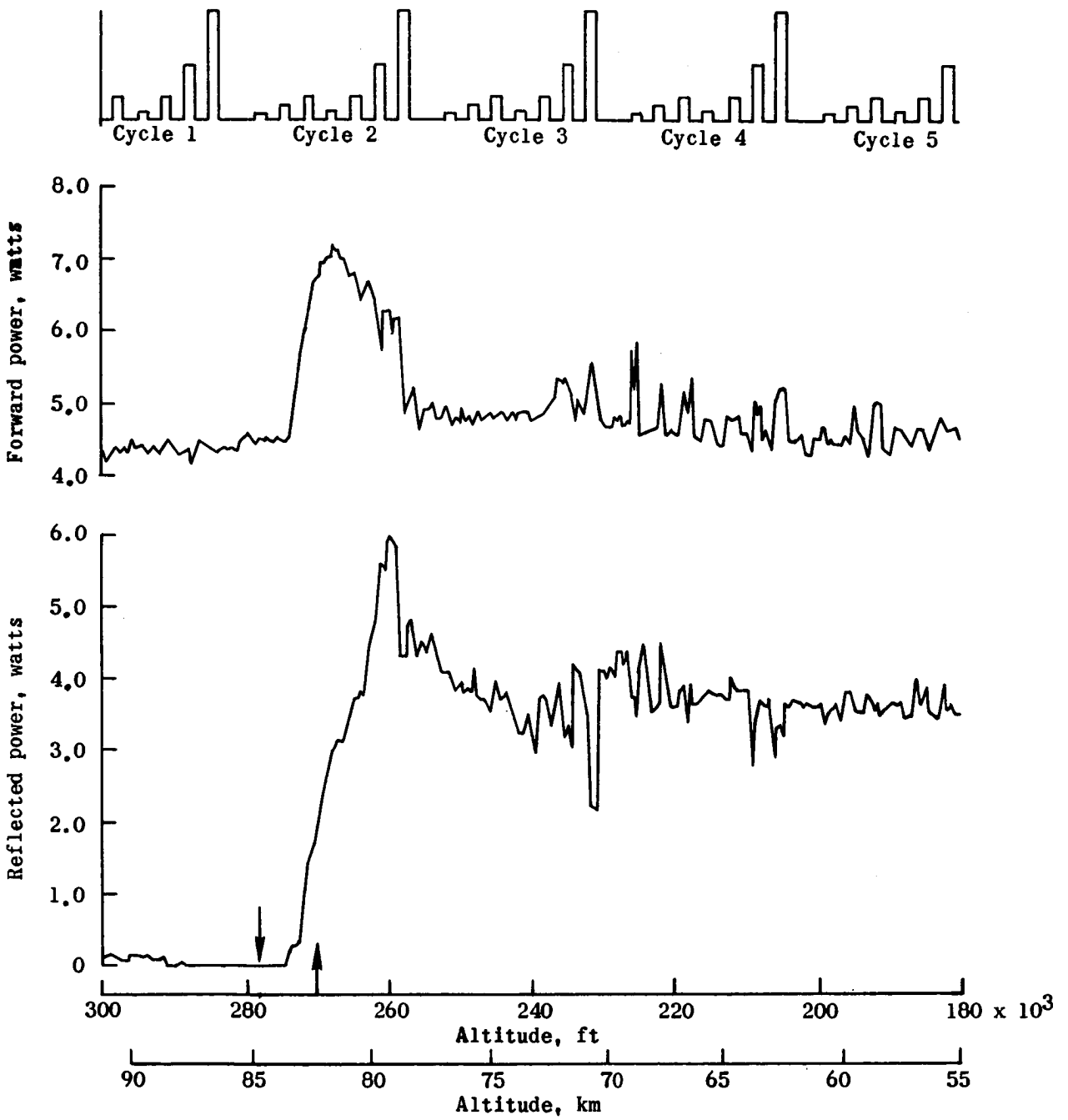

(b) 225.7-MHz system.

Figure 11.- Concluded.

A NON-PROTRUDING CONDUCTIVITY PROBE SYSTEM FOR RE-ENTRY PLASMA DIAGNOSTICS

By Sol Aisenberg and Kuo Wei Chang

Space Sciences Incorporated

SUMMARY

A rugged RF conductivity coil system has been constructed which utilizes a sensitive marginal oscillator to measure the changes of coil Q and inductance, which are closely related to the plasma conductivity. Since the marginal oscillator is constantly on resonance and is sensitive to slight changes in coil Q, this approach is superior to the impedance bridge method. The system has been calibrated over a wide dynamic range of conductivity and was tested in a simulated re-entry plasma. A coaxial multi-coil system capable of measuring the spatial variation of plasma conductivity is also described.

INTRODUCTION

A number of techniques have been used to obtain electrodeless measurements of electrical conductivity of plasmas. One method uses a search coil to measure the distortion of a bias magnetic field by a moving plasma[1-4]. The disadvantage is, of course, due to the need for a moving plasma and for an additional measurement of its velocity. An alternative method measures the change in the oscillator current which represents the energy dissipated in the nearby plasma as a result of an oscillating field[5-9]. The basic difficulty lies in aging, change of temperature and other effects that would result in a change of oscillator current which cannot be differentiated from an apparent conductivity change. Another way of measuring the plasma conductivity has been proposed and used by a number of people[10-12]. This method consists of measuring the change in resistance or reactance of a sensing coil by means of a balanced bridge technique. The main disadvantage of this impedance bridge technique is the strong interaction between resistive and reactive changes in the output, which are difficult to separate. Furthermore, it is necessary to balance the bridge carefully and then measure the resulting slight inbalances within the bridge. Another disadvantage is the extreme sensitivity to drift of the driving oscillator frequency, or of the balancing components of the bridge circuit. For these reasons, the construction of such an impedance bridge for use in the laboratory is already a difficult problem in general, and the construction of a flyable version is considered to be prohibitively difficult. This paper describes a novel RF coil

conductivity probe system which is rugged, reliable, and able to survive the hostile environment of re-entry flight.

SYMBOLS

D	Diameter
$\vec{E}$	Induced electric field
f	Frequency
K, K', K''	Proportionality constant
K_{eff}	Effective surface current
P_{loss}	Total eddy current loss
V	Amplitude of oscillation or DC voltage output
$W(D,z)$	Influence function
$\vec{x}(r,\theta,z)$	Coordinate vector
Γ	Volume of conducting medium
δ	Skin depth
ϵ	Dielectric constant
μ	Permeability
σ	Electrical conductivity

SINGLE-COIL SYSTEM

Marginal Oscillator

A non-immersive RF coil system has been constructed for the measurement of the electrical conductivity of a moving or a stationary plasma in the laboratory or under re-entry flight conditions. The system involves the use of a sensitive radio frequency marginal oscillator to measure the slight changes of circuit Q and coil inductance. A representative circuit of the basic system is shown in Figure 1. The coil of a resonant circuit is placed adjacent to the plasm

being measured and as a result, eddy currents, which are closely related to the plasma conductivity, are induced in the nearby plasma. The resulting energy dissipation, in turn, introduces RF losses into the tank circuit, causing a consequent reduction of system Q, a shift in the resonant frequency and a reduction of the amplitude of oscillation from which information about the plasma electrical conductivity can be extracted. Since the marginal oscillator is constantly on resonance even when its frequency has been shifted by the presence of the conducting plasma, and since it is very responsive to slight changes in the coil Q, this approach is far superior to the impedance bridge method [10,11,12] sometimes used which requires very complex automatic circuitry to balance the bridge, to guard against drifts as well as to maintain frequency and amplitude stability under flight conditions.

Basically, the marginal oscillator system consists of a resonant tank circuit connected to a transistor amplifier with very high feedback. The frequency of oscillation of the entire system is identical to the resonant frequency of the tank circuit. In this way, the system automatically compensates itself for reactive changes in the sensing coil. The tank circuit is operated with a center tapped capacitor divider which is a direct analog of the center tapped coil in a Hartley oscillator. A voltage gain of approximately unity is obtained from the emitter-follower connection of the transistor. In this way the transistor amplifier acts as a current amplifier with a very great amount of feedback so that its voltage gain is relatively immune to changes in the transistor characteristics. The input impedance of the emitter-follower is high, so that it does not load the tank circuit appreciably, while the output impedance is low so that it can drive the relatively low load impedance of the capacitor tap on the tank circuit. The overall stability of the system is high because the voltage gain of the tank circuit is determined essentially by passive elements such as the coil and capacitors, while the voltage gain of the impedance transforming amplifier is stable because of the large amount of negative feedback.

When placed in proximity to a plasma, the tank circuit interacts with the conducting gas and changes its characteristics of oscillation. Two different methods can be used to obtain the plasma electrical conductivity and they are described in the following sections.

Conductivity Deduced from the Amplitude of Oscillation

The feedback voltage drawn from the emitter-resistor is adjusted in such a way that the circuit is essentially oscillating in a marginal mode. In this way a very slight change in the Q of the tank circuit will result in a relatively large change in the amplitude of oscillation. The coil of the tank circuit when placed adjacent to the plasma will induce circulating eddy currents, which are directly related to the plasma's electrical conductivity. The associated ohmic losses within the plasma will cause an increased loss in the tank circuit which results

in a reduction of the circuit Q. This reduction of Q, in turn, causes a decrease in the level of oscillation in the marginal oscillator. Thus, a measurement of the amplitude of oscillation can be used to obtain the electrical conductivity of the adjacent plasma.

The conductivity coil system has been calibrated over a wide dynamic range of about 8 orders of magnitude by using materials of known electrical conductivity. Typical results are shown in Figure 2 for the case of a coil diameter of about 0.635 cm and for a basic oscillator frequency (in the absence of plasmas) of 2 MHz. In the high and low conductivity range, various metals and salt solutions were used respectively, while over the intermediate range, silicon slices doped to various known conductivities were used. Since in practice it will be necessary to provide a protective insulating spacer such as quartz or boron nitride between the plasma and the coil, one of the calibration curves shown was taken with a 0.08 cm spacer to illustrate the effect of coil-plasma separation.

It can be seen from Figure 2 that the output voltage (which is related to the change in the amplitude of oscillation in the presence of a conducting material) is not a single valued function of electrical conductivity, and that in the high conductivity range, the output signal begins to decrease. This can be explained readily in terms of the skin depth factor for the penetration of the RF field into the plasma. At high electrical conductivities the skin depth becomes smaller than the coil diameter, and the RF field is unable to penetrate very far into the conducting material. As a result, the energy coupled from the coil to the conducting medium is reduced as the conductivity gets larger. The conductivity at which the skin depth effect becomes appreciable is expected to correspond to the situation where the skin depth is comparable to the coil diameter.

The above physical observation in the low and the high conductivity limits can also be confirmed analytically. Although in principle the relationship between the plasma conductivity and the amplitude of oscillation can be derived theoretically, this approach is generally not followed on account of the complexity of geometry and circuitry involved. Instead, this relationship will be determined experimentally, with minor analytical manipulations. For an isotropic medium of conductivity σ, the wave equation for the induced electric field $\vec{E}$ can easily be derived from the Maxwell equations:

$$\nabla^2 \vec{E} = i\mu(2\pi f)\sigma\vec{E} - (2\pi f)^2 \epsilon\ \mu\vec{E} \qquad (1)$$

where ϵ is the dielectric constant, μ, the permeability, and f, the frequency. In the low conductivity limit the dominant characteristic length of the problem is the coil diameter D, which is a measure of the extent of the region of significant field strength. With spatial variables normalized by D the wave equation becomes

$$\nabla^2 \vec{E} = 2i \left(\frac{D}{\delta}\right)^2 \vec{E} - \left(2\pi f \sqrt{\epsilon \mu}\, D\right)^2 \vec{E} \qquad (2)$$

where δ is the skin depth or penetration depth defined as follows:

$$\delta = \frac{1}{\sqrt{\pi f \mu \sigma}} \qquad (3)$$

In the low conductivity limit, which is defined by the condition $\frac{D}{\delta} << 1$, the first term on the right hand side of Eq. (2) can be neglected and the induced electric field $\vec{E}$ can be approximated by the induced $\vec{E}$ field in vacuum. That is, as long as $D << \delta$, $\vec{E}$ will be independent of the conductivity σ. Hence, the change of the reciprocal of coil Q (relative to the case in the absence of the plasma) or equivalently, the total eddy current loss within the conducting medium placed adjacent to the RF tank coil can be described as follows

$$\Delta\left(\frac{1}{Q}\right) = k \cdot \sigma \cdot \int\int\int_{\Gamma} \vec{E}(\vec{x}) \cdot \vec{E}(\vec{x})\, d^3 x \qquad (4)$$

or

$$\Delta\left(\frac{1}{Q}\right) \sim \sigma$$

where k is a proportionality constant, $\vec{x}$, the coordinate vector, and Γ, the range or volume of the conducting medium.

The DC voltage output V (V is zero in the absence of the conducting medium) of the marginal oscillator depicted in Figure 1 is a function of $\Delta(\frac{1}{Q})$

$$V = F\left[\Delta\left(\frac{1}{Q}\right)\right] \qquad (5)$$

and this function can be determined from the calibration curve given in Figure 2. Since $\vec{E}$ is independent of σ, V is found to be proportional to $\left[\Delta(\frac{1}{Q})\right]^{3/4}$ or $\sigma^{3/4}$ in the low conductivity limit.

In the opposite high conductivity limit, the RF field penetration is limited by the skin depth and δ becomes the dominant characteristic length. Since δ is now much smaller than D, the induced electric field $\vec{E}$ within the conducting medium becomes dependent on σ. An approximate solution of $\vec{E}$ has been obtained [13] and the total eddy current loss P_{loss} (note that $\Delta(\frac{1}{Q}) \sim P_{loss}$) is

$$P_{loss} = \frac{1}{2\sigma\delta} \int \left|K_{eff}\right|^2 da \qquad (6)$$

where K_{eff} is the effective surface current (which is a quantity independent of σ), da is the surface element normal to the boundary of the conducting medium, and the quantity $1/2\sigma\delta$ plays the role of a surface resistance of the conducting medium. It is therefore obvious that

$$\Delta\left(\frac{1}{Q}\right) \sim \sigma^{-\frac{1}{2}} \tag{7}$$

which is in accord with the observed decline of V in the high conductivity limit (fig. 2). Again, based on the experimental calibration curve, V is found to be proportional to $\left[\Delta\left(\frac{1}{Q}\right)\right]^{\frac{1}{2}}$ or to $\left[\sigma\right]^{-\frac{1}{4}}$, over the range measured.

Conductivity Deduced from Frequency Shift

Associated with the change of the effective resistance of the tank circuit is a change of the effective reactance. Since the induced eddy currents in the plasma always tend to inhibit the penetration of the RF field, a reduction of the coil inductance results, which will cause an increase in the resonant frequency of the marginal oscillator. It should be emphasized that this change in frequency will not affect the performance of the system, since it will adjust itself so that it is always operating at the resonant frequency of the tank circuit. This is an important feature of this system because it eliminates the need for automatic circuits to stabilize the oscillator frequency, as is sometimes required in systems involving impedance bridge circuits.

Thus, one convenient aspect of the marginal oscillator circuit is that the change in oscillator frequency can be used as a direct measure of the change of coil inductance, and therefore, a direct measure of the plasma conductivity. Since the change of coil inductance is also influenced by the change of plasma reactance, this is possible only if the reactive current is relatively small compared to the conductive current. (Obviously, the frequency shift can be used to measure the plasma reactance when it becomes important.) Because re-entry plasmas usually do not exhibit a significant reactive component, except at microwave frequencies, plasma conductivity can also be obtained from a measurement of the frequency shift. A simple integrated circuit has been added to the basic system described in Fig. 1 to convert the change of oscillator frequency into a DC output voltage.

A typical clibration curve of frequency shift versus electrical conductivity is presented in Figure 3. It can be seen that for the low conductivity range where the skin depth is large, there is a significant modification of the operating frequency, but that for higher conductivity the change of operating frequency with increased conductivity becomes very small. The measured frequency shift

can be used to deduce the conductivity, or as a confirmation for the conductivity deduced from the change of oscillation amplitude.

The behavior of frequency shift in both the low and the high conductivity limits can also be deduced analytically by constructing an equivalent circuit in which the conducting medium is represented by a resistor in series with a coil which is inductively coupled to the tank coil of the marginal oscillator. Following a detailed analysis one can show that the change in tank coil inductance is proportional to σ in the low conductivity limit and is independent of σ in the opposite high conductivity limit.

Preliminary Tests and Measurements

The conductivity coil system has been tested in a simulated re-entry argon plasma and preliminary results show that the system is indeed very sensitive to plasma conductivity. Because of its wide dynamic range, the system was further proven to be extremely useful in applications involving plasmas modified by electrophilic chemical additives where the free electron density and plasma conductivity may vary over many orders of magnitude. Results of an argon plasma quenched by gaseous SF_6 are given in Fig. 4 together with results of power transmission of K band (35 kMHz) microwave radiation through the plasma with respect to the value through vacuum. The experimental set-up and a detailed description of the argon plasma torch used can be found in Refs. 14 and 15.

Surface type airborne electrostatic probes are sometimes used for re-entry plasma diagnostics. Because their interaction with a flowing plasma is still not well understood, and because of their strong dependence on flow velocity, their results are somewhat unreliable, and as the vehicle traverses the atmosphere, the probe passes from the collisionless, transition, dense and eventually to the continuum regime so that interpretation of the probe response is very difficult. Furthermore, these electrode-type surface probes are subject to uncertainties due to thermionic and secondary emissions, surface ionization by quasi-steady state particles, contamination, and collection of attached negative molecules. In view of these difficulties and uncertainties, the present conductivity probe system is highly favored and it can conveniently be used to control the injection of electronegative chemical additives by monitoring the re-entry plasma conductivity for the purpose of alleviating the black-out problem.

The output of the present conductivity coil is independent of the flow velocity of the re-entry plasma. However, a modified system consisting of a balanced coil network and marginal oscillators can be constructed to measure both the plasma conductivity and the flow velocity. Such a system has been devised for the in vivo measurement of blood flow velocity.[16]

MULTI-COIL SYSTEM

Preliminary Remarks

The region of significant field strength of an RF coil in vacuum usually extends to a distance of approximately one coil diameter. For re-entry plasma of interest, the electrical conductivity is in general very small (less than 10 mho/m), and it falls within the range indicated in Figs. 2 and 3 where the skin depth for penetration of RF signal into the plasma is much larger than the coil diameter (the skin depth for an oscillator frequency of 1 MHz and for a plasma conductivity of 10 mho/m is about 16 cm). Thus, the effective interaction depth of the coil is not limited by the skin depth but rather by the signal-to-noise ratio of the system. In principle, the RF magnetic field generated by the coil can extend to infinity. The effective interaction or penetration depth of the coil is defined as the distance at which the signal produced by the portion of the plasma beyond that distance is equal to the noise level of the system. This effective penetration depth as determined from experiments is more or less equal to a few coil diameters.

Since coils of different sizes interact with the plasma at different depths, it is possible to devise a multi-coil marginal oscillator system which would provide a convenient measurement of the spatial variation of the plasma conductivity up to a distance equal to the effective penetration depth, when placed in proximity to the plasma whose conductivity profile is to be measured. For definiteness, a coaxially mounted four-coil system with different coil diameters and RF frequencies will be considered. The system to be described will have a lateral resolution approximately equal to the diameter of the largest coil. In situations where the requirement on lateral resolution is critical, the multi-coil system can be adapted easily by utilizing small coils with the same diameter but mounted differentially in axial position relative to each other and to the plasma surface.

Influence Function

While no formal experimental or analytical difficulty is expected in the frequency mode operation, only outputs involving oscillation amplitude will be considered. For simplicity, it is assumed that the conductivity of the plasma has sufficient symmetry so that it is only a function of the distance away from the vehicle or coil surface (i.e., $\sigma = \sigma(z)$, where z is the perpendicular distance out from the coil surface). The coordinate system and the coaxial or concentric multi-coil system used in the analysis are illustrated in Figure 5.

For plasmas with a low and nonuniform conductivity, Eq. (4) becomes

$$\Delta\left(\frac{1}{Q}\right) = K \int_0^{\infty}\int_0^{\infty}\int_0^{2\pi} \sigma(z)\, \vec{E}(r,\theta,z) \cdot \vec{E}(r,\theta,z) r\,dz\,dr\,d\theta \qquad (8)$$

In terms of an influence function W, the change of 1/Q of coil i due to the presence of the plasma can be expressed as follows:

$$\Delta\left(\frac{1}{Q}\right)_i = K \int_0^\infty \sigma(z)\, W_i(D_i, z)\, dz \tag{9}$$

where D_i is the diameter of coil i and W_i is the influence function defined by

$$W_i(D_i, z) = \int_0^\infty \int_0^{2\pi} E^2(D_i, r, \theta, z)\, r dr d\theta \tag{10}$$

The influence function of each coil can be determined either analytically or experimentally. It is independent of the plasma conductivity to a high degree of accuracy as long as the condition $\frac{D_i}{\delta} << 1$ is satisfied. It will be shown here how the influence function can be obtained experimentally.

Although the multi-coil system has only been devised but not built, efforts were made to obtain preliminary results of the influence function of coils of different sizes to demonstrate the feasibility of the approach. The experimental calibration of the influence function is performed using a large slab composed of a uniform material of known conductivity σ_0 in the range where the skin depth is large compared to the coil diameters. By moving this slab vertically in the z direction, the coil response $V_i(z_c)$ can be registered as a function of z_c, the separation between coil center and the lower surface of the conducting slab. After incorporating the known functional relationship between V and $\Delta(\frac{1}{Q})$ obtained earlier, Eq. (9) takes the following form (based in part on data in Fig. 2):

$$\left[V_i(z_c)\right]^{4/3} = K'\Delta\left(\frac{1}{Q}\right)_i = K''\sigma_0 \int_{z_c}^\infty W_i(D_i, z) dz \tag{11}$$

where K' and K" (K" = K'K) are constants which can be obtained from the calibration curve presented in Figure 2. Hence, the influence function can now be determined by simple differentiation

$$W_i(D_i, z) = \frac{1}{K''\sigma_0} \left\{ \frac{\partial}{\partial z_c} \left[V_i(z_c)\right]^{4/3} \right\}_{z = z_c} \tag{12}$$

The measured coil response $V_i(z_c)$ can be represented analytically by a polynomial and a closed form influence function can easily be obtained by differentiation. Preliminary experimental results of $V(z_c)$ obtained for four conductivity coils are given in Figure 6 using a slab of conductivity 17 mho/m. The scatter of experimental points (especially for larger coils) is attributed to the finite, small size slab used.

Determination of Conductivity Profile

After the influence functions have been determined by calibration, Eq. (9) can readily be used to measure the spatial variation of the plasma. Without loss of generality, the conductivity profile is represented by a simple power series

$$\sigma(z) = \sum_j p_j z^j \tag{13}$$

where p_j are unknown constants to be determined. Since only four coils are used, the power series is necessarily a third degree polynomial containing four terms and four unknown constants. Substituting Eq. (13) into Eq. (9), and again incorporating the known functional relationship between V and $\Delta(\frac{1}{Q})$, we have

$$(V_i)^{4/3} = K'' \sum_j p_j \int_0^\infty z^j W(D_i, z)\, dz = \sum_j C_j p_j \tag{14}$$

Thus, by measuring the output signals from each of four coils separately, we obtain four linear algebraic equations which can be used to solve for the four unknown constants p_j (j = 0, 1, 2 and 3) of the power series. The conductivity profile can then be evaluated from the polynomial representation given by Eq. (13). Note that other analytical representations can also be used for faster convergence of the conductivity approximation if some information regarding the conductivity profile is available. Because the influence function can be accurately evaluated from a laboratory calibration, the deduced conductivity profile is expected to be quite accurate.

FUTURE RESEARCH

From the lateral resolution point of view, the coil diameter should be as small as possible. However, for smaller coils the effective penetration depth is also smaller. As a result, the ability to measure the spatial variation of plasma conductivity is reduced. Thus additional research is warranted in areas such as coil configuration and metal sleeving designs for the purpose of augmenting the free space flux penetration depth.

For the multi-coil system, computer processing of the data is desirable and the development of a data recording subsystem involving a multi-channel tape data recorder and an analog-to-digital converter for use with the basic measuring system is recommended. A dedicated computer with appropriate software can also be developed to convert the data from the magnetic tape form to direct display of the conductivity profile or to a computer printout of tabular representation of the conductivity profile as a function of time.

CONCLUDING REMARKS

A non-protruding conductivity probe system utilizing a marginal oscillator has been described which is ideally suited for on-board measurements of electrical conductivity of re-entry plasmas. It was found to be very sensitive to slight changes in conductivity and yet very stable against drift and aging. It differs from other conductivity coil systems by its ruggedness, reliability, wide dynamic range, and the advantageous feature of providing measurements of the spatial variation of plasma conductivity.

ACKNOWLEDGMENT

The research reported in this paper was sponsored by the Air Force Cambridge Research Laboratories, Air Force Systems Command, under Contract No. F19628-68-C-0127.

REFERENCES

1. Lin, S.C., Resler, E.L., and Kantrowitz, A.: J. Appl. Phys., vol. 26, p. 95, 1955.

2. Fuhs, A.E.: AIAA J., vol. 2, p. 667, 1964.

3. Betchov, R., Fuhs, A.E., Meyer, R.X., and Schaffer, A.E.: Aerospace Eng., vol. 21, p. 54, 1962.

4. Rossow, V.J. and Posch, R.E.: Coil Systems for Measuring Conductivity and Velocity of Plasma Streams, Rev. Sci. Inst., vol. 37, p. 1232, 1966.

5. Olson, R.A. and Lary, E.C.: Rev. Sci. Inst., vol. 33, p. 1350, 1962.

6. Olson, R.A. and Lary, E.C.: AIAA J., vol. 1, p. 2513, 1963.

7. Lary, E.C. and Olson, R.A.: Third Symposium on the Engineering Aspects of Magnetohydrodynamics, Gordon and Breach, 1962.

8. Hollister, D.P.: AIAA J., vol. 2, p. 1568, 1964.

9. Koritz, H.E. and Keck, J.C.: A Technique for Measuring the Electrical Conductivity of Wakes of Projectiles at Hypersonic Speeds, AVCO Research Report No. 167, 1963.

10. Fuhs, A.E., Grabowsky, W.R., and Gibb, O.L.: Use of Radio Frequency Bridge for Re-entry Plasma Diagnostics, J. Spacecraft, vol. 4, p. 327, 1967.

11. McPherson, D. A., et al.: RF Bridge Electrical Conductivity Gauge for RMP-B Vehicle, Aerospace Report No. TR-0158 (3220-20)-2, June 1968.

12. Stubbe, E.J.: An Absolute Immersion-Type Electrical Plasma Conductivity Probe, Proc. IEEE, vol. 56, p. 1483, 1968.

13. Jackson, J.D.: Classical Electrodynamics, John Wiley & Sons, Inc., 1962, p. 240.

14. Aisenberg, S.: A Study of the Use of Chemical Additives for the Alleviation of the Plasma Sheath Problem, Scientific Report No. 2 of Space Sciences Incorporated, Waltham, Massachusetts for Contract No. AF19(628)-5097, AFCRL-67-0693, March 1967.

15. Aisenberg, S. and Nydick, S.E.: The Study of Plasma Surrounding Re-entry Bodies and Resultant Interaction with Microwave Radiation, Final Report of Space Sciences Incorporated, Waltham, Massachusetts for Contract No. AF19(628)-5097, April 1968.

16. Aisenberg, S.: A Catheter Coil System for the Measurement of Blood Flow Velocity, Flow Channel Cross-Section and Flow Rate, presented to the Seventh Annual Rocky Mountain Bioengineering Symposium and the Eighth International ISA Biomedical Sciences Instrumentation Symposium, Denver Colorado, May 1970.

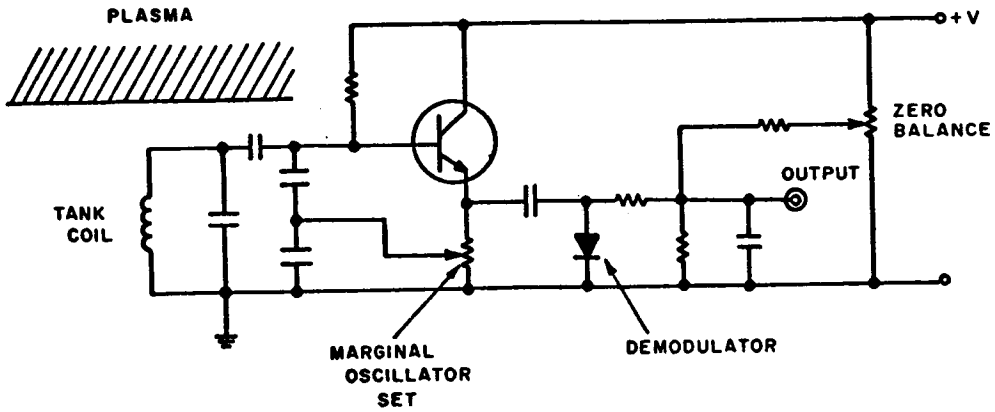

Figure 1.- Basic circuit of conductivity probe.

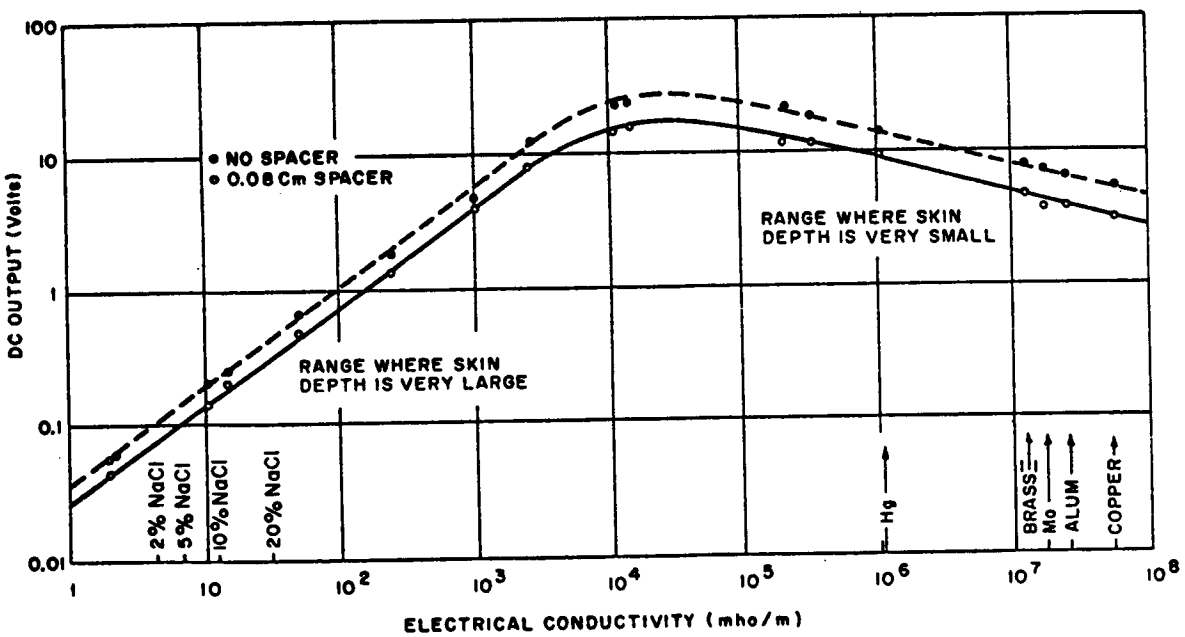

Figure 2.- Calibration curve of output voltage as a function of electrical conductivity.

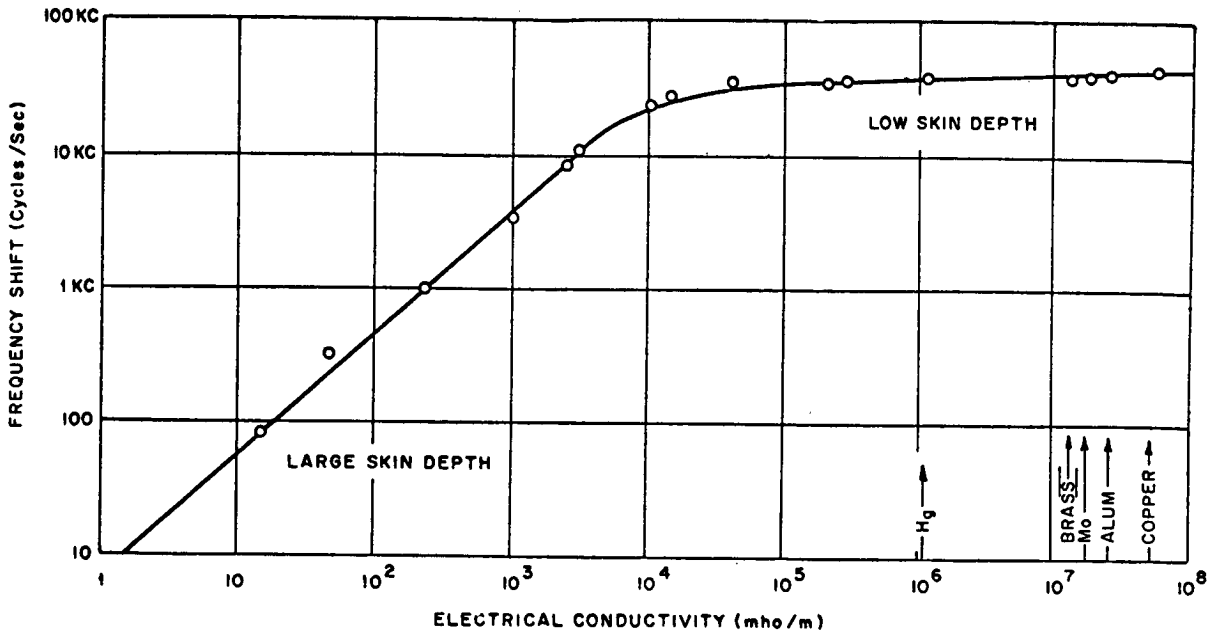

Figure 3.- Calibration curve of frequency shift as a function of electrical conductivity.

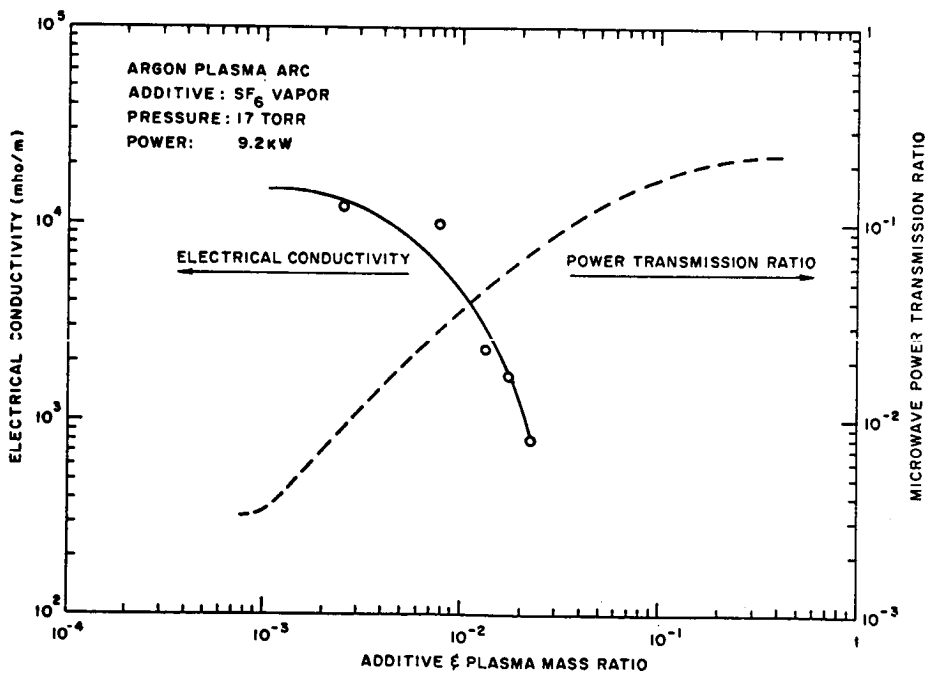

Figure 4.- Additive modification of plasma electrical conductivity as measured by RF conductivity coil system.

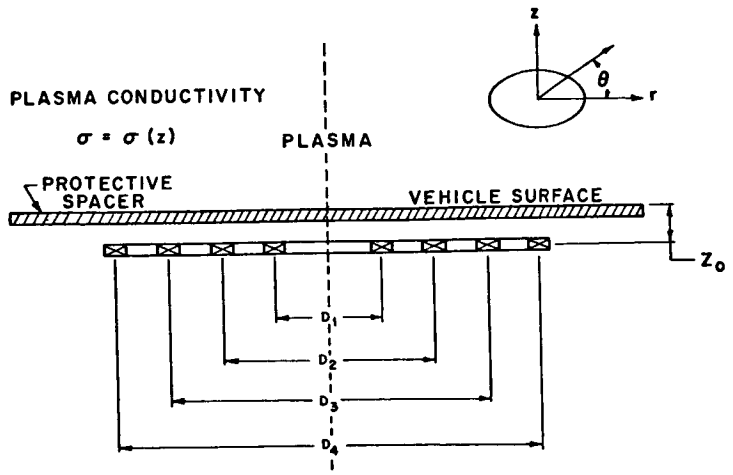

Figure 5.- Illustration of the concentric probing coil system and the coordinate system used in the analysis.

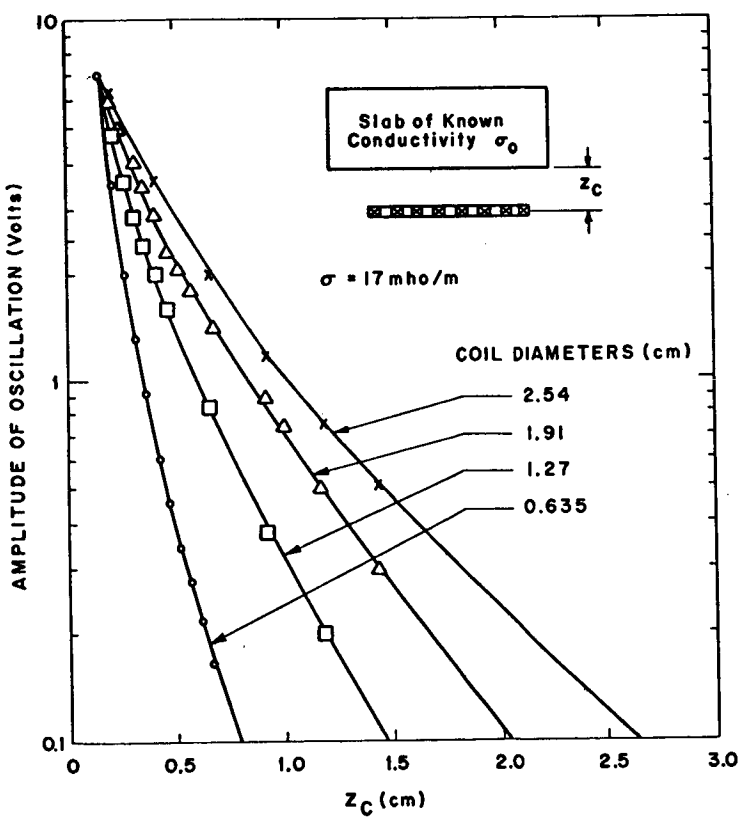

Figure 6.- Variation of output voltage as a function of the spacing between coil center and conducting calibration material.

PREDICTION OF ELECTRON DENSITY IN THE BOUNDARY LAYER ON ENTRY VEHICLES WITH ABLATION

By F. G. Blottner

Supervisor, Numerical Fluid Dynamics
Sandia Laboratories, Albuquerque, New Mexico

13

SUMMARY

A rather general computer code has been developed for the numerical solution of the laminar boundary layer and thin shock layer (stagnation point only) equations for a multi-component gas mixture with finite reaction rates. The purpose of this paper is to indicate the capabilities of this computer program by presenting solutions for pure air flows and flows with carbon ablation. At the body surface the effects of oxidation and sublimation of carbon are taken into account with the following species included in the gas model: O_2, N_2, O, N, NO, NO^+, C_1, C_2, C_3, CN, CO, and CO_2. Results for the boundary layer along a 10° half-angle hyperboloid with ablation of carbon are compared to pure air results. Shock layer results for several wall temperatures and altitudes are presented and compared to pure air results. Other types of problems that can be solved with this computer code are indicated.

INTRODUCTION

The prediction of the electron number density in the flow field around an entry vehicle at certain altitudes can be obtained by following the classical approach of dividing the flow into an inviscid region and a boundary layer. Downstream on slender bodies, the significant ionization occurs in the boundary layer flow and a method of solution is important. For blunt bodies the contribution of the ionization in the boundary layer is small and the importance of solutions is greatly decreased. At altitudes where the flow is laminar, the effects of finite reactions are generally required in the gas model. Therefore, for the laminar boundary layer solutions considered in this paper, the effects of chemical nonequilibrium are taken into account.

The solution of the boundary layer equations along a body has been obtained previously in Ref. 1 for pure air flows. These results are extended in this paper in two respects. First, the edge conditions for the boundary layer have been obtained such that the swallowing of the inviscid flow has been taken into account. This method of handling the boundary layer edge conditions has been shown to be a reasonable approach by Davis[2]. Second, the effect of ablation of the surface material has been taken into account in the boundary conditions applied at the body surface. The boundary condition at the surface takes into account the oxidation and sublimation of carbon. It is assumed that oxidation results from both molecular and atomic oxygen reacting with the carbon surface to produce carbon monoxide. The mass flux of the chemical species at the surface is determined with the use of oxidation probabilities for O and O_2. The

sublimation of the carbon is obtained with the Hertz-Knudsen-Langmuir relation where the vaporization coefficients and the partial pressure of the carbon species are required. In the present model it has been assumed that carbon can sublimate as C_1, C_2, C_3. In addition to the usual air species (O_2, N_2, O, N, NO, and NO^+), the following species are included in the gas model: C_1, C_2, C_3, CN, CO, CO_2. The gas model for the carbon-air system includes 26 homogenous chemical reactions. To illustrate the types of problems which can be solved with this program, the boundary layer flow has been solved along a hyperboloid with an asymptotic half-angle of 10° and 1-inch nose radius.

At high altitudes the viscous effects extend to the shock wave and the solution of the complete viscous shock layer is required rather than inviscid and boundary layer solutions. In reference 3, results were presented for pure air flows where a finite-difference scheme is employed for the solution. This technique has been extended by using the modified Rankine-Hugoniot relations (shock slip) and allowing mass transfer of ablation products at the body surface. To illustrate this part of the program, the viscous shock layer has been determined at the stagnation point of a body with a carbon surface. The same carbon-air gas model is employed as in the previous example. For these solutions it is only necessary to assume the freestream environment and the surface temperature. The ablation rate of the carbon is determined as part of the solution. Results are presented which compare the electron number density with carbon ablation to pure air solutions. The effects of altitude and wall temperature on the electron number density is also considered.

The details of the analysis and computer code are given in reference 4.

SYMBOLS

c_i	mass fraction of species i, ρ_i/ρ
$\bar{M}$	molecular weight of the gas mixture, $1/(\sum_i c_i/M_i)$
M_i	molecular weight of species i
NI	number of chemical species in gas model
NJ	number of chemical species and catalytic bodies
p	pressure
R	universal gas constant
R_N	nose radius
T	temperature, °R
T_K	temperature, °K
u,v	velocity components tangent and normal to body surface

x distance along surface from leading edge or stagnation point

y distance along normal from surface

ρ density

ρ_i density of species i

Subscripts

b conditions at body surface

e conditions at outer edge of shock layer or boundary layer

FORMULATION

Governing Equations and Solution

The finite-difference solution of the conservation equations for a chemically reacting boundary layer are given in reference 1 and the same method of solution is employed in this paper. The governing equations for mass, momentum, energy and species are transformed with the similarity variables. The resulting equations are solved with an implicit finite-difference scheme. To start the solution along the body, initial profiles are necessary and these are obtained from the governing equations which become ordinary differential equations. The solution of the viscous shock layer requires the solution of the same ordinary differential equations but with different boundary conditions. The governing equations and technique for solving these equations are presented in reference 3. The main differences between the present governing equations and those given previously are the forms of the boundary conditions employed and these will be discussed in the next section. Since the finite-difference techniques employed are the same as those given in references 1 and 3, they will not be described. The gas model used in the present study is more complex and is described subsequently.

Surface Boundary Conditions

The boundary conditions at the surface of the body for pure air flows for the case of noncatalytic or fully catalytic walls are given in reference 1. For the case of the ablation of a carbon body, the surface temperature is assumed given and the tangential velocity is zero. The mass flux density, $\dot{m}_i$, of all of the species at the surface must be specified and then the normal mass average velocity can be obtained to use as a boundary conditions for the continuity equation.

The appropriate heterogeneous reactions that can occur at a surface depend on the surface material composition and the chemical species available in the boundary layer flow. For a carbon surface, the following oxidation reactions are considered:

(1) $2C(S) + O_2 \rightarrow 2CO$

(2) $C(S) + O \rightarrow CO$

The detail chemical kinetic mechanisms occurring are not understood for this relatively simple system and many additional chemical species can produce gasification of carbon.

The mass flux density of the chemical species at the surface are zero except for the following:

$$\dot{m}_{O_2} = - \frac{M_{O_2}}{2M_C} \epsilon_{O_2} \rho_b \sqrt{\frac{RT_b}{2\pi M_{O_2}}} c_{O_2} \tag{1a}$$

$$\dot{m}_O = - \frac{M_O}{M_C} \epsilon_O \rho_b \sqrt{\frac{RT_b}{2\pi M_O}} c_O \tag{1b}$$

$$\dot{m}_{CO} = - \frac{M_{CO}}{M_O} \left(\dot{m}_{O_2} + \dot{m}_O \right) \tag{1c}$$

where

$$\epsilon_i = \frac{\text{Flux of carbon atoms away from surface}}{\text{Collision flux of species i with the surface}} \qquad (i = O, O_2)$$

In these relations the collision flux of species i with the surface is obtained from the kinetic theory relation for the rate at which molecules strike a surface in contact with a gas in equilibrium. There have been a large number of experimental papers concerned with the oxidation of carbon or graphite, but adequate information to estimate the oxidation probabilities ϵ_{O_2} and ϵ_O is not available. The best information available on these quantities can be obtained from Allendorf and Rosner[5], but the range of applicability is limited. For the numerical results presented, both oxidation probabilities are taken as one.

In addition to the heterogeneous reactions causing gasification of the carbon surface, sublimation of the surface material also occurs. The mechanisms involved in the sublimation of carbon is very complex and the details are not known. At high temperatures and pressures, particulate matter is lost from the surface and this phenomenon is neglected in the present analysis. A modified Hertz-Knudsen-Langmuir relation is used to determine the mass flux density and is

$$\dot{m}_i = \frac{\alpha_i p_e \bar{M}_b}{\sqrt{2\pi M_i R T_b}} \left(c_{i_{vp}} - c_i \Gamma \right) \tag{2}$$

where

α_i = condensation or vaporization coefficient

$c_{i_{vp}}$ = mass fraction of species i corresponding to the equilibrium vapor pressure

Γ = correction factor for non-equilibrium evaporation

The usual relation employed for non-equilibrium evaporation is expression (2) with $\Gamma = 1$. A more appropriate relation is the expression (2) which is considered in detail in references 6 and 7. The parameter Γ is introduced to modify the relation that is usually applied for the case of molecules hitting a surface with zero mass transfer to the case with surface mass transfer. In the first case, the Maxwellian distribution function is for a gas at rest while a more proper form is the Maxwellian distribution for a moving gas.

The equilibrium vapor pressure is written in the following form:

$$\bar{M} p_e \, c_{i_{vp}} = 2116.22 \, M_i \, A_i \, T_K^{n_i} \, e^{-E_i/T_K} \tag{3}$$

where the coefficients A_i, n_i and E_i are given in Table I. These coefficients are determined from information contained in the JANAF thermochemical tables. The vaporization coefficients are given in Table I and are those given by Zavitsanos[8]. The correction factor Γ has been taken equal to one for the present calculations.

Outer Edge Boundary Conditions

The appropriate edge conditions for the boundary layer flow on a blunt body requires that the swallowing of the non-equilibrium inviscid flow be taken into account. The computer program requires the edge conditions be provided in tabular form and it is the responsibility of the user to provide these quantities.

The technique employed in the example presented subsequently is now described and has resulted in a separate computer code. The mass flow in the boundary layer at distance x_{BL} along the body is matched to the mass flow entering the shock wave which gives the radial distance from the axis to the streamline. The shock shape is determined from either a perfect gas or an equilibrium air inviscid blunt body solution obtained with the NASA Ames computer code[9]. Also from this solution the pressure behind the shock wave and along the body surface is known. The pressure across the shock layer and along the various streamlines is determined from the Maslen[10] relation.

The length of the streamline, s_ℓ, is estimated as

$$s_\ell = \sqrt{\Delta^{*2} + (x_{BL} - x_{sh})^2} \tag{4}$$

where

$\Delta^* = \Delta - \delta$

Δ = shock wave stand-off distance at the stagnation point

δ = boundary layer thickness at the stagnation point

x_{sh} = distance along body where the streamline crosses the shock wave

The distance along the streamline, s, is related to the distance along the body by the approximation

$$s = s_\ell \, (x - x_{sh})/(x_{BL} - x_{sh}) \tag{5}$$

With the pressure known along the streamlines, the one-dimensional inviscid gasdynamic equations for a reacting flow are solved numerically. The conditions behind the shock wave which are obtained from the frozen Rankine-Hugoniot relations are used as initial conditions to start the solution of the ordinary differential equations. When the solution along the streamline is obtained to s_ℓ, the conditions at the edge of the boundary layer will be known at x_{BL}. The total velocity along the streamline, V, is known and the desired boundary condition is the tangential velocity, u_e, which can be obtained from

$$u_e = \sqrt{V^2 - v_e^2} \tag{6}$$

The value of v_e is obtained from the boundary layer solution.

The flow at the edge of the shock layer is obtained from the modified Rankine-Hugoniot relations with frozen chemistry across the shock transition zone. These relations have been given by Cheng[11] and correspond to a one-dimensional shock wave with gradients of the flow properties behind it. It has been shown by Cheng[12] and Tolstykh[13] that these relations are also valid for a curvilinear shock wave if the shock thickness is much less than the radius of curvature of the shock. The modified Rankine-Hugoniot relations are the same as the usual Rankine-Hugoniot relations except slip terms are added to the momentum and energy relations. These slip terms involve normal derivatives of the flow quantities behind the shock wave and are transformed into the similarity coordinates. (See reference 4 for actual equations.) In order to locate where the modified Rankine-Hugoniot relations are to be applied, the interface behind the shock transition zone is defined as where the usual Rankine-Hugoniot pressure jump is completed as used by Cheng[12]. Thus for the viscous shock layer solution, the modified Rankine-Hugoniot relation for momentum is not required since the pressure is known. The mass fraction of chemical species is also required at the interface and requires the solution of the species conservation equations across the shock transition zone. When chemical reactions are neglected in the shock transition zone, a relation for the mass fraction of a chemical species at the interface is readily obtained and has been given by Cheng. The present analysis neglects the chemical reactions and pressure and thermal diffusion effects in the shock transition zone. For air flow, the neglect of the chemical reactions is a reasonable assumption as the results of

Lee and Zierten[14] and Chung[15] have shown. Also Chung states that the thermal and pressure diffusions of atoms are in opposite directions and the neglect of these effects does not imply an excessive approximation.

The boundary conditions with shock slip included are similar to those given previously in reference 3 but the transformed normal velocity relation is changed and the mass fractions of species are no longer equal to the freestream values. Since the boundary conditions and the modified Rankine-Hugoniot relations are coupled, these relations are solved in an iterative manner with the overall iterative solution of the governing equations.

Gas Model

The gas model employed for pure air flows is the same as given in references 1 and 3. For the cases with ablation of carbon, the following carbon-air species are added: C_1, C_2, C_3, CN, CO, and CO_2. For the entry environment conditions considered in this paper, these species should be sufficient based upon equilibrium composition calculation with additional species. At higher entry velocities additional species will contribute to the ionization of the gas such as C^+, CO^+ and CN^+. When these species are taken into account, also the air species O^+, N^+, O_2^+ and N_2^+ must be considered.

The thermodynamic properties of enthalpy and specific heat at constant pressure for the new species are obtained from Browne[16,17,18]. The heats of formation of these species are given in Table II and are from the JANAF thermochemical tables. The transport properties of the gas mixture are obtained as described in references 3 and 4 where the viscosities of the new species are required. The viscosities of C, CO, and CO_2 are obtained from a private communication from Yos which is an extension of the work reported in reference 19. The viscosities of C_2 and CN are from Svehla[20] and the viscosity of C_3 is from Fox and Bernard[21]. The curve fit coefficients for the relation

$$\mu_i = e^{C_{\mu_i}} T_K^{\left(A_{\mu_i} \ln T_K + B_{\mu_i}\right)} \quad \text{(gm/cm-sec.)} \qquad (7)$$

are given in Table II for the various species. The binary Lewis-Semenov numbers have been assumed the same for all of the interactions and equal to 1.4.

The chemical reactions that should be included in the gas model are difficult to determine. From a review of the literature, the following chemical reactions were chosen because information was available on the reaction rates, although some were included that were considered to be unimportant:

r = 1 $\quad O_2 + M_1 \rightleftarrows 2O + M_1$

2 $\quad N_2 + M_2 \rightleftarrows 2N + M_2$

3 $\quad N_2 + N \rightleftarrows 2N + N$

4 $\quad NO + M_3 \rightleftarrows N + O + M_3$

5	$CO_2 + M_4 \rightleftarrows CO + O + M_4$
6	$CO + M_5 \rightleftarrows C + O + M_5$
7	$C_2 + M_6 \rightleftarrows 2C + M_6$
8	$C_3 + M_7 \rightleftarrows C + C_2 + M_7$
9	$CN + M_8 \rightleftarrows C + N + M_8$
10	$NO + O \rightleftarrows O_2 + N$
11	$N_2 + O \rightleftarrows NO + N$
12	$N_2 + C \rightleftarrows CN + N$
13	$CO + N \rightleftarrows CN + O$
14	$CO_2 + N \rightleftarrows CN + O_2$
15	$N_2 + CO \rightleftarrows CN + NO$
16	$CO + NO \rightleftarrows CO_2 + N$
17	$CO_2 + O \rightleftarrows CO + O_2$
18	$2CO \rightleftarrows CO_2 + C$
19	$CO + O \rightleftarrows O_2 + C$
20	$CO + N \rightleftarrows C + NO$
21	$CN + O \rightleftarrows C + NO$
22	$2CO \rightleftarrows C_2 + O_2$
23	$CO + C \rightleftarrows C_2 + O$
24	$C_2 + CO \rightleftarrows C_3 + O$
25	$C_3 + C \rightleftarrows 2C_2$
26	$N + O \rightleftarrows NO^+ + e^-$

The forward reaction rates for the above reactions are expressed as

$$k_{f_r} = T_K^{C2_r} \exp(\ln C0_r - C1_r \times 10^3/T_K) \qquad (8)$$

The backward rates are expressed in the same form with the constant C replaced with D's. The values of the reaction-rate coefficients are given in Table III. The rates for the air reactions (r = 1, 2, 3, 4, 10, 11, and 26) are the same as employed in references 1 and 3 and are from Bortner[22]. The rates for reactions 5, 6, 9, and 12 to 19 are from McKenzie[23], reactions 7, 8, 23, 24 and 25 are from Tunder[24], and reactions 20, 21, and 22 are from Bortner[22]. For many of the reactions only the reaction rate in one direction is given in these references. The equilibrium constant was used to determine the other reaction rate where the JANAF thermochemical tables were used to evaluate the equilibrium constants. For the mass concentration, $\gamma_j = c_j/M_j$, of the electrons and the catalytic bodies, the following expression is used:

$$\gamma_j = \sum_{i=1}^{NI} Z_{ki}\,\gamma_i \qquad j = (NI+1), \ldots NJ \qquad (9)$$

$$k = (j-NI)$$

The quantity Z_{ki} is the third body efficiencies relative to argon and the values used are given in Table IV.

Capabilities of Computer Program

The program is written with the idea to be as general as possible within reasonable limitations. The program solves the boundary layer equations along a body and always starts at the tip or stagnation point for an arbitrary (this will be described subsequently) multi-component gas mixture. At a stagnation point or the tip of a body, the similar boundary layer equations are solved to obtain initial profiles. At a stagnation point the thin viscous shock layer equations with shock slip can be solved but not along the body. The program will handle either two-dimensional bodies (flat plate, blunt wedge with cylindrical leading edge, and hyperbola) or axisymmetric bodies (cone, sphere-cone, and hyperboloid). Also, the nose radius or reference length for a flat plate or cone must be specified. To complete the body geometry the half-angle or asymptotic half-angle for the blunt bodies is required.

The program will handle solutions in an arbitrary freestream where the velocity, pressure, temperature and species mass fraction define the environment. For the shock layer solution no additional information is required. For a boundary layer solution the conditions at the outer edge must be specified consistent with the freestream conditions. The determination of the boundary layer outer edge conditions are to be made by the user. The pressure, tangential velocity, temperature and mass fraction of the various species are required as a function of the distance along the body. The usual relation between the pressure gradient and velocity gradient is not used since swallowing of the inviscid flow can be taken into account.

At the wall a variety of boundary conditions have been included in the program. If gas models other than a binary mixture of oxygen, air or carbon-air are employed, special care should be taken to be sure the boundary conditions employed are appropriate. For all cases it is assumed that the wall temperature is known as a function of the distance along the body in tabular form. The case of an energy balance or a specified heat transfer have not been considered but could be handled with suitable changes in the program. The first four wall options are for noncatalytic and catalytic conditions and the mass transfer at the surface is zero. For the case of mass transfer of ablation products the surface mass flux density must be specified as a function of the distance along the body in tabular form. For the remaining wall options the program will determine the surface mass flux density as part of the solution.

To start the solution along a body or to generate initial profiles, values of the tangential velocity, temperature and species mass fraction must be read in. An iteration procedure is performed to obtain initial profiles or one

iteration is performed on the initial profiles and then the solution proceeds along the body. If a first estimate of the profiles for the iteration of initial profiles is not available, the program will generate profiles for temperature and mass fraction of species where the tangential velocity read in is used.

In the iteration procedure employed to obtain the initial profiles, a choice is available on the procedure to be followed. There is always an iteration performed where the momentum equation is solved first, the species equations solved next, and the energy equation solved last. This iteration is stopped whenever the convergence tolerance has been satisfied or so many iterations have been performed. In the iteration for initial profiles it is necessary in many cases to weigh the calculated solution with the assumed solution. The appropriate values to employ can be determined only from experience.

The gas model allowed in the program has been set up as general as possible. The multi-component gas mixture can consist of as many as 30 species and 30 homogeneous chemical reactions. For each chemical species certain thermodynamic and transport properties are required. The specific heat and enthalpy of each species are required and are given in block data. Data for the following species are presently stored in the program: O_2, N_2, O, N, NO, NO^+, CO, CO_2, CN, C_1, C_2, and C_3. The viscosity of each species and the binary diffusion coefficients between the various species are determined from curve fits. For each curve fit, three coefficients are required. Additional information, such as the molecular weight and heat of formation of each species, is required. For each chemical reaction the names of the species involved in the reaction are read in and also six coefficients to determine the reaction rate coefficients. For reactions involving third bodies and with reaction rates only differing by a constant for the various third bodies, the use of third body efficiencies reduces the amount of computing and is the recommended procedure to be employed. Since the computing time nearly doubles when multi-component diffusion coefficients are being used as compared to Fick's law, these two options are available. For multi-component diffusion, the binary diffusion coefficient information must be supplied for interactions between species. When Fick's law is being used, the value of the Lewis-Semenov numbers for each species is required. In addition to the solution of flows with finite chemical reactions, frozen flows (chemical production terms are zero) can be solved. Also for similar boundary layer solutions with constant Lewis-Semenov numbers, solutions can be obtained for the gas in local chemical equilibrium. If this option is used, the appropriate subroutine must be supplied to determine the equilibrium composition.

Finally, certain information for the finite-difference procedure is required in the input. For many cases the thickness of the boundary layer in terms of the transformed similarity coordinate, η, is nearly constant. For cases where the thickness changes along the body, the value of η_e as a function of x/R_N is required in tabular form. The step-sizes along the body and across the boundary layer or shock layer are required input. The appropriate values to be used depends upon the desired accuracy and are determined from experience with the program. The program also has an option where the step-size across

the boundary layer or shock layer can be variable. A variable step-size can be read in or the program can be used to generate a variable step-size. Other options, such as when to print profiles of the dependent variables and when to punch the final iterations results for the initial profiles on cards, are available.

NUMERICAL RESULTS

To indicate the capabilities of the computer program, the boundary layer solution along a hyperboloid and the stagnation point viscous shock layer solution are presented. For both of these examples the ablation of a carbon surface is taken into account and the gas model described previously is employed.

Boundary Layer Along Hyperboloid

For this case a hyperboloid with an asymptotic half-angle of 10° and 1-inch nose radius is used. The freestream conditions correspond to an altitude of 100 kft and the velocity is 20 kfps. The surface temperature was taken as $3000^{\circ}K$ and constant along the body. For this temperature, ablation results mainly from oxidation and the effects of sublimation were neglected. The solution of the boundary layer and inviscid flow is iterated several times such that the boundary layer is reasonably matched with the inviscid flow. The edge of the boundary layer was taken equal to 15 in terms of the transformed coordinate η_e. For large values of η_e, a sufficient number of points must be taken across the boundary layer to avoid oscillations of the species and for the present case 50 points were used.

The peak electron number density along the hyperboloid is presented in Figure 1 and is compared to results without ablation. It should be noticed that the pure air cases have a wall temperature of $1400^{\circ}K$ and this also influences the electron density. The distribution of electron number density across the boundary layer at different locations along the body is given in Figure 2. For the thickness of the boundary layer employed, the significant ionization in the flow field occurs within the boundary layer downstream on the body.

One solution of the boundary layer flow along the hyperboloid to 50 nose radii requires 11 minutes on a CDC 6600 computer. The program that was described previously to obtain edge conditions requires about 10 minutes for each iteration. The total time for the solution of this problem is approximately an hour.

Viscous Shock Layer

This option of the computer program has been used to obtain the solution of the thin viscous shock layer at the stagnation point of a blunt body with a 1-inch nose radius. The first case investigated has a wall temperature of $3000^{\circ}K$, altitude of 150 kft and the velocity for all cases is 20 kfps. In all of the results for the viscous shock layer, the oxidation and sublimation of

the carbon is taken into account as described previously. The electron number density across the shock layer is given in Figure 3 for the cases with and without carbon ablation. The effect of altitude on the electron density is shown in Figure 4 where the wall temperature is 3000°K. The effect of wall temperature on the electron density at an altitude of 150 kft is presented in Figure 5. With a wall temperature of 4000°K there is significant mass transfer at the surface which increases the thickness of the shock layer and reduces the electron density near the surface. For the cases considered, the ablation of carbon has only a small effect on the electron density when compared to the results of pure air flows without ablation. The ablation rates that have been calculated with the present analysis and computer code are given in Table V for the various cases solved.

The first solution of this problem required approximately 15 minutes on the CDC 6600. In this case initial estimates of the various dependent variables were crudely made for the iteration process. The other solutions were obtained in approximately 5 minutes as previous results were employed as initial values for the dependent variables.

CONCLUDING REMARKS

Some of the capabilities of a computer program developed for solving reacting viscous flows of multi-component gas mixtures have been illustrated. The present investigation has indicated how this program can be used to solve flows with carbon ablation and with complex gas models. The main emphasis has been on the computed results for electron number density. From the computed solutions, the complete details of the flow are known and the usual boundary layer properties are determined. In addition, the importance of any of the chemical reactions can be ascertained from the information available on the contribution of each reaction to the various chemical production terms. For the boundary layer solution in the nose region, the carbon reactions that are important are 5, 7, 8, 12, 13, 16, 17, 19, 23 and 24. The simplified chemical model proposed by Menees and McKenzie[25] is not sufficient for the present flow. The reactions 7, 8, 23, and 24 are required for the prediction of the species C_2 and C_3 which are not included in the model of Menees and McKenzie. The present results indicate reactions 17 and 19 should be included while Menees and McKenzie neglect these reactions.

The computer program has been utilized to solve a variety of viscous flow problems. The type of gas models that have been used are the following:

1. Binary mixture of O and O_2
2. Nitrogen with N_2, N, N^+, N_2^+
3. Air with O_2, N_2, O, N, NO, NO^+
4. Cargon-air as described in this paper.

Boundary layer solutions have been obtained for the following body geometries: flat plate, cone, hyperboloid, sphere-cone, and blunt wedge. Viscous shock layer solutions have been obtained for a blunt body with a 1-inch nose radius

and for an altitude range from 100 to 300 kft. Results also have been obtained for a body with a 1-foot nose radius.

The computer program has been used to predict the electron number density in the boundary layer on a blunt wedge at conditions corresponding to a test performed in a shock tunnel by Boyer and Andre[26]. The edge conditions for the boundary layer solution were obtained from a chemical nonequilibrium inviscid flow solution where perfect gas similar boundary layer solutions were used to account for the displacement effects. This method of matching did not result in smooth profiles near the matching point. In the experimental test two free-stream conditions were employed and both microwave (S-band and X-band) and Langmuir probes were used to determine the electron density. For one test condition the experimental and theoretical results for electron number density were in agreement. For the other test condition, the microwave measurements were 3 times higher than the theoretical results for electron number density. The Langmuir probe results were 4 times higher than the theoretical predictions for electron number density.

The modification of this program to handle other surface boundary conditions can readily be made. There are other extensions of this program which are being considered such as: including curvature terms in governing equations, extending viscous shock layer solutions along the body using the method of Davis[2], and including electron energy and species equations.

The computer program that is described in this paper will be available from COSMIC* in the near future.

REFERENCES

1. Blottner, F. G., "Finite-Difference Methods of Solution of the Boundary-Layer Equations", AIAA Journal, Vol. 8, No. 2, Feb. 1970.

2. Davis, R. T., "Hypersonic Flow of a Chemically Reacting Binary Mixture Past a Blunt Body". AIAA Paper No. 70-805, AIAA 3rd Fluid and Plasma Dynamics Conference, June 29-July 1, 1970.

3. Blottner, F. G., "Viscous Shock Layer at the Stagnation Point with Nonequilibrium Air Chemistry". AIAA Journal, Vol. 7, No. 12, Dec. 1969.

4. Blottner, F. G., and Johnson, M., "Chemically Reacting Viscous Flow Program for Multi-Component Gas Mixtures", Sandia Corporation Research Report SC-RR-70-754, 1970.

5. Allendorf, H. D., and Rosner, D. E., "Primary Products in the Attack of Graphite by Atomic and Diatomic Oxygen Above 1100°K", Carbon, Vol. 7, pp. 515-518, 1969.

6. Schrage, R. W., A Theoretical Study of Interphase Mass Transfer, Columbia University Press, New York, 1953.

*Computer Software Management and Information Center, Barrow Hall, University of Georgia, Athens, Georgia 30601.

7. Kucherov, R. Ya., and Rikenglaz, L. E., "On Hydrodynamic Boundary Conditions for Evaporation and Consideration", Soviet Physics Jetp, Vol. 37, No. 1, pp. 88-89, January 1960.

8. Zavitsanos, P. D., "The Vaporization of Pyrolytic Graphite", General Electric Co., G. E. R 66 SD 31, May 1966.

9. Inouye, Mamoru, Rakich, J. V., and Lomax, Harvard, "A Description of Numerical Methods and Computer Programs for Two-Dimensional and Axisymmetric Supersonic Flow Over Blunt-Nosed and Flared Bodies", NASA TN-2970, August, 1965.

10. Maslen, S. H., "Inviscid Hypersonic Flow Past Smooth Symmetric Bodies", AIAA Journal, Vol. 2, No. 6, pp. 1055-1061, June, 1964.

11. Cheng, H. K., "The Blunt-Body Problem in Hypersonic Flow at Low Reynolds Number", IAS Paper 63-92, New York, Jan. 21-23, 1963; Rept. AF-1285-A-10, 1963, Cornell Aeronautical Lab.

12. Cheng, H. K., "Viscous Hypersonic Blunt-Body Problems and the Newtonian Theory", Fundamental Phenomena in Hypersonic Flow, edited by J. G. Hall, Cornell University Press, Ithaca, N. Y., 1966.

13. Tolstykh, A. I., "On the Structure of a Curvilinear Shock Wave", PMM, Vol. 28, No. 3, pp. 553-556, 1964.

14. Lee, R. H. C., and Zierten, T. A., "Merged Layer Ionization in the Stagnation Region of the Blunt Body", Proceedings of the 1967 Heat Transfer and Fluid Mechanics Institute, edited by P. A. Libby, D. B. Olfe, and C. W. Van Atta, Stanford University Press, Stanford, Calif., pp. 452-458, 1967.

15. Chung, P. M., Holt, J. F., and Liu, S. W., "Merged Stagnation Shock Layer of Nonequilibrium Dissociating Gas", AIAA Journal, Vol. 6, No. 12, pp. 2372-2379, Dec. 1968.

16. Browne, W. G., "Thermodynamic Properties of Some Atoms and Atomic Ions," and "Thermodynamic Properties of Some Diatomic and Linear Polyatomic Molecules", MSD Engineering Physics TM2 and 3, General Electric Co., Philadelphia, Pa.

17. Browne, W. G., "Thermodynamic Properties of Some Ablation Products from Plastic Heat Shields in Air," MSD Aerospace Physics Memo 11, March 16, 1964, General Electric Co., Philadelphia, Pa.

18. Browne, W. G., "Thermodynamic Properties of Some Diatoms and Diatomic Ions at High Temperature," and "Thermodynamic Properties of the Species CN, C_2, C_3, C_2N_2, and C^-", MSD Advanced Aerospace Physcis TM 8 and 9, May 14, 1962, General Electric Co., Philadelphia, Pa.

19. Yos, Jerrold M., "Transport Properties of Nitrogen, Hydrogen, Oxygen, and Air to 30,000°K", RAD-TM-63-7, March 1963, Avco Corp., Wilmington, Mass.

20. Svehla, R. A., "Estimated Viscosities and Thermal Conductivities of Gases at High Temperatures", NASA TR R-132, 1962.

21. Fox, R. L., and Bernard, R. S., "A Tractable Method for Estimating Atomic and Molecular Transport Coefficients", AIAA Journal (to be published).

22. Bortner, M. H., "A Review of Rate Constants of Reactions in Re-Entry Flow Fields", TIS R68SD13, General Electric Co., Philadelphia, Pa., June, 1968.

23. McKenzie, R. L., "An Estimate of the Chemical Kinetics Behind Normal Shock Waves in Mixtures of Carbon Dioxide and Nitrogen for Conditions Typical of Mars Entry", NASA TN D-3287, Feb. 1966.

24. Tunder, R., Mayer, S., Cook, E., and Schieler, L., "Compilations of Reaction Rate Data for Non-Equilibrium Performance and Re-Entry Calculation Programs", Aerospace Corporation Preliminary Report, to be published.

25. Menees, G. P., and McKenzie, R. L., "A Simplified Chemical Model for Estimating the Nonequilibrium Radiant Emission of CN(Violet) in Shock-Heated Mixtures of CO_2 and N_2", AIAA Journal, Vol. 6, No. 3, pp. 554-556, March, 1968.

26. Boyer, D. W., and Andre, S. N., "Theoretical and Experimental Studies of Microwave Interaction Effects in a Hypersonic Air Plasma", Cornell Aeronautical Laboratory, preliminary contractor's report to Sandia Corporation.

Table I

Coefficients for Equilibrium Vapor Pressure

i	Species	A_i	n_i	E_i	α_i
1	C_1	9.3×10^7	0	85,334	0.24
2	C_2	5.8×10^9	0	99,738	0.50
3	C_3	4.3×10^{15}	-1.5	97,597	0.023

Table II

Properties of Species

Species	M_i	Heat of Formation (ft-lb/slug)	A_{μ_i}	B_{μ_i}	C_{μ_i}
C_1	12.011	6.362×10^8	-0.00611	0.7385	-12.71
C_2	24.022	3.718×10^8	-0.02729	1.0639	-14.03
C_3	36.033	2.426×10^8	0	0.8333	-13.516
CN	26.021	1.787×10^8	-0.02572	1.0395	-13.86
CO	28.011	-0.4376×10^8	-0.03242	1.1434	-14.17
CO_2	44.011	-0.9621×10^8	-0.05772	1.5429	-15.76

Table III

Reaction Rate Coefficients

Reaction	CO_r	$C1_r$	$C2_r$	DO_r	$D1_r$	$D2_r$
r = 1	3.61×10^{18}	59.4	-1.0	3.01×10^{15}	0	-0.5
2	1.92×10^{17}	113.1	-0.5	1.09×10^{16}	0	-0.5
3	4.15×10^{22}	113.1	-1.5	2.32×10^{21}	0	-1.5
4	3.97×10^{20}	75.6	-1.5	1.01×10^{20}	0	-1.5
5	1.2×10^{11}	36.85	0.5	1.5×10^{6}	-26.43	1.25
6	8.5×10^{19}	129.0	-1.0	2.4×10^{18}	0	-1.0
7	4.5×10^{18}	70.93	-1.0	1.0×10^{16}	0	-0.5
8	1.6×10^{16}	87.48	1.0	1.0×10^{16}	0	-0.5
9	5.2×10^{19}	94.14	-1.0	7.4×10^{18}	4.12	-1.0
10	3.18×10^{9}	19.7	1.0	9.63×10^{11}	3.6	0.5
11	6.75×10^{13}	37.5	0	1.50×10^{13}	0	0
12	2.0×10^{10}	31.56	1	7.7×10^{9}	8.33	1
13	2.0×10^{10}	45.8	1	2.7×10^{10}	7.1	0.75
14	3.0×10^{8}	49.56	1	6.7×10^{5}	6.96	1.25
15	1.0×10^{3}	92.01	2	3.1×10^{2}	15.59	1.75
16	1.0×10^{3}	20.98	2	1.8×10^{7}	8.75	1.25
17	3.0×10^{8}	18.21	1	5.2×10^{5}	14.30	1.50
18	1.0×10^{3}	72.39	2	2.0×10^{6}	6.97	1.25
19	2.0×10^{10}	69.5	1	1.0×10^{10}	0	1.0
20	9×10^{16}	53.2	-1.0	1×10^{16}	0	-1.0
21	1×10^{12}	14.5	0	6×10^{11}	0	0
22	9.2×10^{11}	163.3	0.75	3.8×10^{13}	36.2	0
23	4.1×10^{10}	59.79	0.5	5.0×10^{11}	2.01	0.5

Table III (Cont.)

Reaction	CO_r	$C1_r$	$C2_r$	DO_r	$D1_r$	$D2_r$
r = 24	1.2×10^{13}	43.24	0	5.0×10^{11}	2.01	0.5
25	1.7×10^{9}	19.58	1.5	5.0×10^{11}	3.02	0.5
26	9.03×10^{9}	32.4	0.5	1.80×10^{19}	0	-1.0

Table IV

Z_{ki}, Third Body Efficiencies Relative to Argon

i =	1	2	3	4	5	6	7	8	9	10	11	12
	O_2	N_2	O	N	NO	NO^+	CO	CO_2	C_1	C_2	C_3	CN
k = 1(e^-)	0	0	0	0	0	1	0	0	0	0	0	0
2(M_1)	9	2	25	1	1	0	2	5	1	1	1	1
3(M_2)	1	2.5	1	0	1	0	2	5	1	1	1	1
4(M_3)	1	1	20	20	20	0	2	5	1	1	1	1
5(M_4)	2	2	2	2	2	0	2	5	1	1	1	1
6(M_5)	1	1	1	1	1	0	1	1	1	1	1	1
7(M_6)	1	1	1	1	1	0	1	1	1	1	1	1
8(M_7)	1	1	1	1	1	0	1	1	1	1	1	1
9(M_8)	1	1	1	1	1	0	1	1	1	1	1	1

Table V

Ablation Rate at Stagnation Point

Altitude (kft)	$T_W(^oK)$	$(\rho v)_b \times 10^4$ (slug/ft^2-sec)
200	3000	2.94
175	3000	4.94
150	3000	7.77
150	3500	8.24
150	4000	31.7

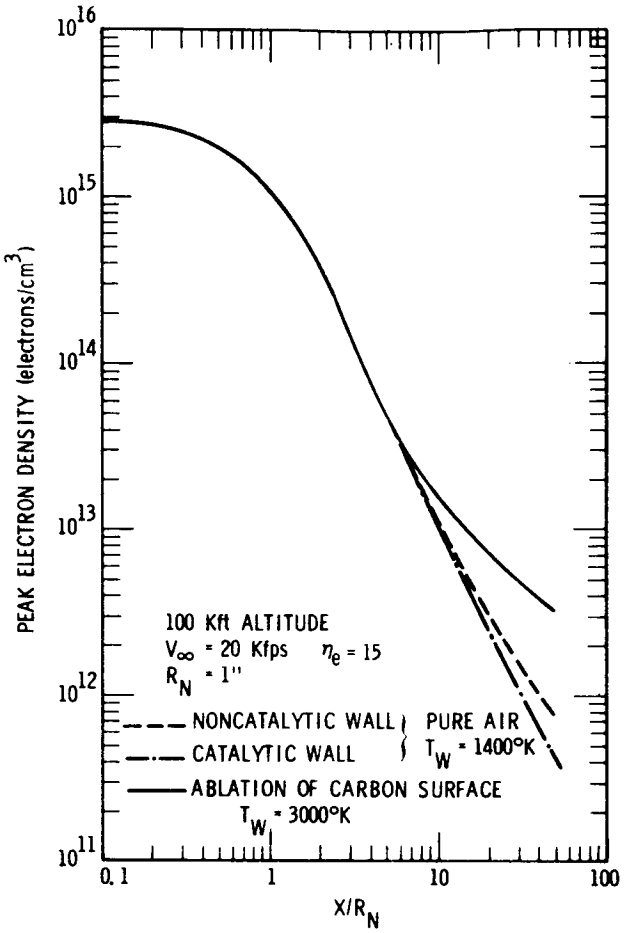

Figure 1.- Peak electron density in the boundary layer along a hyperboloid (10^o half-angle).

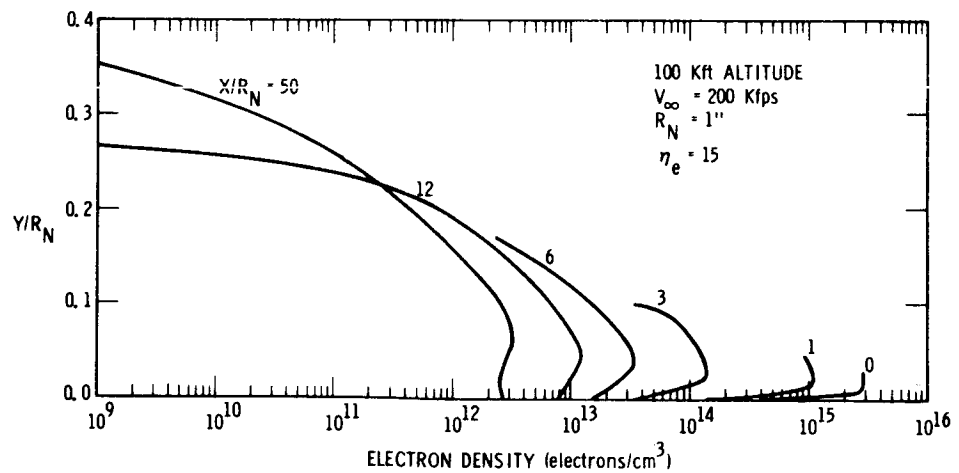

Figure 2.- Profile of electron density across the boundary layer at several locations along a hyperboloid (10^o half-angle).

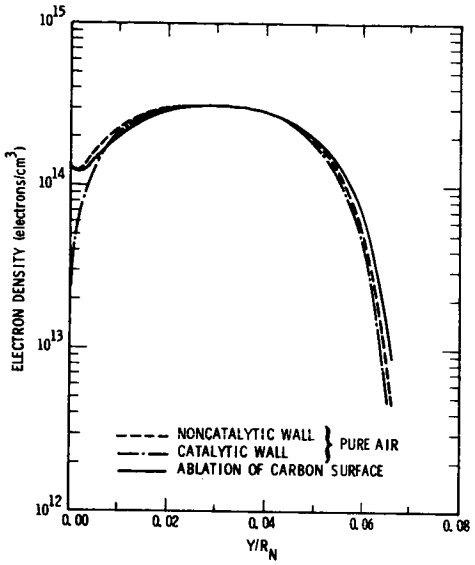

Figure 3.- Effect of carbon ablation on the electron density across the thin viscous shock layer at the stagnation point.

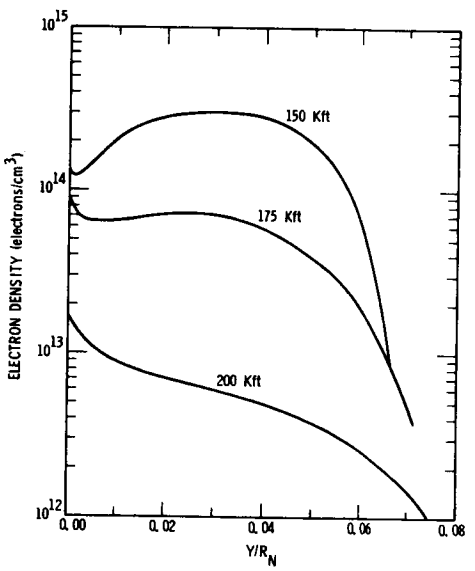

Figure 4.- Effect of altitude on the electron density across the thin viscous shock layer at the stagnation point with carbon ablation. $T_W = 3000^O$ K.

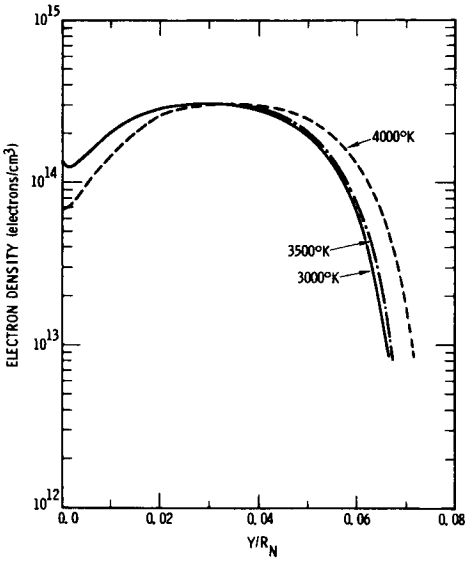

Figure 5.- Effect of wall temperature on the electron density across the thin viscous shock layer at the stagnation point with carbon ablation. Altitude, 150 kft.

A COMPUTATIONAL METHOD FOR UNIFIED SOLUTIONS TO THE INVISCID FLOW FIELD ABOUT BLUNT BODIES

By Ronald H. Aungier*

Air Force Weapons Laboratory

SUMMARY

A computational method is presented for exact, direct and unified solutions to the supersonic blunt body problem. An explicit finite-difference scheme for the time-dependent method is developed which uses stabilizing terms of variable magnitude. This insures that the influence of these terms on the solution can be established negligibly small. Major reductions in the computation time and computer storage required for time-dependent solutions is realized by staging the solution in discrete flow field segments. Results for two-dimensional, axisymmetric and three-dimensional flows are compared with accepted numerical solutions and experimental data.

14

INTRODUCTION

This paper describes recent advances at the Air Force Weapons Laboratory in computational methods for analyzing inviscid compressible flows about blunt-nosed reentry vehicles flying at hypersonic speeds. This work was motivated by a requirement for extremely accurate specifications for the edge boundary conditions used in detailed boundary layer analyses. Boundary layer profiles related to plasma sheath studies are quite sensitive to these edge conditions. An inviscid flow solution capable of considering entropy layers, bluntness induced pressure gradients, angles of attack and a general class of body shapes is required to accurately assign the boundary layer edge conditions. High performance reentry vehicles experience vehicle shape deformation due to ablation mass loss and boundary layer displacement effects. In addition, small to moderate angles of attack may be present and should be included in the analysis. Available methods of sufficient accuracy for this application are generally restricted to axisymmetric flow and to vehicle shapes defined by conic sections or power law profiles. Also, these methods generally require the matching of 2 or more numerical methods to

* Captain, USAF; now at Research Division, Carrier Corporation, Syracuse, New York

describe the entire mixed subsonic-supersonic flow field. A general, exact (no simplifying assumptions used), direct (body geometry is specified as input), and unified (one numerical method is used for the entire flow field) computational method would greatly simplify realizing this and future objectives in the area of blunt body flow analysis. The time-dependent method has been recognized as holding promise for achieving this general solution capability. However, published results have fallen far short of the method's full potential. Difficulties with numerical accuracy and computer efficiency have repeatedly prevented its application to high performance reentry vehicles of practical length. This paper presents a new differencing scheme and computational procedures which effectively eliminate these obstacles.

SYMBOLS

a	sound speed
g	a general function
K	body curvature
M	Mach number
n	coordinate normal to the body
P	pressure
P_∞	free stream pressure
P_o	pressure at the stagnation point
P_{t_2}	total pressure behind a normal shock
R_N	nose radius for a sphere-cone vehicle
r	radial distance from the vehicle symmetry axis
S	non-dimensional entropy
s	streamwise coordinate
T	time required for achieving an approximate steady state flow
t	time
u	velocity component along the s coordinate

v velocity component along the n coordinate

w velocity component along the ϕ coordinate

z distance along the body symmetry axis

γ ratio of specific heats

ζ transformed coordinate defined by equation (14)

η transformed coordinate defined by equation (13)

θ angle between a tangent to the body surface and the symmetry axis

κ 1-Kn

μ stabilizing term coefficient

μ_o constant controlling the stabilizing term influence on the solution; defined by equation (28)

ξ transformed coordinate defined by equation (12)

ρ density

τ transformed coordinate defined by equation (15)

Φ stabilizing term

ϕ azimuthal angle about the symmetry axis

THE TIME-DEPENDENT METHOD

The time-dependent method employs a finite-difference technique to solve the governing equations in their unsteady form. These equations are hyperbolic in form for both subsonic and supersonic flow. This presents a well posed initial value problem for solution, a much simpler task than solving the steady-state form. A description of the steady flow is achieved in the limit of large times. The difficulties usually encountered in applying boundary conditions at an unknown boundary (the bow shock wave) are eliminated, since the bow shock is free to move as the solution is advanced in time to achieve its steady-state position at large times.

An explicit finite-difference scheme for this set of equations is unconditionally unstable. Von Neumann and Richtmyer (Ref. 1) showed stability can be achieved by adding artificial dissipative terms to the governing equations. Since other differencing schemes developed for this problem have added terms of less physical significance, they are better

referred to as stabilizing terms. Attempts to insure that the influence of these terms on the solution is negligible (i.e., the solution is exact) have been, at best, marginally successful. The questionable validity of the numerical models used in available computational methods for time-dependent solutions has seriously limited the method's effectiveness.

The necessity of solving many equations at many points in space and at many times can tax the capabilities of available computers and make practical reentry analyses prohibitively expensive. Consequently, reported time-dependent solutions have been limited to the subsonic-transonic flow region for blunt body problems, with no known attempts to treat high performance reentry vehicles of practical length with a unified time-dependent method.

THE NUMERICAL METHOD

General Remarks

The numerical method is reported in references 2 and 3 in detail. In the interest of brevity, only the more important aspects of the present method will be discussed here. To date, the present method has been restricted to smooth symmetric body profiles, but in other respects the body shape is arbitrary.

Equations and Coordinates

Figure 1 shows the body oriented coordinate system used for this method. The streamwise coordinate, s, is measured along the body surface from the symmetry axis. The normal coordinate, n, is measured normal to the body surface with n = 0 on the body. The third coordinate is the usual azimuthal angle of a cylindrical coordinate system. It is easily shown that

$$r = \int_0^s \sin\theta \, ds' - n\cos\theta \tag{1}$$

$$z = \int_0^s \cos\theta \, ds' + n\sin\theta \tag{2}$$

where θ is the angle between a tangent to the body and the symmetry axis. Using the body curvature, K, to define

$$\kappa = 1 - Kn \tag{3}$$

the governing equations can be written as follows:

$$\kappa r\rho_t + (r\rho u)_s + (\kappa r\rho v)_n + (\kappa\rho w)_\phi = 0 \tag{4}$$

$$\kappa u_t + uu_s + \kappa vu_n + \frac{\kappa w}{r} u_\phi + \frac{1}{\rho} P_s = \frac{\kappa w^2}{r} \sin\theta + Kuv \tag{5}$$

$$\kappa v_t + uv_s + \kappa vv_n + \frac{\kappa w}{r} v_\phi + \frac{\kappa}{\rho} P_n = -\frac{\kappa w^2}{r} \cos\theta - Ku^2 \tag{6}$$

$$\kappa w_t + uw_s + \kappa vw_n + \frac{\kappa w}{r} w_\phi + \frac{\kappa}{r\rho} P_\phi = \frac{\kappa w}{r} (v\cos\theta - u\sin\theta) \tag{7}$$

$$\kappa S_t + uS_s + \kappa vS_n + \frac{\kappa w}{r} S_\phi = 0 \tag{8}$$

where the subscripts imply partial differentation, ρ is the density, P is the pressure, S is the non-dimensional entropy and u, v, and w are the s, n, and ϕ velocity components, respectively.

The equation of state for a perfect gas is

$$S = \ln(P) - \gamma\ln(\rho) \tag{9}$$

where γ is the ratio of specific heats. Equation (4) is singular when s = 0 and is replaced by

$$\kappa^2\rho_t + 2\kappa(\rho u)_s + (\kappa^2\rho v)_n + (\kappa\rho w)_\phi = 0 \tag{10}$$

when axisymmetric or three-dimensional flows are considered. The simplification of these equations for two-dimensional flows is straightforward. To simplify the finite-difference nodal geometry, transformed coordinates are used in solving the governing equations. If δ is defined by

$$\delta = n_{shock} \tag{11}$$

the transformations used are

$$\xi = s \tag{12}$$

$$\eta = n/\delta \tag{13}$$

$$\zeta = \phi \tag{14}$$

$$\tau = t \tag{15}$$

Then, the relevant partial derivatives are given by

$$\frac{\partial}{\partial s} \rightarrow \frac{\partial}{\partial \xi} - \frac{\eta}{\delta}\frac{\partial \delta}{\partial s}\frac{\partial}{\partial \eta} \tag{16}$$

$$\frac{\partial}{\partial n} \rightarrow \frac{1}{\delta}\frac{\partial}{\partial \eta} \tag{17}$$

$$\frac{\partial}{\partial \phi} \rightarrow \frac{\partial}{\partial \zeta} - \frac{\eta}{\delta}\frac{\partial \delta}{\partial \phi}\frac{\partial}{\partial \eta} \tag{18}$$

$$\frac{\partial}{\partial t} \rightarrow \frac{\partial}{\partial \tau} - \frac{\eta}{\delta}\frac{\partial \delta}{\partial t}\frac{\partial}{\partial \eta} \tag{19}$$

Differencing Scheme At Interior Points

At interior points (points not on a boundary) central difference approximations are used to represent the spatial partial derivatives, and forward difference approximations are used to represent the partial derivatives in time. Stability is achieved by adding terms of the form

$$\Phi = \mu^{(\xi)} g_{\xi\xi} + \mu^{(\eta)} g_{\eta\eta} + \mu^{(\zeta)} g_{\zeta\zeta} \tag{20}$$

in the governing equations, where g refers to the flow parameter being advanced in time (e.g., ρ in equation (4)). The second derivatives are represented by second central difference approximations. The coefficients $\mu^{(\xi)}$, $\mu^{(\eta)}$, and $\mu^{(\zeta)}$ were selected from a stability analysis of a one-dimensional linearized momentum equation. This lengthy analysis will be omitted here in the interest of brevity (see Ref. 2) and the results given without proof

$$\mu^{(\xi)} = (|u|+a)^2 \Delta\tau \tag{21}$$

$$\mu^{(\eta)} = (|v|+a)^2 \Delta\tau \tag{22}$$

$$\mu^{(\zeta)} = (|w|+a)^2 \Delta\tau \tag{23}$$

Here, a is the local sound speed. The stability analysis predicts that equations (21) to (23) introduce the minimum value of Φ allowed by stability requirements. This prediction has been verified by numerical experimentation. The Courant-Friedrichs-Lewy stability criterion (ref. 4) requires

$$\Delta\tau \leq \frac{\Delta}{a(M+1)} \tag{24}$$

where Δ is the smallest finite-difference mesh width and M is the Mach number (as stated here, the criterion is conservative, i.e., it can be applied locally). However, the time step can be reduced as much as desired

to reduce the magnitudes of the stabilizing terms. Three features of this differencing scheme distinguish it from others reported. First, the stabilizing terms are independent of the nodal geometry used (thus, variable mesh sizes are easily treated). Second, the stabilizing terms are minimized locally at each point and on each time step consistent with stability requirements. Third, the influence of the stabilizing terms can be reduced as much as desired by reducing the magnitude of the time step used. The differencing scheme, therefore, can generate exact solutions, where exact is used in a practical sense (i.e., the influence of the stabilizing terms can be made as small as is necessary to satisfy the investigator). Since the stabilizing term effects vary with Mach number as well as with time step, a parameter, μ_o, is specified as input.

$$\mu_o = a\Delta\tau(M+1)^2/M \tag{25}$$

For constant μ_o, the same stabilizing term influence is experienced at all Mach numbers.

Differencing Scheme At Boundary Points

A proper finite-difference approximation for boundary points has not been reported. Clearly, the scheme developed for interior points is not applicable since central difference approximations across the boundary can not be generated without introducing questionable assumptions. Consequently, the stability analysis was accomplished again for forward and backward difference approximations. It was found that this differencing scheme would often be stable with no stabilizing terms required. Of interest here, are the cases where one of the velocity components vanishes or is supersonic and positive. Thus, at points on the body, partial derivatives in η are approximated with forward differences and $g_{\eta\eta}$ is assumed to vanish (note: this is not a physical assumption, rather it involves omitting a fictitious term). Similar procedures are used at points where a velocity component vanishes by symmetry arguments. At the downstream boundary, partial derivatives in ξ are represented by backward differences and $g_{\xi\xi}$ is assumed to vanish. This is not a new result, merely formalizing the usual approach of linearly extrapolating the solution at the downstream boundary. However, it points out the necessity of having the relevant velocity component supersonic rather than merely requiring the flow be supersonic (e.g., in reference 5, at small cone angles the radial velocity component may well be subsonic when the flow is supersonic). Thus, at boundary points, backward or forward differences are used along the coordinate normal to the boundary and the related second derivatives are assumed to vanish in Φ. With this exception, the differencing scheme used for interior points is also applied at boundary points. The development of a proper finite-difference scheme for boundary points when body oriented coordinates are used was the major reason for selecting this type of coordinate system.

Shock Point Computations

Computations at points on the shock wave are accomplished with a quasi-one-dimensional method of characteristics scheme developed by Moretti and Abbett (Ref. 5). This method assumes that velocity components and derivatives parallel to the shock can be treated as constant weighting functions, while the velocity component and derivatives normal to the shock are the relevant parameters to determine the shock behavior. Except for the constant weighting functions, the method is very similar to Godunov's scheme (Ref. 6) as described by Masson (Ref. 7). Predictions from the usual shock jump relations and the compatibility relation are generated. An iteration procedure is used to achieve acceptable agreement between these predictions by changing the shock velocity. Since the method has been described in detail in many references, it will not be discussed further in this paper (see, for example, Refs. 2, 3, 5 and 8).

Segmented Flow Solutions

An impressive improvement in computer efficiency can be realized by a simple computational approach developed in this study. Figure 2 shows a typical blunt body problem. If a physical time $\tau = T$ is required to achieve an acceptable approximate steady state solution, segment I, of 1/3 the total streamwise length, will require a physical time $\tau = T/3$. Since only 1/3 as many nodes must be considered, the computer time required to treat segment I is 1/6 of that required for the entire flow field. The solution at the downstream boundary of segment I is then used as constant starting line data for segment II and, similarly, segment III is started with data from segment II. It is easily seen that by using 3 segments the computer time required is reduced by 1/3. Also, the computer storage required is reduced by 1/3 since only data at points in a single segment need be stored in the computer at any one time. Thus, the computation time and computer storage required are reduced by a factor roughly equal to the number of segments considered. In practice, the advantage of this approach is even greater than indicated by this simple example. The maximum computer storage required for any problem is established by the first segment, which must terminate in supersonic flow (the length of other segments is arbitrary). Also, the nodal spacings used can be established locally for each segment based on accuracy requirements. Thus, while 5 nodes across the shock layer is usually adequate for the first segment, well back on the afterbody 20 to 40 may be required. Similarly, fine nodal spacing in the streamwise direction is usually required in segment I, while very coarse spacings are usually adequate well downstream. With this approach, the usual computer limitations encountered in time-dependent methods (e.g., see Ref. 8) are avoided.

RESULTS

Stabilizing Term Influence

Figure 3 shows the error in predicted stagnation point pressure, P_o, relative to the known total pressure behind a normal shock, P_{t_2}, as a function of μ_o. The error increases proportional to μ_o as expected until the Courant-Friedrichs-Lewy (CFL) limit is reached, where the computer code holds $\Delta\tau$ constant. The number of iterations required to achieve a steady flow is seen to vary inversely with μ_o. In other results presented in this paper, a value of $\mu_o = 0.04$ is used. For this value, the error shown in figure 3 is less than 0.53% while the number of iterations required is not excessive.

Blunt Body Results

Figure 4 shows predicted shock shapes for axisymmetric flows about a sphere at Mach numbers ranging from 1.5 to 500. Unlike many computational methods for this problem, no problems are encountered at either very low or very high Mach numbers. Figure 5 shows surface pressure distributions predicted by the present method, other time-dependent methods and the method of integral relations. Belotserkovskii's integral relations solutions (ref. 9, data taken from refs. 7 and 10) are probably the most accurate blunt body results available and, thus, have been selected as a standard for comparison. It is seen that the time-dependent method of Masson, the present method and integral relations results all show excellent agreement. The time-dependent solutions of Godunov et al (ref. 6) and Moretti and Abbett (ref. 5) both exhibit serious local disagreements with the other solutions. Figure 6 shows a comparison of surface density distributions predicted by the present method, Masson's method and integral relations. While the present method and integral relations still show excellent agreement, it is seen that Masson's method is seriously in error, since with the known constant surface entropy Masson's predicted surface densities are not consistent with the pressure predictions in figure 5 (a fact noted by Masson). Thus, it appears the present method is the most accurate of the time-dependent methods shown (which, in the author's opinion, are the best reported to date). Figure 7 shows a comparison of predicted shock shapes from the present method and integral relations for two-dimensional flow over a circular cylinder. Figure 8 shows a comparison of predicted surface pressures from the same two methods for the same case. It is seen that excellent agreement between the methods is realized.

Afterbody Flows

The inverse scheme-method of characteristics solution developed by Inouye, Rakich and Lomax (Ref. 11) at NASA-Ames is generally regarded as one of the more accurate computational methods available. While inverse schemes are always questionable when applied to a specific body shape, this inverse scheme has been shown to be very accurate for the body shapes to be considered in this paper. Figures 9, 10 and 11 show comparisons of surface pressure predictions from the present method and the NASA solution for sphere-cones with various cone half-angles at Mach numbers of 4, 6 and 10, respectively. It is seen that excellent agreement is realized in all cases. Figure 12 shows a comparison of predicted surface pressure from these two methods for flow over ellipsoid-cylinders at Mach 6. Again, it is seen that agreement is excellent.

A Practical Reentry Problem

While previous solutions presented have provided a useful test of the accuracy of the present method, they are of little practical use to the aerodynamicist. Figure 13 shows the predicted surface pressure distributions for a sphere-cone with a 10 degree cone half-angle and an axial length of 50 nose radii in a Mach 20 flow as generated by the present method and a version of the NASA-Ames code used at the Air Force Weapons Laboratory (AFWL). It is seen that excellent agreement is realized between these methods. This case was generated in less than 6 minutes on the AFWL CDC 6600 computer with the present method. It is interesting to estimate the computation time that would have been required if the segmented flow approach had not been used. Based on the known computer efficiency of the basic computer code and the smallest nodal spacings required throughout the flow field, it is estimated that this solution would require more than 70 hours on the same computer. It is easy to see why practical reentry solutions generated with a unified time-dependent method have not previously been reported for these high performance reentry vehicle configurations.

Three-dimensional Flows

The improved computer efficiency realized in this study makes it practical to use the time-dependent method for three-dimensional flow problems. Figures 14 and 15 show shock shapes and surface pressure distributions in 3 azimuthal planes for a sphere-cone vehicle flying at a 5 degree angle of attack. The cone half-angle is 15 degrees and the Mach number is 5.25. Experimental surface pressure data from reference 12 are also shown on figure 15. It is seen that the theory and experiment show good agreement, with the theory predicting slightly lower surface pressures than measured. This is consistent with expected boundary layer displacement effects. Surface pressure predictions for the same flow but with angles of attack of 10 and 15 degrees are compared with experimental data on figures 16 and 17, respectively. Again, good agreement between theory and experi-

mental data is realized. Computation times for these cases ranged from 25 to 40 minutes on the AFWL CDC 6600 computer for an axial length of 20 nose radii.

CONCLUSIONS

An exact, direct and unified computational method for the supersonic blunt body problem has been developed. The explicit differencing scheme presented uses stabilizing terms of variable magnitude. The magnitude of these terms is completely decoupled from the finite-difference nodal geometry used. This facilitates using the differencing scheme with variable nodal spacings. The stabilizing terms are minimized at all computational nodes based on local flow properties, consistent with stability requirements. Stable computations at body points are realized using standard finite-difference approximations, with no additional assumptions. A segmented flow solution procedure is introduced which greatly enhances the computer efficiency obtainable with a time-dependent method. The method has been used to treat practical high performance reentry vehicle flows. Good agreement with accepted numerical solutions and experimental data has been achieved in all cases. References 2 and 3 provide computer codes to apply the method to two-dimensional, axisymmetric and three-dimensional blunt body flows for a general class of symmetric body geometries.

REFERENCES

1. Von Neumann, J., and Richtmyer, R. D., "A Method for the Numerical Calculation of Hydrodynamic Shocks," J. Appl. Phys. 21, pp. 232-237 (1950).

2. Aungier, R. H., "A Computational Method for Exact, Direct and Unified Solutions For Axisymmetric Flow Over Blunt Bodies of Arbitrary Shape (Program BLUNT)," Air Force Weapons Laboratory Technical Report, AFWL-TR-70-16, July 1970.

3. Aungier, R. H., "A Computational Method for Two-Dimensional, Axisymmetric, and Three-Dimensional Blunt Body Flows (Program ATTACK)," Air Force Weapons Laboratory Technical Report, AFWL-TR-70-124.

4. Courant, R., Friedrichs, K. O., and Lewy, H., "Ueber die partiellen Differenzengleichungen der mathematischen Physik," Math. Ann. 100, 32 (1928).

5. Moretti, G., and Abbett, M., "A Time-dependent Computational Method for Blunt Body Flows," AIAA J. 4, pp. 2136-2141 (1966).

6. Godunov, S. K., Zabrodin, A. V., and Prokopov, G. P., "A Computational Scheme for Two-dimensional Nonstationary Problems of Gasdynamics and of the Flow from a Shock Wave Approaching a Stationary State," Zh. Vychislitelnoi Mat. i. Mat. Fiziki 1, pp. 1020-1050 (1961).

7. Masson, B. S., "Two Dimensional Flow Field Calculations by the Godunov Method," Aeronutronic Report No. U-4137 (1967).

8. Moretti, G., and Bleich, G., "Three Dimensional Flow Around Blunt Bodies," AIAA J. 5, pp. 1557-1562 (1967).

9. Belotserkovskii, O. M., "On the Calculation of Flow Past Axisymmetric Bodies with Detached Shock Waves Using An Electronic Computer," J. Appl. Math. Mech. (PMM), 24, pp. 745-755 (1960).

10. Hays, W. D., and Probstein, R. F., "Hypersonic Flow Theory" Vol. I (Academic Press Inc., New York, 1966).

11. Inouye, M., Rakich, J. V., and Lomax, H., "A description of Numerical Methods and Computer Programs For Two-dimensional and Axisymmetric Supersonic Flow Over Blunt-nosed and Flared Bodies," NASA TN D-2970 (1965).

12. Cleary, J. W., "An Experimental and Theoretical Investigation of the Pressure Distribution and Flow Fields of Blunted Cones at Hypersonic Mach Numbers," NASA TN D-2969 (1965).

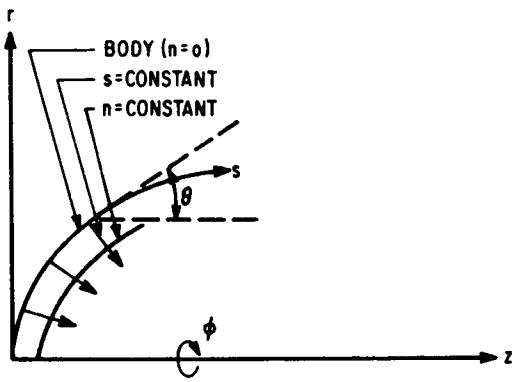

Figure 1.- Body oriented coordinates.

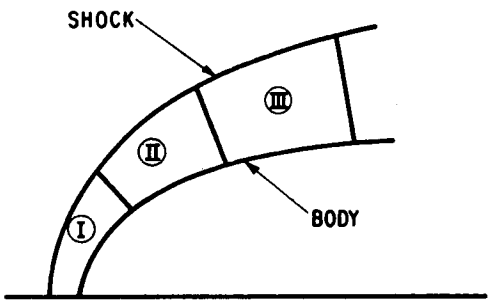

Figure 2.- Segmented solution.

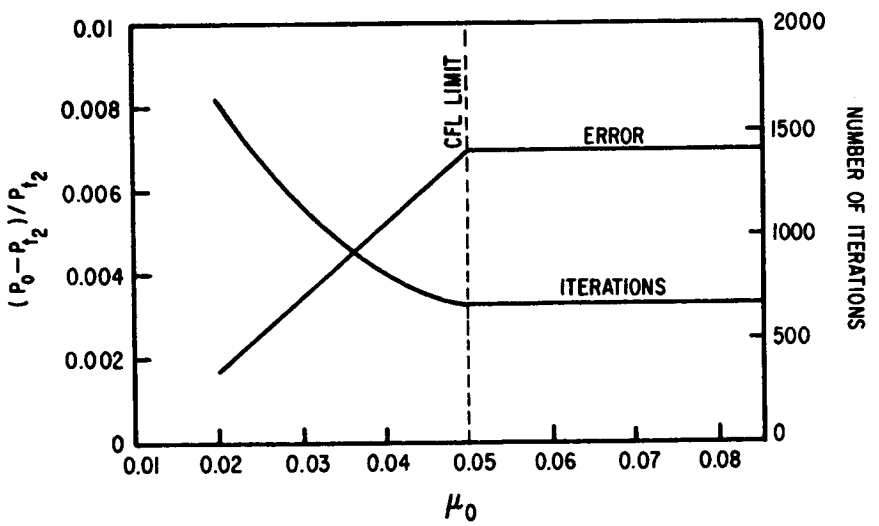

Figure 3.- Investigation of the stabilizing term effects.

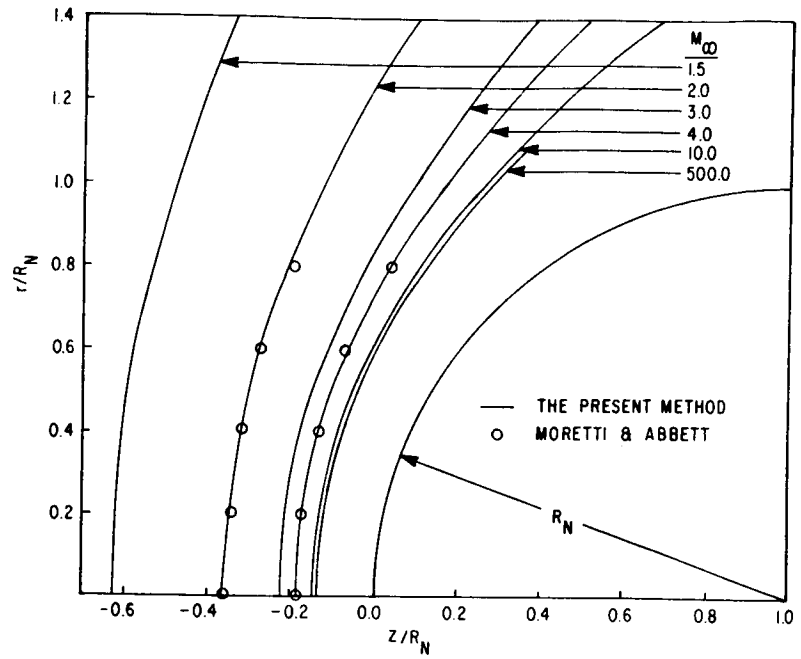

Figure 4.- Shock shapes for flow over a hemisphere at several Mach numbers.

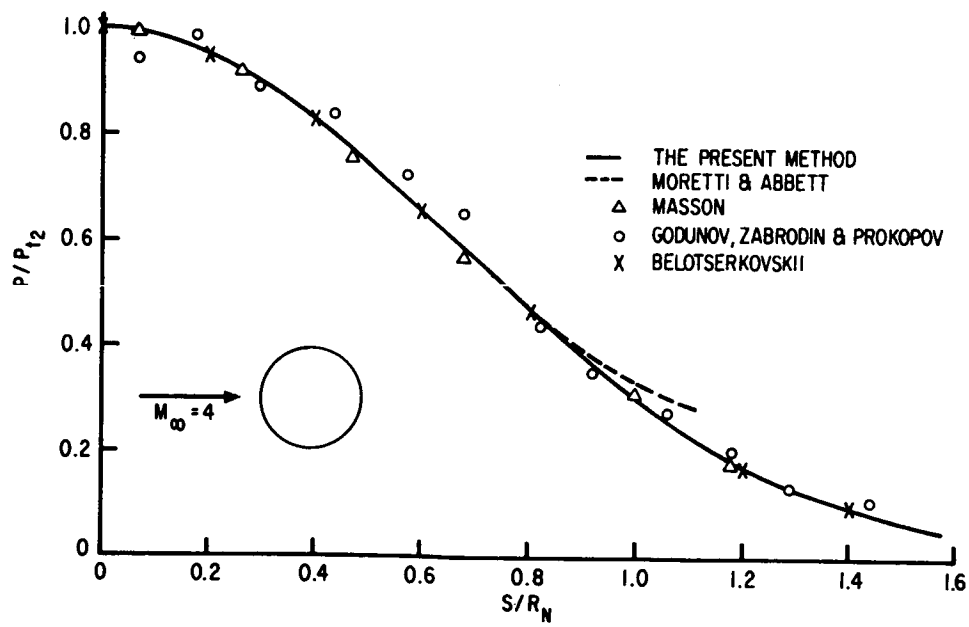

Figure 5.- Surface pressure distribution from time-dependent methods and an integral relations solution.

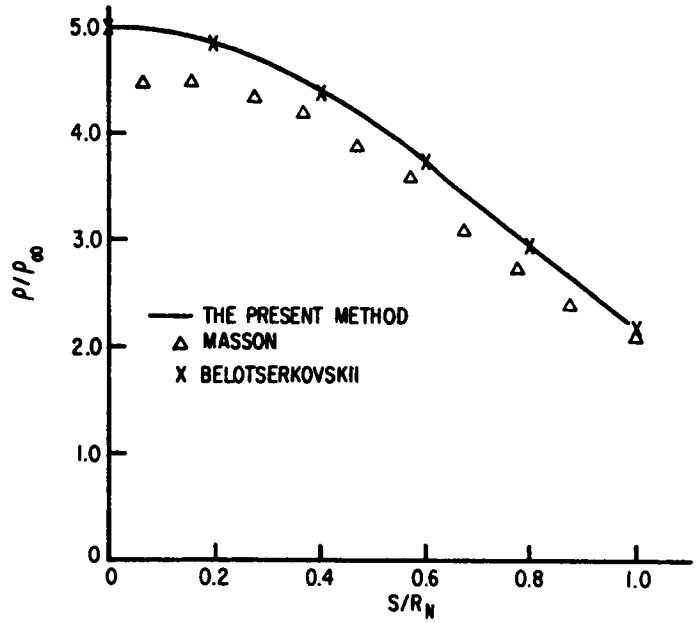

Figure 6.- Surface density distributions for a sphere in Mach 4 flow.

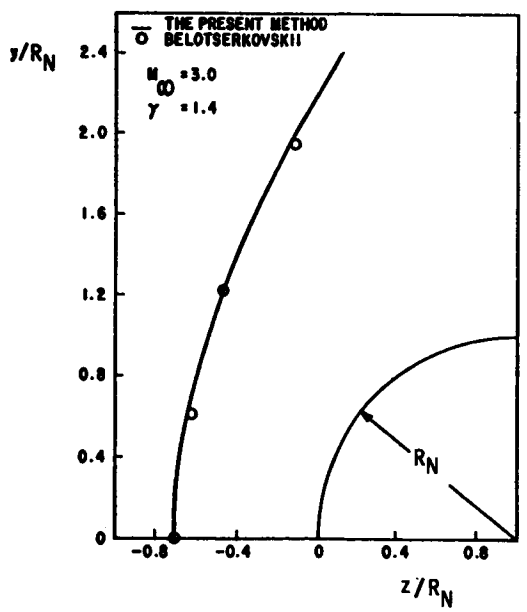

Figure 7.- Shock shape for two-dimensional flow about a circular cylinder.

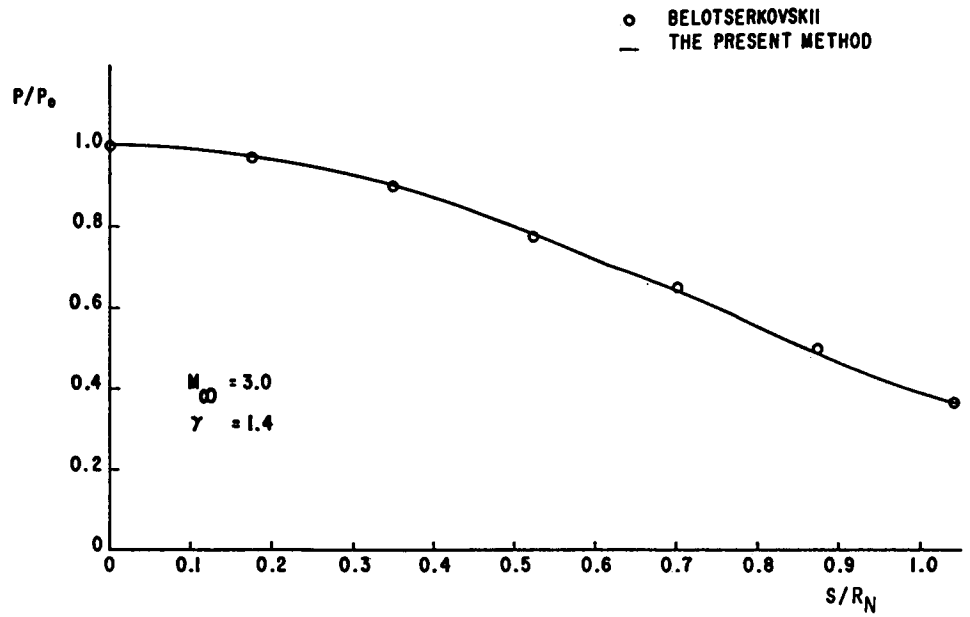

Figure 8.- Surface pressure distribution for two-dimensional flow about a circular cylinder.

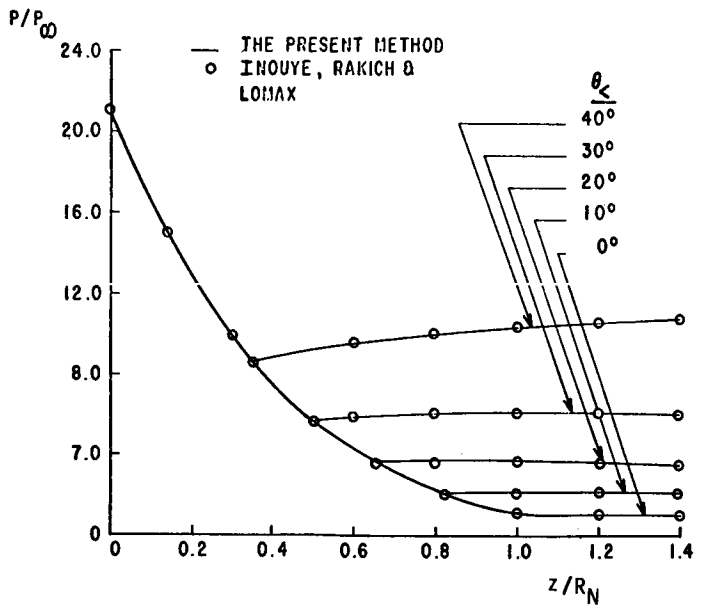

Figure 9.- Surface pressure distribution for sphere-cones in Mach 4 flow.

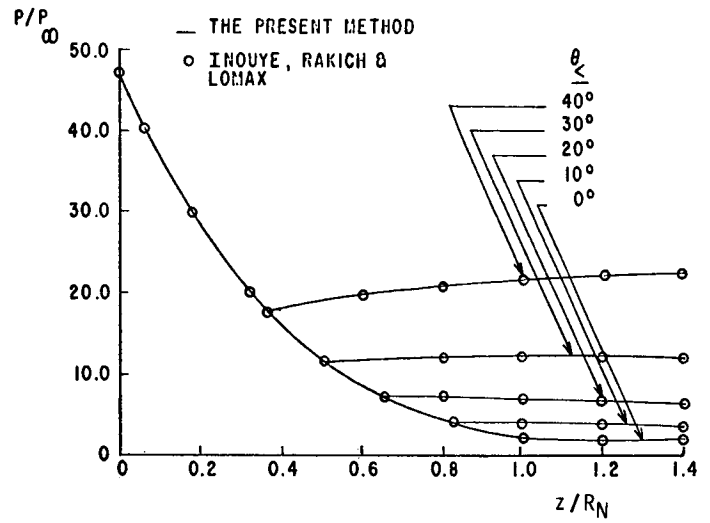

Figure 10.- Surface pressure distribution for sphere-cones in Mach 6 flow.

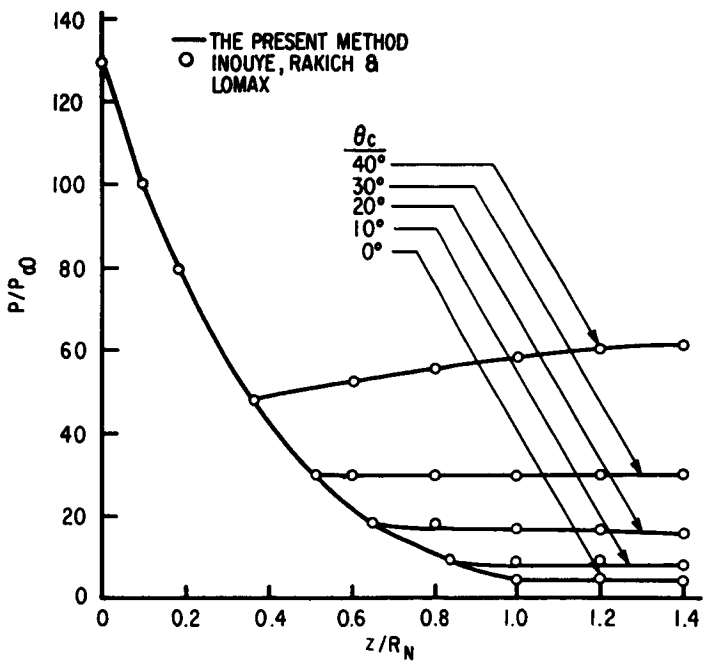

Figure 11.- Surface pressure distribution for sphere-cones in Mach 10 flow.

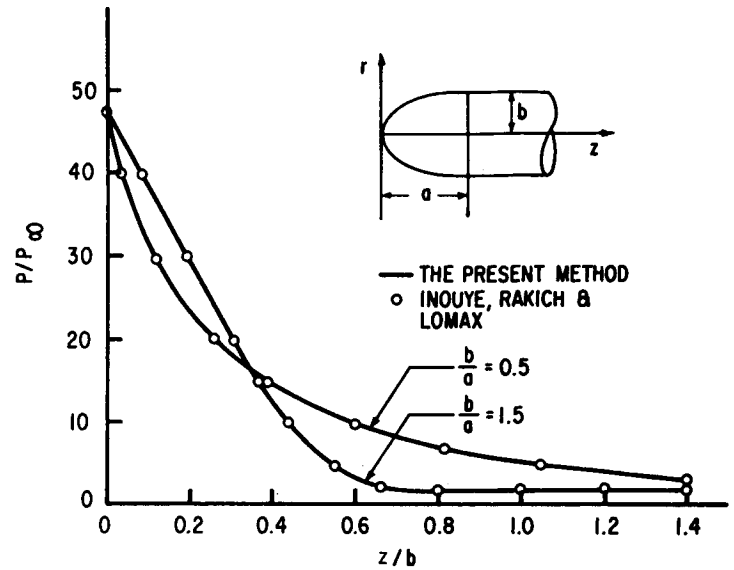

Figure 12.- Surface pressure distribution for ellipsoid-cylinders in Mach 6 flow.

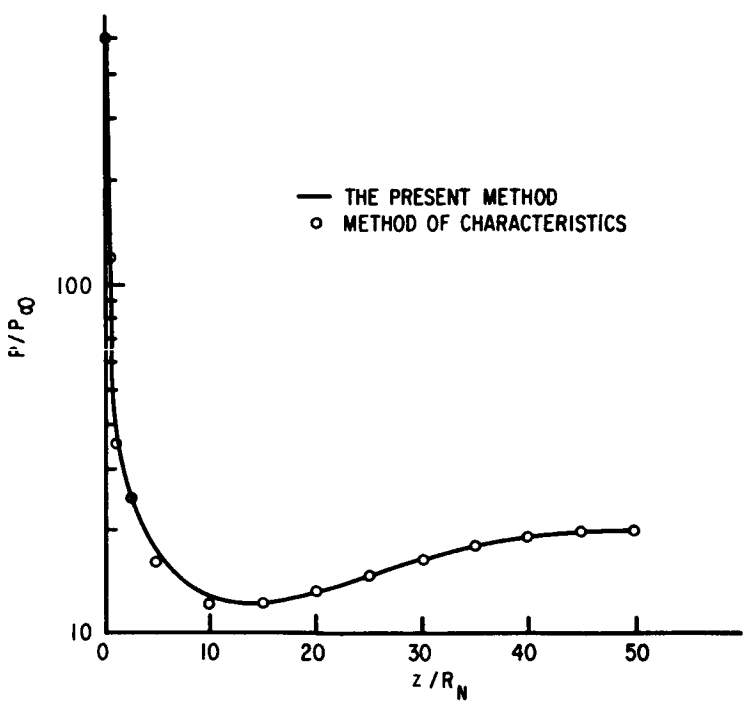

Figure 13.- Surface pressure distribution for a 10^{o} sphere-cone in Mach 20 flow.

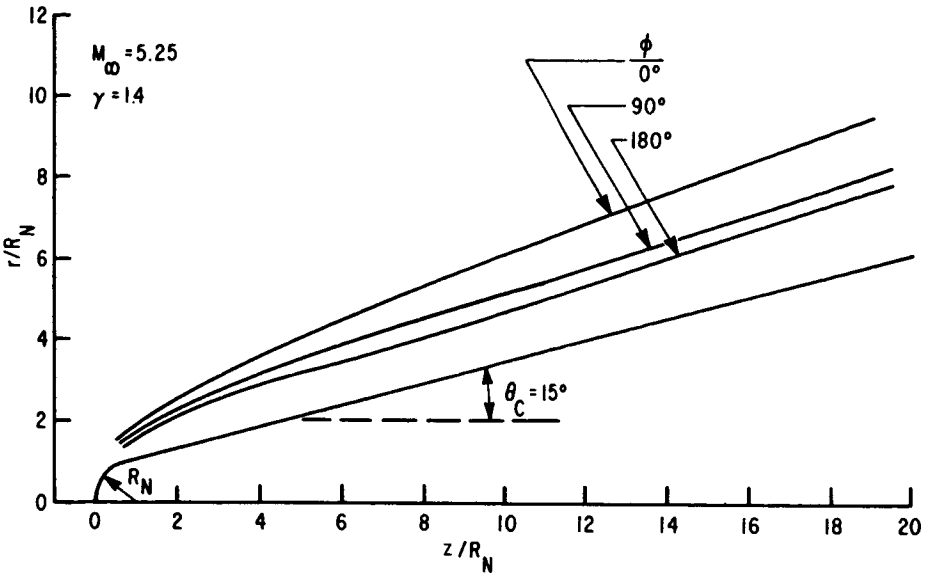

Figure 14.- Shock profiles for a sphere-cone at 5° angle of attack.

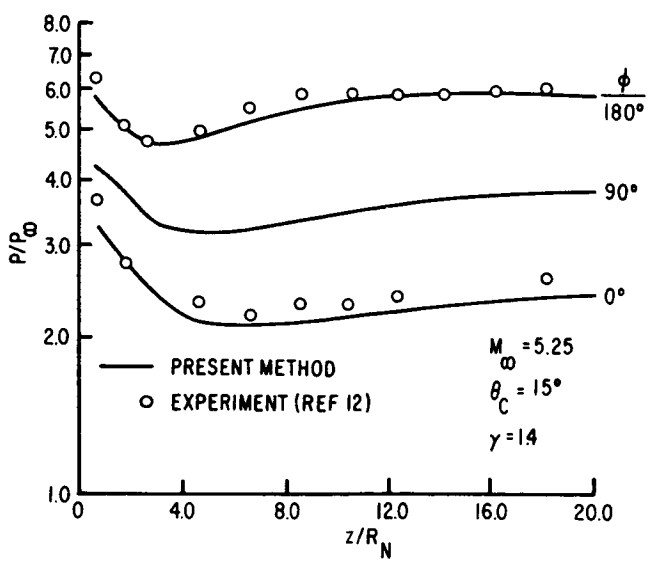

Figure 15.- Surface pressure distribution on a sphere-cone at 5° angle of attack.

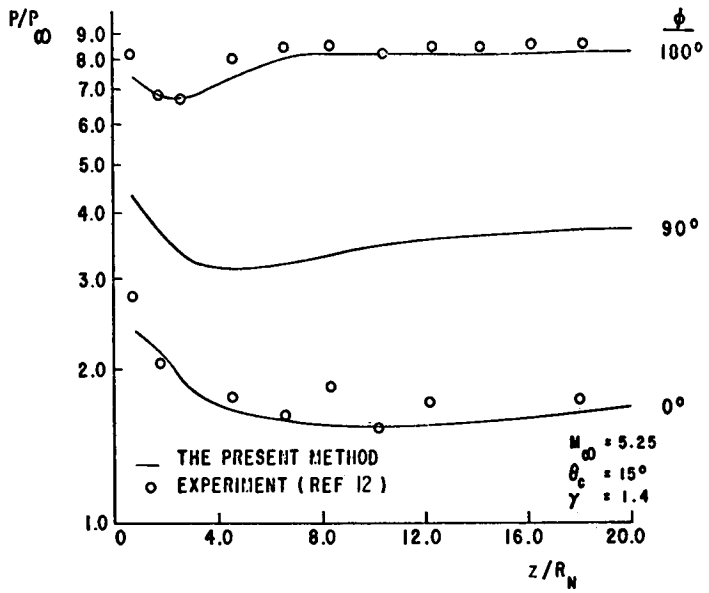

Figure 16.- Surface pressure distribution on a sphere-cone at 10^{o} angle of attack.

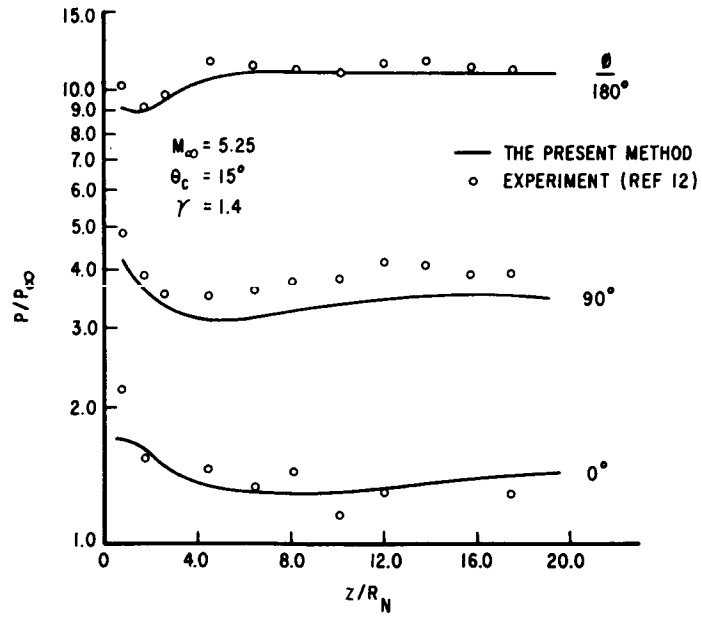

Figure 17.- Surface pressure distribution on a sphere-cone at 15^{o} angle of attack.

LABORATORY MEASUREMENTS OF ELECTRON DENSITY AND ELECTRON TEMPERATURE WITH RAM FLIGHT PROBES * **

By Michael G. Dunn

Cornell Aeronautical Laboratory, Inc.
Buffalo, New York 14221

ABSTRACT

Two types of RAM flight probes (constant bias-voltage wires located perpendicular to the flow direction and swept-voltage wires aligned with the flow direction) have been used to measure electron density and electron temperature in the expanding flow of a short-duration reflected-shock tunnel. Experiments were performed in the inviscid flow with both probes and in the nozzle-wall boundary layer with the constant bias-voltage probe. The electron density in these flows was inferred from the collected ion current and was independently measured using thin-wire Langmuir probes operating in the free-molecular flow regime. Microwave interferometers were used immediately upstream of the probe locations in order to measure the averaged free-stream electron density. The test gas used in these experiments was nitrogen at an equilibrium reservoir condition of 7200°K and 17.1 atm. The constant-voltage probe was used at three axial locations in the inviscid nozzle flow in order to investigate the practical limits of the data-interpretation theory suggested by Smetana. For free-molecular flow, for which the theory was intended, the electron densities deduced agree well with other independent measurements. When the wires were operated in a moderately transition-flow regime (ratio of probe radius to ion-neutral mean free path of approximately 2.8) the free-molecular flow theory underpredicted the electron densities by approximately 20 to 40 per cent. The constant bias-voltage probe was also used to obtain the electron-density distribution in the nozzle-wall boundary layer. The distributions of electron density and electron temperature were independently measured at the same nozzle location using voltage-swept thin-wire probes. The agreement between the electron-density distributions obtained with these two probing techniques was found to be good.

15

---

*This paper is based on research sponsored by the National Aeronautics and Space Administration, Langley Research Center, under Contract NAS 1-9627.

**Editor's note: The designations RAM C and RAM C-C used herein should be RAM C-II and RAM C-III, respectively.

INTRODUCTION

The National Aeronautics and Space Administration has for several years conducted in-flight radio attenuation measurements (RAM) in order to improve understanding of the causes and methods of predicting[1, 2] or preventing[3, 4] the radio-signal degradation during earth entry of a space vehicle. In the last few years, electrostatic probes projecting from the spacecraft into the boundary-layer and inviscid flow have been flown in an attempt to measure in-flight electron-density distributions.[5] On-board diagnostic antennas[6, 7], reflectometers[8] and VHF antennas[9] have also been used to obtain information about the surrounding plasma. Prior to flying the diagnostic antennas, measurements of the admittance of the RAM C and RAM C-C antennas were performed[10] in a shock-tube facility. Such measurements can be very helpful in correctly interpreting the flight data.

The use of electrostatic probes to measure the electron density in the plasma layer of an entering spacecraft has been extensively discussed[11, 12]. Smetana[13] developed a technique for obtaining electron densities from the ion current collected by constant-voltage wires located in a two-dimensional rarefied plasma stream. This theory was used by Scharfman[11, 12] in reducing probe data obtained in an inviscid shock-tube flow to demonstrate the applicability of the theory to within a factor of ± 2 for the RAM C-I probe for conditions at which the flow was free molecular with respect to the wire diameter. It was difficult to investigate the probe operation in a boundary-layer flow in this facility because the boundary layer was too thin for conditions at which sufficient uniform test flow could be obtained.

The purpose of this paper is to describe laboratory measurements of electron density obtained in the inviscid and boundary-layer flow of a conical nozzle using the RAM C-I constant bias-voltage probe and measurements of electron density and electron temperature obtained in the inviscid flow using the RAM C-C voltage-swept thin-wire probes. An important difference between the experiments discussed in this paper and those previously conducted[11, 12] is that relatively thick boundary layers with electron temperatures significantly greater than the heavy-particle translational temperatures can be obtained on the sidewall of the nozzle. Both the previous shock-tube experiments and the present nozzle experiments contribute to establishing confidence in the interpretation of the flight data obtained with the electrostatic probes.

EXPERIMENTAL APPARATUS AND TECHNIQUE

A pressure-driven shock tube was used to produce a reservoir of high-temperature nitrogen which was subsequently expanded in a conical nozzle constructed of Fiberglas as shown in Fig. 1. The test gas used in these experiments was UPC nitrogen supplied by Air Products and Chemicals, Inc. A chemical analysis of the gas indicated the following: oxygen less than 0.5 ppm, total hydrocarbons less than 1 ppm, and water less than 0.15 ppm.

The shock tube was purged with the test gas to approximately 5 torr just prior to each run. A detailed discussion of the nozzle starting process, uniform-flow duration, and boundary-layer growth has been previously presented.[14, 15] The dominant chemical species at the nozzle measuring stations were calculated[16] to be N_2, N and N^+.

The RAM C-I electrostatic probe consists of eight iridium wires with a length of approximately 0.180 inches and a diameter of approximately 0.009 inches. The wires are supported on a wedge-shaped dielectric material with the center to center separation distance between adjacent wires of approximately 0.4 inches. The wires were located in the nozzle so that their length was perpendicular to the velocity vector. These wires were operated in the inviscid flow at axial locations of 14.5, 32.5 and 42.5 inches from the throat and in the boundary layer at 34.5 inches from the throat. The probe voltage was maintained constant at -5 volts relative to the side collectors.

At the nozzle locations noted above, voltage-swept thin-wire probes aligned with the flow direction were used to obtain an independent measurement of the electron density and electron temperature. The ion-current portion of the probe characteristic was used to infer the electron density. The experimental procedure used to obtain the Langmuir probe data in this nitrogen plasma has been described in detail in previous papers.[16, 17]

The RAM C-C flight probe consists of four lengths of iridium wire with diameter and length of approximately 0.0047 inches and 0.41 inches, respectively. These wires were mounted in a wedge-shaped dielectric material similar to the RAM C-I probe, but in this case the wires were oriented parallel to the flow direction. In the present experiments, the voltage on these probes was swept from -5 to +2 volts in approximately 80 μ sec, which is slow enough to avoid transient effects.[18] In some cases the voltage ramp was referenced to tunnel ground, and in other cases it was referenced to the side collectors. The results were insensitive to the voltage reference. However, the inferred electron density and electron temperature were found to be very sensitive to probe contamination as will be discussed later.

During all of the experiments noted above an independent measurement of the integrated free-stream electron density was obtained just upstream of the probe stations using microwave interferometers operating at frequencies of either 35 or 17 GHz.

DISCUSSION OF CONSTANT BIAS-VOLTAGE PROBE RESULTS IN INVISCID FLOW

It was noted above that the RAM C-I probe was used in the inviscid flow at axial locations of 14.5, 32.5 and 42.5 inches. Figure 2 presents the relative magnitudes of the mean free paths $\lambda_{i\text{-}n}$, $\lambda_{n\text{-}n}$, $\lambda_{e\text{-}n}$, $\lambda_{i\text{-}i}$, and $\lambda_{e\text{-}e}$ as a function of inviscid area ratio. These values were calculated using the

expressions summarized by Sonin[19] and the previously reported nozzle-flow properties.[16] For the purpose of estimating mean free paths, the electron temperature can be assumed to be equal to the heavy-particle translational temperature from the reservoir down to 3500°K at which point it can be considered to freeze. Measuring stations at 12.5, 32.5 and 42.5 inches are located on Fig. 2. Also included in Fig. 2 is the relative magnitude of the various probe radii used, i.e., 0.002 and 0.0045 inches. At all of the measuring stations the electron mean free paths are large compared to the probe radius. Figure 2 further shows that at the 14.5-inch measuring station the RAM C-I wire diameter is sufficiently large that interpretation of data using free-molecule theory should not provide the correct electron densities because current collection should be inhibited by the relatively small values of $\lambda_{i\text{-}n}$ and $\lambda_{n\text{-}n}$. At the 32.5-and 42.5-inch stations the 0.009-inch diameter probes should be in free-molecular flow. It was therefore decided to operate the RAM C-I probe at 32.5 and 42.5 inches from the throat to confirm the data reduction technique, and at 14.5 inches to investigate the influence of collisions on the number density deduced using the free-molecular flow theory.

Figure 3 illustrates typical RAM C-I probe and microwave-interferometer data records obtained in the inviscid portion of an expanding nitrogen plasma at 32.5 inches from the throat. Figures 3(a) and (b) are the probe outputs for wires 4, 5, 7, and 8 (see Fig. 4 for relative location) obtained across a 1000-ohm resistor with a constant bias voltage of -5 volts relative to the probe side collectors. The test-flow period is delineated on the data records. The nozzle starting process[14] is also evident on these data records. Figure 3(c) is the 17 GHz microwave-interferometer record obtained one inch upstream of the electrostatic probes. The electron density measured with this interferometer is used as the reference with which the number density calculated from the probe current is compared.

Before calculating the number density from the probe data it is helpful to know the local electron temperature. These temperature measurements were performed[16] in previous experiments and were repeated here for verification. As shown in Fig. 5 of Ref 16 an average value of 3500°K is representative of the plasma at the 32.5-and 42.5-inch locations. The corresponding heavy-particle translational temperature calculated for these stations is in the range 500 to 600°K. It should be noted that the electron densities obtained from the theory are a weak function of temperature. That is, if 500°K were used as the electron temperature instead of 3500°K, then the electron density would be overpredicted by approximately 15 to 20 per cent which is within the experimental scatter presented in Figs. 4 and 5. From the viewpoint of flight-data analysis this insensitivity is important because it suggests that knowledge of T_e is not essential for reduction of the RAM C-I probe data. It should be emphasized that this observation is not true when obtaining electron densities from voltage-swept probes aligned with the flow since in this case the number density is approximately proportional to the square root of the electron temperature. The RAM C-I data analysis procedure has been discussed in detail elsewhere[3, 11, 12] and will not be repeated here.

Figures 4 and 5 present the ratio of the number density deduced from the probe to that obtained from the microwave interferometer with the probe located in the inviscid flow at 32.5 and at 42.5 inches from the throat, respectively. Boundary-layer measurements were previously performed[15] at these stations for similar reflected-shock reservoir conditions but with air as the test gas instead of nitrogen. The boundary-layer thicknesses should not be significantly different for these two gases. At the nozzle stations of interest here the width of the uniform inviscid flow is approximately 21 to 24 inches which is considerably larger than the 3.53-inch width of the RAM C-I probe.

At each location the experiment was repeated approximately 12 to 14 times as indicated by the separate symbols. The centerline of the wedge leading edge was located on the nozzle centerline. Figures 4 and 5 illustrate that for the majority of the measurements the ratio was in the range from 0.80 to 1 20. Part of this scatter is due to the slight nonuniformity of the plasma as illustrated by Fig. 3(c) and part is due to the accuracy with which the data records shown in Figs. 3(a) to 3(c) can be read. On the basis of this comparison it was concluded that the theory predicts the correct electron density when used in the flow regime for which it was intended.

After completing the electrostatic-probe measurements in the free-molecular-flow regime, the probe was moved to a location 14.5 inches from the nozzle throat (where the uniform inviscid-flow width was approximately 5 inches) and the experiment was repeated. From Fig. 2 one sees that at this location both $\lambda_{n\text{-}n}$ and $\lambda_{i\text{-}n}$ were less than the wire radius. The ratio of the probe radius to this ion-neutral mean free path was approximately 2.8. Since the probes were in a transition-flow regime, interpretation of the collected-current data in terms of Smetana's free-molecular flow theory should not be expected to give the correct results. However, this theory was employed to deduce the number densities in order to qualitatively evaluate the sensitivity of the results to collisions. The results of these measurements are presented in Fig. 6 and illustrate that the probe-deduced number densities were approximately 0.6 to 0.9 of the microwave-interferometer values. The lower number densities measured by probes #1 and #8 at the extremities of the 3.53-inch wide probe suggest that the electron density may vary by approximately 10 to 15 per cent across the 5-inch wide inviscid core. However, this variation is not important for the purposes of this study since the remaining data suggest that if the probe is operated in a transition flow, then the number densities obtained in the conventional manner will be somewhat less than actual.

The influence of collisions on the inferred number density discussed above is considerably less than that obtained in previous work by Weissman, et al.[20] These authors performed experiments under conditions for which the ratio of the probe radius to ion-neutral mean free path was the same as experienced here but they found that the inferred number density was approximately 0.05 of the microwave interferometer values. The reason for this difference in results is not clear at the present time.

A simple analysis has been published by Talbot and Chou[21] that has been used successfully[17] to correct thin-wire data (aligned with the flow direction) for collisional effects. The analysis is a scheme for interpolating

between the free-molecular theory of Laframboise[22] and the collision dominated results of Shulz and Brown.[23] The technique of Talbot and Chou in its present form is not applicable to the RAM C-I geometry but it would be helpful for extending the altitude range of the probe data if such a correction technique could be found. A brief but unsuccessful literature search was made for an appropriate correction technique.

DISCUSSION OF CONSTANT BIAS-VOLTAGE PROBE RESULTS IN BOUNDARY-LAYER FLOW

The RAM C-I probe was also used to obtain the electron-density distribution in the nozzle-wall boundary layer at 34.5 inches from the nozzle throat. The electron-temperature distribution and an independent measurement of the electron-density distribution were obtained using voltage-swept thin-wire Langmuir probes. Detailed boundary-layer velocity and density distributions had previously been performed[15] at this nozzle location (using air as the test gas) and the results suggested that the wire probes should be in a free-molecular-flow regime. The velocity distribution from Ref 15 was used in reducing the probe data because of the similarity in test conditions. The measured electron temperatures presented in Fig. 7 were also utilized. The boundary-layer thickness (δ) and displacement thickness (δ^*) noted on Figs. 7 and 8 were calculated using the method given by Burke and Wallace[24] for a turbulent boundary layer. The boundary layer and displacement thicknesses calculated in this manner have been shown[15] to be in good agreement with experimental data for reflected-shock reservoir conditions similar to those used here but with air as the test gas. Calculations indicate that the nozzle-wall boundary-layer growth for nitrogen should be very similar to what it was for air.

The temperature results presented in Fig. 7 suggest that the electron temperature decreases as the nozzle wall is approached. The scatter in the data is approximately + 15 to 20 per cent which is somewhat greater than previously experienced (+ 10 per cent) with the thin-wire probes when they were used in the inviscid-flow environment.

The electron-density distribution measured in the wall boundary layer is presented in Fig. 8. The results obtained with the RAM C-I probe are shown to be in good agreement with the voltage-swept Langmuir probe measurements. As previously mentioned, these latter number densities were obtained from the ion-current portion of the current-voltage characteristic. Typical data records for these probes and the interpretation method has been previously presented.[16, 25] The scatter in the thin-wire electron-density measurements is again somewhat greater than previously experienced using the same diagnostic technique in the inviscid flow.

It was noted in Ref 16 that the indicated number density can be greater than the real value when using thin-wire probes in a region where the ratio of probe radius to Debye length becomes less than one. Care was taken in these

experiments to avoid this problem by using relatively large diameter wire (still within constraints of free-molecular flow) in the low-electron-density region of the boundary layer.

Within the accuracy of the experimental data presented in Fig. 8 the electron-density distribution appears to approach the measured free-stream value at approximately 2.25 inches from the wall. As noted, this is in good agreement with the anticipated boundary-layer thickness. Further, the electron-density distribution obtained with the RAM C-I probe appears to be in good agreement with the distribution obtained with the thin-wire probes.

DISCUSSION OF RAM C-C VOLTAGE-SWEPT PROBE DATA IN INVISCID FLOW

The RAM C-C voltage-swept probe was operated in the inviscid flow at 32.5 inches from the nozzle throat. The probe voltage was swept from -5 to +2 volts referenced to either tunnel ground or the side collectors. The electron-density and electron-temperature results were found to be independent of the voltage reference. At this nozzle location the wires were in the free-molecular flow regime (see Fig. 2) and thus the theory of Laframboise[22] was used in the data reduction.

The electron-density and electron-temperature measurements obtained with this probe were found to be in excellent agreement with previous thin-wire measurements at this nozzle location. The electron-density measurements were also in good agreement with simultaneously obtained microwave interferometer values measured one inch upstream of the probes.

In order to obtain reproducible data from the voltage-swept probes it is essential that the surface be free of contaminants. Experience with these probes indicates that when the surface is contaminated, high electron temperatures are indicated. This observation is consistent with that reported in Reference 26. It is normal laboratory procedure to ultrasonically clean each probe immediately prior to each experiment in a dilute solution of sodium hydroxide if the probe is tungsten or a dilute sodium chloride-hydrochloric acid solution if the probe material is iridium. The probe is used for a single run and then discarded. It thus becomes important for the flight application to have some idea of the susceptibility of the flight probes to relatively small contamination levels. For this reason, the probes were operated for three consecutive experiments without cleaning. For each experiment the probe is exposed to the high-temperature test gas and interface gas for a total time of approximately one millisecond. The electron temperature results obtained in these experiments were reproduced with ± 10 per cent which is within the limits of normal experimental scatter. Further use in the absence of cleaning resulted in increases in indicated electron temperatures by a factor of two to four. The identity or quantity of the contaminant responsible for the increased temperatures is not known at the present time.

CONCLUDING REMARKS

The RAM C-I and RAM C-C flight probes have been used to measure electron density and electron temperature in the inviscid and boundary-layer flow of the conical nozzle of a reflected-shock tunnel. Nitrogen was used as the test gas and was expanded from an equilibrium reservoir condition of 7200°K and 17.1 atm.

The electron densities deduced from the current collected by the RAM C-I probe and Smetana's theory were found to be in good agreement with independent measurements when the conditions of the theory were obeyed. The electron densities and electron temperatures measured with the RAM C-C probe were also in good agreement with independent measurements. However, the electron-temperature measurement is sensitive to probe-surface contamination which could be troublesome at some point in the reentry trajectory.

REFERENCES

1. Huber, P. W.; Evans, J. S.; and Schexnayder, C. J.: Comparison of Theoretical and Flight-Measured Ionization in a Blunt Body Reentry Flow Field. AIAA Paper 70-756, Third Fluid and Plasma Dynamics Conference, Los Angeles, California, 28 June - 1 July 1970.

2. Schexnayder, Charles J., Jr.; Evans, John S.; and Huber, Paul W.: Comparison of Theoretical and Experimental Electron Density for RAM C Flights. The Entry Plasma Sheath and Its Effects on Space Vehicle Electromagnetic Systems - Vol. I, NASA SP-252, 1971, pp. 277-303.

3. Akey, N. D.; and Cross, A. E.: Radio Blackout Alleviation and Plasma Diagnostic Results From a 25,000 ft/sec Blunt-Body Reentry. NASA TN D-5615, February 1970.

4. Schroeder, Lyle C.: Flight Measurements at 25 000 Feet Per Second of Blackout Alleviation by Water and Electrophilic Injection. The Entry Plasma Sheath and Its Effects on Space Vehicle Electromagnetic Systems - Vol. II, NASA SP-253, 1971, pp. 77-100.

5. Jones, W. Linwood, Jr.; and Cross, Aubrey E.: Electrostatic Probe Measurements of Plasma Surrounding Three 25 000 Foot Per Second Reentry Flight Experiments. The Entry Plasma Sheath and Its Effects on Space Vehicle Electromagnetic Systems - Vol. I, NASA SP-252, 1971, pp. 109-136.

6. Swift, C. T.; Beck, F. B.; Thomson, J.; and Castellow, S. L., Jr.: RAM C-III S-Band Diagnostic Experiment. The Entry Plasma Sheath and Its Effects on Space Vehicle Electromagnetic Systems - Vol. I, NASA SP-252, 1971, pp. 137-155.

7. Swift, C. T.; Croswell, W. F.; and Evans, J. S.: Diagnosis of Planetary Atmospheres From Effects of Entry Plasma on Antenna Impedance. AIAA 6th Aerospace Sciences Meeting, New York, January 22-24, 1968.

8. Grantham, William L.: Reentry Plasma Measurements Using a Four-Frequency Reflectometer. The Entry Plasma Sheath and Its Effects on Space Vehicles Electromagnetic Systems - Vol. I, NASA SP-252, 1971, pp. 65-107.

9. Croswell, William F.; and Jones, W. Linwood, Jr.: Effects of Reentry Plasma on RAM C-I VHF Telemetry Antennas. The Entry Plasma Sheath and Its Effects on Space Vehicle Electromagnetic Systems - Vol. I, NASA SP-252, 1971, pp. 183-201.

10. Taylor, W. C.: Shock-Tube Measurement of Admittance of RAM C and RAM C-C Diagnostic Antennas. The Entry Plasma Sheath and Its Effects on Space Vehicle Electromagnetic Systems - Vol. I, NASA SP-252, 1971, pp. 157-182.

11. Scharfman, W. E.: The Use of Langmuir Probes to Determine the Electron Density Surrounding Re-entry Vehicles. Final Report Contract NAS 1-3942, Stanford Research Institute, Menlo Park, California, June 1965.

12. Scharfman, W. E.; and Bredfeldt, H. R.: Use of the Langmuir Probe to Determine the Electron Density and Temperature Surrounding Re-entry Vehicles. Final Report Contract NAS1-4872, NASA 66275, Stanford Research Institute, Menlo Park, California, December 1966.

13. Smetana, F. O.: On the Current Collected by a Charged Circular Cylinder Immersed in a Two-Dimensional Rarefied Plasma Stream. Third Symposium on Rarefied Gas Dynamics, 1962, Paris, France, edited by Laurmann.

14. Dunn, M. G.: Experimental Study of High-Enthalpy Shock-Tunnel Flow: Part I Shock-Tube Flow and Nozzle Starting Time. AIAA Journal, Vol. 7, No. 8, August 1969.

15. Dunn, M. G.: Experimental Study of High-Enthalpy Shock-Tunnel Flow: Part II Nozzle-Flow Characteristics. AIAA Journal, Vol. 7, No. 9, September 1969.

16. Dunn, M. G.; and Lordi, J. A.: Measurement of $N_2^+ + e^-$ Dissociative Recombination in Expanding Nitrogen Flows. AIAA Journal, Vol. 8, No. 2, February 1970.

17. Dunn, M. G.; and Lordi, J. A.: Thin-Wire Langmuir-Probe Measurements in the Transition and Free-Molecular Flow Regimes. AIAA Journal, Vol. 8, No. 6, June 1970.

18. Smy, P. R.; and Greig, J. R.: Transient Response of the Langmuir Probe at Low Pressure. British Journal of Applied Physics, Ser. 2, Vol. 1, 1968, pp. 351-359.

19. Sonin, A. A.: The Behavior of Free Molecule Cylindrical Langmuir Probes in Supersonic Flows, and Their Application to the Study of the Blunt Body Stagnation Layer. UTIAS Report No. 109, August 1965.

20. Weissman, D. E.; Scharfman, W. E.; and Guthart, H.: Electrostatic Probe Measurements in a Short Mean Free Path Plasma. Stanford Research Institute, Contract AF 04(694)-931, July 1966.

21. Talbot, L.; and Chou, Y. S.: Langmuir Probe Response in the Transition Regime. Sixth Rarefied Gasdynamics Symposium, Boston, Mass., June 1968.

22. Laframboise, J. G.: Theory of Spherical and Cylindrical Langmuir Probes in a Collisionless, Maxwellian Plasma at Rest. UTIAS Report No. 100, March 1966.

23. Shulz, G. J.; and Brown, S. C.: Microwave Study of Positive Ion Collection by Probes. Physical Review, Vol. 98, No. 6, 1955, pp. 1642-1649.

24. Burke, A. F.; and Wallace, J. E.: Aerothermodynamic Consequences of Nozzle Nonequilibrium. TR-66-45, February 1966, Arnold Engineering and Development Center, Tullahoma, Tennessee.

25. Dunn, M. G.; and Lordi, J. A.: Measurement of Electron-Temperature and Number Density in Shock-Tunnel Flows: Part I Development of Free-Molecular Langmuir Probes. AIAA Journal, Vol. 7, No. 8, August 1969.

26. Thomas, T. L.; and Battle, E. L.: Effects of Contamination on Langmuir Probe Measurements in Glow Discharge Plasmas. J. Appl. Physics, Vol. 41, No. 8, July 1970, pp. 3428-3432.

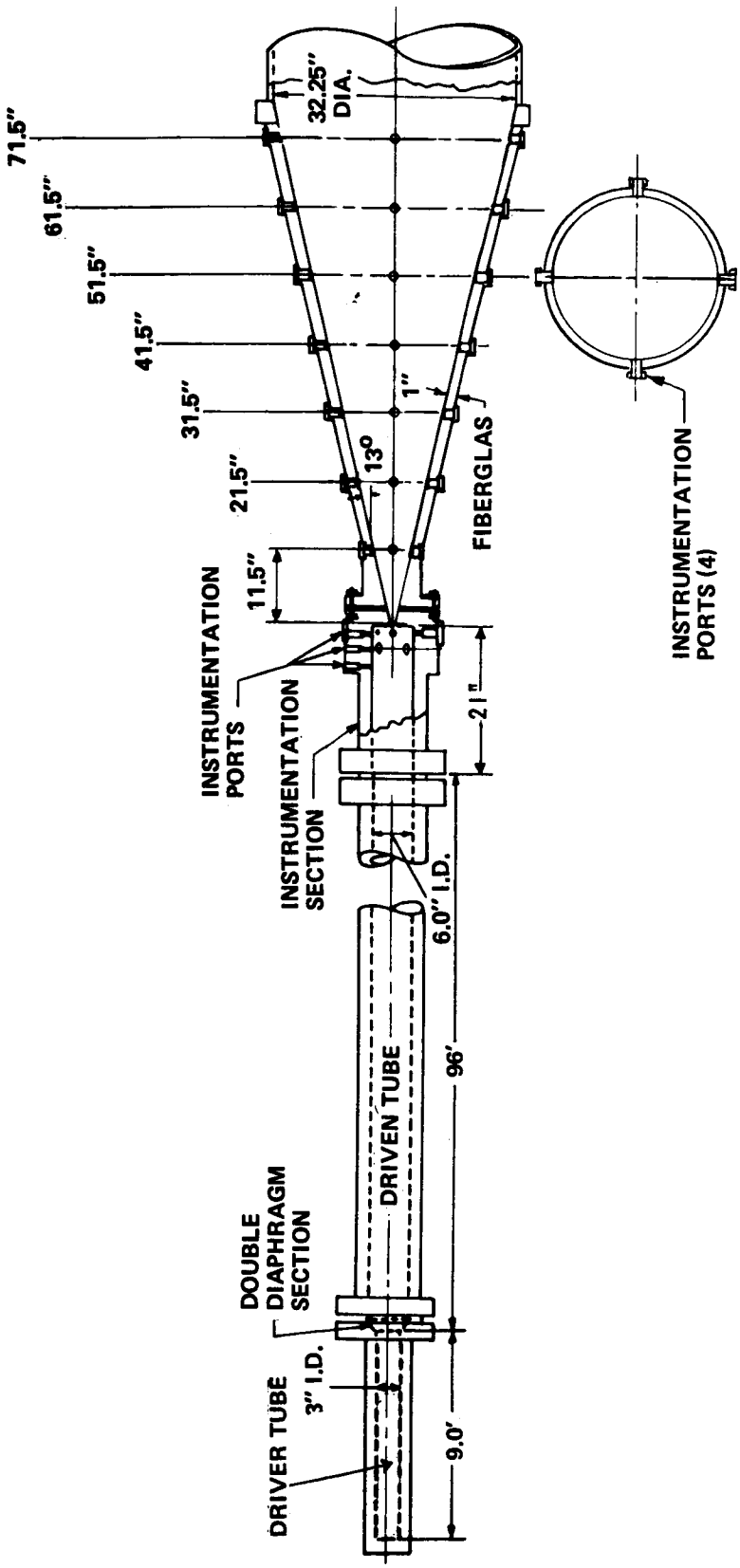

Figure 1.- Schematic of experimental apparatus.

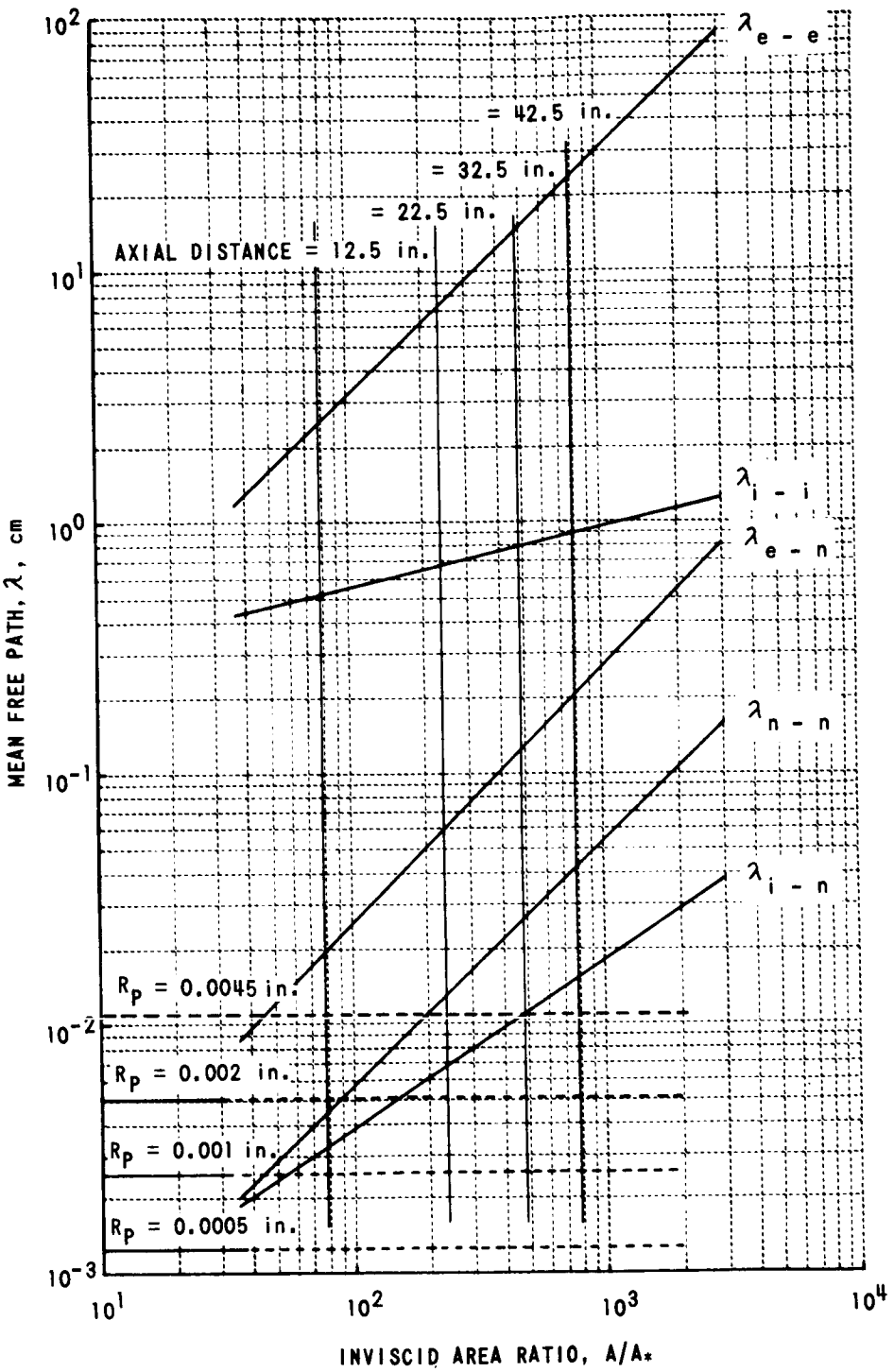

Figure 2.- Calculated mean free paths in expanding nitrogen flow.

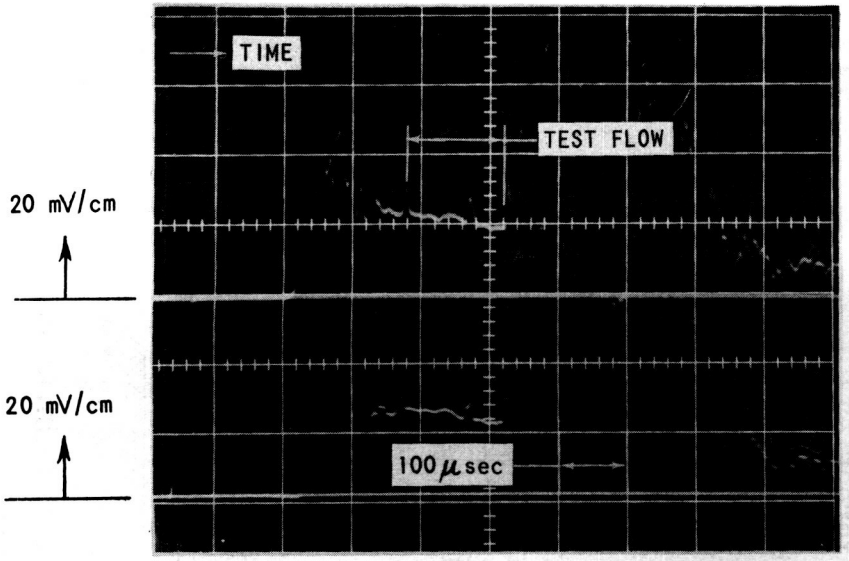

(a) Wedge-probe output at 32.5 in. from throat: upper – probe no. 4; lower – probe no. 5; bias voltage: -5.0 volts; resistor: 1000 ohms

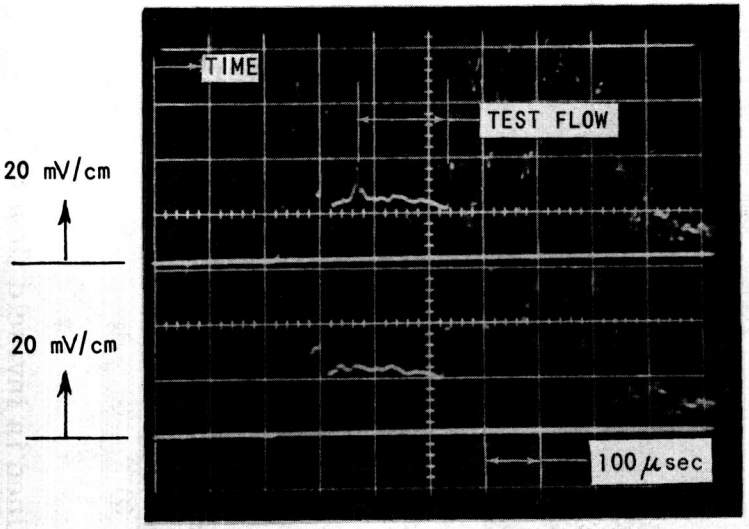

(b) Wedge-probe output at 32.5 in. from throat: upper – probe no. 7; lower – probe no. 8; bias voltage: -5.0 volts; resistor: 1000 ohms

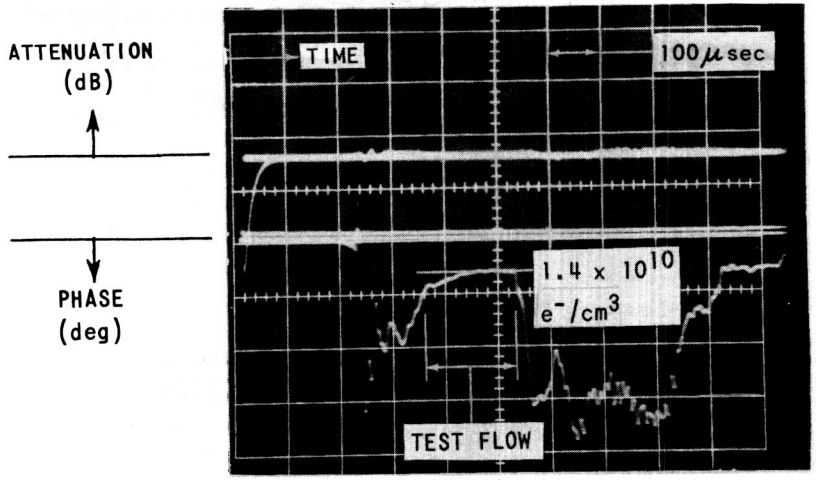

(c) 17 GHz microwave interferometer output at 31.5 in. from throat

Figure 3.- Typical wedge-probe and microwave-interferometer data in a nitrogen plasma.

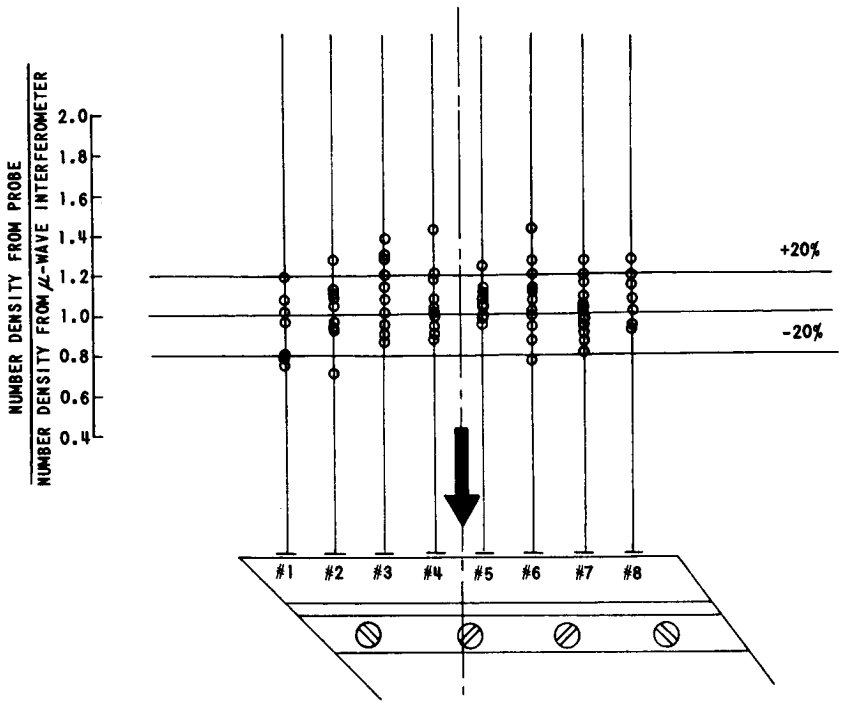

Figure 4.- Wedge-probe results obtained in inviscid flow at 32.5 in. from nozzle throat.

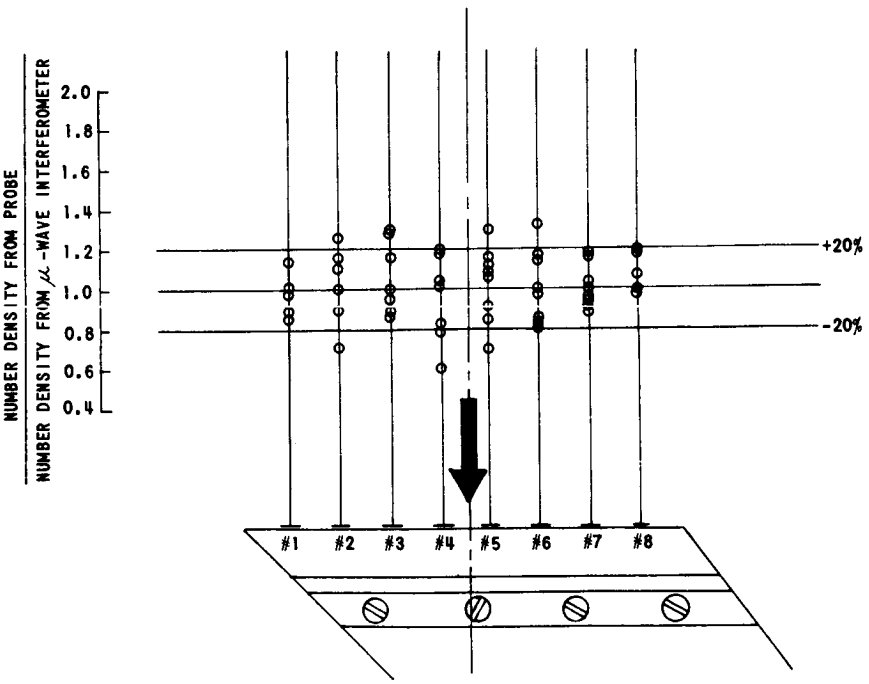

Figure 5.- Wedge-probe results obtained in inviscid flow at 42.5 in. from the throat.

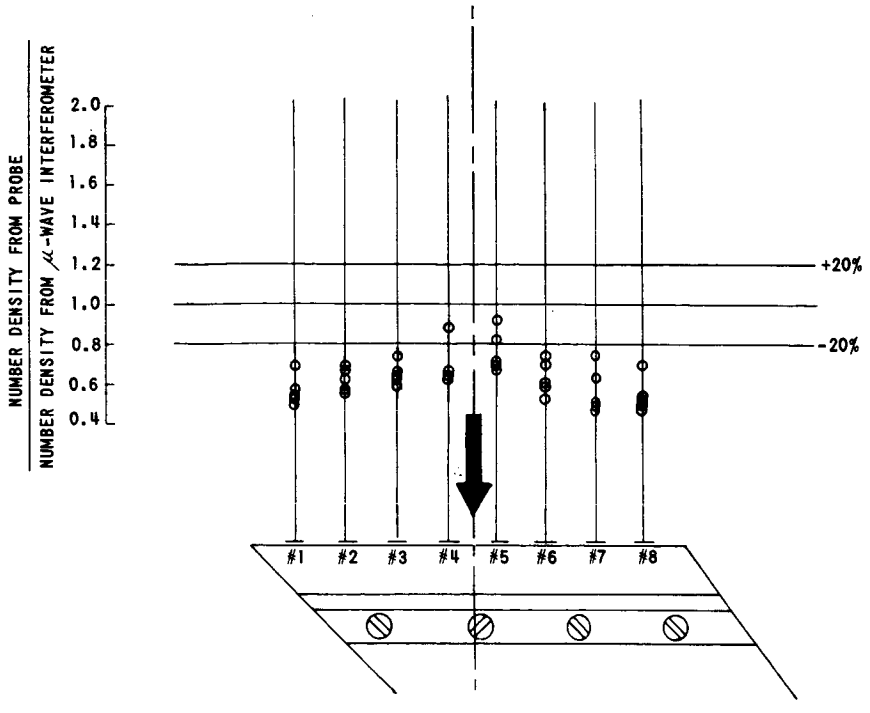

Figure 6.- Wedge-probe results obtained in inviscid flow at 14.5 in. from the throat.

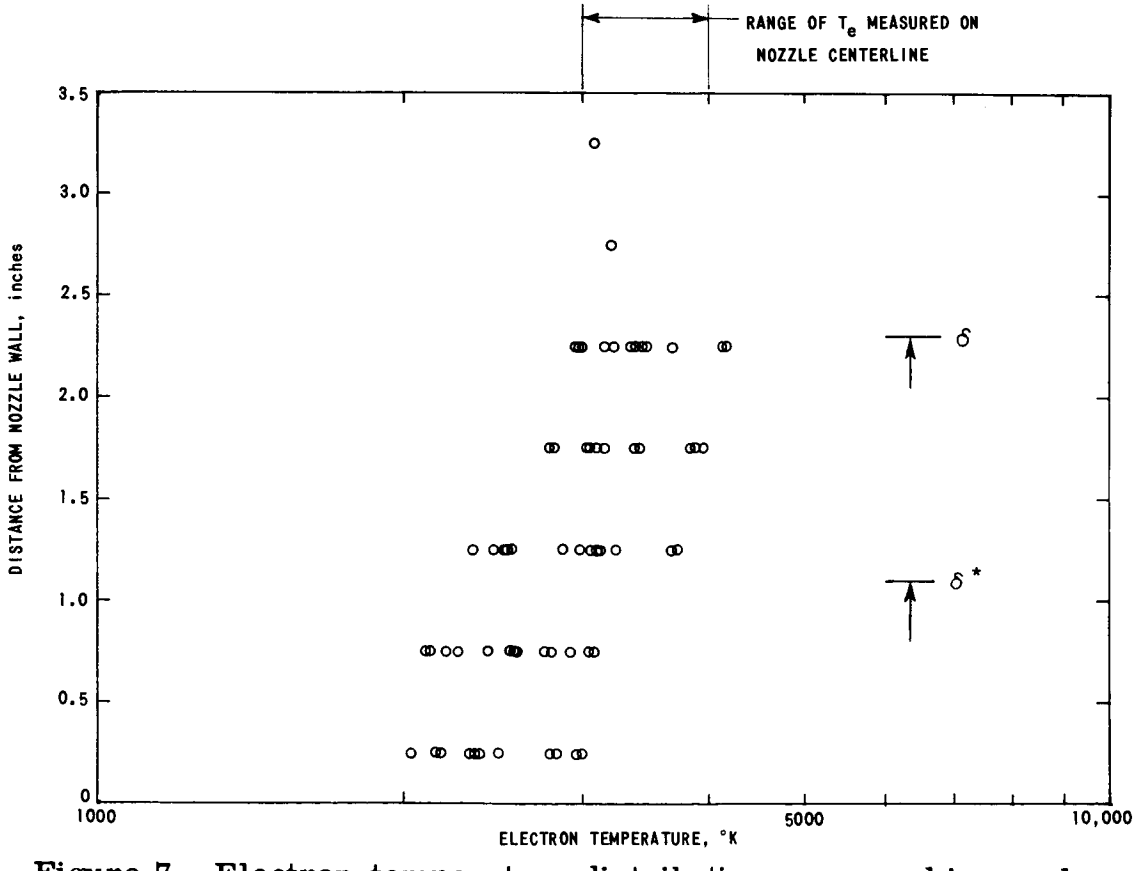

Figure 7.- Electron-temperature distribution measured in nozzle boundary layer.

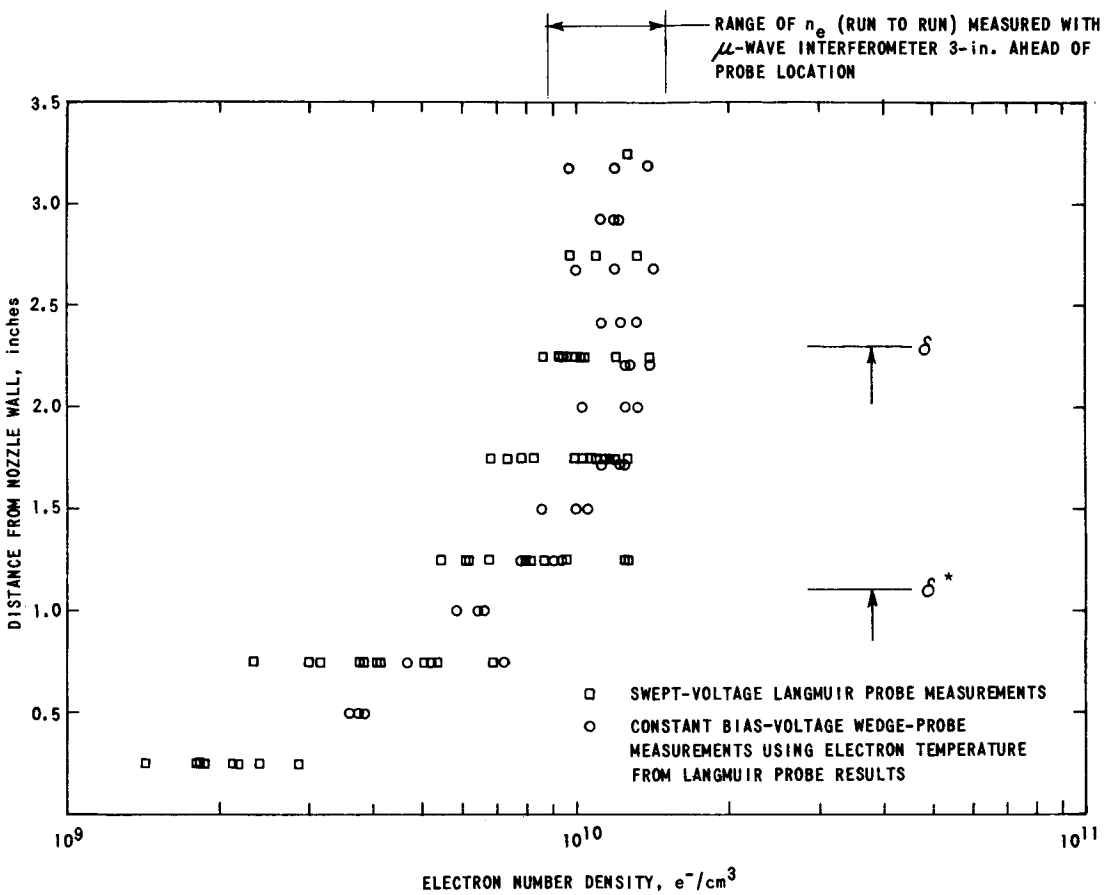

Figure 8.- Electron-density distribution measured in nozzle-wall boundary layer.

COMPARISON OF THEORETICAL AND EXPERIMENTAL ELECTRON DENSITY FOR RAM C FLIGHTS

By Charles J. Schexnayder, Jr., John S. Evans, and Paul W. Huber
NASA Langley Research Center

SUMMARY

Plasma diagnostic data from onboard Langmuir probes, reflectometers, and antenna VSWR, along with passive data from attenuation of beacon and telemetry signals, have been obtained for RAM C reentries at orbital velocity. These data are compared with calculated flow-field ionization and RF signal attenuation along streamlines for both inviscid flow and for inviscid flow merged with a boundary layer. Calculations were made for pure air using nonequilibrium chemistry throughout the flow field and for the same flow field with alkali contamination (in local ionic equilibrium) in the boundary layer. The results show that ambipolar electron-ion diffusion has a large effect on peak concentration and distribution of electrons at high altitudes and that ionization of ablation impurities increases electron concentration in the boundary layer at medium and low altitudes.

INTRODUCTION

The free electrons which are produced in hypersonic flow-field plasmas are the dominant factor in the entry radio blackout phenomenon. Therefore, in order to define, circumvent, or alleviate the blackout problem, it is important that one be able to determine the magnitude and distribution of electrons in the plasma near communications antennas, as well as to determine the interactions which occur between the plasma, the antennas, and the propagating electromagnetic signals. Theoretical evaluation of the electron density levels and profiles for a given entry communications problem requires precise and detailed consideration of complex systems of chemical and thermodynamic processes for the complete shock layer, since free electrons are present only as trace species in time-dependent systems (ref. 1). Even with careful analysis, uncertainties in the flow species to be considered, the reaction-rate coefficients, viscous interactions, antenna near-field effects, and so forth combine to raise doubts about the applicability to many real-life situations. This is especially true of those applications which involve ablation contamination (ref. 2) or blackout at high altitude.

The problem of radio blackout has led to the establishment of a flight project at the Langley Research Center called the Radio Attenuation Measurements Project. The basic objectives of Project RAM have been to obtain a better understanding of the factors which influence transmission of radio waves through plasmas and to search for ways to reduce or eliminate blackout. The RAM C payloads were spherically blunted cones which entered the earth's atmosphere at 7.6 km/sec (25 000 ft/sec) using ablating and nonablating heat shields. (See refs. 3 and 4 for flight descriptions.)

The purpose of this paper is to compare flight results from the RAM C series with theoretical calculations and draw some conclusions from the comparison.

SYMBOLS

d_N	body nose diameter, cm (in.)
f	signal frequency, Hz
k	rarefaction parameter (eq. (1))
N_e	electron concentration, electrons/cm^3
T	temperature, K
u	flow velocity, km/sec (ft/sec)
x	distance along body axis from stagnation point, cm
y	distance from body along normal to body surface, cm
γ	specific-heat ratio
Δ	value of y at shock front for a given value of x/d_N, cm
δ	distance to edge of boundary layer, cm
μ	viscosity, g/cm-sec
ν	collision frequency of an electron with other particles, sec^{-1}
ρ	density, g/cm^3
ω	angular frequency, $2\pi f$, rad/sec

Subscripts:

1,2,3,4	reflectometer body stations for X-, S-, and L-bands (table I)
cr	critical value
p	peak value at given body station
s	normal shock
∞	ambient flight conditions

FLIGHT EXPERIMENTS

The RAM C payloads were 9° half-angle blunted cones with nose diameters of approximately 30.5 cm (12 inches). The entry velocity-altitude profile (common to all C payloads) is shown in figure 1. RAM C-I was a material addition experiment having water injection at the nose and side positions along with four communications antennas as onboard diagnostic instrumentation and a rake of eight Langmuir probes. (See ref. 3 for details of experiment.) RAM C-II was mainly a plasma diagnostic experiment with reflectometers (ref. 4), four communications antennas, and a rake of Langmuir probes. The third payload, RAM C-III, had a material injection experiment which used water and electrophilic fluid for radio-blackout alleviation (ref. 5) and probes to measure positive ion and electron concentrations and electron temperature (ref. 6). Also, there were various communications antennas and an S-band diagnostic antenna (ref. 7) used to obtain information on the ionized layer profile. Table I lists the locations of the diagnostic instrumentation for the three flights.

Even though all three payloads had the same general configuration, there were two different ways of protecting the payloads from the heat generated at the nose. (See sketch in fig. 1.) In the RAM C-I and C-III flights, Narmco 4028, a phenolic graphite charring ablator, was used at the nose. In the RAM C-II flight, for the primary data period 91 to 55 km (300 000 to 180 000 ft), a beryllium (Be) nose cap positioned over a teflon ablator allowed reflectometer data to be taken in a clean airflow. After 55 km, the nose cap was ejected leaving the teflon as an ablator. All payloads used teflon on the afterbody for heat protection.

Analysis of a Narmco 4028 sample showed that it contained up to 5000 μg/g of alkali (Na and K) as an impurity. The Be nose cap and the teflon ablator were found to be free of any significant amounts of alkali.

THEORY

Clean Airflow Field

The techniques described in reference 1 provide a good approximation to the structure of the flow field around a spherically blunted cone such as the RAM payload. Since a knowledge of the electron concentration in the flow field is the major factor in any study involving radio blackout, the ability to calculate the concentration and distribution of the electrons is important. Emphasis for this study (ref. 1) has been placed on the chemical kinetics and the influence of the boundary layer in computing the properties within the blunt-body flow field.

In the inviscid flow portion of the calculations, density, velocity, temperature, and gas composition are computed as a function of distance along a streamline. Velocity and density are then used in a mass conservation program to obtain y coordinates for the streamlines at prespecified x/d_N locations.

At altitudes greater than 30.6 km (100 500 ft), boundary-layer corrections to inviscid results are obtained by following streamlines into the laminar boundary layer, the properties of which are computed separately with edge conditions from the nonequilibrium inviscid results. Thus, the stream-tube method used accounts for the effects of boundary-layer displacement, streamline swallowing, and vorticity interaction normal to the flow direction, as well as the effects of finite-rate chemistry on streamline position and shock shape. A shortcoming of the method (even with boundary-layer corrections) is an inability to include the effects of electron-ion diffusion. This effect, as will be shown subsequently, is not negligible for the profiles of N_e for the RAM C flights at altitudes greater than 70 km (230 000 ft).

Ablation-Contaminated Boundary Layer

Ablation from the heat shield of material known to contain easily ionized impurities such as sodium (Na) and potassium (K) made it necessary to compute boundary-layer profiles of N_e for the RAM C-I and C-III flights from 61.57 km (202 000 ft) to 21.35 km (70 000 ft) by using up to 5000 μg/g of alkali impurity. These calculations (ref. 8) are based on a calculated rate of ablation, on measurements of the ionizable impurities present in Narmco 4028, on theoretical distributions of airflow and ablation material in the boundary layer, and on assumed local equilibrium ionization of the ablation impurities. The curves shown in figure 2 illustrate the effect of impurity ionization in increasing the electron concentration in the boundary layer. The curves designated "Air" are illustrative of the profile results of shock-layer electron concentration obtained from the clean-airflow-field calculations over a range of altitudes.

COMPARISON OF DATA WITH PLASMA CALCULATIONS

High-Altitude Regime

Peak electron concentration.- Values of the peaks of the electron concentration profiles ($N_{e,p}$) are plotted in figure 3 as a function of altitude for several body locations. To show what effect the boundary layer has on electron density, the inviscid peak values are also given. Reflectometer data from reference 4 are given for the same body locations and are plotted as horizontal bars at values of $N_{e,p} = N_{e,cr}$. In figure 3, the length of a bar represents the flight period during which the reflection coefficient rises steeply. A typical example of the region of rapid change in the reflection-coefficient data from reference 4 is shown in figure 4. Shock-tube tests of the X- and S-band reflectometers in reference 9 indicated that critical N_e was associated with the end rather than the beginning of the rise to high reflection coefficient (i.e., the low-altitude ends of the bars). In addition to the reflectometer data, the rise of VSWR in the VHF antenna feed circuits is shown in figure 3(b). Langmuir probe data for the C-I and C-II flights (ref. 6) are shown as the shaded areas representing envelopes (due to spin and angle of attack) of data for the outermost probe (y = 7.08 cm), which were the highest ion concentration

values measured on each profile. That part of the Langmuir probe data from the RAM C-II flight which is shown unshaded indicates the altitude range for which probe temperatures were above 812 K. These data may have been affected by thermal degradation of the beryllium oxide insulation. (See ref. 3.) The VHF pattern data in figure 3(b) represent the altitudes at which the antenna patterns (seen because of vehicle spin) were observed briefly to be circular (ref. 10). The occurrence of a circular pattern is a definite and sharp indicator for the condition $N_{e,p} = N_{e,cr}$. This observation is an excellent check on the other diagnostic data.

Comparison of theory and flight results in figure 3 brings out some interesting points:

(1) Reduction of peak N_e values due to application of boundary-layer theory is small below an altitude of 75 km (245 000 ft) despite the fact that the boundary-layer thickness is more than one-half the shock-layer thickness. This is because the peaks of the N_e curves for altitudes below 75 km do not occur close to the body surface.

(2) There is generally good agreement among the various diagnostic techniques in the altitude range shown in figure 3(b).

(3) A region of slow rise in reflection coefficient for the X_2-band record (ref. 4) is represented in figure 3(a) by a dashed bar. This correlates well with the corresponding slow change in calculated $N_{e,p}$ at $x/d_N = 0.76$ as shown in the same figure.

(4) In view of the agreement of RAM C-I and C-II data, there does not appear to be any effect of alkali ionization at altitudes above 61 km (200 000 ft).

(5) At all body stations, calculated peak N_e values are much higher than those deduced from measurements in the altitude range above 71 km (233 000 ft).

As was pointed out previously, the theoretical model does not allow for inclusion of electron and ion diffusion or for wall recombination effects. Estimated correction factors for these omitted effects were obtained by correlating RAM C data with shock-layer solutions from the literature which included diffusion and wall effects. The results are plotted in figure 5. The shaded region is one which includes theoretically and experimentally determined $N_{e,p}$ reduction factors taken from results of references 11 to 15. The reduction factor is the factor by which $N_{e,p}$ for an inviscid profile is reduced due to the effects of viscosity, ion diffusion, and wall recombination. In order to plot these flight data in the figure, they are divided by $N_{e,p}$ values from the inviscid curves of figure 3. All the reference data are for the nose region of blunt-nosed bodies with the exception of reference 12 which is for $x/d_N = 4$. Values appropriate to the stagnation point are generally near the high-altitude side of the shaded region whereas values for the nose-body juncture are near the low-altitude side. The reference data are correlated on the RAM C altitude

scale on the basis of the rarefaction parameter

$$k^2 = \frac{\gamma_\infty - 1}{2\gamma_\infty} \frac{(\rho u)_\infty d_N}{2\mu_s} \tag{1}$$

The correlation is seen to be quite indicative of the role of ion diffusion and wall effects in the RAM C shock-layer peak N_e. The effects begin at about the altitude predicted $(k^2 \approx 100)$. The nose-region reduction factors as compared with those applicable to aft locations are shifted toward higher altitudes for both flight and reference data.

Electron concentration profiles.- The high-altitude N_e profile shape is affected by diffusion and wall recombination as shown in figure 6. The theory shows that the peak value of N_e occurs at $y = 4$ cm, whereas the values of N_e determined by the Langmuir probe (ref. 3) are seen to be still increasing at $y = 7.08$ cm. Wall effects (surface and gas-phase recombination at low temperature and velocity) act as an electron-ion sink and, being fed by diffusion from the electron concentration peak, will cause a distortion of the profile toward a lower peak N_e and toward a peak located farther from the wall. In the outer part of the profile, diffusion reduces the gradients and hence tends to be self-limiting; whereas, near the wall, the gradients are maintained by recombination. Furthermore, the outer shock-layer flow at high altitude is producing electrons, even at the aft portion of the body, and hence will tend to oppose an N_e reduction due to diffusion. A method given in the appendix is used to extend the experimental N_e profile beyond 7.08 cm. The results are shown in figure 6 as an extension of the curve drawn through the Langmuir probe data.

Intermediate-Altitude Regime

Signal attenuation.- In figure 7 the C- and X-band signal attenuation data from the RAM C-II flight are compared with the theoretical computed signal loss for pure-air N_e profiles using the plane wave nonhomogeneous plasma model given in reference 16. Figure 8 shows a comparison of signal attenuation data for X- and C-band frequencies obtained in the flight of RAM C-I and theoretical attenuation curves obtained both from pure-air profiles and from profiles which contain easily ionizable impurities in the boundary layer. This figure reveals that the lower altitude portion of the data from the RAM C-I flight correlates better with the contaminated boundary-layer model than with the pure-air model. At higher altitudes (>52 km), the experimental data drop off whereas the theoretical curve (air + alkali) is rising. A possible explanation for this is mentioned in the next section. The attenuation data from the RAM C-I flight were definitely higher than the data obtained from the RAM C-II flight (fig. 7). For example, C-band blackout for the RAM C-I flight occurs at an altitude where attenuation of C-band first began for the RAM C-II flight.

Peak electron concentration.- Figure 9 shows a comparison of calculated peak N_e values for the first two RAM flights with the data from the reflectometer experiment (ref. 4) and the signal blackout data from figures 7 and 8.

The attenuation data are converted to $N_{e,p}$ values by using a reverse procedure from that used to get attenuation from the N_e profiles. This is done by first assuming a generalized profile shape (as a function of altitude) and arbitrarily letting the magnitude of N_e vary. Values of $N_{e,p}$ are then found whose profiles yield theoretical attenuations equal to the measured attenuations. The N_e profile shapes assumed in this method are similar to those found in figure 2.

A comparison between the measured data for RAM C-I and C-II flights and the respective theoretical results shows reasonable agreement. (See fig. 9.) The alkali ionization is probably responsible for the difference in the observed attenuation between the two flights. The high-altitude fall-off of the experimental data (see fig. 8 also) at approximately 52 km (171 000 ft) is probably due to failure of the local equilibrium assumption for the Na-K chemistry at high altitude as outlined in reference 8. When comparing the pure-air theory with the flight results of RAM C-II, it must be remembered that the low-altitude end of the reflectometer rise bar is closer to $N_e = 10^{12}$ (ref. 9).

Low-Altitude Regime

Signal attenuation.- Figure 10 shows the comparison of signal recovery and attenuation data for the RAM C-I and C-II flights with theoretical curves plotted as a function of velocity. The theory is computed for a clean-air model and for a model containing the effects of alkali ablation in the boundary layer. Signal recovery data for X-band and C-band for the RAM C-II flight were not obtained because of tracking problems. The fact that the experimental data for the RAM C-I flight and the theoretical curves (air + alkali) show a much larger attenuation than the RAM C-II flight data and theory can be attributed to the alkali impurities in the boundary layer. The large increases in N_e (see fig. 2) produce large increases in calculated signal loss, even though the boundary layer is thin relative to the total plasma layer. The theoretical curves for both flights indicate that there is very little dependence of the predicted recovery on signal frequency. The data from the RAM C-I flight qualitatively confirm this result as there is no particular trend of recovery with frequency except for the 260-MHz VHF signal, which was much more severely attenuated than was predicted. A possible explanation for this lies in the observation that, of the four VHF antennas on the two flights, only this one was a highly tuned slot. The others were ring antennas and were less susceptible to signal strength reduction by loss of antenna gain when in the presence of plasma. The quantitative agreement of each set of flight data with its corresponding theoretical curve is satisfactory.

Peak electron concentration.- The low-altitude signal attenuation data in figure 10 are converted to $N_{e,p}$ values by the method previously mentioned and are plotted in figure 11 along with the reflectometer data and curves representing the previously discussed theoretical models. The reflectometer data from reference 4 are represented by bars whose lengths represent periods of rapid decay in the reflection coefficient. (See sample record in fig. 4.) The attenuation data from the RAM C-I flight agree quite well with the theoretical

curves labeled "Air + alkali theory." The figure also indicates that the $N_{e,p}$ values are two to three decades higher than the theory computed for a clean-air model. The signal attenuation data for the RAM C-II flight agree fairly well with the theoretical curves for clean air, but the reflectometer data do not. The reflectometer data indicate that $N_{e,p}$ is decreasing whereas the theory predicts an increase in $N_{e,p}$. There is apparently no satisfactory explanation for this discrepancy. Several factors which may be helpful in understanding the nature of the impasse will be briefly discussed.

Changing the dissociation rate constants for O_2, N_2, and NO by factors of 10 and 10^{-1} did not improve the overall agreement between the theory and reflectometer data in figure 11. It is expected on the basis of our own calculations, as well as those of reference 17, that chemistry in the flow field is near equilibrium at these low altitudes. In such circumstances, $N_{e,p}$ is insensitive to the dissociation rates of O_2, N_2, and NO. Even though the computer program used in this study includes reactions involving O^- and O_2^- (ref. 1), changes in the rate constants (factor of 10 and 10^{-1}) for $O^- + M \rightleftarrows O + e^- + M$ and $O_2^- + M \rightleftarrows O_2 + e^- + M$ reactions gave only minor changes in the values of $N_{e,p}$. The molecule NO_2 and reactions involving it have been omitted from the calculations. Reference 18, which has equilibrium results for air, reports that NO_2^- becomes a dominating factor in determining the N_e at pressures above 1 atm and temperatures below 4000 K. However, combinations of pressures and temperatures where the reflectometer data are obtained do not match the conditions needed to make NO_2^- important.

One way the air calculation could be appreciably perturbed would be by the combination of large boundary-layer thickening and chemical action of the teflon ablation products. The thickening would presumably occur by the combined effects of early transition (i.e., 38 km instead of 27.5 km) where the vehicle went to an angle of attack as high as 5° in a short body-motion period (ref. 4) occurring at altitudes corresponding to velocities of 6.77 to 7.32 km/sec (22 200 to 24 000 ft/sec), increased mass injection, surface roughness, and so forth. These effects would have to thicken the boundary layer on the nose to about 10 times the computed laminar value for ablation products to reach the required point in the plasma to have any large effect on the peak N_e. This would seem rather unlikely based on the facts that (1) the maximum blowing parameter for the teflon is theoretically only about 0.06 and (2) material injection studies have shown it to be difficult to cause even liquids under pressure to penetrate such high-density flows; therefore, it is very doubtful that gaseous ablation products would be able to penetrate the flow so deeply.

One possible chemical action of teflon ablation products would be attachment of electrons. If the teflon products are confined to a thin boundary layer, the attachment of electrons in the boundary layer will in no way affect the peak N_e since the profiles are relatively flat in this altitude regime. If the teflon could somehow extend into the nose-plasma layer (i.e., 10 times thicker boundary layer), the computed ablation mass is theoretically about

6 percent of the mass within the plasma stream tubes. In the calculations reported in reference 19, only about 1 percent of the electrons attached for a 5-percent teflon-air equilibrium mixture at about the temperature (6000 K) and pressure (1 atm) of RAM C-II nose flow in this low-altitude flight regime. In reference 20 no difference is reported between the conductivities of air and air-teflon mixtures (approximately 3 percent teflon in air behind normal shock waves). (The gas temperature was 3200 to 6500 K and the density on the order of 0.1 to 0.2 of standard density.) It has been shown experimentally in reference 21 that for mixtures of teflon and air at temperatures above 3000 K electron quenching was not obtained. The agreement of RAM C-I low-altitude data with alkali theory tends to rule out any large teflon electrophilic action in the boundary layer $\left(x/d_N > 0.8\right)$ since the body coating injects more teflon into the boundary layer than there are Narmco products present due to nose ablation. With the teflon present and if attachment of electrons occurred, then the N_e curve for the RAM C-I flight would not show a large spike (fig. 2) in the boundary layer and attenuation data would not agree with the air + alkali theory.

For the VHF recovery data to be compatible with the reflectometer results means there must be 25 to 30 dB loss due to antenna mismatch. This is the difference between observed signal loss at recovery (fig. 10) and that computed for the reflectometer-indicated-peak N_e profile at this point (fairing the data) by using plane-wave theory and maximum plasma thickness (upper limit case). However, one would expect much less mismatch loss at low altitude (than at high altitude) because of the greater absorption and lower reflection loss in the plasma at high-electron-collision frequency ($\nu/\omega \geq 10$, compared with approximately 0.01 at high altitude). The measured mismatch losses for RAM C-II in this regime were about 8 dB maximum. (However, this value is as high as the system could accurately measure.) Actually, the VHF recovery data tend to rule against $N_{e,p}$ being constant, or decreasing (such as indicated from fairing of the reflectometer data), in the velocity range from 7.3 to 6.4 km/sec. If this were the case, then attenuation would decrease in this range (because of increasing ν) and recovery would occur earlier than observed. There was a brief period of partial recovery observed (ref. 4) during the body-motion period but actual recovery did not occur until about where the air predictions show a significant decrease in attenuation. Certain factors should be considered which may have affected the performance of the reflectometers during the flight. The possible high-collision cross section for the teflon-air products coupled with a thicker than expected boundary layer might result in large absorption of the signal. Another factor is the long-duration heat pulse of flight (>20 sec) during which there was considerable erosion of the dielectric covering over the reflectometers. Although these factors are only speculative, there were some anomalies in the flight records at low altitude which correspond to the discrepancy period. These include

(1) Shorter decay (nearly discontinuous) of reflected power as a function of time $\left(\text{for } X_1\text{-}, X_4\text{-}, \text{ and perhaps } X_3\text{-bands}\right)$ at low altitude than for the rise at high altitude. The opposite would be expected (ref. 9) because of ν/ω effects. (The value of $N_{e,p}$ as a function of time for stations 3 and 4 is indicated by the reflectometers to be fairly gradual in this regime, and gradual decay is seen in all the S- and L-band records.)

(2) A large perturbation is seen in the X_2-band record prior to or during the decay period.

(3) A reversal in the $N_{e,p}$ values between X_1-band and X_2-band (fig. 11) is observed.

(4) A drop in the level of the reflection coefficient for stations 3 and 4 S- and X-band records is observed exactly at the start of the period of high angle of attack and prior to the decay period.

The above discussions do not establish that the reflectometer were substantially incorrect, nor do they indicate that the theory and the VHF data are correct. The question at this time is unanswered.

CONCLUDING REMARKS

Plasma diagnostic data from onboard Langmuir probes, reflectometers, and antenna VSWR, along with passive data from attenuation of beacon and telemetry signals, have been obtained for the reentry regimes of two RAM C blunt-nosed vehicles. These data are compared with calculations of flow-field ionization and RF signal attenuation based on pure-air nonequilibrium chemistry (both for inviscid flow and for inviscid flow merged with a boundary layer) along streamlines and in a boundary layer contaminated with alkali ablation products in local ionic equilibrium. Based on these comparisons, several conclusions regarding the electron concentration and distribution of electrons in the flow field can be made.

1. There is a large effect on peak concentration and distribution of electrons in the plasma due to ambipolar electron-ion diffusion and wall recombination at altitudes above 71 km (233 000 ft).

2. There is a large increase in the electron concentration in the boundary layer due to ionization of alkali impurities from the heat shield of RAM C-I for altitudes less than 61 km (200 000 ft).

3. Generally good agreement was obtained between theory, diagnostic data, and attenuation data at altitudes greater than 38 km (125 000 ft). At lower altitudes there was reasonable agreement between theory and attenuation data, but disagreement between theory and reflectometer data. Reasons for the disagreement are not understood.

APPENDIX

ESTIMATION OF OUTER PART OF MEASURED N_e PROFILES

In order to make estimates of the outer part of the measured N_e profiles (beyond $y = 7.08$ cm), certain conceptual arguments can be invoked, as detailed in figure 12. This is a plot of N_e contours (from which profiles can be constructed) and other parameters such as the distance to peak gas temperature T_p, the distance to the boundary-layer edge δ, and the distance to the shock point Δ. Theoretical calculations were not made at altitudes above 85 km (279 000 ft) but a point on the peak N_e curve occurs (by definition) where the inner and outer 10^9 (or 10^{10}) contours merge and disappear. Two such merging points are shown in the figure. One was obtained by extrapolation of theoretical calculations without diffusion, (See fig. 3(b).) The other includes electron-ion diffusion, since it is deduced from flight data. The flight measurements in figure 3 and the Langmuir probe profile data from reference 6 are used for this. First, it is assumed that the outer-probe ($y = 7.08$ cm) value of N_e is close to the peak value. This peak value determines the altitude of intersection. Next, the inner 10^9 contour can be roughly drawn by using the probe data, although the intersection in y is not well determined (other than being beyond the point $y = 7.08$ cm). Finally, the peak N_e and the outer 10^9 contours are arbitrarily drawn so as to be self-consistent and consistent with the observations. For example, peak N_e cannot be less than $y = 7.08$ cm at 71 km (233 000 ft) and the departure from theory very probably begins at an altitude less than 70 km (230 000 ft). Using these inferred contours, one can extend the flight measured profiles as illustrated in figure 6. Based on these probable profiles, it would appear that the true $N_{e,p}$ value for RAM C is very little different from that measured by the outer probe and does not occur much beyond $y = 9$ cm. Preliminary data from RAM C-III flight (ref. 6) indicate that the experimental $N_{e,p}$ is further out from the body than shown by the most probable profile curve in figure 6. This could be due to a stronger action of diffusion than was previously estimated. The RAM C-III Langmuir probes extended out 14.02 cm into the plasma as compared with 7.08 cm for the RAM C-I and C-II flight experiments.

REFERENCES

1. Evans, John S.; Schexnayder, Charles J.; and Huber, Paul W.: Computation of Ionization in Re-Entry Flowfields. AIAA J., vol. 8, no. 6, June 1970, pp. 1082-1089.

2. Blottner, F. G.: Chemically Reacting Boundary Layer With Ablation Products and Nose Bluntness Effects. BSD-TR-67-83, U.S. Air Force, June 1967. (Available from DDC as AD 382 026.)

3. Akey, Norman D.; and Cross, Aubrey E. (With appendix A by Thomas G. Campbell appendix B by Fred B. Beck; and appendix C by W. Linwood Jones, Jr.): Radio Blackout Alleviation and Plasma Diagnostic Results From a 25 000 Foot Per Second Blunt-Body Reentry. NASA TN D-5615, 1970.

4. Grantham, William L.: Flight Results of a 25 000-Foot-Per-Second Reentry Experiment Using Microwave Reflectometers to Measure Plasma Electron Density and Standoff Distance. NASA TN D-6062, 1970.

5. Schroeder, Lyle C.: Flight Measurements at 25 000 Feet Per Second of Blackout Alleviation by Water and Electrophilic Injection. The Entry Plasma Sheath and Its Effects on Space Vehicle Electromagnetic Systems – Vol. II, NASA SP-253, 1971, pp. 77-100.

6. Jones, W. Linwood, Jr.; and Cross, Aubrey E.: Electrostatic Probe Measurements of Plasma Surrounding Three 25 000 Foot Per Second Reentry Flight Experiments. The Entry Plasma Sheath and Its Effects on Space Vehicle Electromagnetic Systems – Vol. I, NASA SP-252, 1971, pp. 109-136.

7. Swift, C. T.; Beck, F. B.; Thomson, J.; and Castellow, S. L., Jr.: RAM C-III S-Band Diagnostic Experiment. The Entry Plasma Sheath and Its Effects on Space Vehicle Electromagnetic Systems – Vol. I, NASA SP-252, 1971, pp. 137-155.

8. Huber, P. W.; Evans, J. S.; and Schexnayder, C. J.: Comparison of Theoretical and Flight-Measured Ionization in a Blunt Body Reentry Flow Field. AIAA Pap. No. 70-756, June-July 1970.

9. Taylor, W. C.: An Experimental Investigation of the Interaction of Plasmas With Antennas. NASA CR-1727, 1970.

10. Croswell, William F.; and Jones, W. Linwood, Jr.: Effects of Reentry Plasma on RAM C-I VHF Telemetry Antennas. The Entry Plasma Sheath and Its Effects on Space Vehicle Electromagnetic Systems – Vol. I, NASA SP-252, 1971, pp. 183-201.

11. Lee, Richard H. C.; and Zierten, Thomas A.: Merged Layer Ionization in the Stagnation Region of a Blunt Body. Proceedings of the 1967 Heat Transfer and Fluid Mechanics Institute, Paul A. Libby, Daniel B. Olfe, and Charles W. Van Atta, eds., Stanford Univ. Press, c.1967, pp. 452-468.

12. Kaplan, B.: The Non-Equilibrium Air Boundary Layer on a Blunt Nosed Body. Doc. No. 68SD227, Gen. Elec. Co., Apr. 1968. (Available from DDC as AD 833 789.)

13. Kaegi, E. M.; and McMenamin, D. L., Jr.: Measured and Predicted Air Ionization in Blunt Body Shock Layers. AIAA Pap. No. 69-81, Jan. 1969.

14. Kang, Sang-Wook: Analysis of an Ionized Merged-Layer Hypersonic Flow Over a Blunt Body. CAL No. AI-2187-A-12 (Contract No. NAS 5-9978), Cornell Aeronaut. Lab., Inc., May 1969.

15. Dellinger, T. C.: Computation of Nonequilibrium Merged Stagnation Shock Layers by Successive Accelerated Replacement. AIAA Pap. No. 69-655, June 1969.

16. Swift, Calvin T.; and Evans, John S.: Generalized Treatment of Plane Electromagnetic Waves Passing Through an Isotropic Inhomogeneous Plasma Slab at Arbitrary Angles of Incidence. NASA TR R-172, 1963.

17. Webb, H., Jr.; Dresser, H.; Korkan, K.; and Raparelli, R.: Theoretical Flow Field Calculations for Project RAM. NASA CR-1308, 1969.

18. Peng, T. C.; Doane, P. M.; and Fivel, H. J.: Model Optimization of Equilibrium Air Plasmas From 10^{-4}-10^{3} Atm and 1000 to 10,000° K. Rep. G996, McDonnell Douglas Corp., Mar. 1969.

19. DeBolt, H. E.; and Port, W.: Thermochemical Equilibrium Studies of Ablative Heat-Shield Materials. RAD-TM-63-27 (Contract AF04(694)-239), AVCO Corp., June 7, 1963.

20. Morsell, A. L.: Electrical Conductivity of Shock-Heated Air and Air Plus Teflon Mixtures. Res. Note 20 (Contract No. DA 04-495-AMC-458(Z), Heliodyne Corp., June 1965. (Available from DDC as AD 476 132.)

21. Starner, K. E.: Evaluation of Electron Quench Additives in a Subsonic Air Arc Channel. AIAA J., vol. 7, no. 12, Dec. 1969, pp. 2357-2358.

TABLE I.– LOCATION OF ONBOARD RF AND ELECTROSTATIC PROBES

x/d_N (a)	RAM C-I	RAM C-II	RAM C-III
0.15 (45°) (Station 1)		K-band reflectometer (35000 MHz) X-band reflectometer (10044 MHz) S-band reflectometer (3348 MHz)	
0.76 (Station 2)		K-band reflectometer (35000 MHz) X-band reflectometer (10044 MHz) S-band reflectometer (3348 MHz) L-band reflectometer (1116 MHz)	
2.3 (Station 3)		K-band reflectometer (35000 MHz) X-band reflectometer (10044 MHz) S-band reflectometer (3348 MHz) L-band reflectometer (1116 MHz)	S-band diagnostic antenna (3348 MHz)
2.4 2.6 3.2 3.4	VHF telemetry slots (259.7 MHz) X-band telemetry horns (9210 MHz) VHF telemetry ring (225.7 MHz)	X-band telemetry horns (9210 MHz) VHF telemetry ring (259.7 MHz)	VHF telemetry slots (259.7 MHz) X-band telemetry horns (9210 MHz) VHF telemetry ring (230.4 MHz)
3.5 (Station 4)		K-band reflectometer (35000 MHz) X-band reflectometer (10044 MHz) S-band reflectometer (3348 MHz) L-band reflectometer (1116 MHz)	
3.5 3.7 3.8	C-band beacon horn (5700 MHz)	C-band beacon horn (5800 MHz) VHF telemetry ring (225.7 MHz)	C-band beacon horn (5800 MHz)
3.9 4.0	Langmuir probe rake[b]	Langmuir probe rake[b]	Ion and electron probe rakes[c]

[a]Location of center line of component:
d_N = 12.56 inches (31.90 cm) for RAM C-I and C-III flights, Narmco 4028
d_N = 12.00 inches (30.48 cm) for RAM C-II flight, beryllium
d_N = 12.65 inches (32.13 cm) for RAM C-II flight, teflon

[b]Probes located at y = 0.96, 1.84, 2.70, 3.58, 4.46, 5.34, 6.20, and 7.08 cm.

[c]Ion probes located at y = 0.88, 1.75, 2.63, 3.51, 4.38, 5.26, 6.14, 7.01, 7.89, 8.77, 9.64, 10.52, 11.39, 12.27, 13.15, and 14.02 cm.
Electron probes located at y = 1.5, 3.5, 6.5, and 9.5 cm.

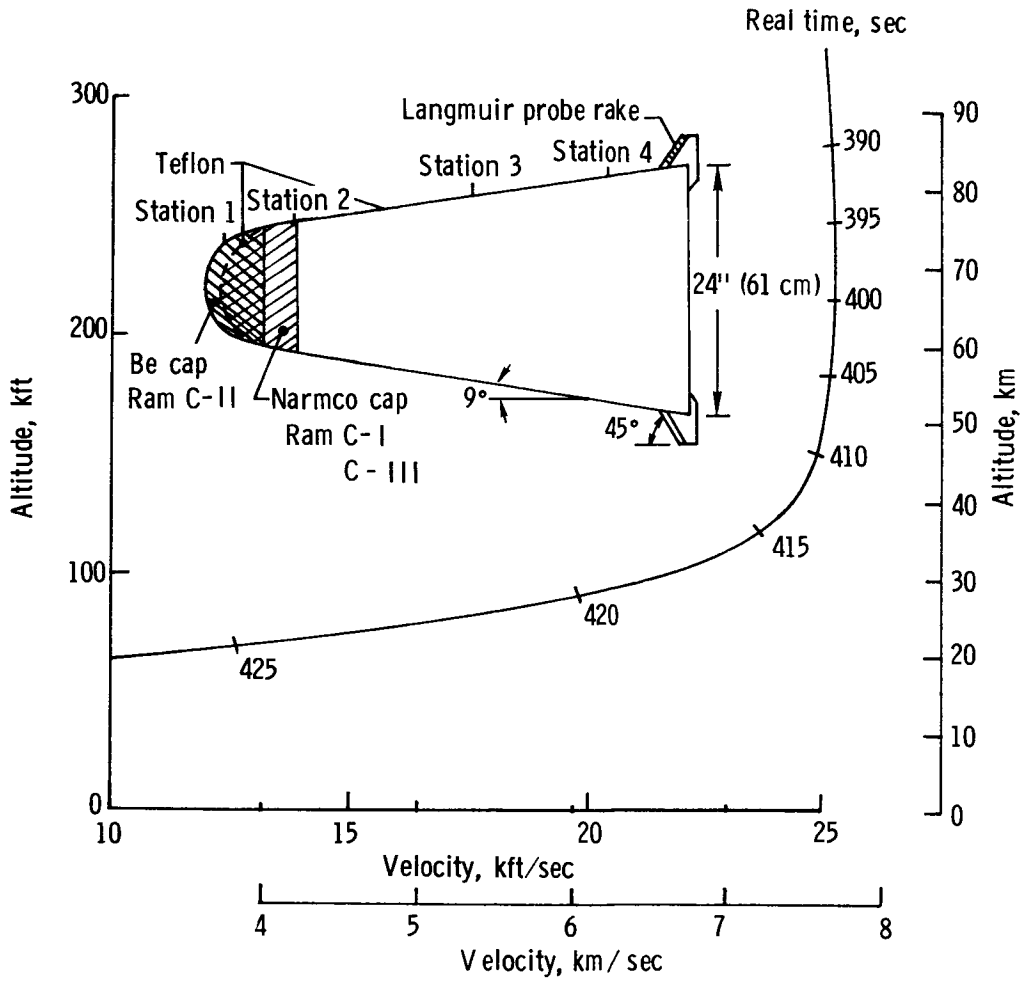

Figure 1.- RAM C configurations and entry profile.

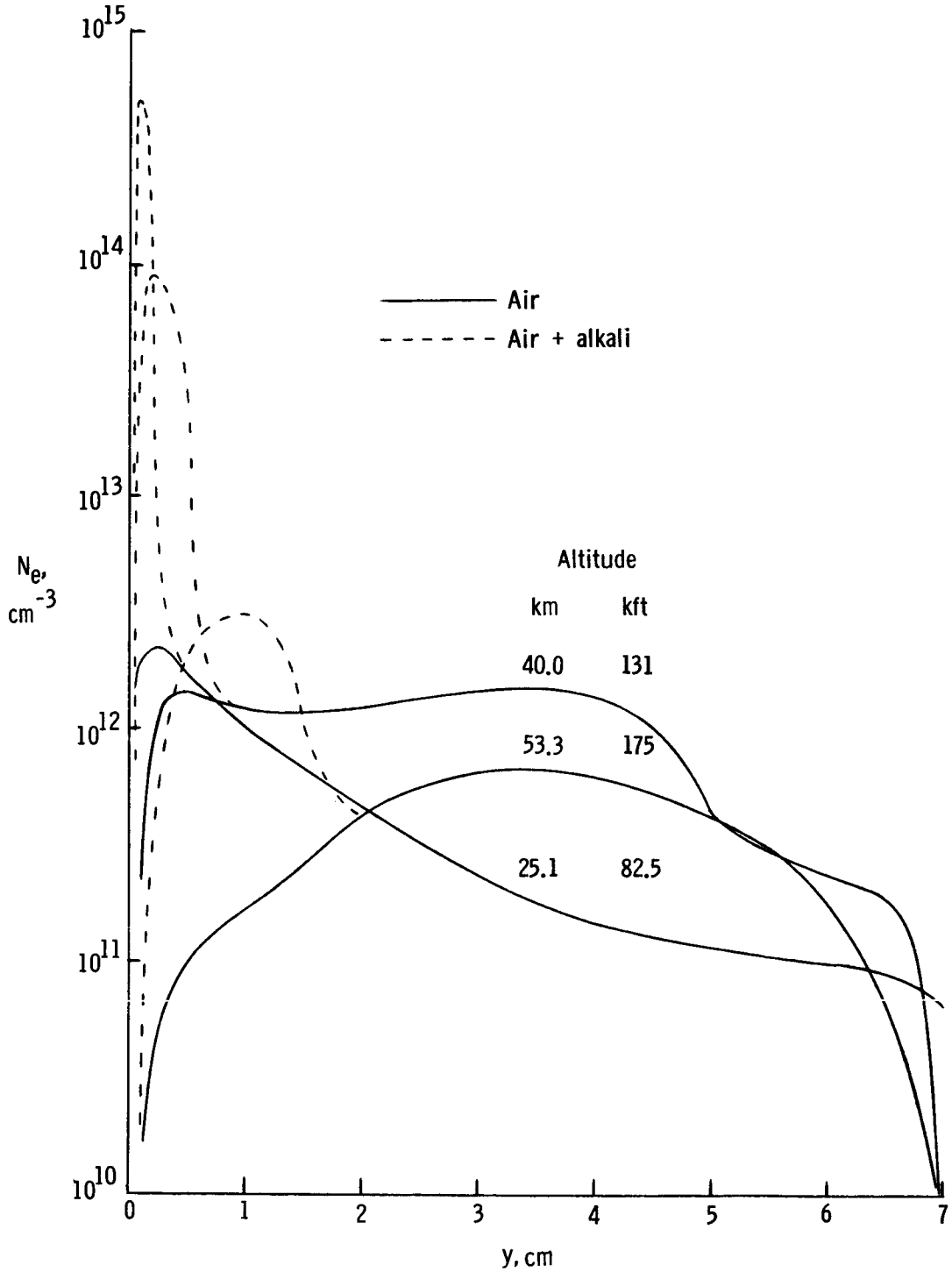

Figure 2.- Electron concentration profiles $x/d_N = 2$.

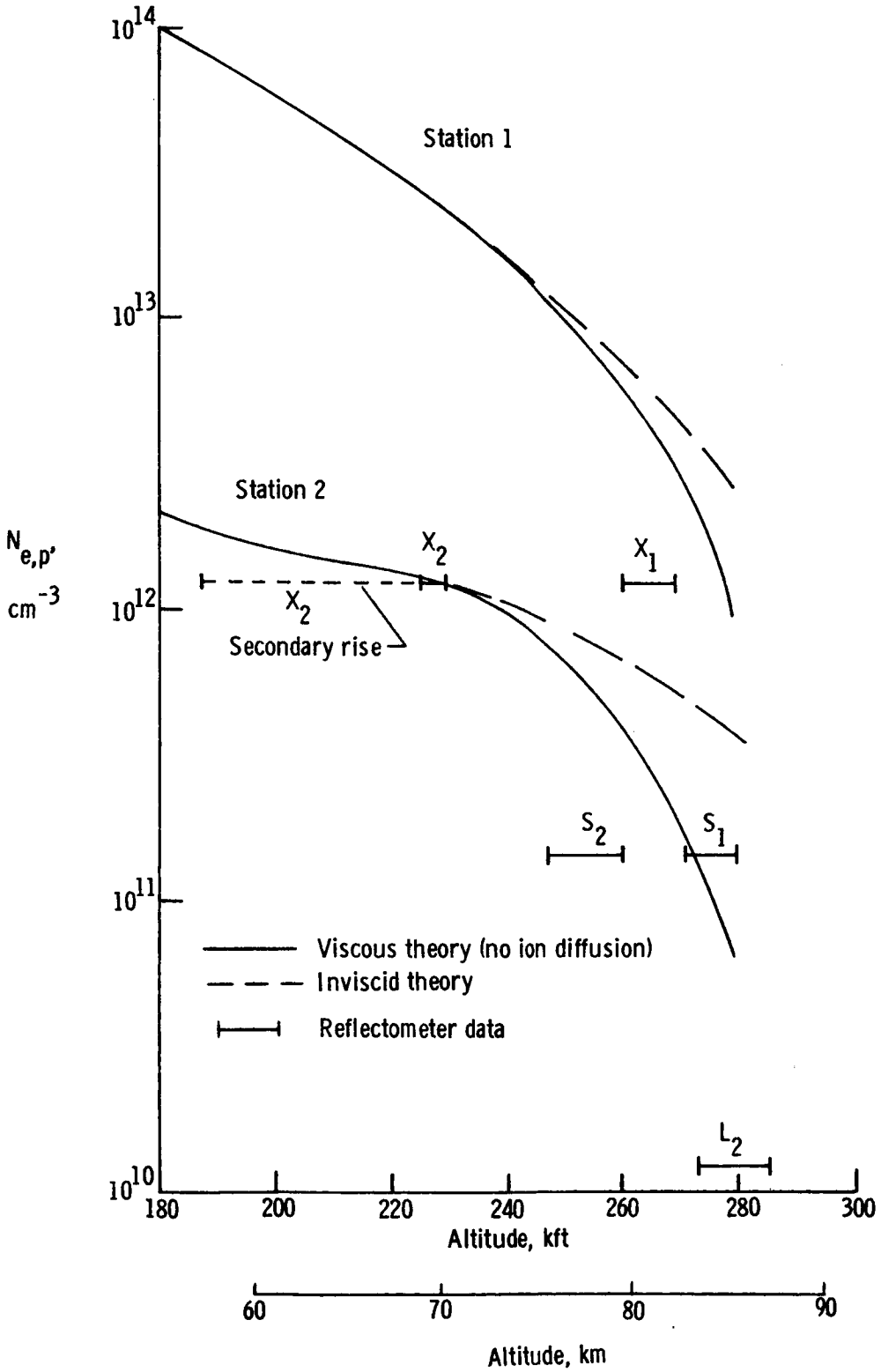

(a) Nose stations.

Figure 3.- Comparison of peak electron concentration at high altitude.

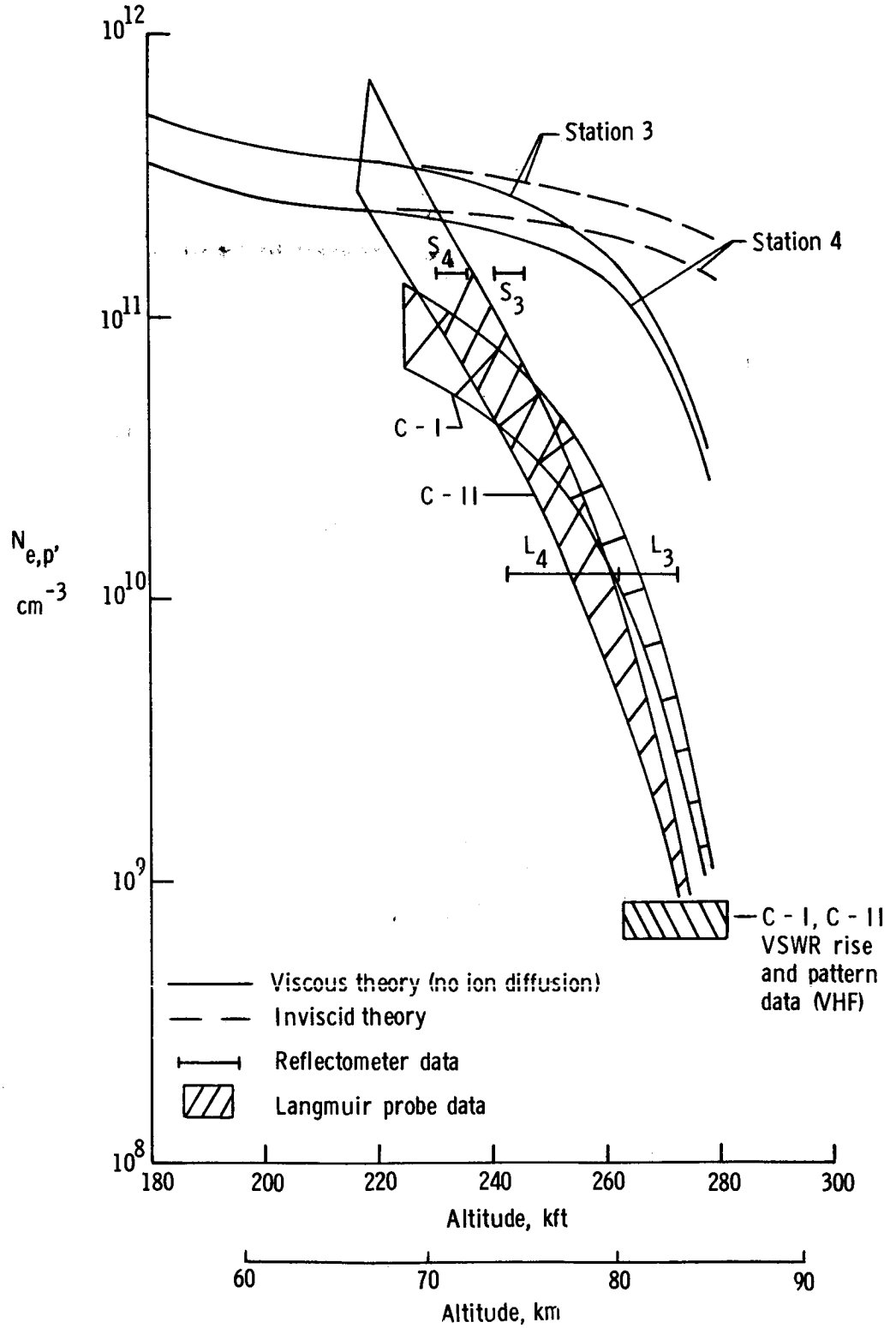

(b) Aft stations.

Figure 3.- Concluded.

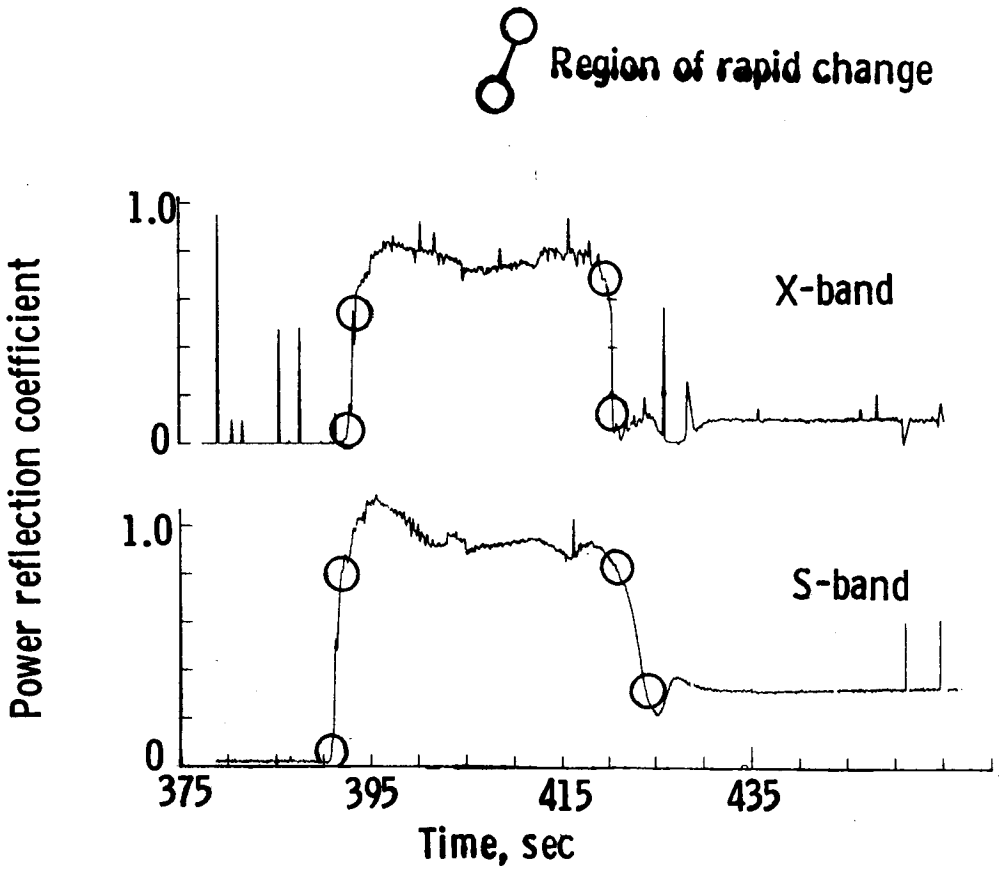

Figure 4.- Reflection-coefficient data (ref. 4) for station 1.

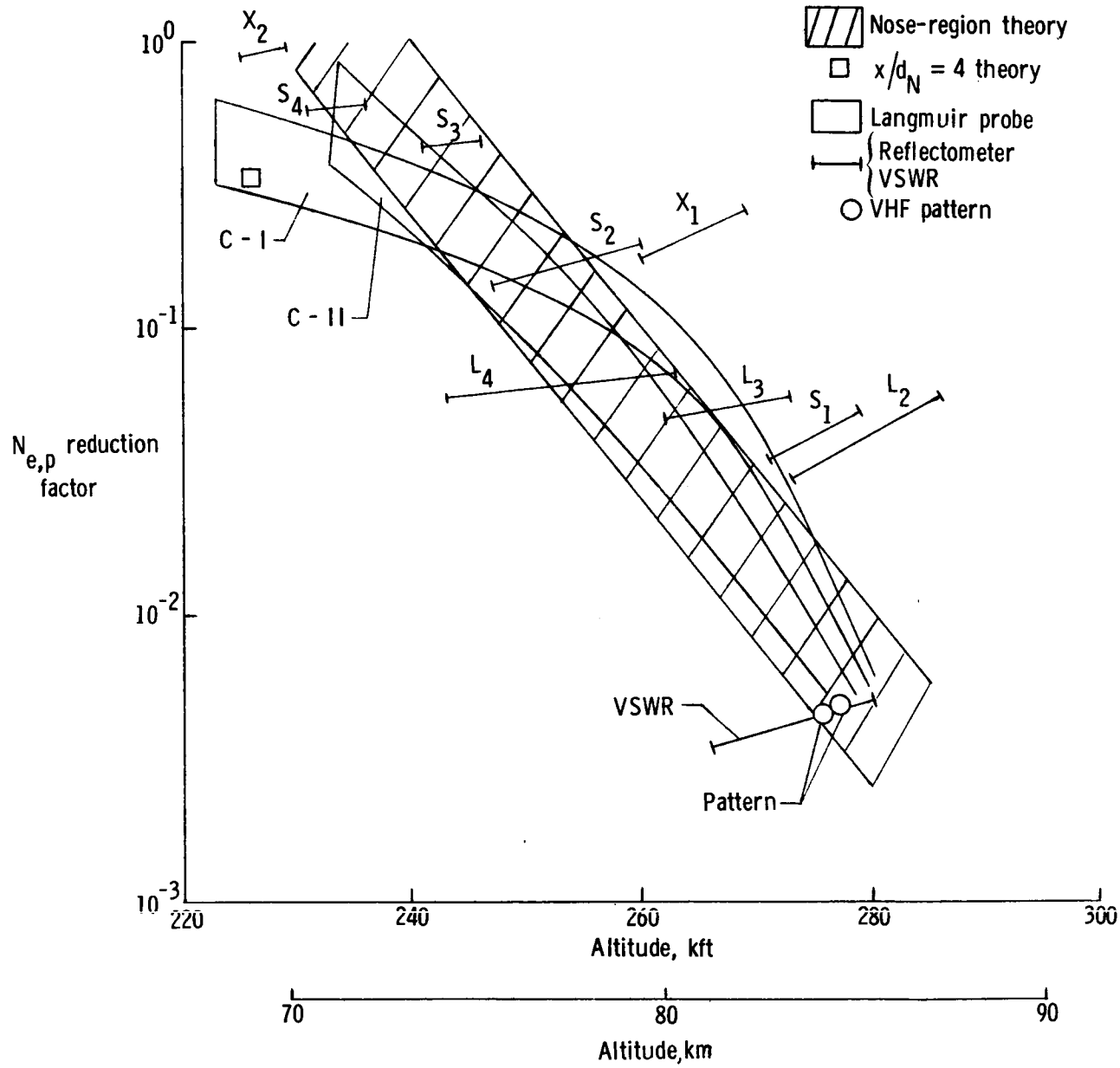

Figure 5.- Correlation of high-altitude data with ion diffusion and wall effects factor. Theory taken from references 11 to 15.

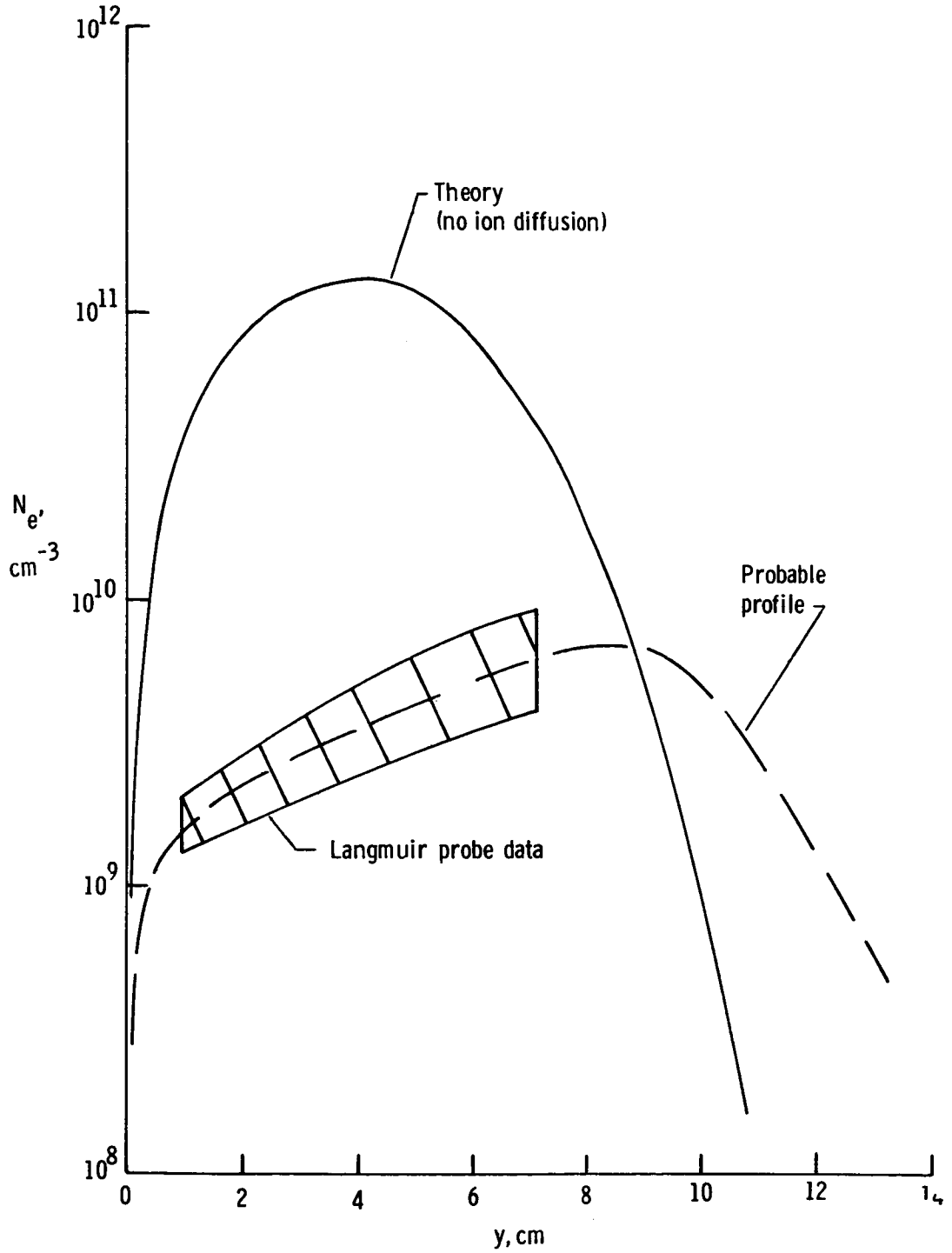

Figure 6.- Comparison of electron concentration profiles. $x/d_N = 4$; altitude, 80.16 km (263 000 ft).

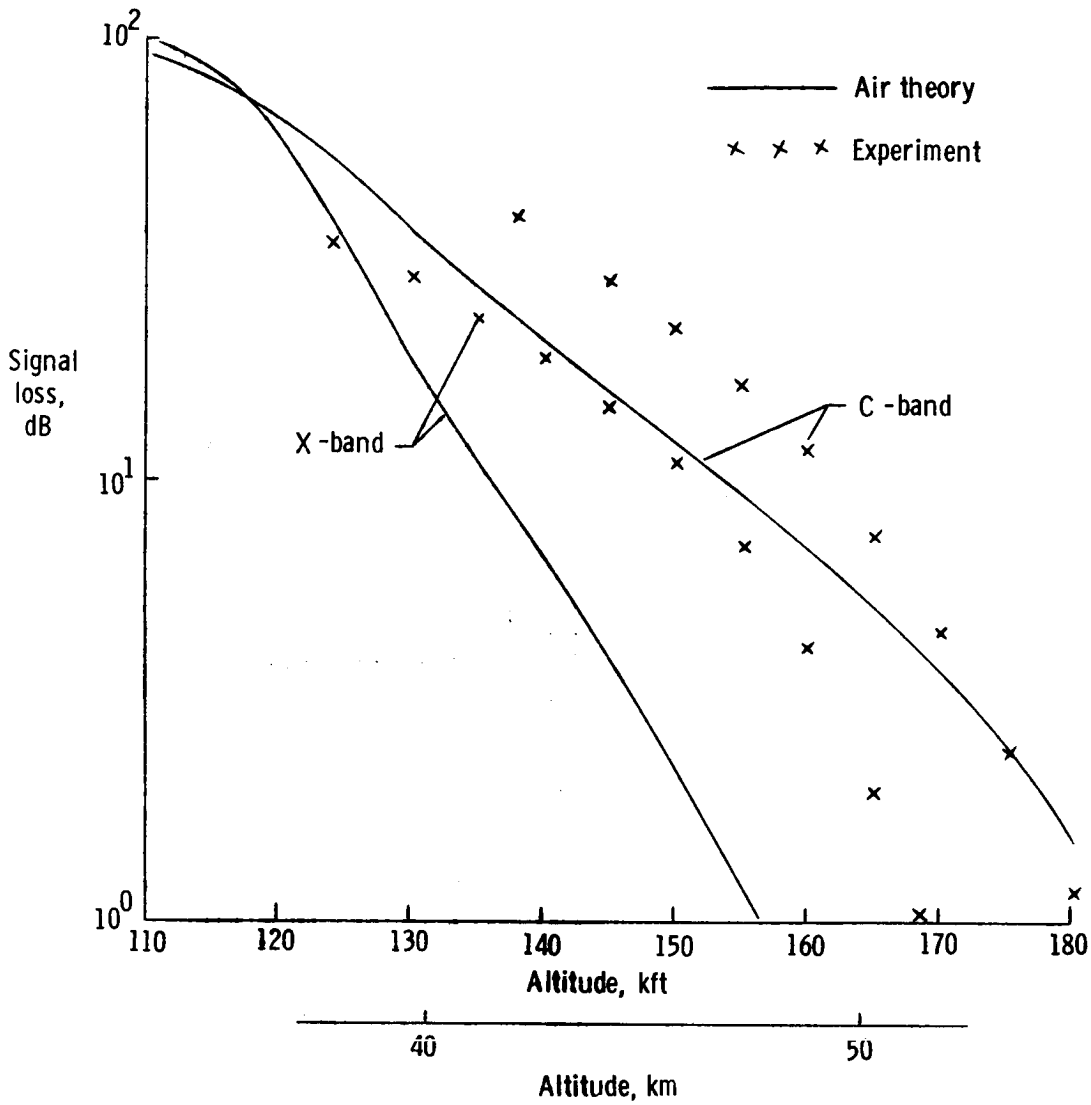

Figure 7.- Comparison of RAM C-II microwave attenuation data with air theory.

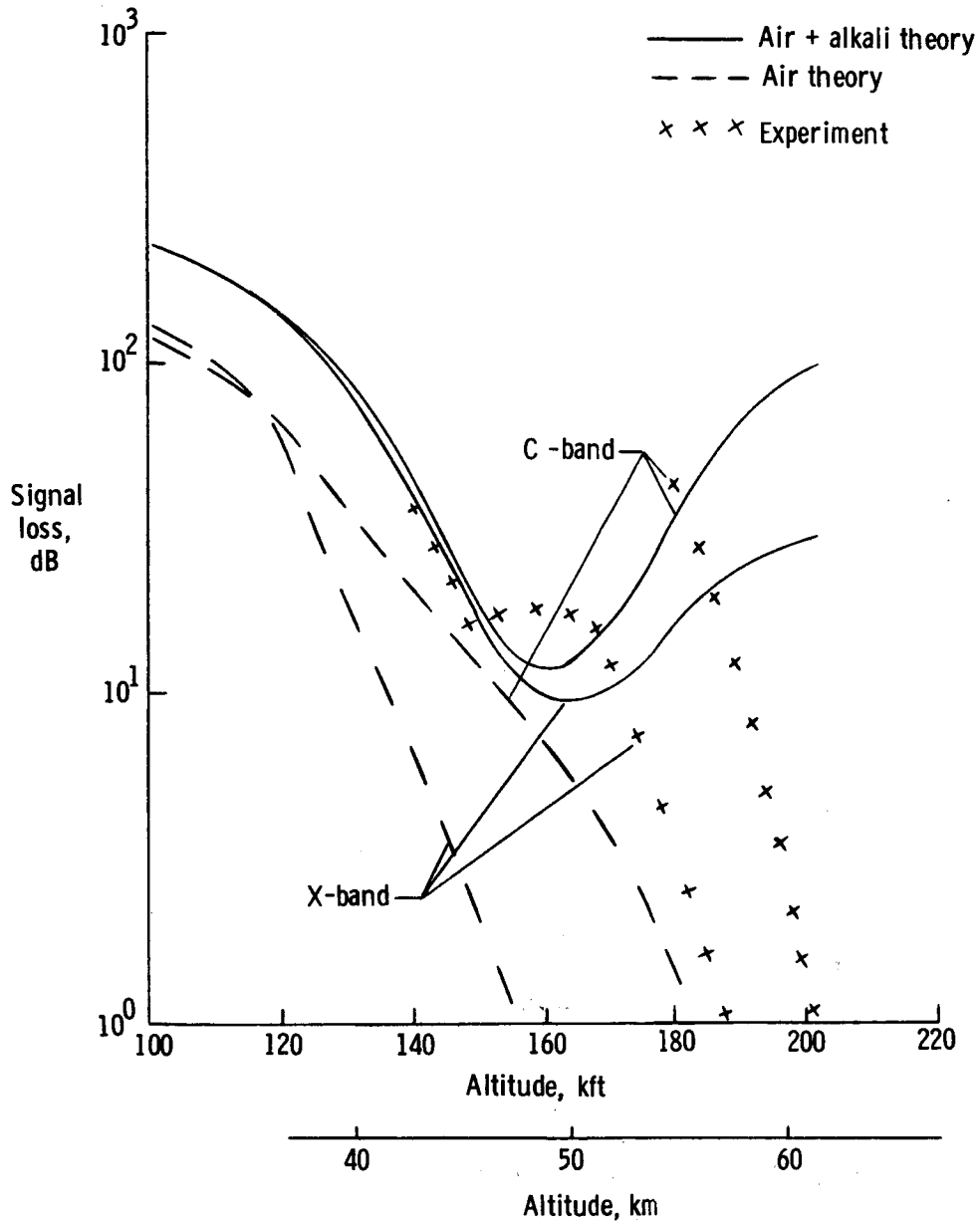

Figure 8.- Comparison of RAM C-I microwave attenuation data with ablation model.

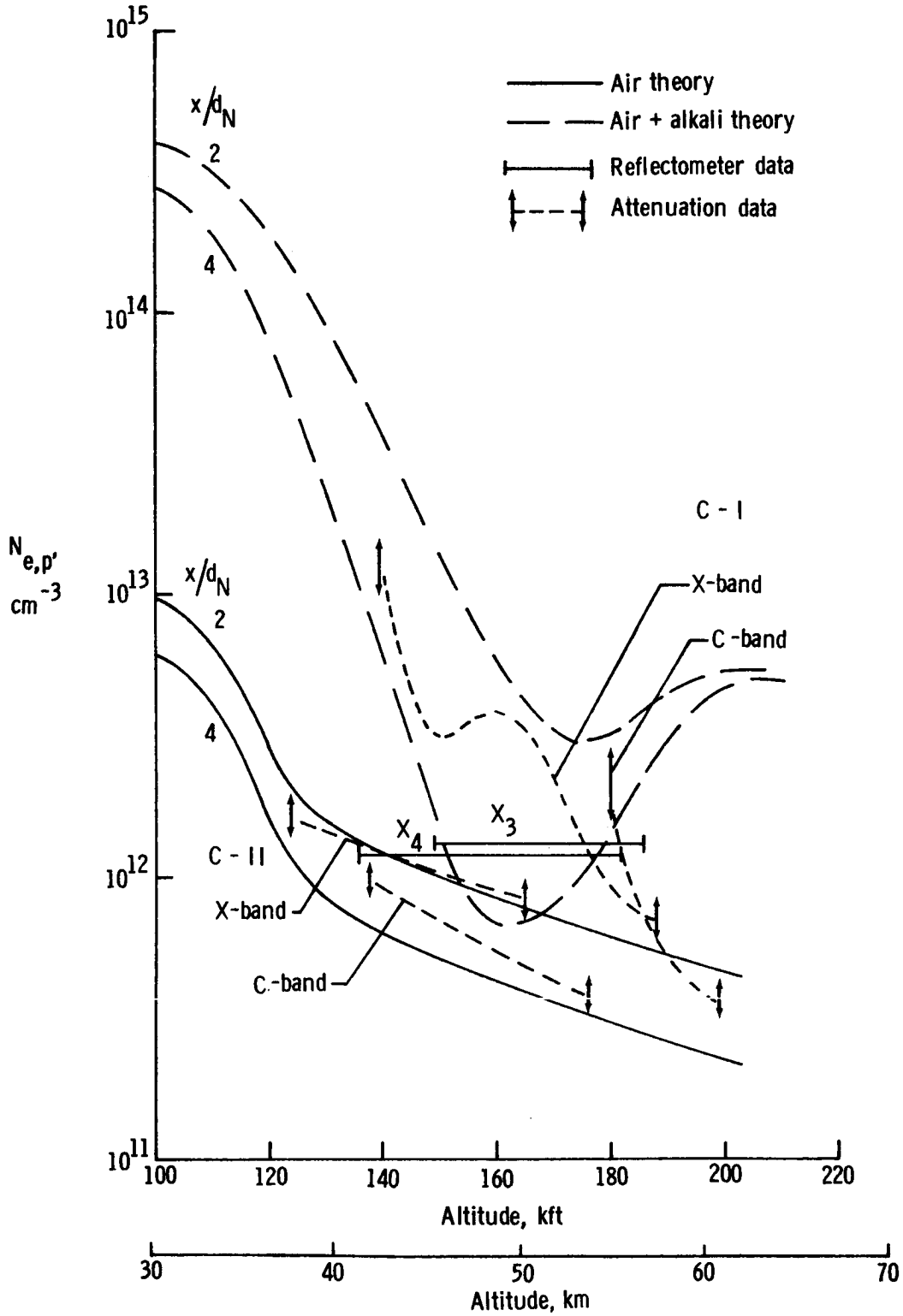

Figure 9.- Comparison of theory with peak electron concentration data at intermediate altitudes.

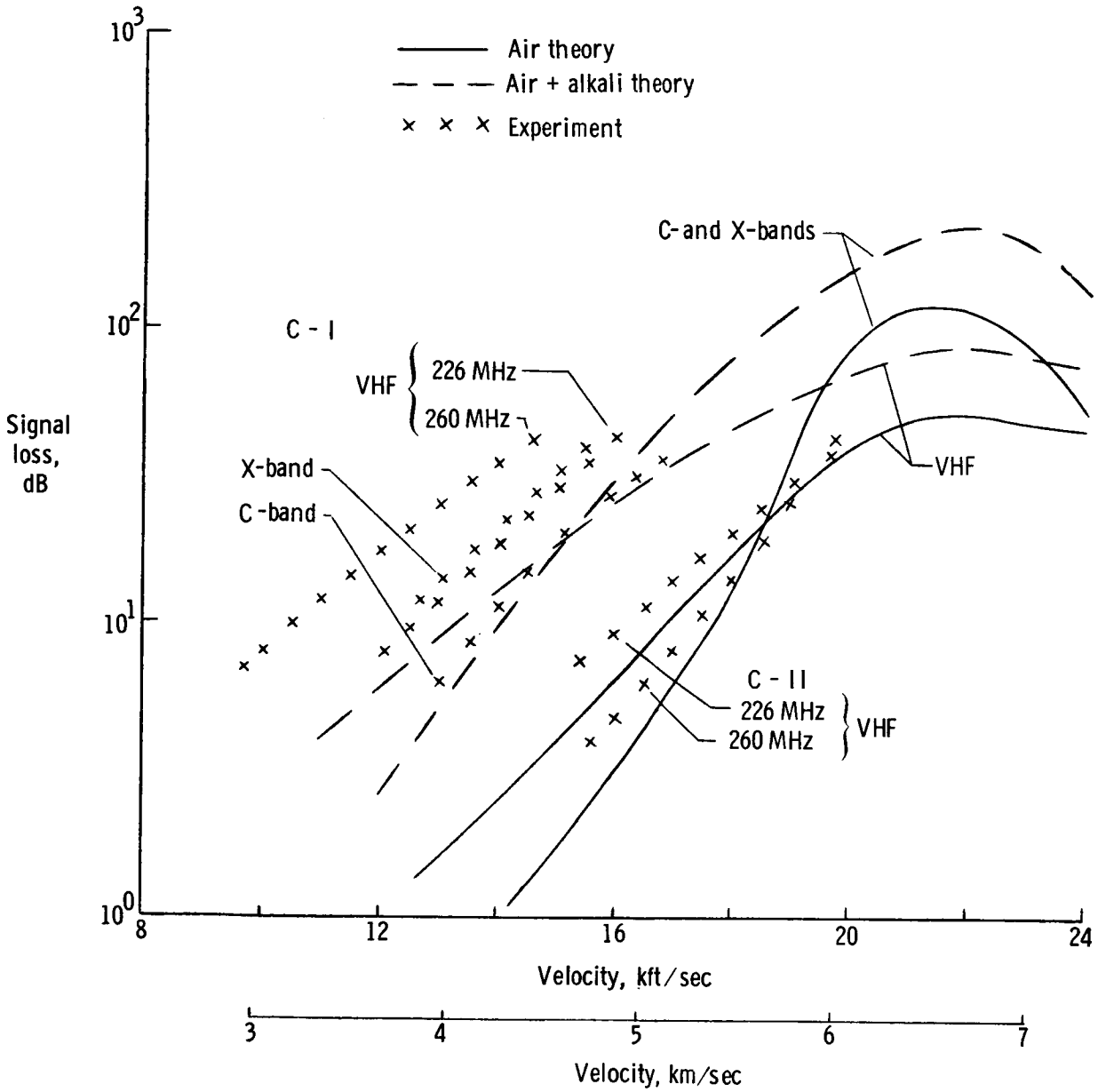

Figure 10.- Comparison of theoretical and experimental attenuation for altitudes ranging from 19.2 to 40.0 km (63 000 to 131 000 ft).

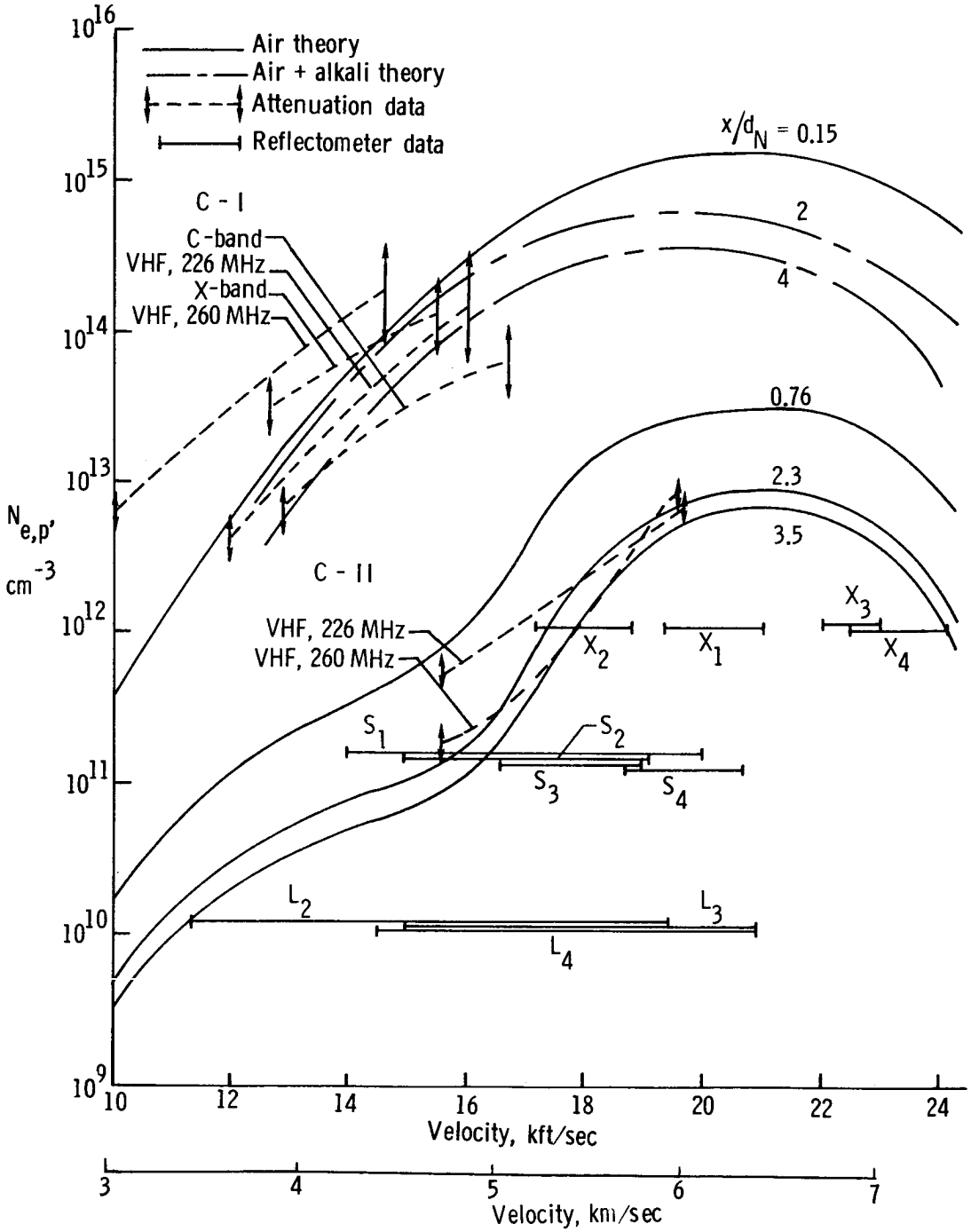

Figure 11.- Comparison of peak electron concentration for altitudes ranging from 19.2 to 40.0 km (63 000 to 131 000 ft).

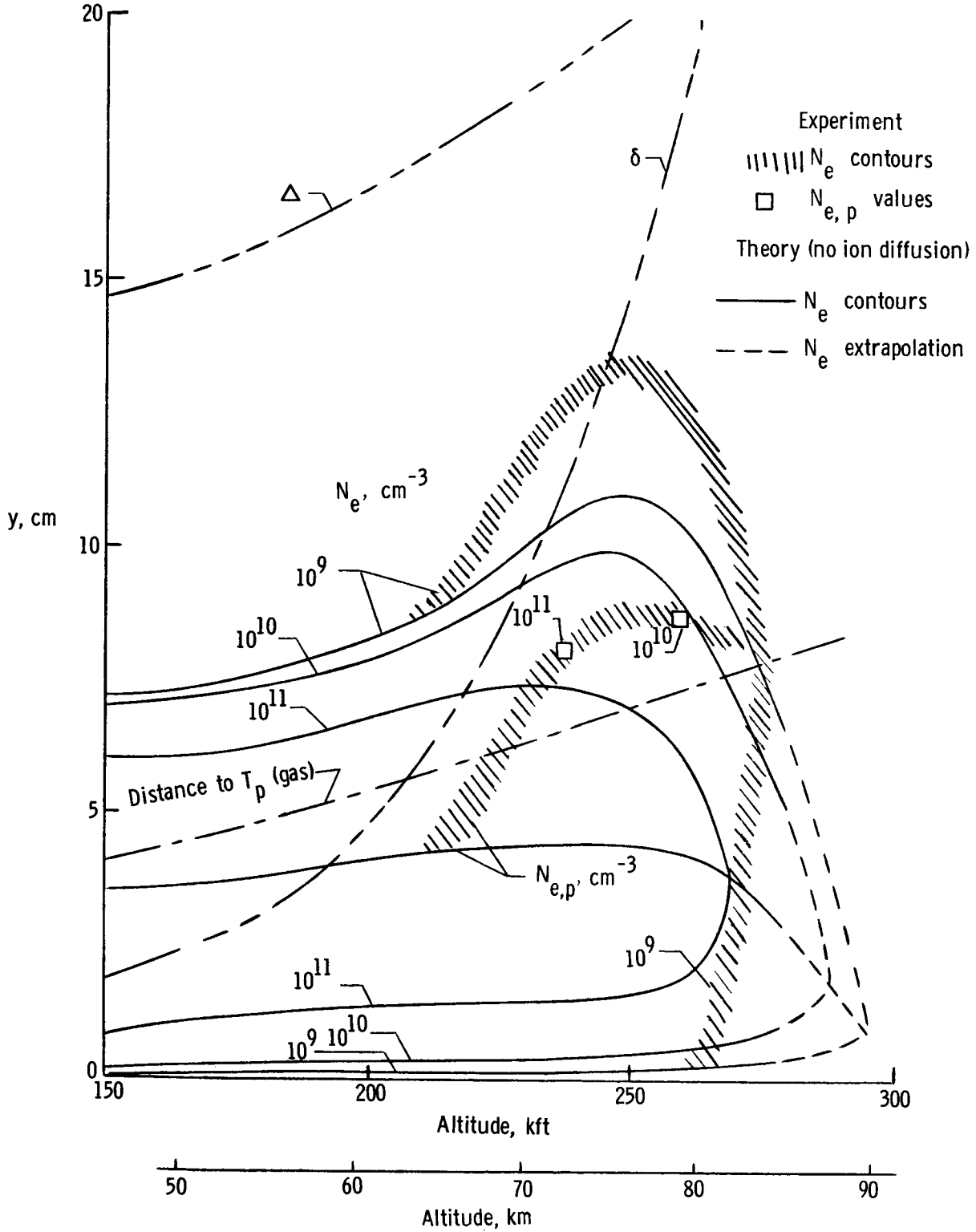

Figure 12.- Effects of ion diffusion on electron concentration contours at $x/d_N = 4$.

REENTRY PRECURSOR PLASMA - DETERMINATION OF THE VACUUM ULTRAVIOLET PHOTOIONIZING RADIATION FLUX*

By Paul V. Marrone and Walter H. Wurster

Cornell Aeronautical Laboratory, Inc.
Buffalo, New York 14221

ABSTRACT

A shock tube research program is described which provides data applicable to VUV radiation from blunt reentry vehicles. The radiation is considered from states in N_2 sufficiently energetic to photoionize ambient O_2 ($E > 12$ eV, $\lambda < 1030$ Å). N_2 absorption coefficients are obtained with a windowless spectrometer using reflected shock radiation to measure absorption in incident-shock heated gases. Additionally, nonequilibrium shock radiation profiles are measured to permit formulation of electronic excitation models and evaluation of rates. Experimental methods, the data and their use in reentry flow field calculations are discussed. Numerical results for precursor plasma properties and RCS effects are briefly presented.

INTRODUCTION

Analyses of radar observations associated with the entry of high-speed objects into the earth's atmosphere have resulted in the consideration of the existence of a cloud of free electrons at substantial distances ahead of the object. Evaluation of the radar return of the MA6-Mercury capsule in 1962[1], for example, showed that the returns could be explained if there existed a precursor cloud of electrons at densities of about 10^7 cm^{-3} at a radius of about 18 m around the capsule. One model for the production of such precursor plasmas in the region ahead of the bow shock considers the shock-heated air as the source of the ionizing radiation, wherein photons leave the shock-heated gas cap and interact with the ambient atmosphere. Thus, the prediction of effects of a precursor plasma on the radar return from blunt reentry bodies involves a knowledge of the photoionizing radiation flux leaving the shock-heated gas cap, the calculation of the precursor plasma electron number densities and finally, the interaction of the incident EM waves with the precursor plasma. Each of these problem components is being studied in a current experimental and analytical research program at CAL, and the present paper will draw upon the results obtained to date on this program. The major emphasis of this paper

17

* Research sponsored by the Advanced Ballistic Missile Defense Agency, Department of the Army, Contract No. DAHC 60-69-C-0130.

will be on the determination of the VUV photoionizing radiation flux emerging from the shock layer gas cap. This involves principally the experimental measurement of the necessary radiative parameters of the shocked gases; namely, the spectral distribution and strength of the radiation in the wavelength region of interest, as well as the electronic excitation rates which govern the excited molecular state populations in the nonequilibrium gas cap flowfield. A discussion of these experiments and the data constitute the major portion of this paper. Finally, the use of several computer codes will be briefly described by means of a numerical example, which demonstrates the coupling of the radiative flux, the generation and properties of the photoelectron precursor plasma, and the subsequent RCS effects for a realistic reentry configuration.

GENERAL CONSIDERATIONS

Of the principal constituents composing the ambient atmosphere, molecular oxygen has the lowest ionization threshold. The lowest energy state of O_2^+ lies approximately 12.1 ev above the ground state of O_2. Considering a one-step ionization process, only photons with an energy in excess of 12.1 ev are capable of producing photoelectrons. This energy corresponds to a wavelength of 1027 A, and hence the photoionization process in air has a sharp onset at this wavelength, and extends to shorter wavelengths. Thus, the ionizing radiation from a blunt body gas cap of interest to the present problem lies in the wavelength range between 1027 A and 800 Å. The upper limit is determined by the O_2^+ photoionization onset and the lower by the decrease of intensity at the temperatures prevailing in the gas cap. This is an important feature for precursor plasma evaluation, since the calculation of the ionizing radiation flux is severely hindered by the lack of experimental data in this wavelength region. The primary source of the ionizing flux has been attributed to radiation from high-lying (> 12 ev) energy states of the nitrogen molecule (Fig. 1), although a preliminary analysis of the results recently obtained on this program indicate that the NO molecule may also have to be considered. These excitation energies are in excess of the dissociation energy, and hence the problem involves the nonequilibrium condition wherein the population of these states and the resultant emission spectra are governed by the electronic excitation rates competing with the subsequent dissociation behind the bow shock. Thus, the required data for the calculation of the ionizing flux include electronic excitation rates as well as the pertinent transition probabilities.

A large number of N_2 states whose energies lie about 12 ev that have been reported in the literature have been classified and ordered in recent papers by Carroll and Collins[2] and Dressler[3]. They showed that most of the separately reported bands can be attributed to the $b'\ ^1\Sigma$ and $b\ ^1\Pi$ states, and two Rydberg series (Fig. 1). Thus, one aspect of the present problem is the determination of which of these states are excited and emit under the highly nonequilibrium conditions behind a bow shock. No applicable intensity data exist for the wavelength region in question; however, Appleton and Steinberg[4] have reported absorption measurements of shock-heated N_2 between 1086 and 1334 Å. By varying the gas temperature, they were able to attribute

the absorption to specific vibration levels of the ground state of N_2, and to deduce f-numbers for the $b'\ ^1\Sigma$ and $b\ ^1\Pi$ states. The key question remains, however, to make spectral measurements in the wavelength region of interest (1027 - 800 Å) to determine whether these states account for all the radiation emitted therein, and to obtain an appropriate f-number. Thus, one part of the experimental work consists of quantitative spectral measurements below 1027 Å to determine the spectral structure and the associated transition probabilities.

Given the spectral data described above, the problem also exists to determine the appropriate excited state populations that govern the emission spectrum. Neither an excitation mechanism nor rate is known for these high-lying energy states in N_2, which involve transitions between singlet states. Most previous radiation measurements in N_2 have been made of transitions involving the triplet states: $N_2(1+)\left[B\ ^3\Pi \rightarrow A\ ^3\Sigma\right]$, $N_2(2+)\left[C\ ^3\Pi \rightarrow B\ ^3\Pi\right]$, and the $N_2^+(1-)$ band system. See Fig. 1. Despite the fact that an electron spin change is involved in terms of direct excitation from the singlet ground state, these states have been shown to be very quickly populated by shock excitation[5].

Thus, the second part of this research program consists of the measurement of the radiation from strong shock waves in N_2 and N_2 - O_2 mixtures. These measurements are designed to provide data from which excitation mechanisms may be postulated, and excitation rates established for the pertinent VUV emitting states of N_2. The present discussion will include the measurements that have been made, and the manner in which the data are presently being used to develop an excitation model for incorporation into the nonequilibrium flow programs.

ABSORPTION COEFFICIENT MEASUREMENTS

Experimental

As mentioned above, the purpose of the absorption measurements includes the determination of the spectrum of N_2, at wavelengths below 1027 Å, appropriate to the high temperatures prevailing in the gas cap. The measurements of Appleton and Steinberg[4] at wavelengths of 1334 Å, 1247 Å, 1176 Å and 1086 Å showed that the absorption occurred primarily from the 13, 11, 8 and 5th vibrational levels of the ground state, respectively. Based on these observations and the pertinent spectroscopic data available from cold N_2 measurements, it is expected that the lowest three vibrational levels of the N_2 are involved in the transitions at wavelengths below 1027 Å. Thus, the absorption spectra must be measured for N_2 at elevated temperatures, under which the vibrational states are suitably populated. It should also be mentioned that the rotational energy distribution plays a significant role in establishing the spectral structure of the gas cap radiation. This is another reason for the inapplicability of cold N_2 absorption data.

The reasons discussed above make clear the advantages of the use of the shock tube to heat the N_2 gas. Equilibrium temperatures between 4000 and 8000°K are readily achieved over a range of gas densities. The price for this

convenience lies in the limited test times during which the state of the shock-heated test gas is known. These times lie nominally between 50 and 200 μ sec. Ultimately, this limitation manisfests itself in the criteria to be met by the light source for the absorption experiment. Ideally, the source should emit a steady, continuum spectrum over the wavelength region of interest, and have a high brightness temperature relative to the test gas. In addition, it should be intense enough to provide good signal-to-noise ratios even when spectrally dispersed to 10 Å resolution, and recorded by detectors with about 5 - 10 μ sec time constants.

Flash lamps are available for the VUV region. Although they have high brightness temperatures, they suffer from the standpoint of repeatability. A more severe drawback is the fact that at wavelengths below 1000 Å, their spectra have changed from continuum to line, and therefore preclude the possibility of absorption measurements at all wavelengths. This feature is illustrated in Ref. 4.

A further complexity in VUV absorption experiments is the lack of window materials to transmit wavelengths below 1050 Å, the transmission cutoff of lithium fluoride. Thus, exposure of a VUV spectrometer-detector system to the shock-heated gases must be accomplished in a windowless fashion, with the entire optical train under hard vacuum. The required vacuum levels ($< 10^{-4}$ torr) are determined by the use of bare photomultiplier detectors in the spectrometer.

The design of the absorption experiment which meets the requirements discussed above has been based in large part on the techniques and results that accrued under an extensive research program conducted at CAL for NASA[6]. The program was directed toward emission measurements of the continuum, recombination radiation of $N^+ + e$ in the wavelength range between 1200 and 700 Å from shock-heated N_2 at temperatures between 10,000 and 13,000°K. The apparatus and techniques developed for that research and the results of the study have been described in detail in Ref. 6. Only the features pertinent to the present experiments will be presented here. They include the following:

(a) A high-purity shock tube, 3 in. inside diameter, with a driven section 30 feet long was utilized (Fig. 2). It is highly instrumented with seven wavespeed measurement intervals, optical ports for both incident and reflected shock radiation measurements, as well as sidewall heat transfer measurement stations. Driver pressures to 4000 psi H_2 have been employed, with initial pressures as low as 0.5 torr. Shock wave speeds up to 17 kft/sec have been utilized in the present experiments.

(b) A three-channel vacuum spectrometer was designed and constructed to permit measurements to be made simultaneously at three wavelengths. First-order dispersion is 16 Å/mm.

(c) The spectrometer is optically coupled to the shock tube (Fig. 2) through an explosively driven plunger, which serves as a fast-acting valve-shutter combination (Fig. 3). It is synchronized with the shock wave, and exposes the spectrometer system to the

shocked gases for a 100 μsec interval that can be adjusted to occur during any part of the test time.

(d) Radiation detection is accomplished by bare photomultiplier tubes placed behind slits in the spectrometer focal plane and operating within the vacuum of the spectrometer chamber itself. The high voltage supply is electronically crowbarred directly after the exposure to protect the tubes from arcing in the event of excessive gas leakage. The use of sodium salicylate to record the VUV radiation with normal tubes was found to be inapplicable, due to the high flux of visible radiation constituting an unwanted background. The bare phototubes have no response at wavelengths longer than about 1500 Å, and thereby circumvent this problem.

(e) The $N^+ + e$ recombination radiation was found to be very strong, requiring N_2 dilution by neon to achieve optically thin conditions. Neon is optically inert in the wavelength interval of interest. Of particular interest to the present problem are the cases of optically thick radiation, since this $N^+ + e$ radiation source provides a convenient source of continuum radiation at wavelengths below 1130 Å, equivalent to a black-body source over the 10,000 - 13,000 °K range.

The features described above were utilized in the design of the present absorption experiments in the following way. A splitter-plate was designed which fits into the shock tube at the reflecting wall (see Fig. 4). The configuration is such that the incident shock wave is divided and proceeds down two channels. One channel is obstructed, and the shock is reflected. This pocket of gas is at reflected shock conditions, and serves as the light source described in (e) above. The light is permitted to pass through an aperture in the splitter plate, passing through the gas in the second channel and into the spectrometer. The gas in this second channel has been processed by the incident shock only, and hence is heated to a significantly lesser degree. The system is feasible because the same test gas composition can be used, over a range of conditions, to serve both functions: a high intensity continuum VUV light source at 10,000 - 13,000 °K, and a chamber of N_2 at 4000 - 8000 °K upon which the absorption measurement is made.

Details of the overall design parameters and the results of splitter-plate performance tests have been reported in Ref. 7. These tests involved the use of various radiometers (and the VUV spectrometer) on each side of the splitter plate. Detectors on the reflected-shock, light source side monitor the total output, while detectors at the opposite, test gas side measure the light source intensity attenuated by any absorption in the test gas. For wavelengths at which the test gas is transparent, the signals have been shown to be equal.

Typical records are shown in Fig. 4b. The lower trace is the signal recorded from an EMR-641-09-18 phototube viewing radiation in the 1150 - 1500 Å interval having a peak sensitivity at 1300 Å. This monitoring phototube shows the total light source radiation history. As can be seen, the

radiation rises to an equilibrium plateau level of about 50 μsec duration. The upper trace is the recorded signal from one channel of the VUV spectrometer set at 760 Å. The plunger open time can be seen, and demonstrates the close synchronization that is achieved with the reflected shock radiation. This 760 Å radiation has passed through the gas heated only by the incident shock, and has been partially absorbed. A comparison of this signal to that obtained with the reflected shock light source on the spectrometer side of the splitter plate (by rotating the splitter plate assembly 180° in the shock tube) gives the fraction of light absorbed, which constitutes the basic datum for the absorption experiments.

The tests to date have revealed no inherent problems in the splitter-plate technique. No damage to the sharp leading edge has been incurred, and no evidence of plate flapping seen. The sidewall heat-transfer gauges that are very sensitive to flow-induced temperature changes showed the channel flow to be free of detrimental shock perturbations. The radiation from the light source channel rose to a fair plateau after shock reflection, and serves as a very suitable source for the absorption experiments. No gasdynamic effects at the splitter-plate aperture have been detected.

Absorption Data

The absorption coefficient measurements made use of the entire system described above; the splitter-plate light source unit, the windowless plunger, and the three-channel VUV spectrometer. Other radiation monitors were also used to obtain radiation profiles behind the incident shock wave. Filter-photomultiplier combinations were used to monitor the N_2 (1+) system at 6600 Å and the N_2 (4+) system at 2500 Å. These radiation records were highly reproducible (within 5%) from test to test, thereby permitting all measurements to be directly compared.

The test gas consisted of a mixture of 10% N_2 - 90% Ne at an initial pressure of 2.0 torr. A constant shock velocity of 13,700 ft/sec was used, producing a reflected shock light source temperature of 11,300 °K and an equilibrium incident shock temperature of 6000 °K. The experimental program was planned so as to initially obtain absorption data at wavelengths overlapping the window region measurements of Appleton and Steinberg[4] (i.e., $\lambda \geq 1086$ Å), and then extend the measurements into the windowless region down to approximately 800 Å. All data was obtained using the VUV spectrometer in first order, with a wavelength bandpass of 16 Å in each channel.

Figure 5 shows the absorption measurements obtained from the experimental series at a temperature of 6000 °K. Two shock-tube tests were required to obtain each data point at a wavelength; first I_o was measured, then the splitter plate rotated 180° so that I could be obtained (see Fig. 4). Two separate detector systems were used to insure test condition repeatability. One was the VUV radiometer at a station opposite the spectrometer. The second was a filter-photomultiplier system inside the spectrometer itself. Set at 5000 Å, for which the test gas was transparent, its constant output signal from test to test verified a constant I_o for the test series.

The experimental data are shown as the ratio of I/I_o as a function of wavelength. Also given on the figure are calculated values of I/I_o using the cross-sections given by Appleton and Steinberg[4] for wavelengths greater than 1086 Å. Their measurements indicated that the N_2 population in the higher vibrational levels was responsible for absorption in the window region. In particular, they attributed absorption from the following vibration levels:

λ, Å	v"
1334	13
1247	11
1176	8
1086	5

Using the temperature of 6000 °K, the N_2 number density in each vibrational level (N_2, v") was computed and I/I_o calculated from

$$\frac{I}{I_o} = e^{-\sigma_\lambda \cdot N_{2,v'',\lambda} \cdot L} \tag{1}$$

where σ_λ is the appropriate absorption cross section (Ref. 4) and L is the absorption path length for the present experiment (L = 3.35 cm). It can be seen that for wavelengths greater than about 1150 Å, the shock-heated gas is transparent, the higher vibrational levels responsible for absorption in this wavelength region not being sufficiently populated at 6000 °K.

The splitter plate absorption data are in excellent agreement with the measurements of Ref. 4 in the region of wavelength overlap. At 1086 Å, for example, the data show about 70% of the incident light I_o is transmitted through the hot gas. However, as the wavelength is decreased, the absorption increases markedly. This is to be expected, since the more highly populated lower vibrational levels (v" = 0, 1, 2) are responsible for absorption in the wavelength region 850 - 1000 Å. Only about 10-15% of I_o is transmitted in this wavelength range. At 1000 Å, for example, the I/I_o ratio has already dropped to about 0.2.

Below 852 Å, the presence of N atoms in the shock-heated gas contributes to absorption of the radiation (852 Å is the photoionization edge of the ground state N atom). Since the N atom absorption cross-section is known[6], the amount of absorption below 852 Å due to this process was calculated, and is also shown on Fig. 5. The splitter-plate data indicate greater absorption in this wavelength region, due to the additional presence of the N_2 absorbing band system.

The absorption data (I/I_o) were converted to an absorption coefficient using

$$\frac{I}{I_o} = e^{-k^* L} = e^{-k \cdot N_{2,tot} \cdot L} \tag{2}$$

where k is in units of $cm^{-1}\ atm^{-1}$.

These data are shown in Fig. 6, and extend the k values given in Ref. 4 into the windowless region. In the wavelength region of high absorption, the k value reaches a maximum near $10^3\ cm^{-1}\ atm^{-1}$. The values of k obtained at wavelengths below 852 Å have a greater degree of uncertainty, since the

dominant N atom contribution must be taken into account. However, the data do show a sharp decrease in absorption at these wavelengths, in substantial agreement with the predicted shape of the band system obtained using a synthetic spectrum generating program[7], and the best available spectroscopic constants for these states[2,3].

From the experimental results, it can be seen that in the critical wavelength region of interest to the precursor problem (1027 Å – 800 Å), it is very important to know the relationship between the rate of excitation of the radiating species and the vibrational relaxation rate which determines the absorption. If these rates are comparable, then it is possible that substantial absorption will occur near the shock front, severely inhibiting the amount of vacuum ultraviolet flux that emerges from the shock. Once the ratio of these two rates have been established (through emission studies to be discussed in the next section), the overall excitation-absorption model will be included in a shock-layer radiation flux computer program to be used in the calculation of the resultant VUV radiation emerging from the shock front.

EMISSION MEASUREMENTS AND DEVELOPMENT OF AN EXCITATION MODEL

At high reentry altitudes, the low densities and correspondingly decreased collision frequencies in the shocked gas produce an appreciable lag in the kinetics which determine species concentrations and energy partition in the internal modes of the molecules. A pronounced effect is seen in the centerline translational temperature of an axisymmetric vehicle, in which the temperature nominally begins at a high value directly behind the bow-shock wave, and then falls markedly toward the equilibrium stagnation value. This striking temperature dependence is dominated by O_2 dissociation. It is clear that the use of the final stagnation temperature in determining the radiation flux would lead to incorrect values.

The corresponding molecular nitrogen density values do not vary markedly; thus, the principal feature of radiation prediction centers upon the highly temperature-dependent populations of the excited radiating states. The limiting case for radiation flux intensity is obtained by assuming that the populations of these excited electronic states are in equilibrium with the local translational temperature. This case corresponds to infinitely fast excitation rates and would predict an extremely large radiative flux in the high temperature nonequilibrium region immediately behind the shock.

Thus, for typical reentry gas cap temperature, the electronic excitation rates for the radiating states dominate the calculation of the nonequilibrium ionizing radiation flux from the bow shock. Since neither an excitation mechanism nor rate data are available, the need exists for direct measurements of these rates for the high lying energy states of N_2. The aims of the emission experiments are to provide the data necessary for the postulation of excitation mechanisms for these high lying energy states of N_2.

Shock-Profile Radiation Measurements

Initial experiments were designed to determine whether radiation overshoots exist behind strong shock waves for the states of N_2 pertinent to the precursor problem. As has been discussed, the $b'\ ^1\Sigma$ and $b\ ^1\Pi$ states, the most likely candidates for the source of radiation below 1027 Å, also extend to wavelengths in excess of 1500 Å. Therefore, direct measurements in this wavelength region were conducted, using an EMR-641-09-18 phototube with an MgF_2 window, viewing the wavelength region from 1150 - 1500 Å.

Although the excitations of these singlet states are the most critical for the present problem, it was decided to make simultaneous measurements of several other triplet states. (See Fig. 1). These states give rise to band systems in more accessible regions of the spectrum, and for this reason have been measured and used as diagnostics in many shock tube studies. Of particular interest is the $D\ ^3\Sigma$ state, which lies at 12.8 ev, well into the energy region of interest, giving rise to the (4+) band system. Thus, as an aid to the interpretation of excitation data, simultaneous measurements were made on the $D\ ^3\Sigma(4+)$, $B\ ^3\Pi(1+)$, and the combined $b'\ ^1\Sigma$, $b\ ^1\Pi$ VUV band systems. Interference filters with 200 Å bandpasses were used at 2500 Å and 6600 Å, respectively, for the (4+) and (1+) measurements. Spatial resolution was determined by 1 x 3 mm apertures at the shock tube wall. Using a lens system, the best resolution was achieved for the 6600 Å channel, where the field of view was a constant 1 x 3 mm across the shock tube. This corresponded to about 0.25 μsec resolution for the shock speeds obtained in the experimental program[7].

A series of experiments was made, in which shock waves at velocities of 15,500 ft/sec were driven into N_2 at 1.0 torr initial pressure. At this velocity, the ideal, post shock temperature is 10,600°K, and rapidly decays to its final equilibrium value. Typical radiation records for these tests are shown in Fig. 7, showing the strong overshoots for each of the states measured. From these records it was shown, therefore, that the molecular populations of the high energy states couple sufficiently quickly to the translational temperature to result in strong radiation prior to molecular N_2 dissociation. Analyses of the data also show that the (4+) and VUV radiation decays more rapidly than the (1+) in the approach to equilibrium. This is to be expected from the strong temperature dependence arising from the fact that the upper states lie at 12 and 8 ev, respectively.

The experiments were then extended to VUV profile measurements in air and pure NO, the results of which are shown in Fig. 8. For these tests, the initial pressure, $p_1 = 1.0$ torr and $V_s = 15,000$ ft sec^{-1}. Several interesting features are evident in the records. In going from (a) N_2 to (b) air, it is seen that the radiation overshoot is much less (in spite of the noted gain change). This effect could be anticipated, since the translational temperature drops much more rapidly behind a shockwave in air, due to the faster O_2 dissociation rate. A feature yet unexplained, however, is the steady plateau of radiation prior to the end of the test time. At the high temperature needed to excite radiation at this wavelength, it would be expected that all the diatomic species would have dissociated appreciably. An identical shock tube test using pure NO as the test gas yields the record (c). It can be seen that

the overshoot is higher and steeper, which is reasonable on the grounds that in this case NO can be thermally excited prior to dissociation, while in air the NO must be chemically formed after O_2 dissociation. The radiation plateau is still present. It seems definite, therefore, that there exists a radiating species in air and NO that is not present in the pure N_2 tests. This feature is of particular significance to the precursor problem, if it is found to persist when these overshoot measurements are extended to wavelengths below 1027 Å.

Development of an Excitation Model

As has been shown, the rate of population of the excited states close to the shock front is the critical parameter in determining the ionizing radiation in the highly nonequilibrium portion of the shock layer. Thus, an excitation mechanism capable of predicting the instantaneous population of the electronic states responsible for the radiation is required. As a first step, an excitation model was developed for the population of the $N_2(B\ ^3\Pi)$ state (see Fig. 1) giving rise of the N_2 (1+) system in the red, since the measurement of this radiation is readily accomplished and has been the subject of numerous experimental observations. On the basis of the knowledge obtained with this excitation model, and the VUV emission profile measurements, a mechanism giving rise to the population of the high lying singlet states of N_2 is currently under development.

The excitation model for the $B\ ^3\Pi$ state follows the mechanism discussed by Wray[5] and Shui, Appleton and Keck[8], who indicated the importance of the first electronically excited molecular state of nitrogen in the overall excitation process as follows:

$$N_2(X\ ^1\Sigma) + M \underset{k_{r_1}}{\overset{k_{f_1}}{\rightleftharpoons}} N_2(A\ ^3\Sigma) + M \tag{3}$$

and

$$N_2(A\ ^3\Sigma) \rightleftharpoons N_2(B\ ^3\Pi) \longrightarrow N_2(A\ ^3\Sigma) + h\nu \tag{4}$$

where M indicates a collision partner to excite the ground state nitrogen molecule, $X\ ^1\Sigma$, to the first excited electronic state, $A\ ^3\Sigma$. Reaction (4) is assumed to be extremely fast, so that the population of the final $B\ ^3\Pi$ state is in local equilibrium with the $A\ ^3\Sigma$ state. It is this $B\ ^3\Pi$ state that is the source of the emission known as the N_2 (1+) system (see Fig. 1 for a schematic of the energy levels involved).

A nonequilibrium normal shock program[9] is utilized to formulate this excitation mechanism, and the resultant computations are correlated with the time-history emission data behind strong shock waves, such as those shown in Fig. 7. To accomplish this, each excited state of the nitrogen molecule is considered as a separate chemical species, populated through a system of finite-rate chemical reactions. The thermodynamic properties of each of these individual species are obtained by describing each species with simple harmonic oscillator relations. This procedure allows for vibrational non-

equilibrium, where the vibrational temperature T_v (which describes the vibrational contribution to the internal energy of the molecule) may be different from the translational temperature T_t. Each electronic state of the nitrogen molecule is considered as a separate species and included with the other components such as molecules, atoms, ions and electrons as part of the kinetic model of a high temperature, reacting gas . The molecular nitrogen dissociation rates were taken from Appleton, Steinberg and Liquornik[10], and the ionization rates were obtained from the survey given by Dunn [11]. With this overall kinetic model, the following excitation rates were obtained after a series of computations which correlated experimentally observed overshoot radiation at 6600 Å with the calculated $B\ ^3\Pi$ state population behind the shock wave:

$$N_2\left(X\ ^1\Sigma\right) + N \underset{}{\overset{k_f}{\rightleftharpoons}} N_2\left(A\ ^3\Sigma\right) + N; \qquad k_f = 1.7\times10^{19}T^{-1.5}e^{-\frac{7.2238\times10^4}{T}} \tag{5}$$

$$N_2\left(X\ ^1\Sigma\right) + N_2\left(X\ ^1\Sigma\right) \underset{}{\overset{k_f}{\rightleftharpoons}} N_2\left(A\ ^3\Sigma\right) + N_2\left(X\ ^1\Sigma\right); \quad k_f = 9.7\times10^{12}T^{-0.5}e^{-\frac{7.2238\times10^4}{T}} \tag{6}$$

$$N_2\left(X\ ^1\Sigma\right) + e^- \underset{}{\overset{k_f}{\rightleftharpoons}} N_2\left(A\ ^3\Sigma\right) + e^-; \qquad k_f = 3\times10^{18}T^{-0.8}e^{-\frac{8.03\times10^4}{T}} \tag{7}$$

$$N_2\left(A\ ^3\Sigma\right) \rightleftharpoons N_2\left(B\ ^3\Pi\right) \text{ in local equilibrium} \tag{8}$$

where k_f is in units of $cm^3\ mol^{-1}\ sec^{-1}$.

The N and N_2 impact excitation rates (reactions 5 & 6) are approximately ten times the value given by Wray[5] as originally estimated from his experimentally observed overshoot radiation results, and within a factor of three of the rates obtained by Flagan[12] upon further analysis of Wray's data. The electron impact rate shown in reaction 7 is 1/10 the value given by Gilmore, Bauer and McGowan[13]. As noted in Ref. 13, the rate coefficient given therein applies to molecules having a rotational temperature of about 300 °K, and the value when the rotational temperature equals the electron temperature (2,000 - 20,000 °K) differs by an unknown but probably small factor.

The computational results indicated that, even though the effectiveness of the N_2 molecule is about 1/100 that of N (see reactions 5 & 6), at low shock velocities this N_2 impact mechanism was dominant, since only a small amount of N atoms is produced. As the shock velocity increases, however, the N impact mechanism soon becomes dominant, while at still higher velocities the electron impact rate becomes important. Figure 9 shows the result for such a computer calculation for a shock velocity of 5.1 mm/μsec in N_2 at a pressure of 0.5 torr. The calculated B state population is shown, normalized with respect to the maximum calculated value. This computed profile can be compared to the experimentally observed N_2 (1+) radiation profile, also normalized with its maximum value.

Also shown in the figure is the contribution of each excitation mechanism in exciting the ground state N_2 molecule to the A state. Immediately behind the shock, the N_2 impact mechanism dominates (due to the finite time required for N and e formation). However, the N excitation soon increases and becomes the dominant mechanism; its maximum value is approximately a factor of 3 greater than the electron impact mechanism for this shock speed. The maximum in the A state population occurs at the time when all excitation contributions go through zero. From this point on, these contributions are negative, leading to a depopulation of the excited state.

A series of shock-tube experiments was performed in N_2 at an initial pressure of 0.5 torr for a range of shock velocities. Radiation profiles were obtained for the three wavelengths discussed earlier: The N_2 (1+) system at 6600 Å, the N_2 (4+) system at 2500 Å, and the VUV radiation at 1150-1500 Å. The experimentally determined profiles were used to obtain the N_2 (1+) excitation mechanism given in reactions 5-8, and are presently being analyzed to postulate an excitation mechanism for the high lying b and b' states giving rise to the VUV radiation.

Figures 10 and 11 present some of the experimental data obtained from this experimental series. Figure 10 shows the time to reach the radiation overshoot peak behind the shock wave (in laboratory time) for the three band systems observed. It can be seen that the VUV radiation reaches a nonequilibrium maximum before the N_2 (1+) red system. This may be expected since the VUV radiation represents an allowed singlet-singlet transition, while the 6600 Å radiation involves states with a spin change. Also shown on the figure are experimentally determined N_2 (1+) time-to-peak values obtained from unpublished results of Wray[5]. These original data were for nitrogen at 1 torr pressure, and was multiplied by 2 for comparison with the 0.5 torr data presented here. It is seen that there is close agreement between the two sets of data. Finally, the calculated time-to-peak, using the excitation model and the nonequilibrium shock program, is also given for the N_2 (1+) system. The calculated value of τ is within about 10% of the experimentally determined results.

Figure 11 presents the amplitude of the peak nonequilibrium overshoot as a function of shock speed for the three band systems. All of the data have been normalized with the peak height obtained at the lowest shock speed. It can be seen that the (4+) and (1+) systems show similar functional relationships with increasing temperature or shock speed. However, the VUV peak radiation increases more rapidly at the higher shock speeds due to a stronger temperature dependence of the population of the high lying states responsible for the radiation. Also shown on the figure is the calculated maximum in B $^3\Pi$-state population using the excitation model, and normalized with the experimental data at a shock speed of 4.8 mm per μsec. It is seen that the prediction is somewhat low at the slower shock speeds, but exhibits the proper relationship at the higher shock speeds approaching reentry velocities.

With the information derived from the development of the N_2 (1+) excitation model, and the experimental VUV data shown in Figs. 10 and 11, a model for excitation to the high lying b and b' states is presently being developed.

RV PRECURSOR EFFECTS ON RCS - NUMERICAL EXAMPLE

The ultimate objectives of the research program are to determine the ionizing radiative flux emerging from the hot gas cap surrounding a reentry vehicle, to compute the properties of the resultant precursor plasma and to calculate the subsequent interaction of electromagnetic waves with this plasma. To this end, a test case calculation was undertaken to evaluate the various aspects of the overall research program for a realistic flight configuration. This section of the paper presents a brief discussion of this test case and gives the results of the subsequent computer calculations for the formation of the precursor plasma and its effect on the radar cross section. Complete details can be found in Ref. 7.

The experimental data discussed in the previous sections constitute the critical parameters required as inputs to the calculations. The spectral distribution of the radiation and the transition probabilities determine both the emissive and absorptive properties of the gas cap. For the nonequilibrium conditions behind the bow shock, these are not equal; the absorption is governed by the vibrational energy distribution of the ground electronic state of N_2, while the emission is related to the local electronic temperature of the high energy, VUV emitting states. Thus, the net flux emerging along a ray from the gas cap depends strongly upon the relative rates of these internal excitation modes.

For a given reentry configuration, the starting point is the calculation of the gasdynamic flow field properties of the gas cap. This calculation uses a computer program developed at CAL[14], which yields the complete solution for the nonequilibrium flow field. Its output yields a grid of points at which not only the chemical species concentrations and translational temperature are specified, but also, by using the new excitation models, the instantaneous populations of the electronic and vibrational energy states relevant to the photoionizing flux calculation are given. A separate program can then calculate the one-dimensional energy transfer along any ray in the gas cap to yield the emergent flux, in a given direction from a point on the shock front.

In the ambient atmosphere ahead of the shock front, the precursor electron density is calculated using a program developed at CAL as a part of the present research effort[7]. The electron density at any point is calculated by integrating the VUV photoionizing flux over the total shocked gas region and over the relevant wavelength interval. It takes into account the wavelength resolved photoionization coefficients of the ambient air, as well as the flux attenuation by absorption; electron bulk depletion mechanisms are also included. The output of this program thus provides contours of local photoionization rates, electron densities and electron temperatures.

These output parameters are then used as inputs to a final program which calculates the EM-wave interaction with this precursor plasma[7]. To predict this interaction, a geometrical optics model is used, and therefore the results obtained from this program serve as good approximations when the shock front nose radius is larger than the inverse of the wave number of the incident electromagnetic wave. This condition holds for the radar frequencies

relevant to the objectives of the research problem. Specifically, the program requires as inputs the plasma electron number density, the collision frequency and their first and second partial derivatives with respect to the precursor plasma coordinate system.

The reentry configuration chosen for the first numerical example was one for which the flow field solutions were in hand, namely:

h = altitude = 201,000 ft

V_s = velocity = 21,950 ft/sec

R_B = nose radius = 57 cm

Since the preliminary emission and absorption measurements pertinent to the VUV radiation were incomplete, an approximate method was used to obtain the VUV flux emanating from the shock layer for the purposes of this example. A temperature was chosen along each integration ray from which blackbody radiation was calculated in the wavelength range 800 - 1080 Å. Although this is only an approximation to the actual radiating flux, it is felt to be realistic due to the large absorption coefficients measured thus far, and the high temperatures existing close behind the shock front. The temperatures chosen for the blackbody radiation were determined near the position of the maximum in electron concentration along each integration ray near the shock front. The blackbody radiation computed from this temperature was assumed to originate at the intersection of the integration ray and the shock surface. Figure 12 shows the actual temperatures used to obtain the blackbody radiation, as a function of distance along the shock, x/R_s. It can be seen that these temperatures are much lower than the initial post-shock temperature (which would correspond to instantaneous excitation to the high-lying radiating states of N_2).

The blackbody distribution for each temperature was divided into ten wavelength intervals, and the blackbody curve integrated over each interval to obtain the total flux originating in that $\Delta\lambda$ interval. The largest contribution to the radiative flux arises from the high temperature region near the centerline, and decreases rapidly away from the centerline due to the falloff in temperature. For the plasma calculation, the intensity was taken to vary from the perpendicular intensity as the cosine of the angle between the emitted ray and the normal to the shock surface. Oxygen photoionization rates were subsequently calculated throughout the precursor region along various streamlines.

Integration of the photoionization rates along streamlines resulted in the final electron number density in the precursor plasma. These results are presented in Fig. 13, showing the electron concentration contours for the region close to the shock. The number density of electrons approaches 2×10^{13} electrons/cm^3 on the stagnation streamline at the shock surface, and decreases from this value by five orders of magnitude within a distance of 10 mean free paths from this shock front. Far from the shock front the number density has dropped sharply; at a distance of 3000 cm, a calculated number density of 5×10^4 electrons/cm^3 is obtained.

Finally, for this numerical example, five sets of cases were computed[7], each set corresponding to one of the radar frequencies listed in the following table.

RADAR FREQUENCIES FOR NUMERICAL EXAMPLE

Radar Frequency Identification	Radar Frequency (GigaHertz)
VHF	0.15
UHF	0.42
L-Band	1.3
S-Band	3.0
C-Band	5.5

The radar cross section computed as a function of aspect angle is presented in Fig. 14 for the five radar frequencies considered. The calculated results indicate that the radar cross section is nearly independent of the aspect angle; note in particular the results for VHF and UHF.

The usefulness of this numerical example is twofold: it serves to demonstrate the successful performance of the various components of the overall calculational procedure, and also to define the limitations and reliability. It was shown, for example, that the accuracy of the RCS calculations depends critically on the spatial resolution of the data that specify electron densities, temperature and collision frequencies, particularly near the body and near the stagnation streamline.

SUMMARY

Results to date have been presented for a research program whose overall objective is the study of the formation and effect of a photoionized, precursor electron plasma on the RCS of reentry vehicles. The importance of the relevant transition probabilities and excitation mechanisms for VUV-emitting states in N_2 has been discussed, experiments to measure these critical parameters have been described, and the data obtained to date have been reported. The overall aspects of this program have been outlined, in which the ionizing flux, the resultant electron densities and subsequent EM-wave interaction are calculated by the successive use of computer programs developed for this problem. A numerical example has been discussed which illustrates this procedure, and for which the RCS as a function of aspect angle has been calculated for a realistic flight configuration.

Current effects of the research are directed toward the assessment of the influence of O_2 in the excitation kinetics of high lying N_2 energy levels, as well as in the formation of NO in the shock-heated-gas cap. In particular, the role of NO absorption and emission in the determination of the VUV photo-

ionizing flux is a question that has resulted from the present study and is currently being assessed.

ACKNOWLEDGEMENTS

The authors gratefully acknowledge the assistance of their colleagues, Dr. J. Curtis, Miss M. Williams and J. Stratton in various phases of the research. Also acknowledged are the contributions of Dr. K. Edwards, Dr. S. Chang, G. Olson and B. Chambers of the Systems Technology Department at CAL, who are responsible for the calculations of the precursor plasma properties and the resultant radar cross sections.

REFERENCES

1. Lin, S. -C., Radio Echoes from a Manned Satellite During Reentry. J. of Geophys. Res., Vol. 67, No. 10, September 1962, pp. 3851-3870.

2. Carroll, P.K. and Collins, C.P., High Resolution Absorption Studies of the $b'\ ^1\Pi \rightarrow X\ ^1\Sigma$ System of Nitrogen. Canadian Journal of Physics, vol. 47, 1969, pp. 563-589.

3. Dressler, K., The Lowest Valence and Rydberg States in the Dipole-allowed Absorption Spectrum of Nitrogen. A Survey of Their Interactions. Canadian Journal of Physics, Vol. 47, 1969, pp. 547-561.

4. Appleton, J.P. and Steinberg, M., Vacuum-Ultraviolet Absorption of Shock-Heated Vibrationally Excited Nitrogen. J. Chem. Phys., Vol. 46, No. 4, 15 February 1967, pp. 1521-1529.

5. Wray, K.L., Excitation Studies on the $N_2(1+)$ and $N_2^+(1-)$ Systems in Shock-Heated N-N_2 Mixtures. J. Chem. Phys., Vol. 44, No. 2, 15 January 1966, pp. 623-632.

6. Marrone, P.V., Wurster, W.H. and Stratton, J.E., Shock-tube Studies of N^+ and O^+ Recombination Radiation in the Vacuum Ultraviolet. Cornell Aeronautical Laboratory Report No. AG-1729-A-7, June 1968.

7. Precursor Ionization from Blunt Body Shock Waves (U); Annual Technical Report. Prepared by W. H. Wurster. Cornell Aeronautical Laboratory Report No. AF-2851-A-2, July 1970.

8. Shui, V.H., Appleton, J.P. and Keck, J.C., The Dissociation and Recombination of Nitrogen; A Comparison Between Theory and Experiment. MIT Fluid Mechanics Laboratory Publication No. 70-2, February 1970.

9. Marrone, P. V., Inviscid, Nonequilibrium Flow Behind Bow and Normal Shock Waves, Part I. General Analysis and Numerical Examples. Cornell Aeronautical Laboratory Report No. QM-1626-A-12(I), May 1963.

10. Appleton, J. P., Steinberg, M. and Liquornik, D. J. Shock-Tube Study of Nitrogen Dissociation Using Vacuum-Ultraviolet Light Absorption. J. Chem. Phys., Vol. 48, No. 2, 15 January 1968. pp. 599-608.

11. Dunn, M. G. Reaction Rate Constants for Ionized Air. Cornell Aeronautical Laboratory Report No. AI-2187-A-1, April 1966.

12. Flagan, R. (MIT Fluid Mechanics Laboratory). Private Communication, July 1970.

13. Gilmore, F. R., Bauer, E. and McGowan, J. W., A Review of Atomic and Molecular Excitation Mechanisms in Nonequilibrium Gases up to 20,000°K. JQSRT, Vol. 9, No. 2, February 1969, pp. 157-185.

14. Curtis, J. T. and Strom, C. R., Computations of the Nonequilibrium Flow of a Viscous, Radiating Fluid About a Blunt Axisymmetric Body, Volume I, Equations and Results. Air Force Flight Dynamics Laboratory Report AFFDL-TR-67-40, Vol. I, June 1967; (Also Cornell Aeronautical Laboratory Report AM-2113-Y-1).

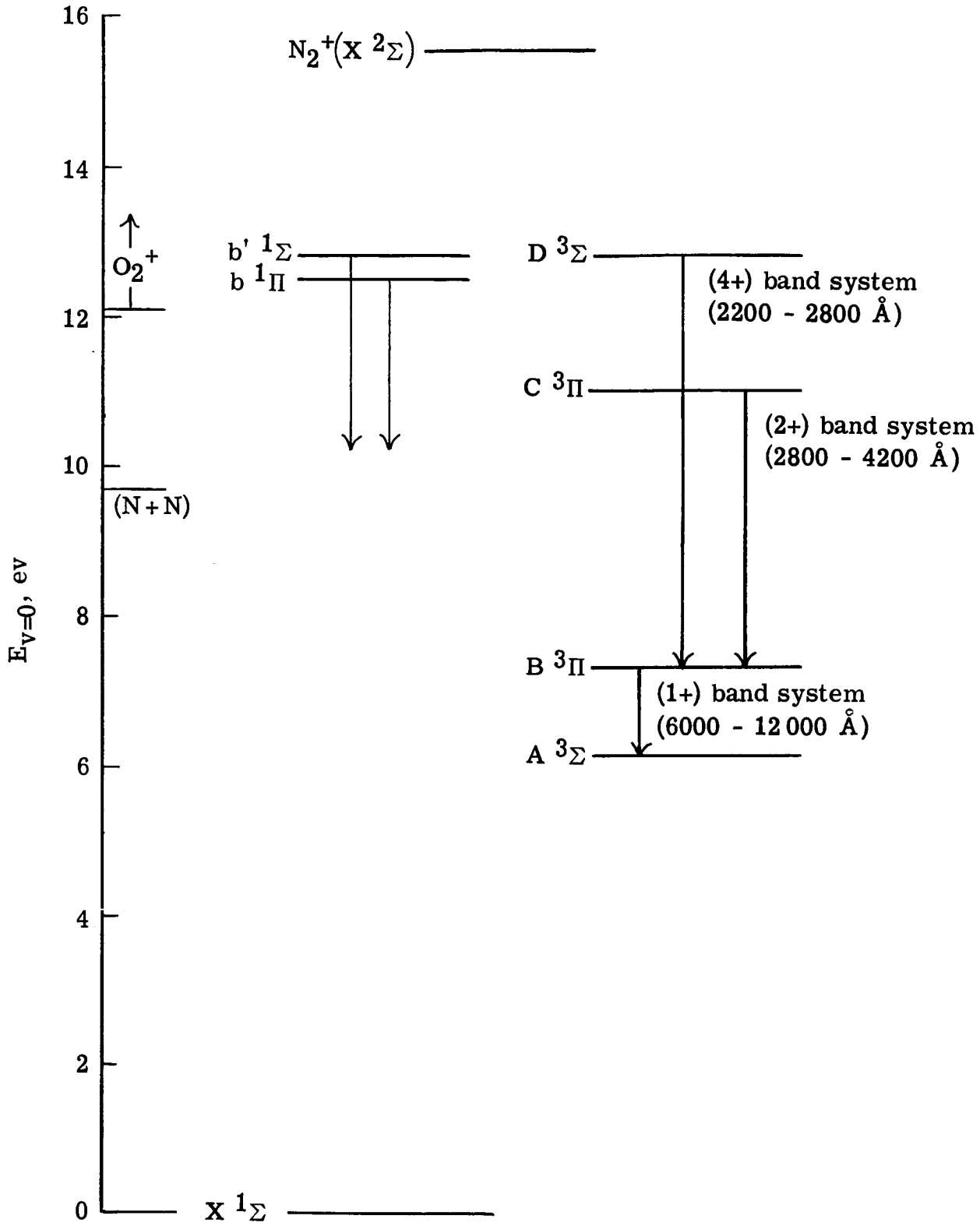

Figure 1.- Some relevant nitrogen energy levels.

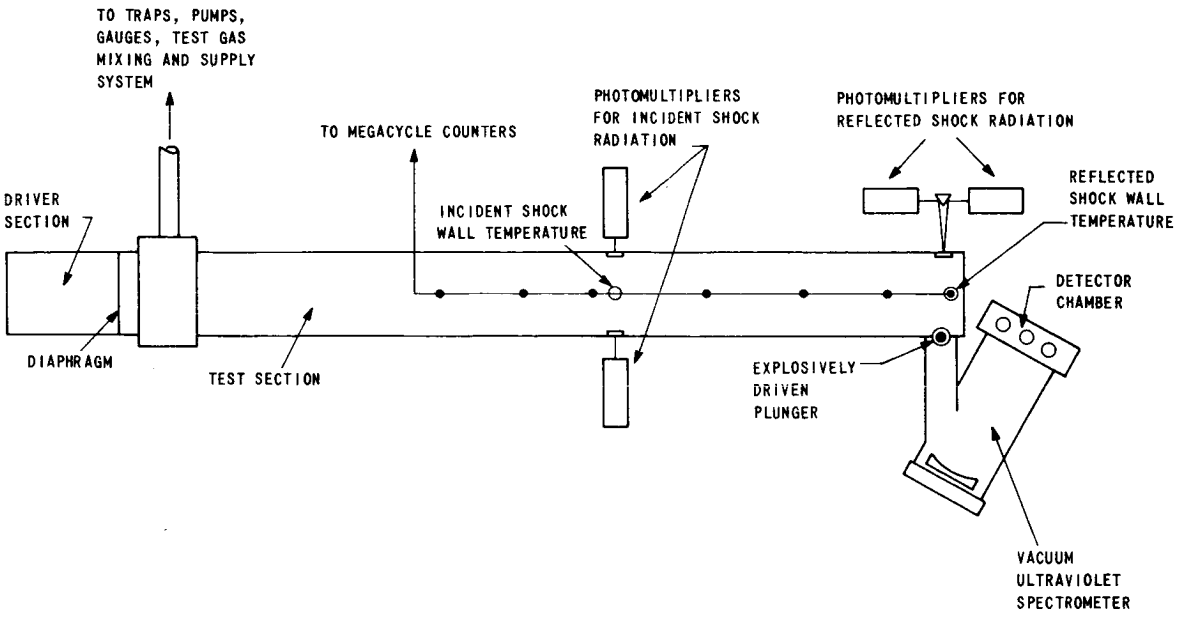

Figure 2.- Schematic of experimental apparatus.

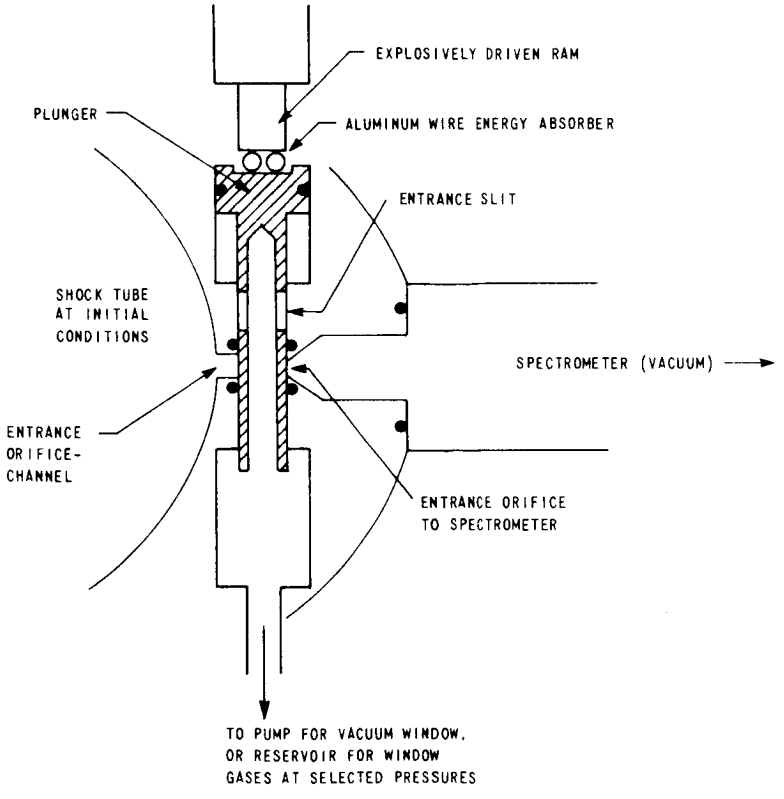

Figure 3.- Schematic of windowless plunger assembly.

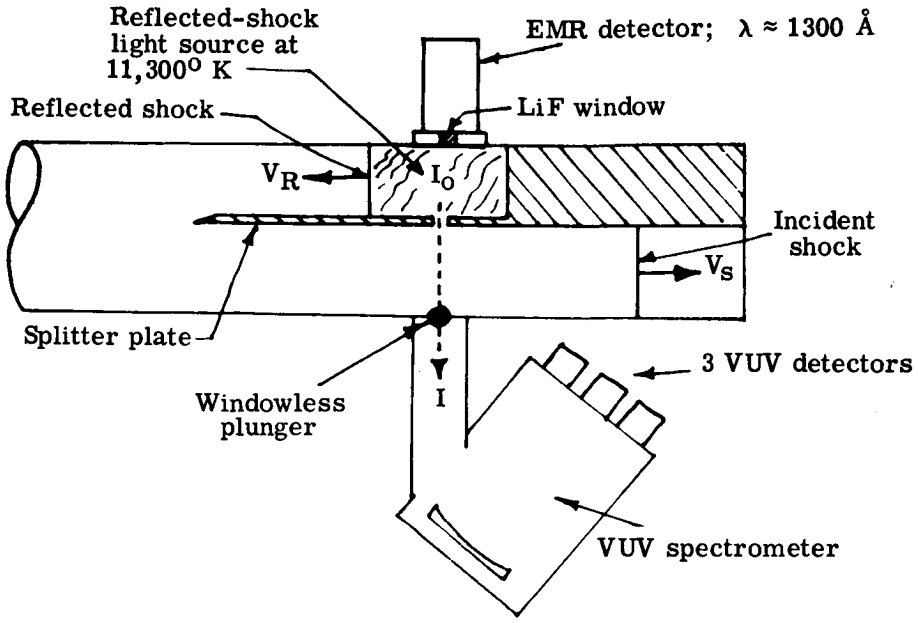

(a) Experiment.

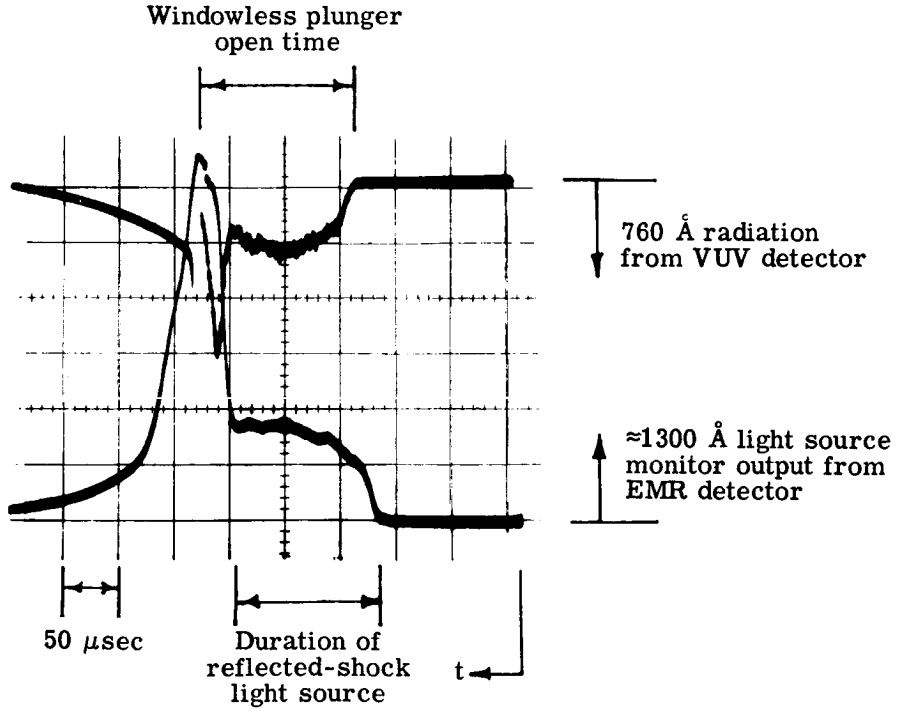

(b) Measurements.

Figure 4.- Vacuum ultraviolet absorption experiment and radiation measurements.

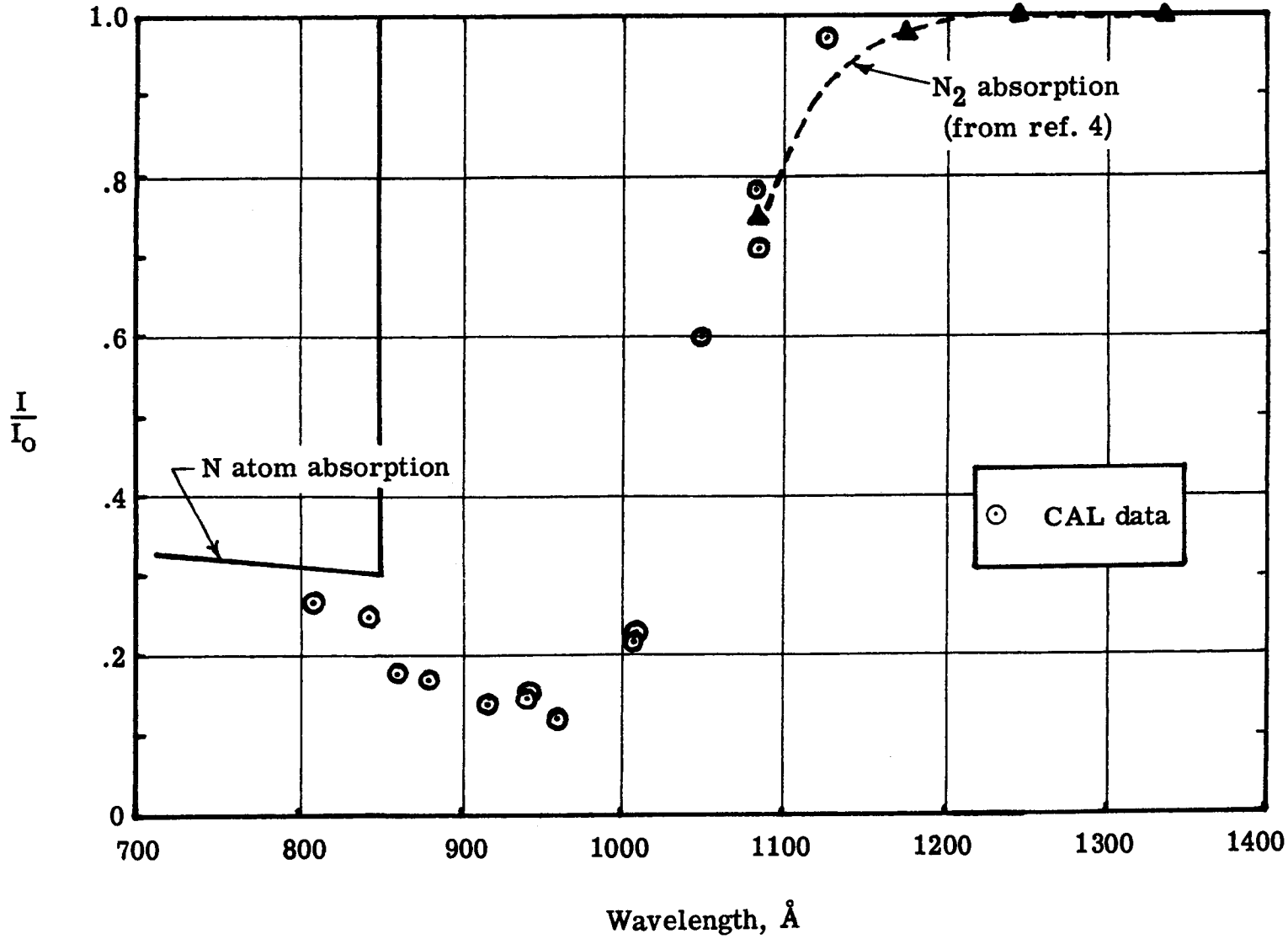

Figure 5.- Vacuum ultraviolet absorption measurements in shock-heated nitrogen. $T = 6000^{o}$ K.

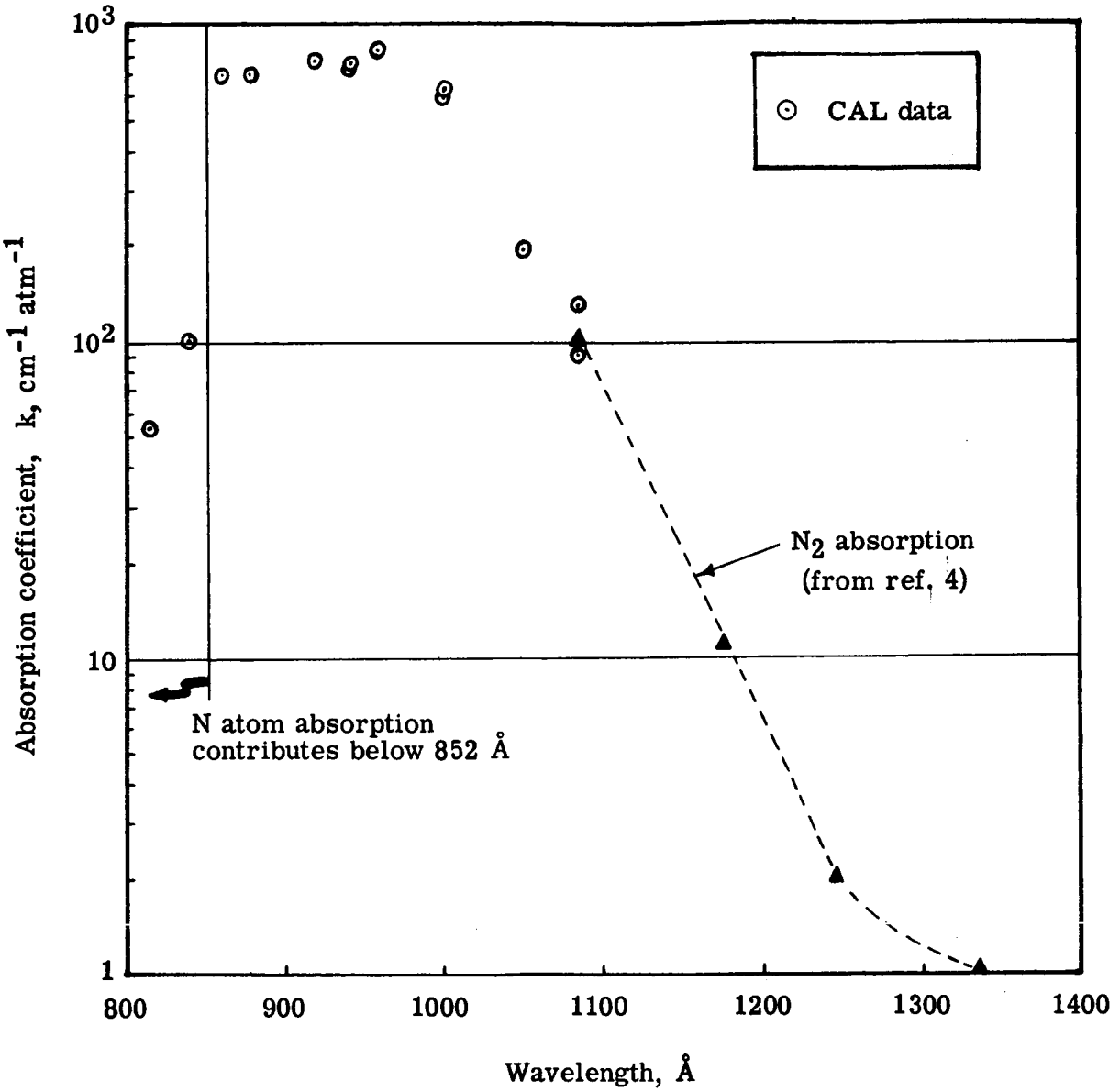

Figure 6.- Vacuum ultraviolet absorption coefficients for shock-heated nitrogen. $T = 6000^{o}$ K.

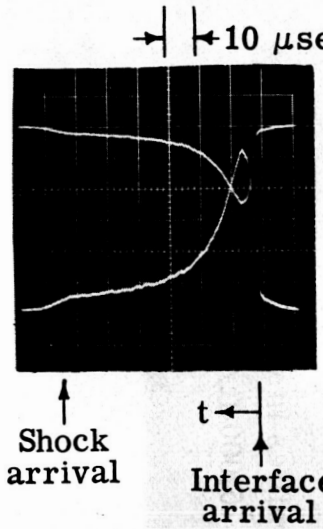

$N_2(1+)$; $B\ ^3\Pi \rightarrow A\ ^3\Sigma$

$\lambda_c = 7060$ Å; $\Delta\lambda = 200$ Å

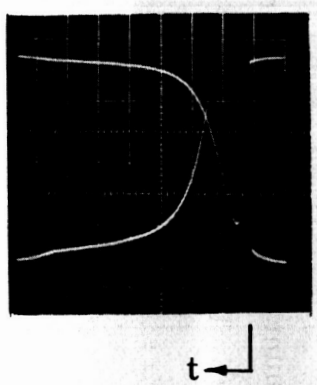

$N_2(4+)$; $D\ ^3\Sigma \rightarrow B\ ^3\Pi$

$\lambda_c = 2500$ Å; $\Delta\lambda = 200$ Å

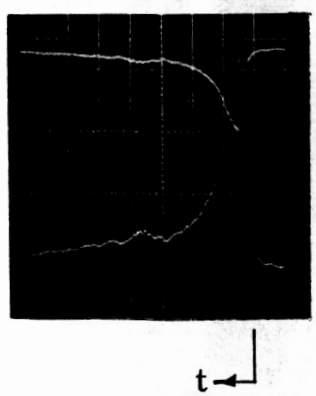

N_2(VUV); $b'\ ^1\Sigma \rightarrow X\ ^1\Sigma$

$b\ ^1\Pi \rightarrow X\ ^1\Sigma$

$\lambda_c \approx 1300$ Å; $\Delta\lambda \approx 1150$ Å to 1500 Å

Figure 7.- Nonequilibrium radiation profiles in shock-heated nitrogen. $p_1 = 1$ torr; $V_s = 15{,}500$ ft/sec; $T_s = 10{,}600^{\circ}$ K.

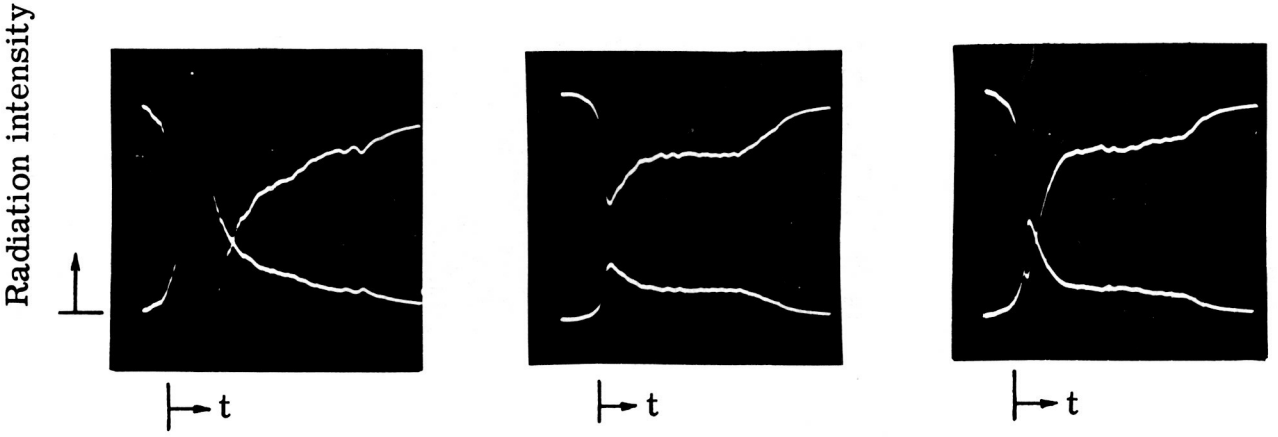

(a) N_2; 100 mV/div. (b) Air; 200 mV/div. (c) NO; 200 mV/div.

Figure 8.- Comparison of vacuum ultraviolet shock profiles in various gases. $\Delta\lambda \approx 1150$ to 1500 Å; $p_1 = 1.0$ torr; $V_s = 15{,}000$ ft/sec; sweep speeds, 10 μsec/div.

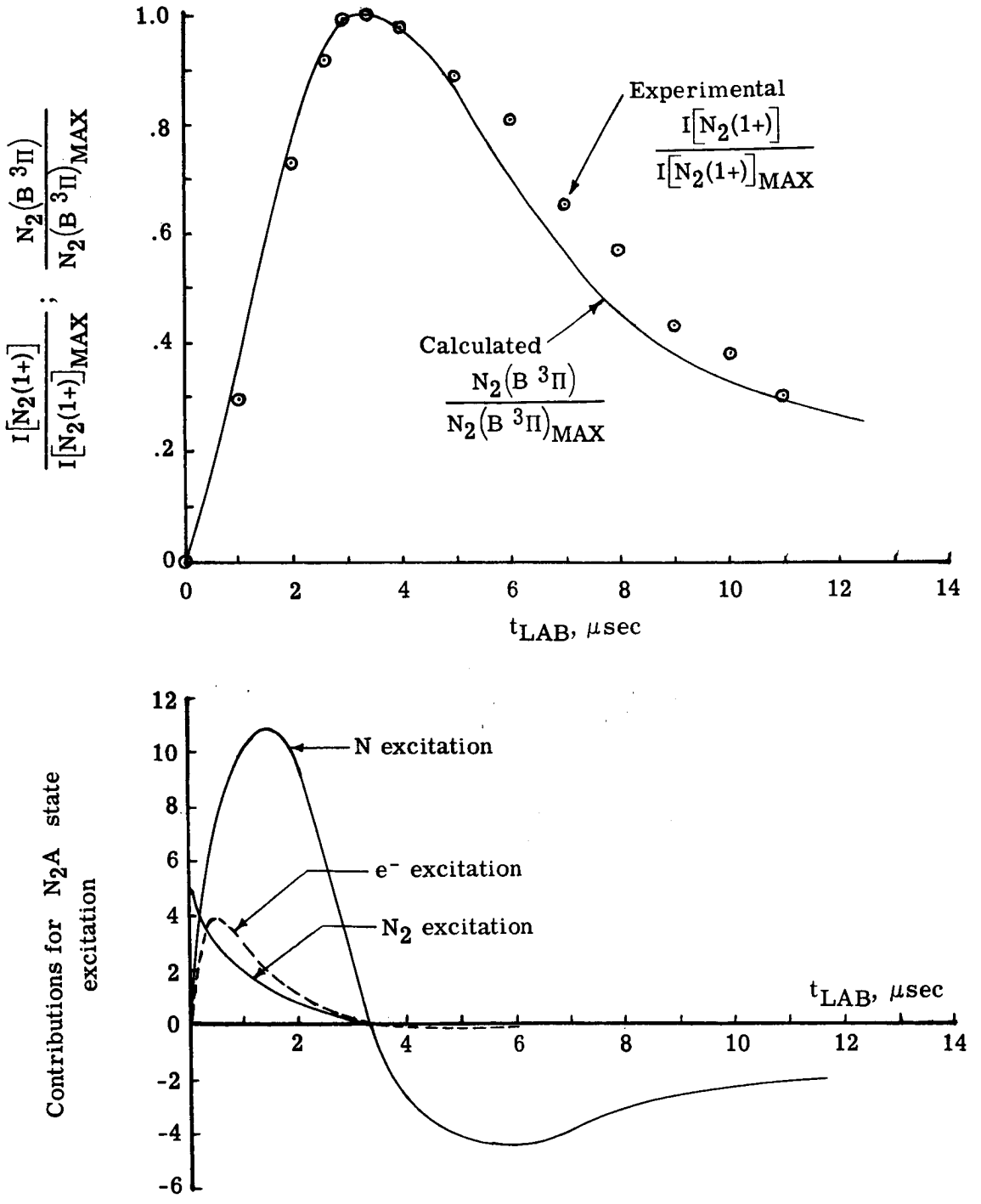

Figure 9.- Experimental and calculated $N_2(1+)$ and $N_2(B\,^3\Pi)$ state concentration and radiation profiles. N_2 at $p_1 = 0.5$ torr; $V_s = 5.1$ mm/μsec.

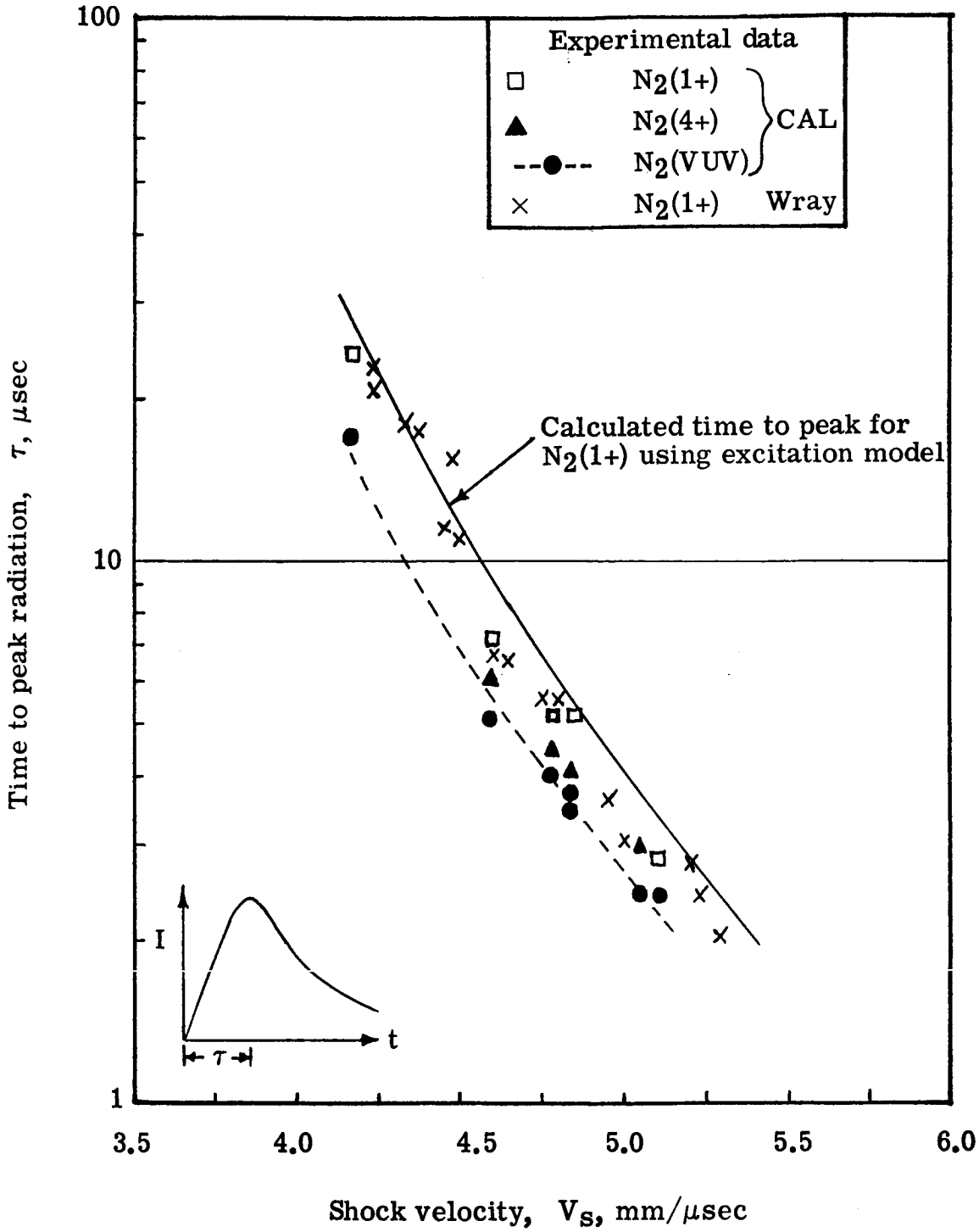

Figure 10.- Time-to-peak radiation overshoot in shock-heated nitrogen. N_2 at $p_1 = 0.5$ torr.

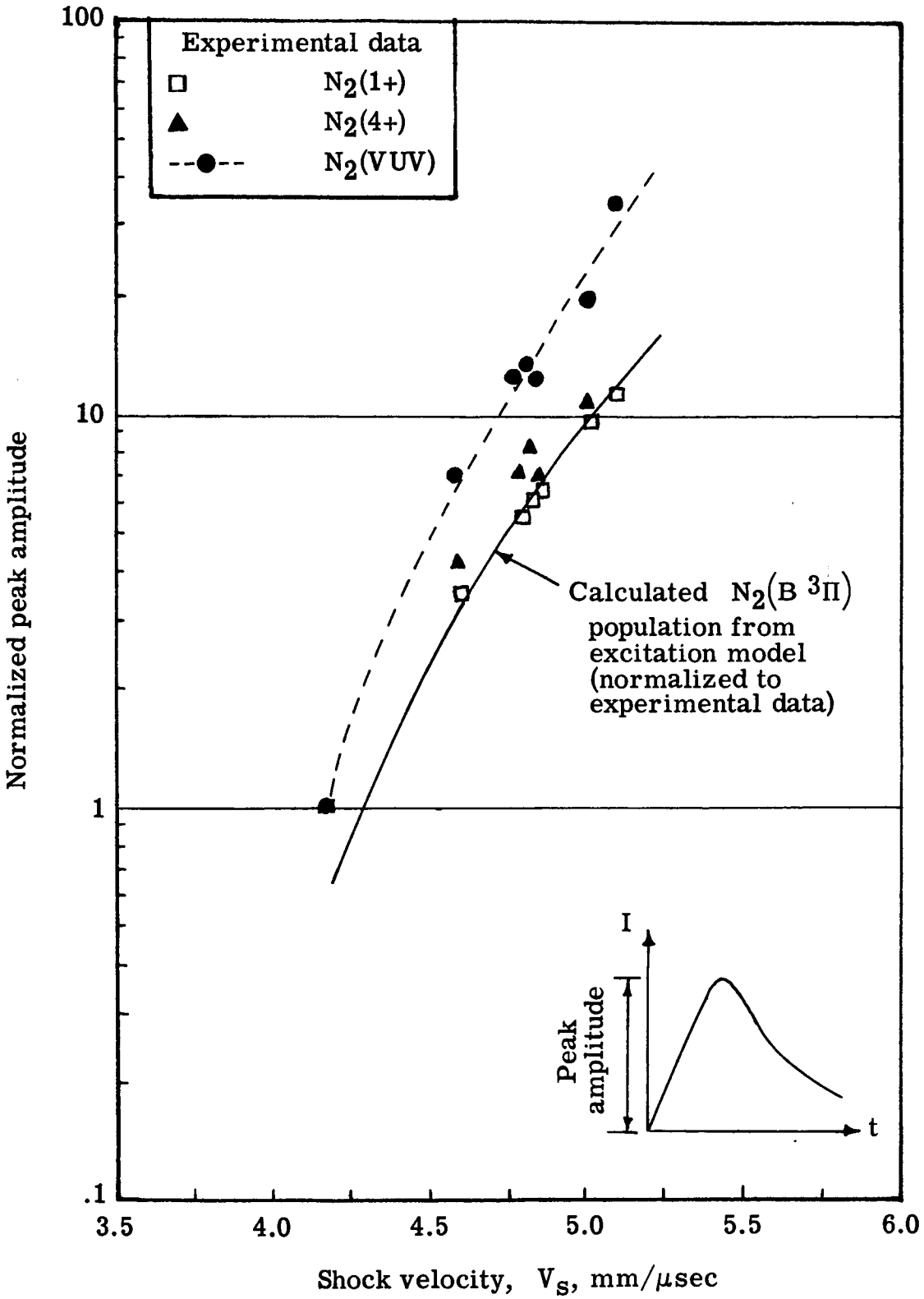

Figure 11.- Normalized nonequilibrium peak radiation in shock-heated nitrogen.

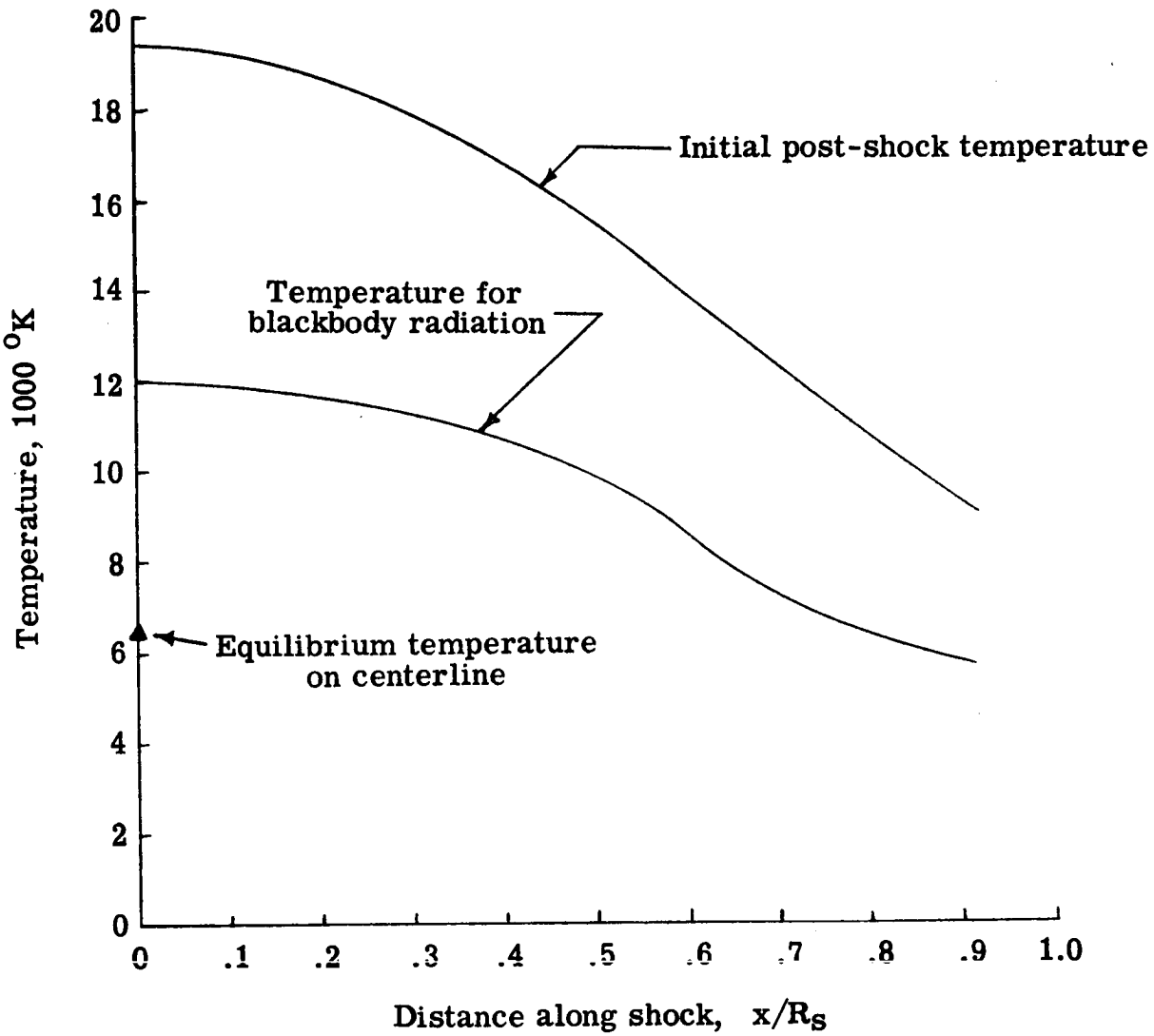

Figure 12.- Temperature distribution in reentry-vehicle shock layer. V_S = 21,950 ft/sec; R_B = 57 cm; h = 201 kft.

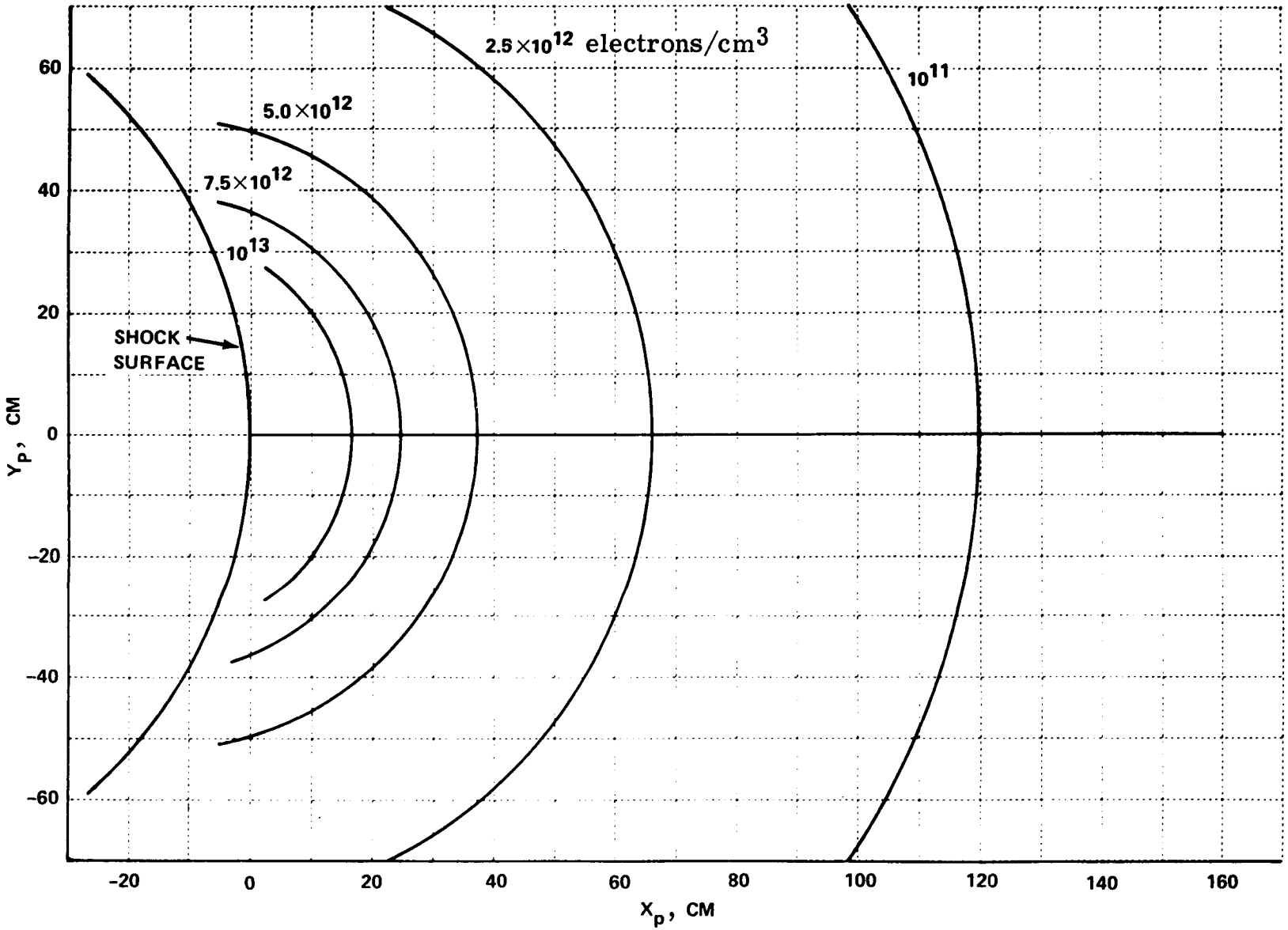

Figure 13.- Contours of constant electron number density in the precursor plasma near the shock front.

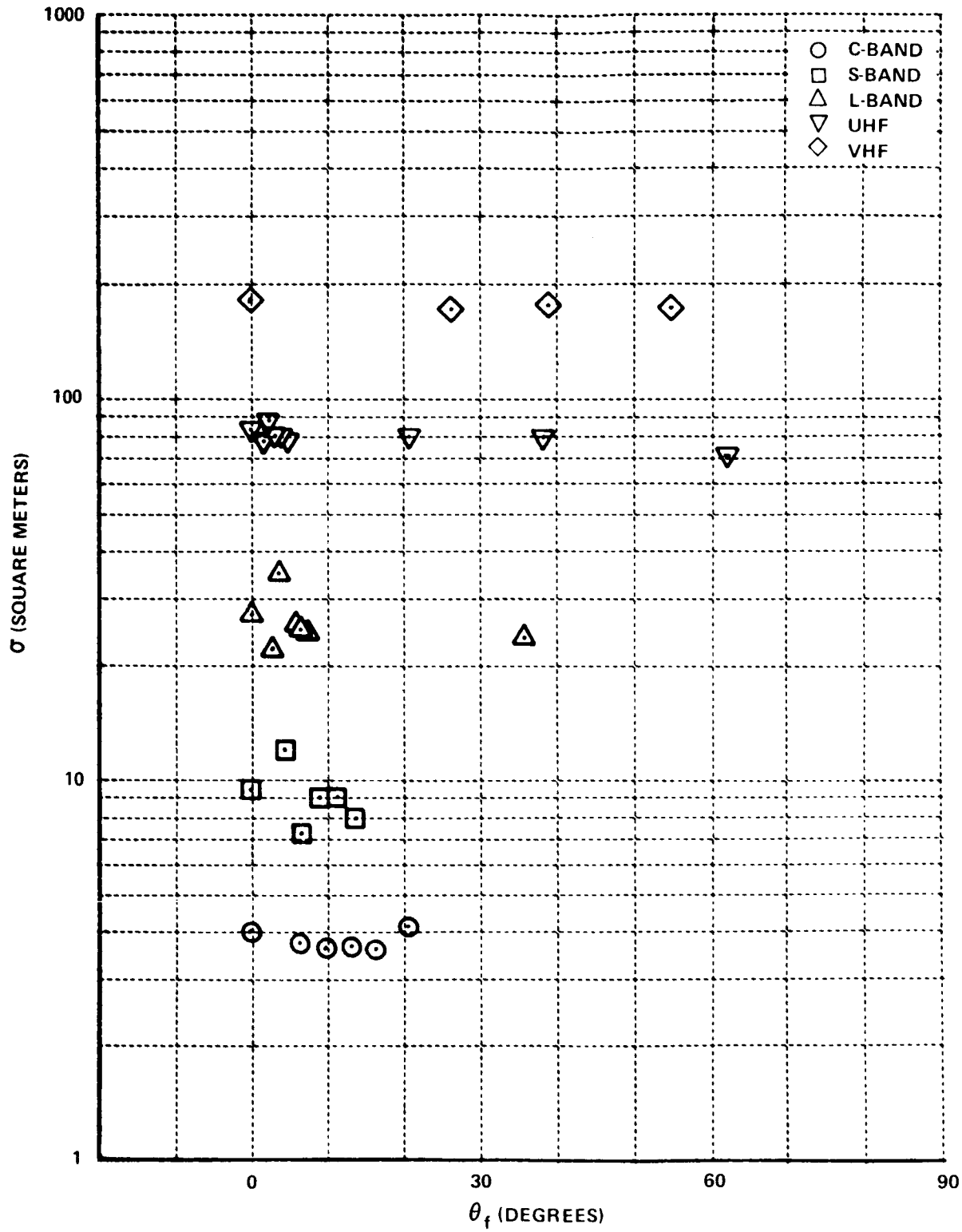

Figure 14.- Computed radar cross section as a function of aspect angle.

FURTHER STUDIES OF PRECURSOR ELECTRON DENSITIES AHEAD OF SHOCK WAVES

By Masayuki Omura and Leroy L. Presley

NASA Ames Research Center

SUMMARY

This paper presents recent results obtained from a study of precursor electron formation ahead of strong shock waves traveling into mixtures of nitrogen and oxygen in a shock tube. Efforts have been made to develop a theoretical model of the ionization process that would provide a satisfactory prediction of the experimental data. It has been found that a qualitatively correct prediction of electron density ahead of a shock wave can be given only by a spectrally detailed model of the photoionization and total absorption coefficients. Experimentally, Langmuir probes were used to study radial electron density profiles in a shock tube. Good quantitative agreement with the electron densities measured with a microwave interferometer was obtained with the Langmuir probes by assuming the electron temperature to be 500°K.

INTRODUCTION

The existence of free electrons ahead of shock waves associated with high-speed bodies entering the earth's atmosphere has been discerned from radar observation of the entry of both meteors and man-made entry bodies. The well documented "head echo" of meteors is due to the existence of free electrons many meters in front of a meteor. The evaluation of the radar observation of the entry of the MA 6 Mercury capsule by Lin (ref. 1) showed the existence of electron densities of 10^7 cm^{-3} at a distance of approximately 15 m ahead of the capsule. The presence of these precursor electrons affects both radar detection and communication with a reentry capsule and to a lesser extent the flow field behind the shock wave.

Laboratory research directed at understanding the mechanism for production of precursor electrons has been conducted by a number of investigators. For the most part, these studies were conducted in pressure-driven shock tubes using argon as the test gas at shock velocities up to about 8.7 km/sec. Recently Omura and Presley (ref. 2) have published some experimental results using nitrogen and oxygen mixtures as the test gases. These data were taken in an arc-discharge shock tube (ref. 3) over a shock wave velocity range of 9.8 to 13.2 km/sec. A discussion of these measurements will be made later.

Several theoretical studies have been conducted to provide predictions of the observed electron densities. Ferrari and Clarke (ref. 4) were among the first to set forth a detailed model for the production of electrons ahead of shock waves in argon. Their analysis considered only photoionization from the ground state and one-dimensional radiative transfer. Dobbins (ref. 5) and Murty (ref. 6) have formulated models that include the effects of resonance line absorption and photoionization from excited states. Dobbins' analysis considers radiative transfer within a shock tube, and is specifically aimed at explaining the precursor electron densities in argon that were observed by Lederman and Wilson (ref. 7) while Murty's analysis is appropriate for a hydrogenic gas with one dimensional radiative transfer. Presley and Omura (ref. 8) have considered photoionization ahead of a shock wave using one dimensional radiative transfer in a gas consisting of nitrogen and oxygen mixtures. They found good qualitative agreement between their theoretical results and much of their experimental data. An extension of their theory and further precursor measurements made with Langmuir probes are presented in this paper.

SYMBOLS

A	area of Langmuir probe
A_o	Avogardro's number
$B(\nu)$	Planck function
c	speed of light
C	constant for Langmuir probe
d_{lr}	dissociative recombination, see Eq. (5)
$d_{\rho r}$	dissociative recombination, see Eq. (7)
e	electronic charge
h	Planck constant, or Debye length
$I(\nu)$	radiative intensity
j_e	Langmuir probe current
j_{e_o}	Langmuir probe current at zero voltage
$J(\nu)$	spatially averaged radiative intensity
k	Boltzmann constant

k_1	collisional rate constant, see Eq. (4)
k_2	collisional rate constant, see Eq. (6)
$k(\nu)$	absorption coefficient
n	particle number density
p	pressure
Q_{1f}	photoionization rate constant for N_2
Q_{2f}	photoionization rate constant for O_2
r_o	shock tube radius
R	universal gas constant
s	particular species
t	time
T	temperature
u	particle velocity relative to shock wave
V	shock wave velocity, or Langmuir probe voltage
w	net mass rate of production per unit volume of particular species
x	distance in front of shock wave
β	ratio of oxygen partial pressure to total pressure
η	moles of particular species per unit mass of mixture
λ_m	mean free path of gas ahead of shock wave
μ	molecular weight
ν	frequency
ρ	mass density
$\sigma_1(\nu)$	photoionization cross section for N_2
$\sigma_2(\nu)$	photoionization cross section for O_2
$\sigma_T(\nu)$	total absorption cross section due to all processes

Ω	solid angle
[ ]	moles per unit volume

Subscripts:

1	ahead of shock wave
2	equilibrium behind shock wave
e	electron
I	ionization
s	particular chemical species
T	total

Note - Chemical symbols such as N_2, O_2, N_2^+, etc., also appear as subscripts.

EXPERIMENTAL PROCEDURE

The experimental measurements described in this paper consist of time dependent observations of the electron density at a fixed location in a shock tube as the shock wave approaches that station. A 12-inch diameter shock tube driven by a 1 MJ arc discharge driver, which is separated from the driven tube by a stainless steel diaphragm, was used for these tests. The driven tube is fabricated of honed stainless steel tubing.

The measurements of electron density were accomplished by two different diagnostic techniques, a microwave interferometer, and an array of electric probes. The microwave interferometer was a standard X-band interferometer operating at 8.5 GHz and was located about 13 m downstream of the main shock tube diaphragm. A schematic diagram of the interferometer is shown in figure 1.

An array of Langmuir probes was also installed about 13 m from the diaphragm and arranged as shown in figure 2, in order to obtain the radial distribution of electrons at various axial locations ahead of the shock wave. The probes were of the guard ring design, as shown in figures 2 and 3, and the time dependent current to each probe was recorded on an oscilloscope. Both the probe and the guard ring were held at the same voltage in order that the probe would appear one-dimensional to an electron that is near the collecting surface. In order that the probe not disturb the plasma, it is necessary that the Debye length be much smaller than the mean free path of the plasma. For typical conditions of this experiment, h would be of the order of 10^{-2} mm, and λ of the order of 10^{-1} mm; therefore this criterion should be reasonably well satisfied. A typical current-voltage characteristic for a Langmuir probe is shown in figure 3. It is seen that in the saturation region, the probe current is only dependent upon electron density and temperature. In this study, the probes were operated at a potential of +6 volts which was felt to be sufficiently high to insure that the probes were

operating in the saturation region. Under such conditions, the electron density can be obtained directly from known probe current and electron temperatures. Although electron temperature can be obtained directly from measurements of the slope of the probe characteristic curve in the transition region, as indicated in figure 3, no attempt to sweep the probe voltage was made for this experiment; therefore the electron temperature was assumed, as will be discussed later.

A complete analysis of the precursor electron density ahead of the shock wave should include the production of electrons by photoionization and the effects of electron diffusion forward through the shock wave. However, for this study, electron densities at distances much greater than the diffusion distance were of primary interest, thus only photoionization and related collisional processes will be included. The overall approach of the analysis is to first consider a simple one-dimensional model for the radiative transport, corresponding to a shock wave of infinite extent, and to investigate the effects of spectral detail of the absorption coefficient. Then consideration is given to the effects of finite shock tube size. The analysis is devloped for an arbitrary mixture of molecular nitrogen and oxygen that is characterized by an initial partial pressure of oxygen, given by $p_{O_2} = \beta p_1$.

Although the details of the theory are presented in reference 7, a synoptic view will be given here for completeness. If steady state conditions are assumed, the conservation equation for a particular species s can be written as:

$$\frac{d}{dx}\left(\rho_s u_s\right) = w_s \tag{1}$$

where ρ_s, u_s and w_s relate to the species s. If, as will be discussed later, the flow velocity relative to the shock wave is constant, and neglecting diffusion the above equation becomes:

$$V \frac{d}{dx} \rho_s = w_s \tag{2}$$

where V is the velocity of the gas relative to the shock wave, i.e. the shock wave velocity. The quantity w_s is given by

$$w_s = \mu_s \frac{d[s]}{dt} \tag{3}$$

where μ_s and $\frac{d[s]}{dt}$ are the molecular weight and net molar rate of change of species s respectively.

The net molar rate of change of a given species is a summation of radiative and collisional processes. If the total number of electrons is small compared to the number of neutral molecules, then to a good approximation,

the number of neutral molecules ahead of the shock wave can be assumed constant. Further, for electron densities less than about 10^{11}, the enthalpy is very nearly constant, and the heavy particle temperature can be taken as constant at the initial temperature, $T_1 \simeq 300^{\circ}K$. A complete model should take into account the variation in electron temperature ahead of the shock wave but Murty (ref. 6), and Nelson and Goulard (ref. 9) show that the electron temperature throughout the region upstream of the shock wave does not differ appreciably from the initial value. Therefore, for this analysis, electron temperature is taken equal to the heavy particle temperature.

Of the many reactions that could be considered in the precursor region, the following are considered in this analysis:

Collisional Reactions

$$N_2 + X \underset{k_{1r}}{\overset{k_{1f}}{\rightleftharpoons}} N_2^+ + e^- + X \tag{4}$$

$$N + N \underset{d_{ir}}{\overset{d_{1f}}{\rightleftharpoons}} N_2^+ + e^- \tag{5}$$

$$O_2 + X \underset{k_{2r}}{\overset{k_{2f}}{\rightleftharpoons}} O_2^+ + e^- + X \tag{6}$$

$$O + O \underset{d_{2r}}{\overset{d_{2f}}{\rightleftharpoons}} O_2^+ + e^- \tag{7}$$

where X is an arbitrary collision partner.

Radiative Reactions

$$N_2 + h\nu \underset{Q_{1r}}{\overset{Q_{1f}}{\rightleftharpoons}} N_2^+ + e^- \tag{8}$$

$$O_2 + h\nu \underset{Q_{2r}}{\overset{Q_{2f}}{\rightleftharpoons}} O_2^+ + e^- \tag{9}$$

Collisional rates for the reactions given in Eqs. (4) to (7) were taken from Bortner (ref. 10). Due to the low translational temperatures and low atomic concentrations that would be expected in the precursor region, the forward collisional reactions were ignored. Comparison of the recombination rates for reactions (4) to (7) shows that the dissociative recombination reactions are much the larger electron absorption mechanisms, and the rates d_{1r} and and d_{2r} are given by (ref. 10)

$$d_{1r} = 5\text{x}10^{18\pm1}\ T^{-\frac{1}{2}}\ \frac{cm^3}{sec\text{-}mole} \tag{10}$$

and

$$d_{2r} = 5\text{x}10^{19\pm1}\ T^{-1}\ \frac{cm^3}{sec\text{-}mole} \tag{11}$$

The photoionization rates, as given by Ferrari and Clarke (ref. 4) are

$$Q_{1f} = 4\pi \int_{\nu_1}^{\infty} \frac{\sigma_1(\nu)}{h\nu}\ J(\nu)\ d\nu \tag{12}$$

and

$$Q_{2f} = 4\pi \int_{\nu_2}^{\infty} \frac{\sigma_2(\nu)}{h\nu}\ J(\nu)\ d\nu \tag{13}$$

where ν_1 and ν_2 are the frequencies associated with the threshold energies for photoionization; $\sigma_1(\nu)$ and $\sigma_2(\nu)$ are the frequency-dependent photoionization cross sections. The spatially averaged radiative intensity, $J(\nu)$, is given by

$$J(\nu) = \frac{1}{4\pi} \int I(\nu)\ d\Omega \tag{14}$$

It should be noted that the photoionization processes considered here are for the ground state processes only. Both Murty (ref. 6) and Dobbins (ref. 5) point out the importance of ionization from excited states and to be physically correct, the present analysis should include this effect. However, excited state photoionization was not included due to a lack of data for the

cross sections of this process.

The local spatially averaged radiative intensity at any point ahead of the shock wave is needed to determine the photoionization rate. This local intensity results from the emission from the hot gas behind the shock wave and is attenuated due to absorption by the cold gas ahead of the shock wave. A representative prediction of the continuum radiation from behind the shock wave is shown in figure 4. These results were calculated using the computer model of Wilson and Grief (ref. 11) for a semi-infinite slab 20 cm thick at a temperature and pressure of $T_2 = 11{,}500^{\circ}K$ and $p_2 = 0.4$ atm respectively. Comparison of the calculated radiative intensity with the black body intensity at wavelengths shorter than 1150 Å shows that the radiative intensity at the shock front can be approximated to a good degree of accuracy by the black body intensity. The presence of oxygen in the test gas will not alter the validity of this assumption. The local radiative intensity for the one-dimensional model is then given by:

$$J(\nu) = \frac{B(\nu)}{2} E_2 \left(k_T(\nu)x\right) \tag{15}$$

where

$$B(\nu) = \frac{2\, h\nu^2/c^2}{\exp\left(\frac{h\nu}{kT_2}\right) - 1} \tag{16}$$

and

$$E_2(\tau) = \int_1^{\infty} \frac{\exp(-\tau z)}{z^2}\, dz \tag{17}$$

where τ is the optical depth, given by $\tau = k_T(\nu)\, x$, and z accounts for the angular integration. For the small optical depths $(\tau < z)$ that will be of importance far ahead of the shock wave, the Milne-Eddington approximation can be used for the E_2 function; thus Eq. 15 becomes:

$$J(\nu) = \frac{B(\nu)}{2} \exp\left[\sqrt{3}\, k_T(\nu)\, x\right] \tag{18}$$

The total absorption coefficient is given by

$$k_T(\nu) = \sigma_{T_{N_2}}(\nu) n_{N_2} + \sigma_{T_{O_2}}(\nu) n_{O_2} \tag{19}$$

where $\sigma_{T_{N_2}}$ and $\sigma_{T_{O_2}}$ are the total cross section for N_2 and O_2 and

n_{N_2} and n_{O_2} are the member densities of the nitrogen and oxygen molecules, herein taken as constants throughout the precursor region and given by

$$n_{N_2} = \frac{(1-\beta)\, p_1\, A_o}{R\, T_1} \tag{20}$$

and

$$n_{O_2} = \frac{\beta\, p_1\, A_o}{R\, T_1} \tag{21}$$

It should be noted that the ionization threshold for nitrogen is $h\nu_1 = 15.57$ electron volts while the threshold for oxygen is $h\nu_2 = 12.15$ electron volts. Thus the total cross section of both nitrogen and oxygen must be used at all energies greater than 12.15 electron volts to evaluate the radiant energy available to ionize the gases from their ground states.

The above expression for $J(\nu)$ considers the source of the radiation to be an infinite surface. Such a condition would be approached if the wall of the shock tube were totally reflecting at all wavelengths. However, such is not the case, particularly at the vacuum ultraviolet wavelengths that are required for photoionization from the ground state. In reality, the emission comes from a cylindrical volume of hot gas and the reflection coefficient of the walls is a function of both the angle and the frequency of the incident radiation. If the source of radiation is considered to be a circular disk, then the spatially averaged radiative intensity at any axial location ahead of the shock and on the center line of the shock tube can be expressed as, see reference 4:

$$J(\nu) = \frac{B(\nu)}{2}\left[E_2(k_T(\nu)x) - \frac{x}{\sqrt{x^2+r_o^2}}\, E_2\left(k_T(\nu)\sqrt{x^2+r_o^2}\right)\right] \tag{22}$$

where r_o is the radius of the emitting surface, i.e. the shock tube radius. Use of this expression to calculate the average intensity ahead of the shock wave assumes that the intensity is uniform across the shock tube and that the walls are totally non-reflecting. Dobbins (ref. 5), discusses the incorporation of an enhancement term that accounts for, in an approximate way, the reflection of walls in the visible portion of the spectra. However, since only ground state photoionization processes are considered in this analysis use of an enhancement factor appropriate for visible light would be inconsistent; therefore Eq. 22 was used directly to obtain a lower limit on the photoionization rate.

The radiative recombination is usually small, and is not included in this analysis. With the above assumptions, the total rate of electron production is

$$\frac{d[e^-]}{dt} = \frac{d[N_2^+]}{dt} + \frac{d[O_2^+]}{dt} \tag{23}$$

where

$$\frac{d[N_2^+]}{dt} = Q_{1f}[N_2] - d_{1r}[N_2^+][e^-] \tag{24}$$

and

$$\frac{d[O_2^+]}{dt} = Q_{2f}[O_2] - d_{2r}[O_2^+][e^-] \tag{25}$$

The spatial gradients of N_2^+ and O_2^+ can be obtained from Eq. 2, where Eqs. 24 and 25 are used for the net molar production of N_2^+ and O_2^+, and are given below:

$$V \frac{d[N_2^+]}{dx} = Q_{1f}[N_2] - d_{1r}[N_2^+][e^-] \tag{26}$$

and

$$V \frac{d[O_2^+]}{dx} = Q_{2f}[O_2] - d_{2r}[O_2^+][e^-] \tag{27}$$

with

$$[e^-] = [N_2^+] + [O_2^+] \tag{28}$$

The additional information needed to solve the above equations is the temperature of the gas behind the shock front and the spectrally detailed absorption and ionization cross sections. The calculation of the temperature behind the incident shock wave for arbitrary mixtures of nitrogen and oxygen is done in the manner described by Vincenti and Kruger (ref. 12). For the absorption and photoionization cross sections, the data of Cook and Ching (ref. 13) was used. Several modeling techniques were used to represent the detailed absorption spectra in a format amenable for efficient computation, and these models will be discussed below.

RESULTS AND DISCUSSION

Typical electron density profiles ahead of the shock wave in air are shown in figure 5 for an initial pressure of 0.2 torr. These profiles were obtained with the microwave interferometer and represent an average electron

density across the shock tube as a function of distance ahead of the shock wave. The most significant results presented in figure 5 are the high electron densities, in excess of 10^{10} cm^{-3} at distances greater than 5 m for the higher velocity shock wave and the large dependence of the data upon shock wave velocity.

When an experimental study of precursor electron densities is made in a shock tube, two phenomena immediately arise that must be considered, both in conducting and analyzing the experiment - reflection of radiation originating behind the shock wave from the shock tube walls, and leakage or outgassing affecting test gas purity. Dobbins has pointed out that wall reflectivity can enhance the radiative intensity at any given location in front of the shock wave, and thus should increase the precursor electron density compared to that in a tube with transparent or absorbing walls. In order to determine the effect of wall reflectivity, comparison was made of two shock-tube firings with differences in wall reflectivity. The first was made after the wall of the driven tube had been cleaned using a swabbing procedure. The second was made with the wall dirty, bearing a thin layer of the black soot-like deposit from the previous firing. This layer of soot is quite black and optically absorbing in the visible wavelength range, and should not alter appreciably the production of photo-electrons from the wall or the diffusion of electrons to the wall. As shown in figure 6, the nonreflective dirty wall considerably suppresses the production of electrons at long distances from the shock wave. (Electron densities close to the shock wave were nearly unaffected.) Since the production of precursor electrons is a function of wall reflectivity, theoretical models for the accurate prediction of electron density ahead of a shock wave in a shock tube must include this effect. All data presented in this note, other than that shown in figure 6 were taken with a clean shock tube wall. A perfectly reflecting wall would produce conditions within the shock tube that would simulate one-dimensional radiative transfer; however, in reality even a polished metal wall would not totally reflect vacuum ultraviolet radiation.

Several tests were made using pure nitrogen (99.99% purity) as the source gas to determine the effects of impurities in the test gas that were induced by the shock tube testing procedure. Due to outgassing and possible leakages, it was not possible to obtain a contamination level in the shock tube less than 0.2% of the test gas concentration. An electron density profile ahead of a shock wave at the above minimum impurity level condition is shown in figure 7. When the impurity level was allowed to build up to 1% by increasing the elapsed time between charging the driven tube with gas and firing the shock tube, nearly a five-fold increase in electron density was obtained, as shown in figure 7. Similar results were obtained consistently (the random scatter of all data was less than ±50%), thus demonstrating that precursor ionization in pure nitrogen is very sensitive to driven gas impurities.

Of the possible impurities in the nitrogen test gas, the most probable were water vapor and oxygen. Since it is difficult to control the concentration of water vapor, a series of firings was made wherein various controlled

mixtures of oxygen and nitrogen were used as the test gas. Although the detailed optical absorption coefficients of water vapor and oxygen are quite different, their ionization potentials are nearly identical; thus to a first approximation they should have similar response to photoionizing radiation. For these firings, the unknown impurity concentration was maintained at the minimum level (0.2%). The electron density one meter in front of the shock wave is shown in figure 8 as a function of the percent oxygen in the mixture. Since shock wave velocity varied over a range of 10 to 12.5 km/sec for these data points, the electron density has been adjusted to a velocity of 10 km/sec using an eighth-power velocity dependence, which will be discussed later. The magnitude of the precursor electron density is seen to be very sensitive to small amounts of oxygen, up to about a 0.2% mixture. An increase in the oxygen concentration beyond 0.2%, however, does not result in a proportionate increase in the electron density. For a 20% oxygen mixture, i.e., simulated air, the difference in electron density with 0.2% and 1.0% unknown impurities was within the accuracy of the experiment. Thus, the air data can be considered to be free of large impurity effects. All data for air that are given herein, however, are for an unknown impurity level of 0.2% or less.

Typical results of the Langmuir probe studies to determine the radial distribution of electrons are shown in figure 9 where the current drawn by four probes is presented for several distances ahead of the shock wave. All of the probes were assumed to have the same sensitivity. The results indicate a radial variation of electrons at all distances ahead of the shock wave, and that the radial nonuniformity tends to increase as the shock wave is approached. The fall-off in probe current near the wall is probably due to a combination of two effects: (1) the intensity of radiation across the shock tube near the shock wave is not uniform and (2) the effects of diffusion near the walls. Of these two effects, the nonuniform radiative intensity is believed to be responsible for most of radial variation of electron density.

In order to obtain quantitative electron density data from Langmuir probes operating at a constant potential that is above the saturation voltage, it is necessary to know the electron temperature in front of the shock wave. However, in this study, no attempt was made to measure the electron temperature, but an estimate of the electron temperature can be inferred from the experimental data. If an electron temperature of 500°K is assumed, then good agreement between the Langmuir probe data and the microwave interferometer data is obtained as shown in figure 10. For this comparison, the Langmuir probe that was inserted deepest into the shock tube was used. This agreement is perhaps fortuitous in light of the radial nonuniformity in probe current that exists and the expectation that the electron temperature would not be a constant ahead of the shock wave. The results, therefore, should be taken only as an indication that the electron temperature is probably only slightly higher than that of the heavy particles.

In order to obtain a theoretical prediction of precursor electron density, the model described in the analysis section was used. Several major questions arise when developing an analytical model for prediction of

precursor electron densities in a shock tube. The first question concerns the proper way to model the radiative transfer within the shock tube such that spectral detail, shock tube geometry and wall reflectivity are included properly. Next, the proper magnitude of the various collisional rate processes must be chosen since these rates can have large effects on the predictions of electron density and temperature. Lastly, effects due solely to shock tube testing procedure, such as introduction of impurities into the test gas must be included in the analysis. Obviously, the model described earlier does not, in its present state of development, include all of these effects. However, some of the important features are included and they will be discussed in the following paragraphs.

Typical absorption coefficients for photoionization of oxygen are shown in figure 11, along with several approximate models that were used in the current study. A comparison of the results of calculating the precursor electron density using the three models is shown in figure 12, where the one dimensional radiative transfer model of Eq. 18 was used for these calculations. It is seen that a simple arithmetic average model is totally inadequate as compared to the experimental data and grossly underpredicts the electron density. A gray band model, see reference 8 for details, on the other hand overpredicts the data, but has the same qualitative behavior. The more realistic sawtooth model, obtained by connecting the maxima and minima of the data of Cook and Ching with straight line elements still overpredicts both sets of data, but provides a slightly better prediction than the gray band model. Since these calculations were performed using a one dimensional radiative transfer model, the comparison with the clean wall data is more appropriate.

In order to determine the geometrical effects, an approximate three dimensional model for the radiative transfer has been used, Eq. 22, and the precursor electron densities are shown in figure 13 for this model using the sawtooth representation for the photoionization coefficient. The agreement between the approximate three dimensional calculation and the dirty wall data, both of which minimize the effects of wall reflectivity, is quite favorable. It should be mentioned however that these results are quite sensitive to the collisional processes, particularly the recombination processes described by Eq's. 5 and 7. Calculations in which the recombination rate for this reaction was varied by an order of magnitude have shown that the electron density can vary as much as a factor of 5. Since there is considerable uncertainty in these rates, better agreement between theory and experiment could be obtained. However such agreement might not be representative of the true value of the recombination rate coefficient.

It was noted earlier, that the experimental electron density profiles ahead of the shock wave were very dependent upon shock wave velocity. Several theoretical solutions were obtained using the gray band model and one-dimensional radiative transfer (improved solutions using the sawtooth model are in progress) and the electron density one meter in front of the shock wave from these solutions is shown as a function of shock wave velocity and ambient pressure in figure 14. Although this model overpredicts the

average electron density for a clean shock tube wall by about an order of magnitude, the dependence on shock wave velocity and ambient pressure is well predicted. The theoretical calculations have about a tenth power velocity dependence at 10 km/sec, decreasing to about a fourth power at 13 km/sec.

The sensitivity of precursor electron density to small amounts of impurities has been noted by other investigators as well as in the present study. In order to determine if the theoretical model used above would indicate the proper sensitivity several cases were run wherein the amount of oxygen in the nitrogen-oxygen mixture was varied, and these results are shown in figure 15. Here the average electron density one meter in front of the shock wave is shown as a function of the O_2 fraction, and again the theoretical predictions are high, but qualitatively accurate.

CONCLUDING REMARKS

From the results of this study, numerous concluding remarks can be made. The most significant are:

(1) Electron densities in excess of $10^{10}/cm^3$ are found several meters in front of shock waves traveling through air in a shock tube at velocities greater than 10 km/sec.

(2) High reflectivity of the shock tube wall significantly enhances the precursor electron density data.

(3) Driven gas impurities play a major role in the photoionization of pure nitrogen ahead of shock waves traveling at velocities greater than 10 km/sec. Air data, however, are much less sensitive to impurities.

(4) Radial profiles of Langmuir probe current indicate that near the shock front the radial nonuniformity of electron density increases.

(5) Langmuir probe data agree within a factor of 2 with the microwave measurements if an electron temperature of $500^{\circ}K$ is assumed.

(6) Theoretical prediction of precursor electron density profiles is very sensitive to the models used for photoionization coefficients, radiative transport, and collisional recombination rates. However by appropriate choice of the ground state absorption coefficient and recombination rates and using an approximate three dimensional radiative transport model that does not include wall reflection, the experimental profiles can be predicted with reasonable accuracy.

REFERENCES

1. Lin, S. C.: Radio Echoes from Manned Satellite During Reentry. J. Geophys. Res., vol. 67, Sept. 1962, p. 3851.

2. Omura, M. and Presley, L. L.: Electron Density Measurements Ahead of Shock Waves in Air. AIAA Journal, vol. 7, no. 12, Dec. 1969, pp. 2363-2365.

3. Presley, L. L., Falkenthal, G. E. and Naff, J. T.: A 1 MJ Arc Discharge Shock Tube as a Chemical Kinetics Research Facility. Proceedings of the Fifth Shock Tube Symposium, Silver Spring, Maryland, 1965, pp. 857-878.

4. Ferrari, C. and Clarke, J. H.: On Photoionization Ahead of a Strong Shock Wave. Supersonic Flow, Chemical Processes, and Radiative Transfer, Pergaman Press, New York, 1964, pp. 375-398.

5. Dobbins, R.A.: Photoexcitation and Photoionization of Argon Ahead of a Strong Shock Wave. AIAA Fluid and Plasma Dynamics Conference, Los Angeles, Calif., 1968, no. 68-666.

6. Murty, S. S. R.: Effect of Line Radiation on Precursor Ionization. Journal of Quantitative Spectroscopy and Radiative Transfer, vol. 8, Jan. 1968, pp. 531-554.

7. Lederman, S. and Wilson, D. S.: Microwave Resonant Cavity Measurement of Shock Produced Electron Precursors. AIAA Journal, vol. 5, no. 1, Jan. 1967, pp. 70-77.

8. Presley, L. L. and Omura, M.: Microwave Measurement of Precursor Electron Densities Ahead of Shock Waves in Air at Velocities Greater than 10 km/sec. AIAA 8th Aerospace Sciences Meeting, New York, New York, Jan. 19-21, 1970. No. 70-83.

9. Nelson, H. F. and Goulard, R.: Structure of Shock Waves with Nonequilibrium Radiation and Ionization. Phys. Fluids, vol. 12, no. 8, August 1969, pp. 1605-1617.

10. Bortner, M. H.: Chemical Kinetics in a Reentry Flow Field. General Electric Space Sciences Laboratory Report R6SD063, August 1963.

11. Wilson, K. H. and Greif, R.: Radiation Transport in Atomic Plasmas. J. Quant. Spectry. Radiat. Transfer, vol. 8, no. 4, Apr. 1968, pp. 1061-1086.

12. Vincenti, W. G. and Kruger, C. H., Jr.: Introduction to Physical Gas Dynamics. John Wiley and Sons, Inc., New York, 1965.

13. Cook, G. R. and Ching, B. K.: Absorption, Photoionization, and Fluorescence of Some Gases of Importance in the Study of the Upper Atmosphere. Aerospace Corporation Report TDR-469(9260-01)-4, January 1965.

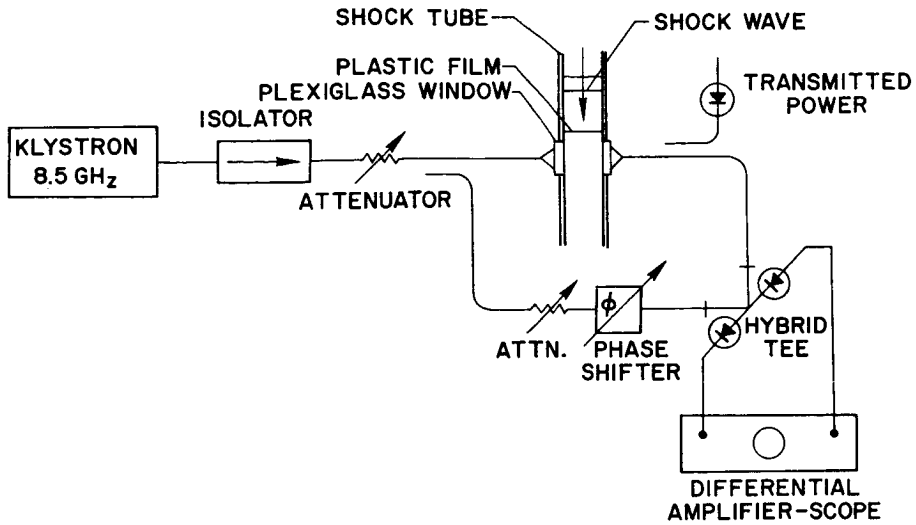

Figure 1.- Experimental setup of microwave interferometer.

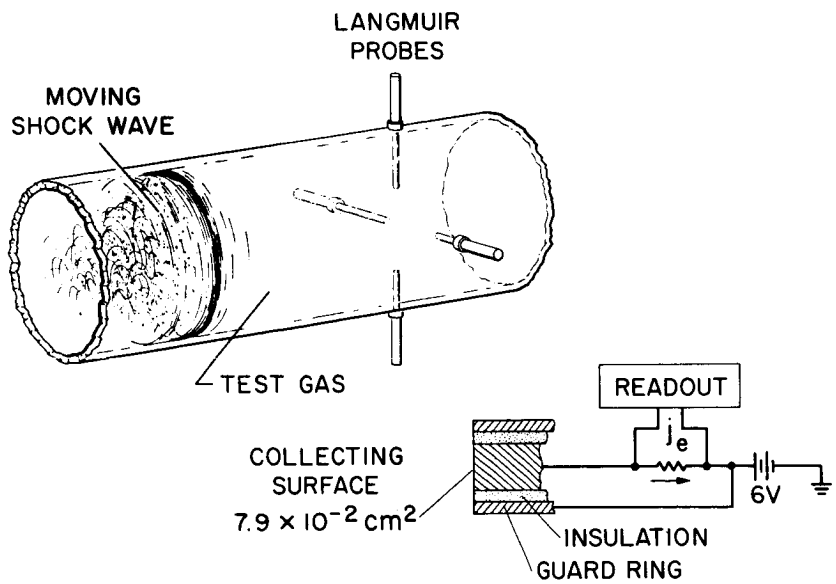

Figure 2.- Schematic of Langmuir probe array in shock tube.

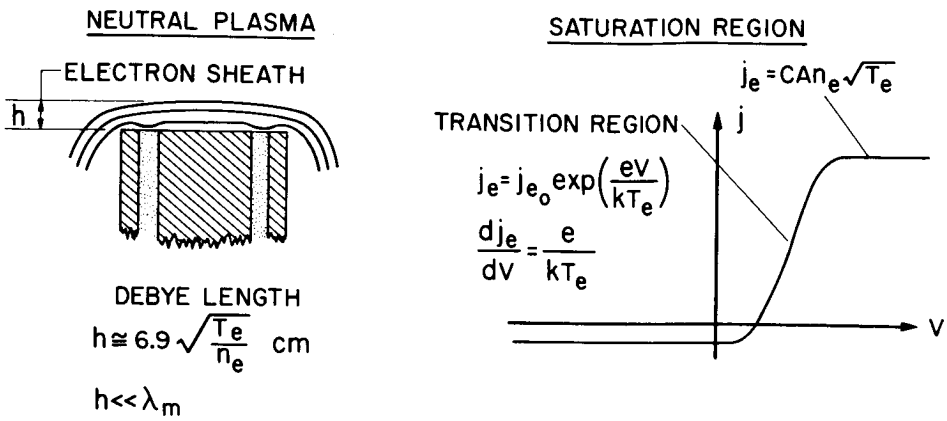

Figure 3.- Concepts of one-dimensional Langmuir probes.

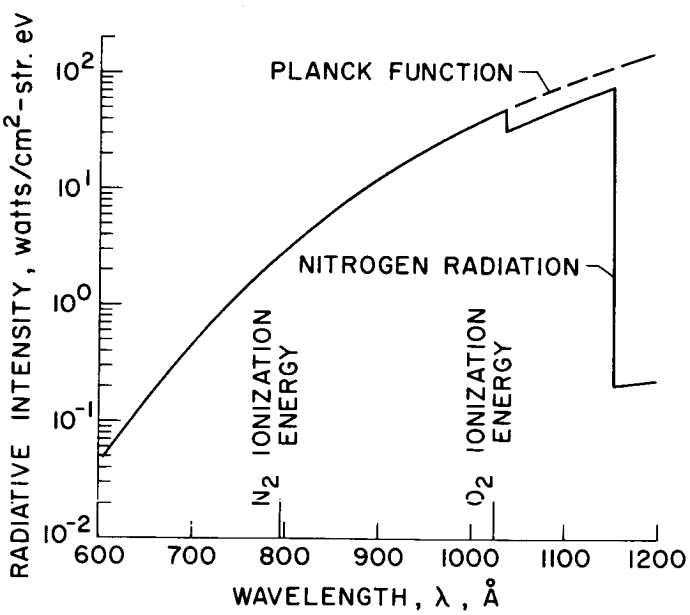

Figure 4.- One-dimensional isothermal radiative intensity from a 20-cm-thick nitrogen plasma. V = 12 km/sec; p_1 = 0.2 torr.

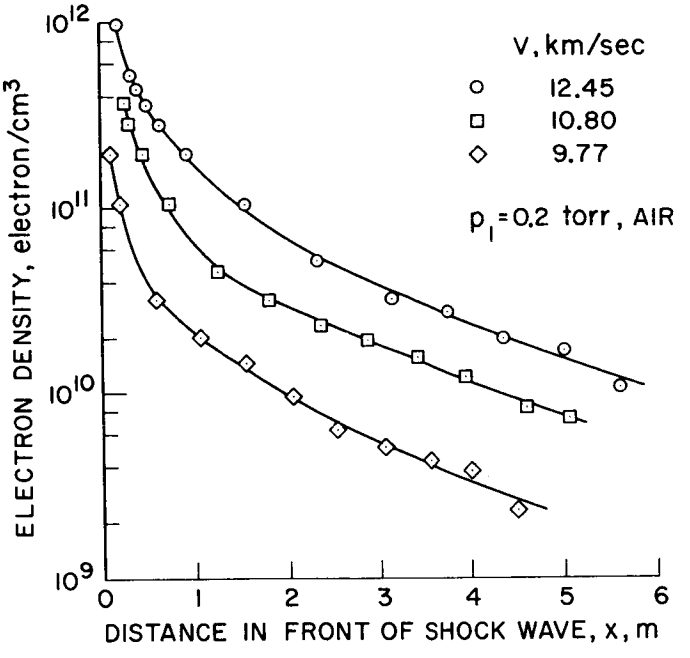

Figure 5.- Typical average electron density profiles in air.

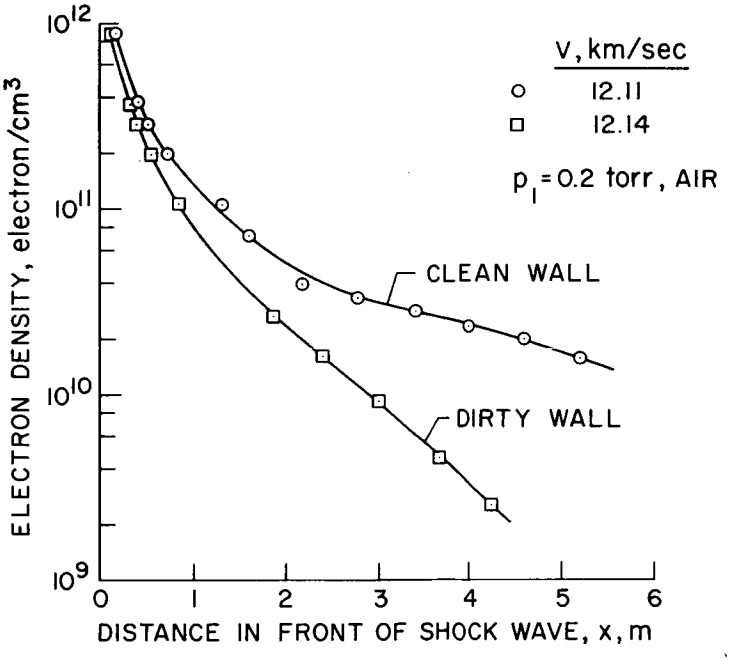

Figure 6.- Variation of average electron density profiles with clean (reflecting) and dirty (nonreflecting) shock tube wall.

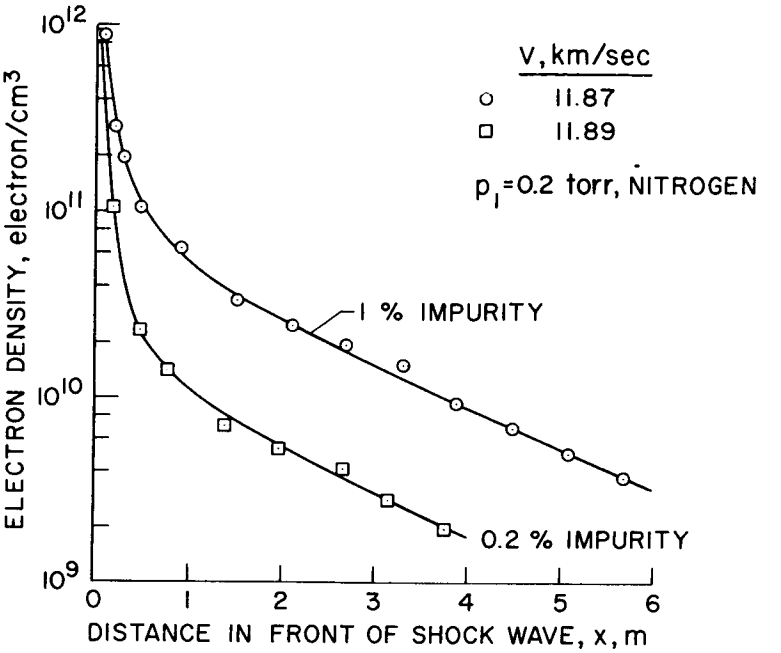

Figure 7.- Effect of impurities of unknown composition upon average electron density profiles in pure nitrogen.

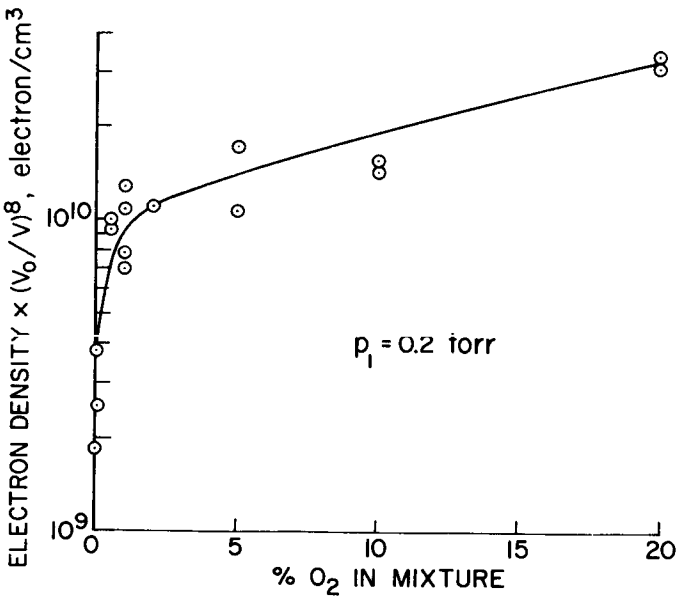

Figure 8.- Average electron density at 1 m in front of shock waves for various mixtures of oxygen and nitrogen. Data adjusted to V = 10 km/sec.

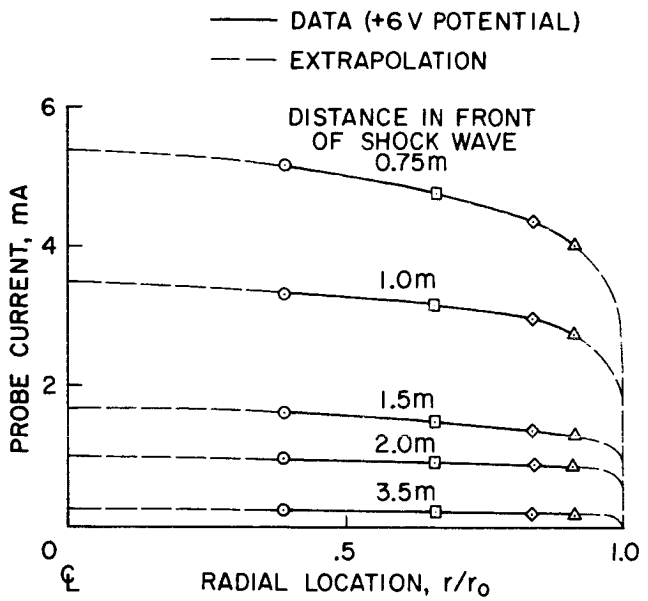

Figure 9.- Radial distribution of Langmuir probe current. V = 12 km/sec; p_1 = 0.2 torr.

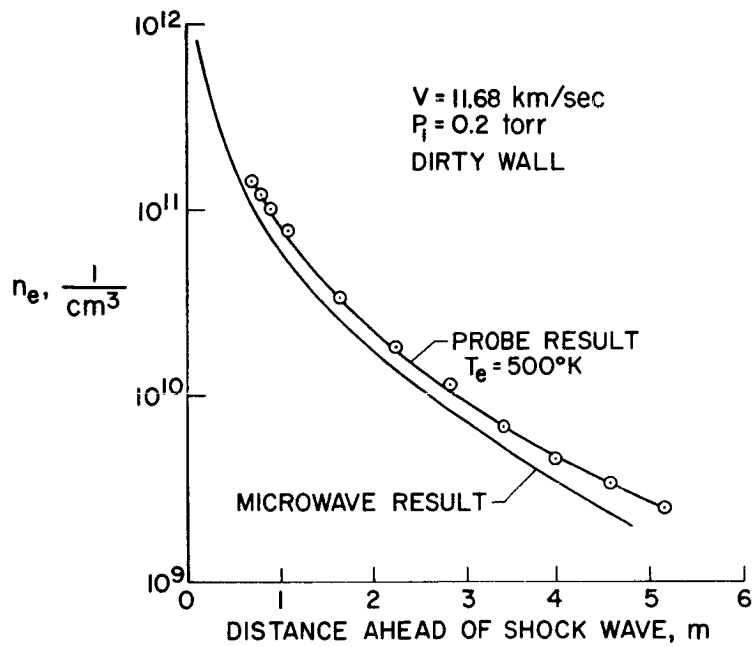

Figure 10.- Comparison of local Langmuir probe results for an assumed $T_e = 500^o$ K with microwave results.

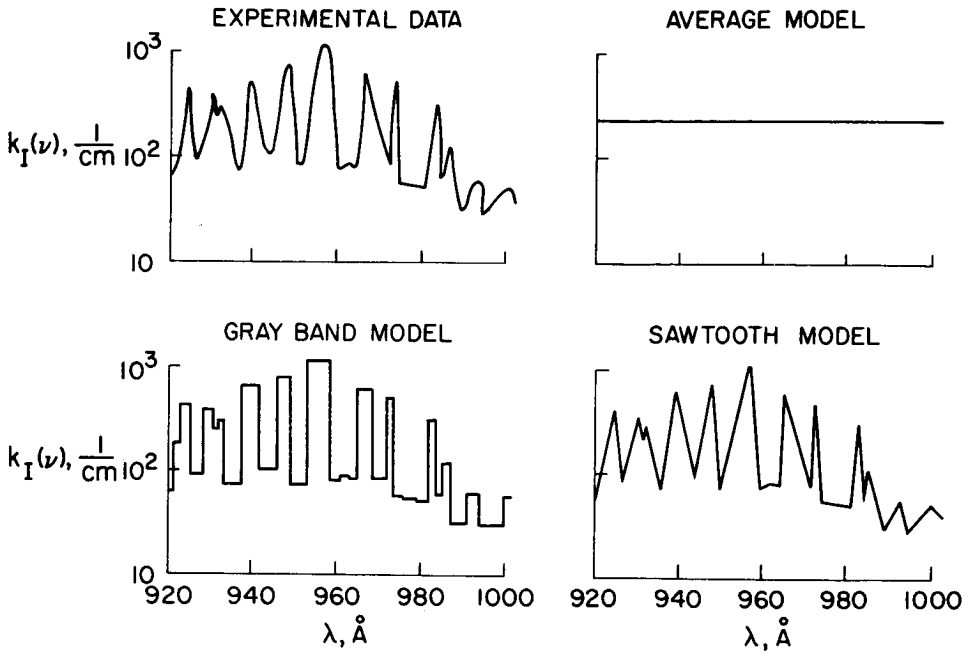

Figure 11.- Typical photoionization coefficients for molecular oxygen and modeling used in this study.

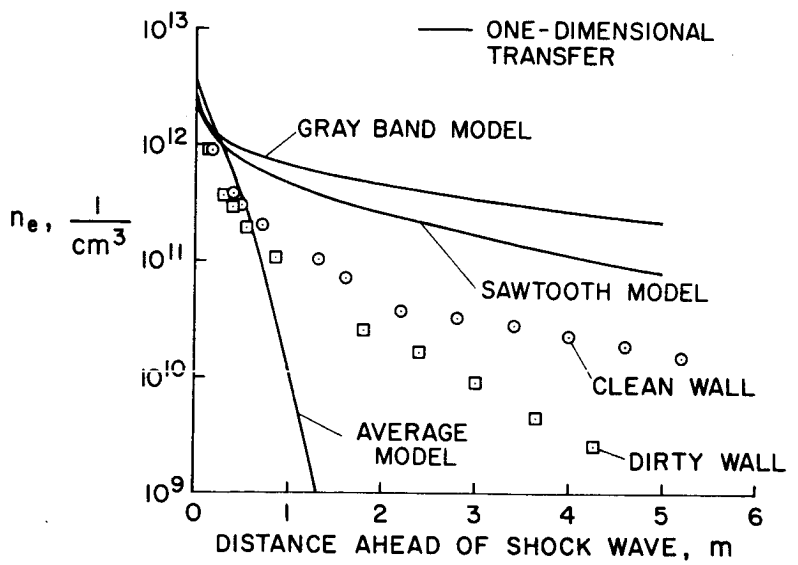

Figure 12.- Comparison of theoretical predictions using different models for absorption coefficients and one-dimensional radiative transfer. V_1 = 12 km/sec; p_1 = 0.2 torr.

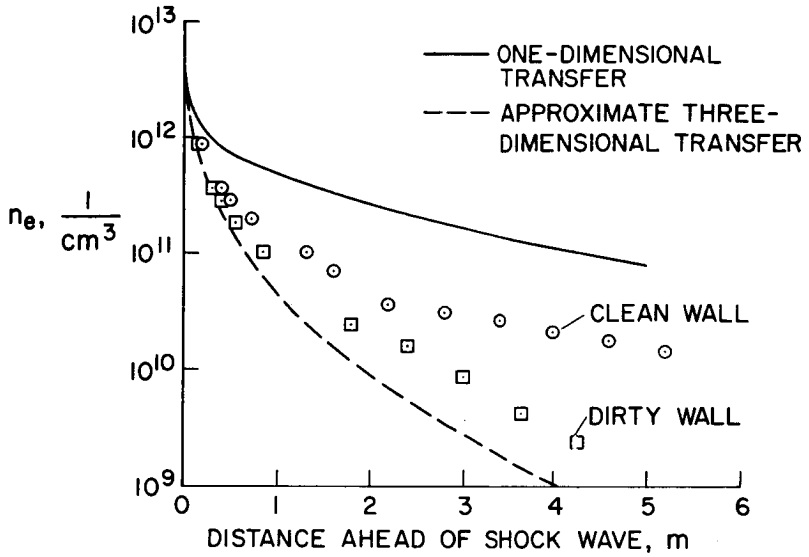

Figure 13.- Comparison of one-dimensional and approximate three-dimensional radiative transfer using sawtooth model of absorption coefficients.

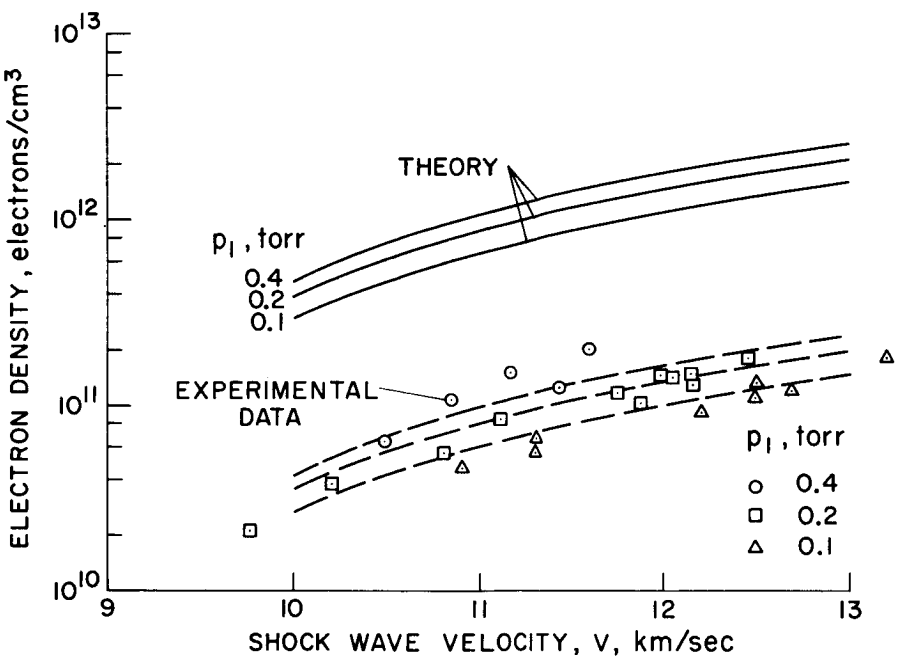

Figure 14.- Variation of electron density 1 m in front of shock with shock wave velocity in air.

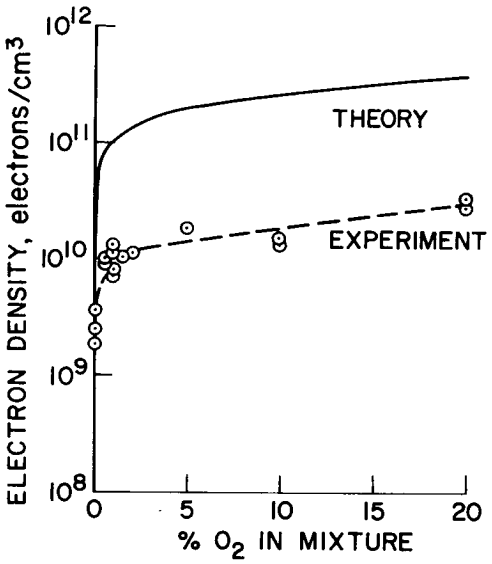

Figure 15.- Theoretical and experimental electron density 1 m in front of shock for nitrogen-oxygen mixtures.

ANALYSIS OF VHF AND X-BAND TELEMETRY SYSTEMS DEGRADATION BY REENTRY ENVIRONMENT*

By Kurt E. Golden and Donald A. McPherson

The Aerospace Corporation, Los Angeles, California

SUMMARY

The degradation of VHF and X-band telemetry by the reentry plasma sheath has been analyzed for recent flight tests of a hypersonic reentry vehicle. A self-consistent technique utilizing the received signal strengths of both the VHF and X-band transmitters was used. It was determined that the attenuation was caused by electrons flowing back over the antennas from the stagnation region at the nose. For the X-band signal, the attenuation was a result of pattern distortion caused by refraction in the plasma layer and distortion of the field distribution in the antenna aperture. At VHF, the plasma layer is electrically thin, and the signal loss resulted from the combined effects of reflection and absorption.

INTRODUCTION

RF signal attenuation data from a reentry vehicle are compared with predictions obtained from theoretical analysis and ground tests of suitable antenna systems. The purpose of this study was to investigate the large attenuation and roll modulation observed in an X-band telemetry signal during a recent flight test. The reentry vehicle was a slightly blunted, slender cone with a velocity of 23 kft/sec. The circumferential slot antennas for the VHF and X-band telemetry were located near the tip of the vehicle as shown in figure 1. The nose tip and heatshield were electrically conducting.

The performance of the telemetry antenna system in both free space and the reentry environment was determined on the basis of aperture admittance, feed network, far-field radiation pattern, and antenna gain effects. Slot antenna calculations for both the VHF and X-band telemetry systems were performed for nonequilibrium laminar boundary-layer plasmas. The results of the study demonstrate that at high altitude the X-band attenuation in the forward direction is dominated by radiation pattern distortion. As the reentry conditions become more severe, degradation of the feed network

*This work was supported by the U.S. Air Force under Contract F04701-70-C-0059.

performance alters the aperture field distribution. The X-band feed network produces the forward-looking pattern and circularly polarized aperture field and is sensitive to changes in the aperture reflection. The performance of the X-band feed network was measured with the reflection characteristics of the plasma simulated by artificial means (ref. 1). For overdense plasmas, the radiation patterns exhibited two roll plane lobes that caused the observed roll modulation in the telemetry signal.

The VHF and X-band signal strength data were analyzed in a self-consistent manner in order to reduce the errors in calculating signal attenuation associated with the uncertainties of the peak electron density predictions from flow field analysis. The shape of the electron density profile over the X-band and VHF antenna apertures was determined from aerodynamic calculations (ref. 2). The peak electron density at the VHF antenna position was inferred from the VHF signal attenuation. The peak electron density at the X-band antenna location was calculated from values at the VHF antenna location, scaled by the Blottner method (ref. 3). The X-band aperture admittance, radiation pattern distortion, and resulting antenna gain calculations were then performed and compared with flight data. The agreement between the measured signal strength received at X-band and the predicted values based on the slot analysis provided verification that the effects of the reentry boundary-layer plasma on the X-band telemetry were modeled in the proper way.

This analysis was first performed for a vehicle with a 0.25-in. nose radius. On the basis of the agreement between the predicted and measured values, the nose radius on a subsequent flight was reduced. Predictions and flight measurements of attenuation for both nose radii are presented.

FLOW FIELD INPUTS

Flow field parameters were calculated for two downstream stations corresponding to the locations of the X-band and VHF antennas (ref. 2). With clean-air chemistry assumed, the solution of the chemically-reacting, air boundary layer was obtained. The estimates for the electron density represent a lower bound, since ablation products from the reentry vehicle nose enhance the electron density. The electron density distributions at the X-band station and the VHF station are shown in figures 2 and 3, respectively. Profiles are shown for two altitudes and for several values of nose radius. The electron neutral collision frequency ν_c was calculated from the density ratio ρ/ρ_0 and temperature data T from the expression:

$$\nu_c = 3 \times 10^8 \, (\rho/\rho_0) \, T \quad \text{Hz} \tag{1}$$

This equation is a curve fit to the equilibrium results of Bachynski, et al. (ref. 4). The equivalent thickness d for the electron density profile is assumed to be

$$d = \int_0^{\delta} N_e(z)\, dz / N_e \text{ (peak)} \tag{2}$$

where δ is the boundary-layer thickness and N_e is the electron density. The collision frequency and profile thickness are shown as a function of altitude in figure 4.

VHF SIGNAL ATTENUATION

The VHF antenna system consists of a coaxial-fed circumferential gap located 11 in. from the virtual tip of the reentry vehicle as shown in figure 1. The complex free-space gap admittance was calculated by means of the method of moments (ref. 5) and is equal to

$$Y^0_{gap} = 6.95 \times 10^{-3} + j\, 4.15 \times 10^{-3} \quad \text{mhos} \tag{3}$$

where the superscript 0 denotes free-space conditions.

The signal attenuation induced by the plasma can be calculated from the thin sheath approximation when: (1) the free-space wavelength is much greater than the boundary-layer thickness; (2) the signal frequency is much less than the peak plasma frequency; and (3) the sheath is in electrical contact with the conducting heat shield. Under these conditions, the plasma does not affect the normalized current distribution on the vehicle except for the fields in the antenna gap. The total admittance of the gap in the reentry environment can be approximated by (ref. 5)

$$Y^P_{gap} = Y^0_{gap} + 2\pi r_{gap}\, Y_s / a \tag{4}$$

where superscript P denotes plasma, a is the gap width, $2\pi r_{gap}$ is the circumferential dimension of the slot, and Y_s is the surface admittance of the plasma,

$$Y_s = \frac{e^2}{(\nu_c + j2\pi f)m} \int_0^{\delta} N_e(z)\, dz \tag{5}$$

In equation 5, e is the electron change, f is the signal frequency, and m is the electron mass. Since the radiation patterns are undistorted, the resulting signal attenuation is given by the change in the voltage developed across the antenna gap and is calculated from the equivalent circuit shown

in figure 5. The VHF signal attenuation is

$$\text{Atten} = \left| \frac{V^{P}_{gap}}{V^{0}_{gap}} \right|^2 = \left| \frac{Z^{P}_{gap}(Z_{gen} + Z^{0}_{gap})}{Z^{0}_{gap}(Z_{gen} + Z^{P}_{gap})} \right|^2 . \tag{6}$$

where V_{gap} is the voltage developed across the antenna gap and Z_{gen} is the characteristic impedance of the coaxial feed. Figure 5 also shows attenuation vs collision frequency for constant values of integrated electron density. The numbers labeling each contour represent the integrated electron density in units of cm^{-2}.

The integrated electron densities at the VHF antenna station can be obtained from the measured VHF signal attenuation and predicted collision frequency. The data points given in figure 5 correspond to the predicted collision frequencies and measured VHF attenuations for a recent flight test of a vehicle with a 0.25-in. nose radius. The line drawn between points represents the "trajectory" of the vehicle in collision frequency-attenuation space. The integrated electron density corresponding to a given altitude can be obtained from the intersections of the trajectory line and the contour lines.

The peak electron density is determined from the integrated values by use of the electron density profile predicted from the flow field analysis. The peak electron densities as inferred from the measured VHF signal attenuation are displayed in figure 6. The error bars in electron density at the X-band station are representative of the uncertainties in scaling the results from the VHF station to the X-band station and the uncertainty in determining the peak electron density from VHF signal attenuation. The electron density results are used for the calculation of the expected X-band signal attenuation.

X-BAND ANTENNA CALCULATIONS

It was not possible to analyze the X-band antenna explicitly because of the complexity of the antenna feed and the conical geometry. However, it can be demonstrated that the reentry plasma sheath causes little change in aperture distribution or dominant mode aperture voltages above 140 kft. Therefore, the internal feed performance can be neglected when calculating the high-altitude X-band attenuation.

At lower altitudes, significant reflection occurred at the aperture and affected the antenna feed. Laboratory measurements of these effects are presented in the following section.

The model geometry used in the analytical calculations consisted of a finite rectangular slot loaded with a dielectric and terminated in a plasma-clad ground plane. The plasma was assumed to be uniform along the ground plane surface and inhomogeneous in the direction normal to the ground plane. The rf properties of the plasma sheath are characterized by the conventional dielectric model for high frequency and zero temperature and by the electron density and collision frequency profiles. The aperture was excited with the dominant TE_{01} mode, and the feed waveguide had the same cross-sectional dimensions as the aperture. The length of the slot was chosen to equal half of the circumferential dimension of the actual reentry vehicle antenna in order that the input admittance calculation would approximate the actual aperture admittance.

The planar slot antenna calculations were not intended to represent all the details of the actual flight antenna system, but to demonstrate the trends and to aid in the flight data interpretation. The applicability of the plane calculations to the axial patterns of a slot on a conical vehicle is discussed in ref. 6. The conclusions are that axial patterns of slot antennas on plasma-clad conical vehicles can be approximated by an equivalent plane with a high degree of accuracy when tip scattering is negligible. For conducting heat shields, the overdense plasma sheaths tended to reduce the effects of tip scattering.

The degradation in the transmitted signal caused by the plasma was equal to the change in the E-plane antenna gain expressed as

$$A(\theta, \phi = 0) = \left| \frac{Y_g + Y_{11}^0}{Y_g + Y_{11}^P} \right|^2 \frac{P_e^P(\theta, \phi = 0)}{P_e^0(\theta, \phi = 0)} \tag{7}$$

where Y_{11} is the aperture admittance, Y_g is the characteristic admittance of the dielectric loaded feed waveguide, and $P_e(\theta, \phi)$ is the radiation pattern of the slot antenna. A more complete discussion of the electromagnetic analysis can be found in refs. 7 through 9. Input admittance, radiation pattern distortion, and signal absorption effects are calculated with the slot antenna analysis. The calculations do not incorporate feed network performance or distortions in the aperture electric field. The actual input admittance and radiation pattern calculations were performed for the normalized plasma electron density profile shown in figure 7. The peak electron density and boundary-layer thickness vs altitude is shown in figure 8 for the X-band station. The profile was approximated by 200 equally thick slabs, which caused less than 0.1 dB error in the calculated attenuation. The aperture admittance results are plotted on the Smith chart shown in figure 9. A three-dimensional plot of antenna patterns vs altitude is shown in figure 10. The data of figures 9 and 10 are combined to obtain signal attenuation vs aspect angle for range of altitudes (fig. 11).

The data shown in figure 11 illustrate that the X-band signal attenuation in the forward direction was caused by the redistribution of the far-field radiation. The apparent increase in antenna directivity in the broadside direction was offset by a decrease in transmitted power caused by an increase in aperture reflection loss. Note that complex aperture reflection coefficient did not change significantly above 140 to 150 kft. This implies that the aperture distribution is relatively unaffected at high altitudes.

As the plasma sheath becomes overdense, the plasma tends to short-circuit the antenna aperture. In the following section, it will be shown that the X-band feed system is sensitive to changes in the aperture admittance and that high aperture reflection can alter the aperture distribution and cause additional pattern distortions.

In figure 12, the X-band flight data for the 0.25-in. nose vehicle is plotted as a function of altitude. The predicted values of attenuation obtained from figure 11 for the appropriate aspect angles are also plotted in figure 12.

The periodic signal attenuation below 130 kft is correlated with the roll of the vehicle. It will be shown that, at low altitudes the antenna feed degradation causes an azimuthal pattern distortion that is roll modulated.

Subsequent to the analysis of the attenuation data from the vehicle with the 0.25-in. nose radius, a vehicle with a 0.10-in. nose radius was flight-tested. Sharpening the nose results in a lower electron density of the X-band station because of the increased separation between the antenna and the nose and the reduced volume of the stagnation region. At 120 kft, the peak electron density of the X-band antenna for a 0.10-in. radius nose is predicted to be eight times lower than for a 0.25-in. radius nose.

Figure 13 shows the measured attenuations for both the 0.10- and 0.25-in. nose radius vehicles. The predicted values at 154 and 120 kft for the 0.1-in. case are also shown on figure 13. It is clear that the reduction in the nose radius resulted in dramatic improvement in the received signal strengths from the X-band telemetry system.

X-BAND ANTENNA MEASUREMENTS

The performance of the X-band telemetry antenna was measured with a prototype flight-test antenna in a simulated plasma environment. The purpose of the measurements was to determine whether or not the reflection properties of the 120-kft plasma sheath were severe enough to alter the aperture distribution and cause the radiation pattern distortion observed at low altitude (figure 12).

The surface admittance technique (ref. 1) used in the pattern measurements only approximates the reflection characteristics of the high-altitude reentry conditions, since the actual boundary-layer sheaths are not thin at X-band frequencies. The refraction of the electromagnetic signal by the thick boundary layer is not reproduced by a single impedance surface. Therefore, the radiation pattern measurements in the simulated plasma environment corresponded to the pattern distortions associated with changes in the aperture distribution induced by the plasma shorting the antenna aperture.

Figure 14 shows the input admittance of the X-band slot antenna, used in this analysis, calculated as a function of the predicted reentry environment and the simulated reentry environment. The surface admittances used were wire grid structures (ref. 1) and thin highly lossy dielectric sheets (ref. 8). The wire grid structures provided a better simulation of the reentry conditions than the lossy dielectric sheets.

The surface admittances of the wire grid structures used to simulate the 154- and 120-kft reentry conditions were experimentally determined by placing the grid structures across an X-band waveguide aperture and measuring the resulting change in the aperture susceptance.

The X-band radiation patterns were measured with the prototype flight-test antenna in an anechoic chamber having -50 dB performance. The aft end of the nose-tip antenna assembly was terminated with absorbing material. The wire grid structures were attached to the graphite heat shield with conducting tape to ensure good electrical contact between the wires and heat shield. Figure 15 shows the antenna assembly installed in the anechoic chamber. The insert illustrates the method of attaching the wire grid.

Circular polarization radiation patterns were measured at a constant roll angle ϕ, with the aspect angle θ, varied ±40 deg. The axial patterns were run every 10 deg in roll. Figure 16 shows pattern vs aspect angles for two different roll angles.

The results of the pattern measurements for free-space simulated 154- and 120-kft conditions are plotted in figure 17 at the flight aspect angles as a function of the roll angle. The results show a 6-dB roll modulation in the radiation pattern for the 120-kft reentry conditions, which closely approximates the flight results shown in figure 12. Since the roll pattern exhibits two nulls, the modulation appearing in the flight corresponds to twice the spin rate of the reentry vehicle.

CONCLUSIONS

For the flight test data studied, it was concluded that the attenuation observed in the X-band telemetry signal was caused by electrons flowing back over the antenna from the nose of the vehicle. This attenuation was caused by two different effects. First, at altitudes above transition to turbulence, collisions are unimportant at X-band frequencies, but the electron density is sufficiently high that substantial refraction of the radiation occurs in the boundary layer of the flow field. Because the pattern of the X-band antenna was highly peaked in the forward direction, this resulted in a significant reduction of gain in the direction of the ground receiver.

Second, at altitudes below transition to turbulence where collisional effects are important, the plasma reflected sufficient rf power back into the antenna-feed waveguide to cause a redistribution of the aperture field. For the particular X-band antenna-feed used in the flight tests, this field redistribution results in an azimuthal pattern distortion consisting of two lobes and two nulls. Because of vehicle roll, the pattern distortion appeared in the received signal as a modulation of twice the spin rate.

The results of this study were immediately useful in identifying the cause of the attenuation observed during the flight test of the vehicle with the 0.25-in. nose radius. Thus, it became possible to prevent this difficulty on later flights. In addition, some general results are summarized as follows:

1. With combinations of analytical and laboratory simulation techniques, the plasma attenuation can be predicted over all of the trajectory for a complex antenna system. The same techniques do not apply at all altitudes, and care must be exercised in selecting the appropriate model for the particular conditions of each altitude.

2. Plasma simulation should be included in research and development tests of all radiating systems on reentry vehicles. Combinations of impedance sheets and wire grids can be used to simulate most plasma effects except those associated with collisionless, thick plasmas. For the latter case, calculations for a plasma-covered slot in a plane will probably suffice.

3. In many cases, measured attenuations at two frequencies can be used to factor out normalizations of flow field parameters such as electron density.

4. For antenna feed networks that are very sensitive to reflection loss, the polarization can be changed from one sense to another by the plasma reflection loss.

REFERENCES

1. Golden, K. E., and Smith, T. M.: Simulation of a Thin Plasma Sheath by a Plane of Wires. IEEE Trans. Nuclear Sci., NS-11, 225-230 (1964).

2. Steiger, M. H., et al.: Reentry Communication: Theoretical Analysis and Flight Test Results. AIAA Paper No. 70-220 (January 1970), Aerospace Science Meeting, New York.

3. Blottner, F. G.: Prediction of the Electron Number Density Distribution in the Laminar Air Boundary Layer on Sharp and Blunt Bodies. AIAA Paper No. 68-733 (June 1968), AIAA Fluid Dynamics Meeting, Los Angeles, California.

4. Bachynski, M. P., et al.: Electromagnetic Properties of High-Temperature Air. Proc. IRE 347-356 (1960).

5. Soo Hoo, K. M.: An Investigation of Plasma Effects on Finite Reentry Bodies. Presented at 1970 Spring URSI Meeting, Washington, D. C. (April 1970), p. 75.

6. Stewart, Gordon E., Golden, Kurt E., and Pridmore-Brown, David C.: Radiation From Circumferential Slots on Plasma-Clad Cones. The Entry Plasma Sheath and Its Effects on Space Vehicle Electromagnetic Systems - Vol. I, NASA SP-252, 1971, pp. 411-425.

7. Golden, K. E., and Stewart, G. E.: Single and Multislot Antennas in an Inhomogeneous Reentry Plasma Environment. Proc. Conf. Environmental Effects on Antenna Performance, Boulder, Colorado (July 1969), p. 156.

8. Golden, K. E., and Stewart, G. E.: Self and Mutual Admittances of Rectangular Slot Antennas in the Presence of an Inhomogeneous Plasma Layer, IEEE Trans. Antennas and Propagation, AP-17, 673-770 (1969).

9. Golden, K. E.: Reentry Plasma Attenuation for S-Band Telemetry Systems. TR-0200(4220-10)-3, The Aerospace Corporation, El Segundo, California, (May 1969).

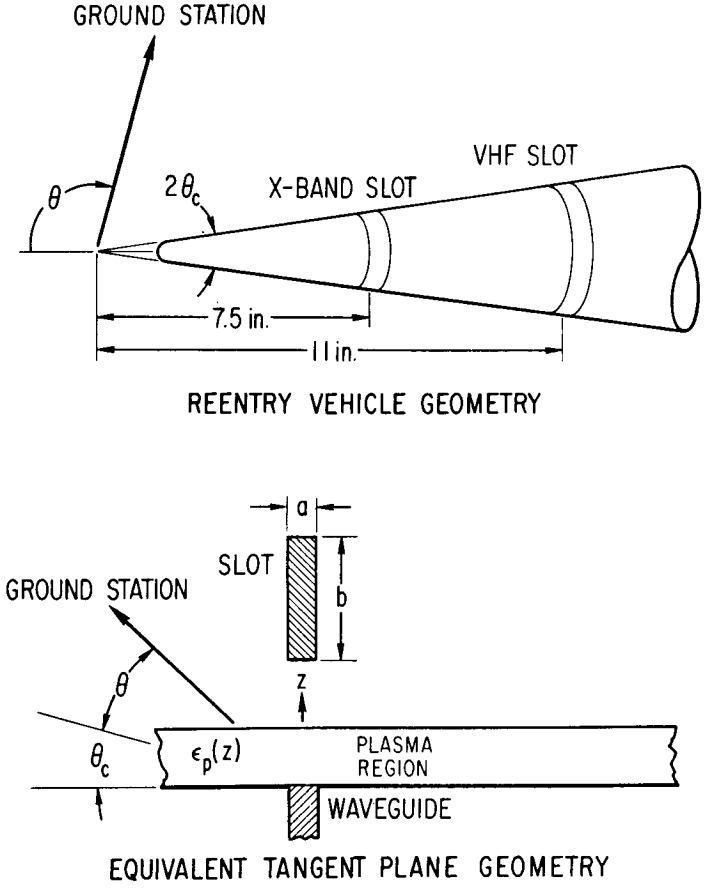

Figure 1.- Telemetry antenna geometry.

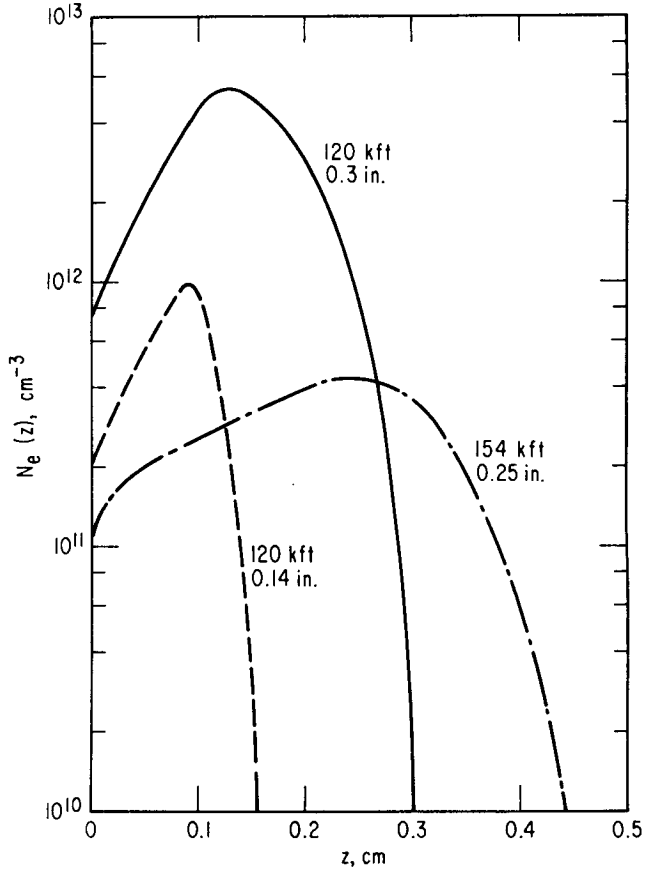

Figure 2.- X-band electron density profiles.

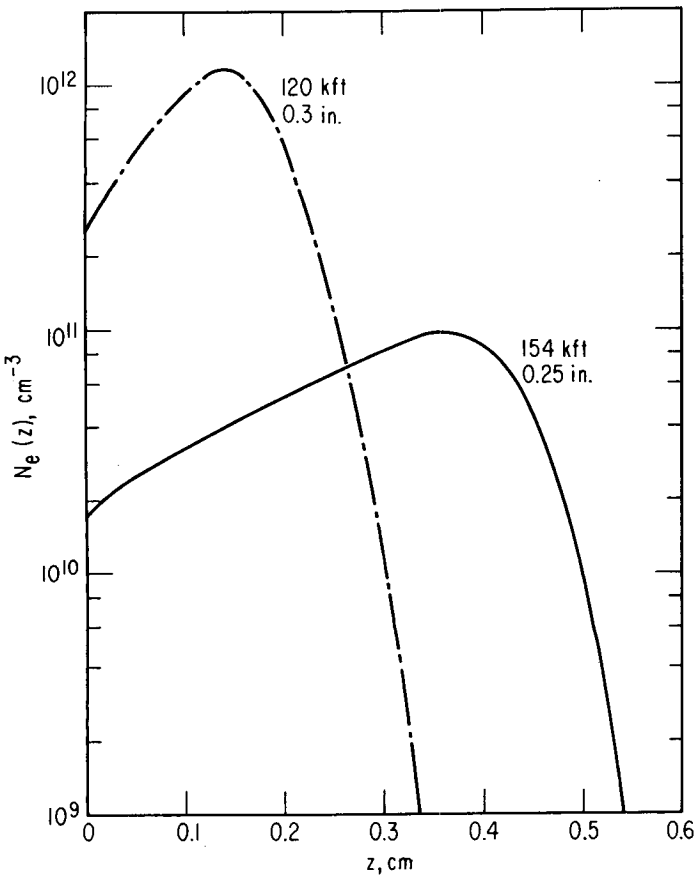

Figure 3.- VHF electron density profiles.

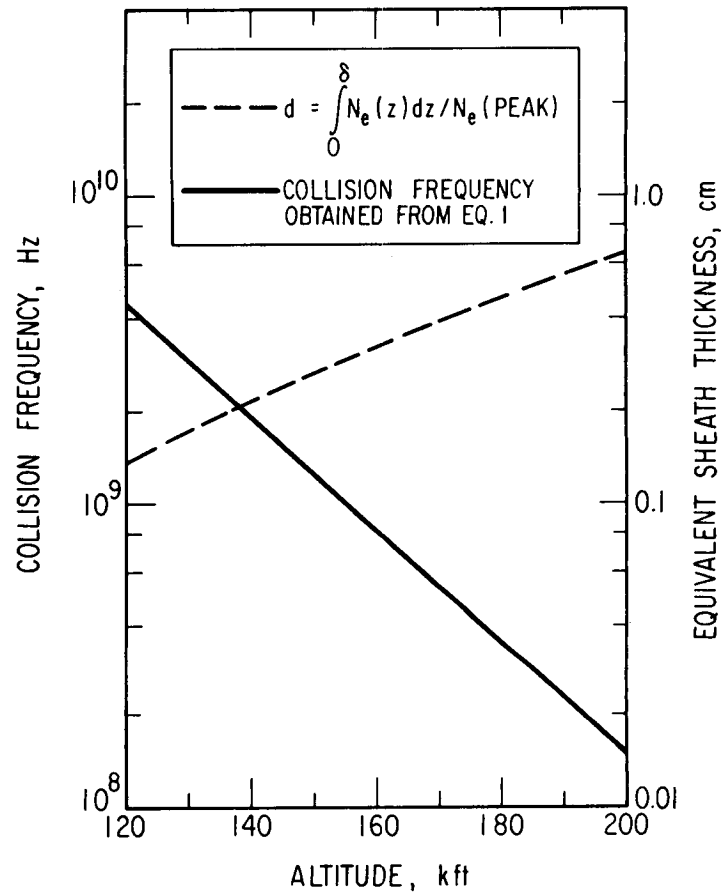

Figure 4.- Postflight average collision frequency and equivalent sheath thickness at VHF antenna body station.

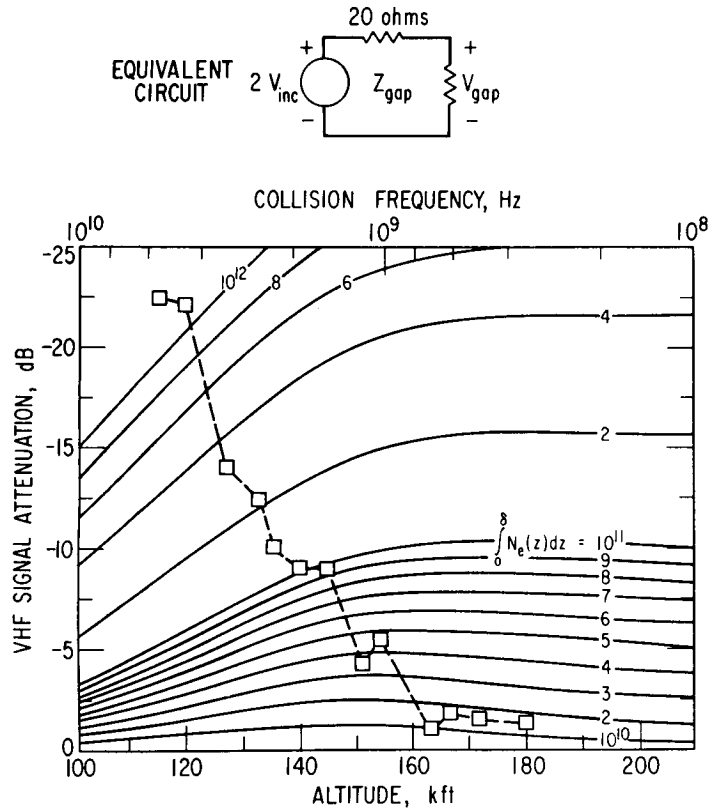

Figure 5.- VHF attenuation as a function of collision frequency, altitude, and integrated electron density.

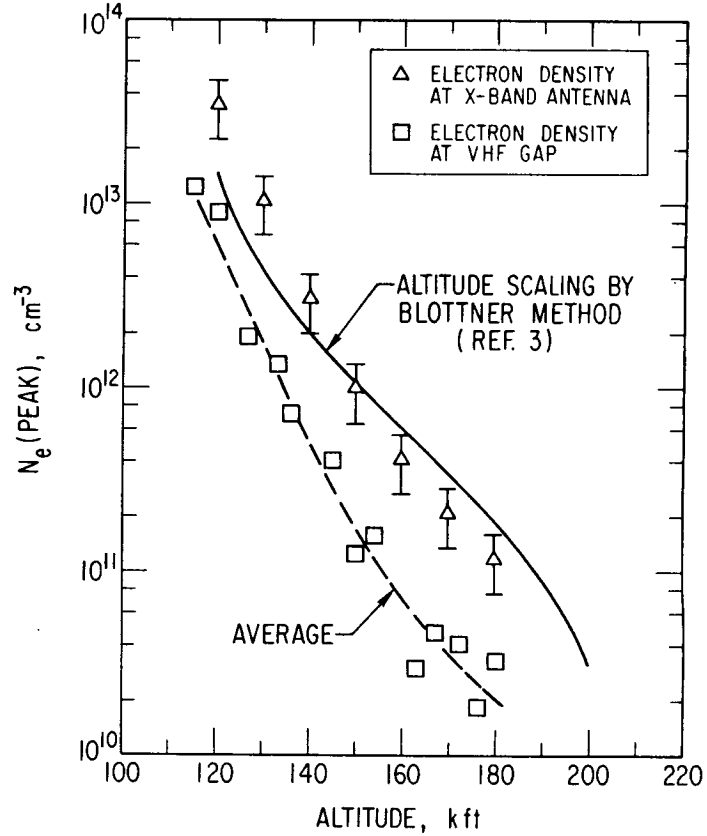

Figure 6.- Peak electron density at VHF and X-band antenna stations.

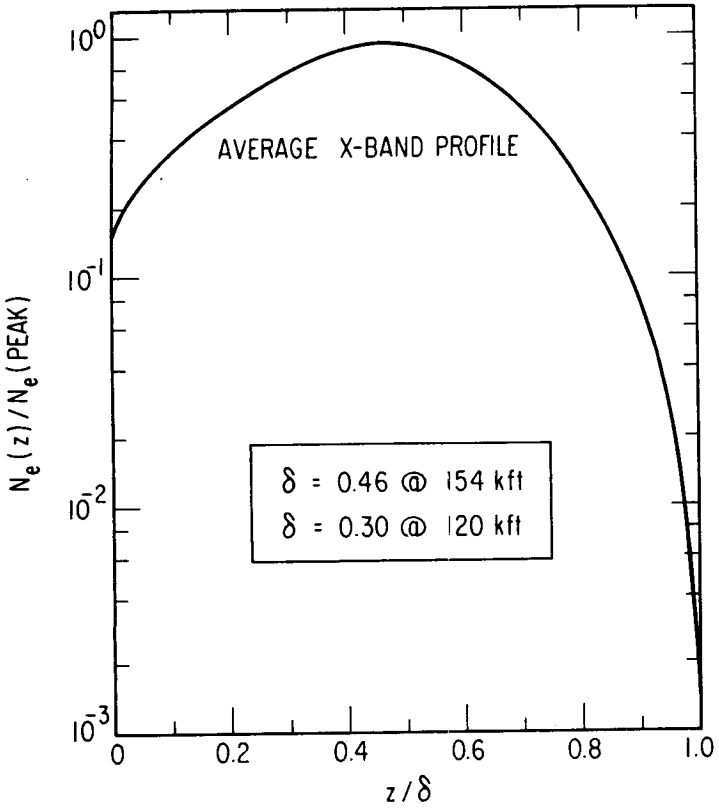

Figure 7.- Normalized electron density profile used in X-band calculations.

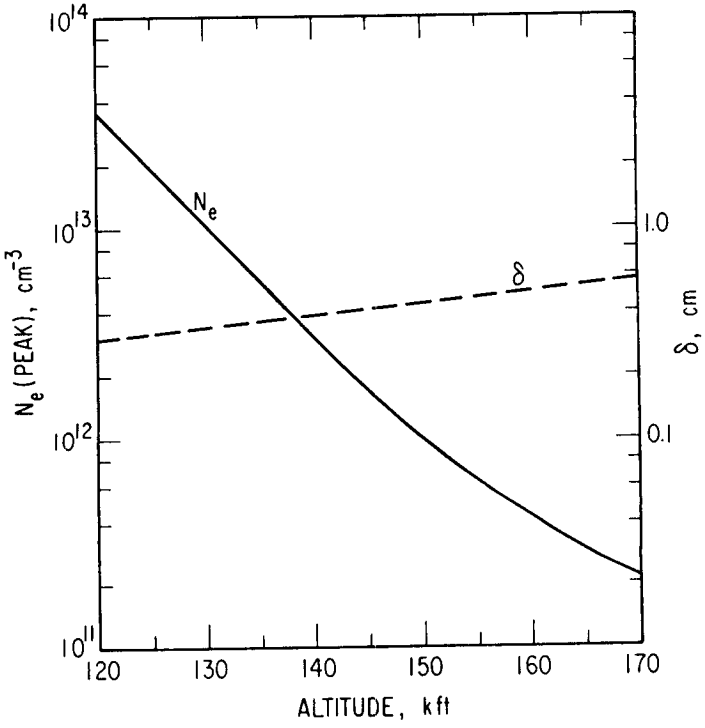

Figure 8.- Peak electron density and boundary-layer thickness at X-band antenna station as a function of altitude.

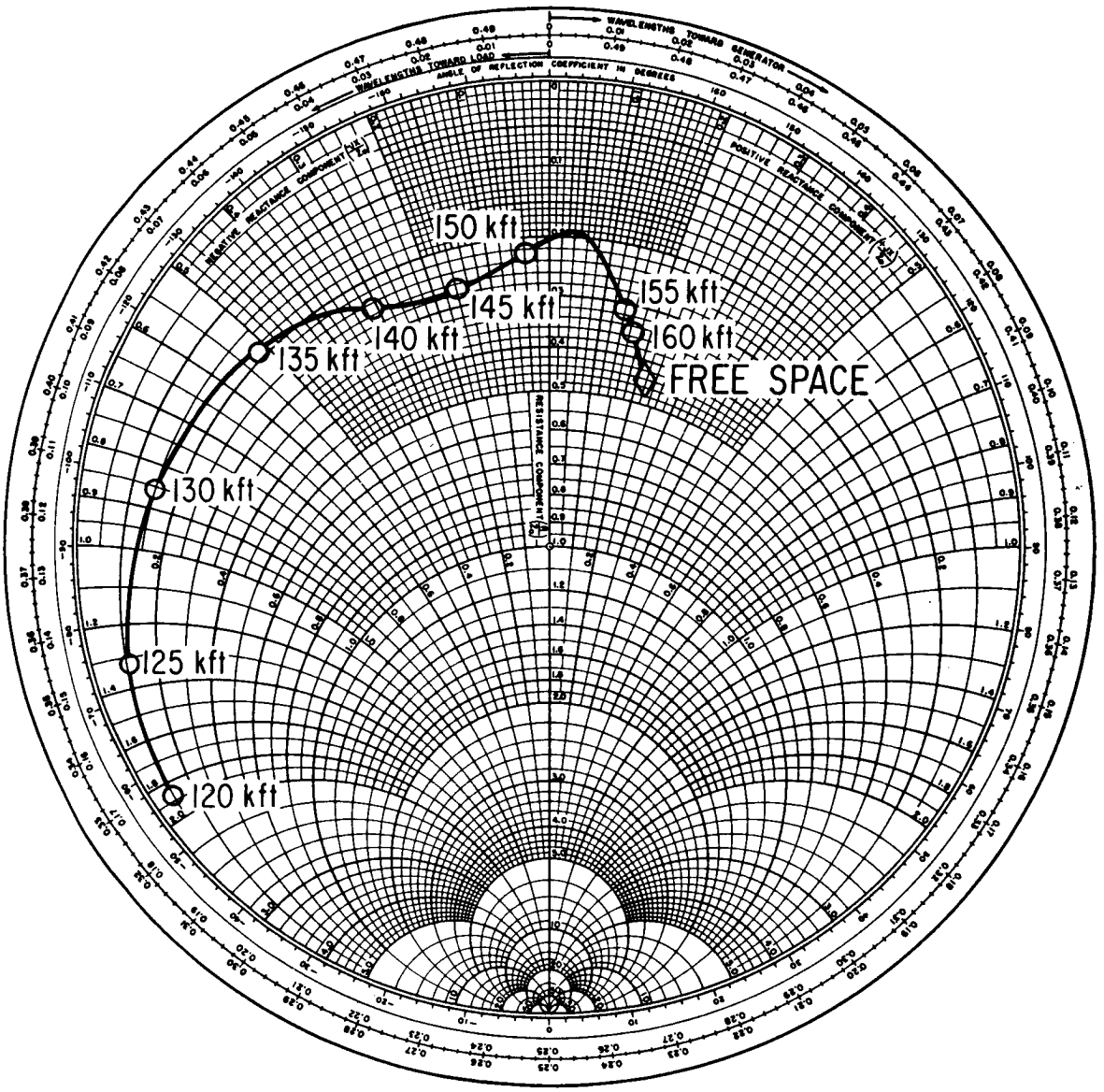

Figure 9.- Aperture admittance calculations for 0.25-in. nose conditions.

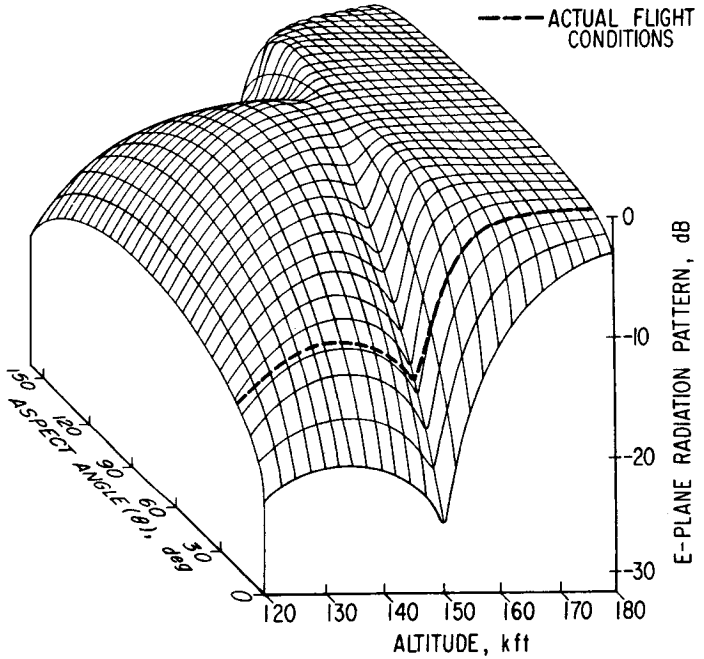

Figure 10.- Radiation pattern distortions as a function of aspect angle and altitude for 0.24-in. nose conditions.

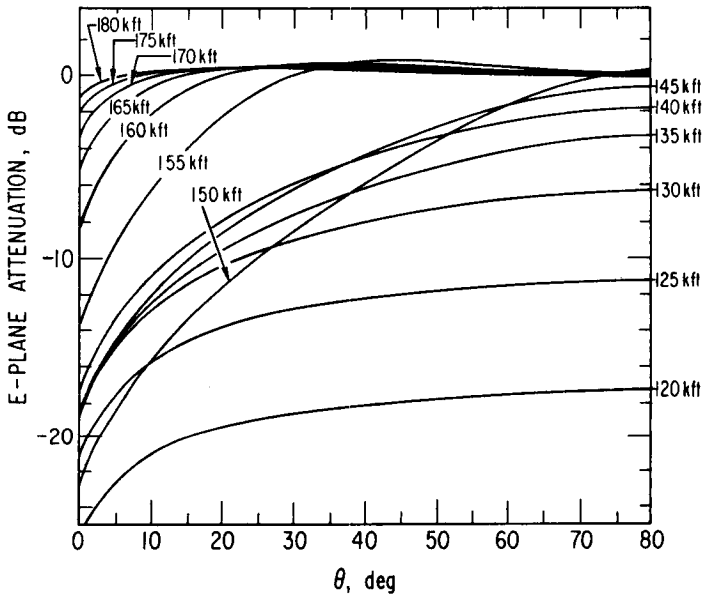

Figure 11.- X-band signal attenuation as a function of aspect angle and altitude for 0.25-in. nose conditions.

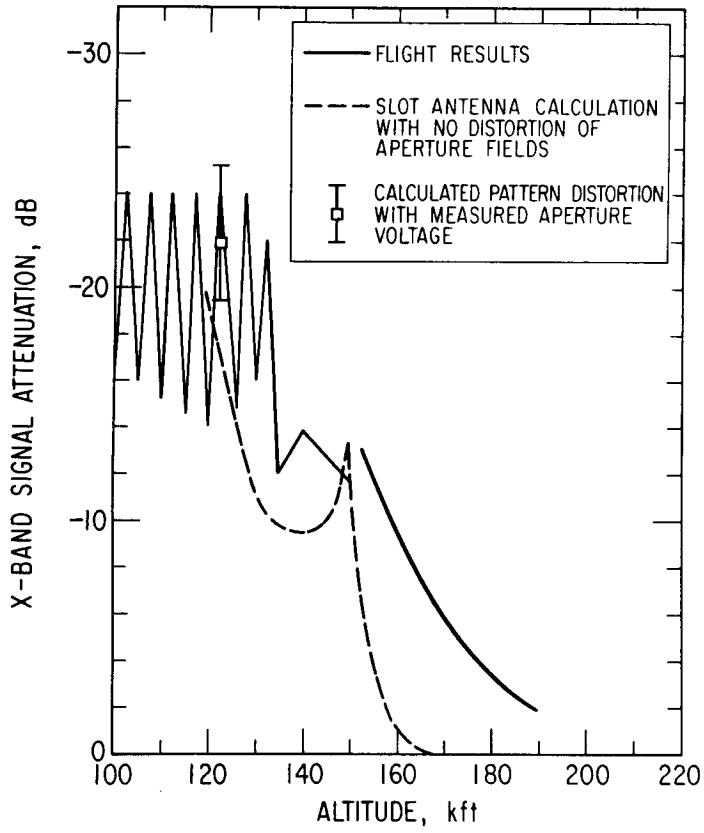

Figure 12.- X-band flight attenuation results for 0.25-in. radius nose tip.

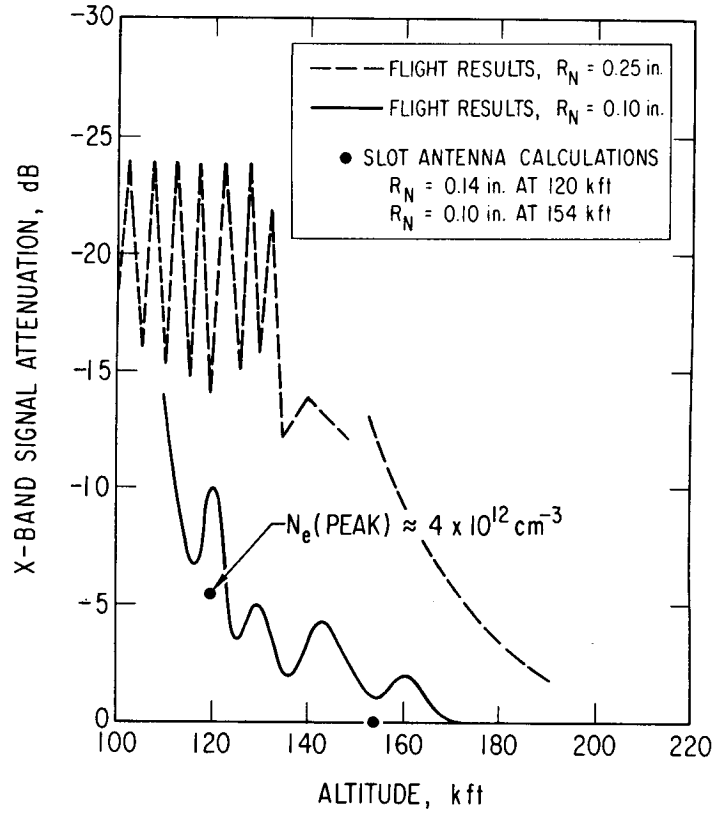

Figure 13.- X-band flight attenuation results for 0.1-in. radius nose tip.

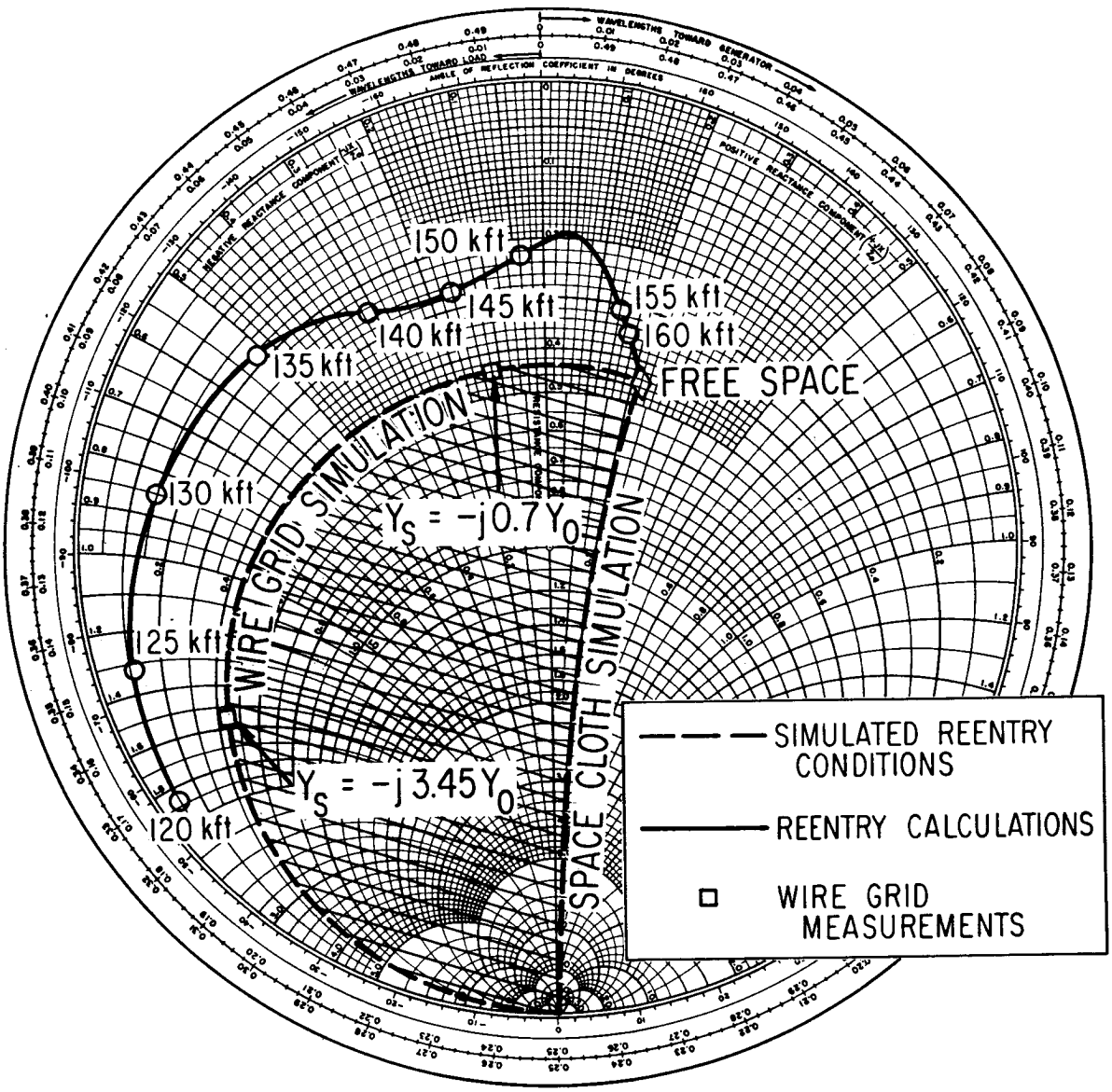

Figure 14.- X-band aperture admittance in simulated plasma environments.

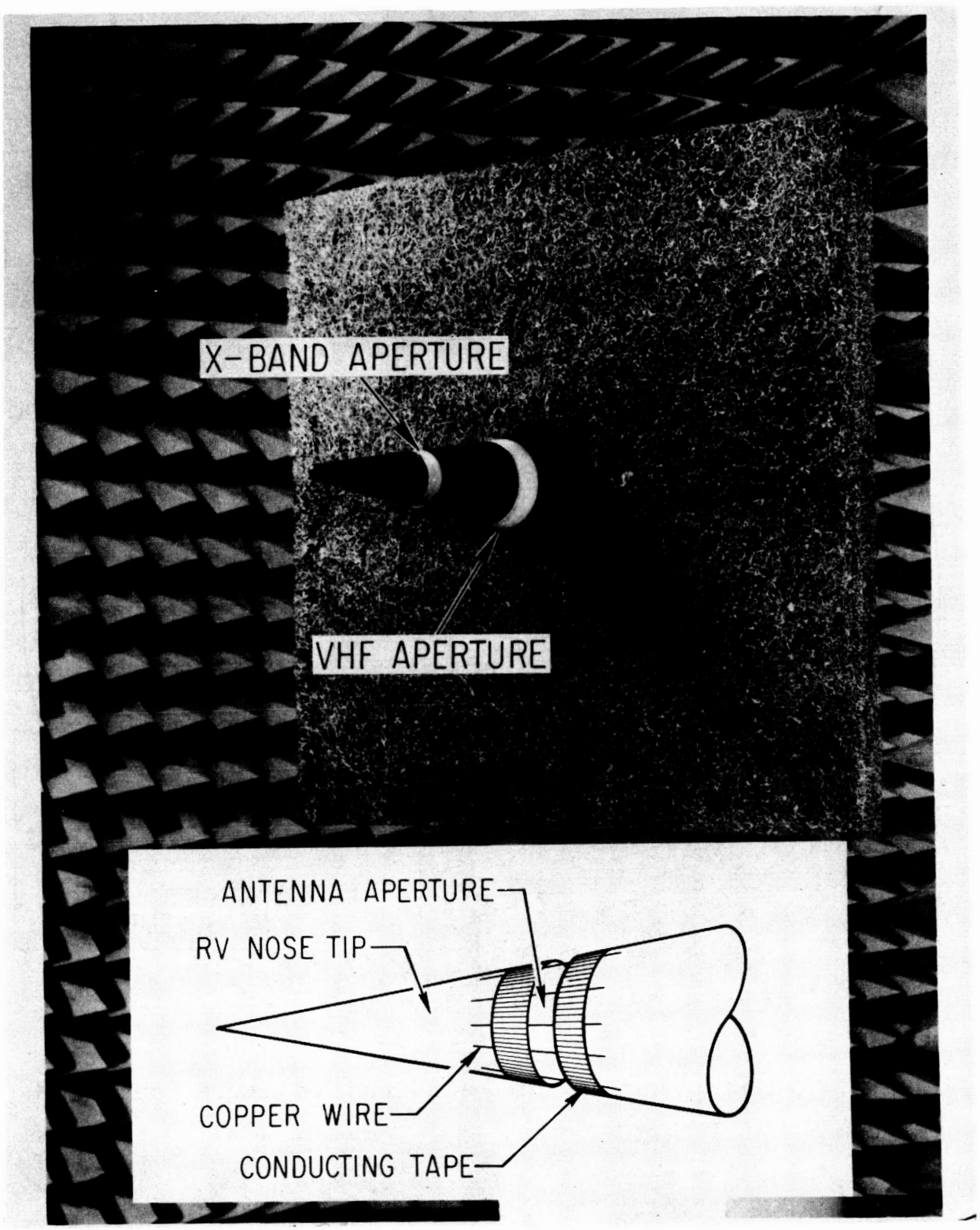

Figure 15.- Nose tip antennas.

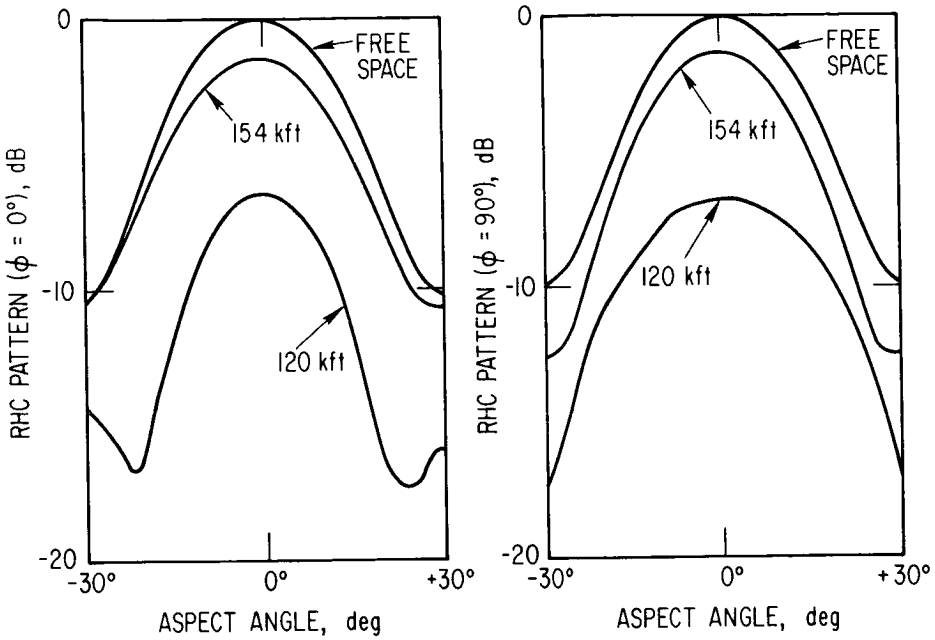

Figure 16.- Measured right-hand circularly polarized radiation patterns in simulated 120- and 154-kft reentry environments.

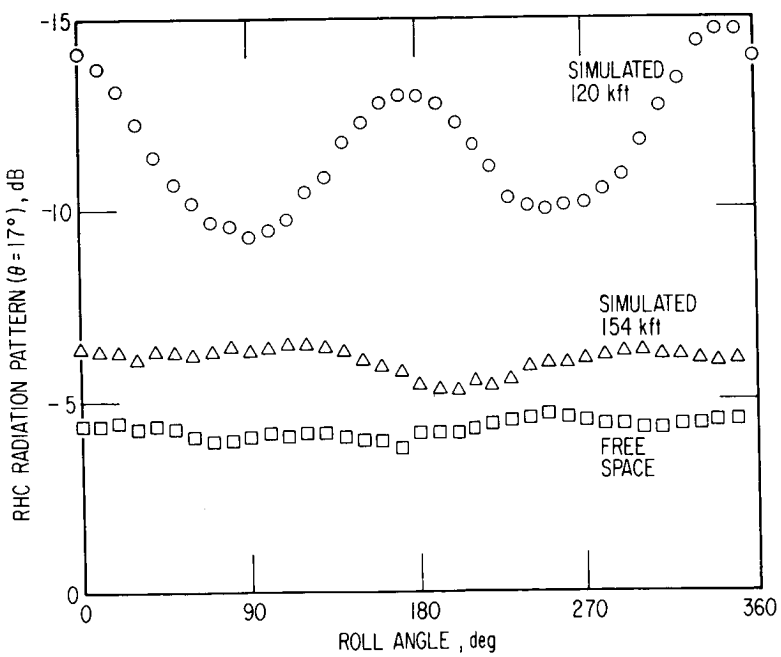

Figure 17.- Roll radiation pattern measurements in simulated 120- and 154-kft reentry environments.

ANTENNA PERFORMANCE IN THE PRESENCE OF A TURBULENT PLASMA

By J. B. Chown

Stanford Research Institute

SUMMARY

This paper reports laboratory experiments undertaken to determine the performance of an antenna with a turbulent plasma in its near field. Diagnostic data to describe the plasma turbulent characteristics for use in theoretical models were obtained using the spatial resolution capabilities of ion probes. In addition to pattern measurements on single- and dual-slot X-band arrays, data were obtained concerning the effect of the plasma on the reflected signal from slot antennas and coupling of signal to adjacent slots in the array. The ratio of peak to critical plasma density was varied from 0.2 to 4. The collision frequency was 1.5×10^{10}, making $\nu/\omega \sim 0.25$.

In general, the radiation patterns obtained using the mean signal level for all antenna configurations could be explained on the basis of a laminar plasma model using the mean density contours of the turbulent plasma. The principal effect of the turbulent medium was phase and amplitude modulation.

INTRODUCTION

In recent years, the problems of transmission from reentry vehicles at altitudes above 100 kft have been investigated both in flight tests and laboratory simulation. The effects of this environment on antenna performance are reasonably well understood. However, the vehicle penetrates to lower altitudes, the flow over the antenna becomes turbulent and overdense, and questions arise concerning the effect of the turbulence on antenna radiation patterns and coupling between elements of the antenna system.

The advantage of working in the laboratory environment is that the plasma characteristics, as well as the effect of plasma on the radiating system, can be determined. Normally, only the latter is available from flight-test data. While a plane-wave solution has proven useful in predicting the effect of underdense turbulent plasma on scattering, at the present time there are no well-established theories dealing with transmission through a turbulent plasma layer, especially in the near-critical and overdense cases.

The electron density profile desired was to simulate the flow around a conical vehicle. The actual flow obtained was thicker than that desired; accordingly, the results give an upper bound on the effect of turbulent flow. The aim of this laboratory program was to assist in the development of phenomenological models and to provide data pertinent to the verification of concepts necessary in the planning of systems and future flight-test programs.

The work reported here was performed by the Stanford Research Institute for the U.S. Air Force Space and Missile Systems Organization under guidance of Aerospace Corporation and consisted of performing laboratory experimental investigations on the effects of a turbulent plasma on the performance of X-band antenna systems.

EXPERIMENTAL TEST SETUP

To investigate the interaction of electromagnetic waves with a turbulent plasma layer, a turbulent plasma was formed by seeding a premixed ethylene-oxygen flame in a combustion chamber and then exhausting the flame through a rectangular nozzle into a low-pressure vessel. Several rectangular nozzles and ground-plane configurations were evaluated on the basis of the ambient electron density and distribution normal to the vertical surface containing the slot antenna. The final configuration selected for the burner slot and ground plane position is shown in Figure 1. The operating pressure in the test chamber was maintained at 10 torr. The ethylene-oxygen mass flow was ~ 2 gm/s. The collision frequency for these conditions turned out to be $\sim 1.5 \times 10^{10}$.

The 6 ft diameter, 8 ft long low-pressure chamber lined with microwave absorbing material is depicted in Figure 2. The antenna ground plane and burner assembly mounted in the chamber is shown in Figure 3. The movable antenna used in making the radiation patterns and a diagnostic ion probe located to measure the ion density normal to the ground plane are also visible in Figure 3.

For monitoring plasma density, a fixed ion probe was mounted 40 cm above the burner (see Figure 3) and calibrated to yield the mean peak electron density in the turbulent plasma occurring at the center of the test area ($x = 25$ cm). All the ion probes used were cylindrical, 0.01 inch in diameter by 0.10 inch long. The probe current was converted to plasma density on the basis of microwave calibrations of identical probes in similar ionized flow conditions. Measurements of the attenuation of signals transmitted from slot antennas located in the ground plane also provided a check on plasma density.

The maximum error in determining the peak electron density using the ion probe monitor is on the order of + 30 percent, which occurs at the higher

electron densities. This is based on a comparison of the calculated attenuation at $\theta = 0°$ for a single slot radiator and using the measured plasma distribution at x = 25 cm as shown in Figure 4. It is difficult to assign the entire error to the ion probe, however, since the plasma is limited in extent in the horizontal plane (yz) and significant energy may be diffracting around the plasma at the higher densities. This would cause the attenuation to be reduced and indicate that the ion probe was overestimating the actual peak density.

PLASMA DIAGNOSTICS

The diagnostic measurements of the turbulent plasma took advantage of the desirable spatial resolution of a 0.1-inch long cylindrical ion probe. The measurements included determination of mean and rms plasma contours and power spectral density of the plasma fluctuations with a single probe. Dual probes were employed in spatial-correlation measurements to establish the mean flow velocity and mean turbulent scale size.

Examination of the mean and rms electron density profiles obtained with ion probes over a range of electron densities indicated that they do not change significantly in shape at a given location in the flow. Using the coordinate system shown in Figure 1, normalized mean and rms density contours normal to the ground plane have been plotted in Figure 4 for three locations in the nominal test area (x = 20, 25, and 30 cm). The peak electron densities occur at approximately 1 cm off the surface. The peak electron density varies in the axial direction decreasing by about a factor of 2 in 10 cm. While the ratio of the rms to mean electron density level varies with the absolute density, the nominal value over the range of interest is ~ 0.4.

Normalized mean and rms electron density contours normal to the flow and the ground plane (zy plane) at x = 25 cm are given in Figures 5 and 6. The relative size of the antenna aperture is shown as well.

Correlation techniques were employed to measure the velocity of the flow. This was done by placing ion probes at two locations in the gas flow and determining the time delay in the signal from the upstream probe that produced a maximum in the correlation coefficient. The velocity was then taken at $\Delta x/\Delta t$, when $R(\Delta t)$ was a maximum. The velocity data obtained indicated a nominal velocity of ~ 675 m/s. An upper limit in velocity would be ~ 785 m/s. This range of flow velocities and the ~ 2 gm/s mass flow rate indicates a Reynolds' number of $\sim 10^3$.

Correlation measurements were made in the flow to determine the mean scale of the turbulence in the three orthogonal directions x, y, and z. In Figure 7

the correlation coefficient $R(\Delta x)$ is plotted as a function of Δx, where Δx is the probe spacing in the x direction. Figure 7 presents data taken at three locations along the flow (x = 20, 25, and 30 cm) 1 cm off the ground plane (y = 1 cm) at the peak value of the electron density contour. As can be seen, the data indicate that the scale size is relatively constant at $\sim$ 1.9 cm over the 10-cm distance. Correlation length is assumed to be the 1/e value of the correlation coefficient.

Correlation data obtained at two electron density levels an order of magnitude apart are shown also in Figure 7 to demonstrate that the scale size does not change significantly with plasma density.

The normalized power spectral density as a function of frequency obtained with an ion probe from four different runs is shown in Figure 8. To check the consistency of the experimental data, cross correlation information in Figure 9 and the velocity data were used to calculate the spectral density distribution. The calculation for two velocity levels is shown as the solid points in Figure 8. The agreement is quite good. An additional check was made by using the solid curve fitted to the spectral density data in Figure 8 and calculating the indicated correlation coefficient. The solid points in Figure 9 are the result of the calculation. The agreement again is seen to be quite good.

Summary of Turbulent Plasma Diagnostics (x = 25 cm)

Correlation lengths	$\ell_x = 1.9$ cm
	$\ell_y = 0.38$ cm
	$\ell_z = 0.63$ cm
Velocity	$U \sim 675$ m/s
Collision frequency	$\nu \sim 1.5 \times 10^{10}$
Reynolds number	$R \sim 10^3$

Figure 10 shows the normalized power spectral density of the turbulent plasma fluctuations obtained from a flush probe (1/8 inch in diameter) in the ground plane surface. The dashed curve in Figure 10 is the power spectral data obtained using a cylindrical probe at the same stream-wise location in the flow and 1 cm off the ground plane surface (Figure 8). The distributions obtained from the two probes are quite similar and differ significantly only at the higher frequencies. The lower high-frequency spectral density for the flush probe is understandable, since the flow velocity decreases near the ground plane and approaches zero at the surface. The probe sheath thickness in this case is $\sim 4 \times 10^{-2}$ cm. The data suggest that flush probes might

provide meaningful information concerning fluctuations in the boundary layer plasma.

ANTENNA IMPEDANCE AND COUPLING TESTS

When the measurement program was initiated, it was planned that data would be obtained at two peak plasma density levels. The final experimental design, however, has made it possible to record certain parameters continuously as a function of plasma frequency, and other parameters at several different plasma density levels during a single experimental run. This makes it possible to observe antenna performance continuously as the plasma density makes the transition through the critical value.

The impedance and coupling tests were carried out at X band (9.1 GHz). The X-band slot apertures consisted of standard 0.9 by 0.4-inch ID guide with $\lambda/2$ boron nitride windows ($\epsilon = 4.4$). The slots were mounted collinearly along the flow direction. The experimental test arrangement employed in collecting the data is shown schematically in Figure 11. The center of the three-slot array was maintained at x = 25 cm. The amplitude and phase of the reflected and coupled signals was obtained using the Hewlett-Packard 8410A Network Analyzer. The mean amplitude and phase, as well as the rms amplitude and phase of the coupled signals, was recorded on two-axis recorders as a function of time. The peak plasma density level was an increasing function with time and was also recorded via the monitor ion probe output.

The amplitude and phase variation of the reflection coefficient (Γ) for a single X-band slot antenna as a function of N_p/N_c are shown in Figure 12, where N_p refers to the peak mean density in the boundary layer and N_c is the critical plasma density at the operating frequency.

The maximum rms level of Γ occurs at the maximum slope of the mean value at $N_p/N_c = 1.3$ (Figure 12). The rms/mean ratio at this point is ~ 0.06. As the plasma density increases, Γ levels off and the rms value decreases. The rms value of θ reaches a maximum at $N_p/N_c \approx 1.5$ and remains reasonably constant with increasing plasma density. The high level of the rms phase fluctuations indicates the sensitivity of the reflection coefficient phase to the location of the critical plasma density in the boundary layer.

The data from Figure 12 have been replotted in Figure 13 to indicate the effect of the plasma on the magnitude and phase of the reflection coefficient.

The mean amplitude and phase, as well as the rms value of their fluctuations, were recorded for the signals coupled from slot antenna No. 1 to slot antennas Nos. 2 and 3. These data were obtained for several incremental spacings (Δx). Typical data for coupling for a slot spacing of 1.8 cm are presented in Figure 14. As one would expect, the change in the mean phase and amplitude increased as a function of both plasma density level and antenna spacing.

The coupling data obtained during the multislot coupling tests are summarized in Figure 15. Data by Golden and Stewart (also plotted in Figure 23) indicate that the general shape of the experimental curves is in good agreement with the zero-order analytical results. It would appear that the plasma density inferred by the downstream ion probe yields electron densities that appear to be higher than the best fit to the computed isolation data. However, as indicated earlier, the plasma varies significantly in peak value and distribution as a function of stream-wise location, which may be responsible for a substantial fraction of the apparent disagreement at higher slot spacings.

The normalized power spectral density for the signal coupled between two slots spaced 1.8 cm apart is presented in Figure 16. Phase and amplitude spectral data presented in Figure 16 were obtained when $N_p \sim N_c$; those quantities are seen to have essentially the same distribution. The spectral density for the phase fluctuations did not vary significantly with plasma density level; however, the spectral density of the coupled amplitude changed markedly, exhibiting a shift of energy to the higher frequencies, as indicated by the data obtained for $N_p/N_c \sim 2.7$.

A comparison of the power spectral density distributions obtained from an ion probe in the turbulent plasma (Figure 8) and that of the coupled signal amplitude for the high plasma density case (Figure 16) reveals that they are quite similar.

Cross-correlation measurements between the reflected signal from the driven slot antenna (No. 1) and received signals at the downstream slots were obtained for several slot spacings and are presented in Figure 17. For all slot spacings except 1.8 cm at low plasma densities the correlation is always negative. This indicates that the increase in reflected signal caused by the plasma produces a decrease in the coupled signal due to the associated mismatch loss. The cause of the positive coupling in the 1.8-cm case is not explainable on the basis of the impedance change of the driven slot. It is assumed that, since the slot spacing is on the order of an eddy size (ℓ = 1.9 cm), common eddy coupling is responsible.

RADIATION-PATTERN MEASUREMENTS

The radiation-pattern measurements were made with the aid of the movable antenna arrangement shown in Figure 3. The pyramidal receiving horn had a gain of ~ 11 dB. The sides of the chamber and the end in which the burner and ground plane were located were covered with 20-dB high-temperature microwave absorbent material; at the opposite end 40-dB low-temperature absorbent material was used.

The E-plane radiation pattern of the mean received signal for a single X-band slot antenna is shown in Figure 18 as a function of plasma density. The flow direction is parallel to the E plane; with this orientation the turbulence size (ℓ_x & ℓ_z) is on the order of three times the slot height and width. On each pattern is indicated the value of the ratio of the mean peak density to the critical density level at $\theta = 0°$. The time required to obtain each pattern (i.e., traverse from -40° to + 90°) is 30 seconds. Since the plasma density varies continuously with time, the radiation pattern is not taken at a constant plasma density. The plasma density changes ~ 20 percent during a pattern cut, contributing to the asymmetrical appearance of the pattern about $\theta = 0°$. A significant contribution to the asymmetry arises from the fact that the plasma thickness increases as the flow moves up the ground plane.

The variations in the no-flame ($N_p = 0$) pattern in Figure 18 are largely due to reflections from the burner top and the downstream end of the ground plane. These variations are greatly reduced for peak densities of only 0.3 N_c due to the attenuation along the ground plane. The mean signal pattern data for a single-slot antenna in the presence of the turbulent plasma can be explained on the basis of a laminar plasma model, the density contours of which are the same as the mean contours of the turbulent plasma. This contention is supported by the fact that the single-slot laboratory measurements are in fair agreement with the patterns calculated by Golden and Stewart, see reference 1, using the measured mean plasma characteristics. (See Figure 17).

The principal effect of the turbulent plasma was expected to be an increase in the sidelobe level. As can be seen, the form of the laminar calculation compares favorably with the measured data. There is no significant rise in the sidelobe level.

While the mean signal pattern data do not exhibit any readily identifiable turbulent effects, the instantaneous amplitude and phase fluctuations are another matter. Figure 19 shows the effects on signals transmitted through the turbulent plasma at various look angles at critical mean peak plasma density. In general, the magnitudes of the variations are increasing functions of both

look angle and mean density. The data in Figure 19 indicate that variations in amplitude greater than 25 dB and phase fluctuations greater than 200° are possible. This suggests that, depending on the particular systems application, the turbulent plasma can be a significant problem.

The H-plane pattern of a slot antenna was also measured with the slot rotated 90° so that the flow direction was also in the H-plane. With this slot orientation, the turbulent size ($\ell_x \sim 1.9$ cm) is on the order of the slot length in the flow direction. As with the E-plane pattern, the H-plane pattern in the presence of the turbulent plasma was similar to the calculated laminar approximation and exhibited no significant increase in sidelobe level.

The E-plane radiation patterns for a dual-slot array with a 1.8-cm center-to-center spacing is shown in Figure 20. No discernible increase in sidelobe level is observed. Several test runs were made with the receiving antenna fixed at θ = 0, 15, 30, and 45°. Figures 21 and 22 indicate the rms/mean ratio amplitude and rms phase variation of the received signal as a function of look angle and plasma density. These data indicate, as before, that considerable phase and amplitude modulation of the signal occurs due to the turbulent plasma. At look angles greater than 30°, there is a marked increase in the turbulent effects.

Figure 23 presents the results of a test that measured the sum and difference pattern (at θ = 0°) of the dual-slot array of Figure 20 (slot spacing = 1.8 cm). The amplitude of the excitation to both slots was the same. The phase, however, was varied continuously by a motor driving the phase shifter. The mean received signal amplitude is shown in the upper curve of Figure 23. The max/min ratio of the sum and difference pattern changes from $\sim$ 43 dB with no plasma, to $\sim$ 22 dB just above critical, and $\sim$ 17 dB at three times critical, illustrating the effect of the plasma on the depth of the minimum. The rms phase variation alone is not sufficient to explain the entire null fill-in. The fact that the plasma profile varies slightly, even over the 1.8 cm, suggests that it is a contributing factor.

Radiation patterns were obtained for slot spacings of 2.3 and 2.8 cm, in addition to the 1.8-cm spacing for Figure 20. As before, the radiation patterns show no readily discernible turbulent effect, such as abnormally high sidelobe levels.

CONCLUSIONS

Based on the plasma conditions existing for these tests, i.e., maximum normal rms phase fluctuations $\ll 2\pi$ and the mean eddy size $\ell_x < \lambda$, the

following conclusions are drawn.

(1) The effects of electrically thin turbulent plasma layer on the mean signal level are second order when considering mean pattern distortion. First-order effects are explicable in terms of the mean plasma properties.

(2) Significant turbulent effects are manifested principally in amplitude and phase fluctuations of the signal.

(3) Therefore, any theoretical interest in the effects of turbulent layers on antenna performance should be applied to predicting the fluctuating quantities.

The following implications of the laboratory program are applicable to flight conditions.

(1) (Electrically) thin turbulent plasmas will always produce only second order changes in mean signal levels. The principal perturbation on the antenna pattern is produced by plasma absorption of the RF.

(2) Thick turbulent plasmas can affect the mean pattern of antenna arrays.

(3) The degree of degradation in performance of an antenna array with a turbulent plasma in its near field will be an increasing function of the aperture size. The effects on the mean radiation patterns of the array are the reduction in directivity and an increase in sidelobe levels.

REFERENCE

1. Golden, K. E. and G. E. Stewart: X-Band Slot Calculations. SAMSO, AFSC, Los Angeles Air Force Station, F0471-69-C-006. Aerospace Report No. TOR-006(5816-41)-1 (15 April 1970).

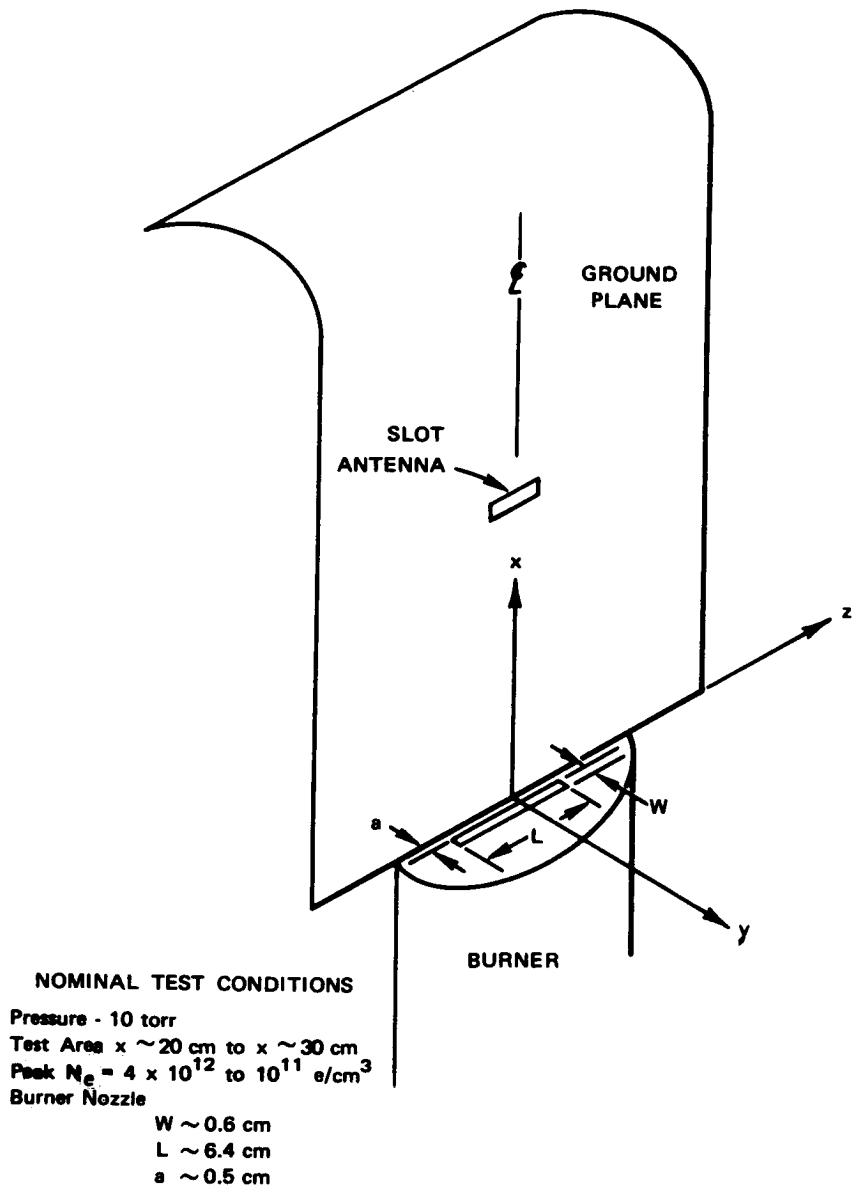

Figure 1.- Coordinate system.

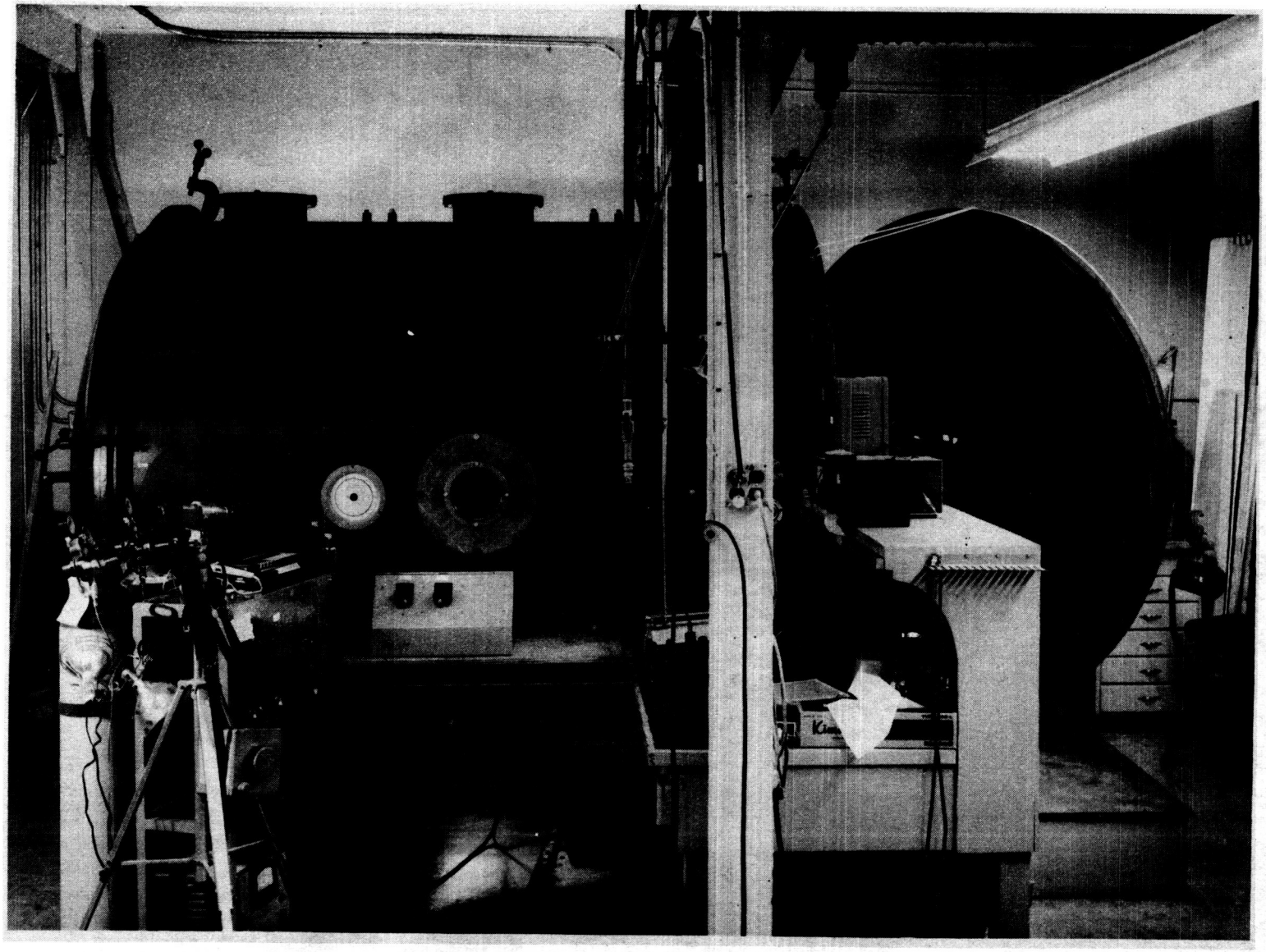

Figure 2.- Low-pressure chamber.

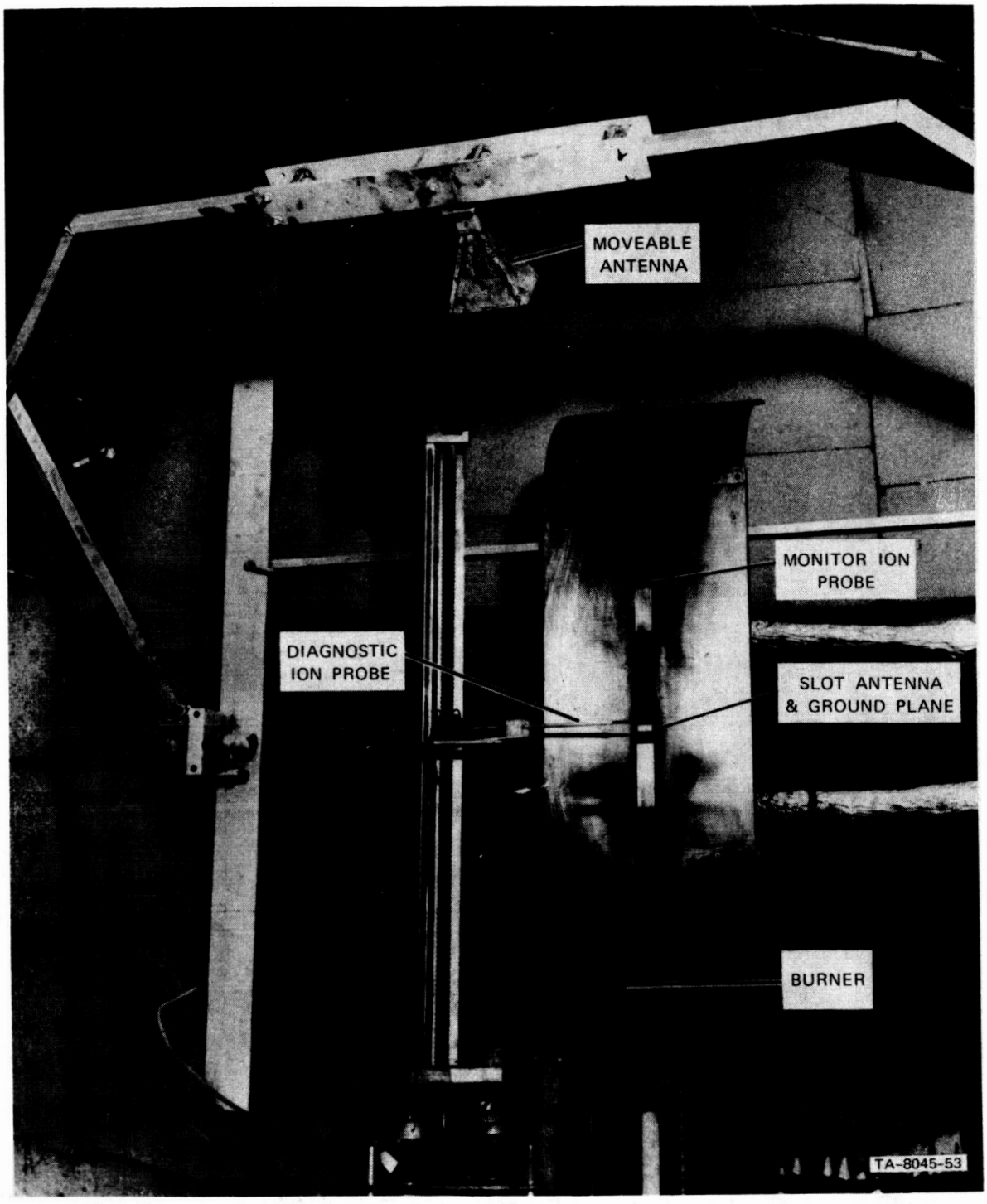

Figure 3.- Interior of low-pressure chamber showing instrumentation.

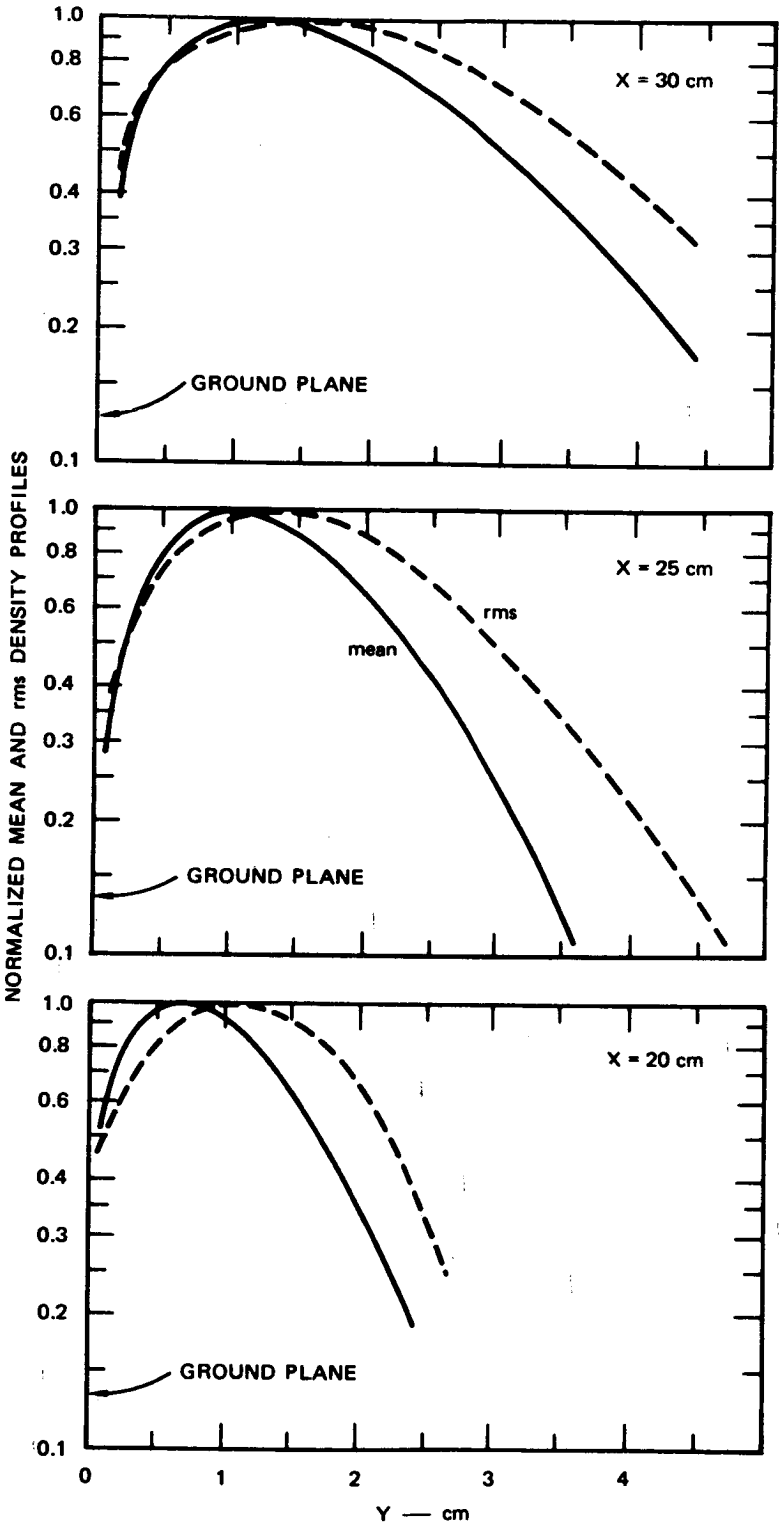

Figure 4.- Normalized mean electron density and rms density fluctuation contours (xy plane).

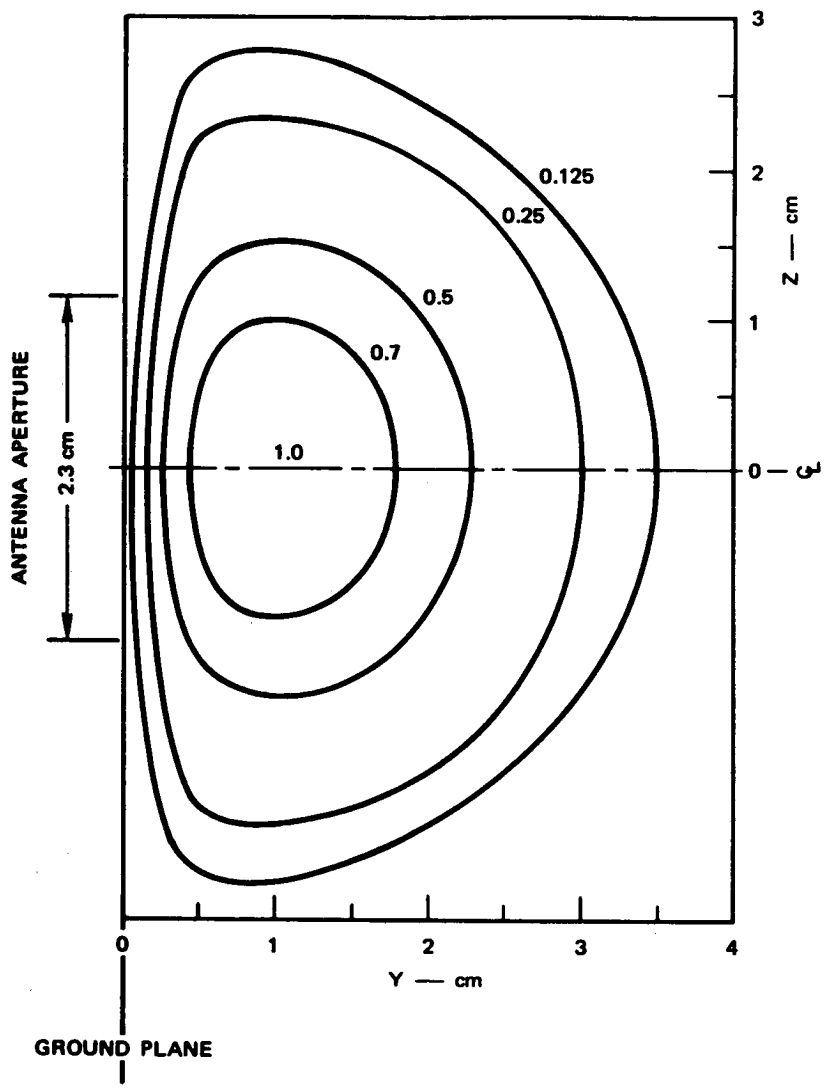

Figure 5.- Normalized mean electron density contours at x = 25 cm (zy plane).

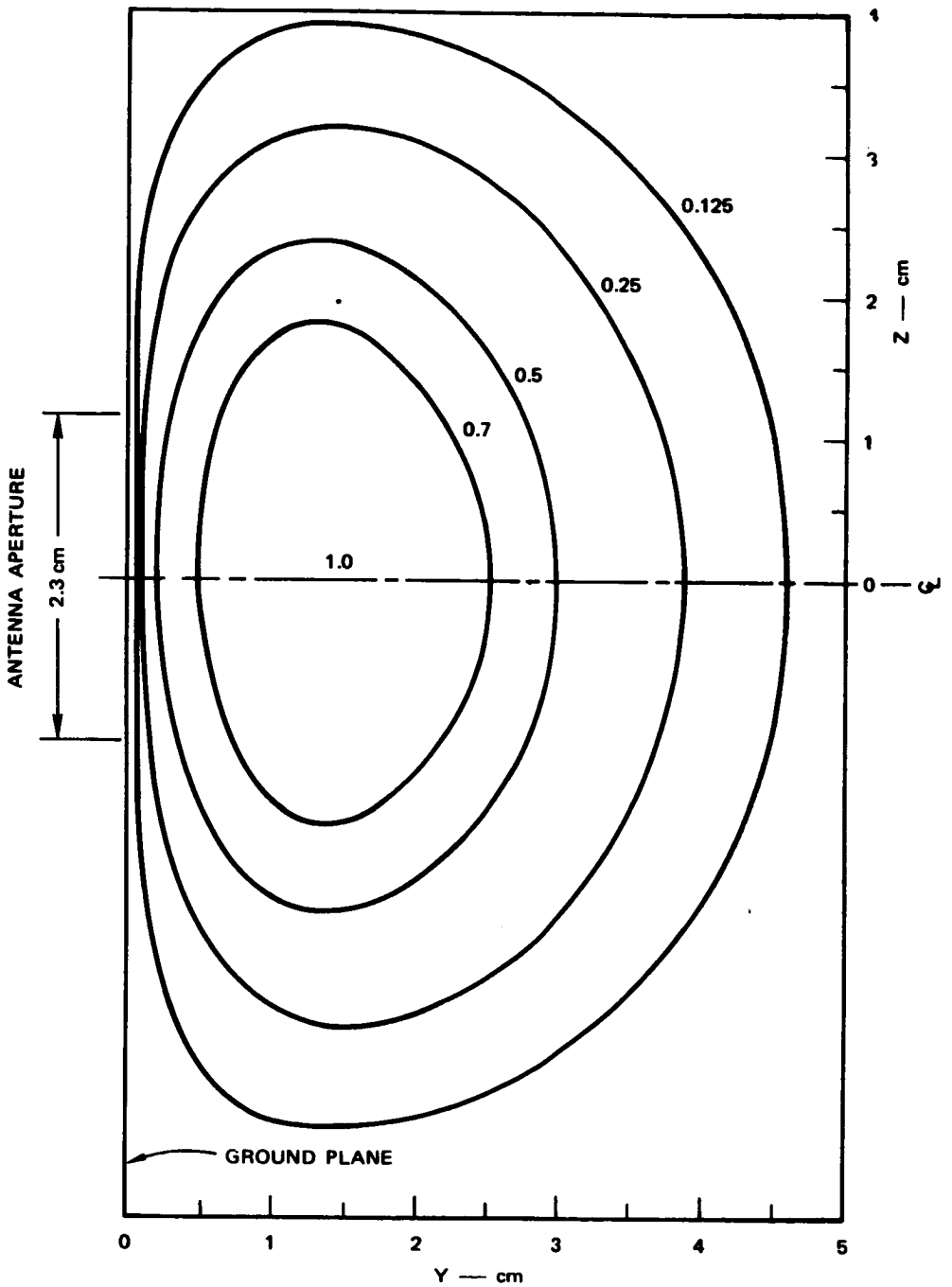

Figure 6.- Normalized rms electron density fluctuation contours at x = 25 cm (zy plane).

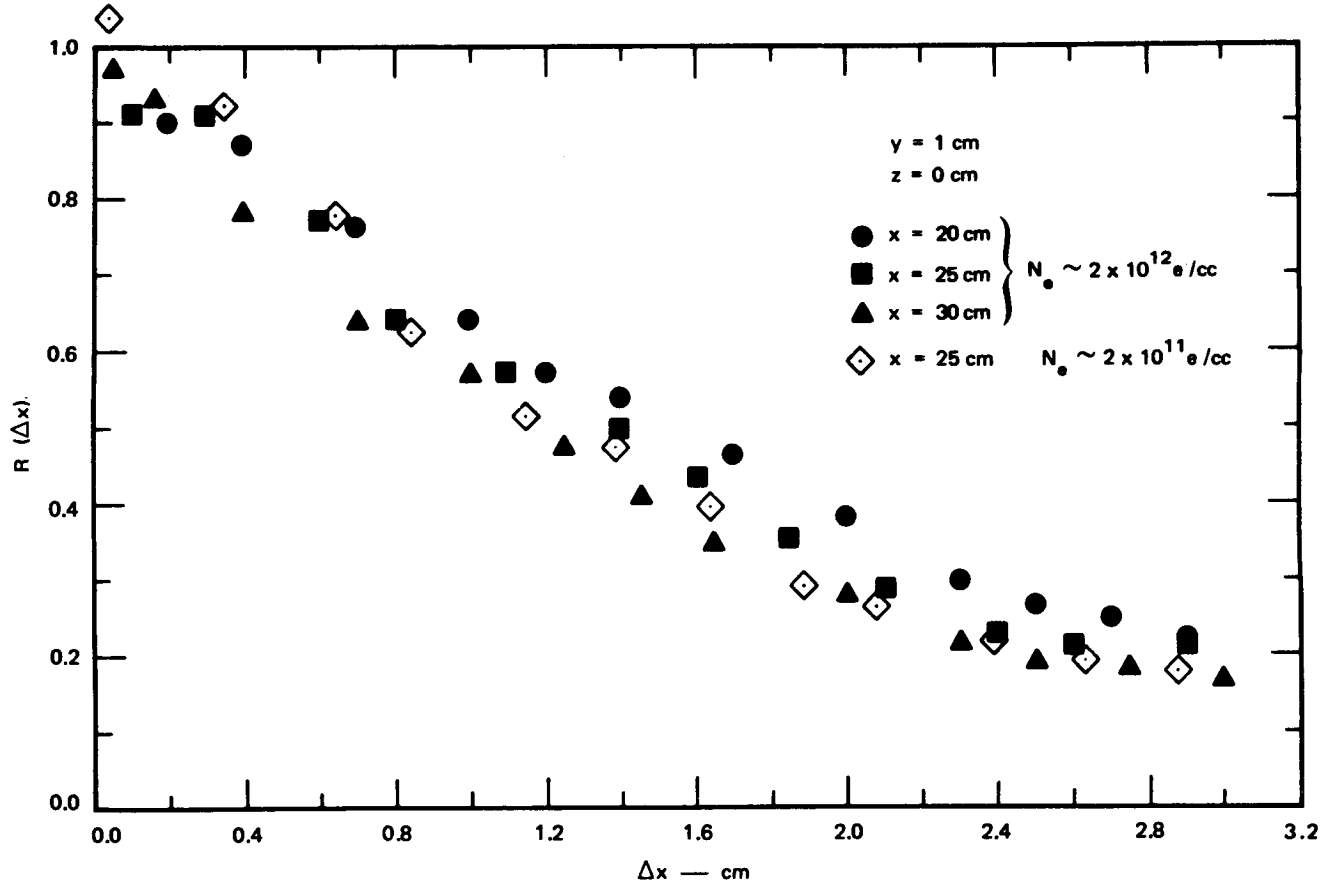

Figure 7.- Correlation coefficient R as a function of ion probe spacing (Δx).

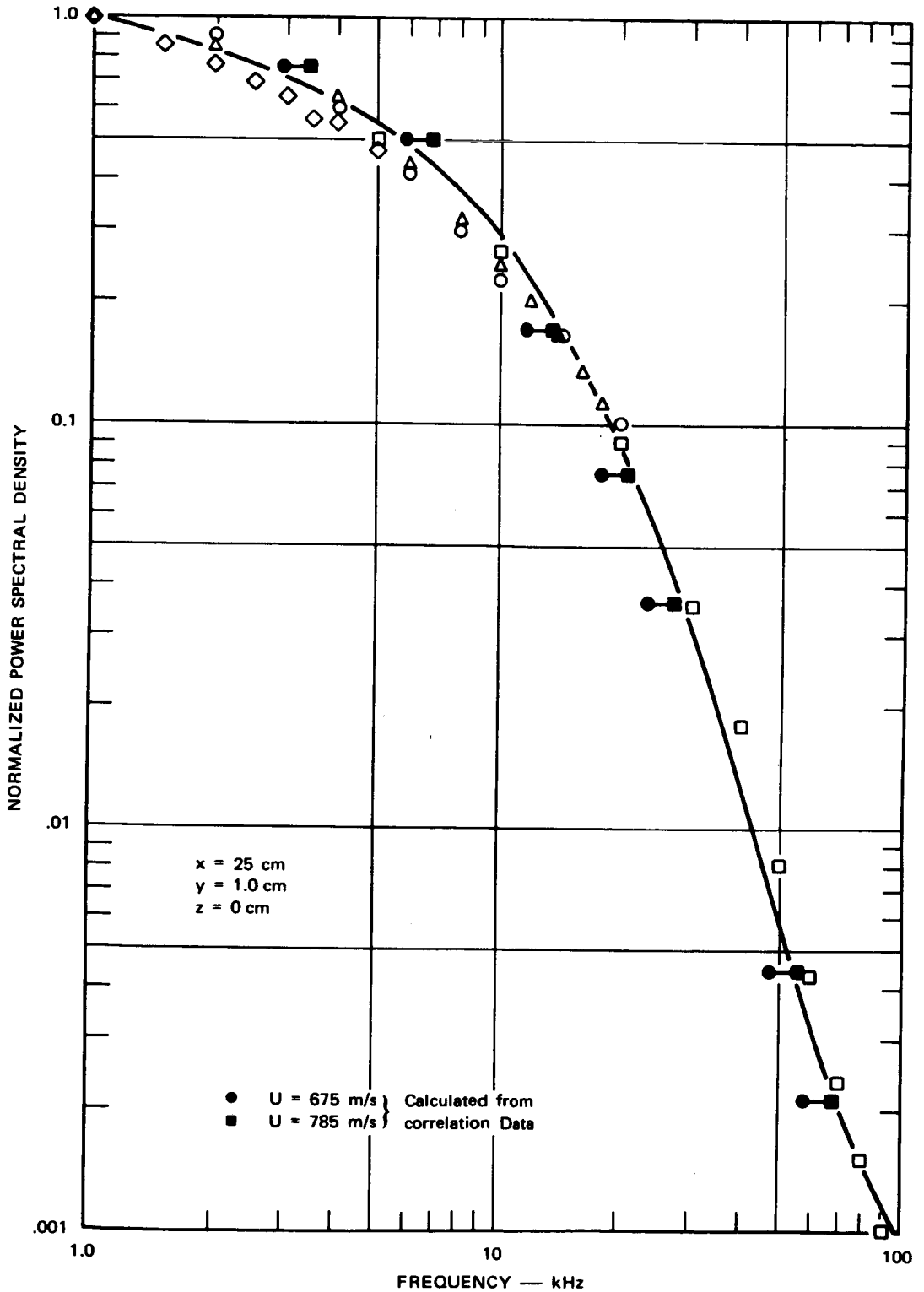

Figure 8.- Normalized power spectral density as a function of frequency.

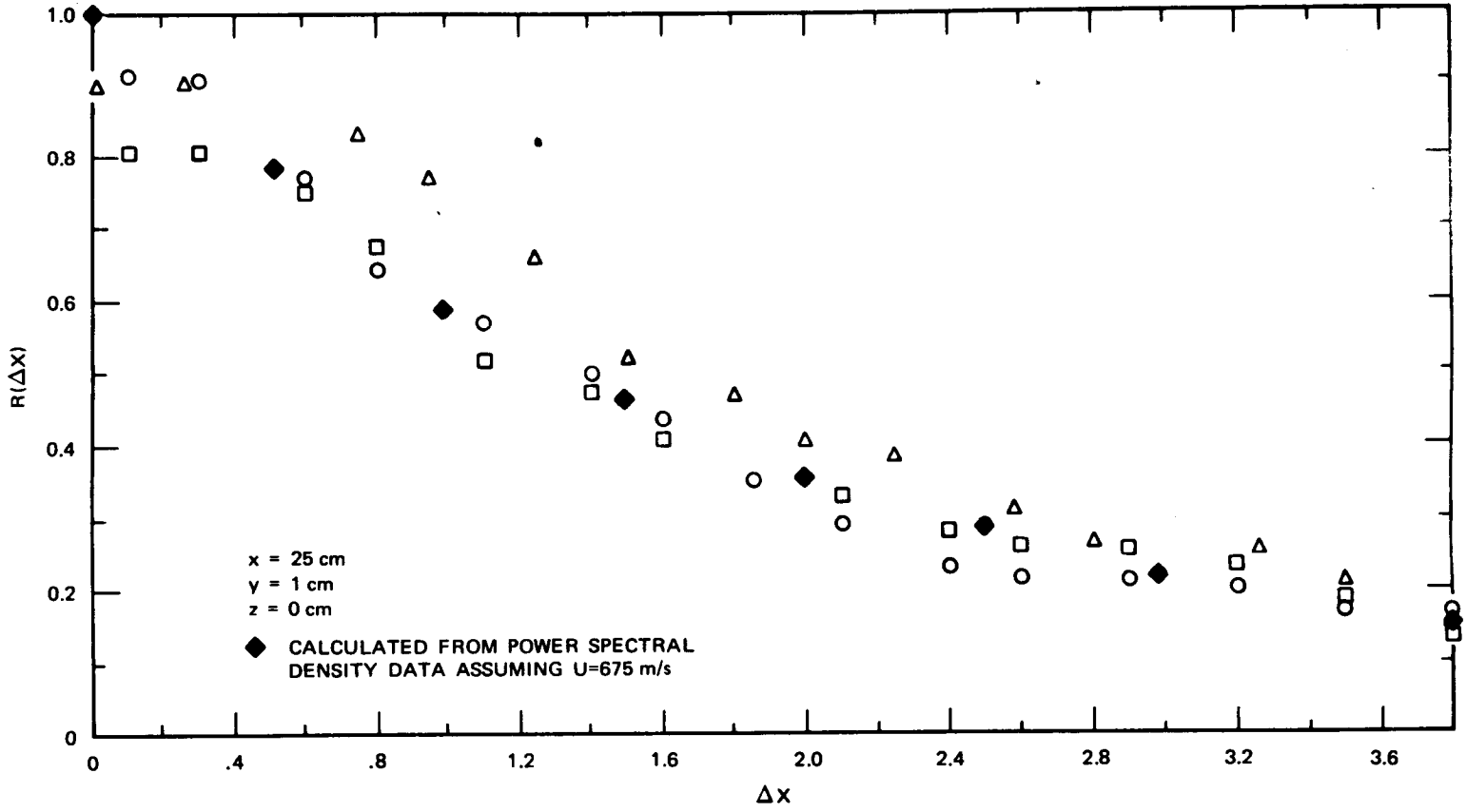

Figure 9.- Correlation coefficient R as a function of ion probe spacing (Δx), compared with calculated values.

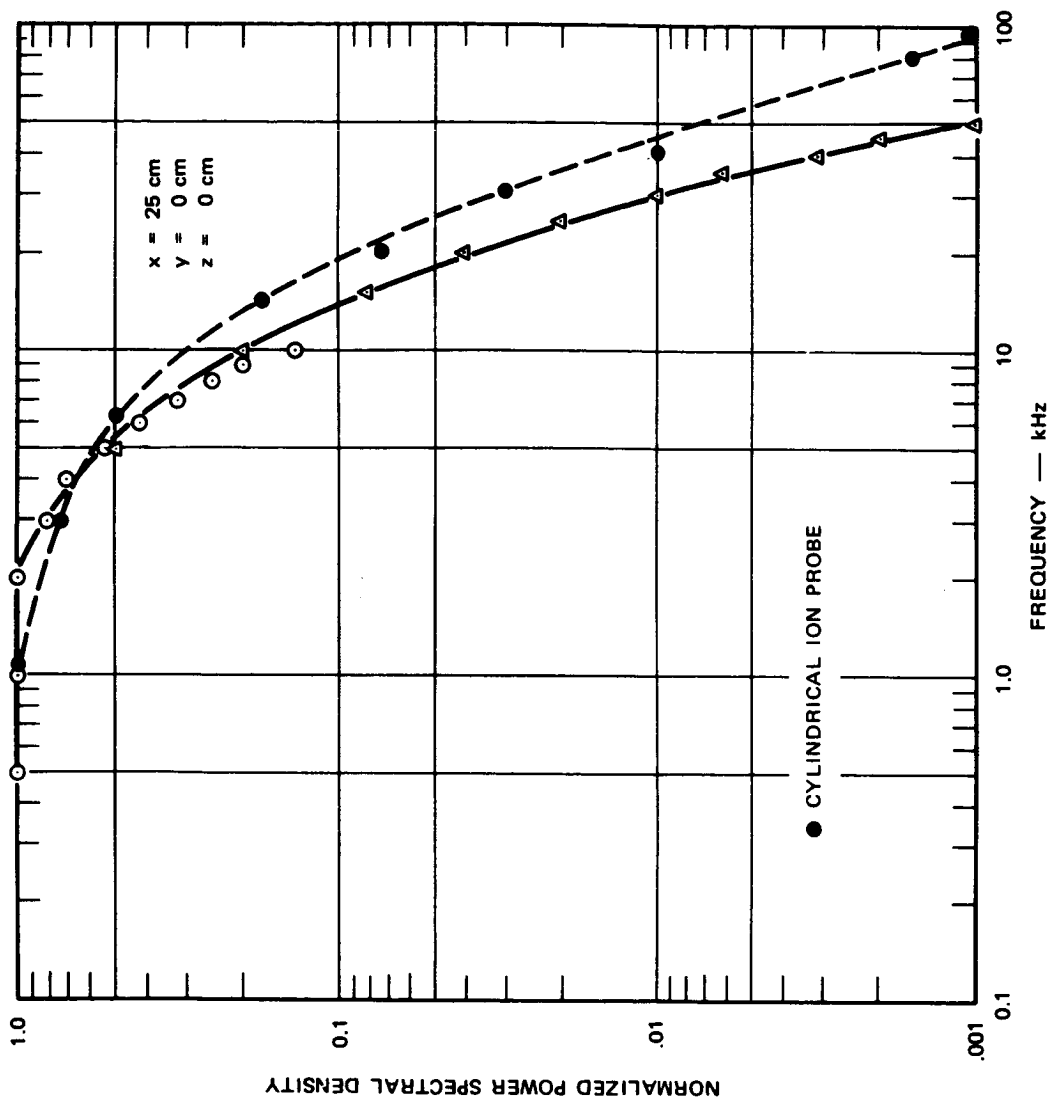

Figure 10.- Normalized power spectral density as a function of frequency (flush probe).

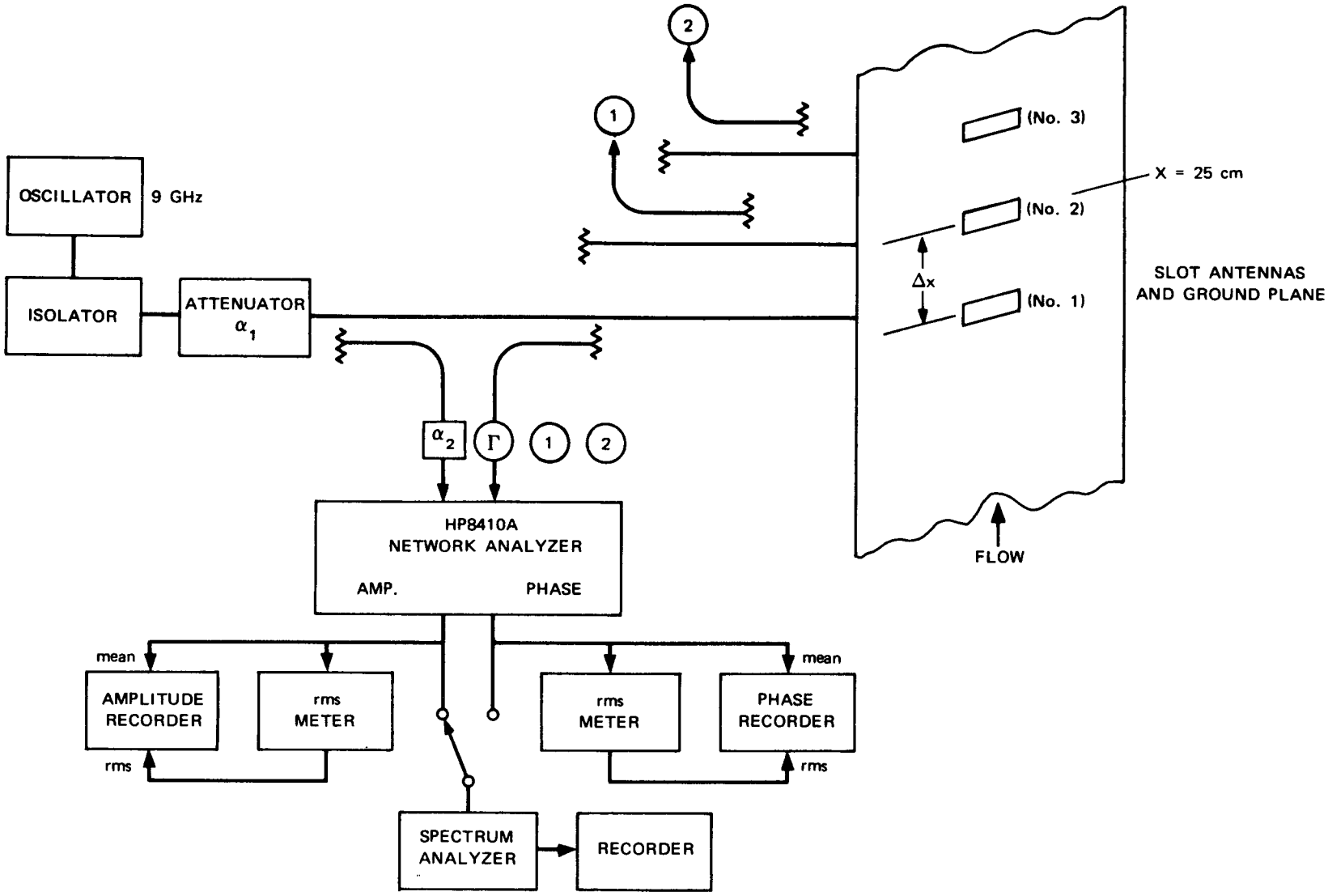

Figure 11.- Multislot test equipment configuration.

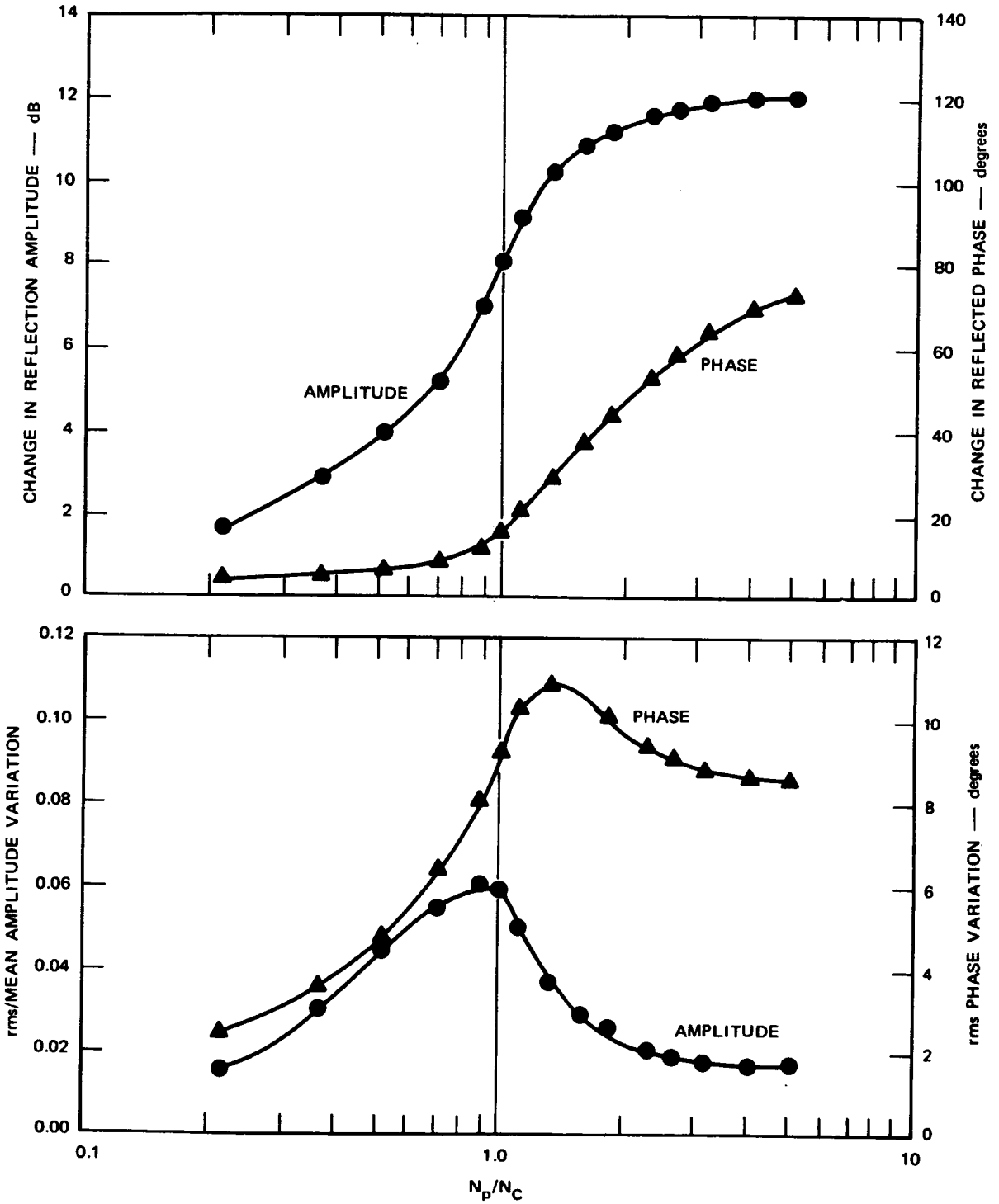

Figure 12.- Effects of turbulent plasma on reflected signal of X-band slot antenna.

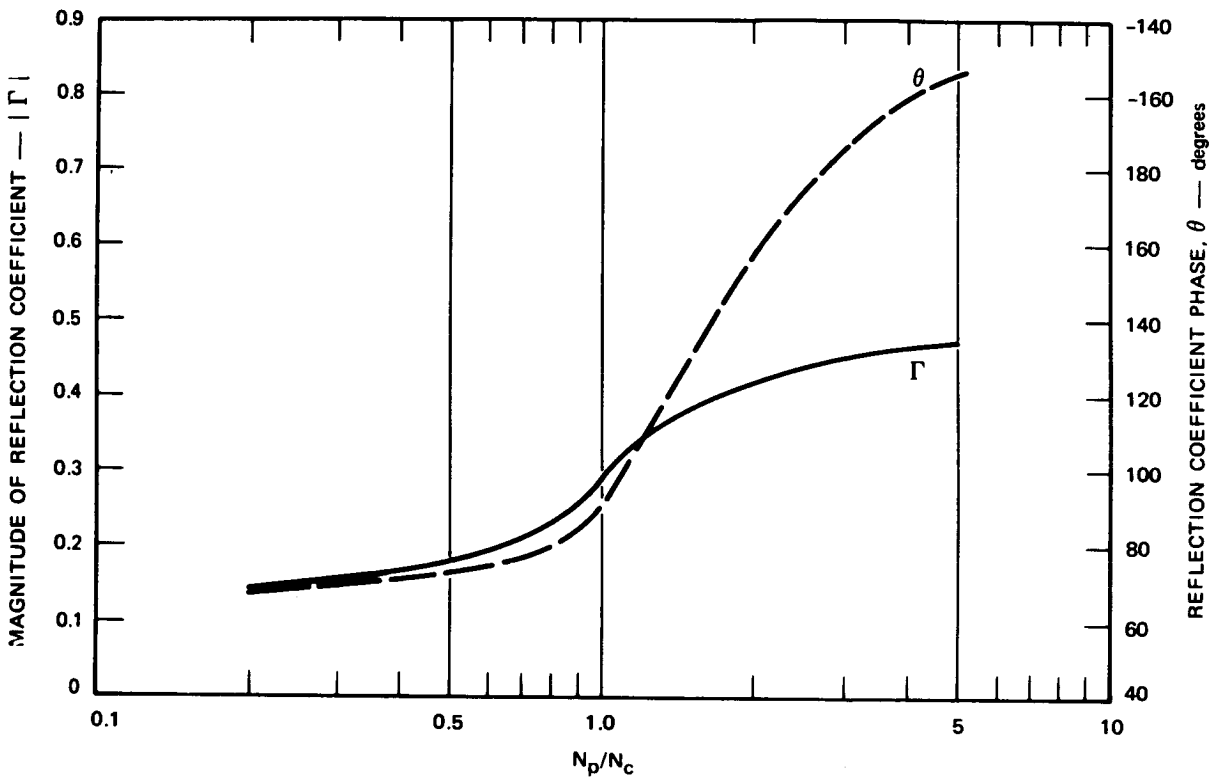

Figure 13.- Effect of plasma on X-band slot antenna reflection coefficient.

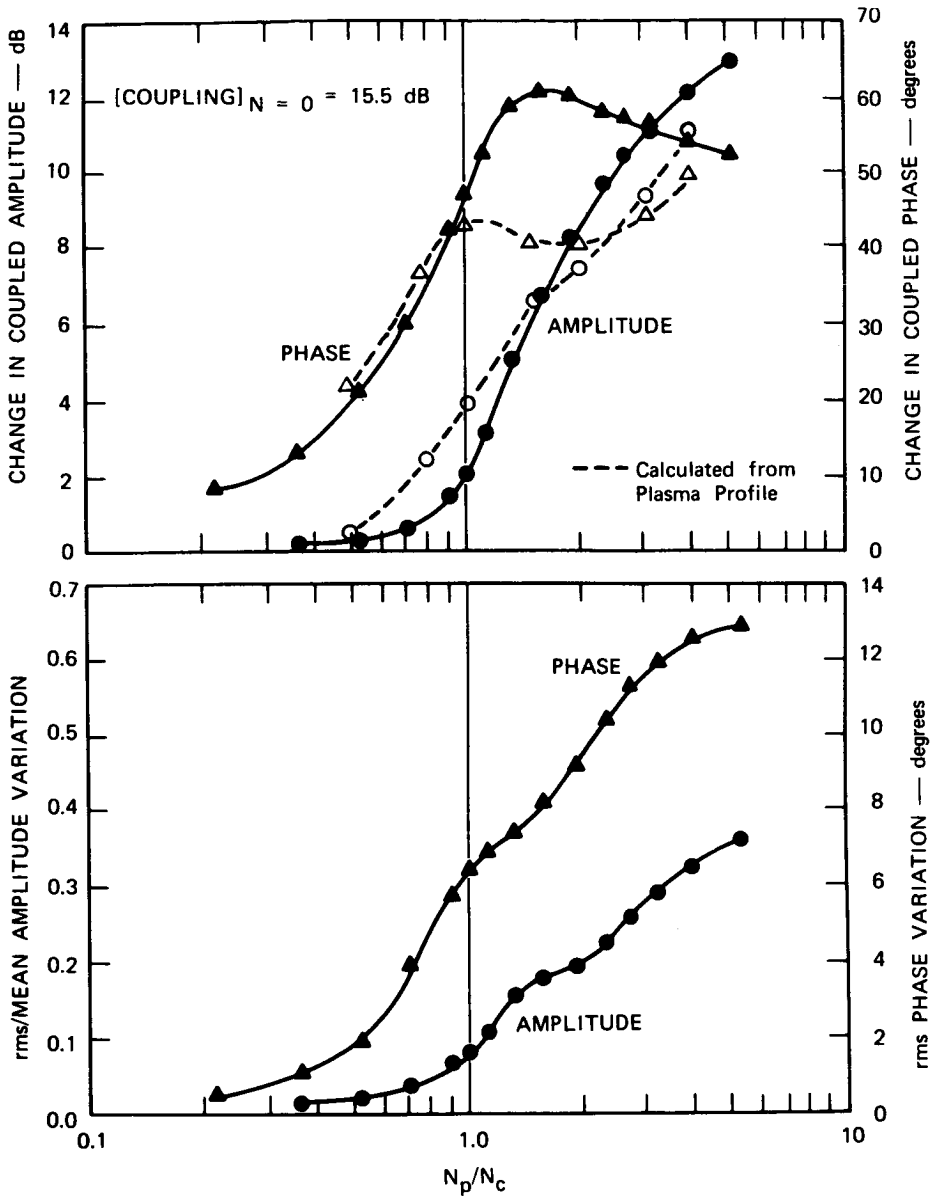

Figure 14.- Effect of turbulent plasma on coupled signal between X-band slot antennas (slot spacing = 1.8 cm, Antenna No. 1 to No. 2).

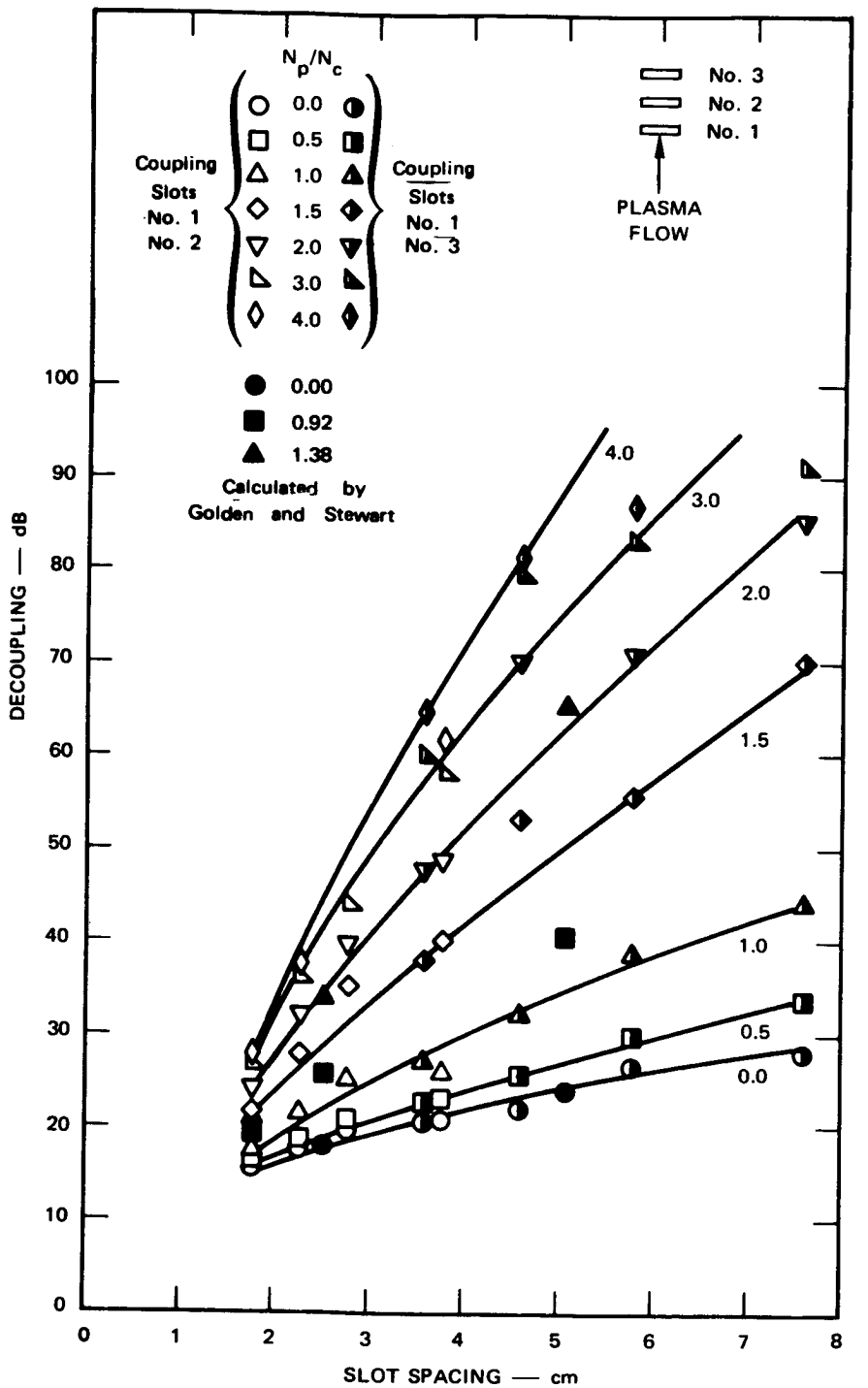

Figure 15.- Effect of turbulent plasma on X-band E-plane slot coupling.

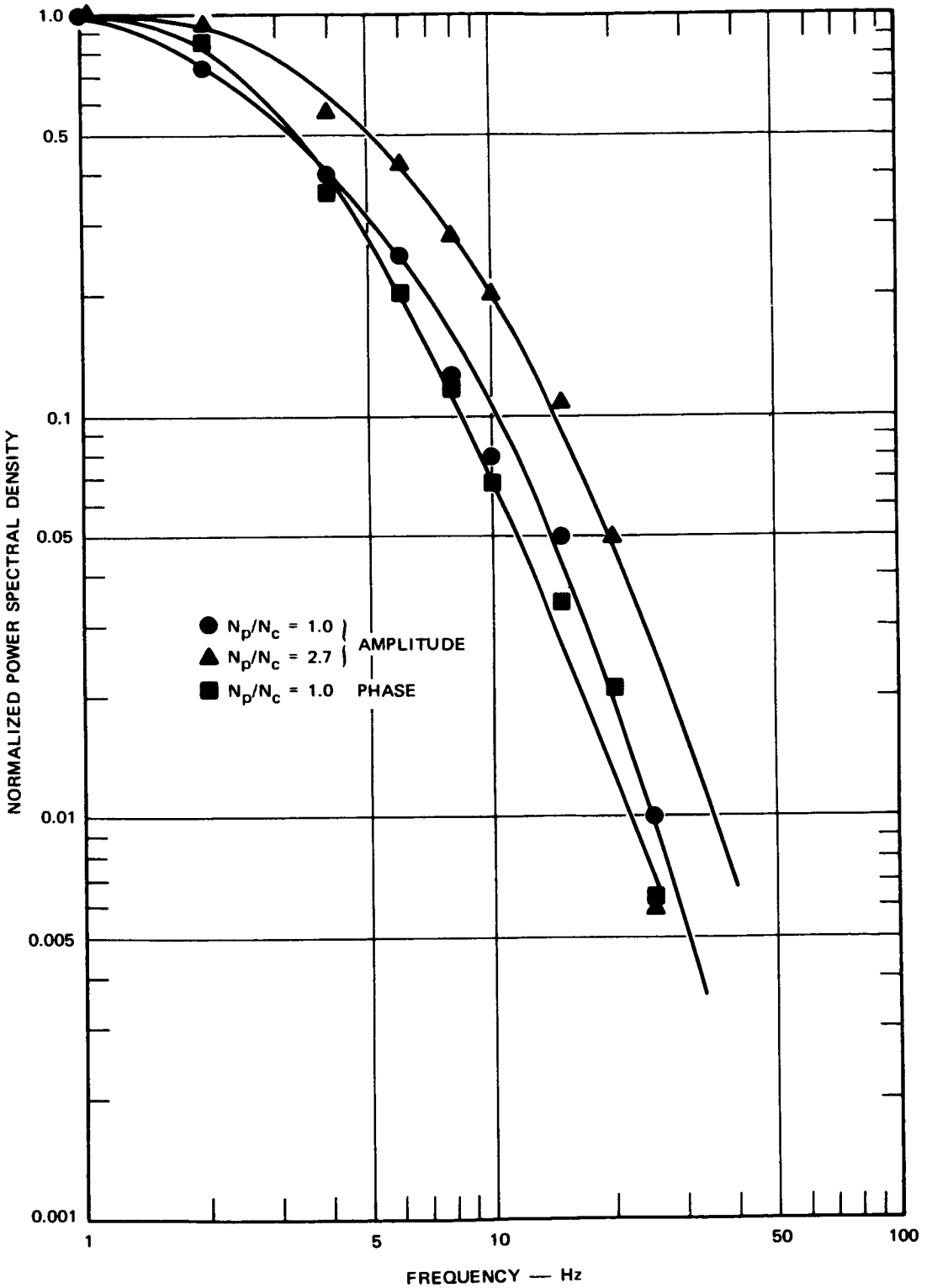

Figure 16.- Power spectral density of signal coupled between two X-band slot antennas in presence of a turbulent plasma (slot spacing = 1.8 cm).

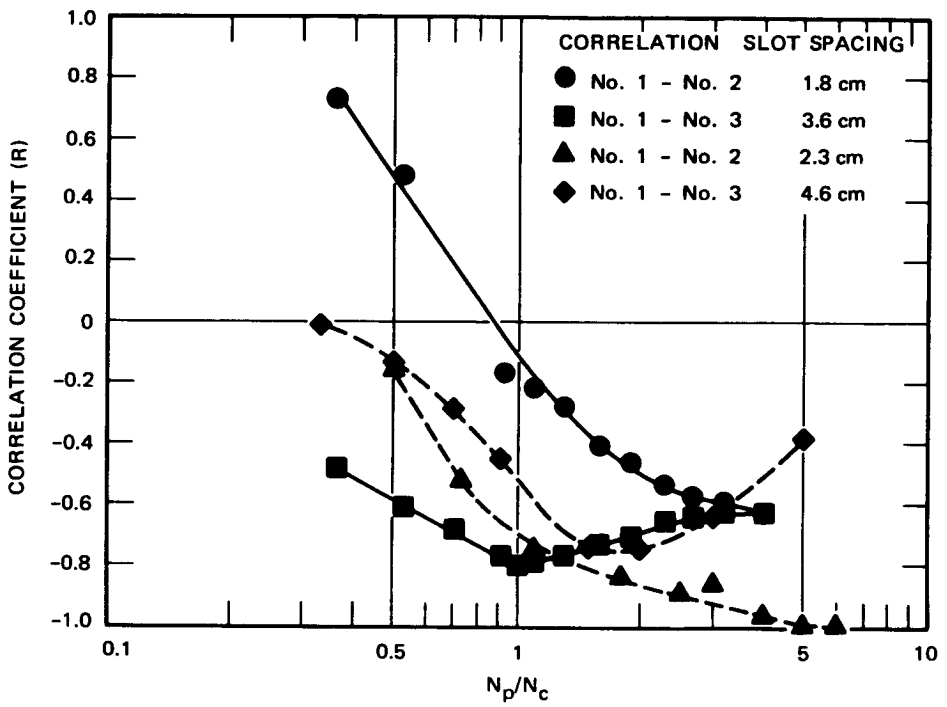

Figure 17.- Cross correlation of reflected signal from driven slot No. 1 and coupled signal to downstream slots No. 2 and No. 3.

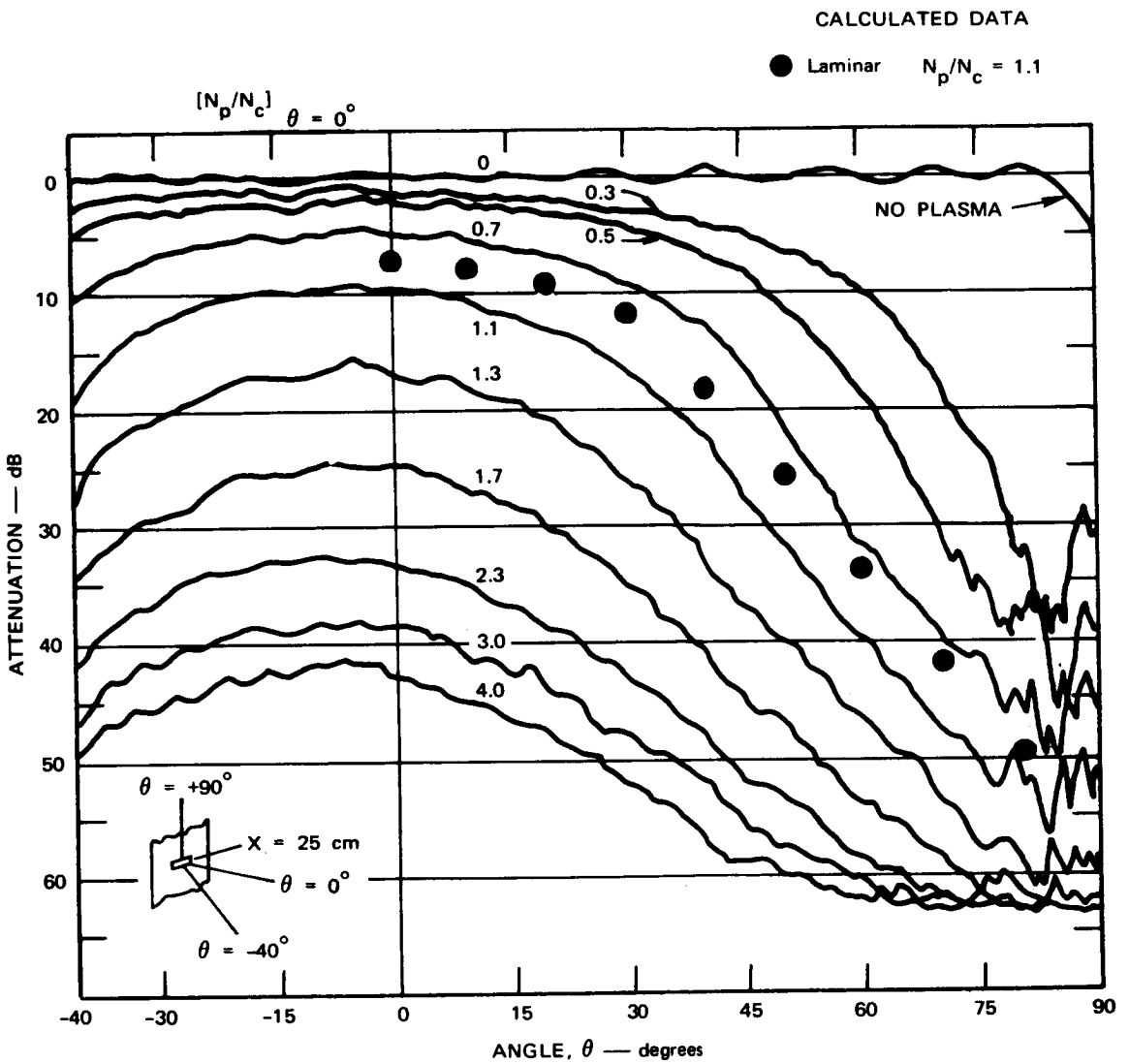

Figure 18.- Effect of turbulent plasma on E-plane pattern of X-band slot antenna.

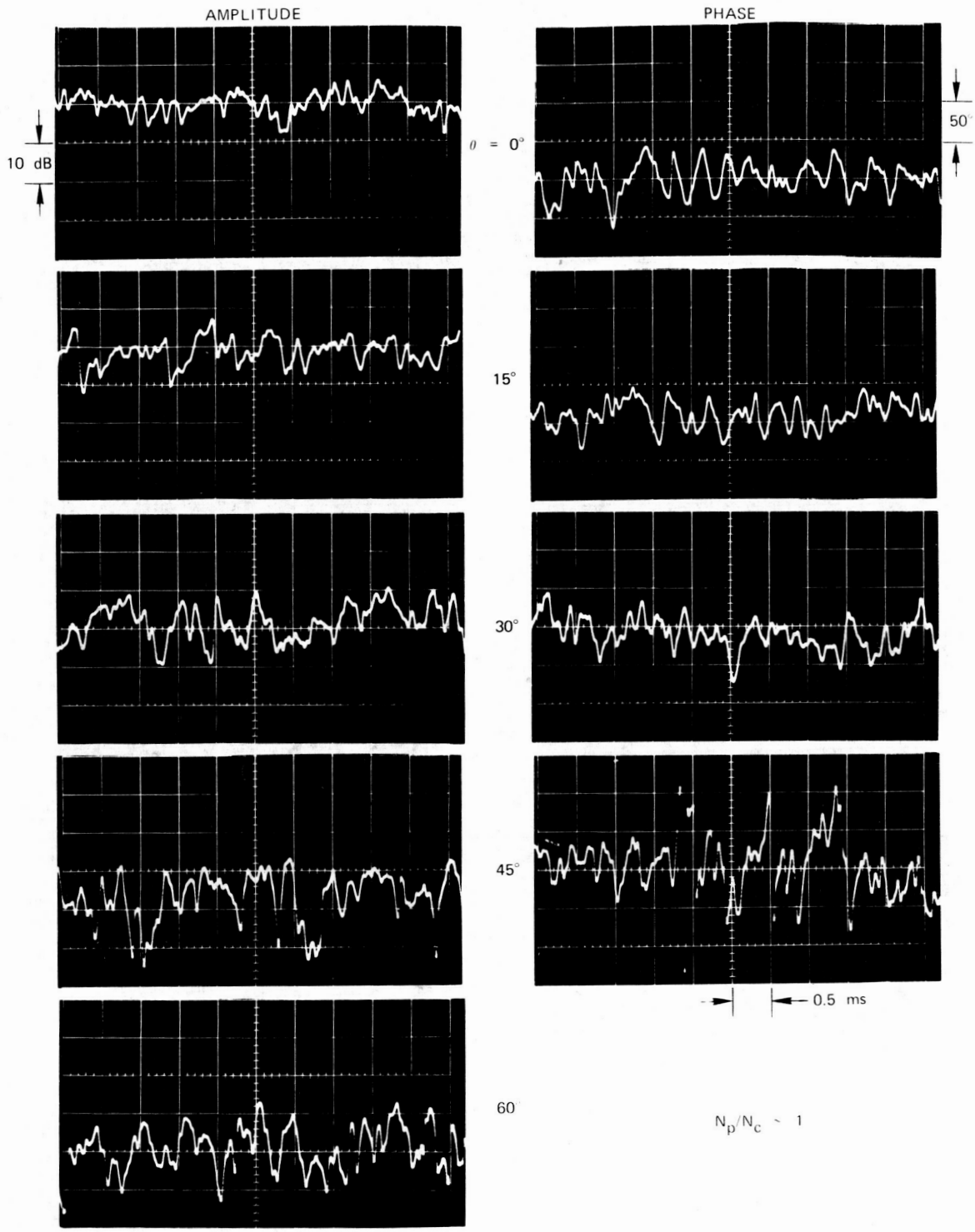

Figure 19.- Effects on signals propagated through a turbulent plasma.

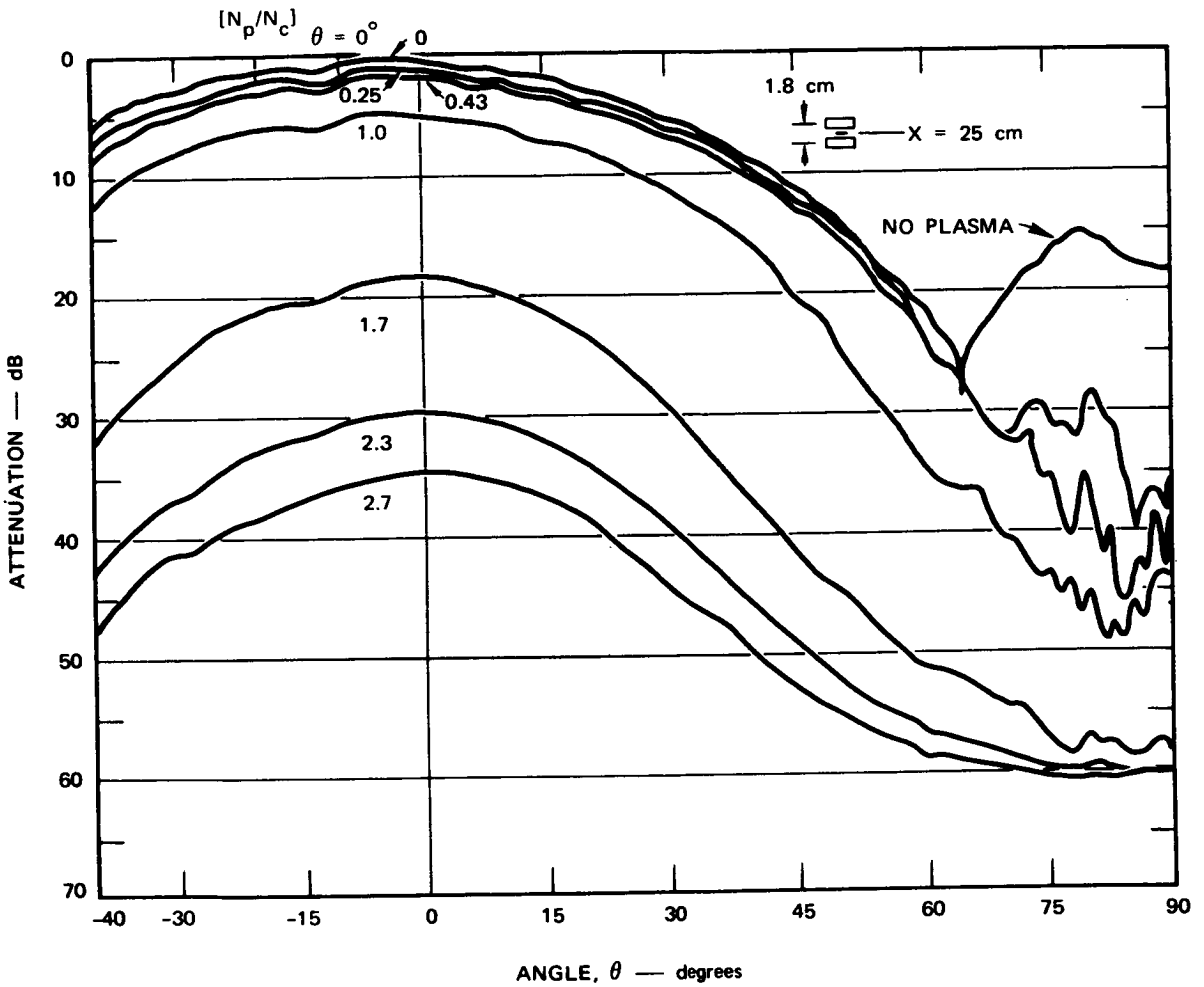

Figure 20.- Effect of turbulent plasma on dual-slot X-band array (slot spacing = 1.8 cm).

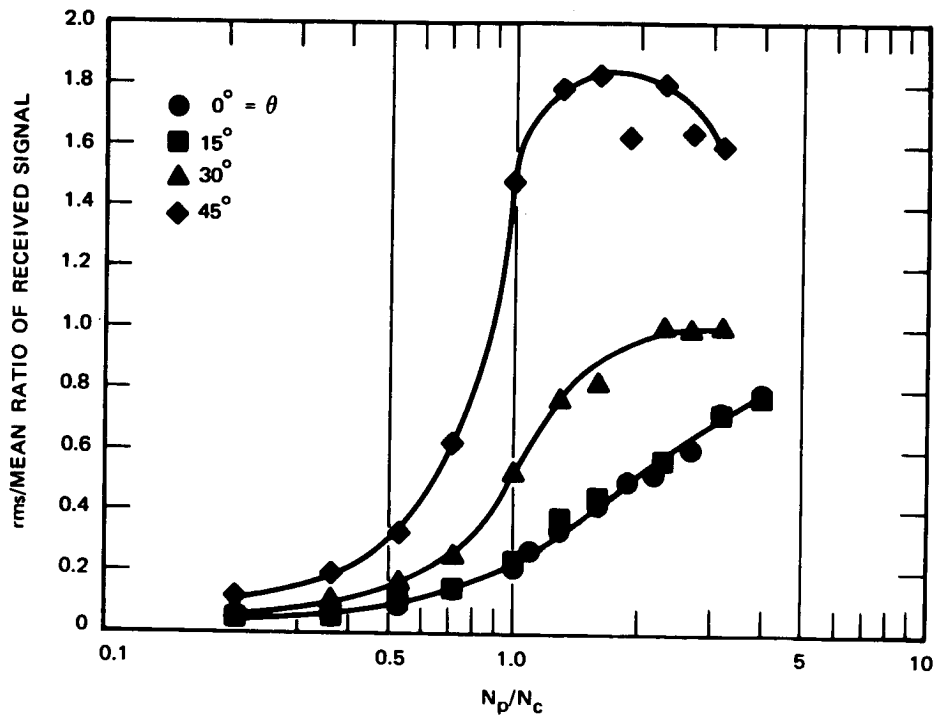

Figure 21.- Effect of turbulent plasma on rms/mean received signal amplitude from dual-slot X-band array (slot spacing = 1.8 cm).

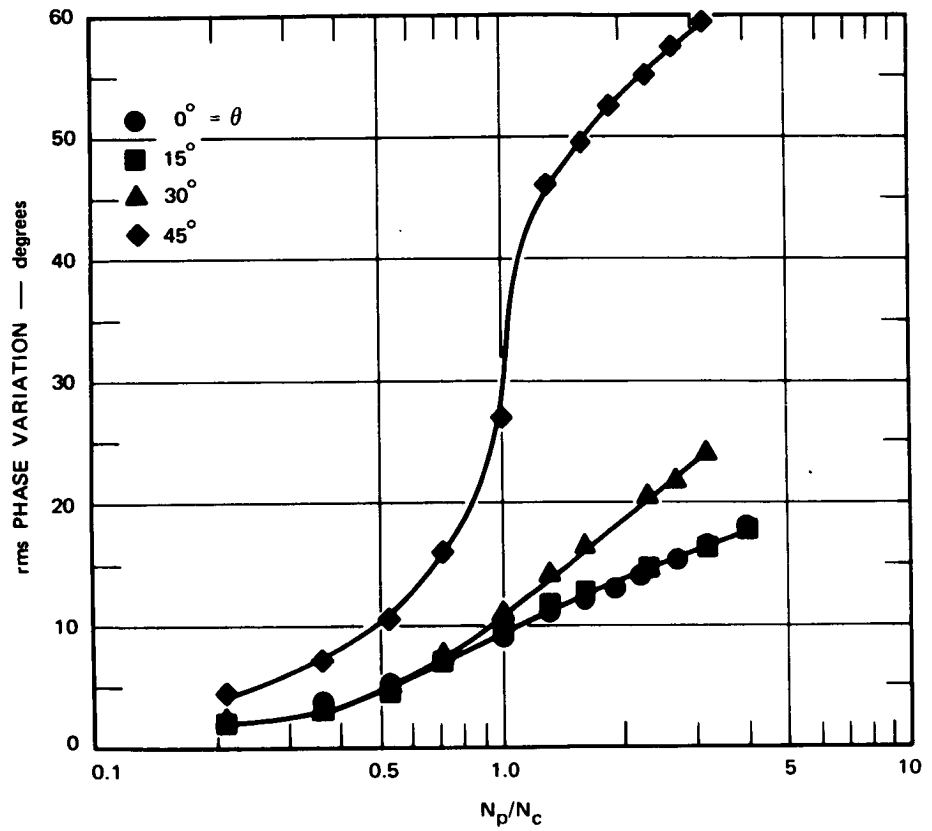

Figure 22.- Effect of turbulent plasma on rms phase variation of received signal from dual-slot X-band array (slot spacing = 1.8 cm).

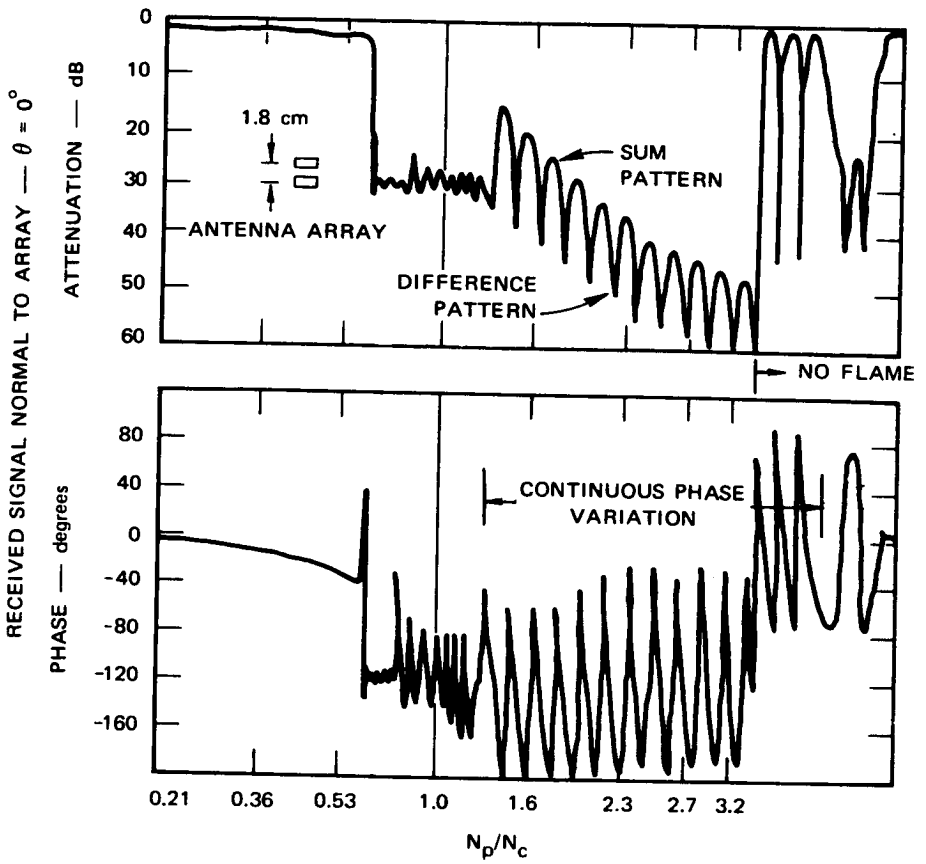

Figure 23.- Effect of turbulent plasma on difference pattern null depth of dual-slot X-band array (slot spacing = 1.8 cm).

RADIATION FROM CIRCUMFERENTIAL SLOTS ON PLASMA-CLAD CONES

By Gordon E. Stewart, Kurt E. Golden, and David C. Pridmore-Brown
The Aerospace Corporation, El Segundo, California

SUMMARY

The radiation pattern distortion produced by a high-altitude, boundary-layer plasma is investigated for both symmetrically and asymmetrically excited circumferential slot antennas on models of conical reentry vehicles that use an electric discharge simulation of the sheath. The slot configurations are selected to conform to nose-mounted telemetry antennas in current use, and the peak electron densities and electron density profiles are selected to approximate high-altitude reentry conditions. Measured patterns and theoretical predictions are compared for both bare and plasma-clad cones. These indicate large modifications of the radiation pattern in the forward direction, even for relatively thin and underdense plasmas.

INTRODUCTION

The analysis and design of antenna systems operating in a reentry environment are greatly facilitated by the use of techniques for simulating the plasma sheath. For sharp, slender bodies at low altitudes and for sufficiently low signal frequencies, the plasma sheath is thin and collision-dominated. The plasma layer alters the self-admittance of slot antennas with little change in the radiation pattern (ref. 1). Under these conditions, the effects of the sheath on antennas can be determined by replacement of the plasma with space cloth of the same conductance (ref. 2). At high altitudes for telemetry frequencies above 3.0 GHz, the collision frequency is low enough and the plasma can be thick enough to introduce significant attenuation, radiation pattern distortion, and changes in mutual admittance between slots as well as altering the self admittance. In a recent paper, the admittance, isolation, and radiation patterns for slots on a ground plane in the presence of an electrical discharge with electronic characteristics similar to those of the boundary layer for a sharp, slender body at high altitudes were measured and compared with theoretical predictions based on probe-measured electron density profiles (ref. 3). For slots at the aft end of large reentry vehicles, ground-plane-based calculations give reasonable estimates of admittance, isolation, and radiation patterns, especially for cuts in which the effective radius of curvature of the cone is infinite. Recently there has been increasing use of nose-mounted telemetry antennas on conical reentry vehicles. Because of the close proximity of the

slot antenna to the cone tip, more careful consideration must be given to the geometry than for slots located further aft. In this paper, the radiation patterns for circumferential slots at the appropriate position for a nose-mounted telemetry antenna are investigated for overdense and underdense plasma layers with electron density profiles similar to those of a high-altitude boundary layer.

There have been two previous laboratory investigations of the use of electrical discharges to study radiation pattern distortion effects on conical bodies. In both of these studies, glass walls were used to confine the discharge. The first of these studies used a hot cathode discharge with the anode located at the apex of the cone (ref. 4). The second group of investigators used a surface wave ionization technique to produce the plasma layer (ref. 5). Neither simulation technique produces a plasma with a profile similar to that of a high altitude boundary layer, and the measured radiation patterns appear to have been distorted by the effects of the glass containers.

HIGH ALTITUDE BOUNDARY LAYER SIMULATION

The plasma layer used in this study is formed by pulsed electron beam emission from the surface of a conducting aluminum cone in a reduced-pressure argon atmosphere. Early investigations with this type of discharge used multiple electrodes inserted into the surface as anodes (ref. 6). In this investigation with models of conical reentry vehicles, the anode consisted of either a small metallic sphere located at the tip or an insulated segment of the aft end of the cone.

In figure 1 the plasma generation technique is shown for a small spherical electrode at the tip of the cone. Kilovolt pulses of 5 μsec duration are applied between anode and cathode at a 500 Hz repetition frequency. Upon application of the voltage pulse, a sheath is developed between the afterglow plasma from the preceding pulse and the body. Positive ions are accelerated into the cone surface, producing secondary electron emission. These electrons are in turn accelerated back through the sheath producing ionization in the plasma, as shown in the inset of figure 1. The thickness of the layer depends primarily on the electron range, which is a function of ionizing pulse voltage and pressure. The discharge requires no confining walls, but only a low-pressure gas environment, typically argon, in which to operate. Since we are here concerned only with the linear, high-frequency properties of the plasma, only the electronic properties — — that is, electron density and collision frequencies — — are of concern in simulation. Therefore, it makes no difference whether the gas is argon or hot air.

Electron densities are measured by use of the ion saturation current drawn by double Langmuir probes with fixed bias at a prescribed time during the afterglow. In this study, all measurements were made 10 μsec after the end of the ionizing pulse. The probe serves as a convenient means of determining relative electron density. Because of the uncertainties in scale factor for relating ion saturation current to electron density, broadside

signal attenuation is used for determination of the peak electron density immediately over the aperture.

The variation of electron density normal to the surface of the cone measured at four stations with probes is shown in figures 2 and 3 for argon pressures of 0.4 and 0.6 Torr, respectively, with the anode located at the aft end of the cone. The curves can be approximated by a parabola between the peak of the profile and the wall. The profile is approximated in the exterior region with an exponential, $\exp(-\alpha x)$, where x is the distance in centimeters normal to the conical surface. The two curves are joined, and the slope is kept continuous at the join. The approximation to the profile over the aperture has been shown as the dashed curves in figures 2 and 3. The thickness of the plasma layer is seen to decrease markedly with increasing pressure because of the reduced range of the electrons. It can be seen that, for excitation at the aft end of the cone, the peak value of the electron density decreases toward the tip. In the case of an electrode at the tip of the cone, the opposite is true. The variation in the peak value of electron density along the surface of the cone depends primarily on the drop in voltage across the sheath as one moves away from the anode. It depends also to some extent on the local radii of curvature of the surface, the peak value being reduced as the radii of curvature of the surface decrease. As can be seen in figures 2 and 3, there is little change in the shape of the profile over the cone.

For electrons generated at the nose tip of a slightly blunted conical reentry vehicle, the peak value of electron density is highest at the tip and decreases as $r^{-3/2}$, where r is the radius in a spherical coordinate system with origin at the projected tip position. The thickness of the layer also increases as one moves away from the tip. For electrons generated by clean air ionization in the high altitude boundary layer, the peak electron density increases toward the aft end of the vehicle. At sufficiently high altitudes, the electrons generated in the tip may be in excess of those produced in the boundary layer over the whole length of the vehicle. At lower altitudes, the electrons generated at the tip can generally be disregarded unless one is very close to the tip.

For a study of nose-mounted telemetry antennas at high altitudes, the electrode mounted at the tip gives the best simulation of the electron density distribution in the nose region; however, as will be shown later, the radiation patterns depend primarily on the electron density in the immediate vicinity of the slot. In figure 4 the shapes of the electron density profiles produced by the discharge at three different pressures are compared with those calculated from flow field analysis for a reentry vehicle with a 0.25-in. nose radius at 154,000 ft at two different stations near the tip. In each case, the peak electron density has been normalized to unity. A plasma layer with the proper thickness can be produced by the discharge with a background pressure of approximately 1.25 Torr. The collision frequencies of both the discharge and the high-altitude boundary layer are sufficiently low that the plasma can be regarded as lossless at the frequencies under consideration.

Evacuable Microwave Anechoic Chamber and Recording Equipment

So that this simulation of the high-altitude boundary layer plasma can be fully exploited, an evacuable microwave anechoic chamber is used as shown in figure 5. With the microwave absorber in place, the chamber can be evacuated to less than 10^{-3} Torr; it is then refilled with argon at a pressure of 0.1 to 2.5 Torr. Models are mounted on an absorber-clad pedestal, which is driven through a rotary seal by a conventional antenna turntable. The anechoic chamber has a reflectivity at X-band of -50 dB.

Since an afterglow plasma is used in this simulation method, radiation pattern measurements are made in a 1-μsec interval of time 10 μsec after the ionizing pulse has terminated; this ensures that plasma conditions do not change during the measurement. A Scientific-Atlanta Series 1671 Pulse Receiving and Recording System has been found well suited to this requirement.

Conical Model with a Symmetrically Excited Circumferential Gap

Figure 6 shows a cross section of the nose of a model having a half cone angle of 11 deg with a circumferential gap that can be symmetrically excited by means of a coaxial feed. For a signal frequency of 9.0 GHz, the k_0a associated with this slot is 24.4. The slot dimension is 1/16 in., which is very small in comparison with the wavelength.

Measurements for the symmetrically excited cone are shown in figure 7. The radiation pattern is for an axial cut with $\theta = 0$ corresponding to the nose of the vehicle. All patterns to be described in this paper have been normalized to 0 dB for the average free space broadside radiation. The cut corresponding to $\phi = 180$ deg has been omitted since it is identical. Both theoretical and experimental patterns exhibit a marked lobe structure, which corresponds to interference between the direct radiation from the slot and power scattered from the tip (ref. 7). The experimental patterns show a small amplitude ripple, which corresponds to scattering from the aft end of the cone. This scattering is not included in the analysis, which is based on a semi-infinite cone.

The effect of a small spherical ball corresponding to an anode located at the tip of the bare cone is shown in figure 8. There is only a small change in the radiation pattern, which is due to modification of the scattering from the tip by such an electrode.

The effect of an underdense plasma layer is shown by the dashed curves of figure 9. There is a severe reduction in the radiation in the forward direction, and the oscillations resulting from the tip scattering have been significantly reduced. This reduction of edge effects has been found for all plasma thicknesses and electron densities investigated in this study, although

a priori one might expect that surface waves could be excited under some conditions that could enhance tip scattering. The reduction of tip scattering leads one to consider whether it would not be possible, for the plasma-clad cone, to use a simplified model, such as a ground-plane-based calculation (ref. 3) for predicting radiation pattern characteristics. In such a model, only the variation of the plasma normal to the surface is considered. The radiation patterns for the plasma-clad ground plane are calculated by use of the multi-layer-type plasma analysis described in refs. 2 and 8. Because of the low loss of the plasma layer, up to 1000 slabs are used to approximate the plasma profile normal to the surface.

In the comparison of the ground-plane-based calculations with the experimental results in figure 9, the curves are remarkably similar. The theoretical calculation corresponding to $N_e(Z_{PEAK}) = 0.4 \times 10^{12}$ cm^{-3} agrees well with the radiation pattern in the forward direction, while 0.8×10^{12} cm^{-3} gives a pattern agreeing well with the radiation in the backward direction. This difference in electron densities occurs because of the gradient in electron density along the cone, which causes the ray paths to traverse different electron concentrations. For the overdense case shown in figure 10, there is again a difference in peak electron density that gives a best fit of the theoretical curves to the experimental curves. The percentage change is significantly smaller, however, since for an overdense plasma, the electric fields are localized more to the immediate vicinity of the aperture.

Conical Model with an Asymmetrically Excited Circumferential Gap

The antenna configuration described in the preceding section provides no radiation in the forward direction. For this reason, it is unsuitable for many flight applications. The simplest excitation for a circumferential slot that provides forward coverage has an aperture field variation of $\cos(\phi)$. A cut-away view of the model used in this study is shown in figure 11. The source is provided by two reduced-height X-band apertures with half-wave boron nitride windows excited 180 deg out of phase with each other. Accurate representation of this source, which has approximately a cosine variation across each aperture, requires a Fourier series. It was found that the first two terms of this Fourier series expansion were sufficiently accurate to compute the radiation patterns for the bare cone

$$E_{ap} = (V_0/a)\left[\cos(\phi) + 0.85\cos(3\phi)\right]$$

The plasma layer can be produced over the model by pulsing the spherical anode either at the tip or at the base cap positively with respect to the conical body.

The theoretical and experimental radiation patterns for this asymmetrically excited cone are displayed in figure 12. Theory and experiment are in good agreement except for the rapid, small-amplitude oscillations resulting from scattering from the back end of the cone, which are not included in the analysis. The small, spherical electrode at the tip produces only a small change in the radiation pattern.

A series of radiation pattern measurements were taken for the plasma-clad cone and again compared with the ground-plane-based theoretical results. These patterns are shown in figures 13 - 16. These values have been selected to cover the range of plasma thicknesses that could occur during reentry at high altitudes. The patterns were taken in the following fashion. A fixed attenuation at broadside was set up for excitation using the tip and for excitation using the back of the model. Since the broadside attenuation depends primarily on the plasma conditions immediately over the slot, this fixed attenuation ensures that, for the two ways of exciting the anode, one is reversing merely the component of the gradient of electron density along the cone, and not the peak value of electron density or the profile normal to the surface at the aperture. Thus, one is able to determine how the component of electron density gradient along the cone affects the pattern. For the overdense plasmas shown in figures 13 - 16, the effect is not large.

Radiation patterns and input admittances were again computed with the use of probe-measured electron density profiles for the four cases shown in figures 13 - 16. The resulting theoretical patterns were selected to have the same broadside attenuation as the experimental data. The agreement in the shape of the patterns is excellent. The ground-plane-based calculations, which do not include the effects of plasma variation in a direction parallel to the ground plane, generally fall between the measured results for the plasma density, increasing forward and aft. At higher pressures of argon, corresponding to plasma thickness of only a few millimeters, there still can be seen some effect of scattering from the tip, although it is considerably reduced in amplitude.

CONCLUSIONS

A plasma layer with an electron density profile similar to that of a high-altitude boundary layer significantly reduces edge effects and radiation in the forward and aft directions. There appears to be no significant surface wave excitation for such a boundary layer profile, even when the plasma is overdense. These results differ from those of other investigators, who have found enhancement of radiation in the forward and aft directions (ref. 5). This difference is probably due to the glass walls used to confine the discharge in their experiments. The present results also contradict the conclusion of Wait (ref. 9), who states that, "the sheath does not have a significant effect on the radiation in the forward direction." It should be noted that this statement was based on work done by Yeh (ref. 10) for a symmetrically excited cone clad with a layer having relative dielectric constant greater than unity.

Because of the reduction in edge effects, the average level of radiated power versus angle for axial cuts can be determined with the use of a ground-plane-based approximation. The fine structure in the pattern cannot, however, be predicted by such an analysis.

REFERENCES

1. Fante, R.L. : Effect of Thin Plasmas on an Aperture Antenna in an Infinite Conducting Plane. Radio Sci., vol. 2, no. 1, Jan. 1967, pp. 87-100.

2. Golden, K.E., and Stewart, G.E. : Self and Mutual Admittances of Rectangular Slot Antennas in the Presence of an Inhomogeneous Plasma Layer. IEEE Trans. Antennas Propagation, vol. AP-17, no. 6, Nov. 1969, pp. 763-770.

3. Stewart, G.E., and Golden, K.E. : Admittance, Isolation, and Radiation Patterns of Rectangular Slot Antennas in the Presence of a Simulated Reentry Sheath. Program and Digest, 1969 G-AP International Symposium, Austin, December 9-11, pp. 215-223.

4. Bates, R.H., Freyheit, P.J., Kristal, R., Lustig, C.D., Meltz, G., and Shizumi, P.K. : ECM Aerospace Antenna Studies. RD-5291-0787, Sperry Rand Corp., September 1969.

5. Sforza, P.F., Samaddar, S.N., Rolfe, E., and Weiss, J.G. : Study of ECM Antenna Optimization. AFCRL-67-0348, Air Force Cambridge Research Labs., June 1965 - March 1967.

6. Stewart, G.E. : Laboratory Simulation of Reentry Plasma Sheaths. IEEE Trans. Antennas Propagation, vol. AP-15, no. 6, Nov. 1967, pp. 831-832.

7. Pridmore-Brown, D.C. : High-Frequency Radiation from Slot-Excited Conical Antennas. Program and Digest, 1970 G-AP International Symposium, Colombus, September 14-16, pp. 161-167.

8. Golden, K.E., and Stewart, G.E.: Single and Multislot Antennas in an Inhomogeneous Reentry Plasma Environment. Proceedings of the Conference on Environmental Effects on Antenna Performance, vol. 1, pp. 156-160. Clearinghouse for Federal Scientific and Technical Information, Springfield, Virginia 1969.

9. Wait, J.R.: Electromagnetic Radiation from Conical Structures. Antenna Theory, pt. 1, ed. R.E. Collin. McGraw-Hill Book Co., New York, 1969.

10. Yeh, C.: An Application of Sommerfeld's Complex-Order Wavefunctions to an Antenna Problem. Journ. Mathematical Physics, vol. 5, pp. 344-350, 1964.

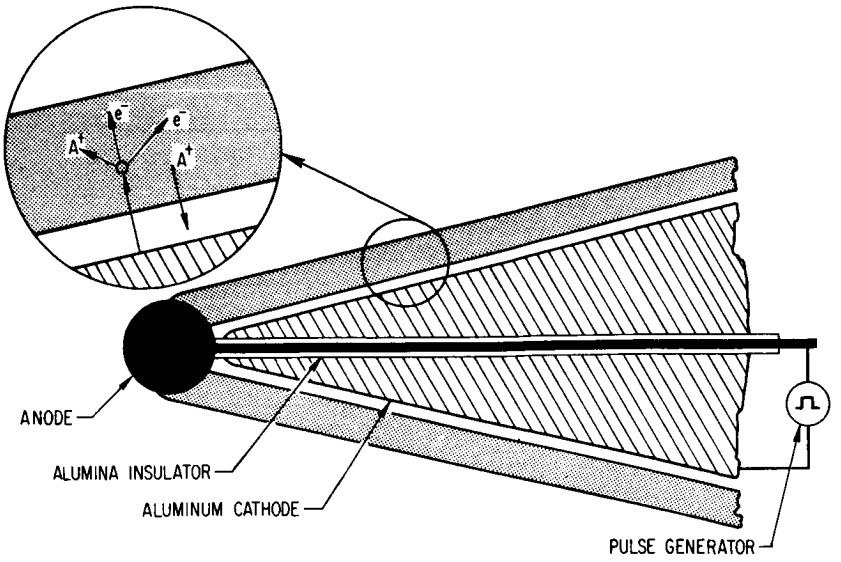

Figure 1.- Plasma layer generation using an anode at the tip.

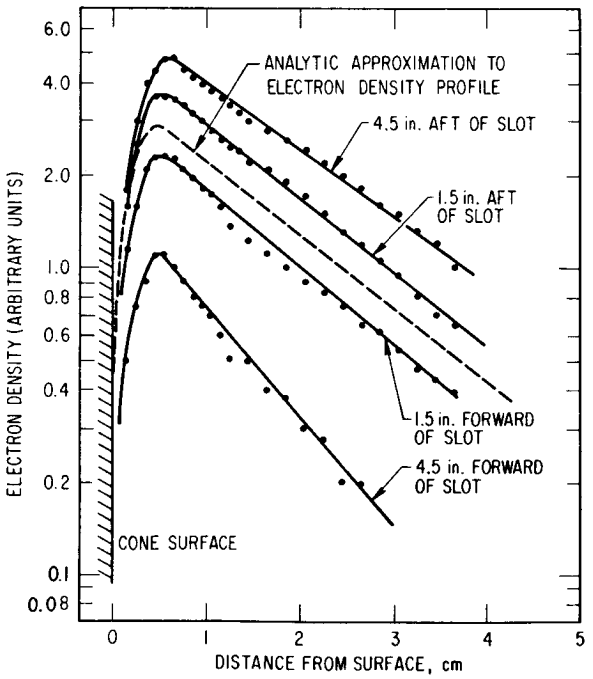

Figure 2.- Electron density profile at 0.4 Torr in argon (dashed line corresponds to an exponential decrease in the exterior region with $\alpha = 0.55\ cm^{-1}$).

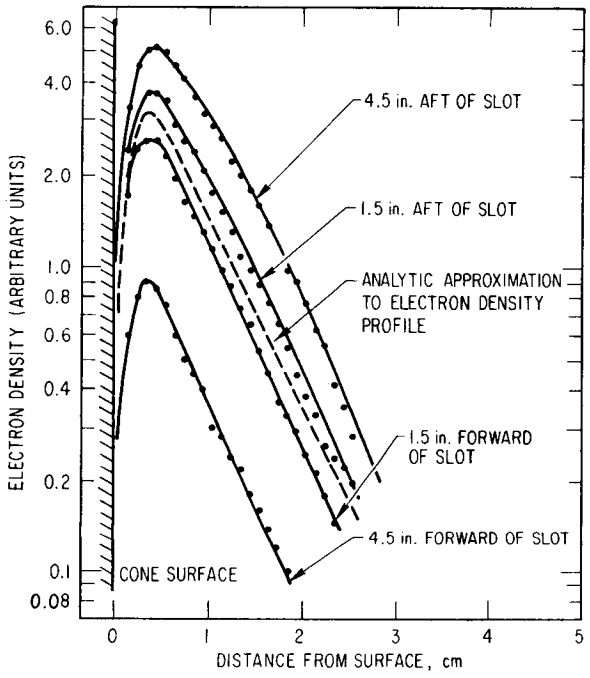

Figure 3.- Electron density profile at 0.6 Torr in argon (dashed line corresponds to an exponential decrease in the exterior region with $\alpha = 1.4$ cm^{-1}).

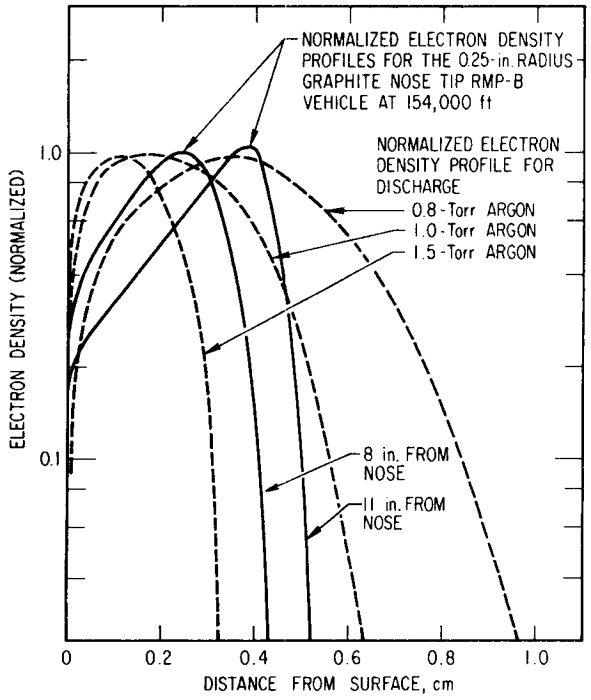

Figure 4.- Comparison of the electron density profiles for the discharge with computed high altitude flow fields.

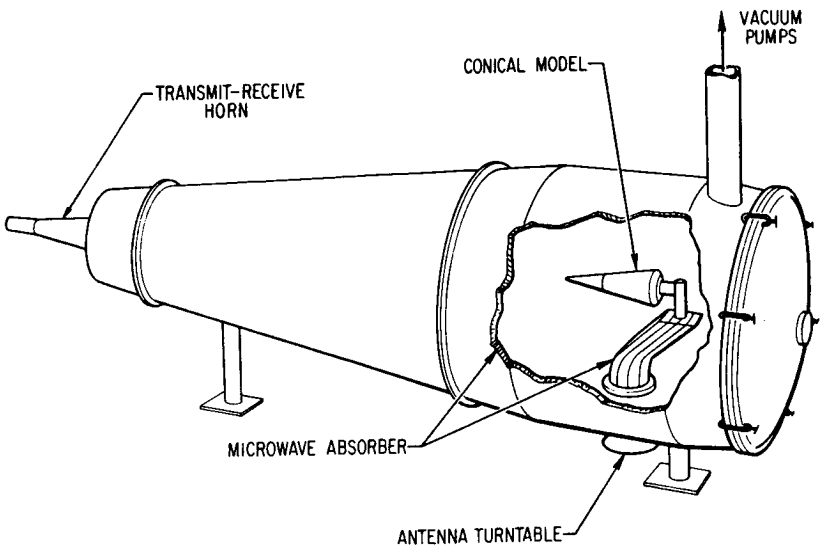

Figure 5.- Conical model mounted in an evacuable microwave anechoic chamber.

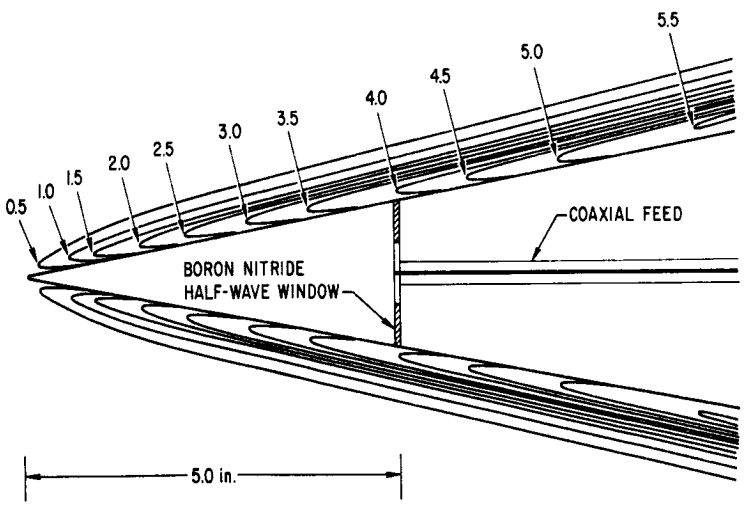

Figure 6.- Tip of conical model with symmetrically excited gap showing coaxial feed and contours of constant electron density for excitation using an anode at the back.

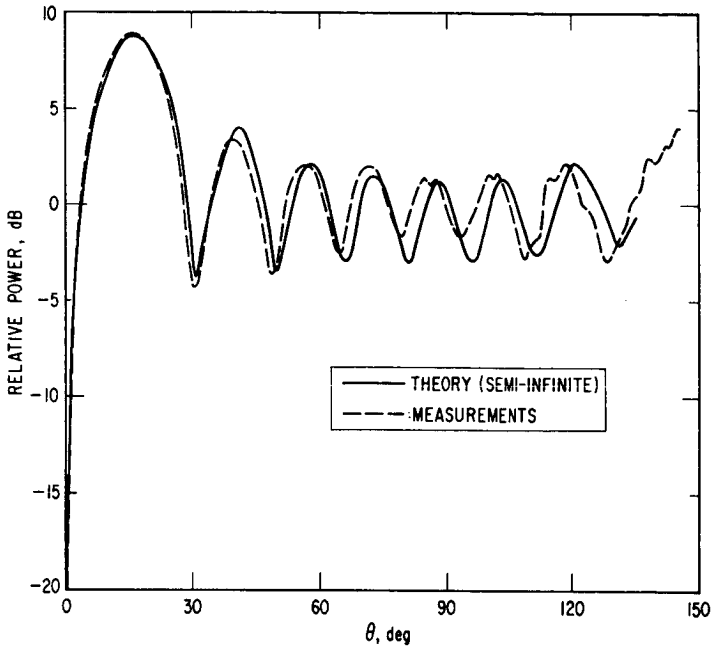

Figure 7.- Axial cut of E_θ radiation pattern for symmetrically excited cone.

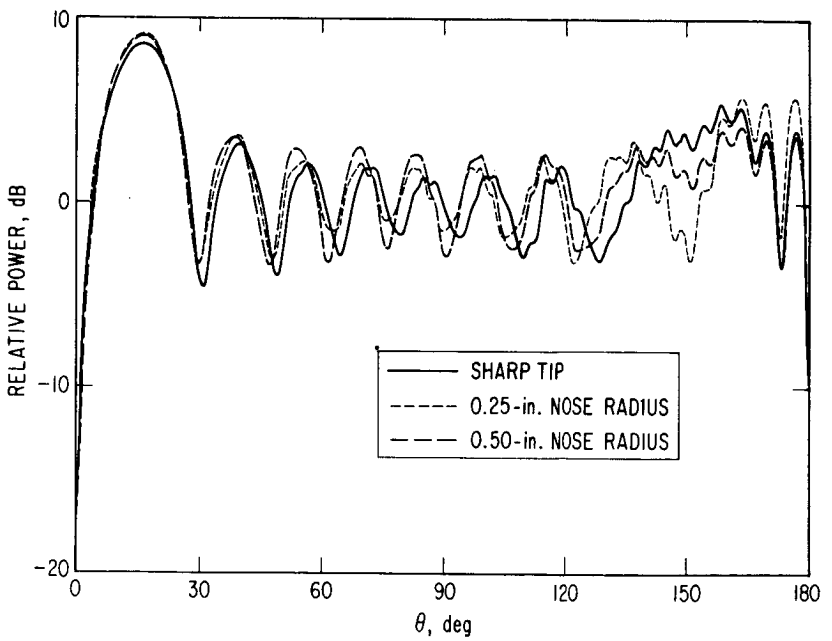

Figure 8.- Axial cut of E_θ radiation pattern for symmetrically excited cone with spheres of various radius at tip.

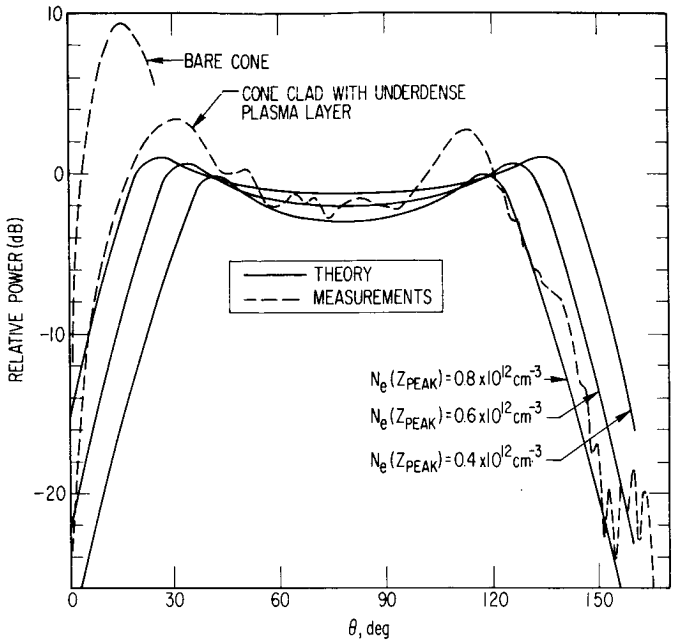

Figure 9.- Axial cut of E_θ radiation pattern for symmetrically excited cone clad with underdense plasma layer. Argon pressure 0.6 Torr.

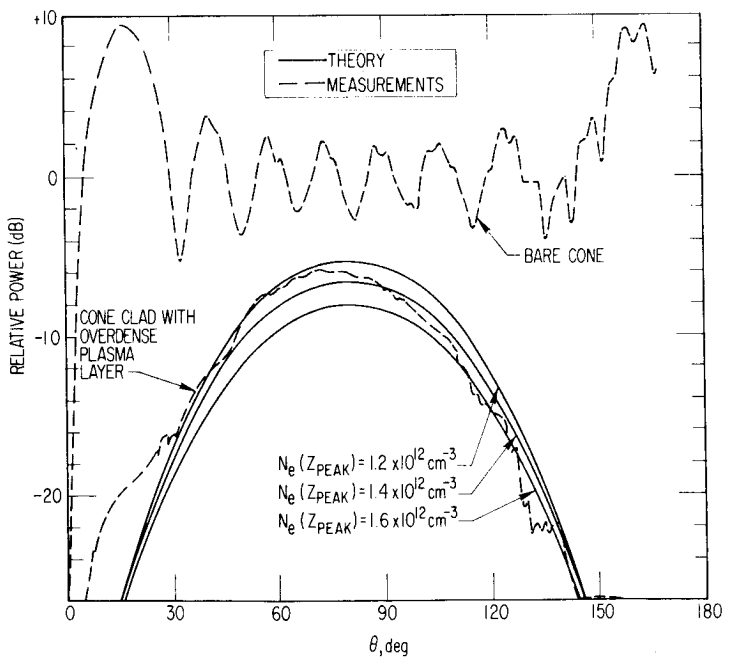

Figure 10.- Axial cut of E_θ radiation pattern for symmetrically excited cone clad with overdense plasma layer. Argon pressure 0.6 Torr.

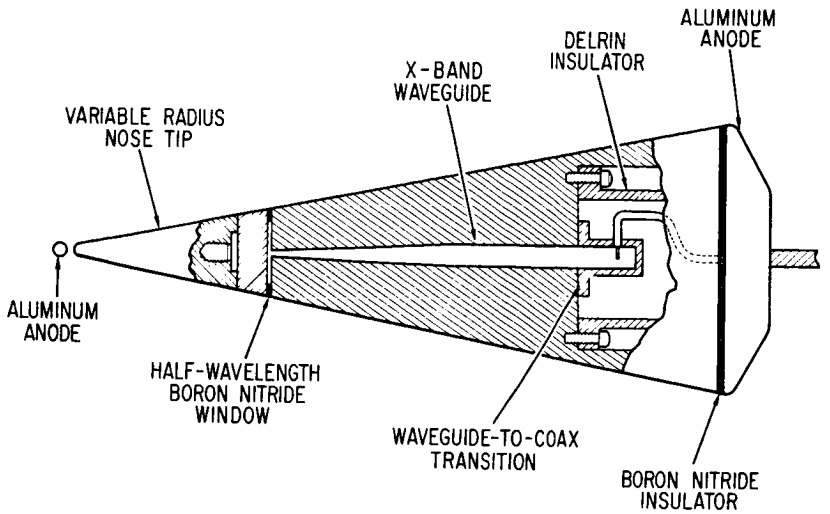

Figure 11.- Conical model with asymmetric excitation of the circumferential gap.

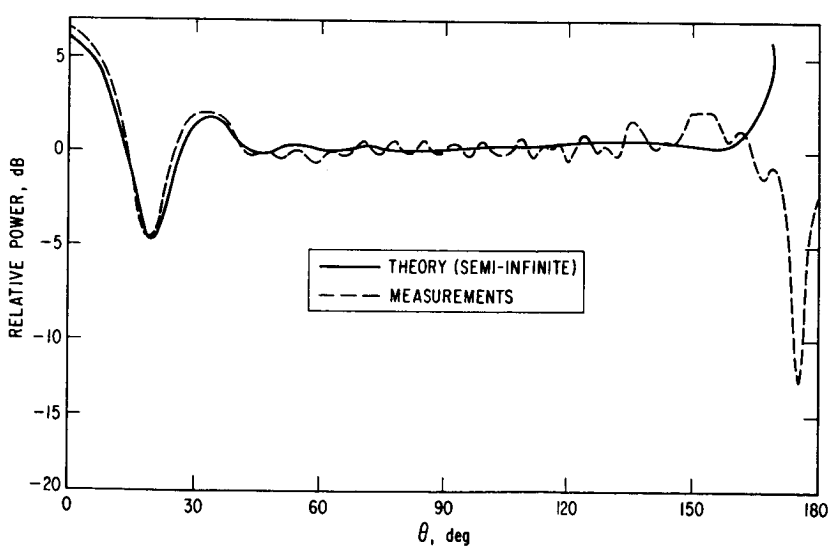

Figure 12.- Axial cut of E_θ radiation pattern for asymmetrically excited cone.

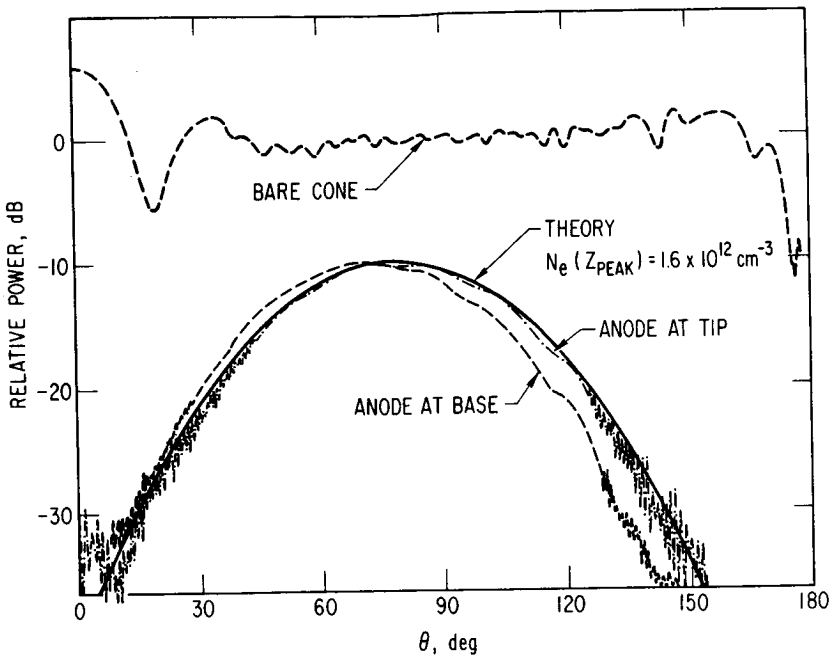

Figure 13.- Axial cut of E_θ radiation pattern for asymmetrically excited cone clad with overdense plasma layer. Argon pressure 0.6 Torr.

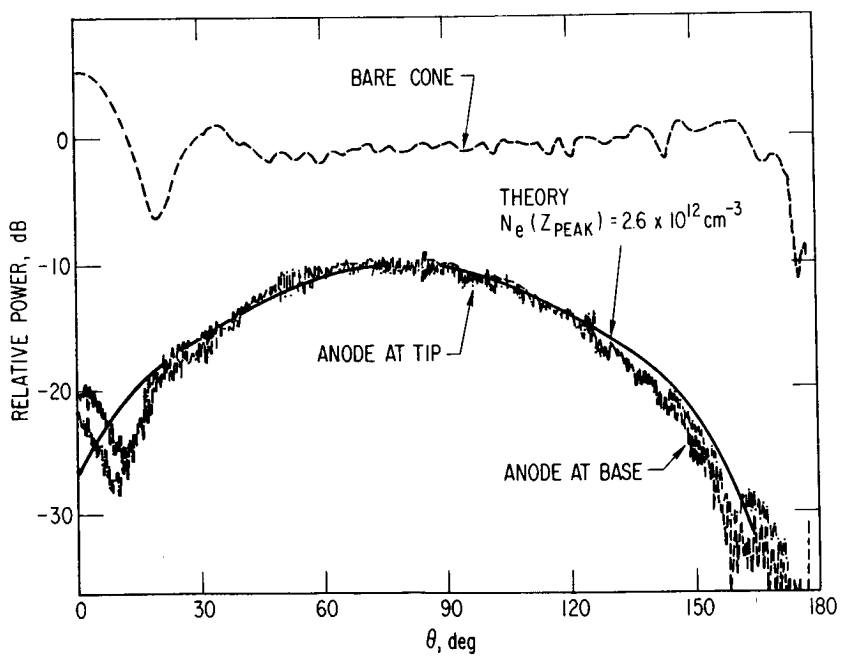

Figure 14.- Axial cut of E_θ radiation pattern for asymmetrically excited cone clad with overdense plasma layer. Argon pressure 0.8 Torr.

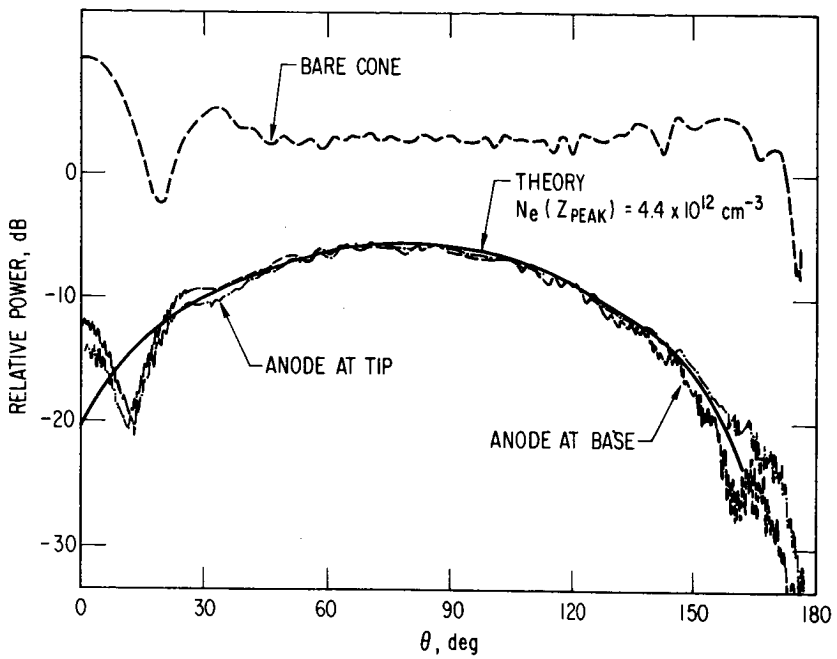

Figure 15.- Axial cut of E_θ radiation pattern for asymmetrically excited cone clad with overdense plasma layer. Argon pressure 1.0 Torr.

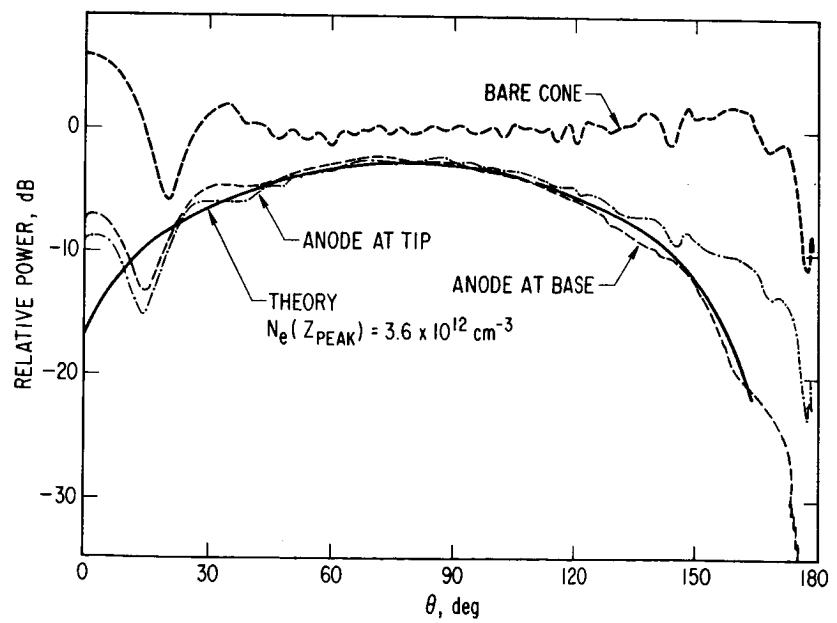

Figure 16.- Axial cut of E_θ radiation pattern for asymmetrically excited cone clad with overdense plasma layer. Argon pressure 1.5 Torr.

22

ELECTROMAGNETIC WAVE PROPAGATION IN A LOSSY PLASMA SLAB WITH A GRADIENT TRANSVERSE TO THE INCIDENT WAVE

By George Gal

Lockheed Palo Alto Research Laboratory

SUMMARY

This paper describes a computer solution of the interaction of a plane electromagnetic wave with a bounded inhomogeneous plasma slab. The electron density gradient is transverse to the incident wave propagation direction. TM and TE polarization are treated.

Transmission and reflection coefficients are obtained and, in addition, refractive defocusing introduced by the transverse gradient has been calculated for a number of electron density distributions. This basic solution is then applied to a bounded plasma slab, flow with a moving shock and communication through a plasma layer.

INTRODUCTION

Microwave diagnostics are widely used to characterize laboratory plasmas (see refs. 1, 2, 3) because thermal protection of the probe is not required and the response time is very short. The scattered and transmitted waves depend upon the overall structure of the plasma. Also, communication through a plasma layer can be affected by refractive defocusing introduced by transverse non-uniformity in the plasma. Clearly, theoretical studies of electromagnetic wave interaction with non-uniform plasmas are required for a correct interpretation of data.

Since the electron density profile is an important variable, the calculations should be carried out for physically realistic profiles. Most previous work studied the effects of an electron density gradient parallel to the electromagnetic wave propagation direction. This assumption may be valid for plasmas confined within a small volume. For plasma flows over a surface or in a channel, or shock tube generated gas, the electron density varies along the flow direction, or behind the ionization shock. (Ref. 4). If appreciable variation of electron density in the transverse direction over the area sensitive to the microwave horn is present, the transmitted and reflected

signal cannot be related to the plasma by simple means.

In the present work we assumed a plasma with an axial gradient and developed a computer program which would provide a numerical solution of Maxwell's equations. The plane incident wave was taken normal to the plasma surface, and both polarizations were treated. The geometric aspect of the problem is described in figure 1. Transmission and reflection coefficients for the plasma slab are obtained and, in addition, refractive defocusing introduced by the transverse gradient has been calculated for a number of electron density distributions, as shown in figure 2. This basic solution is then applied to three specific models, also shown in figure 1:

1. Diagnostics of a plasma slab with a transverse gradient, figure 1a.

2. Propagation through a halfspace, figure 1b. Such a geometry exists in some communication cases over an antenna window, where the refractive defocusing introduced by the transverse electron density gradient cannot be neglected.

3. Shock tube plasma diagnostic, figure 1c, where the electron density is a function of the distance behind the shock and time. Furthermore, the model can be extended to a laminated halfspace, figure 1d, i.e., where electron density is varying in both the x and y directions. Such is the true condition in a boundary layer over an antenna window.

ANALYTICAL PROGRAM AND ASSUMPTIONS

Theoretical analysis consists of the numerical solution of Maxwell's wave equation for a number of different electron density profiles.

The magnetic field $\overline{H}$ and the electric field $\overline{E}$ must satisfy the wave equations

$$\nabla^2 \overline{H} + k_o^2 \epsilon(x)\overline{H} + [\nabla \ln \epsilon(x)] \times [\nabla \times \overline{H}] = 0 \qquad (1)$$

$$\nabla^2 \overline{E} + k_o^2 \epsilon(x)\overline{E} + \nabla [\overline{E} \cdot \nabla \ln \epsilon(x)] = 0 \qquad (2)$$

The above equations are solved in the present work using the following assumptions:

1. the field quantities do not vary in the y-direction;

2. the time dependence can be expressed as $e^{-i\omega t}$;

3. the relative magnetic permeability is constant ($\mu = 1$); and

4. mean free time electron collision model has been assumed.

Hence, the dielectric constant is a scalar and can be written as

$$\epsilon(x) = 1 - \frac{\bar{\omega}_p^2(1-i\bar{\nu})}{1+\bar{\nu}^2} \frac{n(x)}{n_o} \tag{3}$$

$\bar{\omega}_p^2$ is the normalized plasma frequency characterizing the electron density level at the origin ($x = 0$) and can be expressed as

$$\bar{\omega}_p^2 = \frac{3.18 \times 10^9}{\omega^2} n_o \tag{4}$$

where the operating frequency ω is expressed in radians/sec and n_o in particles per cm^3. $\bar{\nu}$ is the normalized collision frequency defined as $\bar{\nu} = \nu/\omega$, $k_o = 2\pi/\lambda$ is the free space wave number, and λ is the free space wavelength.

In the present work, a number of axial profile shapes $n(x)/n_o$ will be investigated and they are given in figure 2.

In a uniform plasma of electron density n, collision frequency ν and thickness L, the phase shift is given by

$$\Delta\varphi = 2\pi \left(\frac{L}{\lambda}\right)\left[1 - \frac{\beta}{k_o}\right] \tag{5}$$

where the phase constant is given by

$$\beta = k_o \left[\frac{|\epsilon| + \epsilon^R}{2}\right]^{1/2} \tag{6}$$

Substituting equations (3) and (6) into (5) allows us to write

$$\Delta\varphi = k_o L \left\{ 1 - \left[\frac{[(1-\delta)^2 + (\bar{\nu}\delta)^2]^{1/2} + (1-\delta)}{2}\right]^{1/2} \right\} \tag{7}$$

where

$$\delta = \frac{\bar{\omega}_p^2}{1+\bar{\nu}^2} \tag{8}$$

For a plasma having an electron density gradient in the x-direction, the phase difference between the wave passing through the slab at a distance x and at a reference point $x = 0$ is given by

$$\Delta\varphi(x) - \Delta\varphi(x = 0) =$$

$$= k_o L \left\{ \left\langle \frac{\left[(1-\delta)^2 + (\bar{\nu}\delta)^2\right]^{1/2} + (1-\delta)}{2} \right\rangle^{1/2} \right. \tag{9}$$

$$\left. - \left\langle \frac{\left\{[1-\delta\bar{n}(x)]^2 + [\bar{\nu}\delta\bar{n}(x)]^2\right\}^{1/2} + [1-\delta\bar{n}(x)]}{2} \right\rangle^{1/2} \right\}$$

The phase front (surface of constant phase) of the wave emanating from the plasma can be determined from equation (9). The surface of the constant optical path length can similarly be obtained from

$$\Phi = \frac{\Delta\varphi(x) - \Delta\varphi(x = 0)}{k_o} \tag{10}$$

Assuming that the phase fronts are orthogonal to the direction of travel, the ray incident upon the slab of plasma at a distance x is refracted so that it emerges at an angle $\theta(x)$ The angle $\theta(x)$ is given by

$$\tan\theta(x) = -\frac{d\Phi}{dx} = \frac{L}{2} f(x) \tag{11}$$

Combining equations (9) and (10), the angle of refraction $\theta(x)$ is obtained as a function of the electron density gradient and collision frequency, and $f(x)$ is defined by

$$f(x) = -\frac{\delta \dfrac{d\bar{n}(x)}{dx} \left\{ \dfrac{[1-\delta\bar{n}(x)] - \bar{\nu}\delta\bar{n}(x)}{\left\langle [1-\delta\bar{n}(x)]^2 + [\bar{\nu}\delta\bar{n}(x)]^2 \right\rangle^{1/2}} + 1 \right\}}{2^{1/2} \left\{ \left\langle [1-\delta\bar{n}(x)]^2 + [\bar{\nu}\delta\bar{n}(x)]^2 \right\rangle^{1/2} + [1-\delta\bar{n}(x)] \right\}^{1/2}} \tag{12}$$

METHOD OF SOLUTION

This method represents the numerical implementation of the Eikonal method given in reference 5. The plasma is divided into a number of subdivisions along the x-direction. The number of subdivisions m depends upon the electron density gradient. It is assumed that in each subdivision the m^{th} ray represents the plane wave. TE and TM mode solutions are obtained using the classical approach of separation of variables in each subdivision.

TM mode solution to equation (1) is

$$H_z(xyt) = X(x)\, Y(y)\, T(t) \tag{13}$$

and the equations for $X(x)$ and $Y(y)$ become

$$X''(x) + \frac{d\epsilon(x)/dx}{\epsilon(x)} X'(x) + k_o^2 [\epsilon(x) - \gamma_m]X(x) = 0 \tag{14}$$

$$Y'' + k_o^2 \gamma_m Y = 0 \tag{15}$$

where γ_m is the separation constant and is given by

$$\gamma_m = \epsilon_2(x = x_m) \cos \theta(x = x_m) \tag{16}$$

but at $y = y_2$; $\theta = 0$, therefore,

$$\gamma_m = \epsilon_2(x = x_m)$$

which is the generalization of the Snell's law of refraction to stratified media (ref. 5). The angle θ is obtained by solving equation (11).

Equation (14) is solved using the Runga-Kutta methods. The boundary conditions for equation (14) are

$$\begin{aligned} X(x = 0) &= 1 \\ X'(x = \infty) &= 0 \end{aligned} \tag{17}$$

x_∞ is defined as the location where the electron density gradient approaches arbitrarily close to zero. x_∞ is obtained from the electron density profiles.

TE mode solution is obtained by solving equation (2). After separation of variables the following differential equations are obtained:

$$X''(x) + k_o^2 \left[\epsilon(x) - \gamma_m\right] X = 0$$

$$Y''(y) + k_o^2 \gamma_m Y(y) = 0 \qquad (18)$$

Solutions of these equations are similar to those obtained for TM mode.

The Z component of the field in each region of figure 1 is represented as follows:

$$\Psi_{To} = Ae^{j(\tau_o - \omega t)}$$

$$\Psi_{Ro} = Be^{-j(\tau_o + \omega t)}$$

$$\Psi_{T1} = Ce^{j(\tau_1 - \omega t)}$$

$$\Psi_{R1} = De^{-j(\tau_1 + \omega t)}$$

$$\Psi_{TII} = FX(x)e^{j(\tau_2 - \omega t)} \qquad (19)$$

$$\Psi_{RII} = GX(x)e^{-j(\tau_2 + \omega t)}$$

$$\Psi_{TIII} = Ke^{j(\tau_3 - \omega t)}$$

$$\Psi_{RIII} = Me^{-j(\tau_3 + \omega t)}$$

$$\Psi_{TIV} = Ne^{j(\tau_4 - \omega t)}$$

$$\Psi_{RIV} = 0$$

where

$$\tau_o = k_o(\epsilon_o)^{1/2}y$$

$$\tau_1 = k_o(\epsilon_1)^{1/2}y$$

$$\tau_2 = k_o(\gamma_m)^{1/2}(y - \ell_1)\cos\theta \qquad (20)$$

$$\tau_3 = k_o(\epsilon_1)^{1/2}[y - (\ell_1 + L)]\cos\theta_{t3}$$

$$\tau_4 = k_o(\epsilon_o)^{1/2}[y - (\ell_1 + \ell_3 + L)]\cos\theta_{t4}$$

Notation is as follows: $\Psi = H_z$ for the TM mode, and $\Psi = E_z$ for the TE mode. A, B, C, through N are complex amplitude constants. The first of the subscripts in Ψ_{mn} describes the direction of the propagation (T = transmitted, R = reflected), while the second subscript specifies the region of interest. The total field in any region is simply the sum of the wave solution having the subscript of that region.

The constants A, B, C through N are calculated using the boundary conditions appropriate at the edges of each layer. The boundary conditions are that the tangential components of the fields are continuous, namely H_z, and E_x for the TM mode or E_z and H_x for the TE mode. From the Maxwell's equation

$$E_x = \frac{j}{\omega\epsilon}\frac{\partial H_z}{\partial y} \qquad \text{TM mode}$$

or (21)

$$H_x = \frac{j}{\omega\mu}\frac{\partial E_z}{\partial y} \qquad \text{TE mode}$$

Equation (21) allows continuity of $\frac{\partial\Psi}{\partial y}$ to use as a boundary condition in place of E_x or H_x for the TM or TE mode, respectively.

Using the boundary conditions, and taking the origin of y to be at the lower face of region 1, eight relations between the nine amplitudes result

$$A + B = C + D$$

$$(A - B) = a_1 (C - D)$$

$$Ce^{j\beta_1} + De^{-j\beta_1} = (F + G)\, X(x)$$

$$Ce^{j\beta_1} - De^{-j\beta_1} = a_4 (F - G)$$

$$X(x)\,(Fe^{j\beta_2} + Ge^{-j\beta_2}) = Ke^{j\beta_3} + Me^{-j\beta_3} \tag{22}$$

$$a_3\,(Fe^{j\beta_2} - Ge^{-j\beta_2}) = Ke^{j\beta_3} - Me^{-j\beta_3}$$

$$Ke^{j\beta_4} + Me^{-j\beta_4} = Ne^{j\beta_5}$$

$$a_2\,(Ke^{j\beta_4} - Me^{-j\beta_4}) = Ne^{j\beta_5}$$

Constants are defined

$$a_1 = \eta_1 \left(\frac{\epsilon_o}{\epsilon_1}\right)^{1/2} + \eta_o \left(\frac{\epsilon_1}{\epsilon_o}\right)^{1/2}$$

$$a_2 = \left[\eta_1 \left(\frac{\epsilon_o}{\epsilon_3}\right)^{1/2} + \eta_o\right]\left[\left(\frac{\epsilon_3}{\epsilon_o}\right)^{1/2} \frac{\cos \theta_{t3}}{\cos \theta_{t4}}\right]$$

$$a_3 = \left[\eta_1 \left(\frac{\epsilon_1}{\epsilon_2}\,(x = x_m)\right) + \eta_o\right]\left[X(x = x_3)\left(\frac{\gamma_3}{\epsilon_1}\right)^{1/2} \frac{\cos \theta_{i3}}{\cos \theta_{t3}}\right] \tag{23}$$

$$a_4 = \left[\eta_1 \left(\frac{\epsilon_1}{\epsilon_2}\,(x = x_m)\right)^{1/2} + \eta_o \left(\frac{\gamma_m}{\epsilon_1}\right)^{1/2}\right] X(x = x_m)$$

$$\left.\begin{aligned}\eta_1 &= 1\\ \eta_o &= 0\end{aligned}\right\} \text{ TM mode} \qquad \left.\begin{aligned}\eta_1 &= 0\\ \eta_o &= 1\end{aligned}\right\} \text{ TE mode}$$

Phase constants are

$$\begin{aligned}\beta_1 &= k_o \sqrt{\epsilon_1}\ell_1\\ \beta_2 &= k_o \sqrt{\gamma_2}\,(L\cos\theta_{i3} + x_3 \sin\theta_{i3})\\ \beta_3 &= k_o \sqrt{\epsilon_3}\, x_3 \sin\theta_{t3}\\ \beta_4 &= k_o \sqrt{\epsilon_3}\,(\ell_3 \cos\theta^*_{t3} + x_4 \sin\theta^*_{t3})\\ \beta_5 &= k_o \sqrt{\epsilon_o}\,(x_4 \sin\theta_{t4})\end{aligned} \tag{24}$$

Since A is the amplitude of the incident wave, it is desirable to find the transmitted signal N and the reflected signal B in terms of A.

Solution of equation (24) requires the knowledge of the propagation angle in the different media. The law of refraction at the interface $y = y_3$ is

$$\frac{\sin\theta_{t3}}{\sin\theta_{i3}} = \frac{\hat{n}_2}{n_3} \tag{25}$$

where θ_i is the incident angle and $\hat{n}_2 = n_2(1 + j\kappa)$ is the complex index of refraction of the plasma. Since the index of refraction is complex, the transmitted angle θ_{t3} is also complex and it therefore no longer has a simple significance as an angle of refraction.

Define

$$\cos\theta_{t3} = qe^{j\varphi} \tag{26}$$

Due to the plasma conductivity, the surfaces of constant amplitude and the surfaces of constant phase do not, in general, coincide with each other; the wave in the plasma is an inhomogeneous wave. An equivalent Snell's law is given by (ref. 5)

$$\sin \theta^*_{t3} = \frac{\sin \theta_{i3}}{\left[\sin \theta_{i3} + n^2 q^2 (\cos \varphi + \varkappa \sin \varphi)^2\right]^{1/2}} \tag{27}$$

where θ^*_{t3} is the true transmission angle and it is real, and

$$n^2 = \frac{\epsilon_3}{n_2^2 (1 + \varkappa^2)^2} \tag{28}$$

Furthermore, the Snell's law at $y = y_4$ is

$$\frac{\sin \theta_{i4}}{\sin \theta_{t4}} = \epsilon_3^{-1/2} \tag{29}$$

Solution of equation (22) yields both the reflection constant (B/A) and the transmission constant (N/A) (K/A for plasma halfspace model) in terms of the incident amplitudes.

The following quantities of interest are evaluated by the program for both polarizations for the m^{th} ray.

Transmission coefficient

$$T\Psi(x)_m = \left| \left(\frac{N}{A}\right)_m e^{j(\tau_5 - \tau_o)} \right|^2 \tag{30}$$

Phase of the transmitted signal

$$PT\Psi(x)_m = \tan^{-1} \left\{ \frac{\mathrm{Im}\left[\left(\frac{N}{A}\right)_m e^{j(\tau_5 - \tau_o)}\right]}{\mathrm{Re}\left[\left(\frac{N}{A}\right)_m e^{j(\tau_5 - \tau_o)}\right]} \right\} \tag{31}$$

Reflection coefficient

$$R\Psi(x)_m = \left| \left(\frac{B}{A}\right)_m e^{-2j\tau_o} \right|^2 \tag{32}$$

Phase of the reflected signal

$$PR\Psi(x)_m = \tan^{-1}\left\{ \frac{\mathrm{Im}\left[\left(\frac{B}{A}\right)_m e^{-2j\tau_o}\right]}{\mathrm{Re}\left[\left(\frac{B}{A}\right)_m e^{-2j\tau_o}\right]} \right\} \tag{33}$$

where

$$\tau_o = k_o \sqrt{\epsilon_o}\, y_o$$

and

$$\tau_5 = k_o \sqrt{\epsilon_o} \left\{ y_5 \cos \theta_{t4} \right\} \tag{34}$$

Deflection path for the m^{th} ray is described by

$$x_{3m} = x_m + \frac{L^2}{4} f(x = x_m)$$

$$\gamma_{3m} = \epsilon_2(x = x_3) \cos^2 \theta_{i3}(x = x_3)$$

$$x_{4m} = x_{3m} + \ell_3 \left(\frac{\sin \theta^*_{t3}}{\cos \theta^*_{t3}} \right)_m \tag{35}$$

$$x_{5m} = x_{4m} + \left[(\ell_3 + \frac{L}{2}) - \frac{D}{2} \right] \left(\frac{\sin \theta_{t4}}{\cos \theta_{t4}} \right)_m$$

APPLICATION

Bounded Plasma Slab or Halfspace

For a bounded plasma slab or in the halfspace models, we define a total power transmission coefficient

$$WT\Psi = \frac{1}{h_1} \left| \int_{x_o}^{x_o + h_1} \left(\frac{N}{A} \right)_m e^{j(\tau_5 - \tau_o)}\, dx \right|^2 \tag{36}$$

where h_1 is the width of the receiver.

Phase of the transmitted signal

$$PT\Psi = \tan^{-1}\left\{\frac{\mathrm{Im}\left[\frac{1}{h_1}\int_{x_o}^{x_o+h_1}\left(\frac{N}{A}\right)_m e^{j(\tau_5-\tau_o)}\,dx\right]}{\mathrm{Re}\left[\frac{1}{h_1}\int_{x_o}^{x_o+h_1}\left(\frac{N}{A}\right)_m e^{j(\tau_5-\tau_o)}\,dx\right]}\right\} \tag{37}$$

Similarly, the total reflection coefficient

$$R\Psi = \frac{1}{h_1}\left|\int_{x_o}^{x_o+h_1}\left(\frac{B}{A}\right)_m e^{-2j\tau_o}\,dx\right|^2 \tag{38}$$

and the phase of the reflected signal

$$PR\Psi = \tan^{-1}\left\{\frac{\mathrm{Im}\left[\frac{1}{h_1}\int_{x_o}^{x_o+h_1}\left(\frac{B}{A}\right)_m e^{-2j\tau_o}\,dx\right]}{\mathrm{Re}\left[\frac{1}{h_1}\int_{x_o}^{x_o+h_1}\left(\frac{B}{A}\right)_m e^{-2j\tau_o}\,dx\right]}\right\} \tag{39}$$

If the beam of incident radiation x_m is intercepted by a plane of a distance d after the ray emerges from the plasma, then the refractive defocusing introduced by the non-uniform electron density variation of the slab, η, is given by

$$\eta(x) = \frac{1}{1 + d\,\dfrac{\tan\theta(x)}{x}} \tag{40}$$

The effect of the non-uniform electron distribution in the plasma slab can be thought of as a plasma lens of constant electron density but shaped so as to give the same phase change to an incident plane wave as does the plasma slab.

For a plasma halfspace the above results are applicable after setting $\epsilon_3 = 1$ and $\ell_3 \to \infty$, i.e., very large, and substituting K/A as transmission constant into equations (36) and (37).

Shock Tube Application

For the shock tube application where the ionization shock front travels past the receivers, the electron density is a function of space and time. Therefore, to evaluate experimental data one must include the electron density profile and also the so-called "partial filling" effect. We define a coordinate system $x = vt$ where v is the velocity of the shock wave and t is the time.

First, we have to obtain the transmission coefficient for the bounded plasma slab which is given by equation (30), and the reflection coefficient equation (31), then define new functions, i.e., perform an integration in the moving coordinate system.

$$U(x) = \int_0^x T\Psi(x)\, dx$$

$$V(x) = \int_0^x R\Psi(x)\, dx \qquad 0 \le x \le x_{test} \tag{41}$$

These new functions represent the transmitted and reflected power per unit area, respectively.

Note that the integration must be performed at the $y = y_5$ plane, and the spacings are no longer even, due to the bending of the m^{th} ray.

Finally, we obtain the microwave response functions:

Transmission response

$$P(x) = \frac{1}{h_1} \left\{ \left[U(x)\right]_{x = x} - \left[U_1(x)\right]_{x = x - h_1} \right\} \tag{42}$$

Reflection response

$$R(x) = \frac{1}{h_1} \left\{ \left[V(x)\right]_{x = x} - \left[V_1(x)\right]_{x = x - h_1} \right\} \tag{43}$$

where

$$\left.\begin{aligned} V_1(x) &= 0 \\ U_1(x) &= x - h_1 \end{aligned}\right\} \qquad 0 \le x \le h_1$$

$$\left.\begin{aligned} U_1(x) &= U(x) \\ V_1(x) &= V(x) \end{aligned}\right\} \qquad h_1 \le x \le x_{test} \tag{44}$$

DISCUSSION OF RESULTS

Three main items are considered, namely, comparison with previous theoretical work, studying the effect of different electron density profiles on transmitted, reflected power, and refractive defocusing caused by the electron density gradient. Finally, application to microwave diagnostics for a shock tube experiment has been shown.

Comparison with Previous Work

This comparison refers to theoretical solutions given by reference 1 for bounded uniform plasma. Excellent agreement is found in figure 3.

Effect of Electron Density Gradient

A plane homogeneous electromagnetic wave entering into the plasma goes through a continuous bending due to the electron density gradient. The emerging wave, as a result of this non-uniform bending, is a nonhomogeneous wave. The ray incident upon the plasma slab at a distance x refracts, so that it emerges at some angle $\theta(x)$. Figure 4 gives the variation of the exit angle $\theta(x)$ of the wave for the electron density distributions given in figure 2.

It is interesting to note that the absolute value of the refraction angle is nearly equal for similar profiles, i.e., increasing or decaying. Furthermore, for actual antenna pattern calculation, the electron density profiles must be included since the refraction angle can vary two orders in magnitude.

Figure 5 shows the effect of maximum electron density and collision frequency on the refraction angle. Higher electron density yields higher refraction. Meanwhile, higher collision frequency tends to decrease the ray bending.

Sample calculations were performed for a plasma slab bounded by dielectric windows with dimensions that would yield minimum reflection. Microwave horn location was $1.0 < x < 4.18$, and the normalized collision frequency was assumed to be equal to $\bar{\nu} = .1$. Figures 6 and 7 show power transmission

coefficient and reflection coefficient, respectively, for the electron density distributions given in figure 2. In general, we can say that depending on the distribution and horn location, the relative differences between various profiles can be as much as an order in magnitude. This implies that proper selection of the plasma profile used in predictions or data interpretation can be critical.

Comparison with Experiment

New results refer to the Gaussian distribution which provides a realistic description of electron density profiles behind an ionization shock front. Configuration for the plasma slab, the window dimensions and material was chosen to be equal to that used by Dr. A. Modica of Avco Systems Division. Pertinent physical parameters are as follows: teflon window thickness $\ell = 1.52$ cm and its dielectric constant $\epsilon_2 = 2.08$, the plasma thickness $L = 3.82$ cm, and the microwave frequency $f = 9.55$ GHz. Gas mixture containing air and excess argon in mole ratios of 5:100 was heated with the reflected shock.

In these experiments, the transmitted and reflected power amplitudes were recorded as a function of time on a dual beam Tektronix oscilloscope. The collision frequency which controls the ohmic losses in the plasma is assumed to be uniform and is an input. The remaining two parameters, namely, α, the Gaussian variance, and the equilibrium plasma density, were estimated from the oscilloscope photo and equilibrium calculation, respectively.

With these inputs, the present work obtained the response function, which is in excellent agreement with those obtained by the experiment. By trial and error method (generally required 2-3 runs) the final parameters were easily obtained. Figure 8 gives results for a collision frequency $\bar{\nu} = 1.89$ and shock velocity $v = 8.23\ 10^4$ cm/sec. The equilibrium electron density is underdense. One can see that at certain time instants the electron density gradient cannot be neglected across the microwave receiver which has $h_1 = 3.18$ cm. The maximum variation across the horn is about a factor of two in electron density. Figure 9 gives the variation of the exit angle $\theta_3(x)$ of the wave. Figure 10 gives the transmission response for an overdense plasma condition.

CONCLUSIONS

This paper describes a computer solution of the interaction of a plane electromagnetic wave with a bounded inhomogeneous plasma slab. The electron density gradient is transverse to the incident wave propagation direction.

A plane homogeneous electromagnetic wave entering into the plasma goes through a continuous bending due to the electron density gradient. The emerging wave, as a result of this non-uniform bending, is a nonhomogeneous wave. Absolute value of the refraction angle can vary two orders in magnitude depending on the transverse gradient and, hence, cannot be neglected in

calculating transmission through a plasma boundary layer.

This model has been applied to a shock tube experiment where the test gas slug moves across the field between the transmitter and receiver. Hence, the electron density is a function of space and time. Results indicate that this experimental data analysis is very accurate and simple to apply.

Both theoretical analyses and application to test data show the importance of using the proper plasma density profile in the calculations.

REFERENCES

1. Bachynski, M. P., et al, "Microwave Measurements of Finite Plasma," RCA Report 7-801-26, May 1963.

2. Gal, G. and Gibson, W. E., "Interaction of Electromagnetic Waves with Plasma Cylinder," IEEE Antenna and Propagation, Vol. 16, No. 4, pp. 468-475, July 1968.

3. Albini, Frank A., "Approximate Evaluation of Slender Radome Performance in Hypersonic Flight," AIAA Journal, Vol. 2, No. 3, March 1964.

4. Ravid, E., "Determination of Longitudinal Shock Wave Profiles in a Microwave Fabry-Parot Interferometer," Physics of Fluids, Vol. 6, No. 7, July 1963.

5. Born, M. and Wolf, E., Principle of Optics, MacMillan Co., New York, New York, 1957.

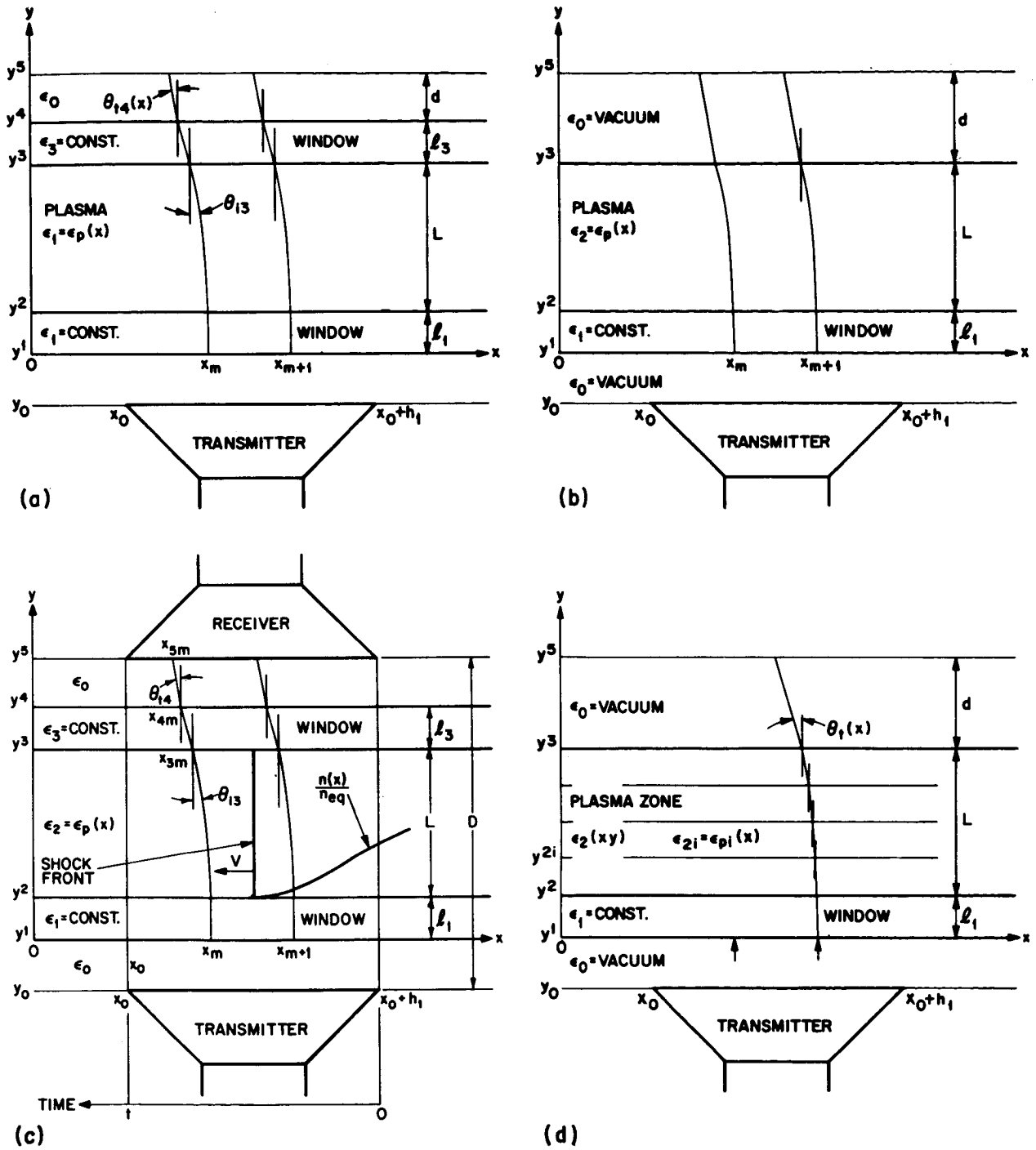

Figure 1.- Geometry of the various problems.

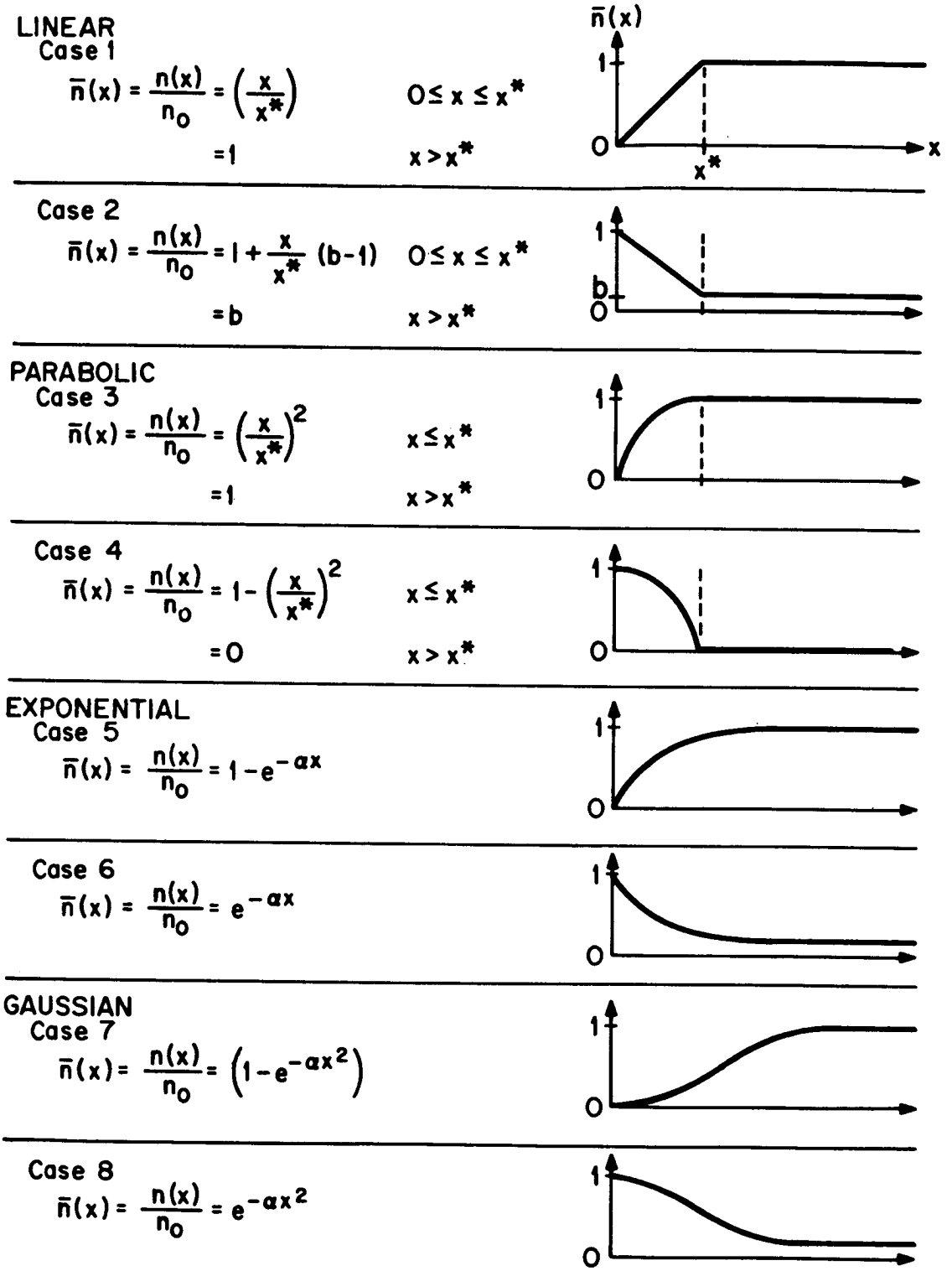

Figure 2.- Typical electron density variations.

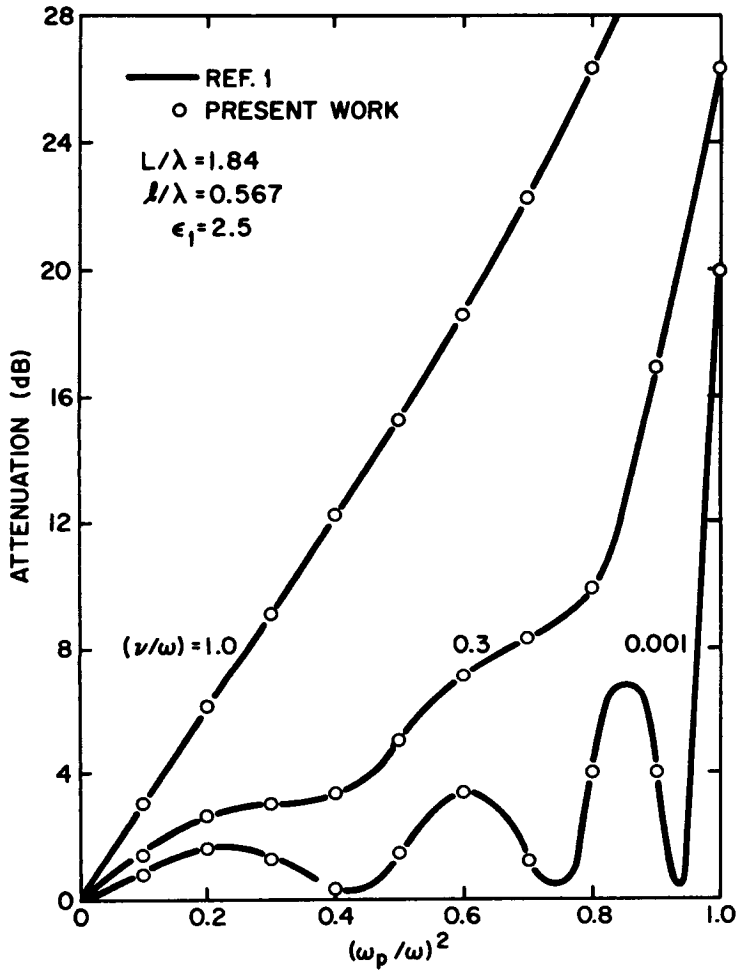

Figure 3.- Variation of attenuation with normalized plasma frequency, for various values of collision frequency.

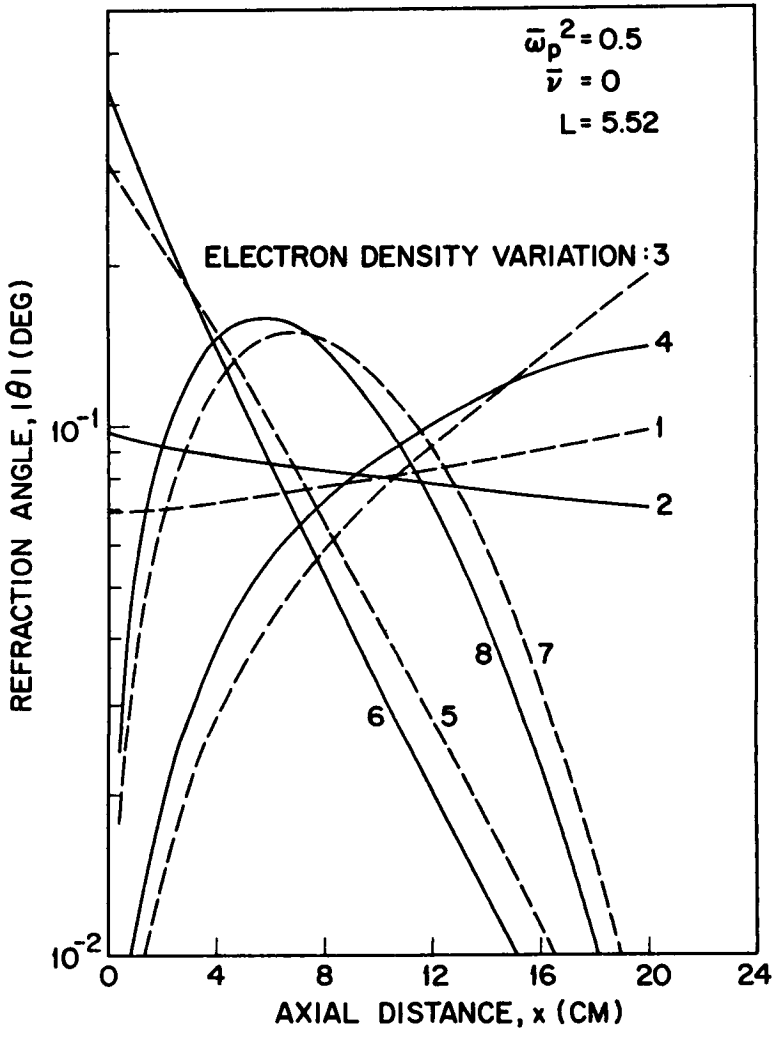

Figure 4.- Refraction angle distribution for different electron density variations.

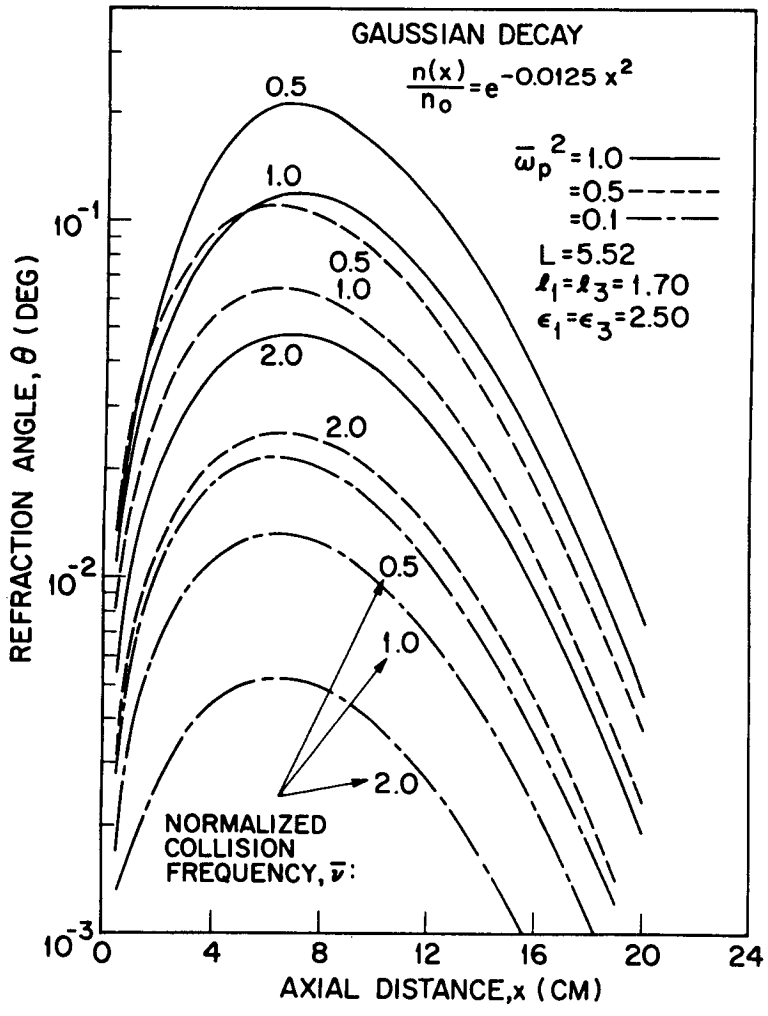

Figure 5.- Influence of plasma and collision frequency on refraction angle for Gaussian electron density decay.

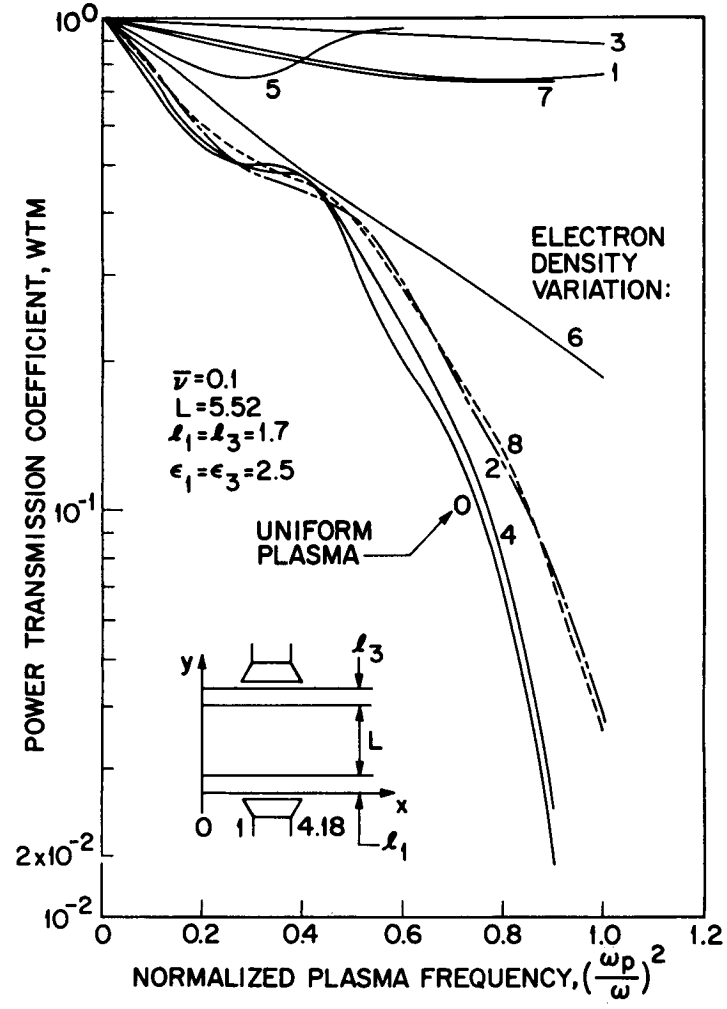

Figure 6.- Variation of power transmission coefficient with normalized plasma frequency for various electron density functions.

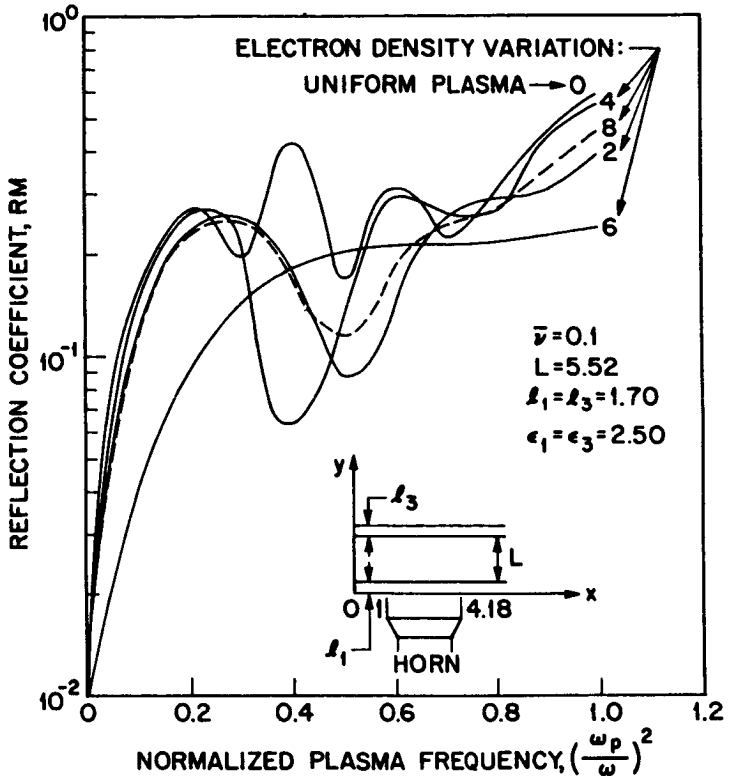

Figure 7.- Variation of reflection coefficient with normalized plasma frequency for various electron density functions.

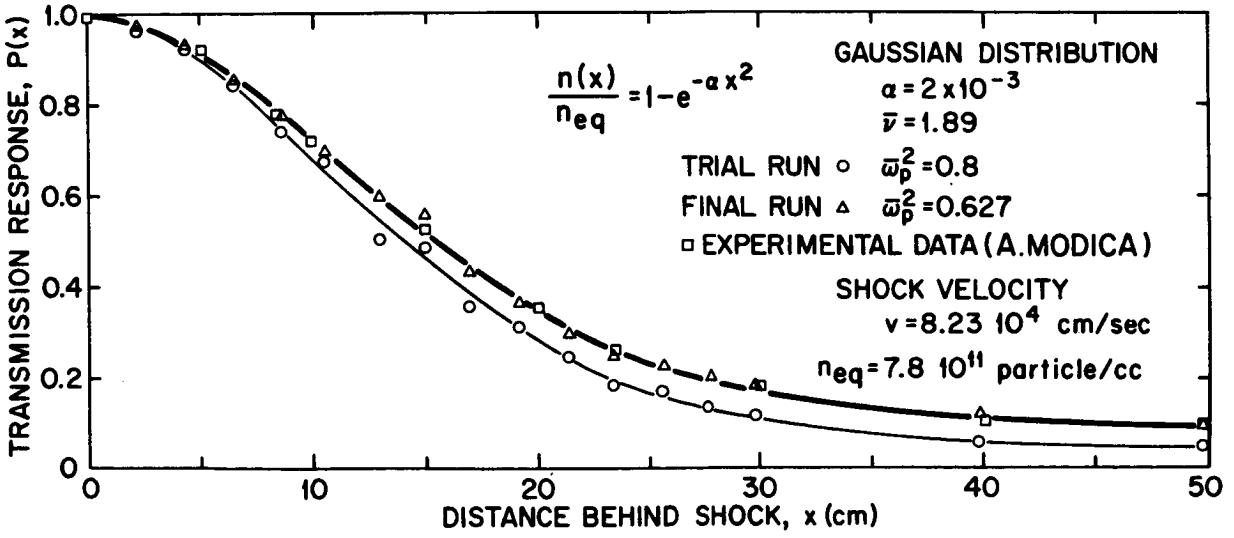

Figure 8.- Transmission response as a function of time for an underdense plasma behind a moving shock front.

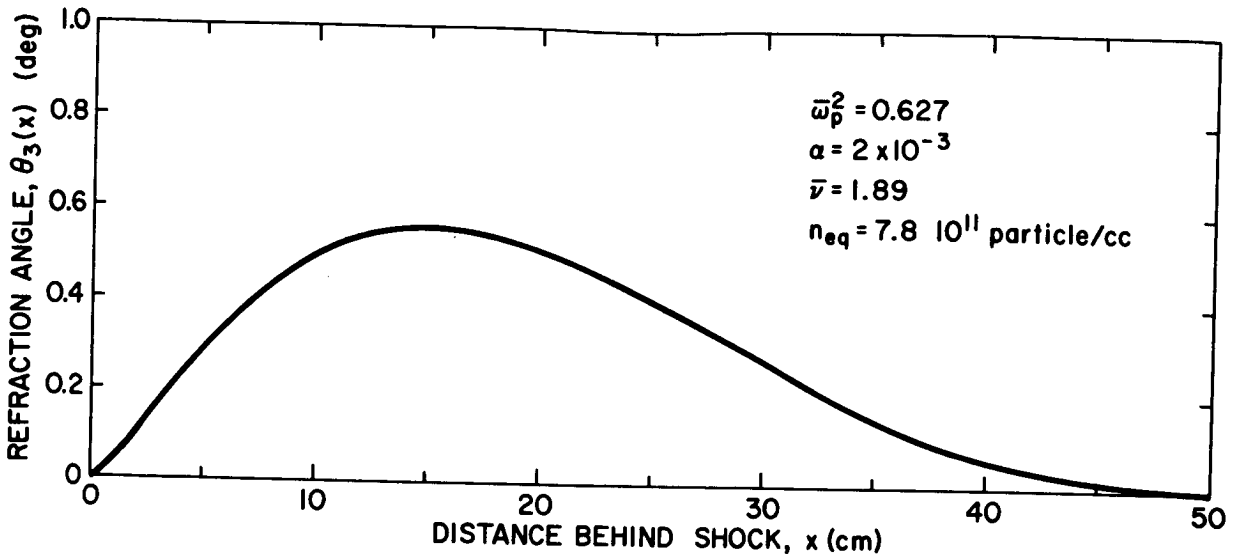

Figure 9.- Refraction angle as a function of time.

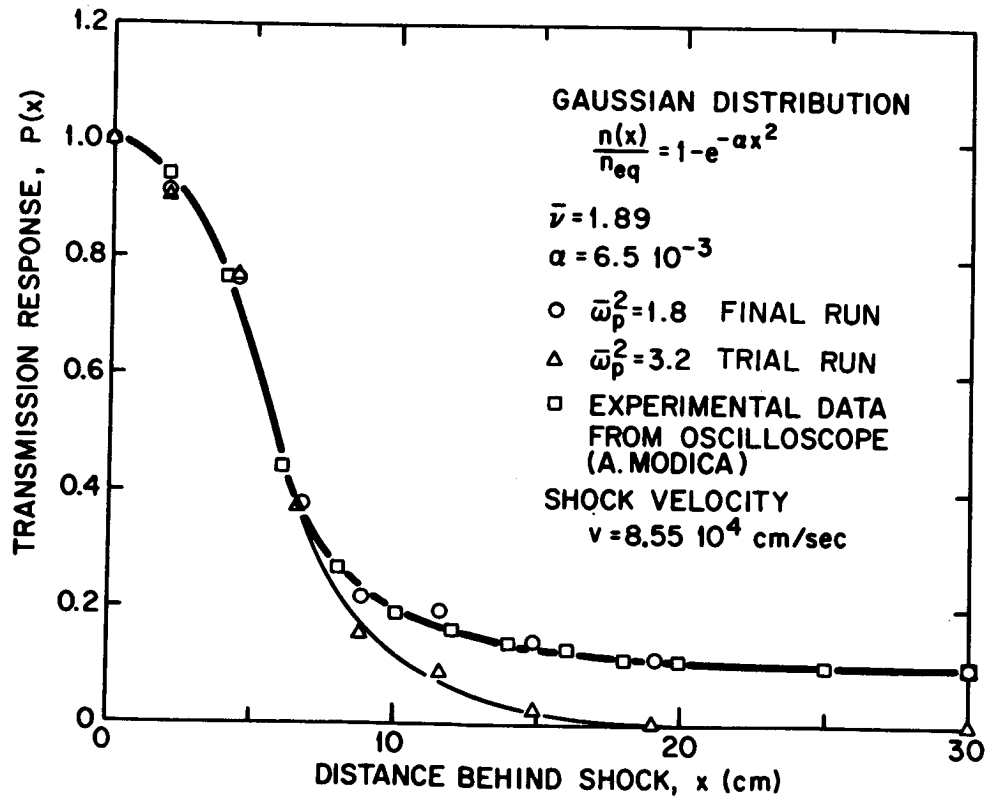

Figure 10.- Transmission response as a function of time for an overdense plasma behind a moving shock front.

AN AUTOMATIC ANTENNA IMPEDANCE MATCHER FOR REENTRY VEHICLE APPLICATIONS

By John S. Potts*
University of Akron, Akron, Ohio

Walter M. Hart, Jr., Lt Col, USAF and
Edward S. Bocian, Jr., Lt, USAF

Air Force Weapons Laboratory
Kirtland Air Force Base, New Mexico

SUMMARY

An antenna impedance compensator which can automatically maximize the power radiated from an X-Band antenna into a time-varying reflective medium is described. The compensator consists of a reflectometer for sensing the complex reflection coefficient of the antenna, two variable ferrite phase shifters which function as an electronic slide screw tuner, and a feedback circuit which processes signals from the reflectometer for use by the tuner. The compensator provides up to a 6 dB improvement in radiated power for a voltage reflection coefficient of 0.97 and responds to any mismatch in less than 3 milliseconds. It is concluded that this technique can provide an effective solution to the communications "blackout" problem for highly reflective time-varying reentry plasma conditions.

INTRODUCTION

The plasma sheath which surrounds a vehicle on reentry into the earth's atmosphere at hypersonic speeds is a lossy, reflective, and time-varying medium. Onboard transmitting antennas adequately tuned before vehicle launch become mismatched by the plasma and heating encountered during reentry.

Signal losses internal to the boundary layer plasma are determined by the heatshield material, the vehicle geometry, and the trajectory. These can be reduced only by changing the vehicle or its environment,

*Formerly of the University of New Mexico, where this work was performed under contract for the Air Force Weapons Laboratory.

or by plasma alleviation near the antenna. But reflective losses produced by the time-varying mismatch of the antenna to its surroundings can be eliminated independently by reducing the VSWR to 1.0 in the line feeding the antenna.

This project developed a device to automatically maximize the power radiated from a reentry vehicle antenna by eliminating the reflected power otherwise dissipated as heat within the transmitter.

SYMBOLS

E_o	flat line voltage
K	a multiplicative factor indicative of transmitter output power variations
V_{pos}, V_{ins}	position and insertion phase shifter control voltages
V_1, V_2	detector output voltages
λ	wavelength of carrier
ρ	reflection coefficient
ψ	reflection coefficient polar angle

THEORETICAL OPERATION OF THE IMPEDANCE MATCHER

General Considerations

The operational environment imposes a number of restrictions on any impedance matcher intended for use on an R/V. The device must respond quickly enough to follow both secular and fluctuating changes in the mismatch imposed by the boundary layer. It should be simple, rugged, lightweight, and, preferably, all electronic with no moving parts. Both operating power and insertion loss should be low. Otherwise the device will dissipate any power gained by canceling reflections.

The basic configuration selected for the impedance matcher is diagramed in figure 1. It is an analog device. A reflectometer and an electronic slide screw tuner are placed between a transmitter and its antenna. The reflectometer senses any mismatch of load to source, and supplies this information to a feedback control signal generator. This, in turn, controls the tuner to produce a matched condition in the line.

The impedance matcher is designed to operate between 9.0 and 10.0 GHz. It differs in hardware, more than theory, from previous designs intended for VHF applications. (See Ref. 1, for example).

The Electronic Slide Screw Tuner

The electronic slide screw tuner includes two phase shifters. One, the "position phase shifter", is placed in the line feeding the antenna. A second, the "insertion phase shifter", is terminated in a short and connected to the branch of a tee in shunt with the position phase shifter. See figure 1.

By varying the effective path length in the position phase shifter, the admittance seen at the plane of the tee is set to the characteristic admittance of the line -- a real quantity -- plus some imaginary part. Then the insertion phase shifter is used to cancel the imaginary part of the admittance at the tee by changing the effective distance to the short.

This matching process is illustrated in the Smith chart of figure 2. For illustration, the phase shifters are assumed lossless, and the distances of antenna and short from the tee are each chosen equal to $\lambda/2$. Then, with zero phase shift inserted in each line, the mismatches produced by both terminations appear unchanged at the plane of the tee. The position phase shifter rotates the load to the unit (normalized) resistance circle along a circular arc. The constant radius corresponds to a reflection coefficient of constant magnitude. The sense of rotation is towards the generator since the phase shifter increases the effective separation of tee and antenna. This control is terminated in the lower half-plane of the Smith chart. Then the insertion phase shifter rotates the short on the locus $|\rho| = 1$, inserting the susceptance required to give a matched line.

All admittances are normalized to the characteristic admittance of the line. This construction, it should be noted, is valid at only a single frequency because component separations and phase shifter outputs are expressed in terms of the wavelength of the carrier.

Figure 3 depicts the theoretical performance of the impedance matcher when various insertion losses are assigned to the two phase shifters. These results were obtained using the equivalent circuit for a waveguide tee given in reference 2. Radiated power is referenced to a lossless matched condition and plotted versus the magnitude of the antenna voltage reflection coefficient. The dashed curve represents the radiated power without compensation. At high reflection coefficients, the compensator can provide a significant gain in radiated power. But notice that a phase shifter insertion loss much over 0.8 dB can completely eliminate this advantage. An 0.2 dB loss in each phase shifter seemed within the state of the art of ferrite phase shifter design and was selected as a

design goal. A loss of 0.2 dB, in figure 3, is an upper limit for realizing a 6 dB improvement in radiated power over the uncompensated case. At this loss figure a 6 dB power boost is expected near a load reflection coefficient of 0.97.

The Reflectometer

For simplicity of construction and to avoid excessive loading of the transmitted signal, a two-probe reflectometer was selected over competing devices for the advanced prototype impedance matcher.

For convenience in description, suppose that the first probe is positioned an integral multiple of $\lambda/2$ from the tee of the tuner. With the second probe $\lambda/8$ beyond the first, ideal square law diodes produce the signals

$$V_1 = E_o^2(1 + |\rho|^2 + 2|\rho| \cos \psi)$$

$$V_2 = E_o^2(1 + |\rho|^2 - 2|\rho| \sin \psi)$$

These equations assume tee and load are likewise an integral multiple of $\lambda/2$ apart. To obtain control signals that will become zero for a matched condition, the flat line readings E_o^2 must be subtracted from both of these signals, leaving

$$V_{pos} = E_o^2(|\rho|^2 + 2|\rho| \cos \psi)$$

$$V_{ins} = E_o^2(|\rho|^2 - 2|\rho| \sin \psi)$$

for the position and insertion phase shifter control signals, respectively. If the transmitter provides a constant output power, E_o^2 may be subtracted from the diode outputs using a constant bias voltage supplied to differential amplifiers in the signal processor. But should transmitter output vary, a directional coupler must be used to sense the transmitted wave and provide this signal. Otherwise, the control signals become

$$V_{pos} = KE_o^2((1-1/K) + |\rho|^2 + 2|\rho| \cos \psi)$$

$$V_{ins} = KE_o^2((1-1/K) + |\rho|^2 - 2|\rho| \sin \psi)$$

where K is a factor proportional to the output power of the transmitter (K = 1 indicates no variation). With $K \neq 1$, when the impedance matcher has reduced V_{pos} and V_{ins} to zero simultaneously, a residual reflection coefficient will exist. Figure 4 plots residual $|\rho|$ as a function of K for several different probe separations. Though several other probe separations indicate an improvement in this respect over the value $\lambda/8$

chosen for the prototype, other considerations affected this choice. Some of these factors are the ease of construction, stability, the speed of correction for an arbitrary mismatch, and phase shifter requirements. It can be shown that some probe separations exceeding $\lambda/6$ permit $V_{pos} = V_{ins} = 0$ at nonzero $|\rho|$ as well as at the matched condition $|\rho| = 0$, so these cases were naturally excluded from consideration.

The Smith chart in figure 5 indicates the circular arcs along which V_{pos} and V_{ins} are respectively zero for the advanced prototype, assuming E_o^2 is correctly monitored. The two arcs intersect only at the matched condition $|\rho| = 0$. Regions where each signal is positive or negative are indicated.

The correction scheme chosen for the impedance matcher can be visualized in figure 5. If $V_{pos} > 0$, the position phase shifter will increase in phase; if $V_{pos} < 0$, it will decrease. A maximum increase in phase shift of 120° -- decreasing the reflection coefficient angle 240° -- and a maximum decrease in phase shift of 90° -- increasing the reflection coefficient angle by 180° -- is sufficient to reach any point on the diagram. These extremes are required on arcs $|\rho| = 1$ and $|\rho| = 0$, respectively, to swing between opposite points on the locus $V_{pos} = 0$. The insertion phase shifter may then be set to zero initially and, if $V_{ins} > 0$, allowed to increase up to a maximum phase shift of 90°.

This scheme provides unambiguous correction to a matched condition. However, a fluctuating mismatch may demand more or less phase shift than is available depending on the instantaneous settings of the phase shifters. In this event, a reset capability must be available to the control system to place both phase shifters to starting locations from which they can converge to a matched condition for any load other than a pure short.

Notice that a total of 210° of phase shift is required of the position phase shifter, 90° of the insertion phase shifter. Also note that the loci of zero V_{pos} and V_{ins} move if the frequency is changed.

The control circuitry will be discussed after the phase shifter and reflectometer hardware are described.

IMPEDANCE MATCHER HARDWARE

The Phase Shifters

Ferrites have resistivities of the order of 10^7 ohm-meters, and very low eddy current power losses. Several investigators have used circular ferrite rods in waveguide for phase shifters. (See Refs. 3 through 6). Other configurations using ferrite slabs have not demonstrated such low insertion losses, and suffer from decreased bandwidth. So it was decided to investigate phase shifters with circular ferrite rods for this application.

The cores chosen for the impedance matcher are pictured in figure 6. These are 1/4" diameter rods, with tapered ends, packed in polystyrene with a relative dielectric constant of 1.3 and placed in aluminum waveguide in a Reggia-Spencer configuration (see reference 3). The material is a Mg-Mn ferrite, Ceramagnetics type MGM-11-MW. The phase shift can be controlled by an externally applied longitudinal DC magnetic field.

The ends of the rods are tapered to reduce reflections, so that the transmitted wave will be as little disturbed as possible. Figure 7 shows the effects of taper on reflection. The taper lengths chosen are compromises between low reflections and unwieldy ferrite lengths. Attempts to eliminate the taper facing the short in the insertion phase shifter, and to attach the core directly to the short merely increased the total ferrite length required for a given phase shift. The portion of the core adjoining the short was ineffective as a phase shifter.

Figure 8 plots phase shift versus control current at several frequencies of interest for the position phase shifter. In general, phase shift increases with frequency and with control current. Similar results are observed for the insertion phase shifter, but, since it is shorter, the corresponding phase shifts are less.

The phase shifter coils were designed for 28 volt operation, at a maximum control current of 80 mA. They consist of about 4900 turns of No. 34 gauge magnet wire, resulting in about 350 ohms of resistance and 0.18 henries of inductance. A narrow silt, 5 to 10 mils wide, was cut along the full length of each phase shifter waveguide with an electrical discharge machine. The resultant gaps allowed negligible leakage losses but prevented eddy current losses in the waveguide structure induced by the control currents. This effectively prevented the degradation of phase shifter time response observed, without the slits, in earlier prototypes.

The phase shifters reflect less than 2% of incident power for all control currents. Figure 9 shows the position phase shifter insertion loss versus frequency at two control current levels. These latter results

are in essential agrement with the losses of a phase shifter without a longitudinal slit. Notice that a resonant absorption occurs near 9.9 GHz, limiting the useful bandwidth of the device in this direction.

Figure 10 shows loss versus control current at several frequencies. The losses are below 0.25 dB for all these control currents and frequencies and are less than 0.2 dB at the center frequency of 9.5 GHz for up to 75 mA of control current. This loss figure was the design goal. Similar results were obtained for the insertion phase shifter.

The Reflectometer

The reflectometer was designed with two HP 444A broad band probes, separated $\lambda/8$ at 9.5 GHz, and mounted in an aluminum block, since it proved impossible to mount them directly on the tee. The aluminum mount was designed to be reversible for testing and to set the insertion probe exactly $9/8\lambda$ from the plane of the tee at either 9.25 GHz, in one direction, or 9.75 GHz in the reverse direction. This permitted testing in the two regimes, 9.0-9.5 GHz and 9.5-10.0 GHz, separately. The detectors were 1N76 diodes.

Control Circuitry

The control circuits include signal amplifiers, phase shifter drivers, and a reset circuit. No attempt was made to miniaturize the electronics in this prototype.

The differential amplifiers receiving outputs from each reflectometer probe can be switched to subtract either a DC reference voltage or an external measurement of the flat line probe outputs from each correction signal. These amplifiers have a slew rate greater than 50 V/μsec; this is necessary for the stability of the entire feedback system.

The reset circuit senses when a phase shifter driver transistor is either cut off or in saturation. In both cases, it bypasses the control signals to the drivers, resets the transistors to an intermediate state, and then returns control to the feedback loop.

The electronic circuitry does not limit the response time of the compensator. The phase shifters do.

OVERALL RESPONSE OF THE IMPEDANCE MATCHER

The impedance matcher was tested with several variable mismatches. One of these was a four-vane metal star, mounted on a shaft and partially inserted into a slotted waveguide. It could be rotated to produce a cyclic mismatch. $|\rho|$ could be varied from 0 to 0.95 in as little as

15 milliseconds. Perfect compensation was obtained except during reset when spikes occurred in the reflection coefficient. Reset time was between 1 and 2 milliseconds with this load, and the reflection coefficient was back to 0 within 3 milliseconds more. The longest reset time observed, for all tests, was 6 milliseconds. It should be noted that reset occurs only with rapid changes in the angle of the reflection coefficient. In normal operation, the compensator is expected to be in a reset condition during only a very small percentage of the time.

Figure 11 depicts the response of the compensator to a step mismatch. Correction occurs within a millisecond.

Figure 12 plots power radiated, with and without the prototype compensator, versus uncompensated reflection coefficient. This data was obtained at four frequencies.

With a detector sensing the output power of the transmitter, the compensator successfully follows variations in this power of as much as 50%.

The maximum instantaneous power dissipated by the device was 3.4 watts. It operated near 2.1 watts minimum and 2.64 watts average, within the design goal of 3 watts on the average.

The bandwidth was near 0.2 GHz for a center operating frequency of 9.5 GHz. Bandwidth was limited because the probes occupied fixed locations and were somewhat mismatched in frequency response.

The prototype, without miniaturization, weighed 4.68 lb, 2.10 lb without the electronics. Corresponding volumes were 266 cu in. and 16 cu in. Reduction in the size of the electronics could be easily accomplished to bring the total system within the 3 lb and 50 cu in. originally envisioned.

CONCLUDING REMARKS

The compensator worked essentially as predicted, but there is some room for improvement. The electronics should be miniaturized, new ferrites tested for the phase shifters as they become available, the probes and reflectometer reduced in size, and more sensitive probes used to reduce the gain required of the electronics. Reset time, as well, can be reduced.

Finally, it is concluded that this project lays the groundwork for flight tests of an impedance matcher.

REFERENCES

1. Wolff, Edward A.: An Automatic Impedance Matcher. Electromagnetic Research Corporation, Report No. 61044-1, 1960.

2. Marcuvitz, N.: Waveguide Handbook, Dover Publications, Inc., New York, 1965.

3. Reggia, F., and Spencer, E. G.: A New Technique in Ferrite Phase Shifting for Beam Scanning of Microwave Antennas, Proc. IRE, Vol. 45, November 1957, pp. 1510-1517.

4. Jones, H., and Reggia, F.: Some Unique Designs of Microwave Ferrite Phase Shifters. HDL TR-1189, 1963.

5. Hodgson, B. A.: The Development of Wideband Waveguide-Mounted Ferrite-Pencil Phase Shifters for X-Band. Royal Aircraft Establishment, TR-66337, 1966.

6. Reggia, F.: C-Band Reciprocal Ferrite Phase Shifters and Amplitude Modulators. HDL TR-1284, 1965.

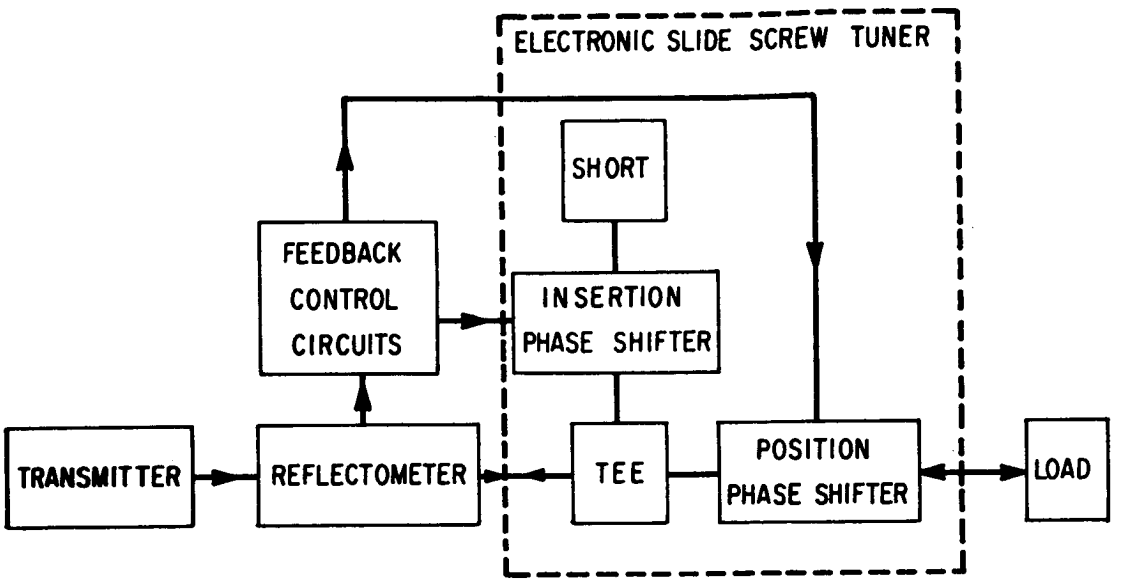

Figure 1.- Block diagram of the automatic impedance matcher.

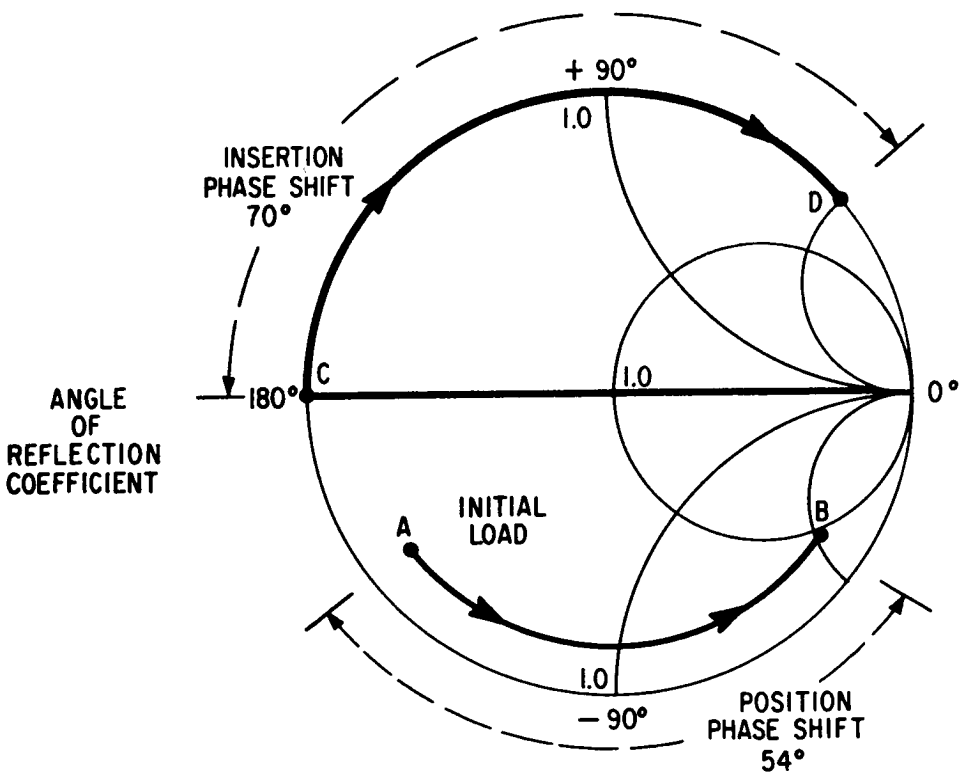

Figure 2.- Electronic slide screw tuner compensation.

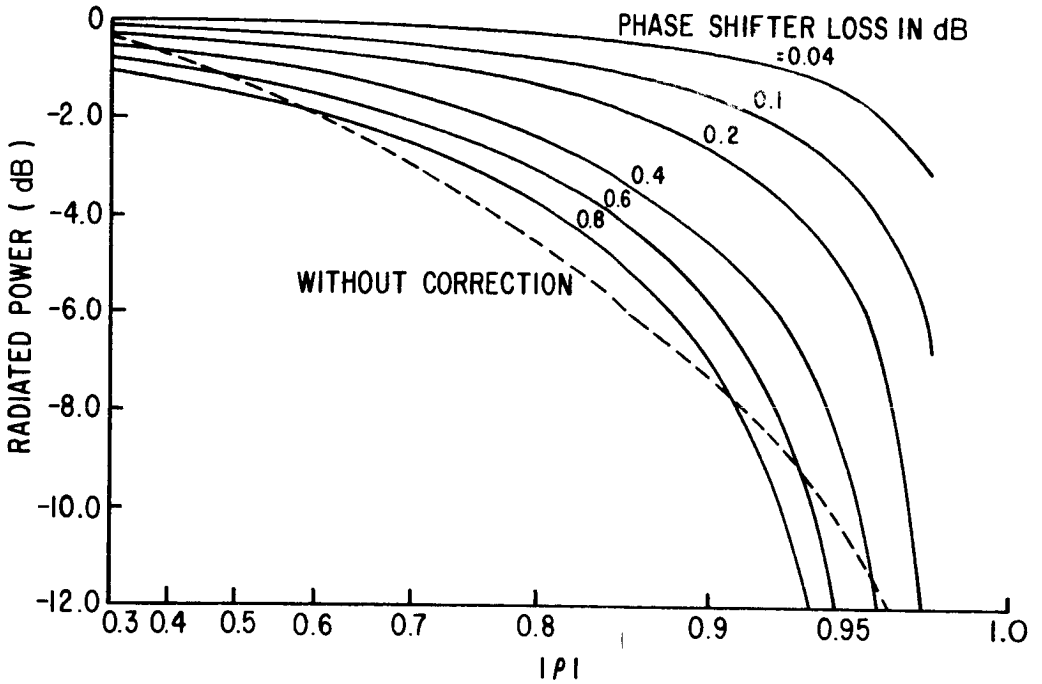

Figure 3.- Theoretical performance of a compensator with various phase shifter insertion losses.

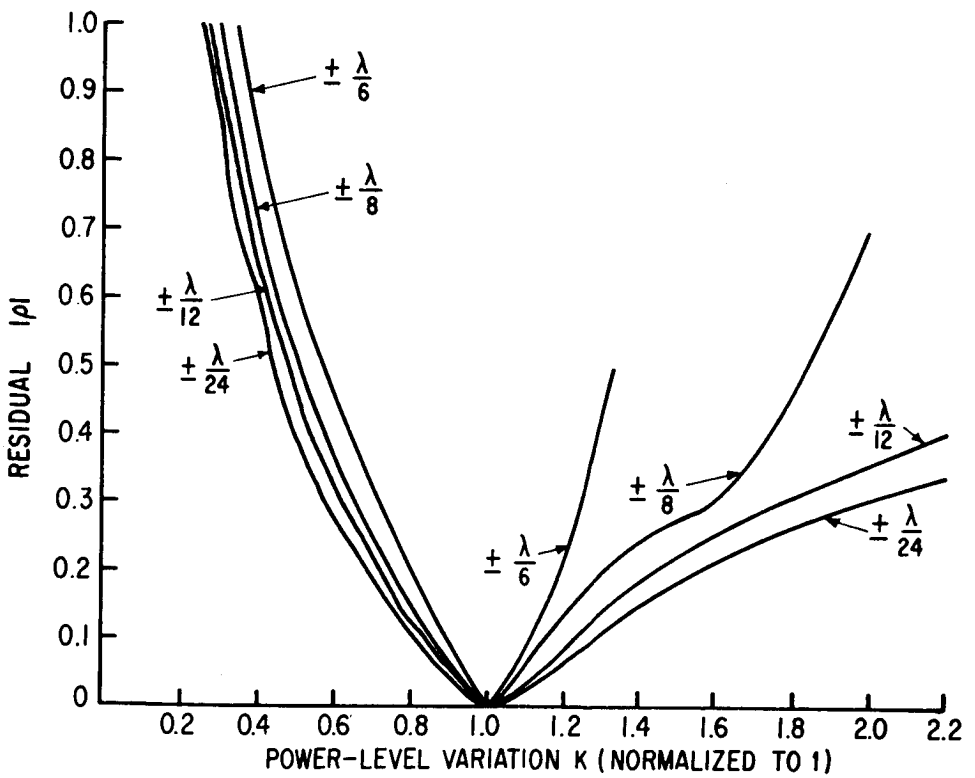

Figure 4.- Residual reflection coefficient versus power level variation.

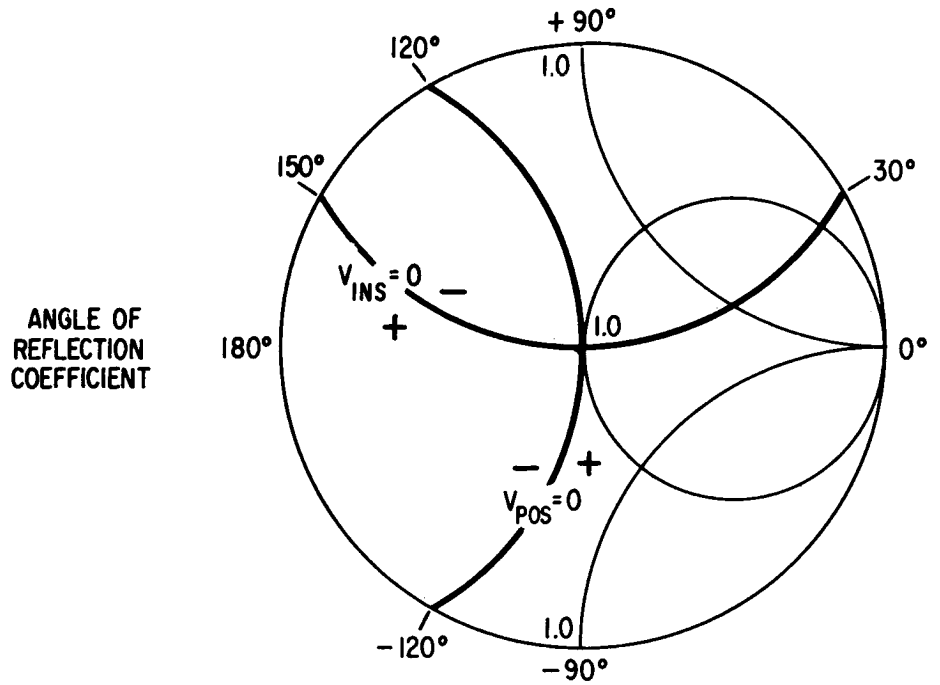

Figure 5.- Phase shifter control signals.

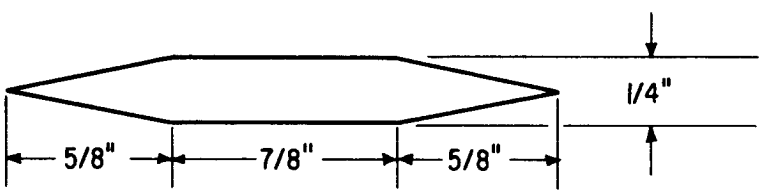

INSERTION PHASE SHIFTER

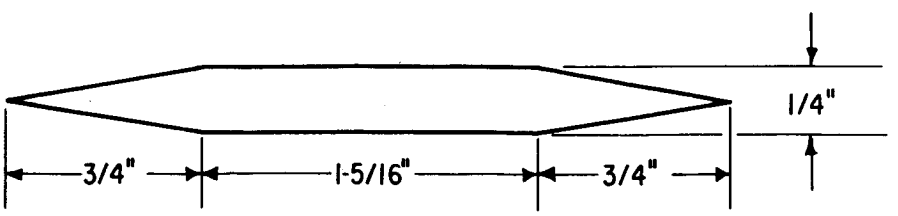

POSITION PHASE SHIFTER

Figure 6.- Construction of the ferrite rods. Cross sections are circular.

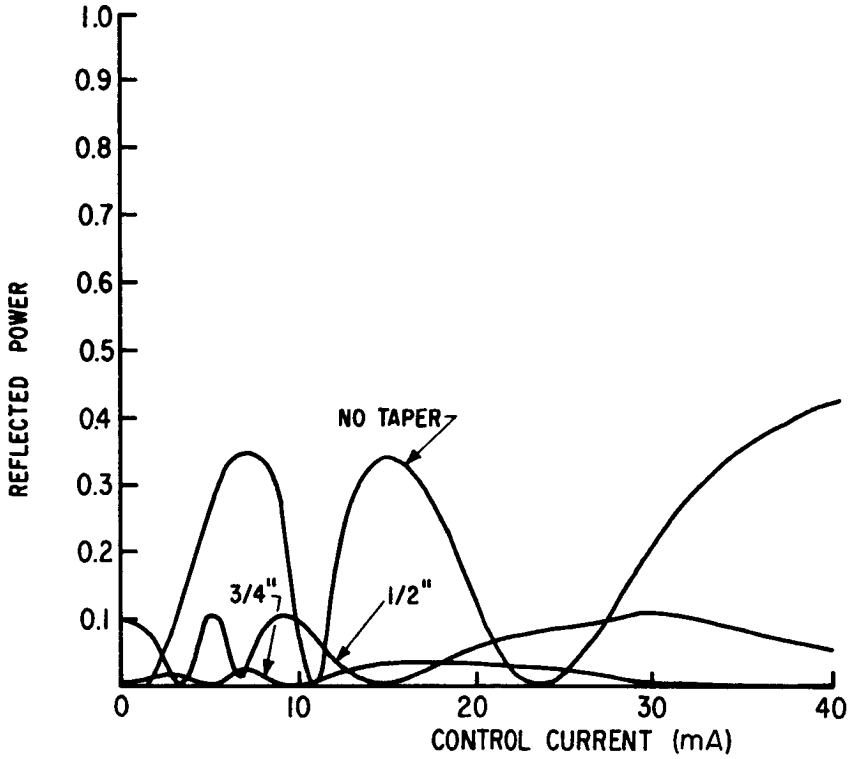

Figure 7.- Effects of ferrite taper on reflections from the phase shifters.

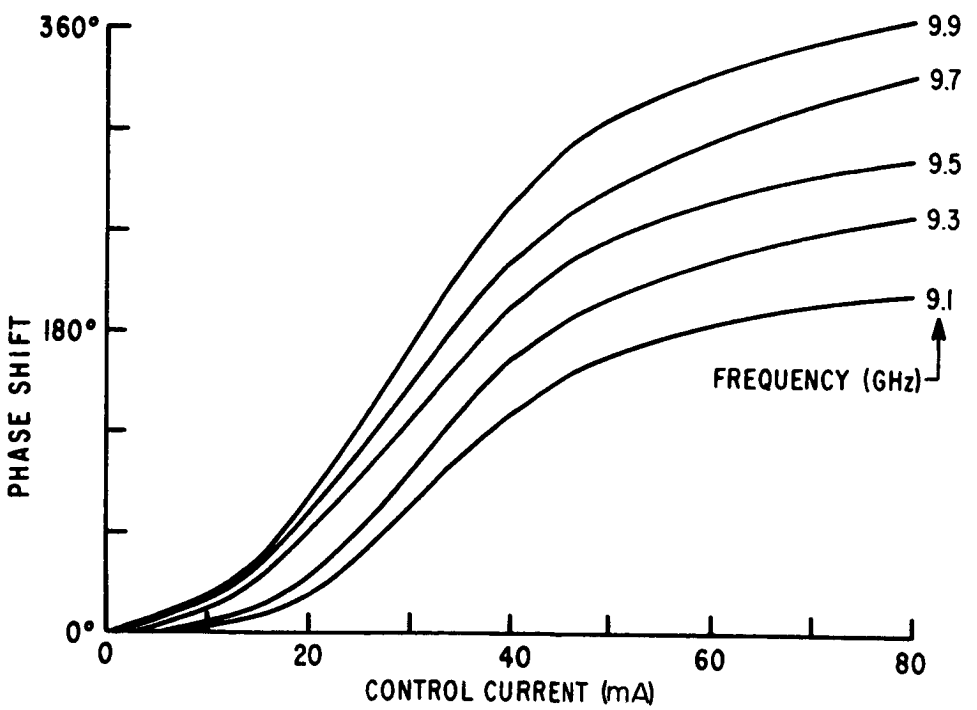

Figure 8.- Phase shift versus control current for the position phase shifter.

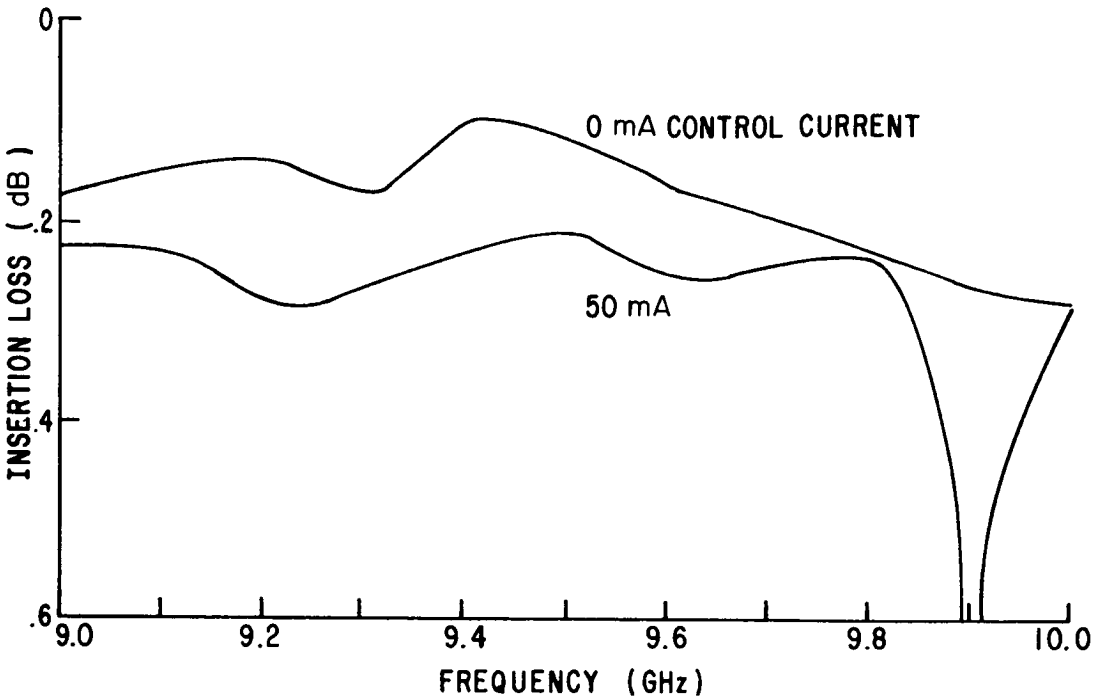

Figure 9.- Insertion loss versus frequency for the position phase shifter.

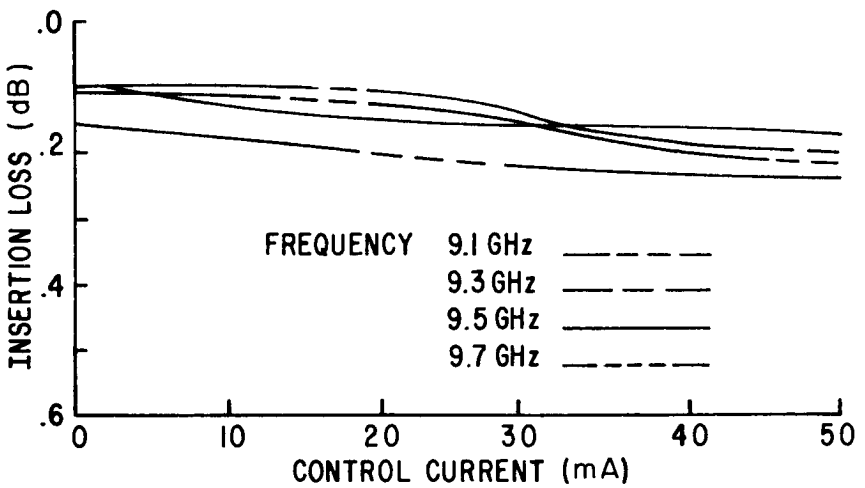

Figure 10.- Insertion loss versus control current for the position phase shifter at 9.1, 9.3, 9.5, and 9.7 GHz.

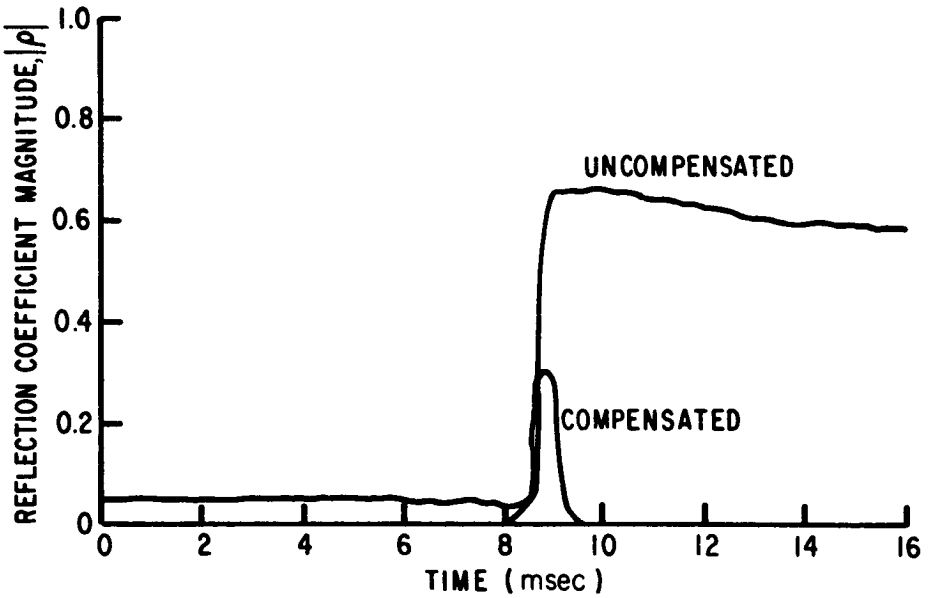

Figure 11.- Correction of a step mismatch.

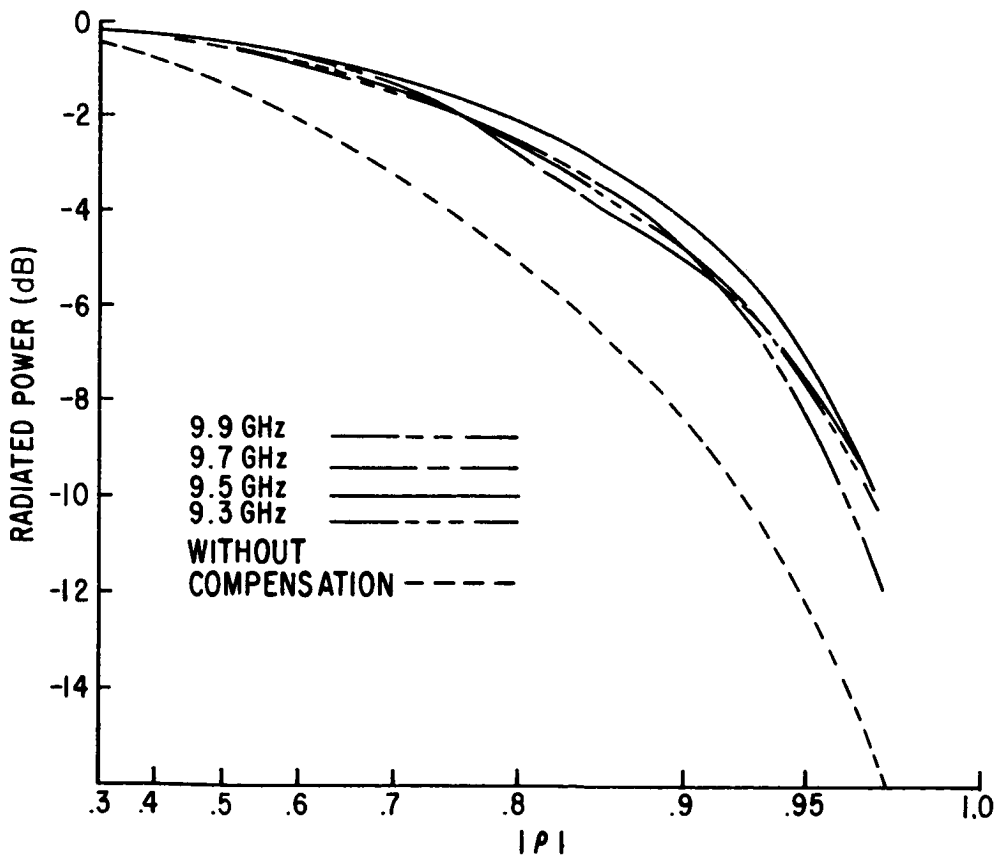

Figure 12.- Measured performance of the compensator.

PROPAGATION OF STRONG FIELD-MODULATED ELECTRO-MAGNETIC WAVES IN PLASMAS

By M.P. Bachynski and B.W. Gibbs

RCA Research Laboratories, Montreal, Quebec*

SUMMARY

The distortion of the waveform of a modulated plane electromagnetic wave propagating in an anisotropic plasma has been experimentally investigated over a range of field strengths of the wave and plasma properties. By using right-hand circularly polarized waves, the effective frequency is $|\omega - \omega_b|$ (where ω is the r-f radian frequency and ω_b the electron cyclotron frequency) and hence the results are also applicable to the propagation of low frequency waves in an isotropic plasma. Severe "overmodulation" of the waveform transmitted through the plasma is found in the regime $|\omega - \omega_b| / \nu < 1$, where ν is the effective collision frequency for momentum transfer. The distortion of the waveform is found to increase with depth of modulation of the incident wave and decrease with increasing modulation frequency.

The "demodulation" is in qualitative agreement with theory for an unmodulated wave with a non-Maxwellian (Druyvesteyn) velocity distribution for the electrons. Many of the effects of the modulation frequencies can also be qualitatively predicted by considering the variation of electron temperature in the presence of the strong field modulated wave. Strong non-linear interaction resulting in marked second harmonic components of the modulation frequency is not predicted by any of the current theories.

INTRODUCTION

The penetration of r-f energy through a re-entry plasma sheath is only part of the problem related to re-entry communications. An equally important problem is the information that can be transmitted via an r-f signal which penetrates through the plasma. Any antenna on board a re-entry vehicle will be located near the enveloping plasma so that the field strength of the emitted r-f fields in the vicinity of the plasma will be large. Hence, the effect of the field strength of the wave on the modulation waveform of the signal transmitted through a plasma is of concern.

A laboratory investigation has been conducted on the propagation of a high frequency (9.2 GHz) plane electromagnetic wave amplitude modulated at low frequencies through an anisotropic plasma. The following sections describe, respectively, the experimental arrangement, experimental measurements, and theoretical explanations for some of the observations.

* This research has been supported by the U.S. Air Force Cambridge Research Laboratories, Bedford, Mass., under contract F19628-67-C-0206.

EXPERIMENTAL ARRANGEMENT

In the laboratory experimental arrangement, a plane electromagnetic wave at 9.2 GHz frequency propagates along the direction of a static magnetic field and is normally incident on an anisotropic plasma, as shown in Fig. 1. The polarization and power level of the incident wave could be varied. The maximum power density used was 2.5 milliwatts/cm^2 which corresponds to an incident electric field of 137 volts/meter. In addition, sinusoidal modulation (modulation frequency (Ω) 10-4,000 sec^{-1}, degree of modulation (μ_0), 0-95%) could be imposed on the incident wave which remained at a frequency of 9.2 GHz. A steady state (d-c) plasma was used so that the modulation waveform of the wave after passing through the plasma could be measured directly.

By using right-hand circularly polarized waves propagating along the direction of the static magnetic field, the effective r-f frequency can be shown[1] to be $|\omega - \omega_b|$, where ω is the r-f radian frequency of the incident wave and ω_b the electron cyclotron frequency. This permitted the investigation of the behaviour of low frequency r-f waves in a laboratory plasma.

The experiment was designed to study the effect of the following parameters on the modulation of the wave passing through the plasma:

(i) Strength of incident wave (E/E_0)

(ii) Effective r-f frequency relative to collision frequency $[(\omega - \omega_b)/\nu]$

(iii) Modulation frequency relative to energy transfer frequency $[\Omega / 2m/M\,\nu]$ (where m, M are respectively the mass of the electron and neutral species)

(iv) Modulation depth (μ/μ_0).

(v) Electron density $(X = \omega_p^2/\omega^2)$ (where ω_p is the electron plasma frequency).

EXPERIMENTAL OBSERVATIONS

Waveform Distortion

Severe effects on the modulation waveform will result in marked distortion of the waveform of the signal transmitted through the plasma. The types of distortion of the waveform which have been measured are shown in Fig. 2 for various magnetic field strengths. These measurements are normalized to the incident waveform, which is also shown.

In order to ascertain the distortion of the waveform, it is advantageous to normalize the distorted wave to the same peak amplitude as the incident wave. An example of distortion of the wave by the plasma resulting in a "demodulated" wave is shown in Fig. 3. The peak of the wave has been somewhat "flattened," but otherwise the waveform remains intact. This is the type of

amplitude distortion that most of the measurements[2] and theory[3] related to ionospheric plasmas have been concerned with. These effects are better known and less interesting than the "overmodulation" case, and hence attention was centered primarily on the "overmodulation" distortion. An example of the "overmodulation" distortion is shown in Fig. 4. This severe type of distortion should occur in an isotropic plasma for $\omega << \nu$. However, by using right-hand circular polarization this condition is $|\omega - \omega_b| << \nu$ and can be achieved by working at frequencies near the electron cyclotron frequency.

Depth of Modulation and Modulation Frequency

Since the maximum effects occur at $Y = \omega_b/\omega \sim 1$, the magnetic field was set at $Y = 1$ and the influence of modulation frequency and depth of modulation of the incident wave were studied for the maximum power level of the incident wave.

The transmitted waveform of different modulation frequencies for an incident wave which is 50% modulated is shown in Fig. 5. As the modulation frequency increases, the transmitted waveform approaches nearer and nearer to the incident waveform. For a greater modulation depth of the incident wave, the distortion by the plasma is greater, as shown by the measurements in Fig. 6 which were taken under similar conditions to those of Fig. 5, except the incident modulation was increased to 90% from 50%. At the low frequencies and high modulation indices, very pronounced distortion of the waveform occurs.

A "phase shift" of the modulated wave as compared to the incident modulation is also observed. The transmitted wave "leads" the incident wave with increasing shift with higher modulation frequency.

Electric Field Strength

Typical results showing the effect of electric field strength for different depths of modulation of the incident wave are shown in Fig. 7. As expected, the greater the field strength or depth of modulation, the more severe is the distortion of the transmitted wave.

Plasma Density

The influence of plasma density for a fixed modulation depth and modulation frequency is shown in Fig. 8. At low plasma densities, the waveform shows a "squaring" or demodulation. At higher electron densities, "overmodulation" corresponding to very deep minima in the modulated wave occurs as described previously. At still higher electron densities, very severe distortion resulting in marked harmonic waveforms occurs. In fact, a condition is possible where almost all the transmitted wave is modulated at the second harmonic (2Ω) of the modulated wave - see result for 1 kHz, 30 mA plasma.

In general, a very complex inter-relation between the plasma and wave parameters (X, Y, E_o, Ω, μ_o) determines the final form of the amplitude modulated wave transmitted through the plasmas. Summarizing, the main features of the modulated waveform emerging through the plasma are

(i) Severe distortion resulting in an "overmodulated" waveform

(ii) The distortion is greatest for large modulation indices

(iii) A shift in position of the maxima of the transmitted wave (compared to the incident wave) is observed

(iv) The strongest distortion is observed at low modulation frequencies

(v) At high electron densities, a strong second harmonic component of the modulation frequency is observed.

EXPLANATION OF EXPERIMENTAL RESULTS

Most theories[4,5,6] for the interaction of amplitude modulated electromagnetic waves with plasma make two major assumptions:

(i) $\Omega << \delta\nu$

where: Ω is the modulation frequency, δ the energy loss parameter, and ν the collision frequency for momentum transfer.

(ii) $\frac{T_e - T}{T} << 1$

where: T_e, T are the electron and gas temperatures, respectively.

The first assumption is certainly true for the experiments described here. However, assumption (ii) is only for very weak interactions. By using right-hand circularly polarized waves and wave-plasma conditions around the electron cyclotron frequency, it has been possible to study strong interactions between a modulated incident wave and the plasma. As evidenced from the experimental results presented here, pronounced interaction can occur at very modest electric field strengths. In particular, the "overmodulated" situation gives rise to severe distortion of the modulated waveform. There is, however, as yet no adequate theory developed for the "strong interaction" case.

If the modulation frequency of the wave (Ω) is much less than the rate of transfer of energy from the electrons to the heavy species of the plasma ($\Omega << \delta\nu$), then the interaction of a modulated electromagnetic wave with the plasma should be similar to that of an unmodulated wave of varying amplitude. Investigations of strong field e-m wave interaction with non-resonant plasmas ($|\omega - \omega_b| >> \nu$) show the effect of a change in collision frequency due to an increase in electron temperature resulting in increased attenuation of the wave with increasing field strength of the wave. In the regime $|\omega - \omega_b| << \nu$, i.e., near the electron cyclotron frequency, a <u>decrease</u> in attenuation with increasing electric field strength of the waves is observed[7]. This phenomenon is not explained by cold plasma theory. Theory based on a non-Maxwellian (Druyvesteyn) velocity distribution of the electrons predicts the correct trends but not the absolute values. Therefore, since even the theory for strong unmodulated e-m waves interacting with plasmas is inadequate, it will be neces-

sary to be content with semi-quantitative theoretical comparisons with the experiment for interaction of strong field modulated waves with plasmas and with predictions of the trends rather than precise quantitative values.

On the basis of the observed interaction of strong field unmodulated electromagnetic waves with plasmas, one would expect the following effect on an amplitude modulated wave in the plasma. In the regime where the stronger the field strength, the greater the attenuation, one would expect the maxima of the modulation to be attenuated more - i.e., the peaks of the waveform transmitted through the plasma would be "clipped". The result would be a "demodulated" wave, as shown in Fig. 9a. In the regime where the strong field wave suffers less attenuation then the low field strength wave, the minima of the modulated wave would be attenuated much more than the maxima resulting in a "overmodulated" waveform, as shown in Fig. 9b. This is qualitatively in agreement with the experimental observations.

In order to put the results in a more quantitative form, one can calculate the attenuation coefficient (α/k) of the e-m wave given by

$$\frac{\alpha}{k} = \sqrt{\frac{|K| - K_r}{2}}$$

where: K is the dielectric coefficient of the plasma with real part K_r and imaginary part K_i; $k = 2\pi/\lambda$ is the free space wave number.

In the region of the electron cyclotron frequency $(Y = 1)$, the imaginary part of the conductivity (σ_i) depends on the factor $(1 - Y)$ so can be neglected. Hence

$$K_r = 1 - \frac{\sigma_i}{\omega\varepsilon_0} = 1$$

Taking[7]:

$$K_i = \frac{\sigma_r}{\omega\varepsilon_0} = X\left(.964\sqrt{\frac{x_0}{E}}\right) << 1 \text{ gives}$$

$$\frac{\alpha}{k} \sim \frac{K_i}{2} = \frac{X}{2}\left[\frac{.964\sqrt{x_0}}{\sqrt{E}}\right] \qquad (1)$$

where: x_0 is a parameter defined in reference 7.

For a modulated electromagnetic wave,

$$E = \frac{E_0}{1+\mu_0}(1 + \mu_0 \cos\Omega t)$$

where: the $(1+\mu_0)^{-1}$ factor is necessary in order to normalize the amplitude of the field to the same peak field regardless of the index of modulation. One thus arrives at

$$\frac{\alpha}{k} \sim \frac{.482\ X}{\sqrt{E_o}} \sqrt{\frac{x_o(1+\mu_o)}{1+\mu_o \cos\Omega t}} \qquad (2)$$

Equation (2) thus predicts that

(i) α/k is proportional to X (electron density) - i.e. the attenuation increases with electron density

(ii) α/k varies as $E_o^{-\frac{1}{2}}$, i.e., the stronger the peak incident electric field strength, the smaller the effect or the attenuation is greatest at the minima of the modulation.

(iii) α/k varies as $\sqrt{\frac{1+\mu_o}{1+\mu_o \cos\Omega t}}$, i.e., the greater the depth of modulation the greater is the effective attenuation with maximum effect occurring at the minima of the modulation waveform.

In order to include the effect of the modulation frequency, it is necessary to solve simultaneously the equation for the electron temperature and the wave amplitude[3,4]. This is generally quite difficult since the collision frequency ν and the energy loss parameter δ which appear in the equation are temperature dependent.

The electron temperature (energy) equation can be written

$$\frac{d(T_e - T)}{dt} + \delta\nu (T_e - T) = \frac{2}{3\kappa n} \vec{J}.\vec{E} \qquad (3)$$

Assume that both δ and ν can be replaced by their average value and that the only important time variation is at the modulation frequency Ω. $\vec{J}.\vec{E}$ can then be replaced by its value averaged over the carrier frequency only, i.e., by

$$\tfrac{1}{2} R_e \vec{J}.\vec{E}^* = \tfrac{1}{2} \sigma_r E_o^2 (1+\mu_o \cos\Omega t)^2$$

which for a right hand circularly polarized wave is

$$\tfrac{1}{2} \frac{ne^2}{m} \frac{\nu}{\nu^2 + (\omega - \omega_b)^2} \; E_o^2 (1+\mu_o \cos\Omega t)^2$$

where: n,e are, respectively, the electron number density and charge.

By writing $(1+\mu_o \cos\Omega t)^2$ as $\left(1 + \frac{\mu_o^2}{2}\right)\left[1 + \frac{2\mu_o}{1+\mu_o^2/2} \left(\cos\Omega t + \frac{\mu_o}{4} \cos 2\Omega t\right)\right]$, Eq. (3) can be written as

$$\frac{d}{dt}[T_e - T] + \delta\nu (T_e - T) = A\left(1 + \frac{\mu_o^2}{2}\right)\left[1 + \frac{2\mu_o}{1+\mu_o^2/2} \left(\cos\Omega t + \frac{\mu_o}{4}\cos 2\Omega t\right)\right]$$

where: $A = \frac{2}{3\kappa n} \tfrac{1}{2} \sigma_r E_o^2$. (4)

Neglecting the 2nd harmonic component, the solution of Eq. (4) is

$$T_e - T = \left[1 + \frac{\frac{2\mu_0}{1+\mu_0^2/2}}{1+(\Omega/\delta\nu)^2} \left\{ \cos\Omega t + \frac{\Omega}{\delta\nu} \sin\Omega t \right\} \right] \left[\frac{A(1+\mu_0^2/2)}{\delta\nu} \right] \quad (5a)$$

$$= \frac{A(1+\mu_0^2/2)}{\delta\nu} \left[1 + \frac{\frac{2\mu_0}{1+\mu_0^2/2}}{\sqrt{1+(\Omega/\delta\nu)^2}} \cos\left\{ \Omega t - \phi \right\} \right] \quad (5b)$$

where: $\phi = \tan^{-1}(\Omega/\delta\nu)$.

At low modulation frequencies, $\Omega/\delta\nu << 1$,

$$T_e - T = \frac{A(1+\mu_0^2/2)}{\delta\nu} \left[1 + \frac{2\mu_0}{1+\mu_0^2/2} \cos\left\{ \Omega\left(t - \frac{1}{\delta\nu}\right) \right\} \right] \quad (6a)$$

At high modulation frequencies, $\Omega/\delta\nu >> 1$,

$$T_e - T \simeq \frac{A(1+\mu_0^2/2)}{\delta\nu} \quad (6b)$$

Since for electron-neutral collisions, $\nu \propto T_e^{\frac{1}{2}}$, then the collision frequency ν and hence the attenuation coefficient α/k will behave in the same general manner as the electron temperature T_e. The temperature equation thus predicts

(i) At low modulation frequencies ($\Omega << \delta\nu$), the strongest influence of the modulation is observed. The wave is shifted in position in the positive time direction by a factor depending on $(\delta\nu)^{-1}$. As the modulation frequency increases, this shift increases. These are the trends observed experimentally.

(ii) At high modulation frequencies ($\Omega >> \delta\nu$), no effect on the temperature and hence on the attenuation is predicted. This is again in accordance with experiment.

If the second harmonic component is included, then the solution of Eq. (4) can be written:

$$T_e - T = \frac{A(1+\mu_0^2/2)}{\delta\nu} \left[1 + \frac{\frac{2\mu_0}{1+\mu_0^2/2}}{1+(\Omega/\delta\nu)^2} \left\{ \cos\Omega t + \frac{\Omega}{\delta\nu} \sin\Omega t \right\} + \frac{\mu_0^2/2 \cdot \frac{1}{1+\mu_0^2/2}}{1+(2\Omega/\delta\nu)^2} \left\{ \cos 2\Omega t + \frac{2\Omega}{\delta\nu} \sin\Omega t \right\} \right] \quad (7a)$$

$$= \frac{A(1+\mu_0^2/2)}{\delta\nu} \left[1 + \frac{\frac{2\mu_0}{1+\mu_0^2/2}}{\sqrt{1+(\Omega/\delta\nu)^2}} \cos(\Omega t - \phi_1) + \frac{\mu_0^2/2 \cdot \frac{1}{1+\mu_0^2/2}}{\sqrt{1+(2\Omega/\delta\nu)^2}} \cos(2\Omega t - \phi_2) \right] \quad (7b)$$

where: $\phi_1 = \tan^{-1} \Omega/\delta\nu$
$\phi_2 = \tan^{-1} 2\Omega/\delta\nu$

At low modulation frequencies $(\Omega/\delta\nu << 1)$,

$$T_e - T = \frac{A(1+\mu_0^2/2)}{\delta\nu}\left[1 + \frac{2\mu_0}{1+\mu_0^2/2}\left\{\cos\Omega(t - \frac{1}{\delta\nu}) + \frac{\mu_0}{4}\cos 2\Omega\,(t - \frac{1}{\delta\nu})\right\}\right] \tag{8a}$$

All this has done is to introduce a phase shift into the modulation frequency components. At high modulation frequencies $(\Omega/\delta\nu >> 1)$,

$$T_e - T = \frac{A(1+\mu_0^2/2)}{\delta\nu} \tag{8b}$$

The ratio of second harmonic component to fundamental of modulation frequency is

$$\frac{F_{2\Omega}}{F_\Omega} = \frac{\mu_0}{4}\left\{\frac{(\delta\nu)^2 + \Omega^2}{(\delta\nu)^2 + (2\Omega)^2}\right\}$$

This predicts a constant ratio between the 2nd harmonic and fundamental components of the temperature variation. This is not what is observed experimentally since under some conditions a very strong second harmonic component has been measured.

Thus, the general trends can be obtained from semi-quantitative considerations of the behaviour of the electron temperature during the modulation cycle. Strong non-linear effects, such as those describing marked second harmonic component content, cannot, however, be obtained from such an approach and await the development of more detailed theory.

CONCLUSIONS

The distortion of the waveform of a modulated plane electromagnetic wave propagating in an anisotropic plasma has been experimentally investigated over a range of field strengths of the wave and plasma properties. By using right-hand circularly polarized waves, the effective frequency is $|\omega - \omega_b|$ and hence the results are also applicable to the propagation of low frequency waves in an isotropic plasma. Severe "overmodulation" of the waveform transmitted through the plasma is found in the regime $|\omega - \omega_b|/\nu < 1$. The distortion of the waveform is found to increase with depth of modulation of the incident wave and decrease with increasing modulation frequency.

The "demodulation" is in qualitative agreement with theory for an unmodulated wave with a non-Maxwellian (Druyvesteyn) velocity distribution for the electrons. Many of the effects of the modulation frequencies can also be qualitatively predicted by considering the variation of electron temperature in the presence of the strong field modulated wave. Strong non-linear interaction resulting in marked second harmonic components of the modulation frequency is not predicted by any of the current theories.

The severe distortions observed indicate that the scheme of using low frequency waves to penetrate the plasma (since the skin depth of the wave will be large compared to the plasma thickness) is not a very good one for amplitude modulated waves since the information transmitted would be severely distorted.

REFERENCES

1. Bachynski, M.P., Gibbs, B.W., and Shkarofsky, I.P., "Strong field electromagnetic wave interaction with anisotropic plasmas", AFCRL Report No. 69-0229, February (1969).

2. King, J.W., "Ionosphere self-demodulation and self-distortion of radio waves", J. Atm. Terr. Phys. 14, 14-49 (1959).

3. Hibberd, F.H., "Ionospheric self-interaction of radio waves", J. Atm. Terr. Phys. 6, 268-279 (1955).

4. Ginsberg, V.L., and Gurevich, A.V., "Nonlinear phenomena in a plasma located in an alternating electromagnetic field", Usp. Fiz. Nauk. 70, 393-428 (1960).

5. Sodha, M.S., and Polumbo, C.J., "Nonlinear propagation of an amplitude modulated electromagnetic wave in a plasma", Proc. Phys. Soc. 80, 1155-1160 (1962).

6. Sodha, M.S., and Arona, A.K., and Aggarwal, A.K., "Non-linear demodulation of an amplitude modulated wave in a plasma elementary approach", Radio Science 3, 1124-1131 (1968).

7. Bachynski, M.P., and Gibbs, B.W., "Propagation of strong-field electromagnetic waves through plasmas near the electron cyclotron frequency", Phys. Rev. Let. 22, 583-587 (1969).

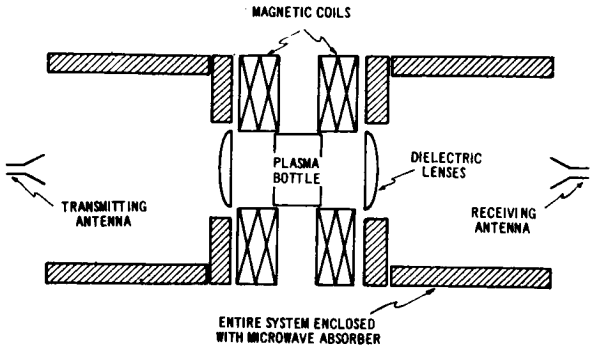

Figure 1.- Schematic diagram of experimental arrangement.

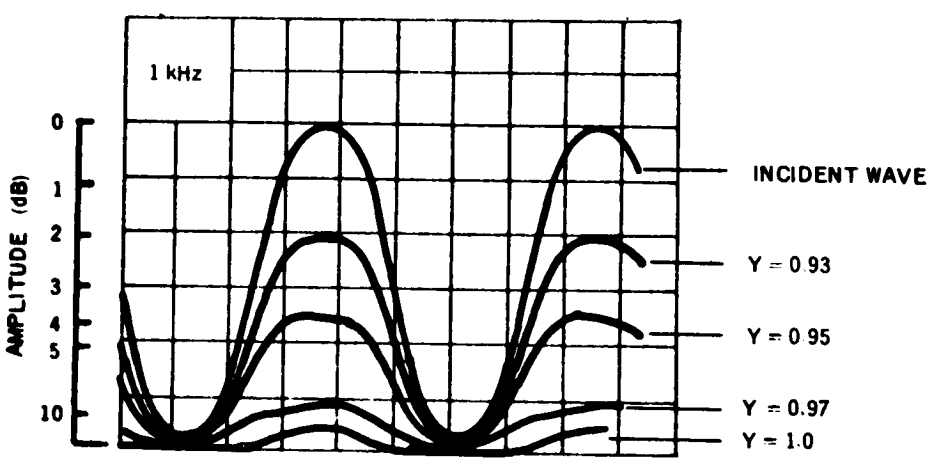

Figure 2.- Distortion of modulation waveform at Ω = 1 kHz showing absolute power levels of incident wave and transmitted wave at various values of magnetic field.

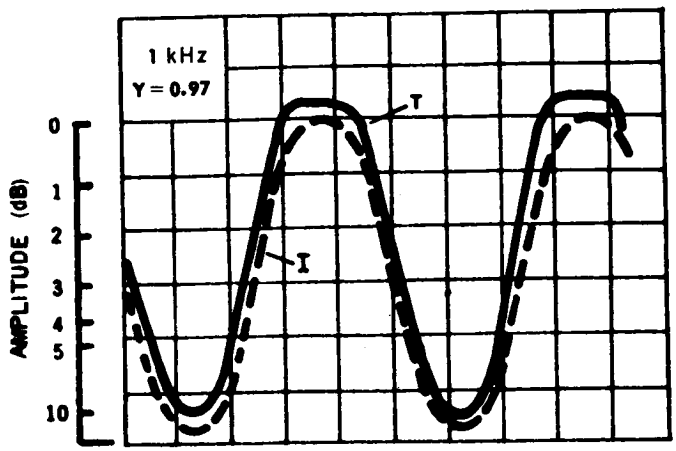

Figure 3.- Distortion of amplitude modulated wave transmitted through plasma resulting in "demodulation" or flattening of peak amplitude.

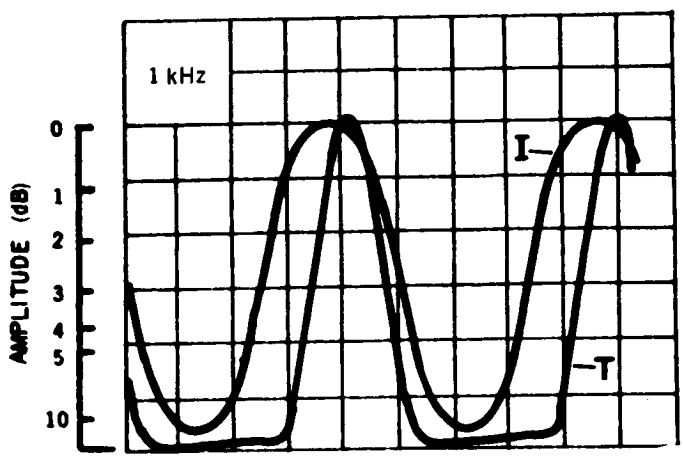

Figure 4.- Distortion of modulation waveform at Ω = 1 kHz showing transmitted wave (T) at Y = 1.0 normalized to incident wave (I). This is an example of an "overmodulated" waveform.

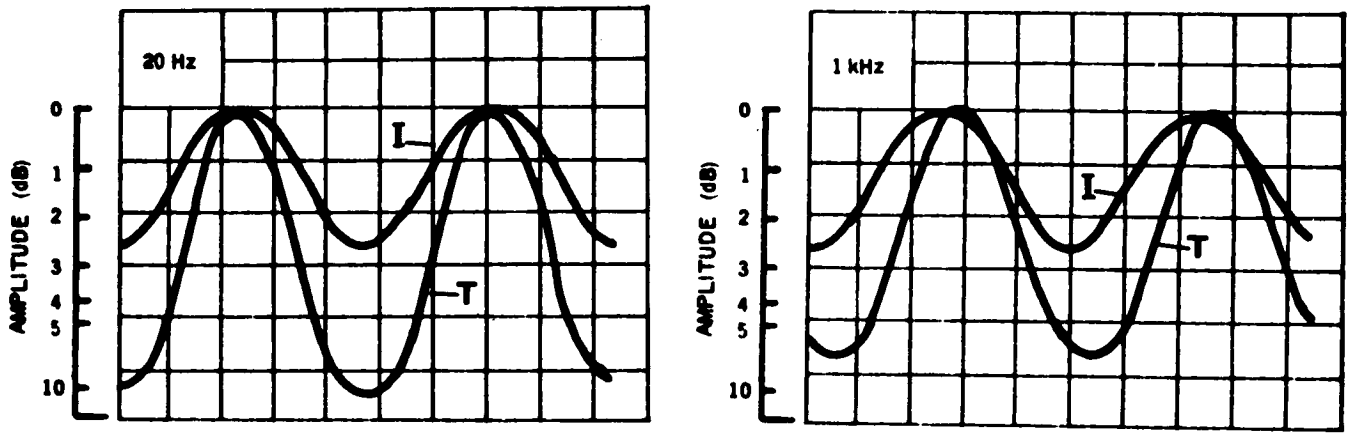

Figure 5.- Change in depth of modulation of a transmitted wave (T) for various frequencies of modulation. Depth of modulation of incident waveform (I) = 50%.

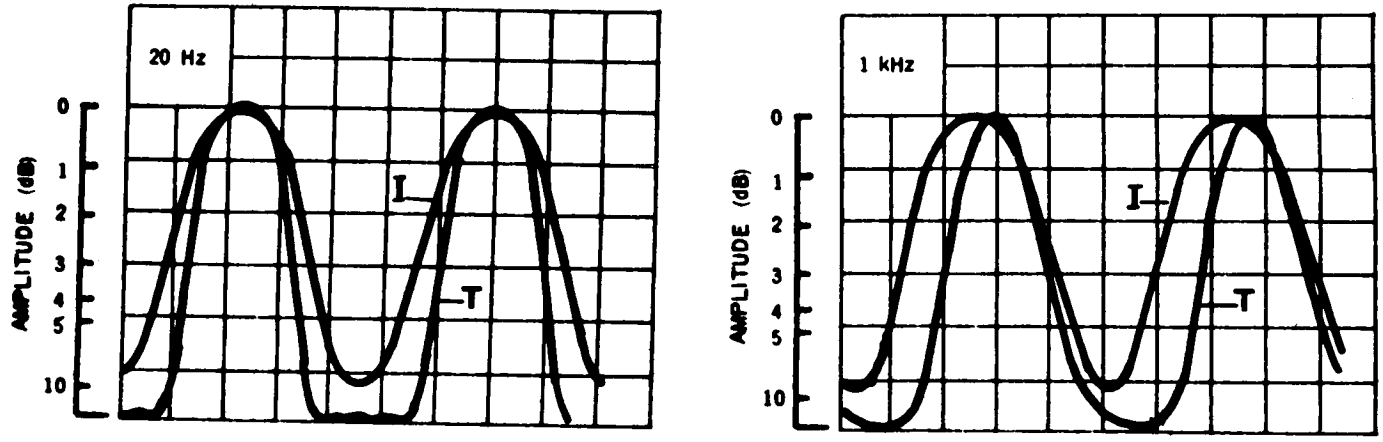

Figure 6.- Change in depth of modulation of a transmitted wave (T) for various frequencies of modulation. Depth of modulation of incident waveform (I) = 90%.

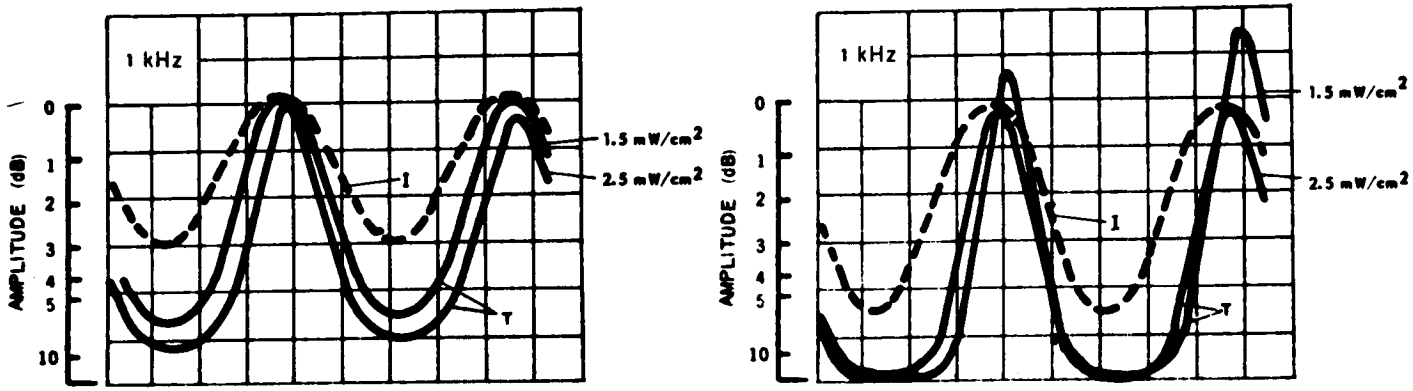

Figure 7.- Effect of power (electric field) of incident wave on modulated waveform transmitted through a plasma (Y = 1).

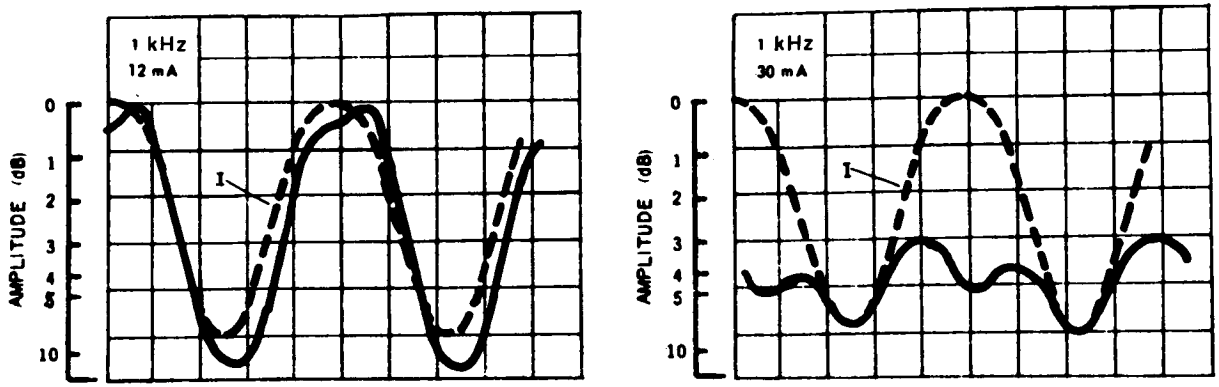

Figure 8.- Effect of a plasma density on modulated waveform transmitted through a plasma (Y = 1).

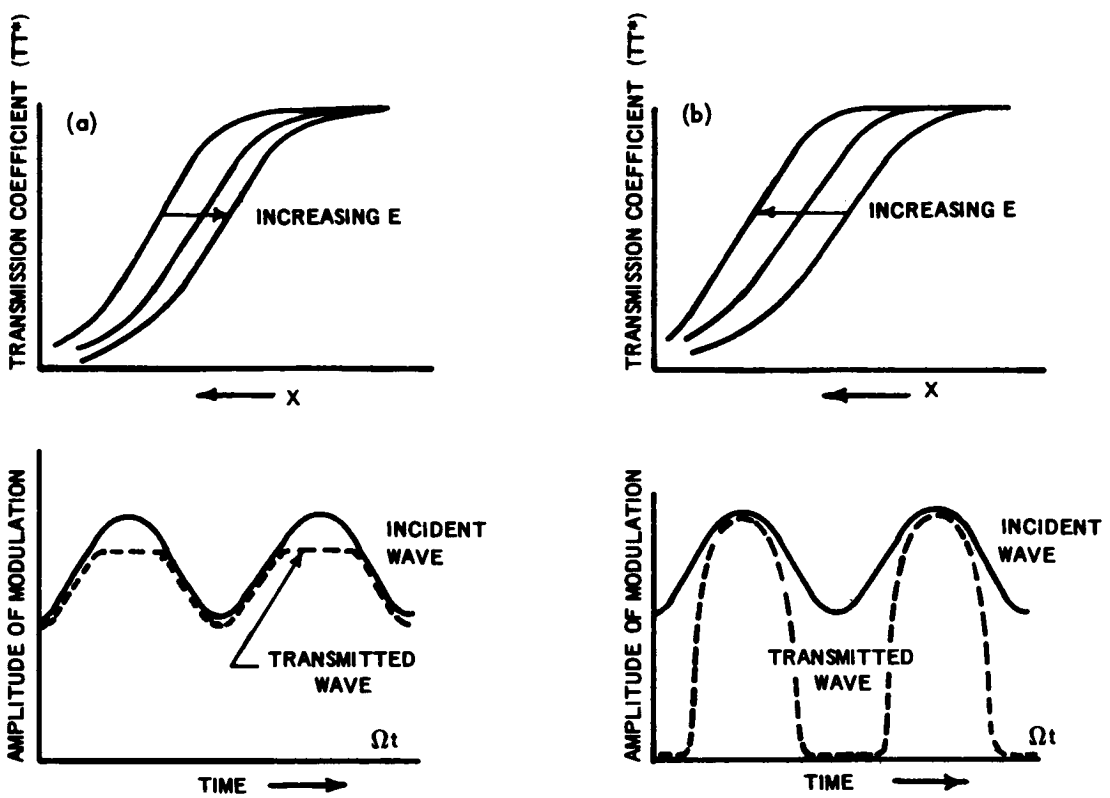

Figure 9.- Waveform of modulated wave transmitted through plasma when

(a) Transmission coefficient decreases with increasing field strength of wave.

(b) Transmission coefficient increases with increasing field strength of wave.

SURVEY OF THE RANT PLASMA AND BREAKDOWN MODELS

By R. L. Fante, J. T. Mayhan, and R. O'Keeffe

Avco Systems Division
Wilmington, Massachusetts

SUMMARY

We outline the theoretical models developed under the RANT program to predict the effect of a plasma on admittance, attenuation, isolation, and breakdown. Some of the salient results obtained from these models are presented.

INTRODUCTION

The RANT program is a study (theoretical plus flight test) of the effect of a reentry environment on the operation of an antenna system. The principal effects of the reentry plasma are (1) an alteration of the antenna radiation pattern, admittance, and attenuation, as well as a change in the isolation for the case of an array of antennas; (2) a change in the breakdown characteristics of high power antennas. To study each of these effects, theoretical models have been developed which are discussed herein.

25

SYMBOLS

a	cylinder radius
c	speed of light
D	diffusion coefficient
d	thickness of plasma layer
$\vec{E}$	electric field strength
e	electron charge
k	equivalent wavenumber in plasma
k_o	free space wavenumber, $2\pi/\lambda$
m	electron mass
n	electron density
n_o	initial electron density before field is applied

n_p critical electron density

P_T transmitted power density

P_{in} incident power density

p^* reduced pressure

q rate of production of electrons due to external sources such as heat

r position

T gas temperature

t time

$\vec{v}$ electron velocity

Y_{11} aperture self-admittance

Y_{12} mutual admittance between apertures

Δ_1, Δ_2 thickness of plasma layers on cylinder

ϵ relative dielectric constant

ϵ_1, ϵ_2 dielectric constant of plasma layers on cylinder

λ free space wavelength

$\mu_o = 4\pi \times 10^{-7}$

ν net ionization rate

ν_c electron collision frequency

ν_r recombination rate

τ time to breakdown

ϕ_1 azimuthal separation between slots on cylinder

ω signal frequency, radian

ω_p electron plasma frequency

LINEAR PLASMA MODELS

Discussion

We have formulated appropriate linear plasma mathematical models and developed several computer programs to determine the mismatch, attenuation, radiation pattern, and isolation for two antenna models, as follows:

(a) Apertures in a plasma-covered infinite ground plane. This model applies to apertures on an actual vehicle in those cases where the frequency of interest is sufficiently high that the curvature of the vehicle can be neglected.

(b) Apertures on a plasma-covered infinite cylinder. This model takes into consideration the effects of the azimuthal curvature of an actual reentry vehicle.

In both models we assume that the plasma is homogeneous in the direction tangential to the vehicle surface but is arbitrarily inhomogeneous normal to the surface. Since the electron temperature on a practical vehicle is usually less than 30 000° K, we shall employ the cold plasma approximation so that the plasma is approximated by a lossy dielectric with local relative dielectric constant (assuming a time variation $e^{-i\omega t}$)

$$\epsilon = \left(1 - \frac{\omega_p^2}{\omega^2 + \nu_c^2}\right) + i\left(\frac{\nu_c}{\omega}\right)\left(\frac{\omega_p^2}{\omega^2 + \nu_c^2}\right) \tag{1}$$

For convenience in setting up the problem for computer solution, the inhomogeneous plasma, in both models, is considered to consist of a series of thin layers, each of which is individually homogeneous. We first solve for the fields in each layer. Then, by applying the boundary conditions on the tangential fields across each layer and across the aperture—heat-shield interface, we are able to obtain variational expressions for the self and mutual admittances. The radiation pattern of the antenna system is obtained by applying the saddle point method to the expressions representing the far fields. The resulting expressions are quite lengthy and will not be written here. The interested reader is referred to references 1 and 2 and also to the recent work of Golden and Stewart (refs. 3 and 4), which has been done simultaneously with the present work.

Results

Since the computer programs have been used by AVCO to predict Y_{11} and Y_{12} for actual reentry profiles, it is difficult to choose cases which can give the reader physical insight or indicate trends. However, one point of interest which can be considered is the comparison of results for Y_{11}, Y_{12}, etc., on

a plasma-covered cylinder with those for the plasma-covered ground plane. A comparison of the self-admittance Y_{11} of axial slots on a bare cylinder with that for a ground plane has been done previously by Knop et al. (ref. 5). For $k_o a > 8$, they found that the value of Y_{11} for a thin axial aperture on a cylinder does not differ significantly from that for the same aperture in a flat ground plane. We have found that these conclusions are not altered when there is a plasma. We have further found that the ground plane value of Y_{11} is generally within 20 percent of the cylinder value, even for $k_o a$ as small as 1.5. In table I we compare the ground plane value of Y_{11} with the value calculated for the same aperture on a cylinder of $k_o a = 1.5$. One can observe that the ground plane values are within 20 percent of the cylinder results. The error is, of course, smaller for larger values of $k_o a$.

Another interesting quantity we can consider is the isolation between slots. We have compared the H-plane isolation between a pair of axial rectangular apertures on a cylinder covered by a plasma with parameters defined by condition* A, with the isolation between apertures on a ground plane covered by the same plasma. We have found that, even though $k_o a$ has the relatively small value of 1.5, there is only about 1 dB difference between the results. From these and other similar results we have concluded that for $k_o a > 1.5$, it is reasonable to approximate the H-plane isolation for rectangular slots on a cylinder with the equivalent results for slots on a ground plane.

The situation for the E-plane isolation is considerably different. We have compared the E-plane isolations for slots on a cylinder and ground plane covered by layers satisfying condition B, as a function of azimuthal separation ϕ_1. We have found that for azimuthal separations of more than 15° there is considerable error in approximating the E-plane isolation on a cylinder by the equivalent ground plane result. As a general rule we do not recommend using the ground plane approximation for E-plane isolation whenever ϕ_1 is 15° or larger.

In all the above analysis it has been assumed that the plasma is homogeneous in directions tangential to the cylindrical surface. However, on actual flight vehicles there are conditions when tangential inhomogeneities may occur. For example, when a space vehicle reenters the earth's atmosphere at an angle of attack, the plasma is inhomogeneous in the azimuthal direction. Using simplified models we have considered this problem. We have concluded that the aperture self-admittance is rather insensitive to tangential plasma inhomogeneities, as long as the plasma is approximately homogeneous over the aperture. This conclusion is not true for the mutual admittance or radiation pattern.

Thin Sheath Approximation

Under certain special conditions it is unnecessary to employ the complex computer program described previously to calculate Y_{11} and Y_{12}. It can be shown that if the plasma is thin, as defined by the condition

*See table I for definition of conditions A and B.

$$k_o \int_0^d \epsilon^{1/2} dz \ll 1$$

and overdense, as specified by the condition $|\epsilon| \gg 1$, then (correct to terms of order $k_o \int \epsilon^{1/2} dz$ and $|\epsilon|^{-1}$ compared with those retained) the self-admittance may be approximated by (see ref. 6)

$$Y_{11} = Y_{11}^{(o)} + Y_s \tag{2a}$$

where

$$Y_s = \frac{2.82 \times 10^{-4}(\nu_c + i\omega)}{\nu_c^2 + \omega^2} \int_0^d n \, dz$$

and n is the electron density and $Y_{11}^{(o)}$ is the aperture admittance when radiating into vacuum. The mutual admittance may be approximated by (see ref. 7)

$$Y_{12} \approx Y_{12}^{(o)} \tag{2b}$$

MICROWAVE BREAKDOWN MODELS

Discussion

We have formulated appropriate mathematical breakdown models as follows:

(a) A linear model which numerically solves the electron continuity equation in an environment with arbitrary distributions of density, temperature, and aperture near field strength. The output of this program is the complete spatial distribution of the electron density as a function of time for a given applied aperture field. From this data one can obtain the time to breakdown, which is defined as the time when the spatial maximum electron density is just equal to the critical density.

(b) A second linear breakdown model developed by using a variational technique. In particular it can be shown (see ref. 8) that the time to breakdown τ is given by

$$\tau = \frac{\ln \frac{n_p}{n_o}}{\lambda_1} \tag{3a}$$

$$-\lambda_1 = \operatorname*{Min}_{\{n\}} \frac{\langle n, Ln \rangle}{\langle n, n \rangle} \tag{3b}$$

$$L = \nabla \cdot (D\nabla) + \nu(r)$$

By expanding n in orthogonal polynomials and varying the coefficients to minimize the variational expression (3b), we then obtain the time to breakdown from equation (3a).

(c) A nonlinear model which includes the coupling between the electron density and the electric field. In this model we consider a plane wave upon a spatially varying plasma and must solve the following set of equations:

$$-\nabla^2\vec{E} + \frac{1}{c^2}\frac{\partial^2\vec{E}}{\partial t^2} = \mu_o e\left[\vec{v}\frac{dn}{dt} + n\frac{d\vec{v}}{dt}\right] \tag{4a}$$

$$m\frac{d\vec{v}}{dt} = -e\vec{E} - m\nu_c\vec{v} \tag{4b}$$

$$\frac{\partial n}{\partial t} = \nabla \cdot (D\nabla n) + \nu n - \nu_r n^2 + q \tag{4c}$$

We can simplify the above set if we assume that the signal frequency $\omega \gg \left(\frac{1}{n}\right)\left(\frac{dn}{dt}\right)$, so that $\vec{v}\frac{dn}{dt} \ll n\frac{d\vec{v}}{dt}$. If we further assume that the breakdown occurs within a few wavelengths of the point of entry of the wave into the plasma, we may then approximate the instantaneous frequency ω_i in the plasma by the signal frequency ω. In this case we can approximate equations (4a) and (4b) by

$$\nabla^2\vec{E} + k^2(n,\nu_c)\vec{E} = 0 \tag{5}$$

where $k^2 = k_o{}^2\epsilon$ and ϵ is defined by equation (1).

A computer program has been developed which simultaneously solves equations (4c) and (5) and prints out a complete time history of the electron density and electric field at all points in the plasma.

Results

In tables II and III we compare the results of linear breakdown models (a) and (b) for VHF and S-band slots operating under conditions present on a typical sharp RV at 200 kft, using the computed near $\vec{E}$ field distribution of the slot. Observe that the agreement between the two models is excellent. Thus the variational technique, which is an approximation to the exact solution, is a very good approximation. For further results see references 9 and 10. In table IV we show the transmitted power as a function of time when a plane wave of frequency 9.4 GHz and a power density of 3000 W/in^2 is incident on a uniform

plasma slab, with initial electron density $n_o = 2 \times 10^{10}/cm^3$, $p^* = 10$ torr, and $T = 4500^o$ K, as calculated from equations (4c) and (5).

We can observe from table IV that the transmitted power changes slowly during the first 0.015 μs after the e.m. pulse has been applied, but then drops radically between 0.015 and 0.017 μs. This rapid drop is coincident with a rapid increase in the electron density of the plasma. At times beyond about 0.02 μs the transmitted power remains approximately constant. In this regime the electron density remains approximately constant, with the source term νn being approximately balanced by the recombination term $\nu_r n^2$.

REFERENCES

1. Fante, R. L.; et al.: RANT Preliminary Report, Vol. 2. AVSD-0374-69-CR, Sept. 12, 1969.

2. Fante, R. L.; et al.: RANT Preliminary Report, Vol. 2 (addendum). AVSD-0374-69-CR, Mar. 25, 1970.

3. Golden, K.; and Stewart, G.: Self and Mutual Admittances of Rectangular Slots in the Presence of a Homogeneous Plasma Layer. IEEE Trans. Antennas Propagation, vol. 17, no. 6, Nov. 1969, pp. 763-771.

4. Golden, K.; and Stewart, G.: Self and Mutual Admittances for Axial Rectangular Slots on a Conducting Cylinder in the Presence of a Thin Plasma Sheath. Presented at the 1969 GAP International Symposium (Austin, Tex.), Dec. 9-11, 1969.

5. Knop, C.; et al.: Radiation Patterns and Admittance of an Axial Slot on a Plasma Covered Cylinder. Presented at the Third Symposium on the Plasma Sheath (Boston, Mass.), Sept. 21-23, 1965.

6. Fante, R. L.: Effect of Thin Plasmas on an Aperture Antenna in an Infinite Conducting Plane. Radio Sci., vol. 2 (New ser.), no. 1, Jan. 1967, pp. 87-100.

7. Fante, R. L.: Mutual Admittance of Infinite Slot Antennas. Proc. IEEE, vol. 55, no. 10, Oct. 1967, pp. 1754-1756.

8. Mayhan, J.; and Fante, R.: A Variational Formulation Specifying Breakdown Criteria for Plasmas Subjected to Spatially Non-Uniform Electric Fields. J. Appl. Phys., vol. 40, no. 2, Feb. 1969, pp. 449-453.

9. Mayhan, J.; et al.: RANT Preliminary Report, Vol. 1. AVSD-0374-69-CR, Sept. 12, 1969.

10. Mayhan, J.; and Fante, R.: RANT Preliminary Report, Vol. 1 (addendum). AVSD-0374-69-CR, Mar. 25, 1970.

TABLE I

COMPARISON OF Y_{11} COMPUTED ON PLASMA-COVERED CYLINDER WITH THE VALUE COMPUTED ON A PLASMA-COVERED GROUND PLANE FOR $k_o a = 1.5$

Condition	Y_{11} for ground plane	Y_{11} for cylinder
[1]A	$1.93 \times 10^{-4} - i2.08 \times 10^{-4}$	$1.56 \times 10^{-4} - i2.11 \times 10^{-4}$
[2]B	$7.88 \times 10^{-3} + i1.30 \times 10^{-3}$	$7.58 \times 10^{-3} + i1.18 \times 10^{-3}$

[1]Condition A is a single layer of plasma of thickness $k_o\Delta_1 = 0.0223$ and relative dielectric constant $\epsilon_1 = 1 + i20$.

[2]Condition B is for two layers with $k_o\Delta_1 = 0.0836$, $k_o\Delta_2 = 0.0836$, $\epsilon_1 = 2 + i30$, $\epsilon_2 = -4 + i20$.

TABLE II

VHF SLOT BREAKDOWN

Aperture $\vec{E}$ field, V/cm	Model (a) time to breakdown, μs	Model (b) (variational) time to breakdown, μs
35	0.020	0.018
30	.050	.040
25	.13	.11
20	.50	.45
15	3.0	3.1

TABLE III

S-BAND SLOT BREAKDOWN

Aperture $\vec{E}$ field, V/cm	Model (a) time to breakdown, μs	Model (b) (variational) time to breakdown, μs
400	0.032	0.03
300	.17	.15
250	.41	.40
200	1.5	1.6
150	9.5	10.2

TABLE IV

TRANSMITTED POWER CALCULATED BY NONLINEAR BREAKDOWN PROGRAM

P_T/P_{in}	t, μs
1.0	0.001
.95	.005
.82	.01
.25	.015
.014	.016
.0027	.017
.0025	.018
.0026	.019
.0029	.020
.0031	.025
.0031	.030
.0031	.04
.0030	.05

THE EFFECTS OF SPATIAL NONUNIFORMITIES ON HIGH-TEMPERATURE MICROWAVE BREAKDOWN

By Glenn C. Light

The Aerospace Corporation

INTRODUCTION

Among the many recent advances in antenna breakdown prediction in the reentry environment are the reported results (refs. 1, 2 and 3) of experimental measurements of microwave breakdown characteristics of high-temperature gases, including air, nitrogen, and argon. A modification of the classical phenomenological theory of breakdown appears to account for the major features of the high-temperature effects in air and nitrogen. However, systematic discrepancies, identified in reference 2, that occur at low pressures in all of these experimental results remain unexplained. Perhaps the most obvious cause of discrepancy is the effect of spatial nonuniformities in electric field and in gas properties.

Recently, several theoretical analyses for predicting the effects of nonuniformities on breakdown have been reported. However, no comprehensive comparisons of data and theoretical predictions have been reported. Fante, et al., (ref. 4) have compared theoretical predictions and experimental data of Scharfman and Morita taken at 1.1 GHz at a fixed pulse duration in room-temperature air. This paper presents experimental results and corresponding theoretical predictions for breakdown in air and in nitrogen for a wide variety of pulse durations, including pulses sufficiently long that the condition of cw breakdown is fulfilled and pulses sufficiently short that diffusion and the effects of nonuniformities are practically negligible. Also included are calculations for the effect of unsteady compressible boundary layers such as were present in all but one of the reported laboratory experiments on the effects of elevated temperature on breakdown.

Epstein and Lenander (ref. 5) recently reported results from a numerical solution of the Boltzmann equation that includes inelastic collision processes appropriate for air at high electric field strengths. The values presented of the fundamental breakdown parameters, ionization frequency, collision frequency, and diffusion coefficient differ from those used in the classical phenomenological breakdown theory. The effect of these new values on breakdown are reevaluated quantitatively.

Calculations for X-band antenna breakdown in an underdense reentry plasma are also presented. Reentry boundary layers typical of slender, sharp-nosed cones are treated. Results are compared for

various simplifying assumptions; (1) uniform gas properties, (2) uniform electric field, and (3) no high-temperature effect.

CALCULATIONS

Of the several theoretical formulations available for the effects of nonuniformities, we use the variational analysis of Epstein (refs. 6 and 7) because it is the only formulation that can evaluate arbitrary flow field nonuniformities. In summarizing the analysis, Epstein showed that the differential electron continuity equation

$$\frac{\partial n}{\partial t} = \nu n - \nabla \cdot (D \nabla n) \tag{1}$$

could be written as a variational statement which, for cw breakdown, becomes

$$\delta \int \left[\lambda f(\xi) n^2 - g(\xi)(\nabla n)^2 \right] d\xi = 0 \tag{2}$$

However, the continuity equation is not correctly written this way. The correct formulation is

$$\partial n/\partial t = \nu n - \nabla \cdot (D \nabla n) - \nabla \cdot (n \nabla D) \tag{3}$$

If we include this term in equation 2, it becomes

$$\delta \int \left[\lambda f n^2 - g(\nabla n)^2 - n \nabla g \cdot \nabla n \right] dV = 0 \tag{4}$$

For pulsed breakdown, this equation becomes

$$\delta \int \left[(\lambda f - p) \tilde{n}^2 - g(\nabla \tilde{n})^2 - \tilde{n} \nabla g \cdot \nabla \tilde{n} + n_i \tilde{n} \right] dV = 0 \tag{5}$$

where $\lambda = \nu_o \ell^2 / D_o$, $f = \nu(\xi)/\nu_o$, $g = D(\xi)/D_o$, ℓ is the spatial extent of the integration, the tilda denotes the Laplace transform with respect to nondimensional time $\tau = D_o t / \ell^2$, p is the Laplace transform variable, and n_i is the initial electron density at t = 0. The inclusion of the term involving ∇D makes, in most cases of practical interest, only a minor modification in the predicted power level. It is included here for generality. Following

Epstein now, we use the Ritz method to find an approximate eigenvalue solution. Trial functions of the form

$$n = C_0 \xi(1-\xi) + C_1 \xi(1-\xi)^k \tag{6}$$

where C_0 and C_1 are functions of time for the pulsed breakdown case as used herein. The trial function is inserted in the relevant above equation, the integrals are evaluated, the variation of the coefficients is set to zero, and the solution is found as outlined by Epstein.

In practice, it has been found that for cw breakdown, a single value of k in equation 6 is sufficient to define a good approximation to the minimum eigenvalue. However, for pulsed breakdown for the field distributions encountered herein, it was found necessary to search through several integer values of $k > 2$ to define a good minimum as the power level was increased; i.e., as the pulse duration for breakdown was decreased. This situation has physical significance since as the pulse duration decreases, there is correspondingly less time available for the diffusion of electrons created by the electric field into regions of lower field strength. Hence, during the buildup of electron density leading to breakdown, the gradients of electron density become quite large in the region of peak field strength. This requires a rapidly varying trial function to better approximate the actual electron density distribution and hence obtain greater values of the exponent k. It has been found that values of k up to 30 are required to find the minimum approximate eigenvalue; such values correspond to pulse durations less than 10^{-8} sec.

Since the experimental geometry (see Experiment section) in the region of breakdown is closely bounded on one side only, the question arises as to how far away from this wall the integration should be carried. Since the electric field decays rapidly with distance near the aperture, one would expect that beyond a certain distance, further integration would make a negligible difference. This concept has been exploited by Fante (ref. 8). In the calculations reported here, it has been found that integration beyond a distance of 2 cm from the aperture produces insignificant refinement to the solution. At 2 cm, the field strength is less than 10% of the peak value. A more detailed description of the computer program used in making these calculations is given in reference 9.

Since this is a one-dimensional analysis, the calculated results for cw breakdown only have been modified slightly to include the first order effects of transverse diffusion; i.e., diffusion parallel to the plane of the aperture. If λ is the calculated eigenvalue from the one-dimensional analysis, then the effective one-dimensional diffusion length is

$$\Lambda_e = \left(\ell^2/\lambda\right)^{1/2}$$

and the modified diffusion length is

$$\Lambda_e' = \left[\frac{1}{\frac{1}{\Lambda_e^2} + \pi^2 \left(\frac{1}{a^2} + \frac{1}{b^2} \right)} \right]^{1/2}$$

where a and b are the aperture dimensions. The modified eigenvalue, then, is $\lambda' = \ell/\Lambda_e'^2$. In all cases, this makes only a minor refinement to the solution.

It is necessary to know the relationships between electric field and gas net ionization frequency ν, and electron free diffusion coefficient D. For this, we apply the "effective field" concept, which states that there is an effective electric field

$$E_e = E_{rms} \left(\frac{1}{1 + (\omega/\bar{\nu}_c)^2} \right)^{1/2}$$

where ω is the microwave radio frequency and $\bar{\nu}_c$ is the appropriate collision frequency for electrons. The effective field concept also states that ν/p and Dp can be expressed as a unique function of E_e/p and $p\lambda$ for a given gas (ref. 10). For air, we will use the data of Brown and Scharfman (ref. 11) for ν/p and the data of MacDonald, et al. (ref. 12) for diffusion coefficient. Gould and Roberts (ref. 10) and Scharfman and Morita (ref. 11) have suggested the expression for collision frequency, $\bar{\nu}_c/p = 5.3 \times 10^9$ $\text{sec}^{-1}\,\text{torr}^{-1}$, which we use. These values for ν/p, Dp, and $\bar{\nu}_c/p$ are referred to as the phenomenological data set.

We also show results of breakdown calculations using a second, independent set of data for these variables, referred to herein as the kinetic theory data set, in air. Epstein and Lenander (ref. 5) have reported results from a numerical solution to the Boltzmann equation that includes inelastic collision processes appropriate for air at high electric field strengths. Their calculations were carried out at three different gas pressures and for a microwave frequency of 9.4 GHz. The effect of a different frequency in the experiment (9.34 GHz) is negligible, and we use a logarithmic interpolation for pressures other than 1, 10, and 100 torr for which calculations are available.

EXPERIMENT

The experimental breakdown data reported here were taken in two different geometries. In both cases, breakdown occurs over a rectangular X-band aperture of 2.286 x 1.016 cm, flush-mounted in a ground plane with a half-wave Pyrex dielectric window flush-mounted in the aperture. In one case, the aperture was positioned 1/2 in. inside the wall of a shock tube as reported in reference 2; in the other case, the aperture was positioned in one wall of an absorber lined vacuum chamber (fig. 1). The data reported here were all taken in room-temperature gas that was continuously flushed through the respective vacuum chamber. Microwave breakdown power was produced by a magnetron operating at 9.34 GHz and driven by a hard tube modulator, which is capable of a wide variety of pulse widths and repetition rates. The occurrence of breakdown was determined by monitoring reflected and transmitted video envelopes as measured with crystal detectors.

It is important in this experiment to ascertain as accurately as possible for a given power level the magnitude of the peak electric field in the plane of the aperture. The apparatus for measuring the incident power at the aperture, including waveguide directional couplers, a precision variable attenuator, and a thermistor power meter were calibrated to an overall accuracy of ±3%. Reflection from the aperture and the aperture conductance were measured with a slotted line and crystal detector. The Pyrex window was made to be one-half of a waveguide wavelength by first measuring the resonant frequency in a terminated waveguide of a Pyrex sample of arbitrary length and then successively cutting and measuring the resonant frequency until the resonant frequency matched the experiment frequency. The power absorbed by the Pyrex window was then measured at the resonant frequency in a closed waveguide system by measuring the power loss across the section of waveguide containing the window. If we make the assumption of dominant mode field distribution in the aperture, then the peak rms electric field can be found from

$$\left(E_{rms}\right)_{peak} = \left[\frac{2\,P_m KT\left(1-\rho^2-\alpha^2\right)}{tabG}\right]^{1/2} \tag{7}$$

where P_m is the measured average power, K is the calibration factor of the waveguide components, ρ is the aperture reflection coefficient, α is the window absorption coefficient, a and b are the aperture dimensions, G is the aperture conductance, t is the pulse duration, and T is the interpulse interval.

For the cw breakdown data, the condition of cw breakdown is approximated by using microwave pulses of sufficient duration that finite pulse time effects are completely negligible in determining the measured threshold. For breakdown in a uniform field and uniform gas, the electron continuity equation can be integrated directly to yield

$$\nu_o - D_o/\Lambda^2 = \ell n\,(n_b/n_o)/t \tag{8}$$

where Λ is the characteristic diffusion length for the breakdown chamber and t is the pulse duration to breakdown. From the cw theoretical calculations described above under Calculations, we directly obtain the value of $\lambda = \nu_o \ell^2/D_o$. Hence, the calculated cw value of effective diffusion length Λ_e is

$$\Lambda_e = \left(\frac{D_o}{\nu_o}\right)^{1/2} = \left(\frac{\ell^2}{\lambda}\right)^{1/2} \tag{9}$$

If this value is used in equation 8, we can readily ascertain the pulse duration that adequately approximates the cw breakdown condition; i.e.,

$$t \gg \frac{\ell_n(n_b/n_o)}{\nu_o - D_o/\Lambda_e^2}$$

For all data reported here, this condition is fulfilled for a pulse duration of 50 μsec.

The magnetron oscillator is pulsed repetitively at a rate of 20 sec^{-1} and the microwave pulse duration, which is continuously adjustable between 0.1 and 100 μsec, is preset to the desired value. After a discharge is obtained, the power level is lowered gradually until the discharge just extinguishes. This power level is considered to be the breakdown power. This technique is simple but has the disadvantage that the gas probably contains reaction products, including neutral species, negative ions, and metastable electronic states.

SPATIAL NONUNIFORMITIES

Electric Field

It is well known that the electric field intensity varies rapidly over a slot radiator. In the absence of flow field gradients, the breakdown will preferentially occur in regions of highest field strength. In the geometry used here (fig. 2), the highest field strength is on the waveguide centerline in the plane of the aperture. Fante and Mayhan (ref. 4) have shown that electric

field gradients in the aperture plane are negligible in determining the breakdown threshold, and that the gradients normal to the ground plane are dominant. We use the description of near field normal to the ground plane given in reference 13.

$$E = E_o \exp(-4\,z/\pi b) \qquad (10)$$

This is an approximation to the exact numerical results which neglects field components in the z-direction. If we neglect the z-component in the calculations, the predicted breakdown power will be slightly high.

Aerodynamic Boundary Layer

We wish to study the effects of the unsteady laminar compressible boundary layer that exists on a semi-infinite flat plate with sharp leading edge in the flow behind a traveling shock wave. Figure 3 schematically depicts this boundary layer.

Such boundary layers have been studied by several investigators. We identify three regimes that occur consecutively in time at a fixed location on the flat plate. For short times after shock passage, there is the shock-induced unsteady boundary layer that has been analyzed in detail by Mirels (ref. 14). We use unpublished boundary layer profile calculations by Mirels to describe this regime. For long times, there is the unsteady boundary layer that originates at the leading edge of the flat plate. We use the calculations of Van Driest (ref. 15) to describe this regime. The intermediate transitional regime has been studied by Lam (ref. 16) and by Felderman (ref. 17). However, no calculations exist for conditions appropriate to this experiment for boundary layer profiles in this regime. We use a linear interpolation between the limiting cases to describe boundary layer profiles in the intermediate regime.

RESULTS AND DISCUSSION

Epstein has previously demonstrated the accuracy of this variational analysis by comparisons with predictions from exact analyses in some simple geometries. We verify the accuracy of our calculations by comparisons with exact predictions for a uniform field in air with uniform properties.

CW Breakdown

The comparison between data and calculations for cw breakdown using the phenomenological data in air are presented in figure 4. Excellent agreement throughout the pressure range is evident.

The result of a calculation based on the theoretical work of Mayhan and Fante (ref. 18) for breakdown in a semi-infinite region is also shown. This theoretical analysis is suitable for uniform gas properties only but has a particularly simple form that facilitates rapid calculation of breakdown levels. Agreement with the prediction based on the present analysis and with the data is quite good. The differences that exist between the two predictions can probably be ascribed to differences in the form of the diffusion term in the continuity equation. Mayhan and Fante use the form $D\nabla^2 n$, whereas the present analysis uses the more general form $\nabla^2(Dn)$.

Experimental data were also obtained in room-temperature air in the shock tube geometry described in reference 2. However, these data do not differ from those obtained in the anechoic chamber and are not shown here. The fact that these data were the same indicates that the near field of the waveguide antenna is not significantly distorted by the shock tube walls. This is an important observation which means that special measurements of the near-field distribution in the shock tube are not necessary, and that the free space near-field distribution of equation 10 can be used for all calculations of breakdown in the shock tube.

A calculation using the kinetic theory data of Epstein and Lenander (ref. 5) is also shown in figure 4. It is evident that for much of the pressure range involved, this calculation falls outside the error brackets of the data. But, it is to be expected that the phenomenological data would yield more accurate results since it is based on experimental data more directly relevant to the microwave breakdown process than the cross-section data necessarily used in the kinetic theory calculation.

A calculation is shown here for the case of a uniform electric field in the region of breakdown. This is shown only to indicate the relative importance of the field nonuniformity, per se, in determining the breakdown threshold. The phenomenological data set was used in this calculation.

As expected, if we calculate a value for effective diffusion length from equation 9 and the calculated value of λ, we find that Λ_e varies with pressure as shown in Table 1. This is unlike the case of a uniform field where the characteristic diffusion length is a property of the bounding surface geometry. Figure 5 shows data obtained for cw breakdown in pure nitrogen gas in the anechoic chamber along with three calculations of breakdown threshold. The curve labelled "Harrison" uses values for ionization frequency given by Harrison (ref. 19), but uses the same values for diffusion coefficient and collision frequency as for air. The curve labelled "Air prediction" uses the phenomenological data for air. The ionization frequency for nitrogen appears to resemble that of air much more closely than the data of reference 19 indicate. Another calculation using the ionization frequency for nitrogen reported by Masch (ref. 20) is intermediate between the other two calculation. However, the assumptions involved in these calculations are such that the calculation should not be used in an attempt to find a new curve for ionization frequency versus E_e/p in nitrogen.

Pulsed Breakdown

Data for pulsed breakdown in air at three different pressures in the form of breakdown power versus pulse duration to breakdown are shown in figures 6, 7, and 8. In all three cases, it is seen that at low power levels and long pulse durations, agreement between the theoretical calculation and the data is quite good, corroborating the cw results of the previous section. However, at higher power levels, there is increasing discrepancy between data and predictions.

The comparison of the calculated curve for aperture breakdown with that for uniform field breakdown in any of these figures reveals that, in both the power and pulse duration, the two curves approach each other as the power increases. This confirms the expectation that, as the pulse duration gets shorter, the importance of electric field nonuniformities in determining breakdown power should diminish; i.e., the breakdown process is increasingly governed only by conditions in the immediate vicinity of the peak field strength. It seems probable, therefore, that the noted discrepancies are not due to improper characterization of the field nonuniformities since these should be most important for cw breakdown where the agreement is excellent; the approach of the experimental data to the "uniform field" calculation is not to be interpreted literally.

As was true for cw breakdown, if we calculate the effective diffusion length Λ_e, using equation 8 and the calculated pulse duration t, Λ_e is a function of power level at a given gas pressure as illustrated in Table 2. As the pulse duration decreases, there is less time available for diffusion processes. Hence, the electron density spatial distribution becomes more asymmetric and, correspondingly, the characteristic diffusion length becomes shorter. Examination of equation 8 reveals that as t, the pulse duration, is made arbitrarily small, the electron continuity equation for a uniform field goes to

$$\nu_o \approx \ell n(n_b/n_o)/t$$

If the effective value of ionization frequency ν is larger than expected, t will be correspondingly smaller. Because of the repetitive pulse technique of gathering data, it is possible to increase the apparent ionization frequency through the existence of either metastable states, negative ions, or neutral species present because of previous discharges in the pulse train. In pure nitrogen gas, however, the existence of negative ions is not probable and neutral species generated by previous discharges are limited to just atomic nitrogen. Breakdown data in nitrogen should help determine the cause of thefall off observed in air. Data taken in pure nitrogen are also shown in figures 6, 7, and 8 for the same three pressures. Unfortunately, at 1 torr, there is no data for ν_i/p in N_2 available from Harrison or Masch. At all

pressures, however, agreement between data and a calculation for air based on Brown's ν_i/p is remarkable. The N_2 data do not show the characteristic falling off at higher power levels as shown in the air data. This situation is consistent with the idea that some form of discharge reactant is present in air that tends to shorten the pulse duration to breakdown. It appears that this reactant is either oxygen or a nitrogen-oxygen molecule. For long pulse durations, the continuity equation becomes $\nu_o \simeq D/\Lambda_e^2$. Therefore, except for inducing ambipolar diffusion at high values of initial electron density n_o, n_o has no effect on cw breakdown, and, since the cw breakdown in air is not affected, either the reactant acts to produce a high n_o or it is not produced at the lower powers required for cw breakdown. Independent evidence exists for an increased effective air ionization frequency in a repetitively pulsed breakdown experiment by Mentzoni (ref. 21). In this work, the ionization frequency was measured more directly by the photometric method, and the data show an increase by about 60% over that taken under single pulse conditions. This could account for a corresponding reduction in observed pulse duration; not enough, however, to account for the present discrepancy. The values for ν_i reported by Mentzoni are measured at about midway between the start of the microwave pulse and achievement of breakdown. If there are negative ions present, it is reasonable to suppose that these ions will lose their extra electrons early in the breakdown formation process because of their relatively low ionization potential. This would cause an enhanced apparent ν_i immediately after pulse initiation, followed by a decrease of ν_i as the number density of negative ions is depleted. The effect is equivalent in our experiment to a constant value of ν_i, with an accompanying high value of n_o. If the electron density n_o at the beginning of each microwave pulse is considerably more than expected (a value of 10^3 cc^{-1} has been assumed in all calculations reported), this will result in a shorter pulse duration to breakdown than shown by the calculations.

Dobrov (ref. 22) has observed electron attachment in air discharge afterglows of this same type. He tentatively concluded that NO_2^- was the dominant negative species in such afterglows.

We conclude, therefore, that the present room-temperature air data are consistent with the presence of negative ions in the air afterglow, which liberate their electrons rapidly at the start of each pulse, before breakdown is achieved, effectively raising the "initial" electron density n_o.

It must be remembered, however, that this mechanism cannot explain any of the observed properties of high-temperature air breakdown because: (1) the high-temperature effect is observed under single pulse conditions where no previous discharges have occurred, (2) there are not sufficient negative ions present at chemical equilibrium in high-temperature air to provide a significant change in n_o even if all negative ions lose electrons, and

(3) the high-temperature effect is also observed in N_2 where no negative ions are possible.

Shock Tube Boundary Layer Effects

The calculated effect of the unsteady compressible laminar boundary layer present in the high-temperature shock tube experiments is shown in figure 9 for two different pressures where data were obtained. For the purpose of isolating the effects of the spatial nonuniformities in the data, the free stream inviscid flow was assumed to be time independent; a constant electron density of 10^9 particle/cc was chosen. The boundary layer was allowed to develop in time, and calculations were made for boundary layer profiles corresponding to flow times in each of the three regimes of unsteady boundary layer development.

As can be seen, the effect of the boundary layer is negligible at the higher pressure, but becomes considerable at the lower pressure. The difference in sensitivity to the boundary layer is due to two factors: first, the breakdown is expected to occur at a point well inside the boundary layer for the lower pressure and out near the edge of the boundary layer for the high pressure case; and second, the diffusion coefficient is about a factor of ten lower at the higher pressure. Any changes in the diffusion geometry due to the boundary layer will have a correspondingly smaller effect on the breakdown level at the higher pressure.

It is interesting to note that the time dependence of the breakdown level is qualitatively different for the two cases; i.e., the breakdown level increases with time at the higher pressure, but monotonically decreases with time for the low-pressure case. In contrast, the high-temperature data of reference 2 show a monotonically decreasing pulse duration to breakdown at all pressures. It appears that some of the data in reference 3 should be discounted on the basis of this analysis. However, the main conclusions of references 2 and 3 are not affected by these results.

Reentry Boundary Layer Effects

Calculations for the effect of the reentry flow field nonuniformities are shown in figure 10 for altitudes of 115 and 150 kft. The boundary layer flow field properties are taken from Pallone (ref. 23), and are valid for pure air chemistry under the following reentry conditions: sharp-nosed conical vehicle, 8-degree cone half angle, u_∞ = 22,000 fps, T_w = 1000 K, and with the antenna 5 ft back from the nose.

These results show widely differing sensitivities to various simplifying assumptions. The lower altitude (115 kft) is approximately the altitude for

minimum breakdown power at this frequency. Breakdown would be expected to occur near the minimum in the boundary layer mass density profile for this case. If we have no knowledge of boundary layer profiles and chose a simplifying assumption of uniform gas conditions with values corresponding to this position of minimum mass density, the resulting breakdown level should differ little from that which incorporates the boundary layer nonuniformities. At 150 kft, however, breakdown will occur at a point close to the wall, where the mass density is appreciably greater than at the minimum in the boundary layer profile. Hence the simplifying assumption of uniform gas having properties of the boundary layer minimum is a poor assumption and leads to breakdown predictions that are too high. On the other hand, if we have no knowledge of the electric field variation over the antenna, and chose a simplifying assumption of uniform electric field at a value equal to the peak field in the aperture plane, somewhat different results will be obtained. At 115 kft, the effect is essentially to increase the electric field at the point of breakdown for a given aperture field. This results in a lower power level required to cause breakdown. At 150 kft, an additional consequence of the uniform field assumption becomes important. At this altitude, the effect of diffusion of electrons is more important in determining the breakdown level because first, the electron density is sufficiently low that the diffusion process is free diffusion rather than ambipolar diffusion, which applies at 115 kft; and second, the number density of neutrals is lower, resulting in a larger diffusion coefficient. Therefore, any assumptions that affect diffusion losses from the breakdown region will have a correspondingly greater effect on the breakdown level. The assumption of a uniform field changes the diffusion geometry in such a way as to decrease the losses of electrons due to diffusion, and this is directly responsible for lowering the predicted breakdown level for this case.

Conclusions

It has been shown that cw breakdown over a rectangular X-band aperture is accurately predicted over a pressure range of two orders of magnitude in room-temperature air. Extensive data have been obtained for pulsed breakdown in air and for cw and pulsed breakdown in nitrogen. All data have been compared in detail with theoretical calculations based on a variational formulation. A breakdown prediction based on recently published results from kinetic theory for ionization frequency, diffusion coefficient, and collision frequency in air have been compared with experimental data. The results are not as good as obtained with the phenomenological data. Discrepancies between the pulsed breakdown data and theoretical predictions are discussed in the light of chemical species produced by previous discharges.

The effects of nonuniformities due to aerodynamic boundary layers, such as found in recent shock tube experiments and on reentry vehicles, are assessed theoretically, and comparisons are made of these results and results obtained if various simplifying assumptions are invoked.

We conclude that the unsteady boundary layers encountered in recent shock tube breakdown experiments do not alter the main conclusions of that work.

REFERENCES

1. Light, G.C.: Jour. Appl. Phys., vol. 39, 1968, p. 1591.

2. Light, G.C.: Jour. Appl. Phys., vol. 40, 1969, p. 1715.

3. Taylor, W.C., Chown, J.B., and Morita, T.: Jour. Appl. Phys. vol. 39, 1968, p. 191.

4. Fante, R.L. and Mayhan, J.T.: Jour. Appl. Phys., vol. 40, 1969, p. 4750.

5. Epstein, M. and Lenander, C.J.: Phys. Fluids, vol. 11, 1968, p. 2753.

6. Epstein, M.: Phys. Fluids, vol. 11, 1968, p. 896.

7. Epstein, M.: Phys. Fluids, vol. 12, 1969, p. 728.

8. Mayhan, J.T. and Fante, R.L.: Jour. Appl. Phys. vol. 40, 1969, p. 449.

9. Light, G.C.: Microwave Breakdown in the Presence of Nonuniformities. TR-0059(6220-10)-4, The Aerospace Corporation, Sept. 1970.

10. Gould, L. and Roberts, L.W.: Jour. Appl. Phys., vol. 27, 1956, p. 1162.

11. Scharfman, W. and Morita, T.: Jour. Appl. Phys., vol. 35, 1964, p. 2016.

12. MacDonald, A.D., Gaskell, D.U., and Gitterman, H.N.: Phys. Rev., vol. 130, 1963, p. 1841.

13. Fante, R.L., Gootkind, D., and Gottesfeld, J.: Radio Sci. (to be published).

14. Mirels, H.: Laminar Boundary Layer Behind a Strong Shock Moving Into Air. NASA TN D-291, 1961.

15. Van Driest, E.R.: Investigation of Laminar Boundary Layer in Compressible Fluids Using the Crocco Method. NACA TN 2597, 1952.

16. Lam, S.H.: Shock-Induced Unsteady Laminar Compressible Boundary Layers on a Semi-Infinite Flat Plate. Ph.D. Thesis, Princeton University, 1958.

17. Felderman, E.J.: AIAA Jour., vol. 6, 1968, p. 408.

18. Mayhan, J.T. and Fante, R.L.: Jour. Appl. Phys., vol. 40, 1969, p. 5207.

19. Harrison, M.A.: Phys. Rev. vol. 105, 1957, p. 366.

20. Masch, K.: Archiv. Elektrotech., vol. 26, 1932, p. 589.

21. Mentzoni, M.: Antennas in Plasma II. Sylvania Electronic Systems, AFCRL-69-0474, 1969.

22. Dobrov, W.I. and MacDonald, A.D.: Phys. Fluids, vol. 12, 1969, p. 1618.

23. Pallone, A.J., et al.: AIAA Jour., vol. 2, 1964, p. 1706.

Table 1

Calculated Diffusion Length vs. Pressure, cw Breakdown in Air

Pressure (torr)	Diffusion Length (cm)
36.4	.0309
16.2	.0602
11.5	.0745
7.61	.0882
5.64	.0963
3.63	.108
2.54	.102
1.89	.108
1.17	.118
.961	.119
.692	.124
.493	.150

Table 2

Calculated Effective Diffusion Length vs Pulse Duration to Breakdown Air at 6.0 Torr

Pulse Duration (μsec)	Diffusion Length (cm)
50	.0929
25	.0871
10	.0793
5	.0707
2.5	.0629
1.0	.0494
0.5	.0427
0.25	.0367
0.1	.0270
0.05	.0237

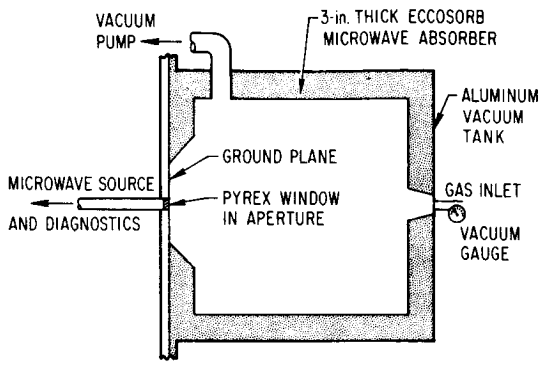

Figure 1.- Absorber lined evacuable chamber for breakdown experiment.

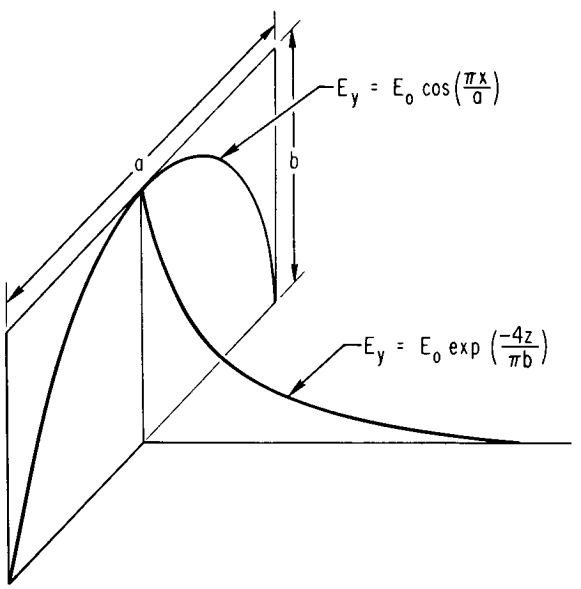

Figure 2.- Waveguide slot geometry and conceptual electric field distribution.

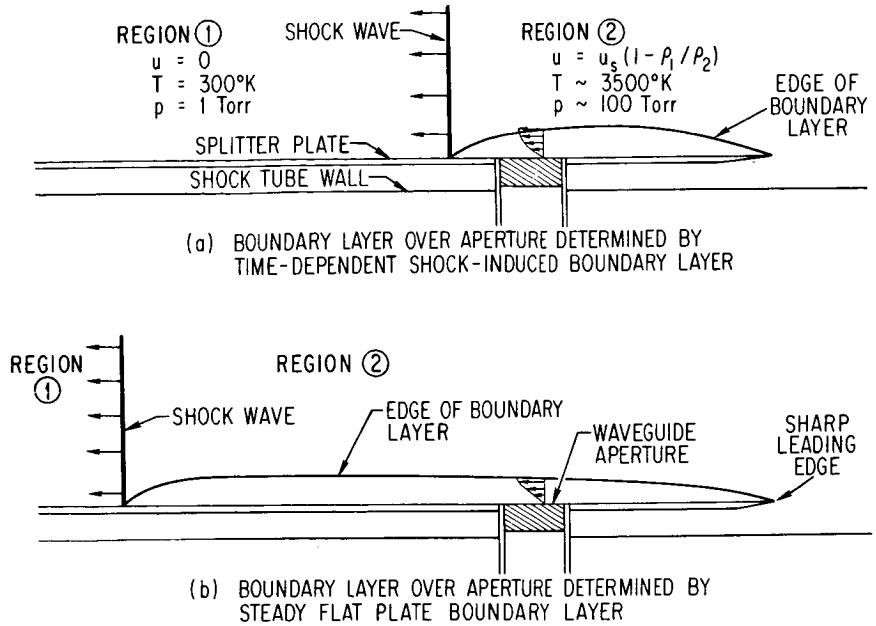

Figure 3.- Shock tube splitter plate boundary layer and its relationship to the waveguide slot.

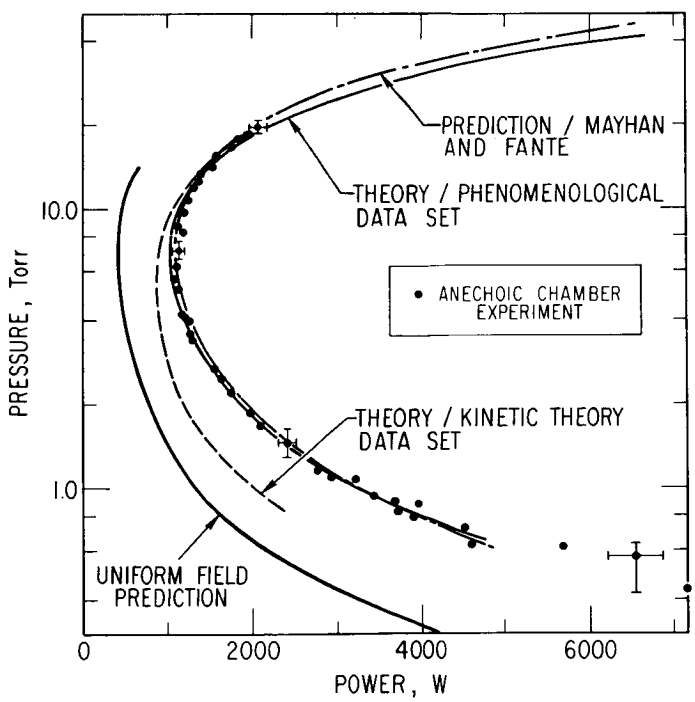

Figure 4.- CW breakdown in air over X-band waveguide slot, showing experimental data and several theoretical calculations.

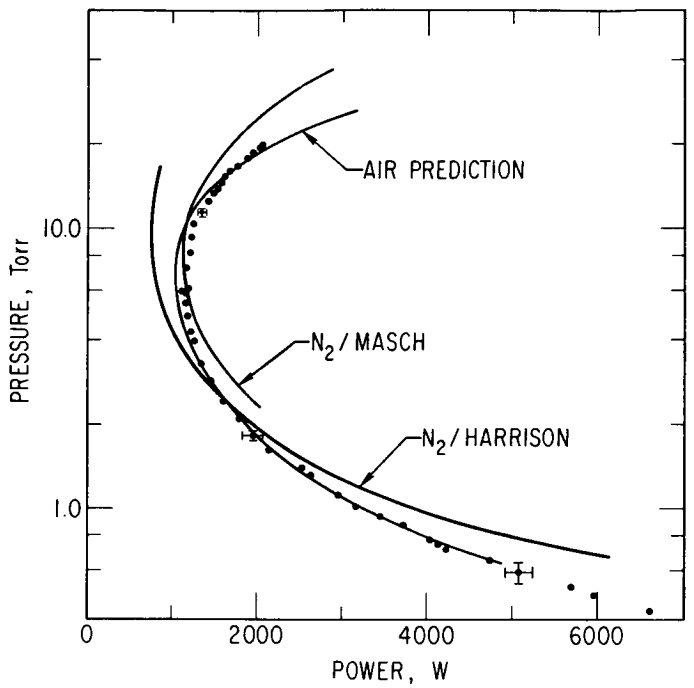

Figure 5.- CW breakdown in nitrogen over X-band waveguide slot, showing experimental data and several theoretical calculations.

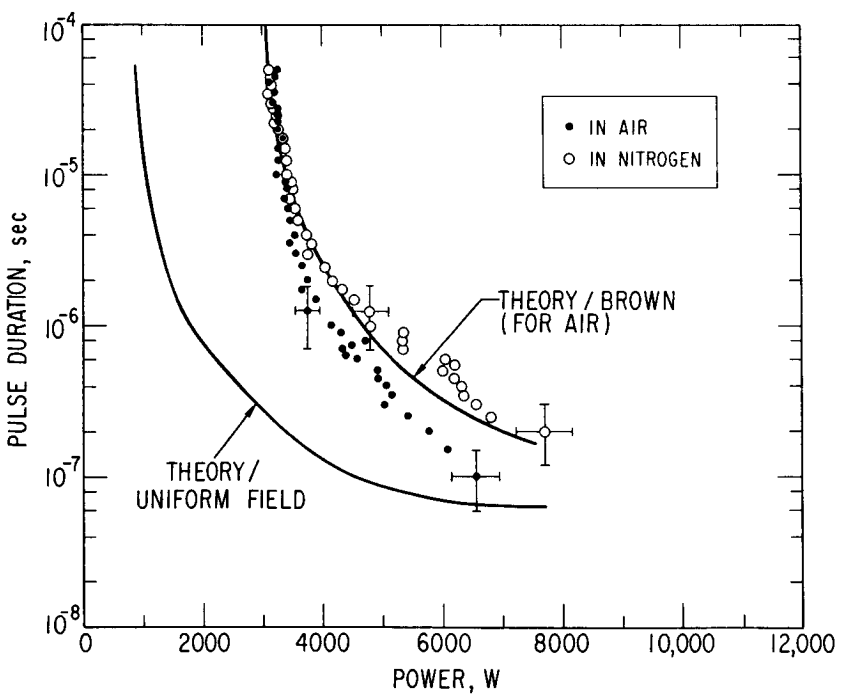

Figure 6.- Pulsed breakdown in air and nitrogen at 1.0 torr, experiment and theory.

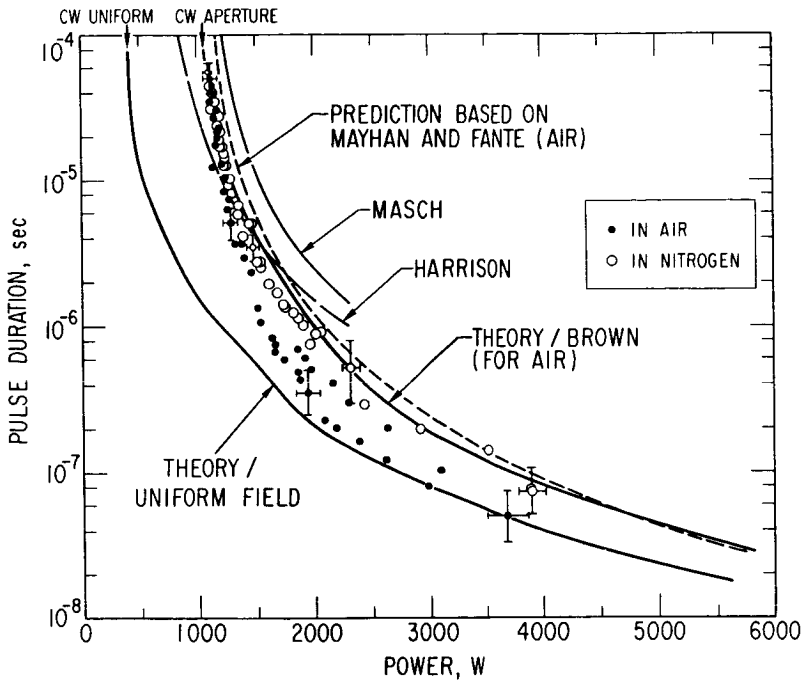

Figure 7.- Pulsed breakdown in air and nitrogen at 6.0 torr, experiment and several theoretical calculations.

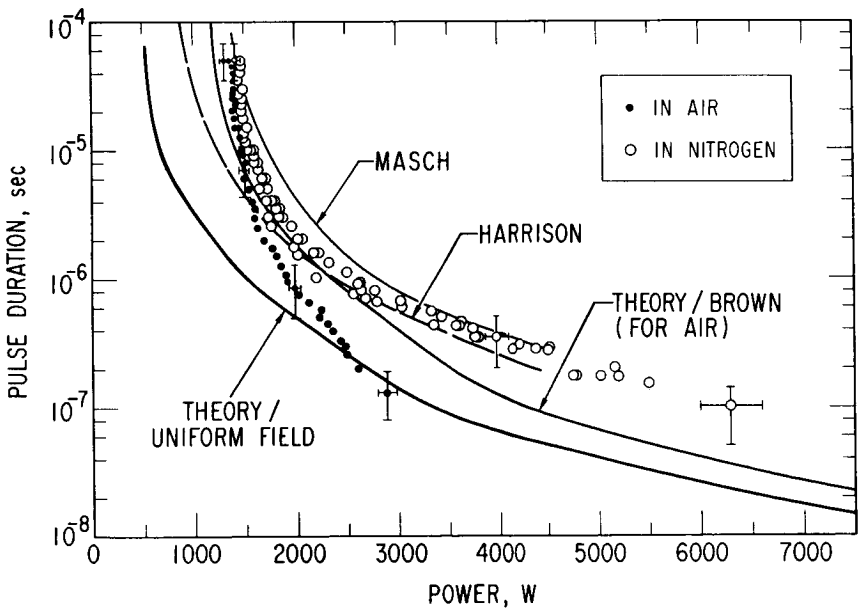

Figure 8.- Pulsed breakdown in air and nitrogen at 12.0 torr, experiment and several theoretical calculations.

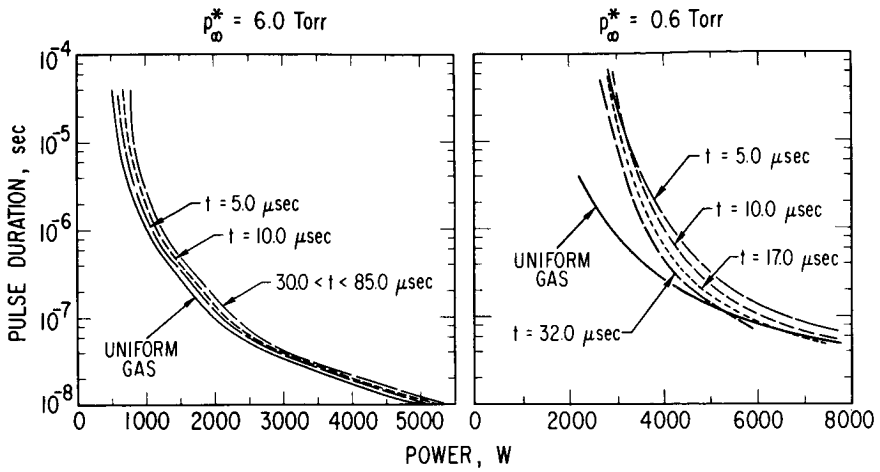

Figure 9.- Breakdown characteristics in a time-dependent shock tube boundary layer at 2 values of free stream density.

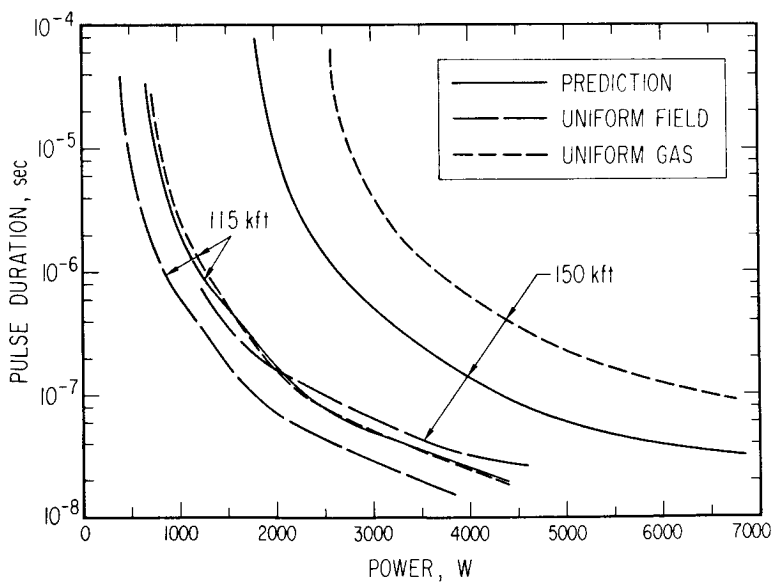

Figure 10.- Predictions of breakdown characteristics in a reentry boundary layer showing the effect of different simplifying assumptions at 2 altitudes.

THE IONIZED STAGNATION REGION FLOW AT LOW REYNOLDS NUMBER

By H. Lew
General Electric Company

SUMMARY

A study is made is this report of the low Reynolds number viscous flow including the merged layer region for a chemically reacting gas of dissociated and ionized air species at the stagnation region of blunt bodies. Use of a two layer model has allowed the inclusion of the effects of heat transfer, shear stress, and heat conduction at the shock. In particular, the electron density in this nonequilibrium regime has been obtained. Results indicate that the production of electrons in the low density regime is still appreciable. Comparison with experimental data tends to indicate that the overall combined scheme of chemical rate constants, species transport, and diffusion properties is a reasonable one.

INTRODUCTION

Re-entry physics of a body in hypersonic flight are complex phenomena involving the dissociation and ionization of air and ablation species. In many applications, it is required to know the detailed distribution of the electron density surrounding the body. These distributions are useful for further studies of their interaction with electromagnetic waves as, for example, communication through the viscous layer or as a source of electrons for the wake. The determination of the electron concentration is a complex problem of chemically reacting fluid mechanics involving the effects of diffusion, surface reactions, mass transfer of ablation species, and finite rate chemistry. This study is concerned with the problem in the high altitude regime at the stagnation region where merged viscous effects and the chemical relaxation of the dissociated air species dominate the flow and are the major factors in the production of electrons.

There have been a number of fluid mechanics models considered for this high altitude regime at the stagnation region of bodies traveling at hypersonic speeds. Cheng[1] has discussed these in detail and placed them in perspective with respect to his two layer model. The principal interests in these previous studies were the heat transfer and skin friction variations at the high altitude. The viscous aerodynamic characteristics for the hypersonic flow through the various altitude regimes of the atmosphere are affected largely by the changing Reynolds number. The regimes of flight where individual phenomena are important can be characterized by this number. This classification has been discussed in detail by Cheng[1] and Hayes and Probstein.[2] The useful Reynolds number is that defined by the free stream density and velocity, the nose radius, and the

viscosity behind the shock, that is, $Re_s = \rho_\infty V_\infty R_N/\mu_s$. Thus, following Cheng[1] the rarefied gas regime of a body traveling at hypersonic speeds can be divided into two regimes I and II as $\infty > \epsilon^2 Re_s \gg 0(1)$ and $\epsilon \leq \epsilon^2 Re_s \leq 0(1)$; regime I contains the boundary layer, vorticity interaction, and the viscous layer with a thin shock, and regime II is the higher altitude regime of the merged viscous layer with a thickened shock so that viscous stresses, conductive fluxes, and diffusion are important. Numerically, if $\epsilon = \rho_\infty/\rho_s$ is taken to be about 0.1, this division gives $Re_s > 100$ and $10 < Re_s < 100$, approximately, for the low and high altitude regimes. Thus, for a one foot nose radius blunt body, the stagnation flow Re_s is 100 and 10 at about 265,000 ft and 300,000 ft altitude, respectively, as can be seen from Fig. 1. Solutions for these regimes involve higher order equations than those given by boundary layer theory. For non-reacting perfect gases, these have been considered by a number of investigators, based on the Navier-Stokes equations simplified by a thin shock layer analysis appropriate for hypersonic speeds. Ho and Probstein[3] have solved the viscous layer regime with a thin shock wave so that the Hugoniot shock equations are the outer boundary conditions. Goldberg and Scala[4] and Goldberg[5] have considered heat transfer and skin friction including mass transfer for chemical equilibrium flows. Cheng[1] has also given some results for an idealized binary gas in nonequilibrium with finite reaction rates. These results tend to emphasize the effect of the cooled wall and the resulting concentration change across the shock. These two effects create a favorable condition for upstream diffusion of the atomic species. In the merged layer regime, Lee and Zierten[6] have integrated the species concentration equations for given pressure, velocity, and static enthalpy functions obtained from frozen solutions of the fluid dynamic equations of the merged layer. Chung (et al.)[7] have considered the merged viscous layer for a binary dissociating gas; the solution of Lee and Zierten[6] utilizes the results for the frozen case. It is evident that a solution for the multi-component dissociated and ionized air species coupled together with the fluid dynamic equations is required in this regime.

It is the purpose of this paper to study the merged viscous layer with reacting air species at the high altitude regime where chemical relaxation and viscous effects dominate. In addition to the complexity introduced by these two effects, a mathematical one arises due to the fact that the set of equations are nonlinear ordinary differential equations with two point boundary conditions whose solutions are elusive to obtain for a multi-species (at least six) mixture if the usual shoot and hunt method of solution for these equations is utilized. The solutions are obtained in this paper by the formulation of the problem into a set of nonlinear finite difference equations and the use of the method of successive accelerated replacements or the method of sweep to obtain their solution by iteration. In the next section, the equations and boundary conditions for the merged viscous layer are developed. The gas model considers a multi-component mixture, with the principal results for air and the thermodynamics and transport properties for the mixture appropriate at high temperatures. The temperatures are relatively high at the shock edge since chemical dissociation begins aft of this point. Then the equations are cast into a set of finite difference equations. Typical results are given for altitude-velocity combinations which show the effects of the heat transfer, shear stress, and diffusion

at the shock edge on the production of the electrons due to the high temperature there and the subsequent diffusion across the layer. Another dominant effect shown is the wall temperature which quenches the production of electrons near the cool wall. Comparison of these theoretical predictions with shock tunnel experimental data is finally given and shows that theory and experiments are in good agreement.

METHOD OF SOLUTION

Nose bluntness is known to be one of the principal mechanisms in the production of electrons for blunted bodies. In most cases, electrons are produced even for slightly blunted conical bodies in the altitude regimes where nonequilibrium effects are not negligible. By a comparison of the boundary layer thickness and detachment distance, it is soon apparent that the boundary layer fills the entire shock layer. For bodies with small nose radii of the order of a fraction of an inch, the boundary layer is thin only below the altitude of 100,000 ft. The Reynolds number based on the body radius at the shock is now sufficiently small that viscosity and heat transfer affects the entire flow and the shock thickness is beginning to grow to an appreciable fraction of the shock layer. At hypersonic velocity, the shock layer is sufficiently thin that the merged viscous layer can be divided into a shock transition layer and body shock layer so that the two layer model as suggested by Cheng[1] is a convenient separation. The equations of motion then include the normal momentum equation for the balance of centrifugal force and then the tangential pressure gradient varies across the layer. The low Reynolds number effect is then embodied in a set of flux boundary conditions at the shock which replaces the usual Rankine-Hugoniot conditions for a thin shock. Of course, the fluid is viscous in the entire region between the body and the shock. With large mass transfer, e.g., due to Teflon ablation, it is expected that the viscous layer (or boundary layer, as the case may be) becomes of the same order as the body radius and the transverse curvature effects become appreciable.

The coordinate system on the surface of the body is denoted by x and y which are the physical distances tangential and normal to the body as shown in Fig. 2. These are transformed by the density function in the usual way to

$$\xi(x) = \int_0^x (\rho\mu)_r u_e r_b^{2j}\, dx$$

$$\eta(x,y) = \frac{u_e}{(2\xi)^{1/2}} \int_0^y \rho r_b^j\, dy \qquad (1)$$

This function r is defined by

$$r = r_b + y \cos \theta_b$$

where r_b is the local body radius at point x, and θ_b is the angle the body slope makes with the axis of the body, $j = 0$ for a two dimensional body, $j = 1$ for an axisymmetric body, $(\rho\mu)_r$ is a reference value of the density viscosity product usually taken to be a constant, u_e the velocity $V_\infty x/R_N$ at the stagnation point. When transverse curvature effects are small, $r \approx r_b$. Utilizing this coordinate system and the thin shock layer assumption, the tangential momentum equation reduces to

$$\frac{\partial}{\partial \eta}\left(l \frac{\partial f'}{\partial \eta}\right) - V \frac{\partial f'}{\partial \eta} + \beta\left[\frac{\bar{M}_e}{\bar{M}} \theta\right] - \frac{1}{(1 + j)} f'^2 = 0 \qquad (2)$$

where $l = (\rho\mu)/(\rho\mu)_r$, f' is the tangential velocity ratio across the layer, $\bar{M}$ is the mixture molecular weight, and $\theta = T/T_e$. In this equation β is the tangential pressure gradient parameter defined by

$$\beta(y) = \frac{1}{(j + 1)} \frac{2R_N^2 \frac{1}{2x} \frac{\partial p}{\partial x}}{V_\infty^2} \qquad (3)$$

The function β depends on the normal distance across the layer and in some cases varies by as much as 30% or more across the layer. In this formulation, consistent for the thin shock layer, the pressure is assumed constant across the layer. Perfect gas computation indicates that this is a reasonable assumption.[1,3]

Thus, it is seen that the pressure p has been expanded from the stagnation point by the series

$$p(x,y) = p_0 + x^2 p_2(y) + \ldots \qquad (4)$$

so that the tangential pressure gradient is given by

$$\frac{\partial p}{\partial x} = 2x p_2(y)$$

and p_0 has been assumed constant across the layer.

The normal momentum equation across the layer, from a balance of centrifugal forces, is given by

$$\kappa \rho u^2 = \frac{\partial p}{\partial y} \tag{5}$$

where κ is the local surface curvature. For the stagnation point, κ is simply the inverse of the nose radius R_N.

Utilizing the transformations (1), this equation becomes

$$\frac{\partial p_2}{\partial \eta} = \left(\frac{V_\infty}{R_N}\right)^{3/2} \sqrt{\frac{(\rho\mu)_r}{(1+j)}} \frac{1}{R_N} f'^2 \tag{6}$$

In addition, conservation of mass at the stagnation point implies the satisfaction of

$$\frac{\partial V}{\partial \eta} + f' = 0 \tag{7}$$

so that V is defined in terms of the mass flux

$$V = \frac{\rho v}{\sqrt{(j+1)(\rho\mu)_r V_\infty / a}} \tag{8}$$

The problem concerned herein is that of a finite rate chemically reacting viscous flow where species diffusion is important. At the lower altitude, it is expected that the species will include, in addition to air, the products of ablation from body material which then leads to chemical reactions of air with hydrocarbon or Teflon species involving species with disparate molecular weights. For this reason only will multi-component diffusion be important. When only air species are concerned, the electron density predicted for a constant Lewis number is only a few percent different from that predicted by the use of multi-component diffusion. The energy equation for the stagnation point can be written in the form:

$$-V \frac{\partial \theta}{\partial \eta} + \bar{c}_p \frac{\partial}{\partial \eta}\left(l \frac{\bar{c}_p}{Pr} \frac{\partial \theta}{\partial \eta}\right) + \frac{l}{Pr} \frac{\partial \theta}{\partial \eta} \sum_{i=1}^{N} \frac{c_{p_i}}{\bar{c}_p} \left\{ (Le_i) \frac{\partial c_i}{\partial \eta} \right\} - \left(\frac{2\xi}{\bar{c}_p T_e u_e \xi_x}\right) \sum_{i=1}^{N} h_i \frac{w_i}{\rho} = 0 \tag{9}$$

where θ is the temperature ratio T/T_e, N is the number of chemical species, $\bar{c}_p$ is the coefficient of specific heat and equal to $\sum_{i=1}^{N} c_{p_i} c_i$ the sum over the individual species value of c_{p_i}, l is the ratio of the product of viscosity coefficient and mass density referenced by a value denoted by $(\rho\mu)_r$, Pr is the Prandtl number, h_i is the species enthalpy, and w_i/ρ is the rate of production of species i per unit volume.

The species distribution is governed by the multi-component diffusion equations and balances the generation of species by chemical production and the diffusion of these species. These equations for the mass fraction c_i for $i = 1$ to N are

$$-V \frac{\partial c_i}{\partial \eta} \frac{\partial}{\partial \eta}\left[\frac{l}{\mathrm{Pr}}\left(\mathrm{Le}_i\right)\frac{\partial c_i}{\partial \eta}\right] + \frac{2\xi}{u_e \xi_x} \frac{w_i}{\rho} = 0 \tag{10}$$

where Le_i is the binary diffusion Lewis number.

The presence of mass transfer is indicated then by the condition

$$V(0) = \left(\frac{R_N}{V_\infty}\right)^{1/2} \frac{(\rho v)_w}{\sqrt{(1 + j)(\rho\mu)_r}} \tag{11}$$

where $(\rho v)_w$ is the normal flux of ablation material entering the viscous layer and can be obtained from a coupled analysis with thermal response of the body material to the heat pulse, or it can be prescribed. The latter analysis also leads to a boundary condition for the body temperature related to its heat flux and dependent on the catalyticity and heterogeneous reaction at the body surface. One condition which is useful for the problem is that the wall temperature T_w is prescribed. Moreover, since the wall temperature is usually low for the altitude concerned the species at the body surface are undissociated.

The problem considers the flow in the entire stagnation region to be fully viscous with a nonzero shock thickness (shock transition layer) affected also by the viscosity. The viscous shock thickness is small compared to other normal dimensions;[1] a first integral of the shock conservation equation can be obtained for the shock heat fluxes, diffusion flux, and shear stress. These conditions, at the shock edge, for the velocity components are

$$u_s = V_\infty \cos \theta_s - \frac{\mu_s}{\rho_\infty V_\infty}\left(\frac{\partial u}{\partial y}\right)_s$$

$$v_s = -\frac{\rho_\infty}{\rho_s} V_\infty \tag{12}$$

where θ_s is the shock angle and is $\pi/2$ for the stagnation point. One notes the coordinate system convention in Fig. 2. The quantities of pressure, enthalpy, and species then are

$$\left.\begin{aligned} p_s &= p_\infty + \rho_\infty V_\infty^2\left(1 - \frac{\rho_\infty}{\rho_s}\right) + \frac{4}{3}\mu_s\left(\frac{\partial v}{\partial y}\right)_s \\ h_s &= \frac{1}{2}V_\infty^2 + h_\infty - \frac{1}{2}\left(u_s^2 + v_s^2\right) - \frac{1}{\rho_\infty V_\infty}\left[k\frac{\partial T}{\partial y}\right. \\ &\quad \left. + \sum_i \frac{\mu}{Pr}\left(Le_i\right)\frac{\partial c_i}{\partial y} + \frac{4}{3}\mu v\frac{\partial v}{\partial y} + \mu u\frac{\partial u}{\partial y}\right]_s \end{aligned}\right\} \tag{13}$$

and

$$c_{i_s} = c_{i_\infty} - \frac{1}{\rho_\infty V_\infty}\left(\frac{\mu}{Pr}\right)\left(Le_i\right)\frac{\partial c_k}{\partial y}$$

for $i = 1,\ldots,N$.

The equations are to be applied at the shock edge defined by the equality of the normal velocity of the external flow and the viscous region. The Rankine-Hugoniot conditions are recovered for a thin shock for negligible effects of the heat transfer, shear stress, and diffusion. The parameter (as mentioned in the Introduction) indicating the regime of validity of the additional terms (i.e., nonzero values of these gradients) is given by

$$K^2 = \frac{1}{2}\left(\frac{\rho_\infty}{\rho_r}\right)\frac{\rho_\infty V_\infty R_N}{\mu_r} \tag{14}$$

where K is composed of the product of the density ratio across the shock and a Reynolds number based on body nose radius and shock viscosity. Thus, if K is large, the shock slip terms are negligible. For low Reynolds number where K has moderate values, the effect of the transport terms is contained above. For the low temperature in the shock thickness regime which is almost free

stream, the chemistry is essentially frozen; the frozen transition zone is consistent with the differential equation to the order of reciprocal of the Reynolds number. The variation of typical Reynolds number with altitude is shown in Fig. 1.

The boundary conditions as given in equations (16) and (17) are applied at the shock front. The location of the shock front can be found by requiring the transformed velocity to attain the following value there:

$$V_s = -\rho_\infty \sqrt{\frac{V_\infty R_N}{(\rho\mu)_r (1 + j)}} \tag{15}$$

This condition essentially leads to the detachment distance, although the shock transition zone is the outer flow and is viscous. The entire viscous region between the free stream and the body can then be found by combining the two layers.

GAS MODEL

The gas model is usually composed of the species and reactions listed in Table I. As can be seen, it is a combination of dissociated and ionized air. The results presented here for the stagnation region are for air species as given by the seven reactions.

For the chemically reacting flow, the enthalpy is obtained by the summation of the individual species values; thus,

$$h = \sum_{i=1}^{N} c_i h_i \tag{16}$$

where the pure species enthalpy of Browne[8] has been utilized. The thermodynamic properties for the diatomic molecules were obtained utilizing the second virial coefficient approach which essentially leads to the thermodynamic properties departure from the monatomic gas at the higher temperature; the Morse potential is utilized. At the lower temperature, the diatomic species are considered as rigid rotator harmonic oscillators with corrections for rotational stretching and vibrational anharmonicity. Comparisons of these data with others are excellent and have been given by Browne.[8] The individual species values of the enthalpy are given in Fig. 3.

The mixture specific heat is obtained similarly as

$$\bar{c}_p = \sum_{i=1}^{N} c_i c_{p_i} \tag{17}$$

TRANSPORT PROPERTIES

The transport properties involve the coefficients of viscosity and conductivity. The individual species coefficients have been obtained from a number of sources. The species viscosity in terms of the collision integrals is given by the relation

$$\mu_i = 26.693 \times 10^{-6} \frac{(M_i T)^{1/2}}{\Omega_i(2,2)} \tag{18}$$

with units of μ_i in poises. Collision integrals from Yun and Mason[9] for dissociated air species are utilized in the computations; the integrals are dependent on the intermolecular potential. The conductivity k_i of the species is related to μ_i by

$$k_i = \frac{\mu_i R}{M_i}\left[c_{p_i}\frac{M_i}{R} + 1.25\right]$$

where k_i is in g-cal per (cm sec ^{o}K). Finally, the mixture values of the viscosity and conductivity are given by Wilke's rules whereby

$$\mu = \sum_{i=1}^{N}\left(\frac{X_i\mu_i}{\sum_{j=1}^{N} X_j\phi_{ij}}\right)$$

$$k = \sum_{i=1}^{N}\left(\frac{X_i k_i}{\sum_{j=1}^{N} X_j\phi_{ij}}\right) \tag{19}$$

where $X_i = c_i\bar{M}/M_i$

$$\phi_{ij} = \frac{\left[1 + \sqrt{\frac{\mu_i}{\mu_j}\left(\frac{M_j}{M_i}\right)^{1/4}}\right]^2}{\sqrt{8}\sqrt{1 + \frac{M_i}{M_j}}} \tag{20}$$

CONSERVATION OF ELEMENTS

It is convenient for the study of chemically reacting flows to consider the element equations since they do not involve the chemical source terms. These equations express the condition that except for the introduction of material at the ablating surface no elements are created or destroyed at any point of the flow field. Thus, by summing the species equation according to the relation

$$c^j = \sum_{i=1}^{N} \alpha_i^j \frac{M^j}{M_i} c_i$$

for $j = 1, J$ elements, and where α_i^j = number of atoms of element j in species i,

$$-V \frac{\partial c^j}{\partial \eta} + \frac{\partial}{\partial \eta}\left[\frac{l}{Pr} (Le) \frac{\partial c^j}{\partial \eta}\right] = 0 \tag{21}$$

since $\sum \alpha_i^j \frac{M^j}{M_i} w_i = 0$; i.e., mass fractions of chemical elements are preserved in chemical reactions. There are J elements and N species in the system. In addition, the mass fractions obey the relation

$$\sum_{i=1}^{N} c_i = 1 \tag{22}$$

implying $(N - 1)$ independent species equations or $(J - 1)$ element equations.

The boundary conditions for the species equations depend on the reactions with the body material. For the high altitude regime, the wall temperature and pressure are low and it appears appropriate to assume that the species are undissociated.

In general, both species and elements, equations (10) and (21), have to be considered together. Due to the condition (22), there are only $(N - 1)$ species equations but only $(N - J)$ need to be considered when $(J - 1)$ independent element equations are utilized. The boundary conditions at the body surface for the elements are specified by the fact that only surface elements are created there and, in the absence of a mass transfer, the following conditions holds:

$$\sum_{i=1}^{N} \frac{M^j}{M_i} \alpha_i^j \dot{m}_{i_w} = 0 \tag{23}$$

for $j = 1,\ldots,J$ where it is remembered that in general

$$\dot{m}_i = c_i \rho v + j_i \tag{24}$$

in terms of the diffusion flux j_i. Equations (23) essentially give relations for the slopes of the species profile at the wall and lead to $(J - 1)$ values for the element concentration at the surface. A second implication of equations (23) is that J values of the mass flux of the N species are uniquely determined and that only $(N - J)$ species mass flux can be prescribed, for example, as surface material reactions or mass transfer of coolant. For consideration in this problem as mentioned above, the species are prescribed as undissociated (same as equilibrium conditions here because of low pressure) with the elements condition providing the c_w^j. Note that if the equilibrium condition is applied at the surface, the c_w^j is utilized to obtain the species c_{i_w}.

METHOD OF SOLUTION

The finite difference method is utilized for the iterative solution of the two point boundary value problem. The system of equations consists of $(N + 4)$ equations of which all are second order except for two. A central difference scheme is written and the entire system of nonlinear algebraic equations resulting from this is solved. The solutions presented herein are obtained by two techniques which are both iterative. Since the systems of linearized equations are tri-diagonal, the sweeping method is utilized efficiently with a resubstitution of the average correction to the coefficient. Another method considered for these solutions was the method of successive accelerated replacement which operates on the nonlinear set of equations; an example of this method has been given in reference 10.

It has been found that the latter method is indeed a rapid convergent algorithm for the iterative solution of these nonlinear equations.

RESULTS

Results for the high altitude regime where the Reynolds number is low have been obtained and are presented here. The discussion is concerned with air species, and the components O_2, N_2, O, N, NO, NO^+, and e^- for air are included; this system is appropriate for the body velocities of the order of 20,000 fps. The rate constants are those suggested by Bortner.[11] These constants and their reactions are listed in Table I. Although a more elaborate set of chemical reactions has been considered, the results for this simpler system suffice to indicate the production of species, especially that of electrons. As can be seen from Table I, the dissociation processes for O_2, N_2, and NO and the

rearrangement reactions between the O, N atoms and their molecular species are considered.

Consider the slightly blunted body with nose radius of 1/4". As can be seen from Fig. 1, for a velocity of 20,000 fps, the flow about the stagnation region is in the merged viscous layer regime from about 150,000 ft altitude up. The Reynolds number Re_s based on the frozen Rankine-Hugoniot conditions behind the shock is 251 at 150,000 ft and becomes 43.2 at 200,000 ft. Note that the actual temperature is about 0.9 the Rankine-Hugoniot value at 200,000 ft. Consider the flow at 200,000 ft where the example calculations are shown and where the shock is sufficiently thick to affect the slopes of temperature and concentration. The temperature and velocity distributions are shown on Fig. 4. The velocity f' at the edge of the layer is about 0.88 and approaches unity in the free stream; in other words, the velocity has decreased from the value of 1 to 0.88 through the shock transition zone. The maximum temperature occurs just aft of the edge of the shock. Figure 4 also shows the molecular species O_2 and N_2, indicating a slight dip in the middle of the layer. The species wall condition is that of a non-dissociated gas. This is also apparent from Fig. 5 showing that O and N atoms and nitric oxide NO achieve their maximum inside the shock layer and are driven to zero at the surface by the low wall temperature. Diffusion of the atomic species upstream occurs. It is interesting to consider the production of these species and to note their variation in Fig. 6.

The production of species is shown on Fig. 6 and this gives an illuminating picture of species generation. As expected, the production of atomic species occurs largely at the high temperature end of the shock layer and diffusion establishes the distribution of the species. For example, the maximum electron density occurs at the midpoint of the layer ($\sim\eta = 2.16$) whereas the maximum production is at $\eta = 3$. Due to the low density, the three body recombination process is not an efficient one so that the atomic oxygen produced in the dissociation process practically never recombines by the reaction $O + O \rightarrow O_2$. This is also true of the dissociation reaction for nitrogen molecules. The loss of atomic species is due to the production of nitric oxide. In this example, the reaction $N_2 + O_2 \rightleftarrows 2NO$ was included but the contribution in both directions to the overall kinetics is negligible. Since recombination is small, two body processes dominate the flow field and it is expected that binary scaling as in inviscid flow is a useful means of obtaining information from flow fields with different altitude-velocity histories. The most significant item from this type of study is the distribution of electron density through the layer. This is shown on Fig. 7, and again, as expected, the maximum occurs inside the shock layer and about the midpoint. It should be kept in mind that these figures are plotted with respect to the transformed distance so that the bottom 1/2 of the physical thickness corresponds to about 2/3 of that in the η coordinate system. In these results, the Lewis number has been taken equal to the constant value of 1.4. The effect of multi-component diffusion is small for air species, as noted before. It is interesting to note that the Prandtl number varies throughout the layer but is sensibly close to the value of 0.75. This variation together with the density-viscosity product through the shock layer is given on Fig. 8.

PRESSURE GRADIENT PARAMETER

The tangential pressure gradient varies across the layer in these flows. A typical variation is shown on Fig. 9 for the $\frac{1}{4}$" nose radius case at 200,000 ft. At the wall, p_2 has a value of 0.61 and drops to about 95% of this value at the shock. The thin boundary layer assumes a constant value.

COMPARISON WITH EXPERIMENTAL DATA

A comparison of this theory with experimental data of Kaegi and McMenamin[12] can be made. Kaegi has measured air ionization in stagnation region of blunt body shock layer with Langmuir probes for air densities corresponding to the high altitude regime. The nose radius of the 10 degree sphere cone body considered was 3". The test conditions are given by Kaegi.[12] The free stream tunnel conditions include dissociated and ionized mixtures of air with values of mass fraction of oxygen atoms equal to 0.18 and of NO^+ equal to 4.2×10^{-6} and with a free stream density of 3.49×10^{-7} slug/ft^3 which corresponds to an appreciable number of electrons there. The Reynolds number Re_∞ is high in this case, being 3160 with a $Re_s = 300$. These values of Reynolds number place this flow at the border line between a merged layer flow and a viscous layer; that is, the flow inside the shock layer is viscous but the shock transition layer is thin. Figure 10 shows this through the velocity profile which has a shape similar to that of a viscous layer near the body tied to a vorticity layer in the upper half of the shock layer. The edge values of temperature and velocity are close to the Rankine-Hugoniot shock values. The species concentrations are also shown on Fig. 10 and on Fig. 11. Due to the cold wall existing in the experimental conditions, the NO and N species peak in the middle of the layer whereas the O atoms are not able to, since there are a large number already in the free stream. The experimental measurement of electron density distribution along the stagnation line is shown on Fig. 12. Since this is a two layer model, only the body viscous layer is shown and, as can be seen, there is excellent agreement between the two. Note that the inviscid approximation to this flow is not adequate to describe the ionization, especially near the wall.

CONCLUDING REMARKS

A study has been made of the low Reynolds number viscous flow including the merged layer region for a chemically reacting flow which may be composed of dissociated and ionized air species and ablation species. The use of a two layer model has allowed the inclusion of the effects of heat transfer, shear stress, and heat conduction at the shock. Results have been obtained which tend to confirm that the nose bluntness is an important factor in the production of electrons even at the low density regime; an appreciable number are obtained. The dominant features of these flows are the diffusion of the species generated at the shock front toward the body and upstream and the quenching effect of the

low temperature in recombining these species as the flow approaches the body. Comparison with experimental data tends to confirm these results for the electron density distribution and that the overall combined scheme of chemical rate constants, species transport properties, and diffusion coefficients is a reasonable one.

REFERENCES

1. Cheng, H., "The Blunt Body Problem in Hypersonic Flow at Low Reynolds Number", IAS Paper 63-92 (Jan. 1963).

2. Hayes, W. D., and Probstein, R. F., "Hypersonic Flow Theory", Academic Press, New York (1959).

3. Ho, H., and Probstein, R., "The Compressible Viscous Layer in Rarefied Hypersonic Flow", Rarefied Gas Dynamics, Academic Press (1961).

4. Goldberg, L., and Scala, S., "Mass Transfer in the Hypersonic Low Reynolds Number Viscous Layer", IAS Preprint 62-80, Jan. 1962. Also GE TIS R65SD27, 1965.

5. Goldberg, L., "The Structure of the Viscous Hypersonic Shock Layer", GE TIS R65SD50, 1965.

6. Lee, R. H. C., and Zierten, T. A., "Merged Layer Ionization in the Stagnation Region of a Blunt Body", Proceedings of the 1967 Heat Transfer and Fluid Mechanics Institute, Stanford University Press.

7. Chung, P. M., Lui, S. W., and Holt, J. F., "Merged Stagnation Shock Layer of Nonequilibrium Dissociating Gas", AIAA Journal.

8. Browne, W. G., "Thermodynamic Properties of Some Atoms and Atomic Ions", "Thermodynamic Properties of Some Diatoms and Diatomic Ions at High Temperatures", and "Comparison of Thermal Functions Generated for Species in the High Temperature Air System with Literature Values", GE-RS, Physics TM No. 2, 8, and 10, 1962.

9. Yun, K. S., and Mason, E. A., "Collision Integrals for the Transport Properties of Dissociating Air at High Temperatures", Physics of Fluids, Vol. 5, No. 2, 155-164, Feb. 1962.

10. Lew, H. G., "Method of Accelerated Successive Replacement Applied to Boundary Layer Equations", AIAA Journal, Vol. 6, No. 5, May 1968.

11. Bortner, M., "A Review of Rate Constants of Reactions in Re-Entry Flow Fields", GE TIS R68SD13, June 1968.

12. Kaegi, E. M., and McMenamin, D. L., Jr., "Measured and Predicted Air Ionization in Blunt Body Shock Layer", AIAA Paper No. 69-81, Jan. 1969. GE-ARP Report.

TABLE I AIR REACTIONS

REACTION RATES

REACTION	Forward Rate a	Forward Rate c	Forward Rate b	Reverse Rate a	Reverse Rate c	Reverse Rate b
1.	2.5×10^{16}	59,380	- .5	8.9×10^{14}	0	- .44
2.	2.0×10^{21}	113.174	-1.5	1.91×10^{20}	0	-1.57
3.	5.5×10^{20}	75,483	-1.5	1.67×10^{20}	0	-1.52
4.	3.2×10^{9}	19,676	1.0	2.67×10^{10}	3,540	.92
5.	6.8×10^{13}	377,000	0	2.13×10^{13}	0	- .04
6.	6.4×10^{9}	32,400	.5	7.0×10^{18}	0	- .9
7.	6.69×10^{24}	64,600	-2.54	2.4×10^{23}	32,380	-2.5

REACTION

1. $O_2 + M_1 \rightleftarrows 2O + M_1$
2. $N_2 + M_2 \rightleftarrows 2N + M_2$
3. $NO + M_3 \rightleftarrows N + O + M_3$
4. $O + NO \rightleftarrows O_2 + N$
5. $O + N_2 \rightleftarrows N + NO$
6. $O + N \rightleftarrows NO^+ + e^-$
7. $N_2 + O_2 \rightleftarrows 2NO$

$k = aT^b e^{-c/T}$

(gm-mole, cm^3, sec, ^oK)

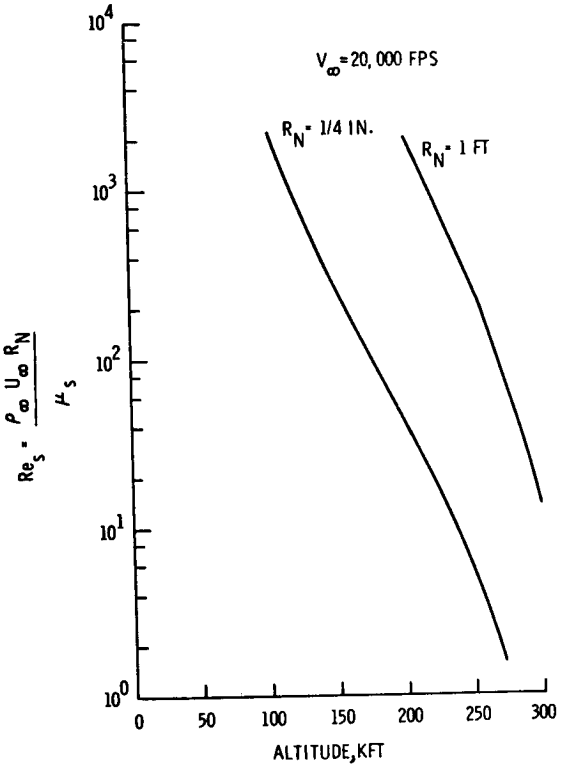

Figure 1.- Flow Reynolds number at stagnation point.

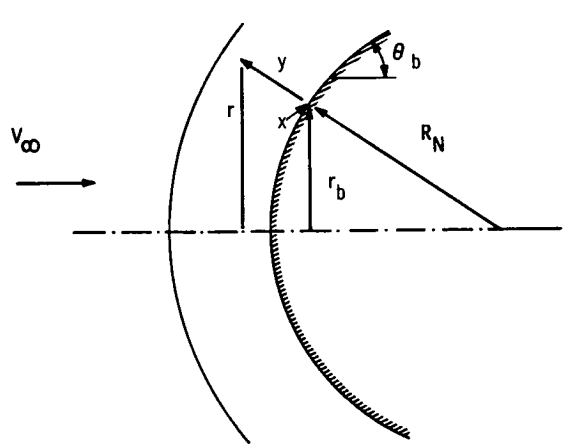

Figure 2.- Coordinate system and body geometry.

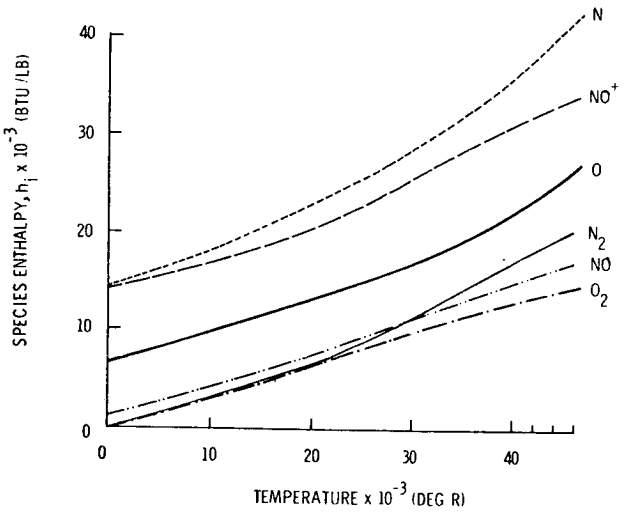

Figure 3.- Species enthalpy.

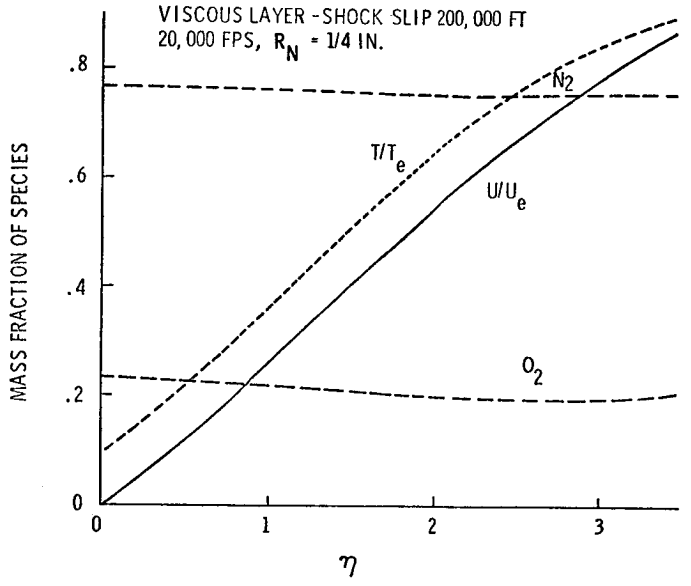

Figure 4.- Velocity, temperature, and species distribution for stagnation region merged viscous flow.

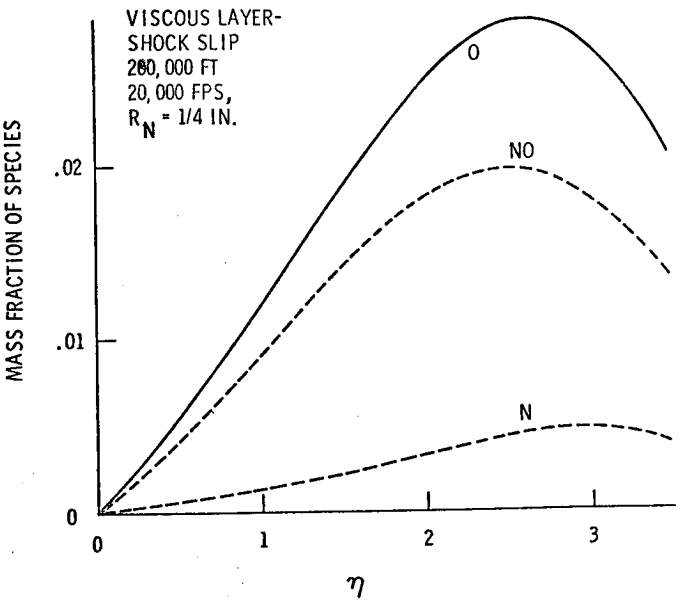

Figure 5.- Species distribution.

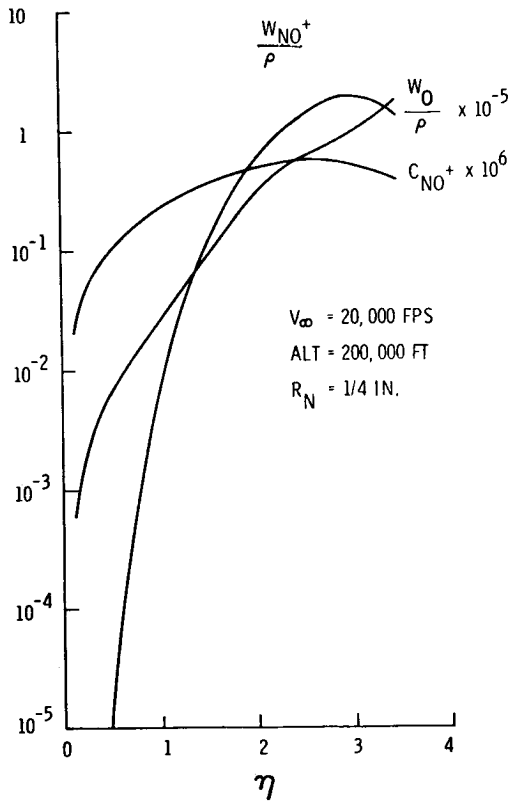

Figure 6.- Production of species across the viscous layer.

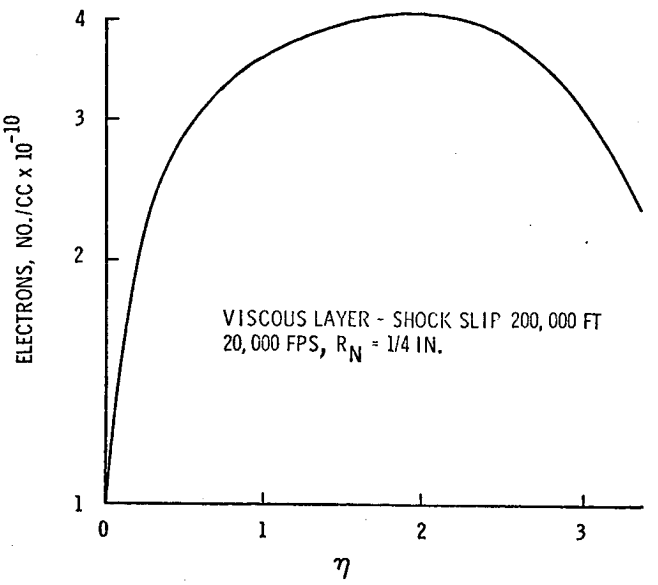

Figure 7.- Electron density distribution.

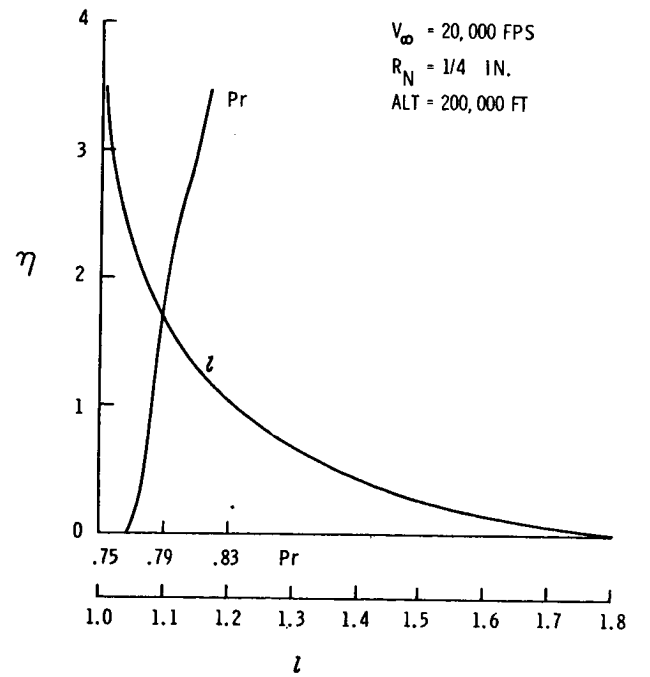

Figure 8.- Prandtl number and viscosity-density ratio across the viscous layer in stagnation region.

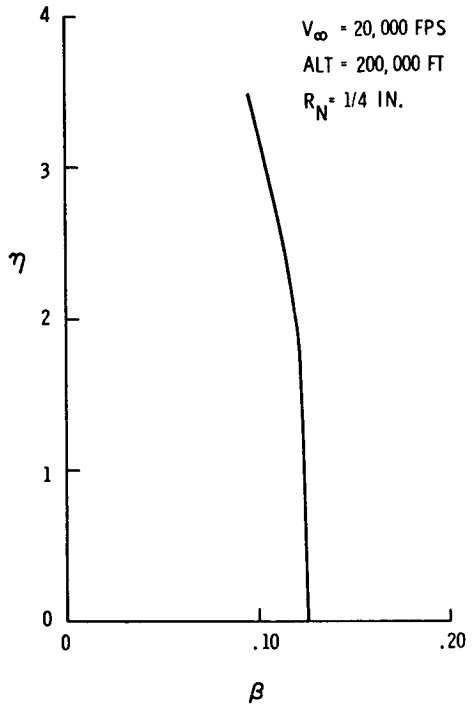

Figure 9.- Tangential pressure gradient across the layer at stagnation point.

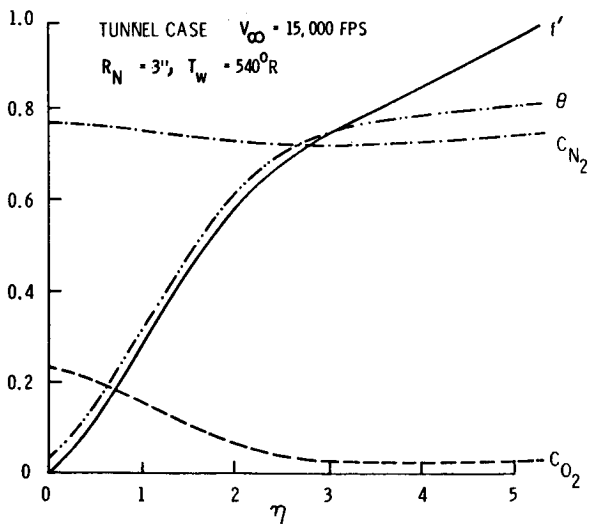

Figure 10.- Velocity, temperature, and species distribution for tunnel flow.

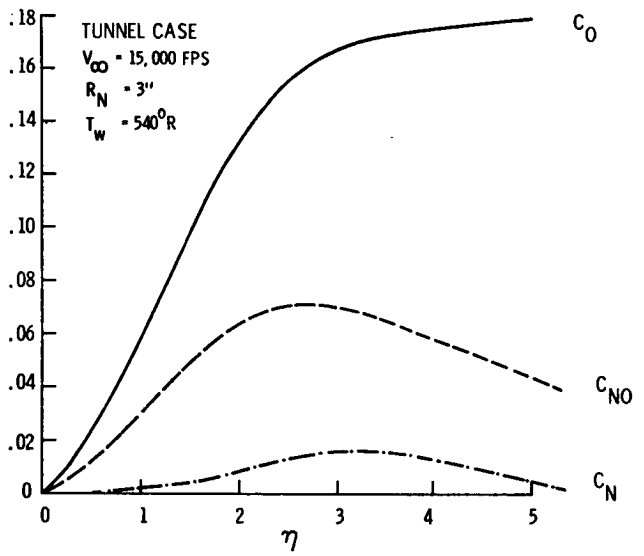

Figure 11.- Species distribution for tunnel flow.

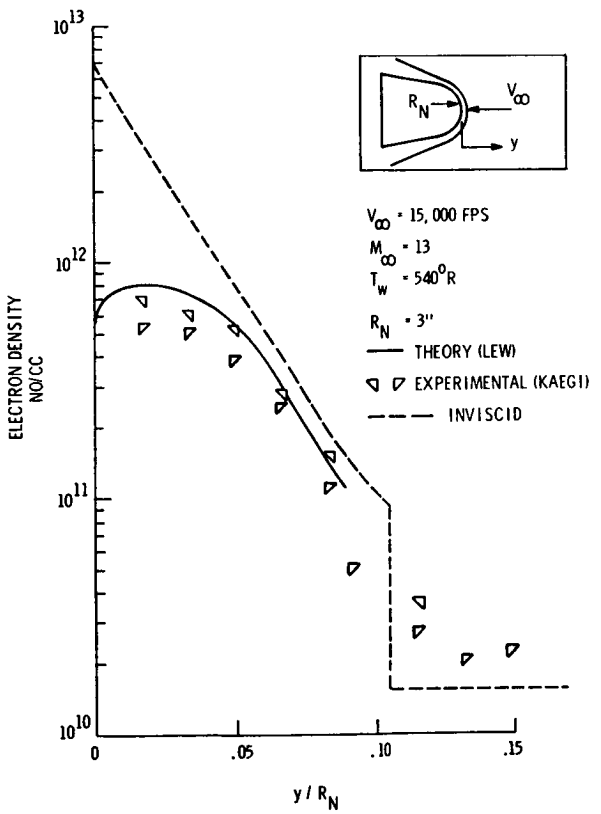

Figure 12.- Comparison of theory and measurement of stagnation region shock layer ionization distribution.

A SHOCK TUBE STUDY OF PLASMA ALLEVIATION BY OXIDE DUST

A. Modica, G. Stepakoff, and H. Rosenbaum

Avco Systems Division
Wilmington, Massachusetts

SUMMARY

Plasma alleviation has been observed in shock heated tungsten oxide-air suspensions at temperatures near 3200°K and 1 atm total pressure. Electron density histories were followed with X-band microwaves and oxide particle concentrations were measured by light scattering. For 3 micron size WO_3 particles at concentrations of 3.6 (10^4) particles/cm^3 (0.03 weight fraction) electron densities were reduced by a factor of 3 below that of clean-air plasmas. The results are interpreted by an electron attachment mechanism including thermionic emission, air ionization, electron-particle attachment, three-body surface ion recombination, oxide gas-phase attachment and catalytic surface attachment. A nonequilibrium stream tube program is used to compare calculated electron densities with experiment.

INTRODUCTION

During hypersonic vehicle reentry the ability to control the electron formation processes, which take place in the plasma sheath, has important applications associated with communication blackout, microwave transmission through the plasma and turbulent wake radar observables. A review of the literature on plasma alleviation by additives[1-8] leads to the conclusion that for high temperature environments refractory metal oxides would be effective quenchant agents,

provided thermionic emission is negligible. The important properties of the refractory oxides are that the materials can exist at high temperatures to provide "catalytic" surface sites for electron-ion recombination, reduce electrons by thermal electrification, and vaporize to give electrophilic gas-phase oxides having large electron cross sections. In the present paper some experimental data and theoretical analysis are given on the electron attachment performance of tungsten oxide in a shocked air plasma. The study involved preparing a suspension of 3 micron diameter tungsten oxide powder in a dust cyclone chamber, introducing a sample of the oxide dust-air mixture into a shock tube and passing a shock wave through the test gas mixture. Particle concentrations in the dust sample were quantitatively determined by measuring the transmitted intensity of a scattered beam of monochromatic light of 2500°A wavelength. Electron densities in the shocked plasma were monitored by measuring the transmitted power of X-band microwaves at 10.3 Gc. The microwave attenuation signals were calibrated against clean air shock waves using a theoretical stream tube computer program to calculate electron densities from high temperature air chemistry. Metal oxide particle trajectories and ablation rates are calculated from one dimensional flow considerations using continuum-flow Stokes-law drag coefficients and average Nusselt numbers for convective heat transfer. The rate of ablation of metal oxide powder was also determined experimentally behind the shock wave by monitoring the gas-phase ultraviolet absorption of WO_3 molecules. A stream tube computer program modified to include ablation of solid particles and particle surface area changes was used to calculate theoretical electron density profiles. An electron attachment model and electron collision frequencies based on kinetic theory were used in the calculations. The numerical analysis allows an assessment of the relative importance of

surface attachment and gas-phase electron attachment in terms of particle size, ablation temperature, mass fraction, particle number density, and electron attachment cross sections.

EXPERIMENTAL TECHNIQUE

Dust Shock Tube Facility

The shock tube used in the study is assembled from stainless steel tubing having a 3.8 cm interior cross section diameter. The driver chamber is 103 cm in length separated by a diaphragm from a driven section 393 cm long (Figure 1). A teflon test section for microwave measurements has been inserted in the end region of the shock tube 315 cm upstream of the diaphragm section. Powdered dust suspensions are prepared in an auxiliary chamber attached to the shock tube. This dust cyclone chamber is 70 cm long with a 15.2 cm inside diameter. A strong vortex is built up in the chamber by a fan located at the base. The fan is driven by a 1/10 H.P. (1500 R.P.M.) motor through a vacuum rotary seal. The dust is expanded into the evacuated shock tube test section through a stainless steel Veeco valve, prior to passage of the shock.

The shock tube and gas handling system is pumped down (.001 torr) by a 10.2 cm water cooled oil diffusion pump. A gravity separator and an oil trap are incorporated in the vacuum pumping line between the shock tube and diffusion pump in order to remove harmful abrasive additives and protect the Kinney (KCV-5 two stage) high vacuum rotary pump.

Microwave Test System

The teflon section was fabricated with microwave-horn bosses to allow radiation and detection of the probing field perpendicular to the shock tube axis. A pair of identical pyramidal horns are situated across the test section with the

edge of the H-plane coincident with the plane of the normal shock flow. In this configuration, the time resolution with respect to the shock flow is approximately 10 microseconds. The microwave circuitry is erected from standard X-band components (Figure 2). The transmitted signal is measured by a crystal detector attached to the receiving horn, and the rejected amplitude is measured by a detector on a directional coupler. In the present setup use is made of the transmitted amplitude to monitor the increase in ionization density following the passage of the shock wave through the test gas. The reflected amplitude is used to note the time at which the electron density exceeds the initial frequency of the plasma. The transmitted and reflected power amplitudes are recorded as a function of time on a Tektronix 555 dual-beam oscilloscope. A single-pulse generator is used to bias the accelerating voltage on the klystron to give the amplitude of the incident microwave beam immediately before shock arrival.

Ultraviolet Light Scattering System

Dust particle densities in the shock flow are determined from the transmitted intensity of scattered monochromatic light with a wavelength of 2500°A. The light scattering system consists of a continuous ultraviolet light source (Hanovia 200-watt xenon - mercury arc lamp, type D-9018-1), two collimating slits each 1 mm in width, a Schoeffel f/4 quartz prism monochromator, and a 1P28 photomultiplier (Figure 3). The light is viewed through Suprasil quartz windows on the shock tube.

Reagents

Metal oxide dust-air suspensions are prepared with commercial grade air (Matheson 99.9% purity). Micron size tungsten oxide powder having a stated purity of 99.6% are

obtained from Electronic Space Products, Inc.

Microwave Calibration

The theory of microwave absorption by free electrons is derivable from the usual Maxwell equations which give, for a plane wave incident normally on a uniform plane slab of ionized gas, the expression[9]

$$A = \ln\left(\frac{I_0}{I}\right) = \epsilon L [e^-] \qquad (1)$$

where A is the absorbance, I_0 and I are the incident and transmitted amplitudes, $[e^-]$ is the number of free electrons per cm^3, L is the path length in centimeters, and ϵ is a complicated function of the electron concentration, the angular frequency of the microwaves, the dielectric constant, electrical conductivity, and electron-atom collision frequency. For values of the electron density below the critical frequency of the plasma, the absorption coefficient is independent of electron density and the absorbance A is linear in both electron concentration and path length, regardless of the spacial distribution of the electrons. With the present experimental setup, because of the complicated geometry between the rectangular microwave beam interacting with the shock tube plasma column, a simple calibration scheme was adopted to determine empirically an effective absorption cross section (ϵL) for the free electrons in the shock tube. The microwave absorption signal is correlated to a single nonequilibrium electron density calculated from a theoretical clean-air chemistry shock tube program[10]. A comparison of the experimental nonequilibrium electron profile and that calculated from the kinetics of air (Table 1) is shown in Figure 4. The agreement between theory and experiment based on a given calibration electron density permits the calibration constant to be checked against different electron

densities during the chemical relaxation time period. An advantage of the internal microwave calibration is that errors caused by shock tube impurities are essentially cancelled in the data reduction.

Light Scattering Particle Measurements

The obscuring power of particles in suspension is used to determine the average projected area A_p of the particles and can be made to yield number densities for particles of known radii. The basis of the method is that the intensity of a beam of light passing through a suspension of particles large compared to indirect wavelength is diminished in proportion to the projected area of the particles[11]. This is expressed by an equation derived from the Lambert-Beer law in the form

$$\ln\left(\frac{I_o}{I}\right) = K l [N_p] A_p \qquad (2)$$

in which the first term is the absorbance of the suspension measured with a parallel light beam, N_p is the number density of particles per cm^3, l is the cell length in centimeters, and K is the total scattering coefficient which is the ratio of the scattering cross section to the geometric cross section of the particle. Theoretical calculations from both the Mie theory and the diffraction theory show that K approaches the value 2 for particles large compared to the incident wavelength. Preliminary number density measurements of tungsten oxide suspensions were made with 3 micron and 10 micron size particles. Transmitted light intensity measurements were made at shock tube loading pressures of 550, 300, and 100 mm Hg. The transmitted ultraviolet light beam (2500°A) was chopped mechanically and the A.C. output of the photomultiplier was displayed on an oscilloscope (Figure 5). The square wave amplitudes were reduced to transmittance values and plotted against shock tube loading pressure (Figure 6). The data were

least squares fitted with a second-order polynomial function and used to infer an initial particle density for a loading test pressure of 10 mm Hg. The results showed 0.53 (10^4) particles per cm^3 for 3 micron size particle suspensions. The uncertainty in these number densities is approximately $\pm$ 40 percent due to scatter in the data.

Ultraviolet Absorption Measurement

Ultraviolet absorption was found to occur in shocked clean-air samples. In similar experiments with the metal oxide suspension, the ultraviolet absorption trace is depicted by a sharp rise in absorption at the shock front and a gradual increase to a steady-state absorption level. These absorption traces were corrected for the background air ultraviolet absorption (Figure 7). The increased ultraviolet absorption in the WO_3 dust suspension is attributed to the absorption of WO_3 molecules produced from the evaporation of the WO_3 crystals in suspension. The basis of this contention is that equilibrium calculations for the tungsten oxide-air system show WO_3 and W_2O_6 to be the dominant tungsten oxide species in the gas phase at 3200°K for a mole fraction of 0.0043 metal oxide and a total gas pressure of 1 atmosphere (Figure 8). The nonequilibrium rise in ultraviolet absorption is attributed to the finite evaporation rate of the crystals. For isoelectronic molecules, the magnitudes of the spectral absorption coefficients for the 2500°A electronic absorption band are similar:

Species	ϵ, liter-mole^{-1}-cm^{-1}
NO_2	113
NF_2	240
CF_2	2450
SO_2	3000

Assuming an absorption coefficient for WO_3 to be 3000 liter-mole^{-1}-cm^{-1} (strongest known band system of SO_2), from the steady-state absorption measurement, the experimental gas-phase WO_3 concentration is 5.8 (10^{-8}) mole per cm^3. The relative agreement between the WO_3 particle concentration, 1.7 (10^{-8}) mole per cm^3, and u.v. absorption gas-phase WO_3 concentration serves as an independent check on the light scattering particle density determination.

Theoretical Particle Trajectory and Evaporation Rate

The vaporization process for refractory metal oxides in the present analysis is assumed to be governed by the convective heat transfer rates from the hot flow field environment. The metal oxide particles are treated as having zero thermal conductivity from the surface to within the particle. The heat balance equation for each particle is given by the relation

$$\Delta h_v \frac{dm_v}{dt} = A_p \bar{h} (T_g - T_v) \qquad (3)$$

where A_p is the surface area of the droplet, $\bar{h}$ is the convective heat transfer coefficient, T_g is the temperature of the environmental gas, Δh_v is the heat of vaporization of the particle and T_v is the ablation temperature of the particle. The particle shapes of WO_3 commercially obtained are stated to be spheres and octahedra. Introducing the relations

$$A = \pi D^2 \quad , \qquad m_v = \pi \rho_p (D_o^3 - D^3)/6$$

and expressing $\bar{h}$ in terms of the Nusselt number Nu, equation (3) can be written in the form

$$D \frac{dD}{dt} = - \frac{2 K_g Nu (T_g - T_v)}{\rho_p \Delta h_v} \qquad (4)$$

where K_g is the thermal conductivity of the gas. Since the

particles are initially at rest and become accelerated by the flow after shock passage, equation (4) must be coupled with the trajectory equation to define the variation of the convective heat transfer coefficient $\bar{h}$ along the path.

The momentum equation is given by

$$m \frac{dU_p}{dt} = \frac{-C_D \rho_g (U_s - U_p)^2}{2} \cdot \frac{\pi D^3}{4} \qquad (5)$$

where U_p is the particle velocity, U_s is the gas stream velocity, and C_D is the particle drag coefficient. In the present experimental study (1 atm total air pressure and 3200°K) the gas mean free path is calculated to be less than the particle width by a factor of 10 for 3 micron size particles, and hence the particles are considered to be in the continuum flow regime.

Equations (4) and (5) were solved on an IBM 1130 computer using a modified Stokes drag law[12],

$$C_D = \frac{24}{Re}\left(1 + \frac{3}{16} Re\right) \qquad (5.1)$$

where Re is the Reynolds number,

$$Re = \frac{\rho_g U_s D}{\mu}\left(1 - \frac{U_p}{U_s}\right) \qquad (5.2)$$

The average Nusselt number for continuum flow is taken from **reference 13.**

$$Nu = 2 + 0.459 (Re)^{0.55} (Pr)^{0.33} \qquad (5.3)$$

where Pr is the Prandtl number. The transport properties of air were taken from an Avco Technical Report by Yos[14]. Particle evaporation rates and the rate of surface area change were calculated for 3 micron and 10 micron tungsten oxide particles in the temperature range 3000-3400°K at one atmosphere total pressure in air. The calculated mass and surface area change of the particle were fitted by an ex-

ponential decay law

$$\text{Mass:} \quad m = m_o e^{-t/\tau_m T^{0.5}}$$

$$\text{Surface:} \quad S = S_o e^{-t/\tau_s T^{0.5}}$$

where τ is the relaxation time constant (Figure 9), with a collisional temperature dependence of $T^{0.5}$. These functions are used in the nonequilibrium stream tube program to numerically provide the solid particle evaporation rate and surface area change for the electron attachment and ion recombination terms (see next section).

Theoretical Gaseous Diffusion Rate

In the theoretical calculation of electron densities with solid and gas phase WO_3 attachment, the ablated WO_3 concentration is assumed to be homogeneous through the reaction medium. The following diffusion calculation shows that this condition is reasonably achieved for about one-third of the total ablated gas-phase concentration. The binary diffusion relation is given by Fick's law of diffusion,

$$n V_d = -D \frac{dn}{dZ} \qquad (6)$$

for a swarm of particles diffusing in the Z direction with a draft velocity V_d. Integration of Eq. (6) gives an exponential decay law

$$\frac{n}{n_o} = exp\left(-\frac{V_d Z}{D}\right) \qquad (7)$$

Based on Eq. (7) for a 0.005 mole fraction of WO_3 particles (1.84×10^{-2} cm) in argon at 3200°K and 1 atm total pressure, calculations show that the characteristic time for the evaporated WO_3 concentration to diffuse to one-half the distance between particles and to decrease to 1/e of the total gas phase WO_3 concentration at the particle site was around 10 μsec laboratory shock time. The calculated binary diffusion coefficient used is D = 6.02 cm^2/sec.

METAL OXIDE PLASMA ALLEVIATION

The various physical processes occurring when solid additives are introduced into a thermal plasma include vaporization cooling, thermal electrification, surface ion recombination, surface neutral molecule electron attachment, all of which tend to reduce the electron properties of the plasma. Because of the high surface temperatures experienced by refractory materials, thermionic emission or the Saha-Langmuir ionization, where gas atoms with high kinetic energy striking the hot surface convert through surface ionization to electrons and positive ions, could lead to adverse quenching properties of the solid additive. In order to assess the performance of solid additives to quench electrons in a high temperature plasma environment, a preliminary shock tube study was carried out using a tungsten oxide-air suspension and shock heating it to plasma temperatures between 3000°-3300°K at a total pressure of 1 atmosphere. Nonequilibrium electron densities were monitored behind the incident normal shock wave with an X-band probing frequency. Typical microwave data for clean-air and WO_3-air plasmas are compared in Figure 10 for nearly identical shock conditions. The experimental electron densities in the shocked tungsten oxide-air samples were analyzed with a theoretical stream tube computer program. The various electron producing and removing processes are numerically described by the mass action equation,

$$\frac{dn_e}{dt} = \underbrace{\frac{1}{4} N_g \bar{u}_g S \int_{\epsilon}^{\infty} e^{-e/kT} d\epsilon}_{\text{thermionic emission}} + \underbrace{k^f_{NO^+}[N][O]}_{\text{air ionization}}$$

$$\underbrace{- N_p n_e \bar{u}_e e^{-ne^2/4\pi\epsilon_0 r kT}}_{\text{electron-particle attachment}} \quad \underbrace{- \frac{1}{4}\sigma_{\pm}^2 \left(\frac{8\pi kT}{\mu}\right) n_+ n_e S}_{\text{3-body surface ion recombination}} \qquad (8)$$

$$\underbrace{- k^b_{NO^+}[NO^+][e^-]}_{\text{air ion recombination}} \quad \underbrace{- N_a n_e \bar{u}_e Q_a}_{\text{gas-phase attachment}}$$

$$\underbrace{- N_a n_e \bar{u}_e S}_{\text{catalytic surface Attachment}} \quad \underbrace{- \frac{2kT_e}{e} \mu_+ \nabla^2 n_e}_{\text{ambipolar diffusion}}$$

By way of comparison, it is noted that only the first and third terms of Eq. (8) are treated in the Anderson-Rosen theory (Ref. 3). The rate constants associated with the above model in an electron-solid particle system are shown in Table 2 and were derived as a first-order approximation from simple kinetic theory. Figure 11 shows a comparison between the electron density profile measured in a shocked suspension of WO_3 particles in air and that calculated by the stream tube computer program with the air chemistry of Table 1, and the electron kinetics of Table 2. The model is seen to be in good quantitative agreement with experiment, and when electron attachment is deleted from the calculation, the results compare with a clean-air plasma test. A plot of the rates for the different electron kinetic processes (Figure 12) shows at first sight that during the early phases of attachment, "catalytic" surface electron-quenchant attachment dominates due to the large available surface area. At later times when particle ablation is going to completion, dissociative attachment of the quenchant-neutral becomes im-

portant and controls the electron attachment mechanism. In the present experiment, since the plasma is bounded, ambipolar diffusion losses are neglected in the theoretical analysis, although such a process could take place with the finite cold boundary layer at the cell wall. However, Aisenberg's calculations tend to show that the ambipolar diffusion would be insignificant compared to the other processes near 1 atmosphere (Ref. 5).

CONCLUSIONS

Metal oxides of micron size particles can be made in a suitable gas suspension to study their electrophilic properties in a high temperature plasma environment by a shock tube technique. A light scattering procedure has been developed to determine particle number densities and is capable of being independently checked by either gas-phase ultraviolet absorption or infrared spectrophotometric techniques.

A phenomenological electron attachment model for solid metal oxides has been derived to correlate particle surface and gas-phase attachment processes. The model allows one to assess various possible electron attachment processes in terms of particle ablation temperature, size, electrophilic cross section of the gas-phase metal oxide and ablation cooling effects. An interesting test of the proposed metal oxide plasma alleviation mechanism is to apply the present shock tube technique to the investigation of oxides with widely different boiling points. The low temperature oxides would have lower surface temperatures, thereby favoring low thermionic emission and predominately gas-phase electrophilic attachment and thermal quenching. The high temperature refractory oxide would have a longer survivability life time to promote surface

attachment processes, but could be hindered by thermionic emission effects.

REFERENCES

1. S. L. Soo, "Thermal Electrification and Removal of Electrons by Solid Particles in a Gas," Phys. of Fluids 6, 145 (1963).
   (See Also)
   S. L. Soo, "Gas-Solid Suspension at High Temperatures," J. Appl. Phys., June 1963.
2. S. L. Soo and R. C. Dimick, "Experimental Study of Thermal Electrification of a Gas-Solid System, "Proc. of the Winter Annual Meeting of the ASME, Philadelphia, Pa., (17-22 Nov. 1963) p. 43.
3. W. L. Anderson and G. Rosen, "On the Refractory Dust Method", J. App. Phys. 36, 3760 (1965)
4. J. S. Evans, "Reduction of Free Electron Concentration in a Reentry Plasma by Injection of Liquids, "Proceedings of the Third Symposium on the Plasma Sheath, Vol. III (AFCRL, Massachusetts, May 1967) p. 343.
5. S. Aisenberg, "A Study of the Use of Chemical Additives for the Alleviation of the Plasma Sheath Problem," Scientific Rept. No. 2 (Space Sciences Inc., Waltham, Massachusetts, 18 Dec. 1967).
6. S. Atallah and W. A. Sanborn, "The Effect of Chemical **Additives on Microwave Transmission in an Air Plasma,"** Proceedings of the Third Symposium on the Plasma Sheath, Vol. III (AFCRL, Massachusetts, May 1967) p. 319.
7. A. P. Modica, "Microwave Measurements of Nonequilibrium Air Plasmas Behind Shock Waves Containing Electrophilic Gases," J. Phys. Chem. 71, 3463 (1967).
8. A. P. Modica, "Shock Tube Studies of the Sulfur Hexafluoride-Hydrogen Reaction, "Avco Tech. Rept. AVATD-

0163-69-RR (Avco Wilmington, Massachusetts, 15 Sept. 1969).

9. H. S. Johnston and W. Koregay, "Rate and Mechanism of the Thermal Ionization of Xenon,"Trans. Faraday Soc. 57, 1563 (1961).

10. A. P. Modica, "Chemical Kinetics of Carbonyl Fluoride Decomposition in Shock Waves, "J. Phys. Chem. 74, 1194 (1970).

11. Physical Methods of Organic Chemistry, Vol. I (Ed., A. Weissberger, Interscience Publishers, Inc., New York, 1959) p. 232.

12. H. Schlichting, Boundary Layer Theory (McGraw-Hill Book Company, Inc., New York, 1960) p. 98.

13. D. J. Carlson and R. F. Hoglund, "Particle Drag and Heat Transfer in Rocket Nozzles, "AIAA J. 2, 1980 (1964).

14. J. M. Yos, "Transport Properties of Nitrogen, Hydrogen, Oxygen, and Air to 30,000°K, Avco Tech. Rept., RAD-TM-63-7 (Avco Wilmington, Massachusetts, 22 March 1963).

TABLE 1 AIR CHEMISTRY AND RATE CONSTANT[a]

RATE EQUATIONS

02	+02	+	=0	+0	+02	RC= 9.710D 22T**(-2.00)EXP(-59300./T)
0	+0	+02	=02	+02	+	RC= 8.010D 19T**(-1.50)EXP(0./T)
02	+0	+	=0	+0	+0	RC= 2.720D 23T**(-2.00)EXP(-59300./T)
0	+0	+0	=02	+0	+	RC= 2.240D 20T**(-1.50)EXP(0./T)
02	+N2	+	=0	+0	+N2	RC= 7.220D 18T**(-1.00)EXP(-59300./T)
0	+0	+N2	=02	+N2	+	RC= 6.020D 15T**(-0.50)EXP(0./T)
02	+N	+	=0	+0	+N	RC= 3.610D 18T**(-1.00)EXP(-59300./T)
0	+0	+N	=02	+N	+	RC= 3.010D 15T**(-0.50)EXP(0./T)
02	+NO	+	=0	+0	+NO	RC= 3.610D 18T**(-1.00)EXP(-59300./T)
0	+0	+NO	=02	+NO	+	RC= 3.010D 15T**(-0.50)EXP(0./T)
N2	+M	+	=N	+N	+M	RC= 4.740D 17T**(-0.50)EXP(-113100./T)
N	+N	+M	=N2	+M	+	RC= 2.880D 17T**(-0.50)EXP(0./T)
N2	+0	+	=NO	+N	+	RC= 7.150D 13T**(0.0)EXP(-37500./T)
N	+NO	+	=N2	+0	+	RC= 1.590D 13T**(0.0)EXP(0./T)
NO	+0	+	=02	+N	+	RC= 3.600D 09T**(1.00)EXP(-19700./T)
N	+02	+	=NO	+0	+	RC= 2.930D 10T**(0.50)EXP(-3010./T)
N	+0	+	=NO+	+E-	+	RC= 9.030D 09T**(0.50)EXP(-32400./T)
NO+	+E-	+	=N	+0	+	RC= 1.810D 19T**(-1.00)EXP(0./T)

[a] Units in °K, Sec, Mole, cm^3

TABLE 3 TUNGSTEN OXIDE ELECTRON ATTACHMENT MECHANISM[a]

1.	*WO3	+M +	=WO3	+E-	+M	RC= 1.350D	03T**(0.50)EXP(	0./T)
2.	NO+	+E- +S	=NO	+S	+	RC= 1.810D	24T**(-1.00)EXP(	0./T)
3.	WO3	+E- +	=WO2-	+O	+	RC= 6.360D	15T**(0.50)EXP(-39255.	/T)
4.	WO3	+E- +S	=WO3-	+S	+	RC= 6.360D	20T**(0.50)EXP(	0./T)
5.	S	+ +	=*S	+	+	RC= 1.130D	03T**(0.50)EXP(	0./T)
6.	S	+M +	=S	+E-	+M	RC= 4.570D	07T**(0.50)EXP(-81300.	/T)
7.	S	+E- +	=S	+*E-	+	RC= 1.550D	10T**(0.50)EXP(-11615.	/T)

[a] Units in °K, Sec, Mole, cm^2, cm^3

* **Indicates solid phase**

Explanation of Equations

1. Thermal Collisional Detachment.
2. Catalytic Recombination of NO+.
3. Dissociative Gas Phase Attachment.
4. Surface Catalyzed Attachment of WO_3.
5. Surface Recession Rate.
6. Thermionic Emission.
7. Electrostatic Electron Collection (probe effect).

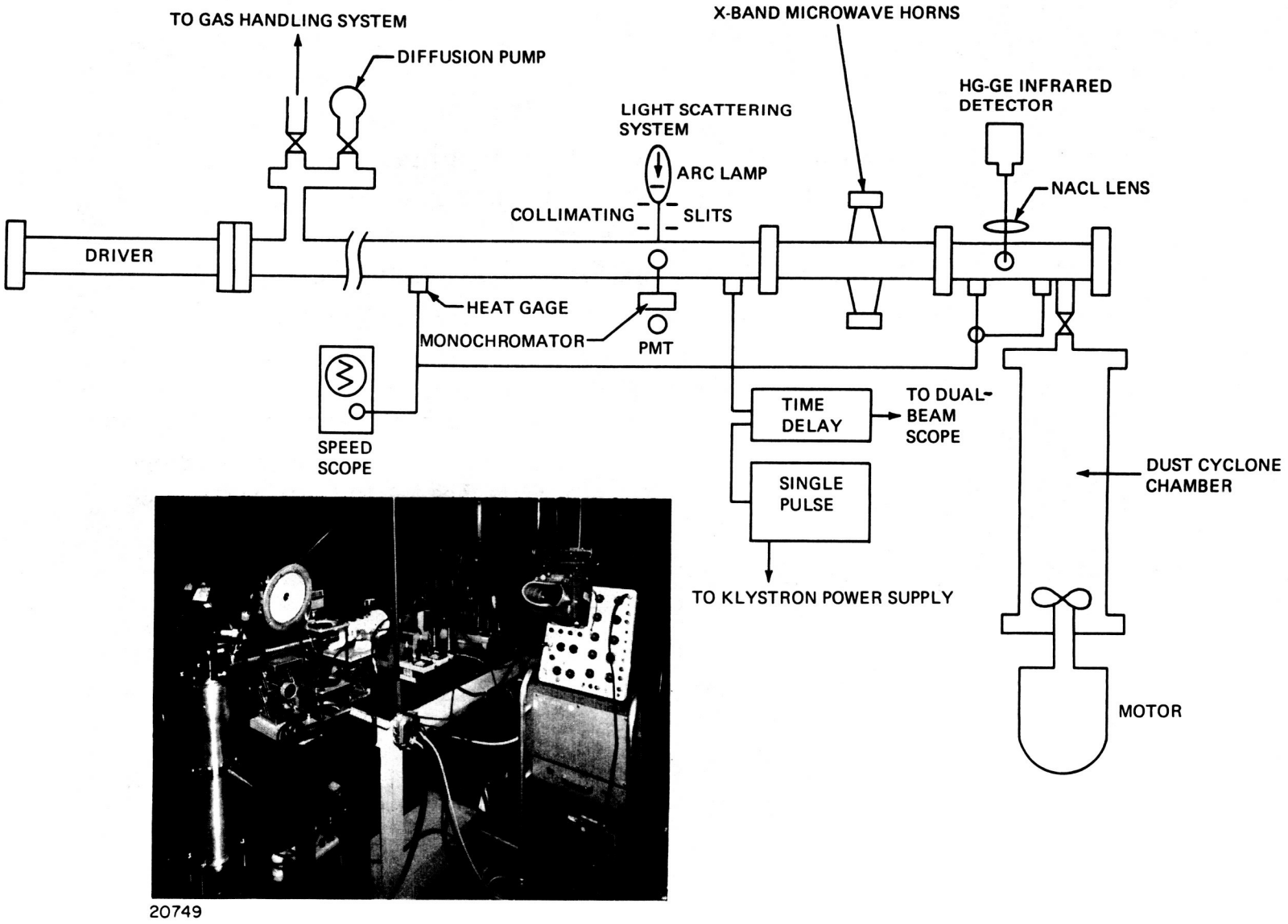

Figure 1.- Schematic of dust shock tube facility.

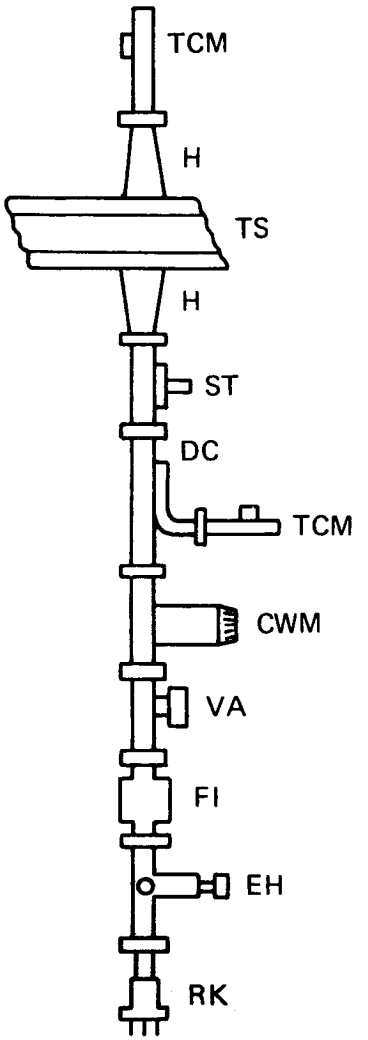

Identification of labels:

RK	reflex klystron
EH	E and H plane tuner
FI	ferrite isolator
VA	variable attenuator
CWM	cavity wave meter
TCM	tunable crystal mount
DC	directional coupler
ST	stub tuner
H	horn
TS	Teflon section (dielectric)

Figure 2.- Diagram of microwave circuitry.

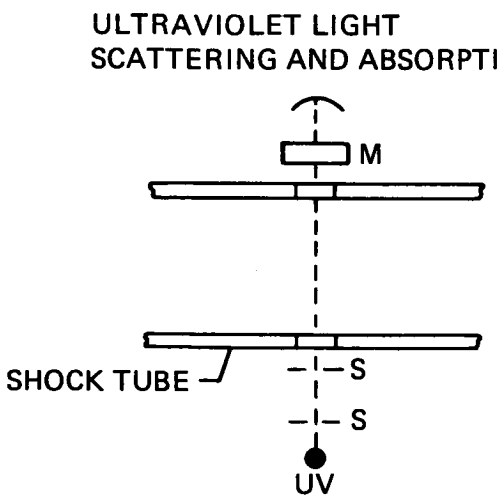

Identification of labels:

M	monochromator
S	collimating slits
UV	ultraviolet light source

Figure 3.- Experimental arrangement of optical shock tube experiments.

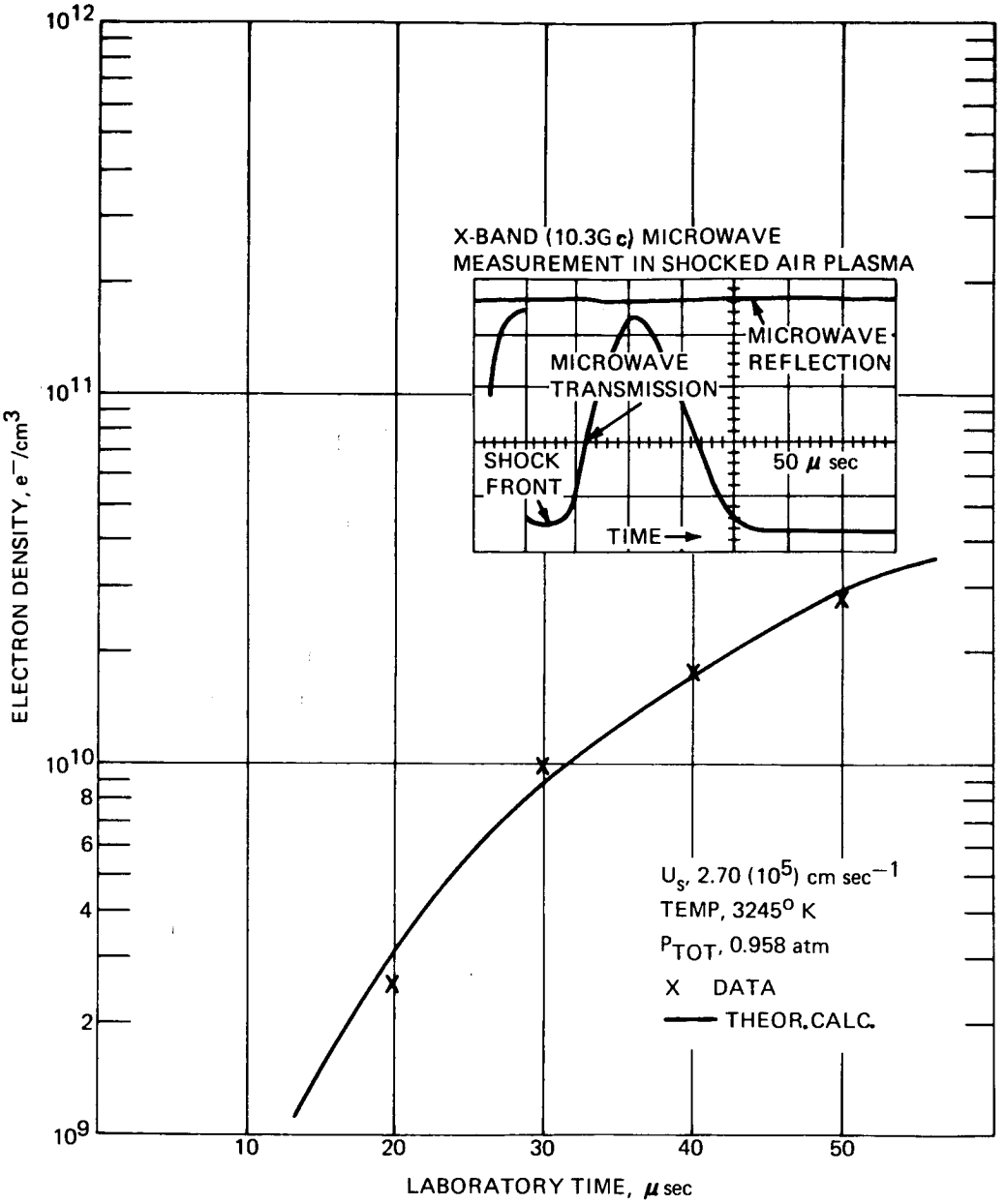

Figure 4.- Experimental and calculated electron density profile in shocked air plasma.

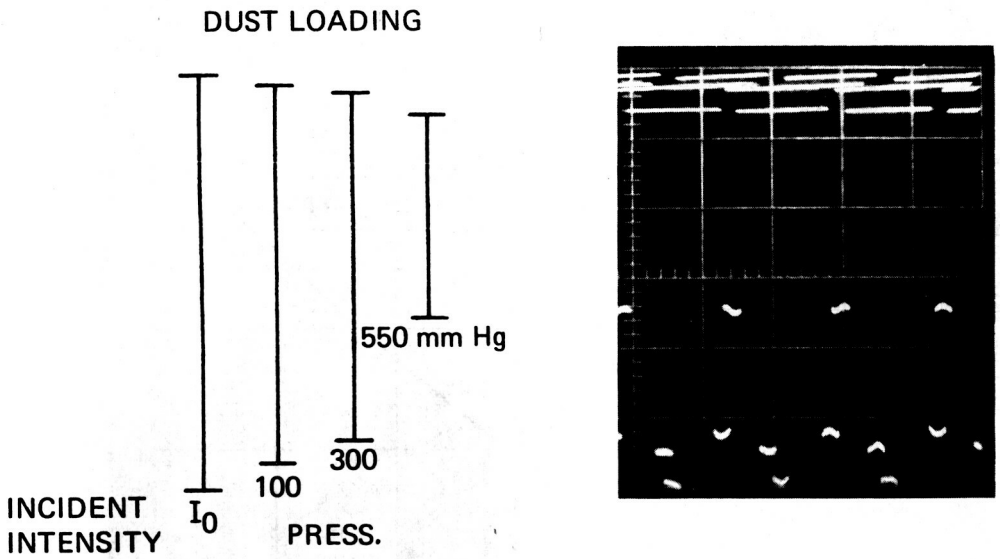

Figure 5.- Ultraviolet light scattering transmittance with loading pressure for dust-air mixtures.

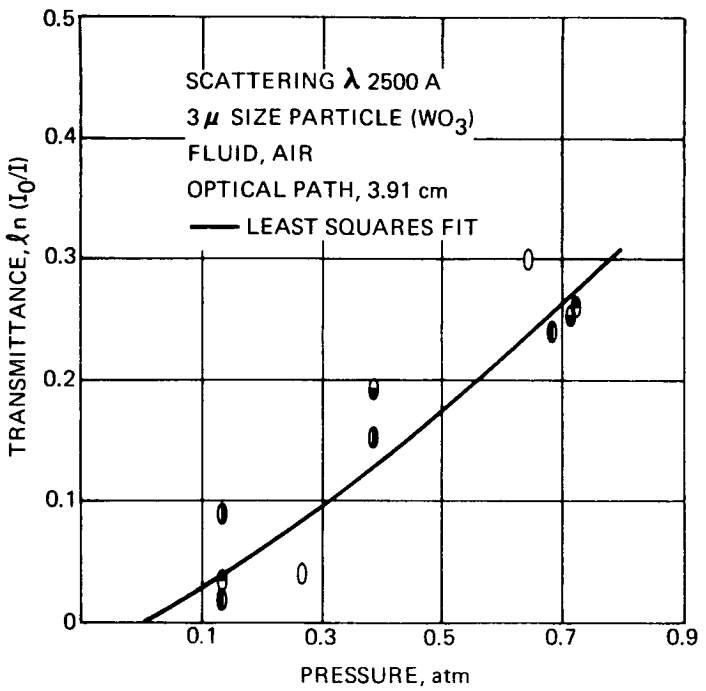

Figure 6.- Variation of transmittance as a function of dust sample pressure in 3 micron size WO_3 particle air mixture. (Different symbols signify individual determinations.)

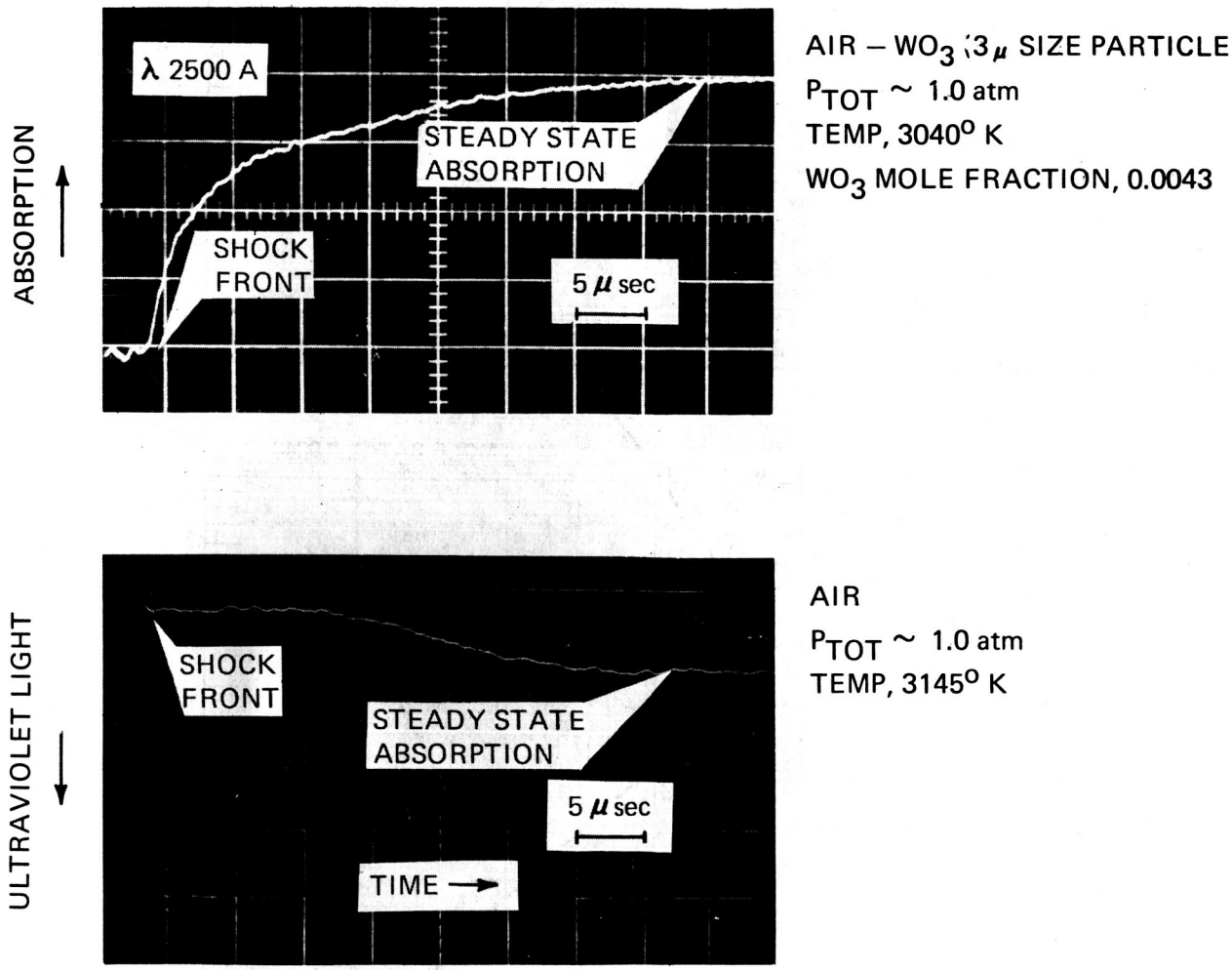

Figure 7.- Gas-phase ultraviolet absorption in clean-air and WO_3-air plasmas behind incident shock.

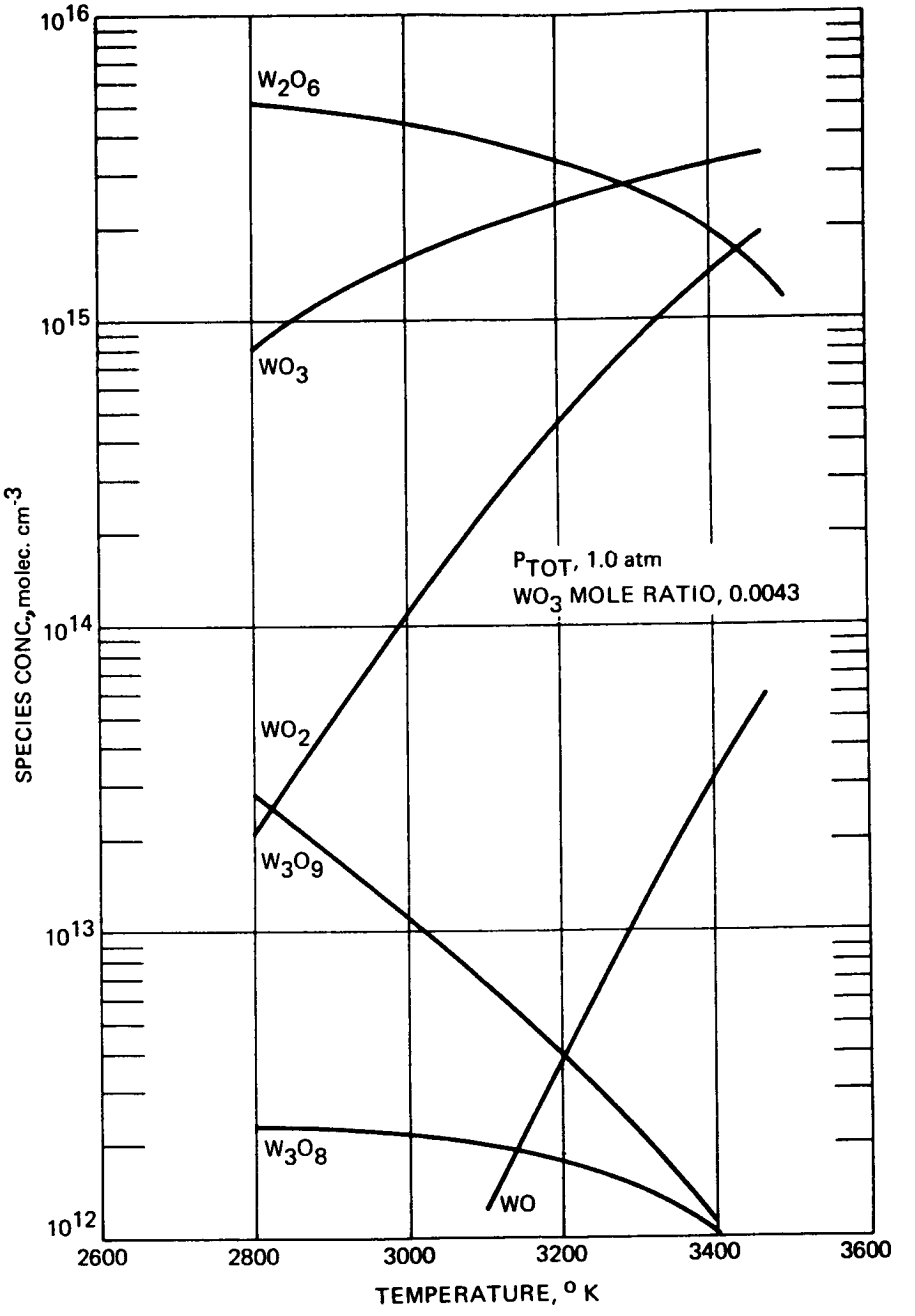

Figure 8.- Equilibrium tungsten oxide-air calculation.

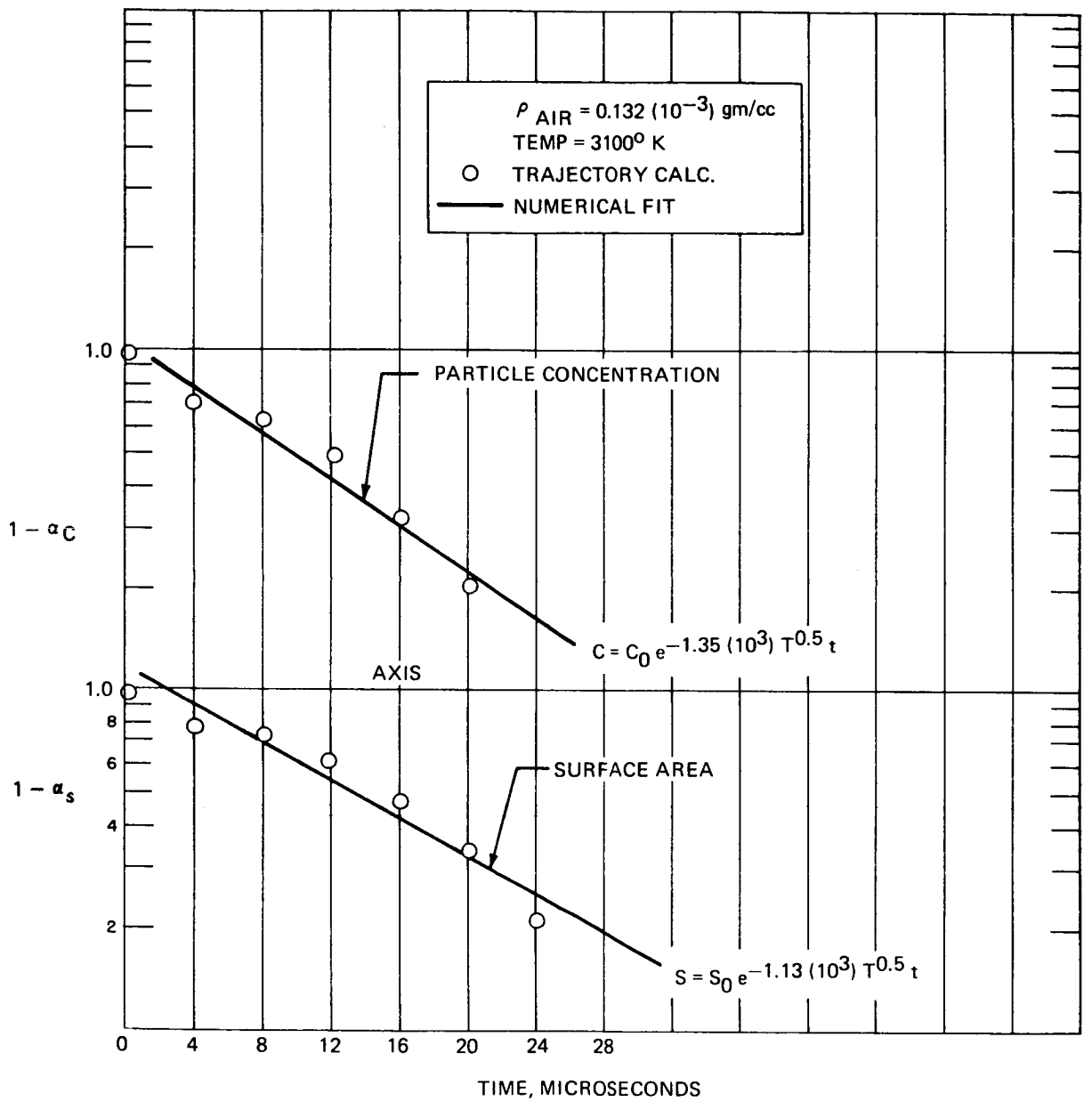

Figure 9.- Arrhenius fit to ablation rate and surface area change for 3 micron size WO_3 particles.

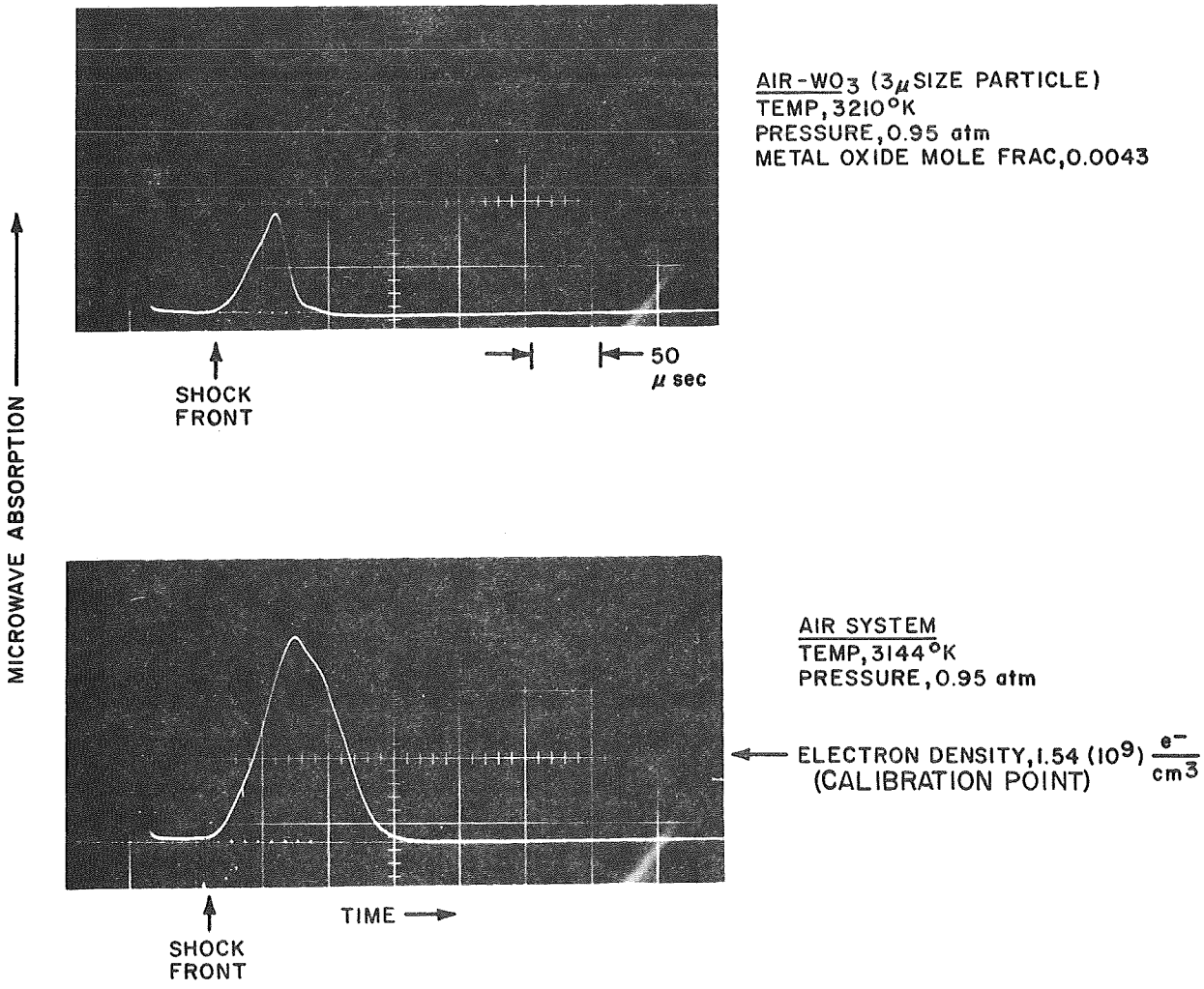

Figure 10.- Microwave oscillogram record of nonequilibrium electron density in clean-air and WO_3-air shocks.

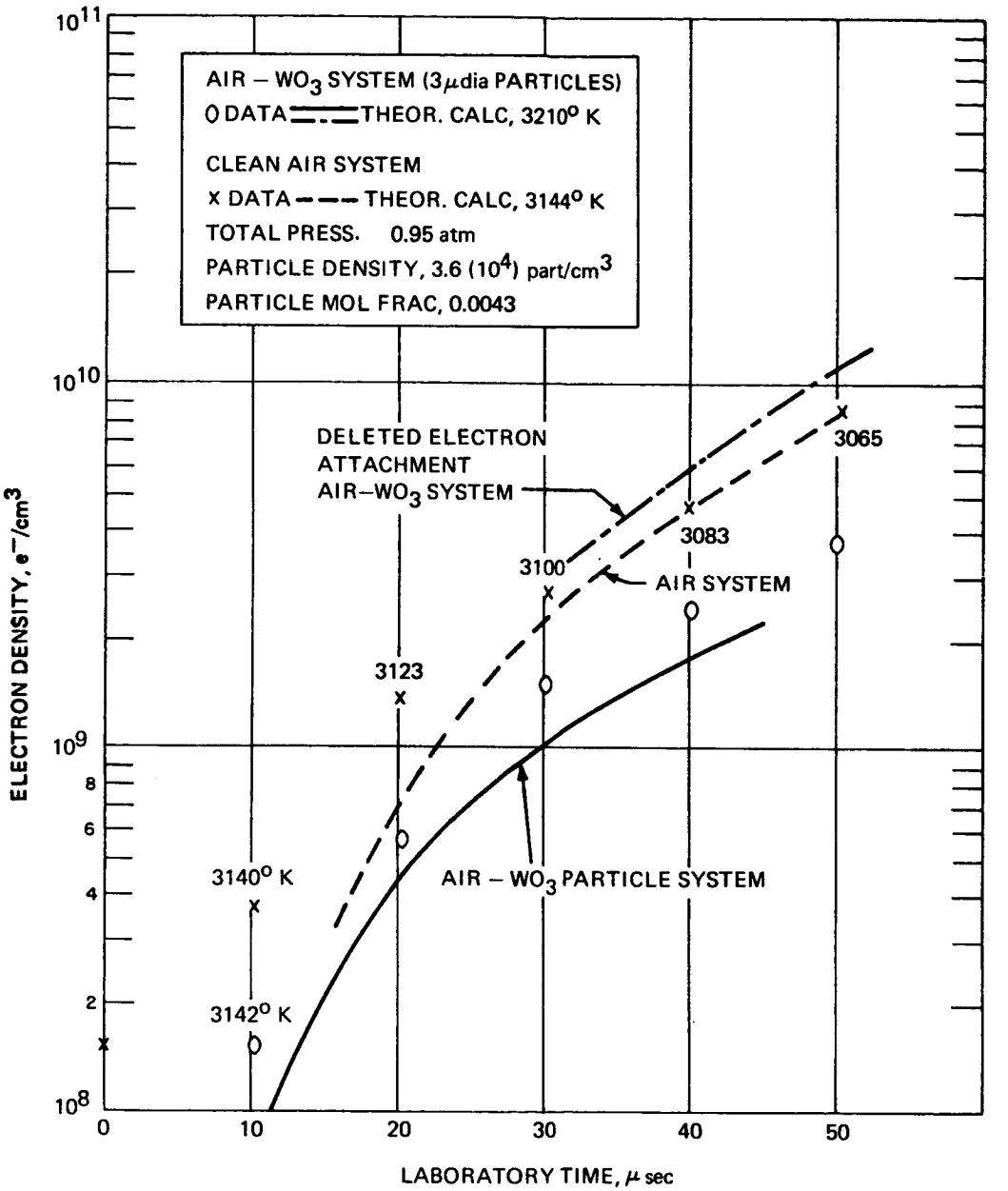

Figure 11.- Stream tube calculation of electron density profiles for shocked WO_3 dust-air mixtures.

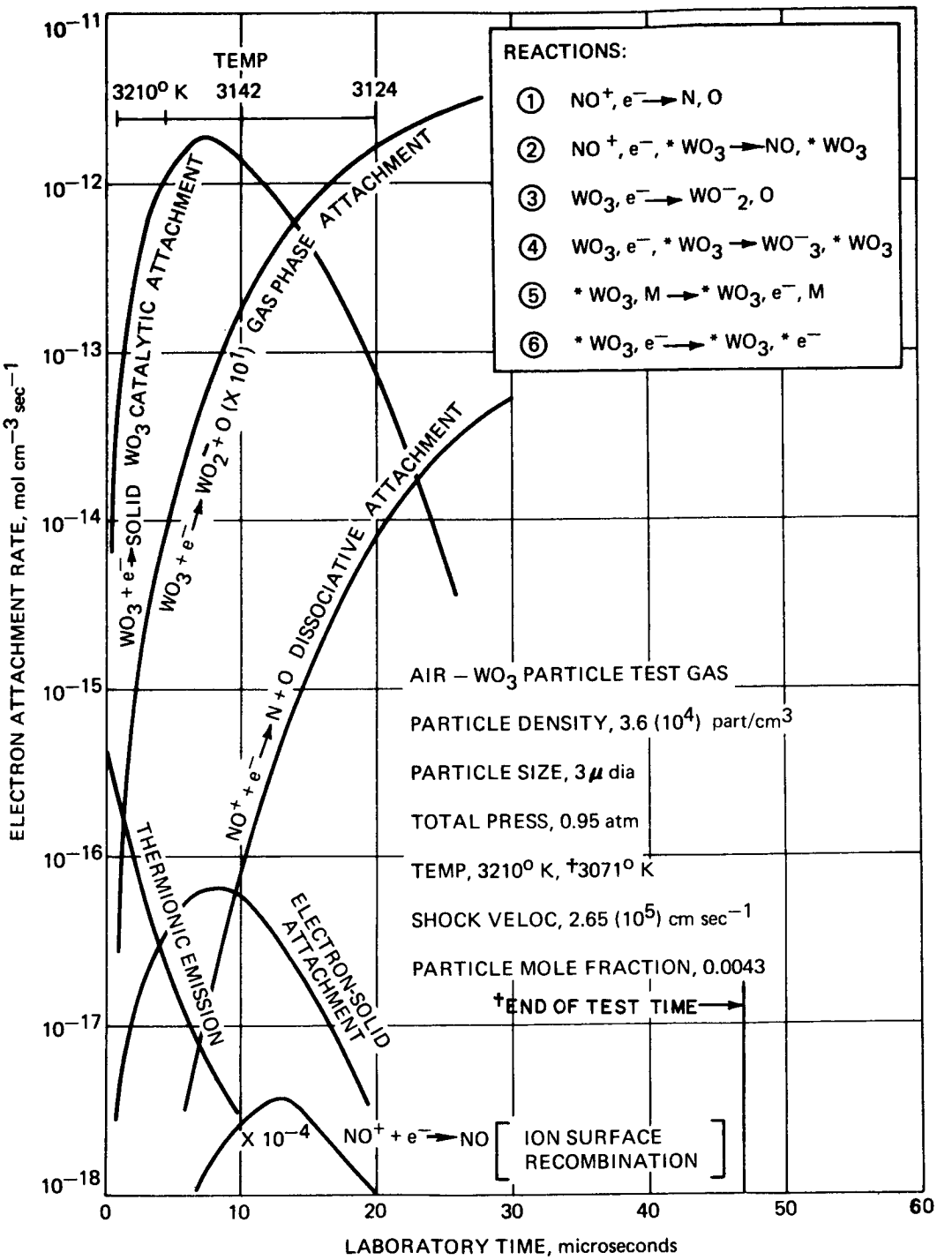

Figure 12.- Theoretical electron production rates and attachment rates for WO_3 dust-air mixtures.

STUDIES OF ELECTRON ATTACHMENT FOR THE ALLEVIATION OF RADIO COMMUNICATIONS BLACKOUT

R. L. Cowperthwaite, H. Myers, and E. P. Bialecke

McDonnell Douglas Astronautics Company

St. Louis, Missouri 63166

SUMMARY

The removal of electrons from reentry flowfields by dissociative attachment is examined. Below electron concentrations of $\simeq 10^{14}/cm^3$, and for attachment times in the range of 1 - 100 microseconds, electron conversion is rate-determined and insensitive to the initial electron density. Additive number densities in the range 10^{13} - 10^{15} particles/cm^3 are required to reduce the electron number density to $10^9/cm^3$. Dissociative attachment cross sections are described by a model that depends mostly on the electron energy. A substantial number of peak cross sections are found to be consistent with the model, with model parameters independent of the target molecule. Further, the model gives the energy dependence of the cross section. The attachment model is then extended to include rotational effects for the case of diatomic molecules.

INTRODUCTION

The plasma sheath generated by a high velocity reentry vehicle degrades radio communications with the vehicle. A way to reduce this problem is to convert the free electrons in the flowfield to gaseous negative ions. The reason that this technique works arises from the fact that the energy extracted by the plasma from the electric field goes roughly as M_c^{-1}. Thus if the free electrons in an illuminated volume of gas are completely converted to negative fluorine ions, the energy extracted from the electric field is 2.9×10^{-5} as large as that for free electrons.

Since parameters other than the mass of the charged particle are present in the energy loss equation, it is worth while to examine these relationships

explicitly. If a negatively charged particle of mass M_c in an electric field $E_o \sin \omega t$ has an initial velocity component V_o parallel to E_o, its one dimensional equation of motion is

$$M_c \frac{dV}{dt} = -eE_o \sin \omega t \tag{1}$$

giving

$$V(t) = V_o + \frac{e}{M_c} \frac{E_o}{\omega} (\cos \omega t - 1) \tag{2}$$

for its velocity, and

$$W(t) = \frac{M_c}{2} V^2(t) \tag{3}$$

for its kinetic energy.

The energy extracted from the electric field is

$$W(t) - W(0) = V_o e \frac{E_o}{\omega} (\cos \omega t - 1) + \frac{1}{2M_c} \left(\frac{eE_o}{\omega}\right)^2 (\cos \omega t - 1)^2 \tag{4}$$

When Eq. (4) is averaged over a symmetric distribution with a mean value of zero for V_o (the Maxwell-Boltzmann distribution, for example.), the first term drops out and

$$W(t) - W(0) = \frac{1}{2M_c} \left(\frac{eE_o}{\omega}\right)^2 (\cos \omega t - 1)^2 \tag{5}$$

After some characteristic time, some fraction of this energy is removed from the electric field by collisions of the charged particle with neutral gas particles.

The only conclusion we wish to draw from Eq. (5) is that the energy loss from the electric field depends on the mass of the charged particle roughly by a factor of M_c^{-1}.

The above introduction is a great oversimplication of the problem of designing an alleviation system for a real vehicle. The following sections explore additional considerations of the relevant physics.

SYMBOLS

B	Spectroscopic rotational constant for diatomic molecules
E	Electron energy for cross section calculations
E_T	Electron attachment threshold energy for a ground state molecule
E_{rot}	Rotational energy of a diatomic molecule
E_o	Amplitude of a periodic electric field
J	Rotational quantum number
K_{att}	Total attachment rate constant
K_{rot}	Rotational contribution to the attachment rate constant
K'	Contribution to the attachment rate constant for electron energies greater than E_T
M_c	Mass of any charged particle
M_e	Electron mass
$N(0)$	An arbitrary number of electron-molecule associations at time zero
N	The number of electron - molecule associations at a time other than zero
$N_{att}(0)$	Attaching compound number density at time zero
N_{att}	Attaching compound number density at a time other than zero
$N_e(0)$	Electron number density at time zero
N_e	Electron number density at a time other than zero
P	The probability that rotational energy is conserved for an electron molecule collision when $E < E_T$
R_o	Additional separation of the nuclei required to assure dissociative attachment
T	Gas temperature

U	Potential energy of the separating fragments in a dissociative attachment reaction
$V(t)$	The velocity of an electron in an electric field
V_o	The initial velocity of an electron in the absence of an electric field
$W(0)$	Kinetic energy of an electron with velocity V_o
$W(t)$	Kinetic energy of an electron with velocity $V(t)$
c	Speed of light
e	Magnitude of the electron charge
df/dJ	Probability density of rotational quantum numbers for a diatomic molecule
h	Planck's constant
$\hbar$	$h/2\pi$
k	Boltzmann's constant
r	Nuclear separation of molecular fragments during dissociative attachment
r_o	Initial value of r
r'	$r - r_o$
$\dot{r}'$	Time derivative of r'
t	Time
α	Scale constant for the uncertainty principle
γ	Parameter in the attachment cross section model
η	Scale factor for the separation potential
μ	Reduced mass of the separating fragments
π	3.1416
σ	Dissociative attachment cross section
σ_o	Dissociative attachment cross section at zero collision energy

τ_a Electron - molecule association time

τ_s Time required for the dissociating fragments to acquire their final kinetic energies

$\langle\tau\rangle$ Average electron - molecule association time

ϕ $E^{1/2}$

ω Electric field angular frequency

ATTACHMENT TIME REQUIREMENTS

If an important gain in transmission through the plasma sheath is to be achieved, the conversion to negative ions must be sufficiently rapid to convert most of the electrons to negative ions in a few μsec. This aspect of the problem can be explored in a simple way by assuming the only process is electron attachment. When this assumption is made the differential equation for the loss of electrons is

$$\frac{dN_e}{dt} = -K_{att} N_e N_{att} \tag{6}$$

If we assume each reaction removes one attaching molecule, particle conservation requires

$$N_{att}(0) = N_{att} + N_e(0) - N_e \tag{7}$$

and Eq. (6) becomes

$$\frac{dN_e}{N_e[N_{att}(0) + N_e - N_e(0)]} = - K_{att}\, dt \tag{8}$$

which integrates to

$$\frac{N_e}{N_e(0)} \quad \frac{N_{att}(0)}{N_e + N_{att}(0) - N_e(0)} = \exp\left(-N_{att}(0) - N_e(0))K_{att}t\right) \tag{9}$$

provided $N_{att}(0) > N_e(0)$. If a significant reduction in electron concentration is to be achieved, $N_e(0) >> N_e$, and Eq. (9) reduces to

$$\frac{N_e}{N_e(0)} = \frac{N_{att}(0) - N_e(0)}{N_{att}(0)} \exp\left(-N_{att}(0) - N_e(0))K_{att}\, t\right) \qquad (10)$$

Equation (10) explicitly displays three parameters available to the vehicle designer: $N_{att}(0)$, K_{att}, and t.

It is fruitful to ask the question, "what value of $N_{att}(0)$ is required to reduce $N_e(0)$ to 10^9 electrons/cm^3 for reasonable values of $(K_{att}t)$?" Figure (1) gives the answer to this question. It is interesting to note how the solution breaks up into two regions when $K_{att}t \approx 10^{-14}$ cm^3/particle. If $N_e(0) < 10^{-14}$ electrons/cm^3, the solution depends quite weakly on $N_e(0)$, and above 10^{14} electrons/cm^3 the solution depends mostly on $N_e(0)$. For this simple case a major change in additive scaling rules might be expected at electron densities of $\approx 10^{14}$ per cm^3.

If time scales of 1 - 100 μsec are estimated for the $K_{att}t$ range of 2 - 20 x 10^{-14} cm^3/particle, the range of attachment rate constants is 2-2000 x 10^{-10} cm^3/particle-sec. Many attachment rate constants fall in this range. Further, the minimum required attaching compound number density is in the range of 10^{13} - 10^{15} particles/cm^3.

ATTACHMENT RATE CONSTANTS

From the preceding analysis it is apparent that gas phase electron attachment can lead to major reductions in electromagnetic energy losses and that these reactions are fast enough. What is now required are accurate attachment rate constants. For a Maxwell-Boltzmann gas the rate constant is given by

$$K_{att} = \frac{2}{(kT)^{3/2}} \left(\frac{2}{\pi M_e}\right)^{1/2} \int_0^\infty \sigma(E)\, E \exp\left(-E/kT\right)\, dE \qquad (11)$$

Thus a knowledge of the cross section, the energy distribution independent quantity, permits an evaluation of the rate constant. The actual situation is more complicated because the cross section depends on more quantities than the collision energy. In particular, it may depend on temperature via the

rotational, vibrational, and electron levels of the target molecules. The remainder of this paper will be devoted to our attempts to devise methods to predict attachment cross sections. Further, we shall restrict the discussion to endothermic attachment and energy transfers that occur below the electronic levels of the target molecules.

ATTACHMENT CROSS SECTIONS

In 1951 Holstein (Ref. 1) suggested that the dissociative attachment cross section could be represented by

$$\sigma(E) = \sigma_o \exp(-\tau_s/\tau_a) \tag{12}$$

Numerous applications of this formula exist in the literature. Usually τ_a is considered to be constant, and various methods are used to estimate τ_s. Further, more complicated derivations of the attachment cross section have been made, with O'Malley's (Ref. 2) being representative.

We wish to show that very simple arguments lead to an equation of form given by (12), and further, that this model leads to useful results. First, we phenomenologically replace the target molecule with a circle of area σ_o. There is only one restriction placed on this circle: Any electron that penetrates this circle must have a non-zero probability of ending up as a negative ion. Second, we assume that the time an electron spends "inside" the circle is not unique, but that a distribution of times must be considered. Third, we examine a large number, N, of target molecule-electron pairs with respect to some arbitrary time zero, and calculate the rate that the molecule-electron pairs revert back to independent particles. The conversion rate is

$$dN = \frac{-N}{\langle\tau\rangle}\, dt \tag{13}$$

Thus the fraction of molecule-electron associations left after time τ_s is

$$\frac{N(\tau_s)}{N(0)} = \exp(-\tau_s/\langle\tau\rangle) \tag{14}$$

Thus if the unique time τ_s is required for attachment to be assured, the attachment cross section is given by

$$\sigma = \sigma_o \exp\ (-\tau_s/\langle\tau\rangle) \qquad (15)$$

the equation given by Holstein. The above discussion still is not a derivation because of several implicit assumptions. Some of the assumptions are cleared up as follows: First, in equation (13) the dependence of dN on N is nothing more than a statement that the N(0) electron-molecule pairs are independent. Second, the use of only one $\langle\tau\rangle$ means that on the average only one type process need be considered for electrons "leaving" the circle σ_o. Third, it is not at all clear what physical picture is associated with the relation $dN \propto dt$. At this stage of the development we leave this as an assumption without a physical picture. The use of a unique time for τ_s is qualitatively justified by the relatively large nuclear masses. In fact τ_a will be computed using quantum mechanics and τ_s using classical mechanics; the large mass difference between the electron and the nucleus is the qualitative justification for this.

There is a time interval when it is not possible to predict the details of the mechanics of a single incoming electron. The average value of this time duration can be estimated for the case of a strong electron-molecule interaction, and is

$$\langle\tau\rangle = \frac{\alpha\hbar}{E} \qquad (16)$$

Equation (16) is an application of the uncertainty principle. The strong interaction allows us to use the incident electrons' energy to scale the energy term in the uncertainty principle. The strong coupling assumed for the calculation of $\langle\tau\rangle$ has an important physical implication: For a time $\simeq \langle\tau\rangle$, it is not possible to associate the incident electron with any "part" of the target molecule.

If the collision results in electron attachment, two heavy particles, the neutral fragment and the fragment that ends up as a negative ion, must separate. Thus, τ_s is calculated by relating it to a potential energy of the separating fragments. This is accomplished as follows: Before separation begins, the potential energy associated with the separating forces is scaled to the incident electron energy giving

$$U(r_o) = \eta E + \text{Arbitrary Constant} \tag{17}$$

Equation (17) follows from the classical conservation of energy when the incident electron is "stopped", and all of the incident electron kinetic energy is converted to potential energy for separating the fragments, in which case $\eta = 1$. η is thus viewed as the efficiency of the conversion of electron kinetic energy to potential energy for the separation of the fragments. r_o is the initial separation distance of the fragments. At large separations the force between the negative ion and the neutral fragment must be small. To account for this space dependence, the potential given by Eq. (17) is modified as follows:

$$U(r) = \eta E \left[1 - \frac{(r - r_o)}{R_o}\right] + \text{Arbitrary Constant} \tag{18}$$

We note that Eq. (18) is the first two terms in the Taylor's expansion of

$$\eta E \exp\left[-(r - r_o)/R_o\right] \tag{19}$$

about r_o. Rewriting (18) in terms of the change in separation, $r' = r - r_o$, gives

$$U(r') = \eta E \left[1 - r'/R_o\right] + \text{Arbitrary Constant} \tag{20}$$

The classical equation of motion for the separating fragments is

$$\mu \frac{d^2r'}{dt^2} = -\frac{dU}{dr'} \tag{21}$$

giving

$$\mu \frac{d^2r'}{dt^2} = \frac{\eta E}{R_o} \tag{22}$$

Integration gives

$$r'(t) = \frac{\eta E}{2\mu R_o} t^2 + \dot{r}'(0)t + r'(0) \tag{23}$$

and $r'(0) = 0$. What to do about $\dot{r}'(0)$ is much more difficult since it depends on the vibration velocity and the separation geometry, but as a first approximation we assume $\dot{r}'(0) = 0$. Then Eq. (23) becomes

$$r'(t) = \frac{\eta E}{2\mu R_o} t^2 \tag{24}$$

To obtain τ_s we assume that attachment is assured when the change in relative separation is R_o. Because of the way the separation potential energy curve is defined, Eq. (18), this is the position where the separating fragments have acquired their final kinetic energies. Then

$$\tau_s = R_o \sqrt{\frac{2\mu}{\eta E}} \tag{25}$$

Inserting (25) and (16) into (15) gives

$$\sigma(E) = \sigma_o \exp \left[- \frac{R_o}{\alpha\hbar} \sqrt{\frac{2\mu}{\eta}} E^{1/2} \right] \tag{26}$$

Equation (26) gives the predicted dependence of the attachment cross section on the energy of the incident electron. Further, we note that it is not possible to determine the parameters R_o, α, and η from measured values of the cross section, but a combined parameter,

$$\gamma = \frac{R_o}{\alpha\hbar} \sqrt{\frac{2\mu}{\eta}} \tag{27}$$

can be determined.

Finally, we introduce the threshold energy, E_T, as the minimum energy at which attachment can occur for target molecules in ground rotational and vibrational states. Thus the final form for the cross section is

$$\sigma(E) = \sigma_o \exp (- \gamma E^{1/2}) \qquad E \geq E_T \tag{28}$$

Perhaps the most striking thing about the above development is the large number of assumptions and approximations. Further, the cross section model contains two unknown parameters. This situation is reasonably typical when one replaces a very complex problem with a model. Further, we have chosen to emphasize the approximations in our derivations. Our only option now is to explore the consequences of the model. This is done, in part, in the following paragraphs.

First, the model should predict the proper energy dependence of the cross section above the threshold energy. An example of this is shown in Fig. (2), where the model is fit to the 3.72 ev dissociative attachment of H_2. The experimental data are that of Schulz and Asundi (Ref. 3). The

unfolding calculations can be found in reference 4. The cross section parameters with approximate error estimates are given on the Figure. (For the moment ignore the rotational considerations.) The fit is seen to be reasonably good. Table I gives a summary of parameters for molecules that we have examined in some detail. The parameter estimates for all of the molecules except H_2 can be found in Reference 5. The most striking thing about the parameter summary is that σ_o is approximately independent of the target molecule. As the peak cross section for these molecules at room temperature varies by about 10^7, this result is rather convenient. The average value of σ_o is $(5.1 \pm 1.3) \times 10^{-14}$ cm^2.

Second, with the model we should be able to estimate peak cross sections. To do this we assign a value of 9 ev$^{-1/2}$ to γ. Figure (3) shows the results of these calculations for a number of processes. The bars indicate various experimental differences. Thus it appears that the dependence of the attachment cross section on electron energy is predicted reasonably correctly. We point out that there is no reason to believe that the parameters should be independent of the target molecule, they just turn out to be approximately so.

Lest simple results be extended too far, we point out that when the electron energy is greater than some electronic state of the target molecule, the formula fails quite badly.

That the electron energy is the dominant variable was first pointed out by Christophorou and Stockdale (Ref. 6). These investigators also pointed out the effects of electronic states. The two cross section models are quite different, however, because of the way τ_s and τ_a are calculated. In our calculation, the energy dependence of each cross section and the peak cross sections are predicted using an almost constant set of parameters. Further, we have included H_2 within the scope of our model.

EFFECTS OF PURE ROTATION FOR DIATOMIC MOLECULES

A relatively simple extension of the model allows estimation of the effects of rotation for diatomic molecules. Since the attachment cross section depends mostly on the incident electron's energy, the rotational energy can be treated as a static effect. For diatomic molecules all of this

energy can be recovered and hence rotational effects have the appearance of a threshold lowering. The calculation then amounts to extrapolating

$$\sigma(E) = \sigma_o \exp(-\gamma E^{1/2}) \tag{29}$$

to energies below E_T and weighing the curve by the probability that the collision is one that permits energy to be conserved. The situation is illustrated schematically by Fig. (4). Thus the cross section is given by

$$\sigma(E) = P[E_{rot} \geq (E_T - E)] \; \sigma_o \exp(-\gamma E^{1/2}) \qquad E < E_T \tag{30}$$

Treating the rotational quantum numbers as continuous and in equilibrium, the normalized distribution function is (Ref. 7),

$$\frac{df}{dJ} = \frac{hcB}{kT}(2J+1)\exp(-hcB\,J(J+1)/kT) \tag{31}$$

the rotational energy is

$$E_{rot} = hcB\,J(J+1) \tag{32}$$

the transformation from J to E_{rot} is

$$\frac{df}{dE_{rot}} = \frac{df}{dJ}\frac{dJ}{dE_{rot}} \tag{33}$$

from (32)

$$\frac{dJ}{dE_{rot}} = \frac{1}{hcB(2J+1)} \tag{34}$$

Thus

$$\frac{df}{dE_{rot}} = \frac{1}{kT}\exp(-E_{rot}/kT) \tag{35}$$

Therefore

$$P(E_{rot} \geq (E_T - E)) = \frac{1}{kT}\int_{E_T-E}^{\infty}\exp(-E_{rot}/kT)\,dE_{rot} \tag{36}$$

$$= \exp[-(E_T - E)/kT] \tag{37}$$

Then the expression for the cross section becomes

$$\sigma_o(E) = \sigma_o \exp(-\gamma E^{1/2}) \exp(-(E_T - E)/kT) \qquad E < E_T \quad (38)$$

Figure (5) shows the predicted effects of rotation as a function of temperature. Above ≈ 2000°K the effects become rather pronounced. It is difficult to check these calculations with experimental data because of the lack of instrumental resolution. Indirect checks might be made from rate constant data as they become available. To facilitate this comparison we note that the rotational contribution to the rate constant is

$$K_{rot} = \frac{24\,\sigma_o}{\gamma^4 (kT)^{3/2}} \left(\frac{2}{\pi M_e}\right)^{1/2} \exp(-E_T/kT)$$

$$\left[1 - [\exp(-\gamma E_T^{1/2})]\ [1 + \gamma E_T^{1/2} + 1/2\ \gamma^2 E_T + 1/6\ \gamma^3 E_T^{3/2}]\right] \quad (39)$$

This accounts for the cross section values below E_T. There is a contribution by the cross section at energies above E_T, which is given by

$$K' = \frac{2\sigma_o}{(kT)^{3/2}} \left(\frac{2}{\pi M_e}\right)^{1/2} \int_{E_T}^{\infty} E \exp(-(E/kT + \gamma E^{1/2}))\ dE \quad (40)$$

$$K' = \frac{4\sigma_o}{(kT)^{3/2}} \left(\frac{2}{\pi M_e}\right)^{1/2} \int_{E_T^{1/2}}^{\infty} \phi^3 \exp(-(\phi^2/kT + \phi\gamma))\ d\phi \quad (41)$$

The integral in (41) cannot be done in closed form, but must be evaluated numerically.

CONCLUDING REMARKS

Some of the aspects of negative ion formation have been explored. In particular, the emphasis of this paper is a simple procedure for the prediction of dissociative attachment cross sections, and some of the extensions required to include excited states. The electron energy is no doubt one of the major variables for many dissociative attachment processes. This strong energy dependence suggests a simple model for diatomic rotational effects. More calculations and careful experiments are required to evaluate the usefulness of simple cross section models.

ACKNOWLEDGEMENT

The research reported in this paper was sponsored in part by the Air Force Cambridge Research Laboratories, Office of Aerospace Research, under Contract No. F1962-70-C-0134, but publication does not necessarily reflect endorsement by the sponsor.

REFERENCES

1. T. Holstein, Phys. Rev., 84, 1073 (1951).
2. T. F. O'Malley, Phys. Rev., 150, 149 (1966).
3. G. J. Schulz and R. K. Asundi, Phys. Rev., 158, 25 (1967).
4. R. L. Cowperthwaite and H. Myers, J. Chem. Phys. 53, 1077, (1970).
5. R. L. Cowperthwaite, MDAC Report H358, McDonnell Douglas Corp., St.Louis, Missouri, June 1969.
6. L. G. Christophorou and J.A.D. Stockdale, J. Chem. Phys., 48 1956 (1968).
7. G. Herzberg, Molecular Spectra and Molecular Structure, Vol. I., D. Van Nostrand Inc., New York, 1945.
8. I. S. Buchel'nikova, Zh. Eksp. Teor. Fiz., 35, 1119 (1958); English Translation in JEPT 35 783 (1959).

TABLE I

DISSOCIATIVE ATTACHMENT CROSS SECTION PARAMETERS

Process	$\sigma_o(cm^2)$	$\gamma(ev^{-1/2})$
$SF_6 \rightarrow SF_5^- + F$	$(3.4 \pm 0.9) \times 10^{-14}$	6.06
$HI \rightarrow H + I^-$	$(7.8 \pm 1) \times 10^{-14}$	5.7
$DI \rightarrow D + I^-$	$(4.5 \pm .8) \times 10^{-14}$	6.86
$HBr \rightarrow H + Br^-$	$(6 \pm 2) \times 10^{-14}$	9.6
$DBr \rightarrow D + Br^-$	$(3.5 \pm 2) \times 10^{-14}$	9.2
$HCl \rightarrow H + Cl^-$	$(6 \pm 3) \times 10^{-14}$	9.0
$DCl \rightarrow D + Cl^-$	$(4 \pm 2) \times 10^{-14}$	8.8
$CCl_4 \rightarrow CCl_3 + Cl^-$	$(7.5 \pm 1.5) \times 10^{-14}$	6.6 ± 1.4
$H_2 \rightarrow H + H^-$	$(6.2 \pm 3.0) \times 10^{-14}$	8.88 ± 0.30

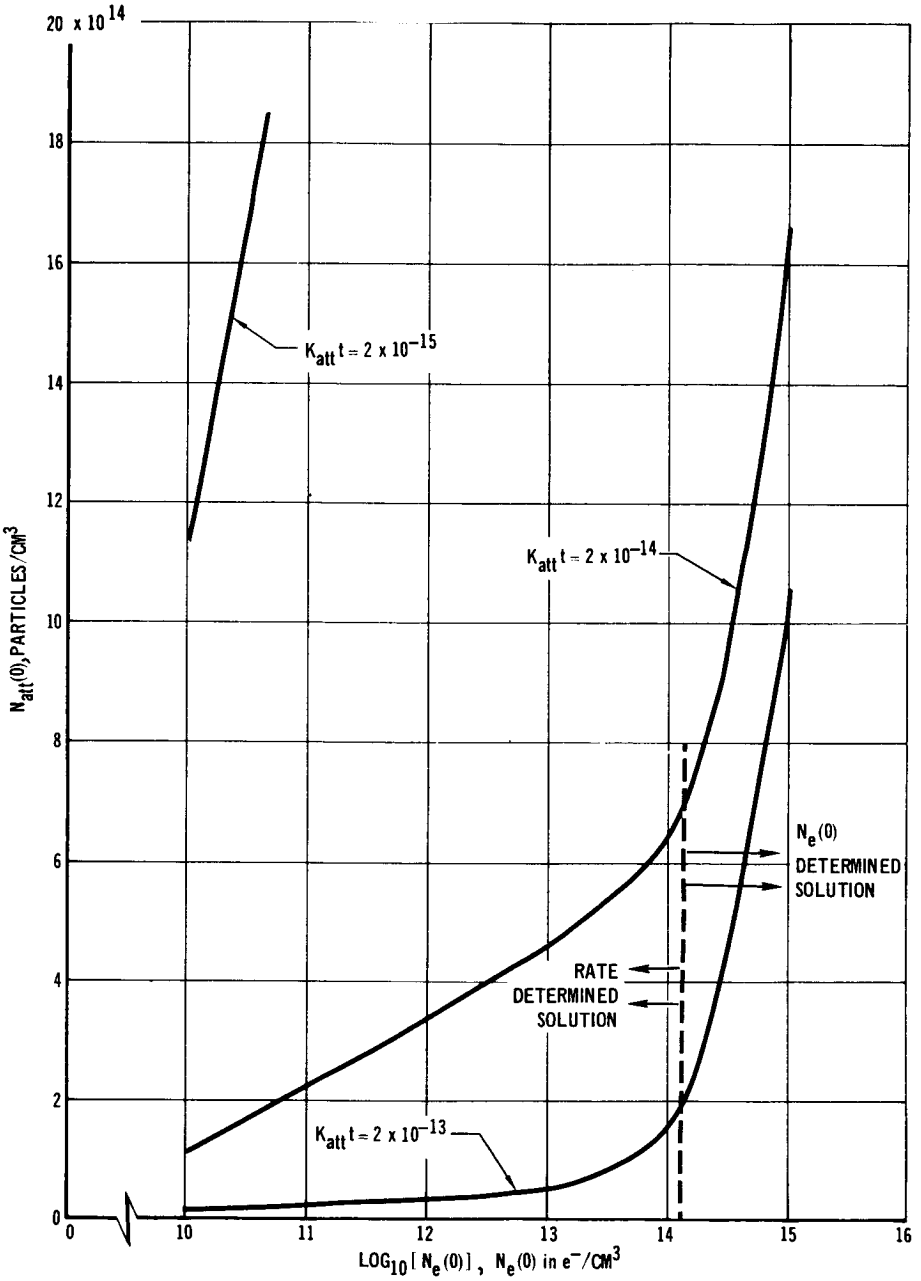

Figure 1.- Additive number density required to reduce initial electron concentrations to 10^9 e^-/cm^3 for various values of $K_{att}t$.

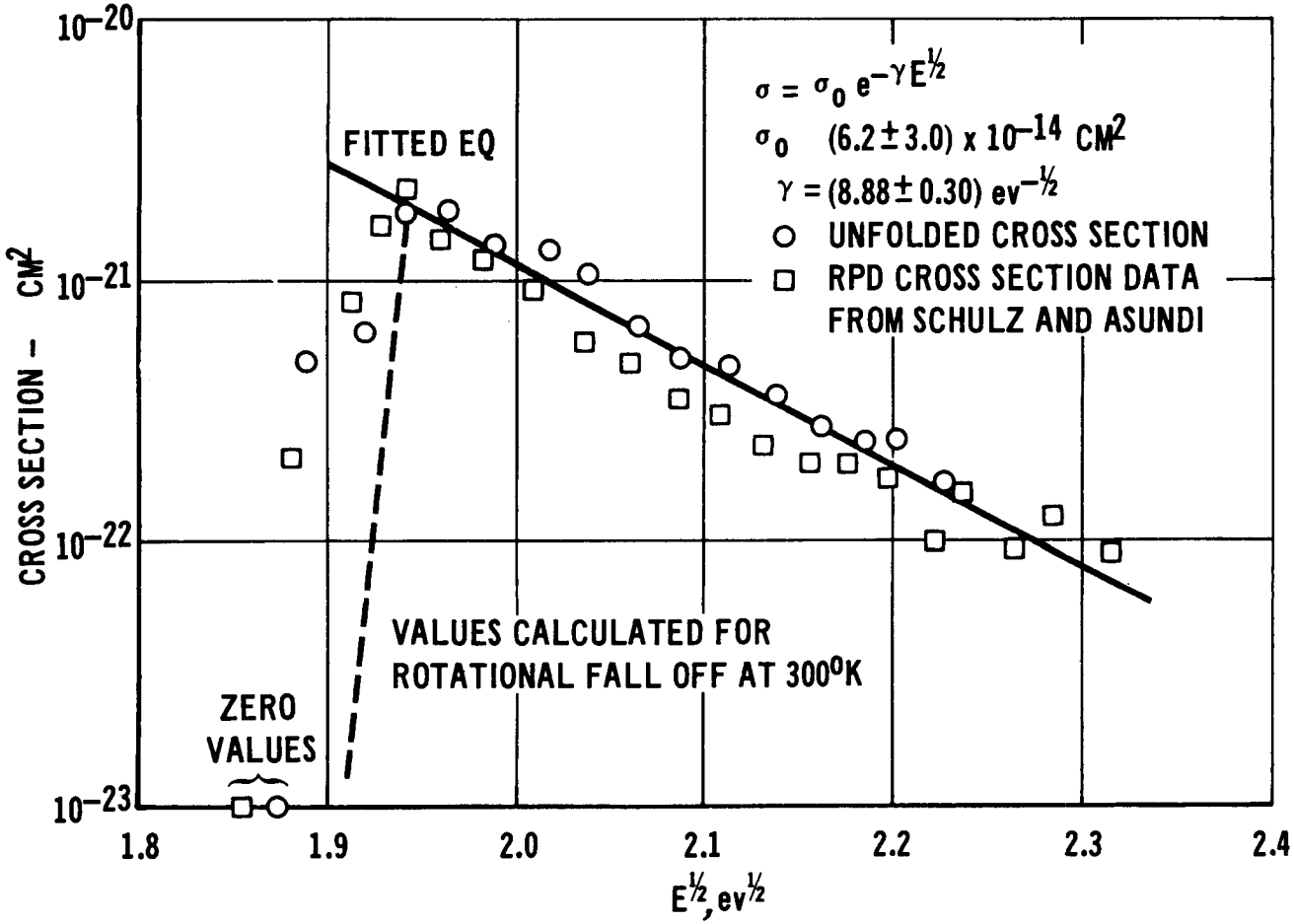

Figure 2.- Model fit to 3.72 eV H_2 cross-section data, illustrating the ability of the model to reproduce the energy dependence of the cross section.

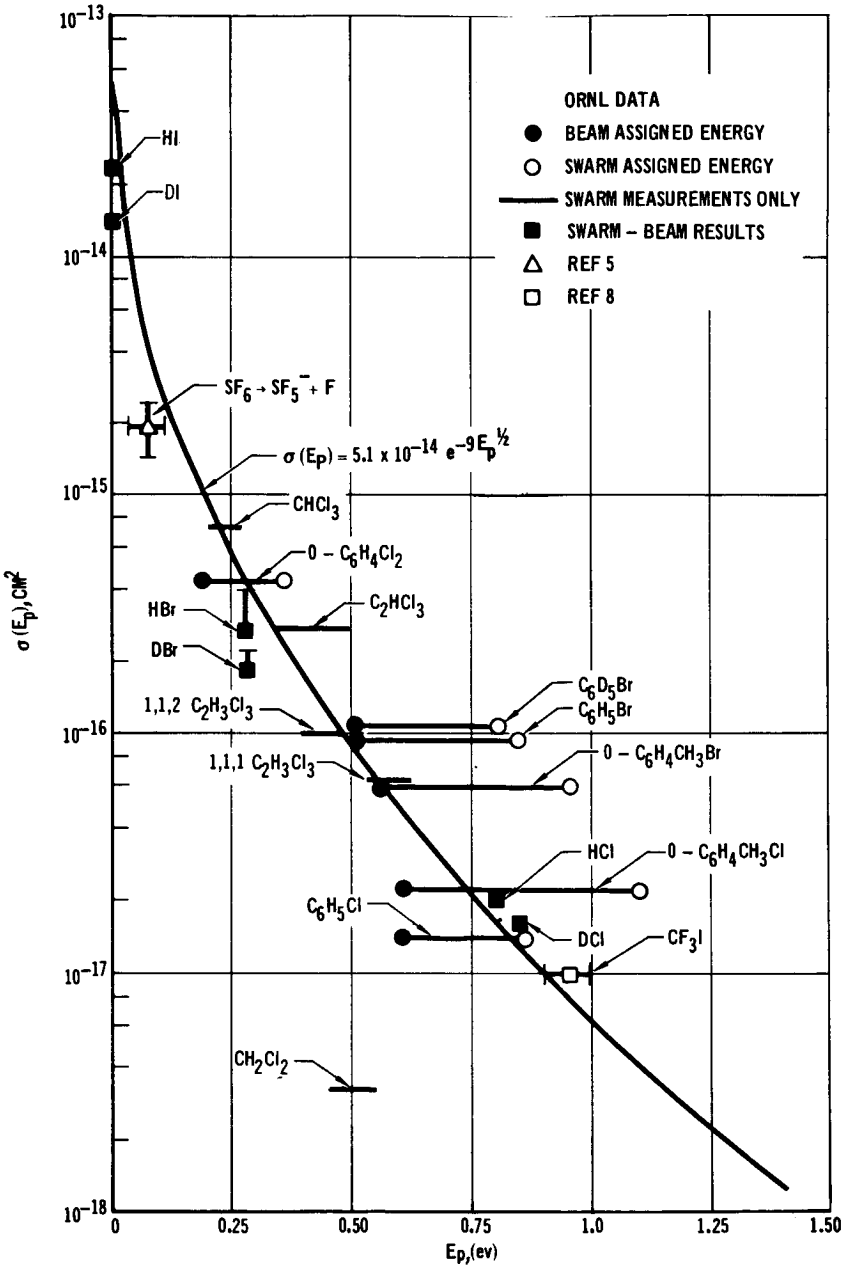

Figure 3.- Comparison of predicted peak cross sections, using constant model parameters, and measured peak cross sections.

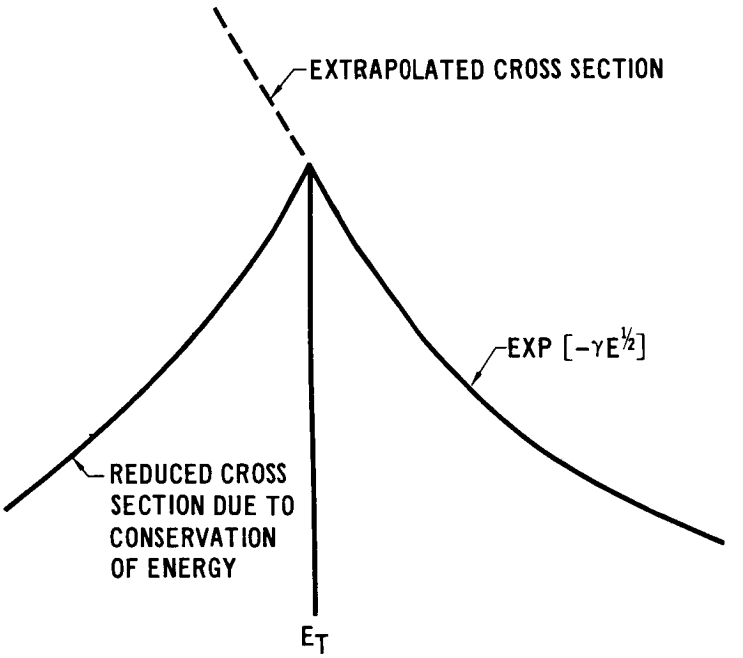

Figure 4.- Schematic of the rotational effects treatment, suggested by the strong energy dependence of the cross sections.

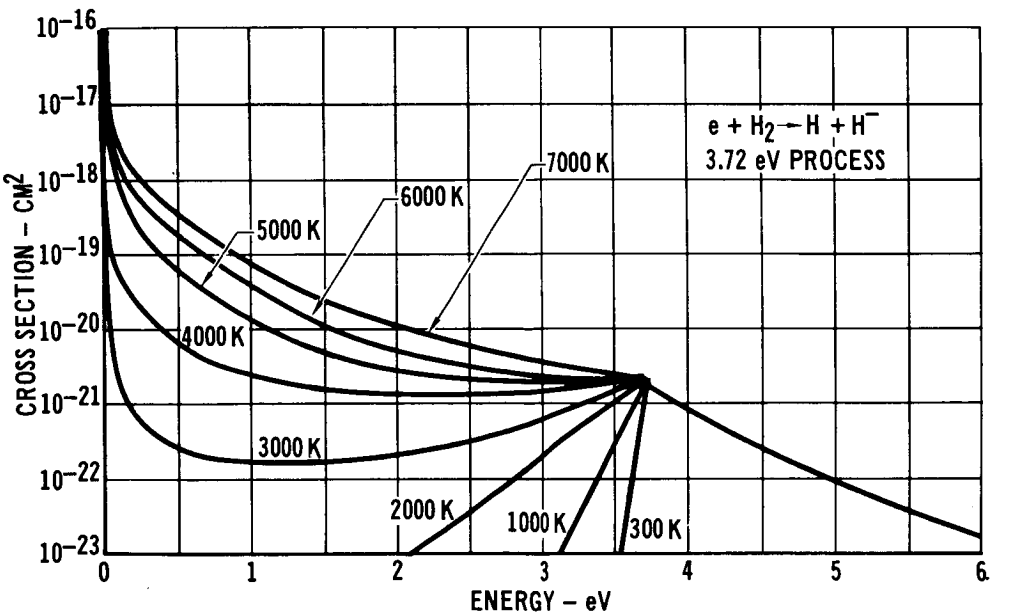

Figure 5.- Parametric calculations of predicted rotational effects for H_2. The calculations suggest that the attachment rate constant will strongly increase with temperature.

AEROPHYSICAL PLASMA ALLEVIATION*

By E. M. Parmentier, K. L. Wray, and R. F. Weiss
Avco-Everett Research Laboratory

SUMMARY

Two techniques for alleviating the reentry plasma sheath on a slender vehicle have been analyzed. The objective of both techniques is to reduce the boundary layer electron density in the field of view of an antenna and so reduce the attenuation of transmitted signals and prevent breakdown.

The chemical technique considers the effects of the addition of small amounts of SF_6 (~1% by volume) to the boundary layer. The objective is to keep the electrons attached as F^- for a time long enough to accomplish alleviation. Our results indicate that if full or partial equilibrium is attained, alleviation cannot be accomplished. However, if electron attachment rates are sufficiently fast at the high temperatures in the boundary layer, a factor of 10 decrease in electron concentration is possible at high altitudes (above 100 kft), provided the necessary steady state SF_6 concentration could be maintained for the required flow time. At lower altitudes increased H-atom concentration prevents any significant reduction of electron density.

Furthermore, our results indicate that the concentrations of SF_6 required for alleviation at low altitudes (and probably high altitudes) would certainly be sufficient to blow off the boundary layer. This suggests that an entirely aerodynamic solution might be possible in which a plume of electron-free gas is injected into the vehicle shock layer to divert the boundary layer around an antenna window. Aerodynamic disturbances must be kept weak to prevent additional electron production. An injection technique has been identified which assures minimum aerodynamic disturbances while efficiently diverting the boundary layer. For a hydrazine gas source, a mass flow of approximately 200 gm/sec at 100 kft can provide at least a factor of 5 reduction of integrated electron density. The mass flow required at other altitudes is proportional to the ambient pressure.

INTRODUCTION

The formation of the plasma sheath surrounding a vehicle reentering the atmosphere and its resulting effect on the transmission of electromagnetic signals are well known. In this investigation we have analyzed two techniques - one chemical and the other aerodynamic - for alleviating this plasma sheath in the neighborhood of an antenna window on a slender reentry vehicle.

---

*This research was supported by the Advanced Research Projects Agency of the Department of Defense and Space and Missile Systems Organization, Air Force Systems Command and was monitored by Space and Missile Systems Organization, Air Force Systems Command under Contract F04701-70-C-0128.

Chemical techniques using a variety of alleviants have been investigated with some success on the RAM vehicle which is a 9° half angle blunt cone. However, no studies of the effectiveness of electrophilics to attach electrons on slender vehicles when the electrons are confined to the boundary layer have yet been presented. SF_6 is selected as the alleviant studied since its high temperature chemistry is relatively well known and its success as a quenchant has been demonstrated. The rates of addition of SF_6 considered are less than the boundary layer blow-off limit.

The aerodynamic concept makes use of a plume of electron-free gas injected into the vehicle shock layer to divert the boundary layer from the field of view of the antenna window. The success of this technique does not depend on the electrophilic properties of the injectant, but only on the manner in which it is injected. The injectant may be chosen to minimize the mass flow required to divert the boundary layer.

The vehicle considered is the RANT vehicle - a typical slender reentry vehicle: an 8° half angle cone with a 1/4" nose radius and a carbon phenolic heat shield. An antenna window is located at a station 30" back from the nose. The effectiveness of the chemical technique is evaluated for a reentry velocity of 23,500 ft/sec and in the altitude range of 160 kft to 40 kft. The aerodynamic technique is analyzed for the vehicle at a free stream Mach number of 20 from 120 kft to 60 kft.

SYMBOLS

A	area
(A)	concentration of species A
C_D	drag coefficient
C_p	pressure coefficient
c_p	specific heat at constant pressure
k	reaction rate constant
K	equilibrium constant
$\mathcal{M}$	molecular weight
M	Mach number or non-specific gas species
$\dot{m}$	mass flow
N_e	integrated electron density

n_e	electron density
p	static pressure
p_o	stagnation pressure
r	radial coordinate (figure 11)
Re	unit Reynolds number
(R,ω,θ)	spherical coordinates (figure 9)
(R,ξ,y)	boundary layer coordinates (figure 11)
T	static temperature
T_o	stagnation temperature
u	velocity
(v_R,v_ξ,v_y)	sublayer velocity components
α	injection angle
δ	boundary layer thickness
δ_s	sublayer thickness
δ_e	integrated electron density thickness
ϵ	eccentricity of ellipse
γ	ratio of specific heats
τ_{AB}	relaxation time for process A + B $\rightarrow$ products
μ	viscosity
ρ	gas density

Subscripts:

c	at fully expanded plume cross section
e	edge condition
j	at injection port
o	initial value

s	in vehicle shock layer
ss	steady state
∞	free stream

CHEMICAL ALLEVIATION WITH SF_6

The objective of the chemical technique is to attach free electrons in the boundary layer. Attachment of electrons occurs by the formation of SF_6^- (or some fragment thereof) by the reaction of a free electron with SF_6. Alleviation can be accomplished if enough electrons can be kept attached for a time sufficiently long compared to the flow time over the antenna window.

Theoretical Model

In this study we superimposed the alleviant chemistry onto the aerodynamic flow fields computed without the presence of the alleviant. For simplicity, we make the assumption that the position of the maximum temperature in the boundary layer is the relevant one; hence, we need only superimpose the alleviant chemistry onto the temperature and density of various species at this point in the boundary layer. We can then obtain the answers to such questions as how fast do the electrons attach, what is the thermal and chemical stability of the alleviant, what is the detachment mechanism, etc. The justification for this approach is 1) it is a problem that can be solved, whereas the machinery for handling the problem in all detail is non-existent; 2) it was recognized early in this study that one of the main difficulties in boundary layer alleviation is the stability of the quenchant materials - the peak temperature in the boundary layer is where this problem is most severe; 3) the peak temperature in the boundary layer also approximately coincides with the position of the peak electron concentration.

The important chemical processes occurring in the SF_6/air-ablation product system are presented in Table 1 along with an evaluation of the rate constants. The thermal decomposition of SF_6 has been the subject of several investigations; however, none of them have been in the density/temperature regime of interest in the present problem and, hence, extrapolations must be made. Unfortunately, 1) there is some conflict in the data and 2) theoretical extrapolations are somewhat uncertain. The most extensive data are those of Bott and Jacobs[1] who fit their data to the theory of Rice, Ramsberger and Kassel; we have used their RRK parameters to extrapolate[2] to the T and p regimes of interest. The data of Bott and Jacobs have been substantiated in the unpublished work of K. L. Wray and E. V. Feldman of AERL. The results of Kurzius and Raab[3] are anomalous. The mathematical representation of their data, $k_d(K)$, does not extrapolate into the data of Bott and Jacobs. We have serious doubt as to the validity of $k_d(K)$; however, for completeness we include it in our study.

There is no doubt that SF_6 attaches electrons to make SF_6^- with an attachment rate $\approx 2 \times 10^{-7}$ cm^3 sec^{-1} in the vicinity of room temperature independent of the "buffer gas" and that this process is two-body in the density regime of interest in the present study.[4-6] Unfortunately, the situation at high temperature is not nearly so clear although indications are that the rate decreases somewhat at higher temperatures. Perhaps more importantly, it is clear that the rates of formation of SF_5^- and, at very high temperatures, F^- increase steeply. With the presently available data it is not yet possible to separate the effects of the electron temperature from those of the heavy gas temperature. However, at high temperatures, and when the heavy temperature is equal to the electron temperature, we feel that the predominant negative ion formed is SF_5^- and/or F^- with attachment rate constants of the order of 10^{-8} cm^3/sec.

The electron detachment processes are important because if they are slow enough it might be possible to keep the electron bound up in the form of F^- for a sufficiently long time so that alleviation can be successfully accomplished. We list some of these processes in Table 1. In recent work (not yet published) A. Mandl of AERL has measured k_{F^-M} for M = N_2 and CO; k_{F^-F} is extrapolated from measurements on the Iodine system[7]. We include the probably fast reaction with atomic hydrogen[8], which, as we will see later, dominates. We also include in Table 1 the processes for ionization k_i and neutralization $k_{F^-NO^+}$ which a priori could be important. k_i is very accurately known as the result of a large number of investigations, while $k_{F^-NO^+} = 10^{-7}$ is typical for such reactions, but could be an order of magnitude slower.

In figure 1 we have plotted the rate constants given in Table 1 as a function of temperature; k_d(RRK) cannot be plotted since in the RRK formulation the effective rate constant depends on the concentration of collision partners. We wish to compare the reaction <u>times</u> of these processes at the boundary layer conditions of interest. The chemical relaxation time for the the process $A + B \xrightarrow{k} \text{products}$ where (B) $\gg$ (A) is defined as $\tau_{AB} = 1/k(B)$ so that, for bimolecular reactions, τ_{AB} is the time in which (A) will be decreased from its initial value by a factor of 1/e.

Aside from kinetic considerations we must also look at the equilibrium situation as it is not correct to consider only the forward reaction path but one must also take into account the backward reaction. We outline three such considerations.

I. Assume that the electrons are in local equilibrium with SF_6^-; i.e., $(e)_f(SF_6)_f/(SF_6^-)_f = K(T)$, where the subscript f on the concentrations refers to the "final" values. If we wish to reduce the initial electron density $(e)_i$ to a final density $(e)_f$ we see that the SF_6 required to survive is given by

$(SF_6)_f = \left\{\left[(e)_i/(e)_f\right] - 1\right\} K(T)$. Hence, to reduce $(e)_i$ by a factor of 10 we must add SF_6 concentration at least to the extent of 10 times the equilibrium constant.

II. Completely similar considerations are applicable for the system where $e + F \rightleftarrows F^-$ equilibrium is assumed.

III. It is conceivable that instead of the system going to a local equilibrium, that the electrons could temporarily get tied up as F^-. This could come about if the electron attachment to the SF_6 (or some fragment thereof) was fast compared to the F^- detachment process, so that a steady state F^- concentration above that of full equilibrium could be achieved. Thus, for the reactions $e + SF_6 \xrightarrow{k_1} F^-$ + products and $F^- + H \xrightarrow{k_{F^-H}} HF + e$, the steady state F^- concentration $(F^-)_{ss}$ is related to the SF_6 by: $(SF_6)_{ss} = (F^-)_{ss}/(e)_{ss}\left(1/k_1\tau_{F^-H}\right)$. Again, when $(F^-)/(e) \gtrsim 1$, reduction in electron concentration is accomplished.

Concentrations and Temperatures

Five altitudes were considered, i.e., 160, 130, 100, 70 and 40 kft. For the three highest altitudes where ablation effects are not overwhelming, finite chemical kinetics boundary layer solutions were obtained for pure air chemistry. These were Blottner type calculations using the correct wall temperature and wall boundary conditions for the system under consideration. In order to evaluate the number density of ablation material products in the boundary layer, results from separate trajectory-heating computer programs were used for a carbon phenolic heat shield which gave the mass ablation rate at various positions on the body for the altitudes of interest. We used the current state of knowledge on the nature of the primary ablation products of carbon phenolic to convert this mass ablation rate into a particle density in the boundary layer. At the lower altitudes of 70 and 40 kft, which are below transition, the boundary layer is turbulent and very probably equilibrium; here we used preliminary computer code calculations which yielded the desired enthalpy and mass ratio of ablation product to air profiles. Via chemical equilibrium programs, these were converted into temperature and species concentration profiles. It should be emphasized that the low altitude peak temperatures resulting from these calculations are currently suspected to be too high.

The results of these calculations are shown in Table 2 where we have listed at the various altitudes the concentrations of the chemical species of interest in making chemical time calculations. Also shown are the ablation rates $\dot{m}$ and the mass fraction of ablation products in the boundary layer $\dot{m}_A/\dot{m}_{BL}$ at high altitudes. The following comments are noteworthy. The peak temperature in the high altitude boundary layer at 160 kft is 5000° K and only as low as 4190° at 100 kft. For the low altitude cases the very high temperatures are doubted, as work in progress at AERL is leading to temperatures of ≈4400° K. The atomic

hydrogen concentration is of order 1% of the total species concentration at the high altitudes above transition; below transition in the equilibrium boundary layer, it is more like 10%. We have assumed for the purpose of calculation that the SF_6 concentration is 1% of the total concentration.

Results of Calculations

Figures 2, 3 and 4 show the chemical relaxation times as a function of temperature for 3 of the 5 altitudes for which detailed calculations were carried out. At each altitude the number density of the relevant chemical species for that altitude was used but not the peak temperature itself. Also indicated on the figures is the characteristic flow time for the problem which would be between 10^{-4} and 10^{-5} sec for an injection nozzle located a short distance upstream from the antenna window.

We note that there is an extremely significant difference in the dissociation time for SF_6 depending on whether we use the RRK extrapolation or the extrapolation supplied by the Kurzius-Raab report[3]. (Note, however, the experimental data point τ_d on Fig. 4.)

At all altitudes the electron attachment time is comparable with or even a factor of 10 shorter than the SF_6 (RRK) dissociation time. This is, of course, a critical point. At high altitudes, the electron detachment time by H is 10 times longer than the attachment time, while at low altitudes these two times are about equal. Furthermore, even at the highest altitude the attachment time is short compared to the characteristic flow time for the problem, but, unfortunately, so is the (RRK) dissociation time.

In figure 5 the concentration of SF_6 needed to start reducing the electron density in the boundary layer is plotted as a function of temperature. The curves are calculated on the basis of the local equilibrium and steady state considerations discussed earlier. Also shown for comparison are ticks on the concentration axis indicating the total number density (M) in the boundary layer for the various altitudes. This figure makes it readily apparent that when the electrons are in equilibrium with SF_6^- the amount of SF_6 needed to survive to tie up a significant number of electrons is much larger than the total number density at the location of the peak temperature in the boundary layer. At temperatures above about 3500° the same statements can be made when the electron is tied up in F^-. However, it is true that when the boundary layer temperature falls below about 3500° one can begin to significantly reduce the electron density by the addition of SF_6 allowing full equilibrium.

On the other hand, to tie up the electrons in a steady state F^- concentration which is bottlenecked by the detachment process is seemingly possible as indicated by the curves labeled F^-_{ss} in figure 5. These calculations are based on the detachment mechanism being $F^- + H \rightarrow HF + e$ for which we have certainly used an upper bound for its rate constant. It is doubtful that any other detachment process in the boundary layer would have a smaller time than τ_{F^-H}.

For a 1% SF_6 addition, the high altitude cases show about a factor of 10 decrease in electron concentration, but at low altitudes, due to the increased H-atom concentration, electron reduction barely starts. Unfortunately, the $(SF_6)_{ss}$ needed to accomplish this reduction is not available due to its decomposition in times short compared to the flow time.

Summary

As outlined above we have identified the important chemical processes for SF_6 alleviation in ablating carbon phenolic boundary layers. We have evaluated the rate constants for these processes and have obtained temperatures and concentrations at the position of boundary layer peak temperature as a function of altitude. We have calculated reaction times as a function of temperature and, furthermore, have calculated equilibrium and steady state electron densities for several cases as a function of temperature for SF_6 addition. We have concluded that for SF_6 addition amounting to 1% by volume, alleviation cannot be accomplished if the system goes to partial or full equilibrium. However, if the SF_6 global electron attachment rates to form F^- are sufficiently fast at the high temperatures encountered in these boundary layers, then the results of this study indicate that sufficient F^- may be formed to significantly reduce electron concentrations at high altitude provided that the required SF_6 steady state concentration is available; this would not be true if the k_d (RRK) is correct, but only if k_d(K) is correct. The rate constant of 10^{-8} cm^3/sec used in this study is at best an educated guess and if $k_{6,5,1} \lesssim 10^{-10}$ then quenching would not be successful at any altitude, independent of the value of k_d. In the absence of hydrogen, we speculate that the dominant detachment process would be $F^- + O \rightarrow FO + e$, also with a very high rate constant.

The success of various quench experiments performed in the laboratory ought to be noted; however, these have been carried out at significantly lower temperatures than those encountered under the present situation. Furthermore, they were not carried out in the presence of hydrogen and, to be sure, the mass additions of alleviants in these various experiments have often exceeded the concentrations necessary to blow off the boundary layer. It is not clear whether these experiments were successful due to 1) steady state F^- formation, 2) sufficient mass addition so that the boundary layer was cooled to the point where electrons could be equilibrium attached or 3) simply causing the plasma sheath to deviate from the detector.

AERODYNAMIC ALLEVIATION

The results of the chemical alleviation analysis indicate that for altitudes below about 100 kft, the concentration of SF_6 needed to significantly reduce the electron density at the peak temperature point in the boundary layer is large. In fact, it would exceed the total number density in the boundary layer at that point. Clearly, the injection of such large amounts of SF_6 will blow off the

boundary layer. This suggests that an entirely aerodynamic solution to achieve low altitude alleviation might be feasible.

The objective of the aerodynamic technique is to inject a plume of electron-free gas into the vehicle shock layer in a manner favorable to diverting the high electron density boundary layer around an antenna window. The concept is shown schematically in figure 6. The plume shape, in addition to diverting the boundary layer, must minimize further electron production in the plume shock layer. This is strongly emphasized by the results in figure 7 which show the electron density behind oblique shock waves in the vehicle shock layer at 50 kft. To make the resulting electron density at least two orders of magnitude below the peak value in the boundary layer ($\approx 10^{13}$/cc at 65 kft for a 30" station on the vehicle considered) over a typical length of 10 cm requires that the plume shockwave angle be restricted to no more than approximately 20 degrees.

Theoretical Model

In order to estimate the behavior of the boundary layer as it interacts with the plume of injected gas, a simplified model is necessary. The model chosen is suggested by the behavior of the dynamic pressure through the boundary layer. As shown in figure 8, in the laminar hypersonic boundary layer the dynamic pressure decreases sharply to an order of magnitude less than that in the freestream near the outer edge. For the laminar boundary layer, R. Vaglio-Laurin[9] has developed rigorously a two-layer approximation for the boundary layer structure. In his model the inner layer, comprising the bulk of the boundary layer, has negligible momentum and is treated as a Couette flow. There, the motion of the gas is determined by balancing shear forces and pressure gradients. However, in the thin outer layer both acceleration and viscous forces are important. Then adopting the shear flow approximation for the inner region (referred to as the sublayer) and assuming that the high dynamic pressure outer region is completely inviscid, this approximate model is applied to both laminar and turbulent boundary layers. In the laminar boundary layer $\delta_{s_o} \approx \delta$. In the turbulent boundary layer the model is less exact as can be seen from the turbulent dynamic pressure profile in figure 8 and the choice for δ_{s_o} is not as clearly defined. However $0 \leq \delta_{s_o} \leq \theta_D$

where

$$\theta_D = \int_0^{\delta} \left(1 - \frac{\rho u^2}{\rho_e u_e^2}\right) dy$$

is the momentum thickness. It is easily seen in figure 8 that when $\delta_{s_o} < \theta_D$ the momentum flux in the modeled boundary layer is greater than in the actual boundary layer.

If the scale of non-uniformity in the boundary layer model, δ_{s_o}, is small compared to the size of the plume, the shape of the injected gas interface is determined by the interaction of the injectant with the inviscid external flow. The sublayer can then be treated separately in a way to be discussed later.

The flow in the shock layer of the vehicle is approximated as a uniform and parallel stream. This approximation should be accurate as long as the diameter of the vehicle at the injection station is large compared to the plume size.

To minimize electron production the most desirable interface would be one that is conical in shape since this ensures a shockwave that is everywhere weak. An injection scheme which can produce such an interface is shown in figure 9. The gas is injected uniformly and supersonically at an angle α from a triangularly shaped injection port in the vehicle surface. Since the injected flow is supersonic, the back edge of the injection port does not influence the flow upstream of the first wave of the expansion from the back edge. The flow in this undisturbed region is conical and generators of the interface surface are rays extending from the apex of the injection port. The angle α is determined so that the turning angle across the inner shock wave is everywhere less than the maximum turning which can be accomplished across an oblique shock wave.

The spherical coordinate system chosen to describe the interface is also shown in figure 9. In order to simply estimate the shape of the interface both the injected gas and the external stream will be assumed Newtonian. For the external stream the assumption is a reasonable one since the Mach number is high ($\approx$11.5). The assumption is much more approximate for the internal flow where in general Mach numbers less than 3 are considered. Across the interface the pressure must balance. Considering an element of the interface surface as shown in figure 9, matching Newtonian pressure on each side gives

$$p_j + \gamma_j p_j M_j^2 \left(\vec{\ell}_j \cdot \vec{n}^2\right) = p_s + \gamma_s p_s M_s^2 \left(\vec{\ell}_s \cdot \vec{n}^2\right) \tag{1}$$

where $\vec{n}$ is a unit vector normal to the surface, $\vec{\ell}_s$ is a unit vector in the direction of the external stream, and $\vec{\ell}_j$ is a unit vector in the direction of the stream of injected gas. The shape of the interface in a coordinate surface of constant R is then $\omega = \omega(\theta)$ and in these terms

$$\vec{\ell}_j \cdot \vec{n} = \cos\psi \sin\alpha \cos\omega \cos\theta - \cos\psi \cos\alpha \sin\omega - \sin\psi \sin\alpha \sin\theta$$

$$\vec{\ell}_s \cdot \vec{n} = \cos\psi \sin\omega$$

(The angle ψ is defined in fig. 9.) Then substituting these expressions into equation (1), and after some algebraic manipulation

$$\frac{1}{\sin \omega}\frac{d\omega}{d\theta} = \frac{-\frac{\Lambda}{C_p}\beta \sin\alpha \cos\theta + \sqrt{\left(\frac{1}{C_p}\sin^2\omega - 1\right)\left(1 - \frac{\Lambda}{C_p}\beta^2 \sin^2\alpha \cos^2\theta\right)}}{1 + \frac{\Lambda}{C_p}\sin^2\alpha\cos^2\theta} \tag{2}$$

where

$$\beta = \sin\alpha \cos\omega \cos\theta - \cos\alpha \sin\omega$$

and

$$\Lambda \equiv \frac{\gamma_j p_j M_j^2}{\gamma_s p_s M_s^2}$$

$$C_p \equiv \frac{p_j - p_s}{\gamma_s p_s M_s^2}$$

are the two dimensionless parameters which along with the injection angle α and the boundary conditions determine the shape of the interface. The subscript j refers to conditions at the injection port and s to conditions in the vehicle shock layer upstream of the injection port. For given values of M_j and p_{o_j}/p_s, the parameters Λ and C_p can be calculated. The boundary conditions required are that $\omega = \omega_s$ (the half angle of the injection port) at $\theta = \pi/2$ and the condition of symmetry, $\frac{d\omega}{d\theta} = 0$, in the plane $\theta = 0$. The equation governing $\omega(\theta)$ is, however, only first order and the solution for arbitrary ω_s cannot satisfy the symmetry condition at $\theta = 0$. Including centrifugal forces in the shock layers, due to their dependence on the curvature of the interface, can introduce a second derivative of ω with respect to θ. However, if the streamline pattern in the inner shock layer is analyzed by determining its laminar Newtonian structure, a Newtonian shock line[10] occurs on the symmetry plane. This is a singularity of the Newtonian shock layer structure for which no uniformly valid solution has yet been obtained. The singular behavior indicates that the calculated interface shape is not correct in the immediate vicinity of $\theta = 0$.

A typical family of interface shapes resulting from a numerical solution of Eq. (2) is plotted in figure 10. As shown by the dashed line the shape is nearly an elliptical cone over the top portion of the interface if its behavior near $\theta = 0$ is ignored. For the remainder of this discussion the interface is assumed to be a half cone of elliptical cross section. This will permit

physically realistic order of magnitude estimates of the boundary layer behavior without the anomalous effects introduced by the singularity at $\theta = 0$. The elliptic shape is completely specified by its eccentricity, ϵ, and the angle ω at $\theta = 0$ which is denoted ω_0.

The attenuation due to a plasma sheath above an antenna window is determined by the integrated electron density, N_e, through the sheath. As the boundary layer interacts with the plume of injected gas, it is important to determine how quickly the portion of the boundary layer containing high electron concentrations is diverted.

The behavior of the inviscid portion of the boundary layer as it flows over the conical body can be calculated by application of the three-dimensional Newtonian shock layer theory discussed by Hayes and Probstein.[10] Detailed calculations have shown, however, that for $\epsilon \gtrsim .8$, the integrated electron density, N_e, on the interface surface decays almost as it would on an axisymmetric shape, i.e., $N_e \propto 1/R$, due to the geometric stretching of the portion of the plume shock layer containing electrons from the boundary layer.

The effect of the deviation of the interface from an axisymmetric shape on the behavior of the sublayer is more pronounced. To make a conservative estimate of the rate at which the sublayer is diverted, it is assumed that the sublayer negotiates the adverse pressure gradient near the nose of the interface and then flows onto the interface surface. There a cross flow will develop due to the transverse pressure gradient created by the departure of the interface from an axially symmetric shape. The momentum and continuity equations written in boundary layer coordinates of the interface surface (fig. 11a) become

$$\mu \frac{\partial^2 v_\xi}{\partial y^2} = \frac{1}{R} \frac{\partial p_e}{\partial \xi}$$

$$\mu \frac{\partial^2 v_R}{\partial y^2} = \frac{\partial p_e}{\partial R} = 0$$

$$\frac{\partial}{\partial R}\left(R v_R\right) + \frac{\partial v_\xi}{\partial \xi} + \frac{\partial}{\partial y}\left(R v_y\right) = 0$$

where the temperature and consequently the density have been assumed uniform through the sublayer and the acceleration terms in the momentum equations have been neglected. The momentum equations then give for the velocity profiles

$$v_R = v_{R_e}\left(\frac{y}{\delta_s}\right) ; \quad v_\xi = \beta y^2 + \left(\frac{v_{\xi_e} - \beta \delta_s^2}{\delta_s}\right) y$$

where

$$\beta = \frac{1}{\mu R}\frac{\partial p_e}{\partial \xi}$$

and δ_s is the sublayer thickness. The subscript e refers to conditions at the outer edge of the layer. As shown in figure 11b, the R-velocity profile is just Couette-like and the cross flow profile is Poussielle-like. Here the interface surface, because of its relatively low velocity, is being treated as a solid boundary and the effect of the mixing layer that forms along the interface has been neglected. The velocity gradient is discontinuous at the outer edge of the layer as a result of neglecting viscous effects in the outer layer. Physically, the outer layer acts locally like a solid wall driving the inner motion. The low momentum gas is dragged up the interface surface by the R-velocity of the inviscid flow while the layer is simultaneously thinned by the pressure gradient induced cross flow.

Integrating the continuity equation over the y coordinate gives

$$\frac{\partial}{\partial R}\left(v_{R_e} R\delta_s\right) + \frac{\partial}{\partial \xi}\left(v_{\xi_e}\delta_s - \frac{1}{3}\beta\delta_s^3\right) = 0 \ .$$

To esimate how quickly the thickness δ_s decays, a solution is sought near the symmetry plane $\left(v_{\xi_e} = 0, \frac{\partial \delta_s}{\partial \xi} = 0\right)$ where the equation for δ_s reduces to

$$\frac{d}{d\bar{r}}\left(\bar{r}\bar{\delta}\right) - \frac{\Omega}{\bar{r}}\bar{\delta}^3 = 0$$

where

$$\bar{\delta} = \delta_s/\delta_{s_o} \text{ and } \bar{r} = R/R_{s_o} \ .$$

Then taking $\bar{\delta} = 1$ when $\bar{r} = 1$ as approximate initial conditions

$$\bar{\delta} = \frac{1}{\bar{r}\sqrt{1 - \frac{2\Omega}{3}\left(1 - 1/\bar{r}^2\right)}}$$

where with $v_{R_e} = u_s \cos \omega_o$ and $\mu \propto T$

$$\Omega = \frac{1}{3}\tan \omega_o \mathrm{Re}_s\left(\frac{T_s}{T}\right)\delta_{s_o}\frac{d^2}{d\xi^2}\left(\frac{p_e}{\gamma_s p_s M_s^2}\right) \ .$$

T is the temperature in the sublayer taken to be a value near the peak temperature in the boundary layer. Typical order of magnitude estimates of the parameters involved for the shock layer of the vehicle considered in the altitude range of interest give

$$\frac{T_s}{T} \approx .2; \quad Re_s \approx 10^6/ft;$$

$$10^{-3} \lesssim \delta_{s_o} \lesssim 10^{-2} \text{ ft} .$$

Using the Newtonian pressure distribution near the symmetry plane, given analytically by the righthand side of equation (1), and performing the indicated differentiation,

$$\frac{d^2}{d\xi^2}\left(\frac{p_e}{\gamma_s p_s M_s^2}\right) = -2\left[\left(\frac{1-\epsilon^2}{\epsilon^2 \tan\omega_o}\right)^2 + \cos\omega_o\left(\frac{1-\epsilon^2}{\epsilon^2 \tan\omega_o}\right)\right] .$$

With the above order of magnitude estimates, the distance along the interface required to divert the sublayer $\left(\delta_s/\delta_{s_o} \approx 10^{-2}\right)$ is small $\left(R \lesssim 10\, R_{s_o}\right)$ for even a slight deviation of the interface from axial symmetry ($\epsilon \lesssim .95$). For a plume size which satisfies the initial assumption that it be an order of magnitude larger than δ_{s_o}, the sublayer will always be diverted. Since $N_e \propto \frac{1}{R}$ in the inviscid portion of the plume shock layer and the sublayer is completely diverted,

$$\frac{N_e}{N_{e_o}} \approx \left(1 - \frac{N_{e_{\delta_s}}}{N_{e_o}}\right)\frac{R_o}{R} \quad . \tag{3}$$

Here N_e is the integrated electron density through the plume shock layer, N_{e_o} is the initial integrated electron density through the boundary layer and $N_{e_{\delta_s}}$ is the integrated electron density through the sublayer. R_o is the distance along the interface surface at which the last streamline (convecting electrons from the boundary layer) enters the interface shock layer.

For given injection conditions, the shape of the conical portion of the interface and its ability to divert the boundary layer may be estimated. The resulting interface shape provides an important constraint on the injection conditions chosen, but another constraint enters into this choice. Downstream of the injection port the injected gas will continue to expand and the size of the plume will grow, but its shape will become less efficient for diverting

the boundar layer. To maximize the fraction of the boundary layer diverted, injection conditions must be chosen which make the size of the injection port as large as possible compared to the overall size of the plume. Using the approach first discussed by Zukoski and Spaid[11], an estimate of the overall plume size is made by use of the simple adiabatic quasi one-dimensional conservation equations

$$\frac{1}{2}\rho_s u_s^2 C_D A_c - p_s A_c = \rho_c u_c^2 A_c - \rho_j u_j^2 A_j \cos\alpha$$

$$\rho_c u_c A_c = \rho_j u_j A_j$$

$$c_p T_j + \frac{u_j^2}{2} = c_p T_c + \frac{u_c^2}{2}$$

The subscript c refers to conditions at the fully expanded plume cross section where $p_c = p_s$. The first equation conserves momentum in the streamwise direction, and C_D, the drag coefficient of the interface, is an expression of its efficiency to impart streamwise momentum to the injected gas. The second equation conserves mass and the last conserves total enthalpy. The area, A_c, is taken as a measure of the overall plume size and it is desired to make the ratio A_c/A_j as close to unity as possible. Then using this set of conservation equations the ratio $\frac{A_c p_{o_j}}{A_j p_s}$ is easily computed as a function of only α and M_j. The results are shown in figure 12 where $C_D \approx .2$ has been taken as an estimate of the interface drag coefficient (20° half angle cone-cylinder interface shape with base area A_c).

As can be seen from the curves of figure 12, the size of the injection port relative to the plume size is maximized by injection at the highest possible Mach number for a given stagnation pressure. However, as indicated by the family of interface shapes in figure 10, increasing the Mach number of the injected gas at fixed stagnation pressure decreases its dynamic pressure and hence the angle ω_o. To maintain $\omega_o \approx 20^\circ$, the limit set by electron production, $p_{o_j}/p_s \approx 100$ and $M_j \approx 2$ are required. A higher stagnation pressure increases the mass flow per unit area of the injection port and for a fixed mass flow makes its size smaller. For the present flow conditions in the shock layer $(M_s \approx 11.5)$ the choice of $p_{o_j}/p_s = 100$ and $M_j = 2$ represents an optimum in that A_c/A_j is minimized while maintaining $\omega_o \approx 20^\circ$. For these injection conditions $A_c/A_j \approx 2$ is the smallest value obtainable subject to the other imposed constraints. The interface shape corresponding to these injection conditions has $\epsilon \approx .8$.

Application of Model

These results are now applied to estimate the reduction of electron density which is possible for a given plume size. The boundary layer thickness on the cone at a station 30 inches from the nose is shown as a function of altitude in figure 13. Attention is centered on the turbulent boundary layer following transition when the boundary layer has maximum thickness. The mean electron density profile in turbulent boundary layers is not well understood and has never been measured directly, but figure 14 shows a typical mean integrated electron density profile in a turbulent boundary layer from a recent calculation by S. Glickler of AERL. A thickness δ_e is defined representing the portion of the boundary layer which must be diverted. A value of $\delta_e \approx .6\delta$ is obtained from figure 14.

In general, the required plume size can be governed by either the thickness δ_e or by the size of the antenna window. To estimate the mass flow required to create a significant reduction of integrated electron density, the thickness δ_e is the more important of the two sizes. Choosing as a reasonable size $h = 2\delta$, where h is the penetration height of the interface at the back edge of the injection port as shown in figure 15, the integrated electron density at that point on the interface may be estimated using Eq. (3) with the injection conditions identified in the previous discussion. The result is plotted in figure 16 as a function of δ_{s_o}/δ. The theoretical approximations which have been made assume $\delta_{s_o} \ll h$ so that the calculated value of N_e/N_{e_o} is accurate only for $\delta_{s_o}/\delta \lesssim .2$ $\left(\text{i.e. } \delta_{s_o}/h \lesssim .1\right)$. But from the dynamic pressure profile of figure 8, $\delta_{s_o} = .2\delta$ overestimates the momentum flux in the boundary layer (making it more difficult to divert), and so $N_e/N_{e_o} \approx .2$ must be taken as a conservative estimate of the reduction of electron density possible for a plume of the size considered. Clearly, if the theoretical result is believable for larger δ_{s_o}, the reduction of electron density can be an order of magnitude or more.

Details of the plume structure downstream of the injection port are difficult to estimate so that the size of the antenna window, i.e. the width w in figure 15, cannot be calculated precisely. An estimate of the size can be made by assuming the plume to be semi-circular in cross section. Then for a plume of the size being discussed, a simple computation gives $w \approx 8\delta$.

For an injection port of fixed size, for a fixed stagnation pressure, and for a given γ, $\dot{m} \propto \sqrt{\frac{m}{T_{o_j}}}$. So to create a plume of given size with minimum mass flow, the injected gas should have a low molecular weight and a high stagnation temperature. An upper limit on the temperature is determined by the onset of ionization of the injected gas. Hydrazine decomposition[12] $\sqrt{\frac{m}{T_{o_j}}} \approx .1$

can provide such a gas source which should be suitable for flight application. For an injection port of the size discussed above and with $\delta \approx .5$ cm, the mass flow as a function of altitude, maintaining a constant plume size, with a hydrazine gas source is shown in figure 17. For continuous operation from 120 kft to 60 kft, approximately 7.5 lbm of hydrazine is required.

Since mixing occurs along the plume interface, the use of SF_6 or another chemical alleviant as the injectant would permit electron attachment in the mixing layer. The mass flow of SF_6 which would be required for a plume of the same size calculated for hydrazine injection is also shown in figure 17 where the SF_6 at reservoir conditions is assumed to be in the vapor phase at a temperature of 300° K. Due to its high molecular weight ($\mathcal{M} = 146$) and low stagnation temperature the mass flow of SF_6 required is 7 times that of hydrazine. Furthermore, the vapor pressure of SF_6 at 300° K is approximately 20 atm, which is less than that required for the injection technique described for shock layer pressures above .2 atm (below 90 kft). Therefore the use of SF_6 does not seem feasible and the same is true of other frequently discussed alleviants such as water and various fluorocarbons.

Summary

The concept of aerodynamically diverting a high electron density boundary layer around an antenna window by the use of a plume of injected gas has been investigated. Electron production in the plume shock layer provides a severe constraint on the plume shapes which can be considered. The conical injection technique discussed should prevent electron production while efficiently diverting the boundary layer.

An approximate analysis to determine the fraction of the boundary layer diverted for a given plume size and injection conditions has been developed. The results show that for the vehicle and reentry conditions considered, a mass flow on the order of 200 grams/sec at 100 kft can provide at least a factor of 5 reduction in integrated electron density above the antenna window. This estimate was noted to be conservative, and perhaps an order of magnitude or more is a realistic estimate of the electron density reduction which can be achieved for this mass flow.

A hydrazine gas source was chosen since it gives reasonable mass flows for a given plume size and should be compatible with flight vehicle systems requirements. For continuous operation between 120 kft and 60 kft approximately 8 lbs of hydrazine would be consumed.

CONCLUDING REMARKS

Future research in chemical alleviation should improve existing knowledge of the rate constants involved. In particular, high temperature, low pressure

attachment rates and SF_6 decomposition rates should be measured. Our work with the aerodynamic technique has been an attempt to construct a simple model to describe a highly complex flowfield. Further research of an experimental nature is clearly needed to confirm the effectiveness of the technique.

REFERENCES

1. J. F. Bott and T. A. Jacobs, J. Chem. Phys. 50, 3850 (1969).

2. G. Emanuel, "Table of the Kassel Integral", The Aerospace Corp., Jan. 1969. TR-0200 (4240-20)-5.

3. S. Kurzius and F. Raab, "Vaporization and Decomposition Kinetics of Candidate Re-entry Blackout Suppressants in Low-Pressure Flames", Aerochem Research Lab., Inc., Aug. 1968, TP-181.

4. Mahan and Young, J. Chem. Phys. 44, 2192 (1966).

5. Chen, George, and Wentworth, J. Chem. Phys. 49, 1973 (1968).

6. F. C. Fehsenfeld, J. Chem. Phys. 53, 2000 (1970).

7. Biondi and Fox, Phys. Rev. 109, 2005, 2008, 2012 (1958).

8. Michels, J. Chem. Phys. 48, 2821 (1968).

9. R. Vaglio-Laurin and G. Miller, "On Three Dimensional Laminar Boundary Layers with Large Cross Flow", AIAA Paper 69-710 (1969).

10. W. D. Hayes and R. F. Probstein, "Hypersonic Flow Theory", Academic Press, New York (1966).

11. E. E. Zukoski and P. W. Spaid, "Secondary Injection of Gases into a Supersonic Flow", AIAA Journal, Vol. 2, No. 10 (1964).

12. G. P. Sutton, "Rocket Propulsion Elements", Wiley, New York (1956).

TABLE 1

CHEMICAL PROCESSES FOR SF_6 ALLEVIATION

I. Thermal Decomposition[1-3]

$$SF_6 \xrightarrow{M} SF_5 + F$$

a) Bott and Jacobs $1600 \lesssim T \lesssim 2050^\circ$ K; $0.13 \leq p \leq 30$ atm.

Data fit to RRK theory:

$$k_d(RRK) = A\, e^{-E^*/RT} I\left(S,\ E^*,\ A/\lambda T^{1/2}(M)\right)$$

where I is the Kassel integral (see ref. G. Emanuel)

$S = 6$, $\lambda = 0.25$, $A = 9 \times 10^{12}$ sec^{-1}, $E^* = 75.9$ kcal/mole

b) Kurzius and Raab $T \approx 2500^\circ$ K; $10 \leq p \leq 40$ torr

$$k_d(K) = 3 \times 10^{-10}\, e^{-35{,}200/T}$$

c) Note: possible competition by H attack

II. Electron Attachment[4-6]

		$T = 300^\circ$ K	$T \approx 3000 - 6000^\circ$ K
$e + SF_6 \rightarrow$	SF_6^-	$k_6 = 2 \times 10^{-7}$	$\sim 10^{-8}$
	SF_5^-	$k_5 = 2 \times 10^{-11}$	$\sim 10^{-8}$
	F^-	k_1 not observable	$\sim 10^{-8}$

III. Electron Detachment[7-8]

$$F^- + M \rightarrow F + M + e;\ k_{F^-M} = 6 \times 10^{-11} \exp(-40{,}000/T)$$

$$F^- + F \rightarrow F_2 + e;\ k_{F^-F} = 1.3 \times 10^{-19}\, T^2\, e^{-21{,}114/T}$$

Note: possible competition by H

$$H + F^- \rightarrow HF + e;\ k_{F^-H} = 10^{-9}$$

IV. Ionization and Neutralization

$$N + O \rightarrow NO^+ + e;\ k_i = 3.2 \times 10^{-12}\, e^{-31{,}900/T}$$

$$F^- + NO^+ \rightarrow F + NO;\ k_{F^-\,NO^+} = 10^{-7}$$

TABLE 2

PROPERTIES AT T_{peak} IN BOUNDARY LAYER

alt (kft)	(M) (#/cc)	(e) (#/cc)	(O) (#/cc)	(N) (#/cc)	p (atm)	T (^{o}K)
160	1.9^{16}	8.9^{9}	3.8^{13}	1.1^{11}	.013	5000
130	7.2^{16}	2.3^{10}	2.9^{14}	7.2^{11}	.05	4750
100	3.3^{17}	1.0^{11}	5.0^{15}	6.6^{12}	.185	4190
70	9.2^{17}	5.9^{13}	4.2^{16}	9.0^{16}	.70	(5600) ?
40	2.3^{18}	1.2^{14}	6.5^{16}	1.7^{17}	1.78	(5700) ?

alt (kft)	$\dot{m}_A$ (lbs/ft^2-sec)	$\dot{m}_A/\dot{m}_{BL}$	(H) (#/cc)	(C) (#/cc)	(CO) (#/cc)
160	4.7^{-3}	1.0^{-2}	1.9^{14}		
130	9.1^{-3}	1.2^{-2}	8.6^{14}		
100	1.7^{-2}	1.6^{-2}	5.3^{15}		
70			7.7^{16}	1.4^{16}	2.4^{17}
40			2.1^{17}	3.7^{16}	6.4^{17}

$(SF_6) \equiv 0.01$ (M) at all altitudes

[A number in the exponent position represents multiplication by that power of 10; for example, $1.9^{16} = 1.9 \times 10^{16}$.]

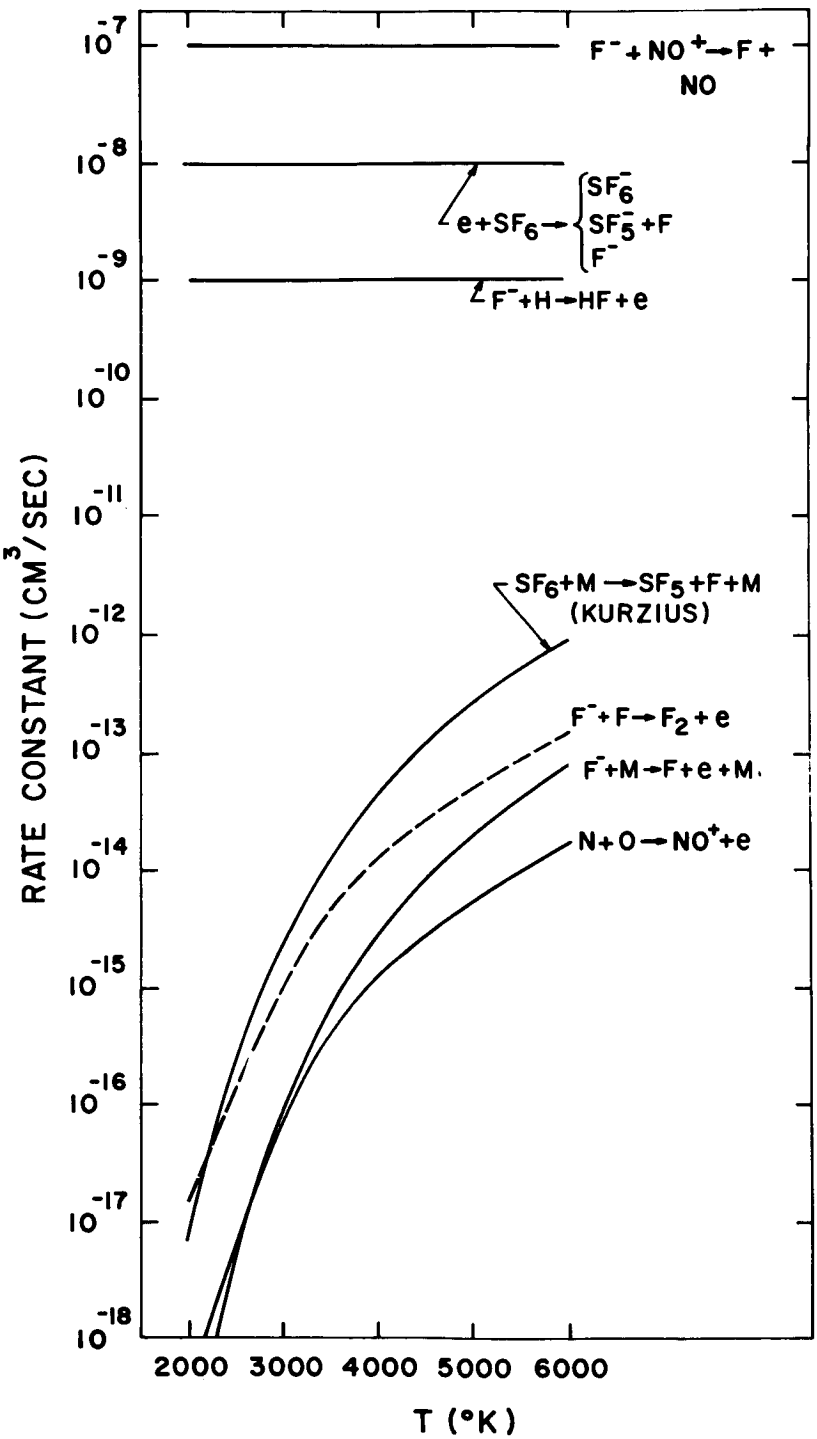

Fig. 1 Chemical rate constants for important processes in SF_6 alleviation.

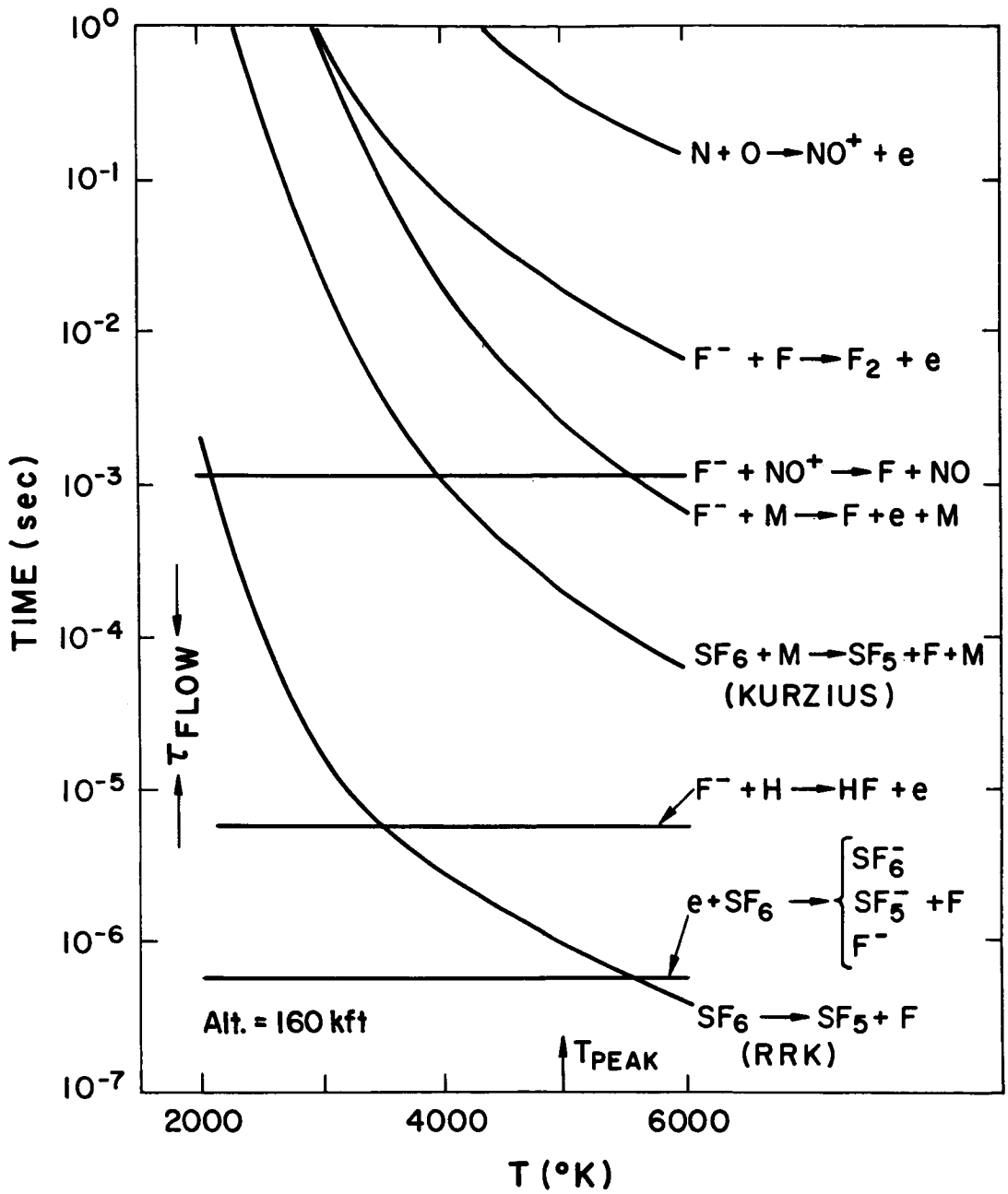

Fig. 2 Chemical relaxation times as a function of temperature for concentrations at 160 kft.

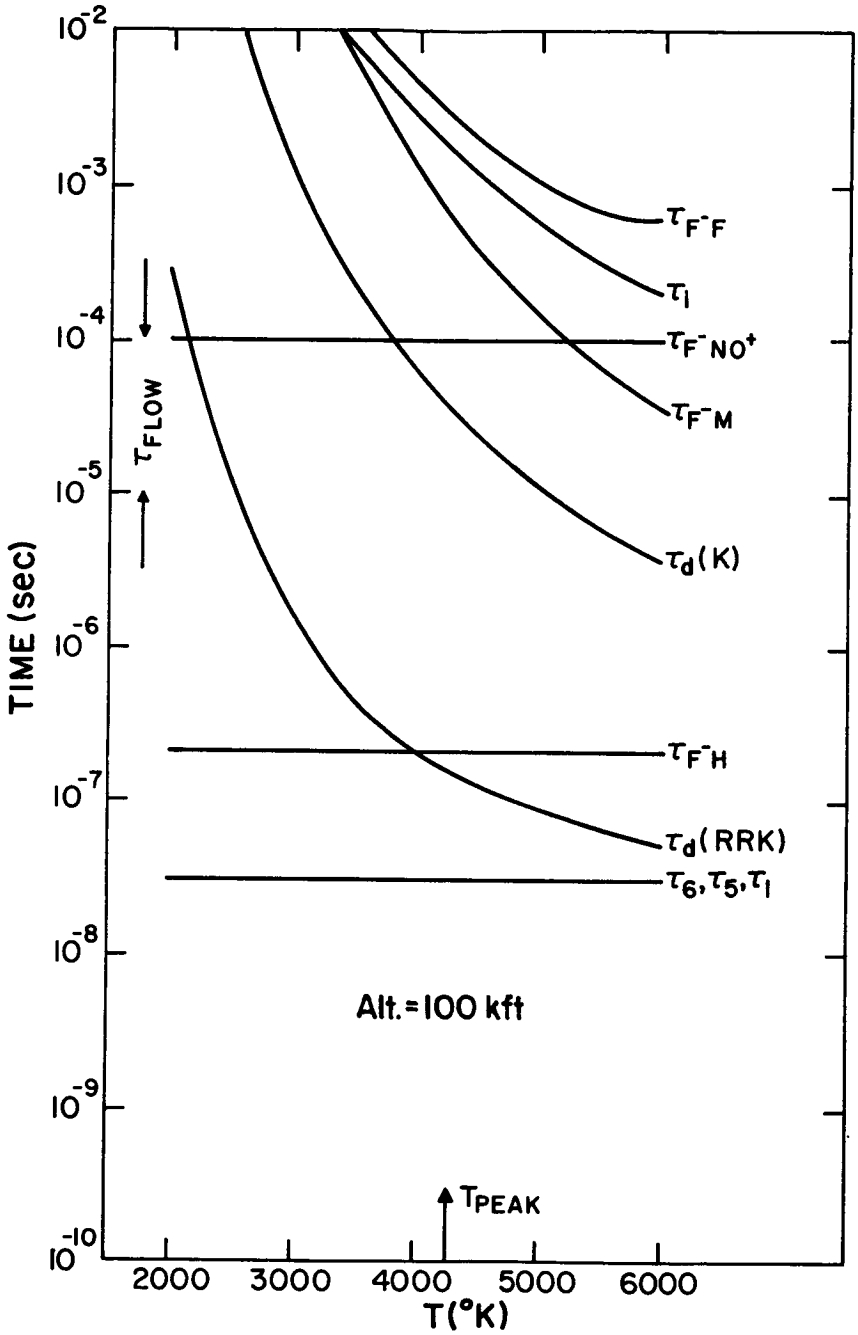

Fig. 3 Chemical relaxation times as a function of temperature for concentrations at 100 kft.

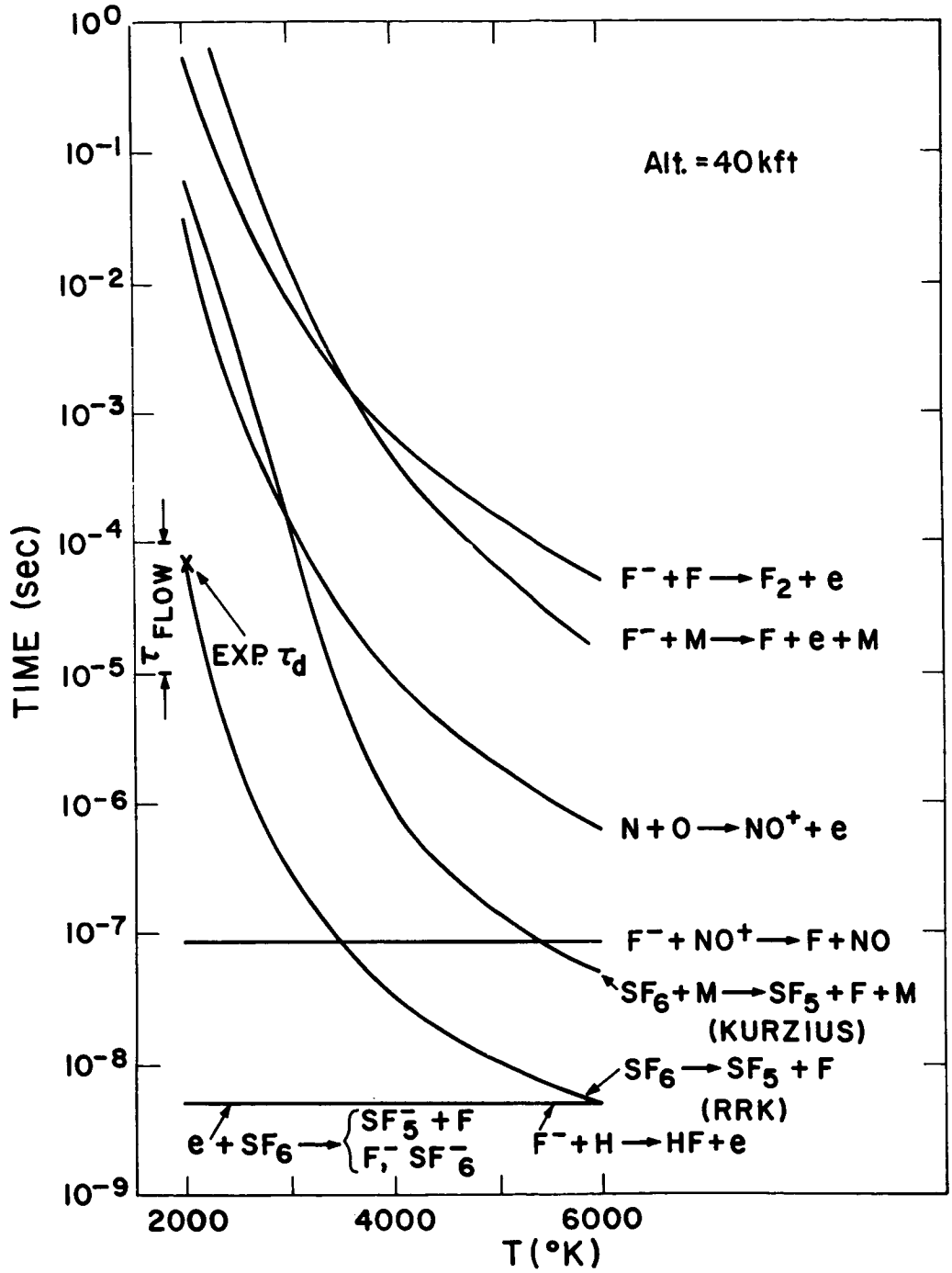

Fig. 4 Chemical relaxation times as a function of temperature for concentrations at 40 kft.

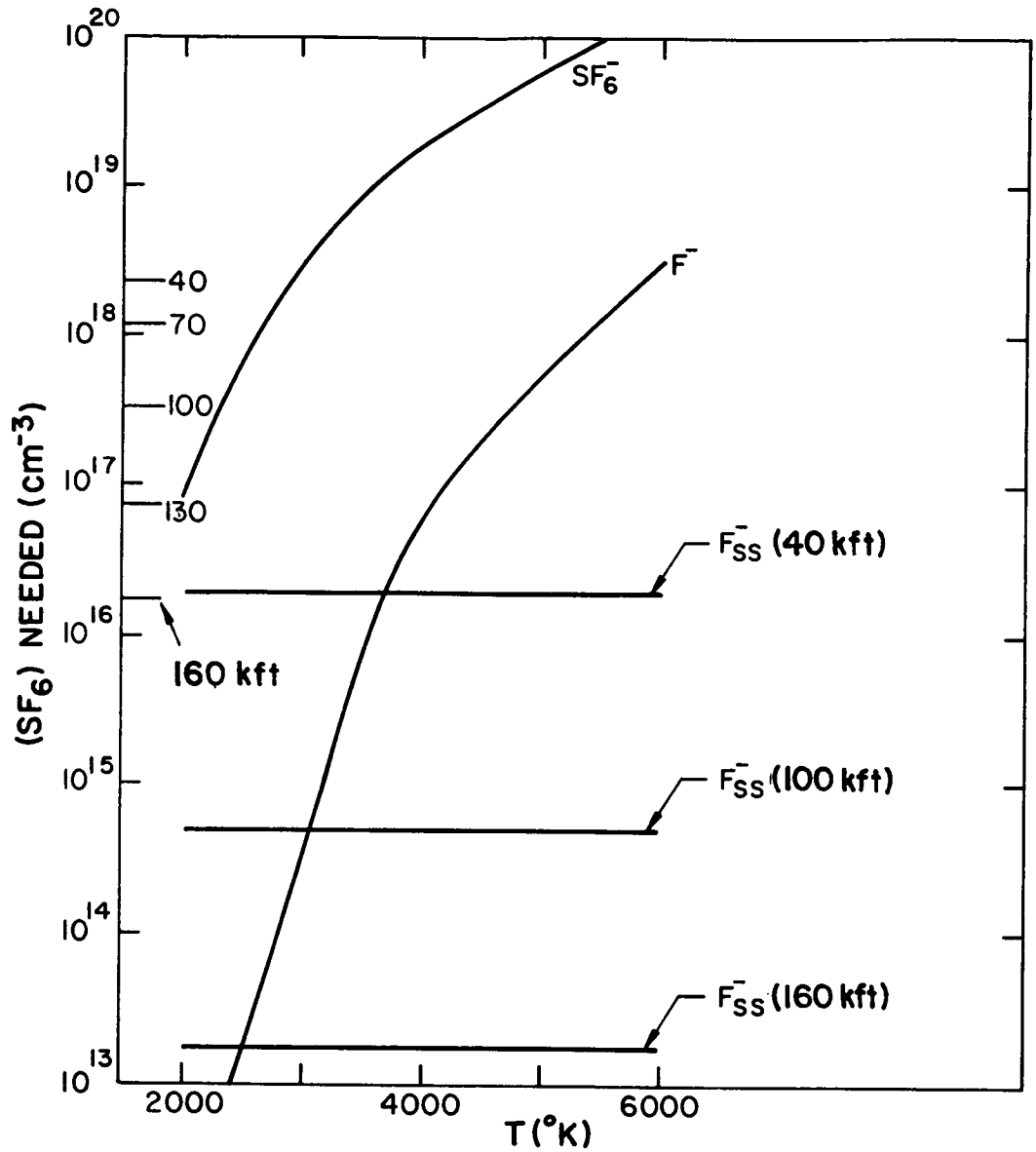

Fig. 5 SF_6^- curve - SF_6 needed to survive to accomplish onset of electron reduction assuming $e + SF_6 \rightleftharpoons SF_6^-$.

F^- curve - SF_6 needed to be converted into F^- to accomplish onset of electron reduction assuming $e + F \rightleftharpoons F^-$.

F_{ss}^- curves - SF_6 needed to be converted into F^- to accomplish onset of electron reduction assuming $F^- + H \rightarrow HF + e$ as major detachment mechanism.

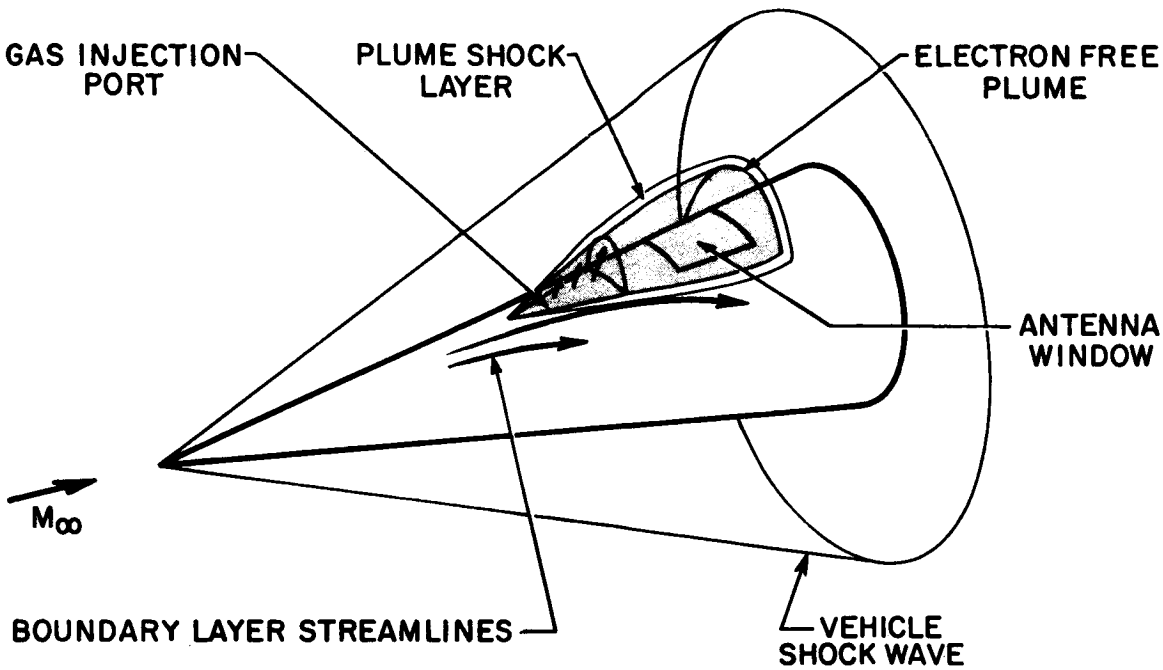

Fig. 6 Schematic of aerodynamic alleviation concept.

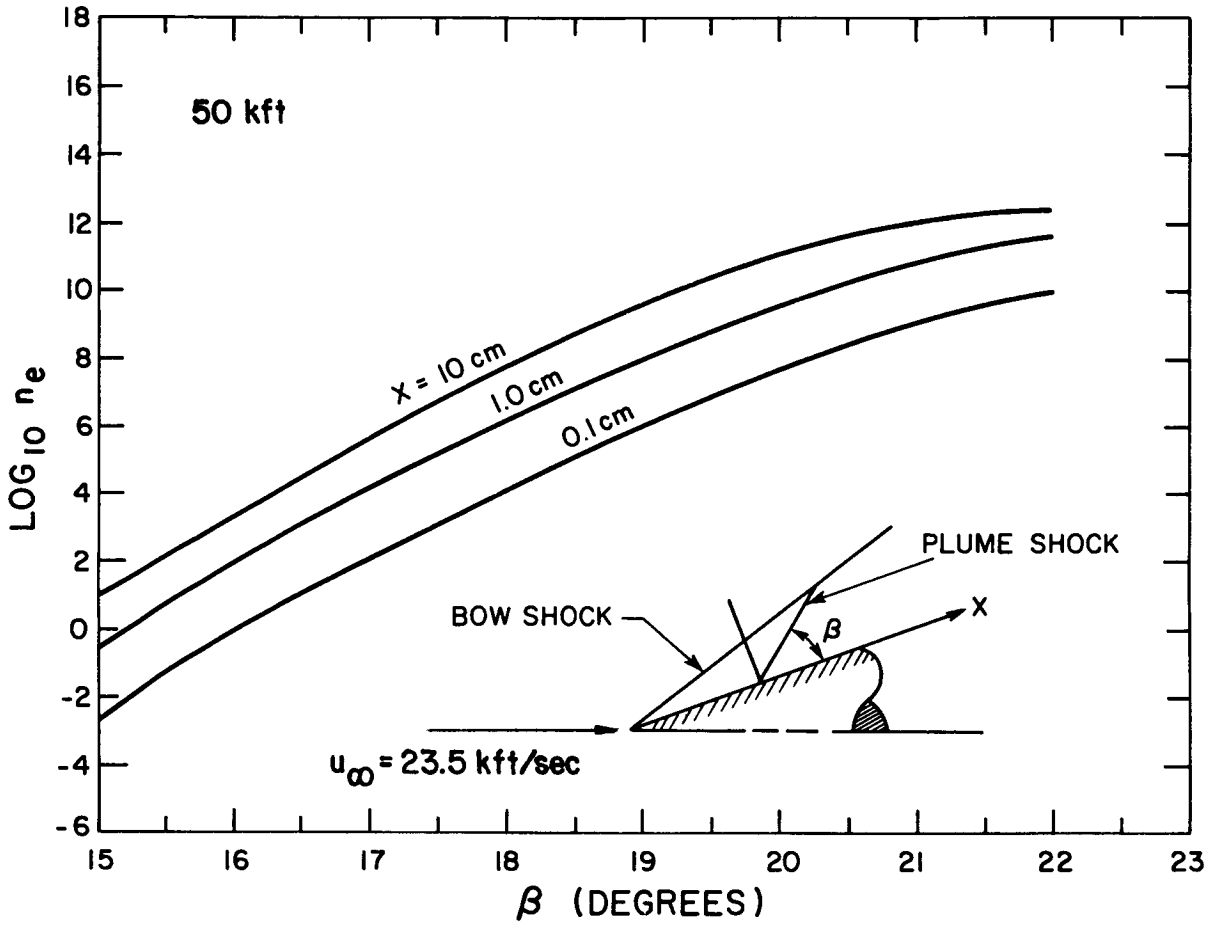

Fig. 7 Electron density due to plume shock.

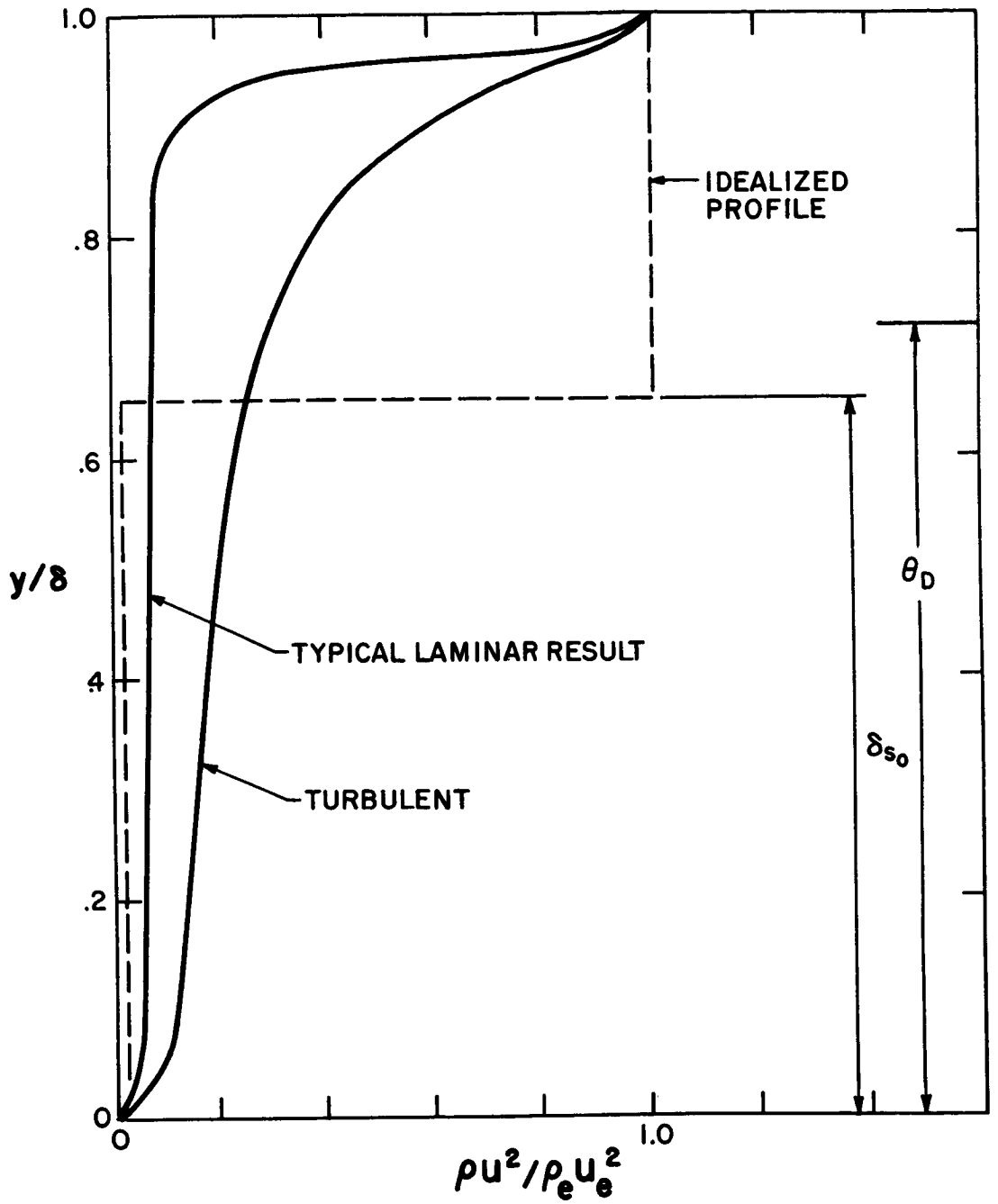

Fig. 8 Boundary layer dynamic pressure profiles.

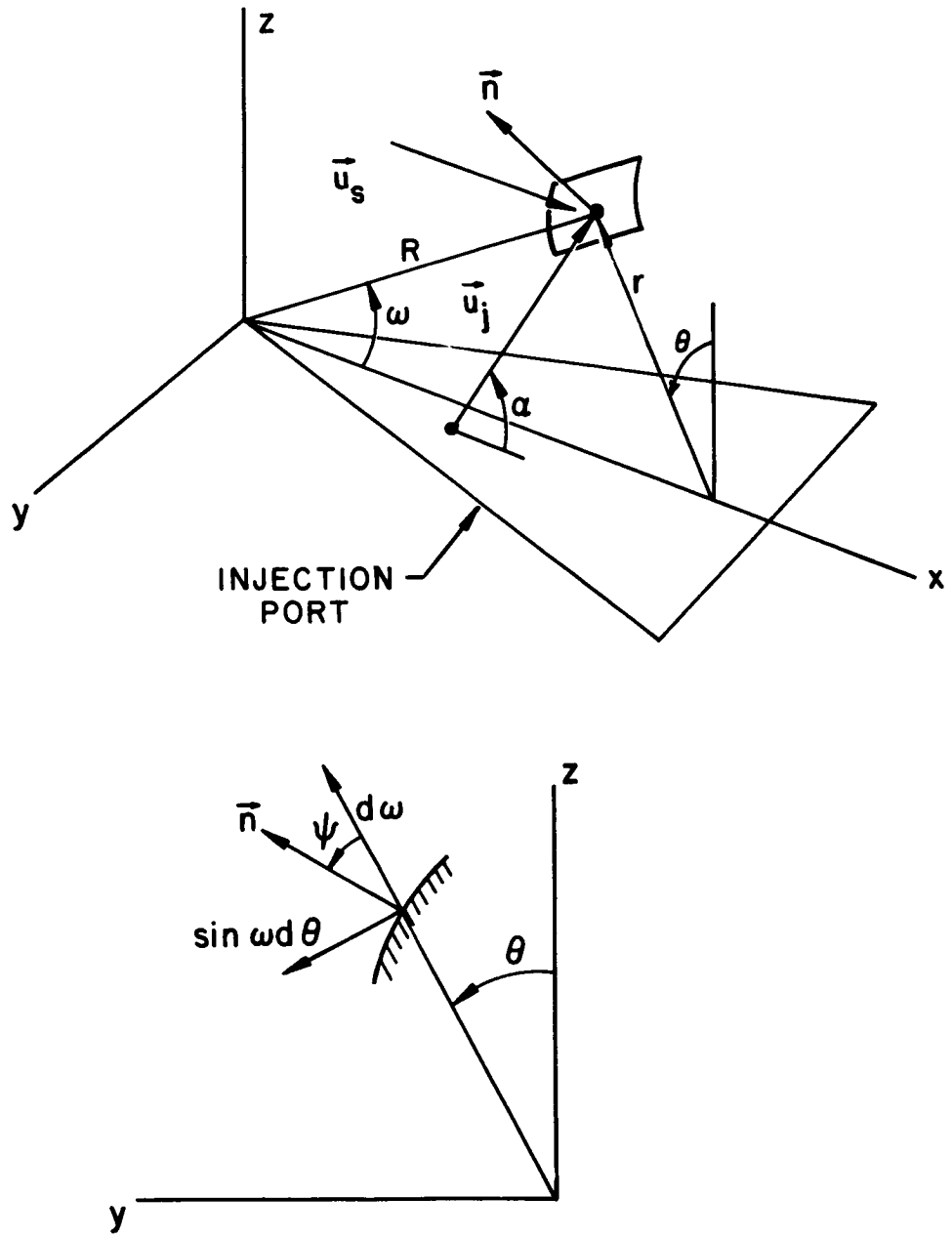

Fig. 9 Coordinate system for conical interface.

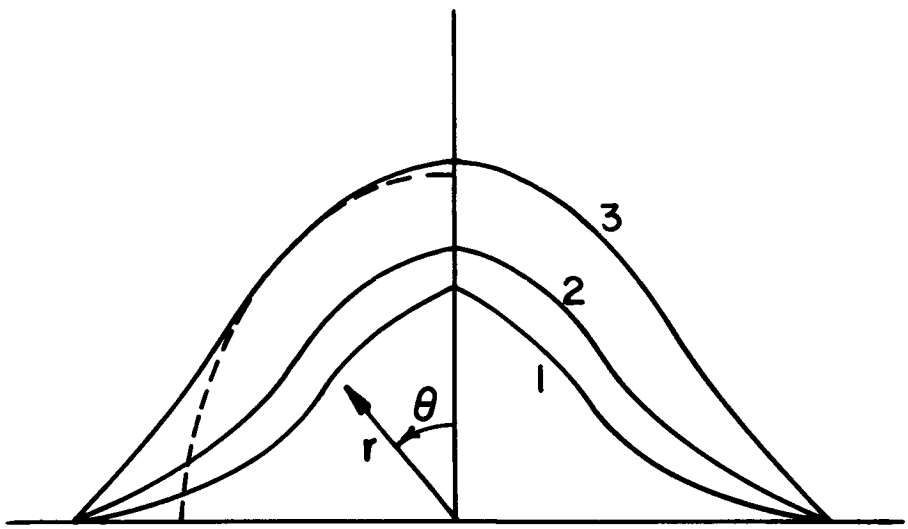

$p_{o_j}/p_s = 100$ $\omega_s = 20°$

	M_j	α	C_p	Λ
1	3.0	55°	.0092	.160
2	2.5	50°	.0240	.225
3	2.0	45°	.0650	.330

Fig. 10 Newtonian estimate of interface shape.

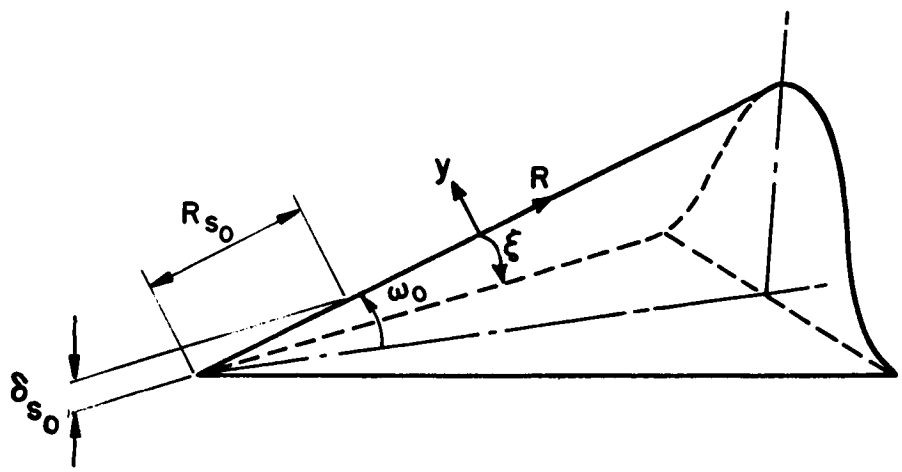

Fig. 11a Boundary layer coordinates on interface surface.

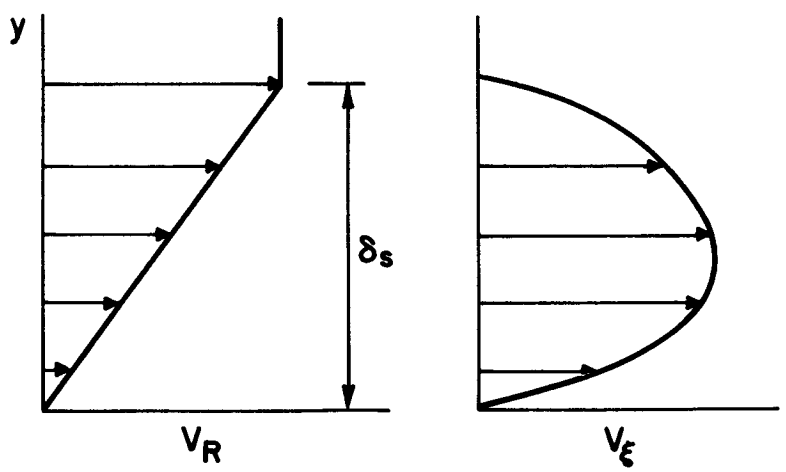

Fig. 11b Sublayer velocity profiles.

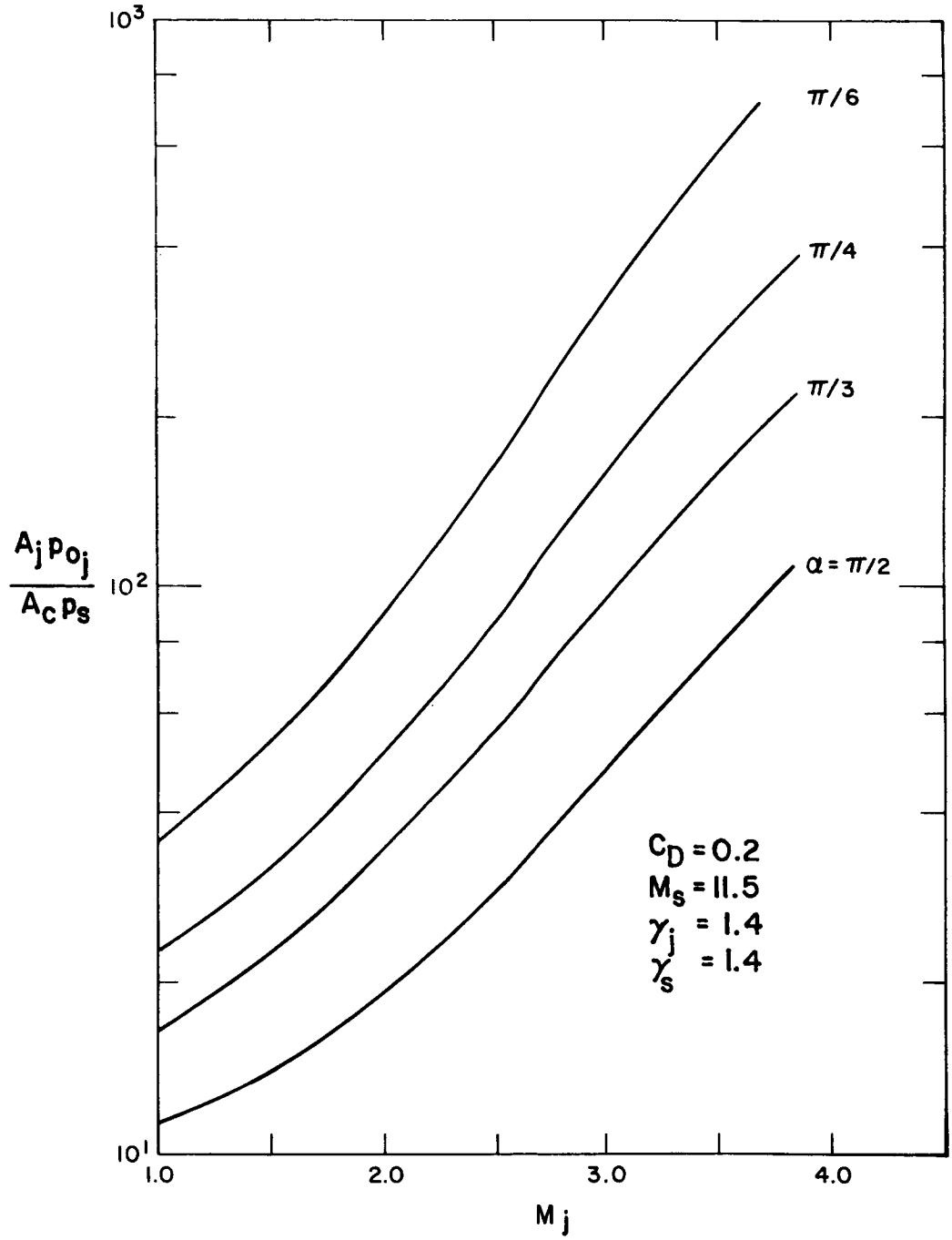

Fig. 12 Parameters for calculation of plume size.

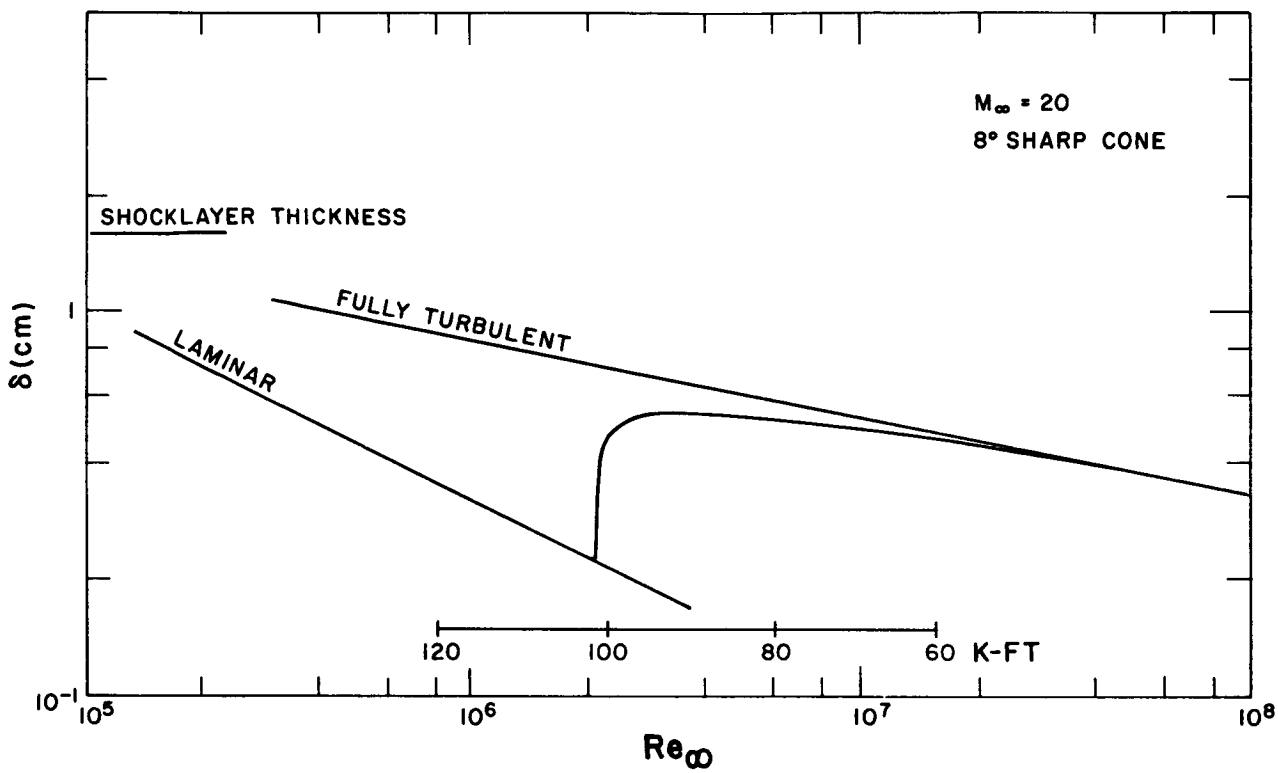

Fig. 13 Boundary layer thickness at antenna window.

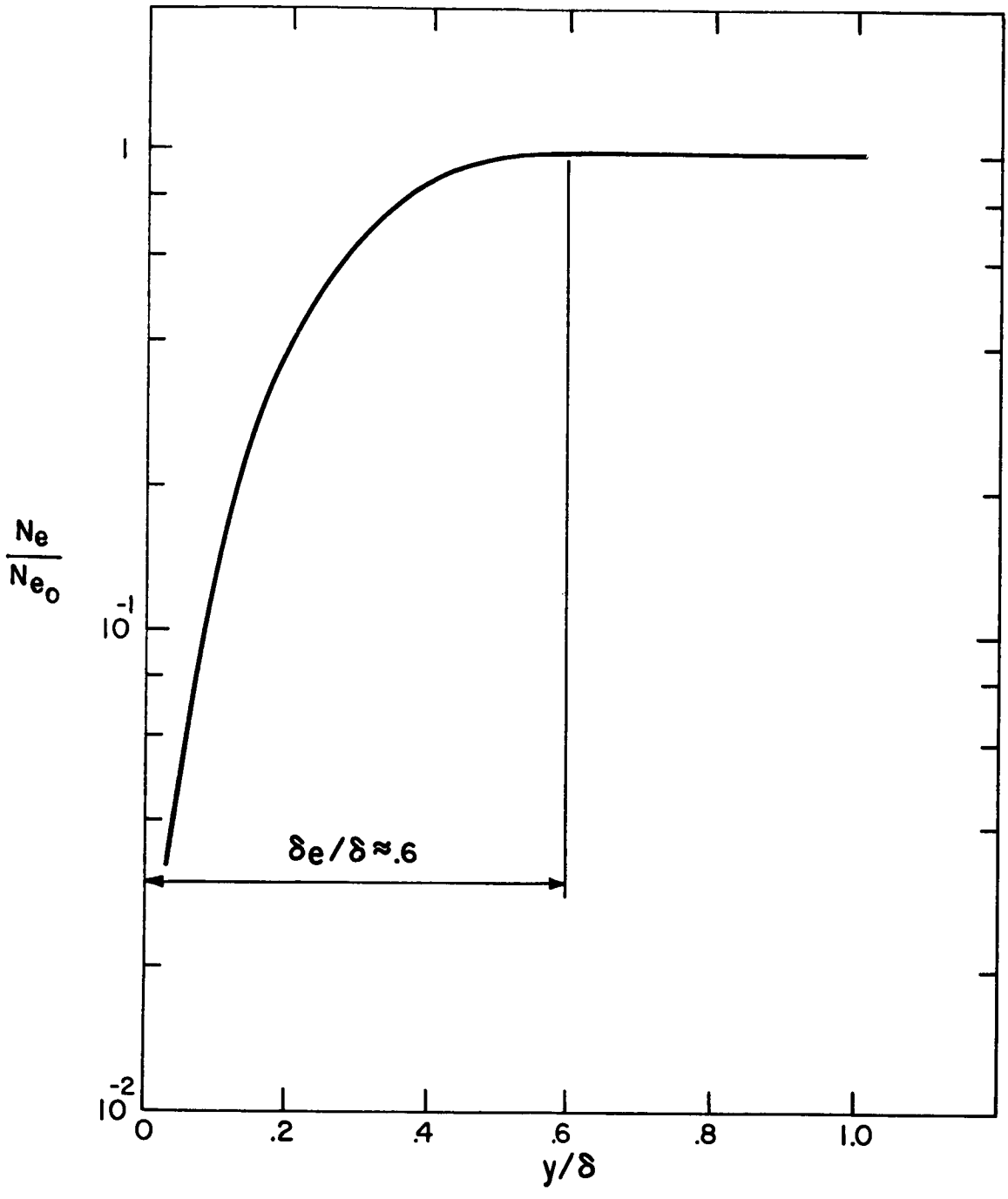

Fig. 14 Typical integrated electron density profile in turbulent boundary layer.

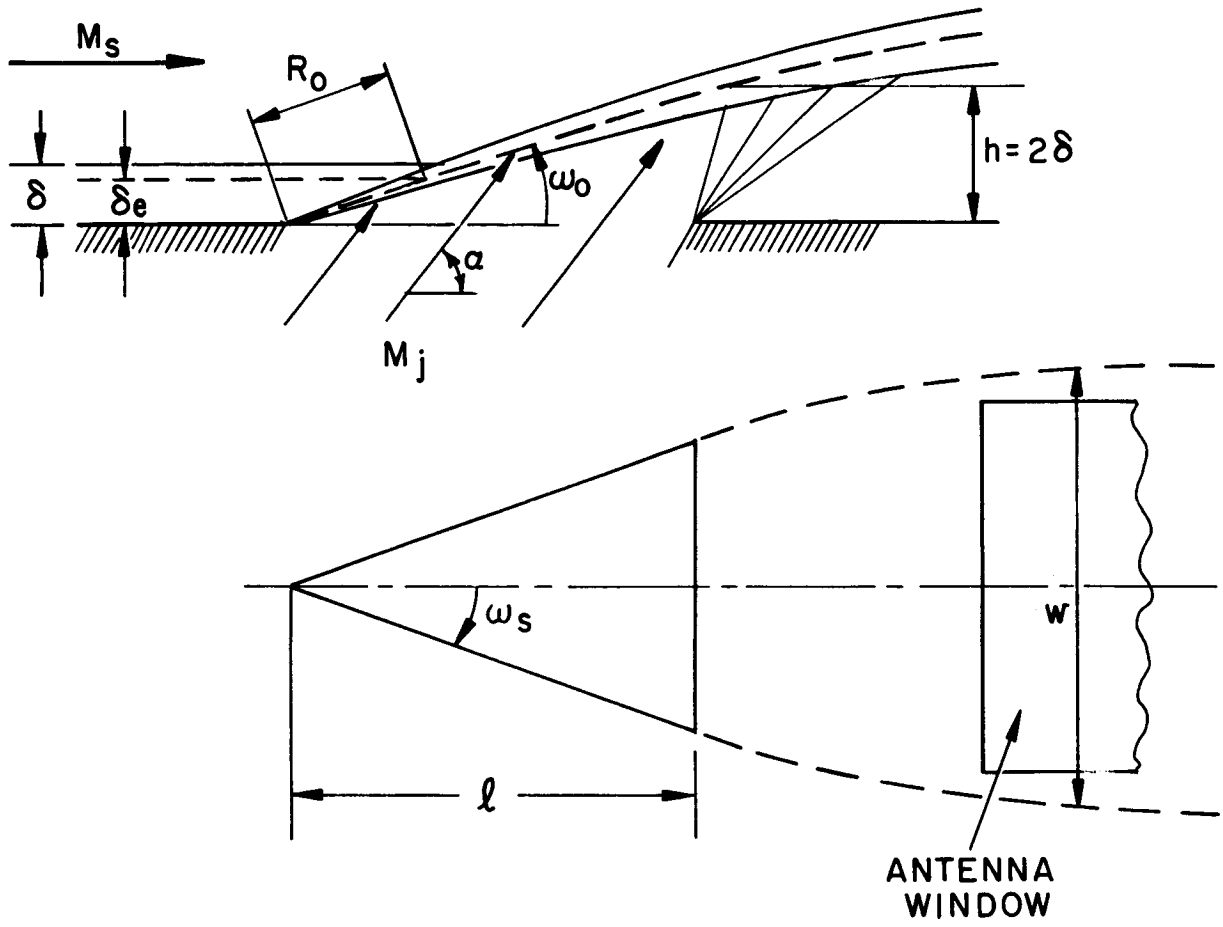

Fig. 15 Size of injection port chosen to accomplish integrated electron density reduction.

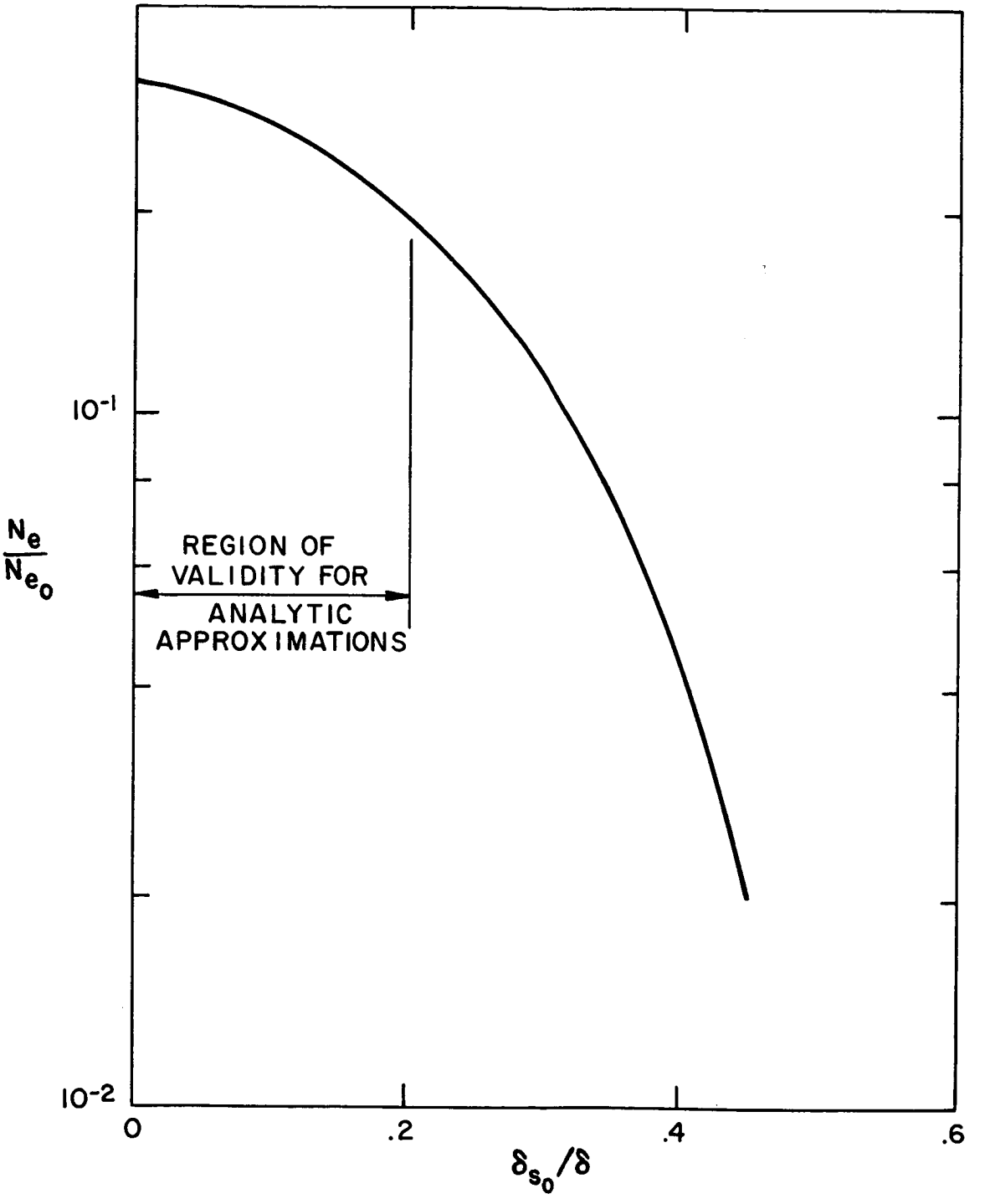

Fig. 16 Reduction of integrated electron density.

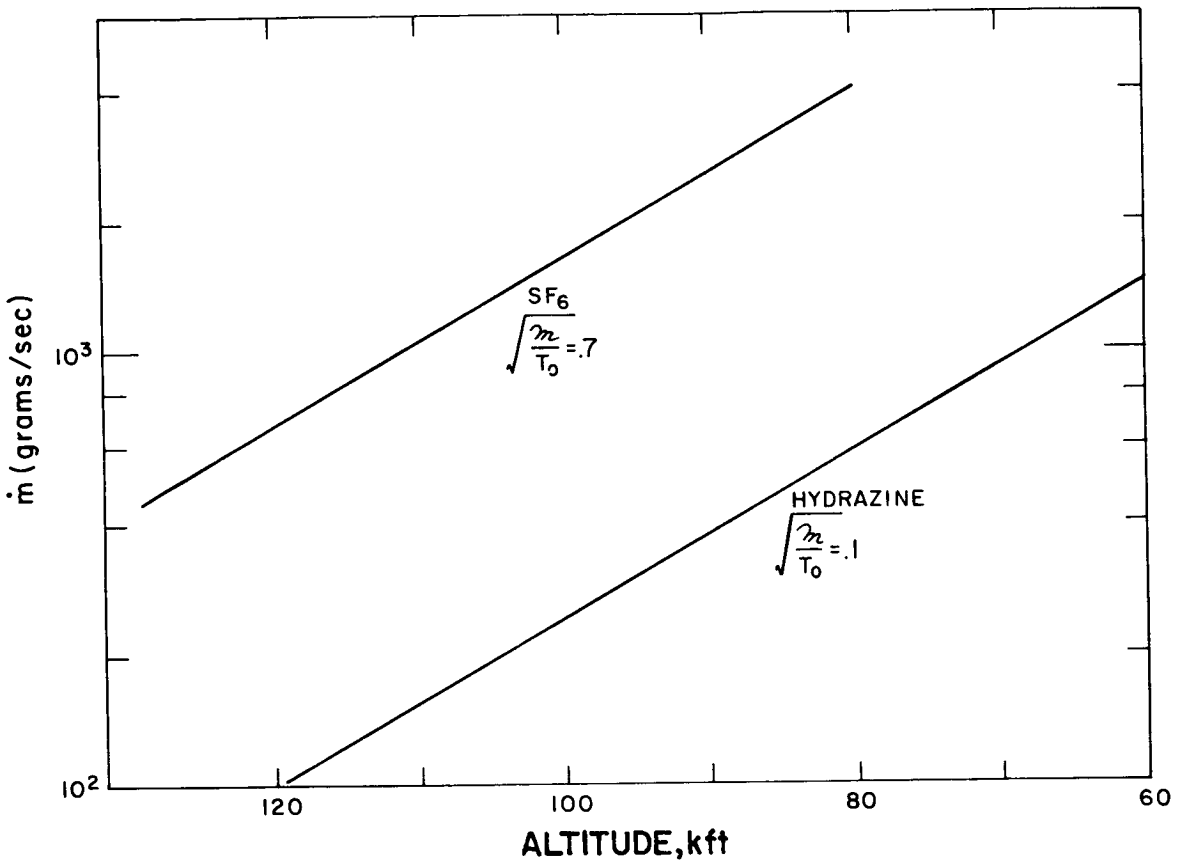

Fig. 17 Mass flow required to achieve integrated electron density reduction.

THE REMOVAL OF FREE ELECTRONS IN A THERMAL PLASMA BY MEANS OF RAPIDLY EVAPORATING LIQUID ADDITIVES*

By Sol Aisenberg and Pung Nien Hu

Space Sciences Incorporated
Waltham, Massachusetts

INTRODUCTION

This paper describes a study of various mechanisms whereby different additives and additive processes increase the microwave transmission through the plasma sheath. A comparison is made of the role of the relative effectiveness of various gaseous and liquid additives in reducing the free-electron concentration and in enhancing the microwave transmission through the plasma sheath. Based upon an interpretation of the results that have been obtained so far, a number of techniques have been postulated as being important for increasing the effectiveness of chemical additives for use in the plasma sheath.

In particular, it has been found that additives when introduced into the plasma in the form of rapidly evaporating droplets (and of liquids with low boiling points) appear to be much more effective in increasing the microwave transmission than additives introduced in the vapor form or introduced in a slowly vaporizing liquid droplet form. As a result of this observation, it is postulated that the vaporization itself of the additive can be an extremely important process in the plasma-sheath modification.

DISCUSSION

It has been found that different additives when put into an argon thermal plasma produced the following results:

(1) Some liquid additives are better than the best gaseous additives studied.

(2) The effectiveness of the additive is increased by aspirating it into the plasma with a carrier gas (such as argon) which is used to break the liquid additive into the form of small droplets.

(3) The lower the boiling point of the liquid additive, the more effective the additive appears to be in reducing the microwave transmission loss.

*The research reported herein was sponsored by the Air Force Cambridge Research Laboratories, Office of Aerospace Research, under Contract No. F19628-68-C-0127.

(4) Additives with very high boiling points such as silicone oils are less effective in spite of their ability to survive plasma heating for longer times.

(5) Additives such as SF_6 that are introduced in the already gaseous form are not as effective as the rapidly evaporating additives.

(6) There appears to be no correlation between only the cooling effect of different liquid additives (such as H_2O and CCl_4) and the measured effectiveness.

(7) The effectiveness of an additive appears to be directly related to the presence of the evaporation process of the additives and does not appear to be related strongly to the presence of the droplet alone or to the presence of the vapor alone.

One mechanism that could explain the improved effectiveness of rapidly evaporating droplets is the possibility that these droplets are evaporating in large part as negatively charged molecules. This can be explained by the following process: Droplets in a plasma will rapidly become negatively charged through the collection of electrons. Because of the lower electron mass, the random electron current density is orders of magnitude larger than the random positive-ion current density. As a result, the electron current to a surface is larger than the ion current to the same surface so that the surface charges negatively and thereby reduces the electron current until it is equal to the ion current. This negative charge on the droplet reduces the rate of removal of free electrons from the plasma until it is equal to the much lower rate of removal of positive ions. Because of the small size of the droplet, the electric field at the surface of the droplet can be very large and can result in the subsequent evaporation of the droplet molecules with a negative charge attached. (It is easier for a negatively charged molecule to evaporate from a negatively charged droplet than for a neutral to evaporate from this same droplet, since in the former case the system terminates in a lower energy state.) This negative-ion evaporation would explain why the vaporization process itself seems to augment the rate of removal of free electrons from the plasma. In addition, it would explain why droplets introduced by aspiration are more effective: since the resulting droplets are smaller, there are more droplets per unit mass of additive, and the electric field associated with a smaller droplet is larger.

Some results are shown in figure 1 where the transmitted microwave power ratio is plotted as a function of additive mass fraction (that is, the weight per unit time of the additive relative to the weight per unit time of the argon gas introduced into the plasma torch producing the thermal plasma).

Of the liquid additives studied, the following four have been found to be most effective and much more effective than water or SF_6:

(1) Freon C-51-12 (DuPont) (Liquid A)

(2) Trichloroethylene (Liquid B)

(3) Carbon tetrachloride (Liquid C)

(4) Freon 113 (Liquid D)

These additives were measured in their most effective form by using argon carrier gas to introduce the additive droplets in the form of finely aspirated droplets, rather than as larger droplets. It was found that the use of the aspiration injection of the additive significantly increased the effectiveness of the additive, presumably because of the smaller droplet sizes. This is shown in figure 2 where measurements are shown for one of the more effective additives, C-51-12. The results show the average transmission without the aspiration compared with the average transmission with the aspiration. The unusual behavior of the additive at very low flow rates and when a carrier gas is not used is related to the intermittent flow of additives at the very low rates.

There is an apparent correlation between the volatility of the additive and its effectiveness for increasing microwave transmission. It appears that the more volatile the liquid droplet additives are, the more effective they are in increasing the microwave power transmission for the same relative mass fraction of additive. The lower the boiling point of the additive, the more readily the material will vaporize. Associated with the low boiling point is a higher vapor pressure and also a lower latent heat of vaporization. Thus, the additive liquid with the lower boiling point will vaporize more molecules per unit time in the same plasma than a liquid with a higher boiling point. The survival time of droplets with a lower boiling point will be shorter than for the case of higher boiling point materials. However, for droplets of reasonable size and reasonable transit times, the survival time in general will be longer than the transit time. The present measurements were taken under conditions at which the transit time from the torch to the diagnostic microwave system was about 25 to 50 microseconds, which is relatively short compared with the droplet survival time. The additives in the liquid form will survive longer before thermal dissociation than additives in the gaseous form. Thus a much larger fraction of the liquid additive molecules can form negative ions than for the case of gaseous molecules.

The relative effectiveness of the different additives does not appear to be primarily related to the additional plasma cooling by the rapidly vaporizing droplets. There are several reasons for this conclusion. First, calculation of the electron removal rate by a plasma that has been only cooled shows that the characteristic time for electron loss by recombination, by normal attachment, and by diffusion, is relatively long compared with the time allowed by the transit of the plasma past the microwave antenna. It is only through a mechanism such as enhanced attachment that the electron density can decrease as much as is permitted by plasma cooling. Cooling alone is not sufficient to supply electron density reductions as rapidly as is required by the transit-time limitations. Second, a calculation of the heat per unit mass absorbed by vaporization indicates that the cooling by water is slightly more effective than the cooling by carbon tetrachloride. The measured plasma modification effectiveness shows that water, on the other hand, is much less effective than carbon tetrachloride and similar materials. This is at variance with what would be expected on the basis of the relative ability to cool the plasma alone.

It is postulated that the reason carbon tetrachloride (and similar volatile materials) is more effective than water (assuming that the droplets introduced are about the same size distribution for both liquids) is that the latent heat of vaporization (and the boiling point) of carbon tetrachloride is less than that of water, and therefore for a given energy flux from the plasma, many more carbon tetrachloride molecules will evaporate from a carbon tetrachloride droplet than water molecules can evaporate from a water droplet. Therefore, the carbon tetrachloride additive will vaporize more rapidly, will supply many more vaporizing molecules, and at the same time will survive long enough compared with the transit time so that its existence as a droplet is not jeopardized.

The mechanism for the removal of free electrons from the plasma is postulated to operate as follows: A vaporizing droplet in the plasma rapidly collects electrons because of the much larger random electron current. The droplet therefore quickly acquires a negative charge and a large local electric field. As a result of this negative charge and the local electric field, the molecules can vaporize as negatively charged molecules, thus removing part of the droplet charge and making it able to collect additional electrons from the plasma. Therefore, electrons striking the vaporizing droplet can leave in the form of a negative molecule. The surface thus acts as a catalytic surface to convert free electrons into negative molecules. Introducing the droplets by aspiration to break the additive liquid into a larger number of smaller droplets increases the effectiveness of the additive because (1) there are more droplets per unit mass introduced, (2) there is more surface area per unit mass introduced, and (3) the electric field at the surface of the smaller droplet is larger. A negatively charged molecule vaporizing from a negatively charged droplet leaves the system in a lower energy state and therefore energetically it is more likely that a negatively charged molecule will vaporize than an uncharged molecule.

SUMMARY

The removal of electrons from the plasma by means of vaporization cooling by liquid additives is not expected to be important because of the frozen flow limitations. The decay of electron density to a lower value characteristic of a lower thermal equilibrium temperature is not sufficiently fast if it depends upon normal attachment, recombination, and diffusion. When additives in the form of liquid droplets are introduced into the plasma, it is found that the rate of removal of free electrons is much faster than when additives in the vapor form are introduced into the plasma. This corresponds to the situation in which free electrons impinge on the droplet surface and then leave the droplet in the form of negative molecules. The negative ions vaporizing from the droplet surface are usually stabilized by collisions among the molecules of the additive liquid and hence should be more resistant to electron detachment than those formed in the gaseous phase and which exist at a high energy level.

If the vaporization rate from a droplet is less than the electron arrival rate, then the electrons accumulate on the droplet and charge it negatively with a resultant reduction of subsequent electron collection. The rate of

conversion of free electrons into negative molecules is then limited by the slower of the two processes of electron collection and molecular evaporation. Thus, in the case where the vapor pressure is low (and the boiling point is high), the negative-ion formation is limited by the vaporization of the liquid additive droplet because the vaporization number rate from the droplet is less than the electron collection rate. An improvement in the effectiveness of liquid additive droplets can therefore be obtained by going to liquid additives with lower boiling points. It was observed that there was an increase in liquid droplet effectiveness as materials with lower boiling points were used.

It should be noted that once the rate of vaporization from the droplet is greater than the electron arrival rate, the conversion of electrons to negative ions is limited essentially by the slower rate of electron arrival. Then any further enhancement of the vaporization rate by selecting liquid additives with even lower boiling points will be of no real help. Too rapid a vaporization for liquid additives can even be harmful in the sense that a larger fraction of the additive will vaporize as uncharged molecules rather than as negative ions. It is apparent from this that there is an optimum value of the latent heat of vaporization for given plasma conditions.

It should be noticed, therefore, that while the vaporization of liquid additives may be a limiting factor in a plasma with a high degree of ionization (because the electron collection rate is then greater than the molecular evaporation rate), this same additive in a plasma with a lower degree of ionization will have more than adequate vaporization to interact with the reduced electron current.

In evaluating the relative effectiveness of various liquid additives it is important to consider the vapor pressure, which is related to the boiling point and the latent heat of vaporization. If the degree of ionization of the plasma is large and the boiling point of the additive is high, then the electron arrival rate at the droplet is larger than the molecular evaporation rate. Thus, the limitation on the vaporization of negative ions is the droplet vaporization, and the additive effectiveness can be enhanced by going to additives with lower boiling points. Once a material with a sufficiently low boiling point has been selected, however, then the limitation is on the electron arrival rate and a further reduction of additive boiling point is of no additional value. The optimum latent heat of vaporization can be shown to depend on the degree of ionization of the plasma, the plasma temperature, and the plasma molecular weight.

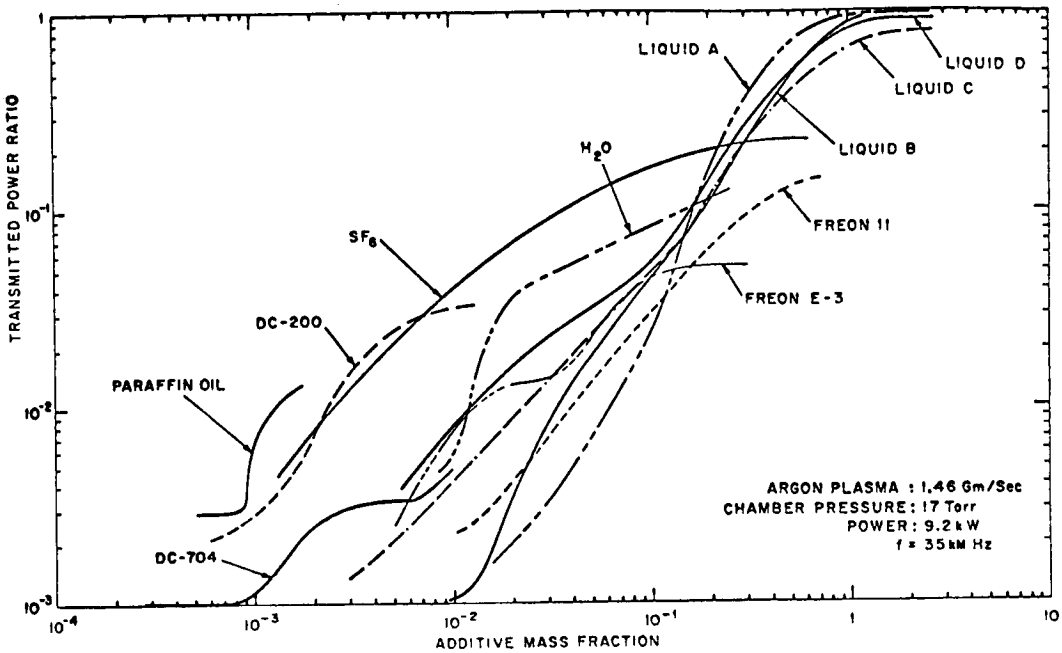

Figure 1.- Effect of aspirated liquids on microwave transmitted power ratio.

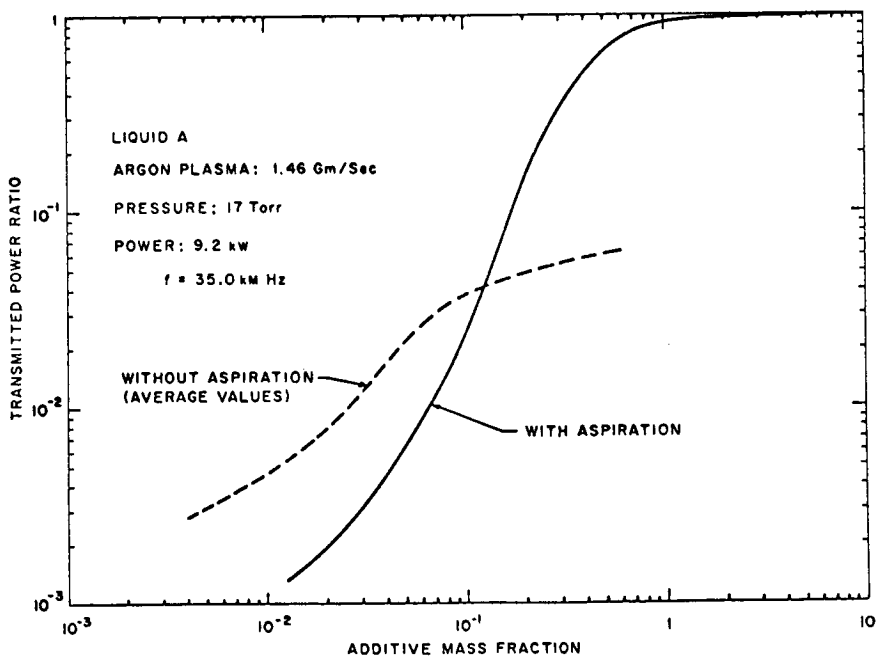

Figure 2.- Effect of liquid injection system on microwave transmitted power ratio.

"The aeronautical and space activities of the United States shall be conducted so as to contribute . . . to the expansion of human knowledge of phenomena in the atmosphere and space. The Administration shall provide for the widest practicable and appropriate dissemination of information concerning its activities and the results thereof."

— NATIONAL AERONAUTICS AND SPACE ACT OF 1958

NASA SCIENTIFIC AND TECHNICAL PUBLICATIONS

TECHNICAL REPORTS: Scientific and technical information considered important, complete, and a lasting contribution to existing knowledge.

TECHNICAL NOTES: Information less broad in scope but nevertheless of importance as a contribution to existing knowledge.

TECHNICAL MEMORANDUMS: Information receiving limited distribution because of preliminary data, security classification, or other reasons.

CONTRACTOR REPORTS: Scientific and technical information generated under a NASA contract or grant and considered an important contribution to existing knowledge.

TECHNICAL TRANSLATIONS: Information published in a foreign language considered to merit NASA distribution in English.

SPECIAL PUBLICATIONS: Information derived from or of value to NASA activities. Publications include conference proceedings, monographs, data compilations, handbooks, sourcebooks, and special bibliographies.

TECHNOLOGY UTILIZATION PUBLICATIONS: Information on technology used by NASA that may be of particular interest in commercial and other non-aerospace applications. Publications include Tech Briefs, Technology Utilization Reports and Technology Surveys.

Details on the availability of these publications may be obtained from:

SCIENTIFIC AND TECHNICAL INFORMATION OFFICE

NATIONAL AERONAUTICS AND SPACE ADMINISTRATION

Washington, D.C. 20546